SERDP

FINAL REPORT

Strategies and Methods for Effective UXO Classification

Leonard Pasion
Black Tusk Geophysics

Lin-Ping Song
University of British Columbia

May 2021

SERDP Project MR-2318

DISTRIBUTION STATEMENT A
This document has been cleared for public release.

This report was prepared under contract to the Department of Defense Strategic Environmental Research and Development Program (SERDP). The publication of this report does not indicate endorsement by the Department of Defense, nor should the contents be construed as reflecting the official policy or position of the Department of Defense. Reference herein to any specific commercial product, process, or service by trade name, trademark, manufacturer, or otherwise, does not necessarily constitute or imply its endorsement, recommendation, or favoring by the Department of Defense.

REPORT DOCUMENTATION PAGE

Form Approved
OMB No. 0704-0188

The public reporting burden for this collection of information is estimated to average 1 hour per response, including the time for reviewing instructions, searching existing data sources, gathering and maintaining the data needed, and completing and reviewing the collection of information. Send comments regarding this burden estimate or any other aspect of this collection of information, including suggestions for reducing the burden, to Department of Defense, Washington Headquarters Services, Directorate for Information Operations and Reports (0704-0188), 1215 Jefferson Davis Highway, Suite 1204, Arlington, VA 22202-4302. Respondents should be aware that notwithstanding any other provision of law, no person shall be subject to any penalty for failing to comply with a collection of information if it does not display a currently valid OMB control number.
PLEASE DO NOT RETURN YOUR FORM TO THE ABOVE ADDRESS.

1. REPORT DATE *(DD-MM-YYYY)*	**2. REPORT TYPE**	**3. DATES COVERED** *(From - To)*
5/30/2021	SERDP Final Report	9/30/2013 - 9/30/2018

4. TITLE AND SUBTITLE

Strategies and Methods for Effective UXO Classification

5a. CONTRACT NUMBER
13-C-0078

5b. GRANT NUMBER

5c. PROGRAM ELEMENT NUMBER

6. AUTHOR(S)
Leonard Pasion: Black Tusk Geophysics

Lin-Ping Song: University of British Columbia

5d. PROJECT NUMBER
MR-2318

5e. TASK NUMBER

5f. WORK UNIT NUMBER

7. PERFORMING ORGANIZATION NAME(S) AND ADDRESS(ES)
Black Tusk Geophysics
401 / 1755 West Broadway
Vancouver, British Columbia V6J 4S5

8. PERFORMING ORGANIZATION REPORT NUMBER
MR-2318

9. SPONSORING/MONITORING AGENCY NAME(S) AND ADDRESS(ES)
Office of the Deputy Assistant Secretary of Defense (Energy Resilience & Optimization)
3500 Defense Pentagon, RM 5C646
Washington, DC 20301-3500

10. SPONSOR/MONITOR'S ACRONYM(S)
SERDP

11. SPONSOR/MONITOR'S REPORT NUMBER(S)
MR-2318

12. DISTRIBUTION/AVAILABILITY STATEMENT
DISTRIBUTION STATEMENT A. Approved for public release: distribution unlimited.

13. SUPPLEMENTARY NOTES

14. ABSTRACT
Advanced geophysical classification (AGC) uses information derived from geophysical sensor data to make dig/no‐dig decisions at sites contaminated with unexploded ordnance (UXO). AGC techniques have been developed through Strategic Environmental Research and Development Program (SERDP) funded projects and other research efforts for several decades. Data processing workflows that incorporate AGC have been implemented in publicly available software packages such as Geosoft's UXAnalyze and UXOLab. These workflows and have been successfully used on multiple Environmental Security Technology Certification Program (ESTCP) Live‐Site demonstrations and Military Munitions Response Program (MMRP) projects featuring AGC. These successes have confirmed that AGC can reliably identify targets of interest (TOI) and reduce the number of digs at remediation sites. Indeed, many MMRP projects now prefer ‐ or even require ‐ the use of AGC when remediating sites contaminated with UXO.

15. SUBJECT TERMS
modeling and signal processing, UXO, cluttered environment, target identification, EMI, Electromagnetic Induction, terrestrial environment

16. SECURITY CLASSIFICATION OF:			**17. LIMITATION OF ABSTRACT**	**18. NUMBER OF PAGES**	**19a. NAME OF RESPONSIBLE PERSON**
a. REPORT	**b. ABSTRACT**	**c. THIS PAGE**			Leonard Pasion
UNCLASS	UNCLASS	UNCLASS	UNCLASS	287	**19b. TELEPHONE NUMBER** *(Include area code)* 604-428-3380

Executive Summary

Advanced geophysical classification (AGC) uses information derived from geophysical sensor data to make dig/no-dig decisions at sites contaminated with unexploded ordnance (UXO). AGC techniques have been developed through Strategic Environmental Research and Development Program (SERDP) funded projects and other research efforts for several decades. Data processing workflows that incorporate AGC have been implemented in publicly available software packages such as Geosoft's UX-Analyze and UXOLab. These workflows and have been successfully used on multiple Environmental Security Technology Certification Program (ESTCP) Live-Site demonstrations and Military Munitions Response Program (MMRP) projects featuring AGC. These successes have confirmed that AGC can reliably identify targets of interest (TOI) and reduce the number of digs at remediation sites. Indeed, many MMRP projects now prefer - or even require - the use of AGC when remediating sites contaminated with UXO.

AGC consists of two steps: (1) Extracting information from sensor data, and then (2) using that information as input into classification algorithms to estimate the probability that a buried target is a TOI. The objective of SERDP MR-2318 was to improve the quality of classification decisions by improving the accuracy of information derived from sensor data. Our plan was to identify potential shortcomings in data processing workflows and develop practical solutions to address them.

In UXO detection and classification applications, target information is derived from the parameters of a forward model that is estimated from sensor data. The point dipole source model is the most common method for representing the electromagnetic induction (EMI) response of a compact metallic target. The parameters of the dipole model are the dipole source location and the polarizability tensor. The eigenvectors of the polarizability tensor are related to the orientation of the target. The eigenvalues are the principal polarizabilities, which are intrinsic properties of the target. The amplitude and decay characteristics of the dipole polarizabilities are a function of the size, shape, wall-thickness, and electromagnetic material properties (i.e., magnetic permeability and electrical conductivity).

The dipole model parameters are estimated from EMI data through the process of data inversion. EMI data acquisition surveys generate a larger number of data than unknown dipole parameters, resulting in an overdetermined inverse problem. Therefore, we generally seek a single set of dipole parameters - i.e., location, orientation and principal polarizabilities - that best represent the sensor data. In practice, we invert for 1, 2, and 3 source models. In each case, an optimal set of parameters minimizes a data misfit function that compares the recorded sensor data with data predicted by the point dipole forward model.

Advanced EMI sensors are purpose built for AGC. That is, they are designed to produce data from which dipole parameters can be more reliably estimated. Advanced EMI sensors have multiple transmitters that illuminate a buried target with a primary magnetic field at multiple angles, thereby improving the ability to resolve the 3 principal polarizabilities. Advanced sensors are multi-static, featuring multiple 3-component, "vector" receivers simultaneously sampling the secondary field over multiple time channels. Multiple receivers improve the accuracy with which target location can be estimated.

The combination of improved electronics increasing the Signal-to-Noise ratio (SNR) of the data and the improved integration of inertial measurement unit (IMU) and global positioning system (GPS) data streams with EMI sensor data, has led to the feasibility of reliable classification with "one-pass" systems, i.e., EMI sensors that acquire dynamic, full-coverage EMI dataset suitable for AGC. Of course, "one-pass" classification might not be suitable at some sites depending on site conditions and classification problem. For these cases, a "two-pass" approach is used. A first pass dynamic data set is acquired and processed to identify locations of potential targets. A second survey involves collecting cued measurements over each of the potential targets. Since the data are acquired in a static mode, data can be stacked and averaged to improve SNR and positioning error is eliminated.

The advent of new advanced EMI instruments has led to significant improvements in the accuracy with which dipole parameters estimated and, consequently, have improved the reliability of classification. However, there still exists scenarios for which AGC data are unable to constrain the parameters of the dipole model, resulting in unreliable estimates of the target location and polarizabilities. Examples include:

- *Dipole forward modelling inaccuracy.* Reliable data inversion requires the forward model to accurately describe the physics of the problem. For example, inaccurate positioning and orientation information will result in inaccurate inversion results. Non-dipole signals such as artifacts from inaccurate removal of background soil signals can bias dipole parameters.
- *Highly cluttered Sites.* At highly cluttered sites, there can be multiple targets within the view of the instrument. Multiple dipole sources are required to model the physics of the EMI measurement. Multi-source inversions have local minimum leading to incorrect solutions. Model complexity must also be considered. If too few sources are used, then resulting polarizabilities are potentially inaccurate. If too many sources are used, then spurious models result. These spurious models can have polarizabilities that appear similar to TOI. Therefore, criteria for identifying these models improve the efficiency of classification.
- *Data quality*. Due to the limited number receivers and transmitters of EMI systems and SNR considerations, there are only a finite number of targets that an instrument can resolve accurately. It is important to understand the limitations of the data. Poor data quality due to a low SNR or survey design (for example, insufficient coverage during dynamic data surveys or poor positioning of cued sensors over a target, resulting in inadequate illumination of principal polarizability directions) limit the quality and reliability inversions.

The objective of SERDP MR-2318 was to address these and other challenging scenarios by understanding the impact on processing performance and developing practical solutions. The sections in this report match the "Tasks" listed in the research proposal. Below we summarize the work.

Dynamic data processing: Target picking and Informed Source Selection

Section 1 begins with a method for correcting instrument lag corrections and IMU biases. Lag corrections were implemented by comparing the statistics of the data stream and GPS time series to match their reference start time. Methods to correct several lines together based on the assumption

that the digital acquisition unit clock drift is a linear function of time during acquisition periods only were also created. These corrections were validated on large datasets by ensuring that anomalies that appear on opposite lines are not distorted. These methods were implemented in our software package to improve inversion results. We developed a method for biases in the IMU and lag by solving an inverse problem where a depth constrained dipole model is estimated along with the survey correction values. Using TEMTADS 2x2 IVS data, we found that a lag correction can be reliably estimated. IMU offsets were less reliably estimated.

A detrend filter – usually a de-median filter – is commonly used to remove background signals from dynamic data. Filtering errors can result from algorithms being unable to properly handle data acquired over high target density regions of a site, data at the beginning or end of a collected line, and data collected over short lines. At the target picking stage, filtering artifacts can lead to additional anomalies being chosen (e.g., when the background response is underestimated), or targets being missed due to negative biases when the background response is over estimated. Filtering artifacts also lead to inaccurate data inversion results, as filtering artifacts are coherent signals that are poorly handled by least squares inversions. Methods developed here have improved the performance of filtering for short lines and the end of lines. These improved filters have been implemented in the UXOLab software and are applied regularly on our AGC projects.

We performed a study to determine the accuracy of the Geonics EM61 sensor for target picking. Geonics EM61 data are not usually inverted for source locations, since the combination of EM61 transmitter and receiver geometry, positional accuracy, and SNR limit the reliability of dipole source estimates. In general, data amplitude peak picking algorithms are used to identify potential targets. We assessed the likelihood of missing TOI when using image-based target picking approaches using synthetically generated EM61 data and TEMTADS 2x2 data. The larger transmitter and receiver loops of the EM61 led to more “smeared” out images, which becomes particularly problematic when multiple targets are present. We highlighted situations where EM61 based cued locations lists would not have the accuracy required by cued systems such as the TEMTADS/MetalMapper 2x2 or the MPV. These results guided the target picking strategy at Hawthorne Army Depot, NV and led to the target pick tiling methods being implemented into our software and adopted for the project.

We investigated alternatives to the standard data amplitude-based approaches for picking targets with dynamic AGC data. Our objective was to utilize more of the information that is available in AGC sensors. We tested an equivalent source-based approach, in which a group of dipole sources was defined that could be used to accurately reconstruct the data set. By using equivalent sources to reconstruct the data, we can choose optimal Tx/Rx combinations for creating the data image, and we can filter out small spatial scale features in the data not related to metallic targets. Both steps can improve the SNR of the map used for detection. Also, data variations due to sensor height and orientation variability can be removed by re-modeling the data on a level plane.

The distribution of sources used to represent the data can be used to assist in target picking. We used MetalMapper 2x2 data collected at the former Savanna Army Depot in Illinois to evaluate the limitations of the technique. A Quality Control (QC) seed target (small Industry Standard Object (ISO): 4 inch length of steel pipe, at a depth of 35cm) was not detected using standard techniques due to low SNR.

However, dipole clustering methods were able to detect the target. By not using polarizabilities to "screen" unlikely targets, dipole clustering may result in more target picks. Although less efficient, dipole clustering may be more robust than conventional methods. Further testing involved synthetically seeding targets into the Savanna data set. We then determined parameters that optimized each target picking method, and then identify scenarios for which some methods have superior performance.

We observed that dipole clustering is a promising approach, in part due to a decreased reliance on polarizability accuracy. However, our current implementation of dipole clustering is computationally intensive, and refinements and parallelization are necessary for practical application. In the current UXOLab processing steps, we do not use the equivalent sources to filter the data. However, examining source clustering results is a step in the analyst review process during Informed Source Selection (ISS) processing of dynamic data.

At locations where a data anomaly exceeds the detection threshold, the dynamic data are inverted for dipole sources. These inversion results can be used in two ways. If the data quality and classification problem allow for making reliable classification decision from the dynamic data, then the results can be used for "one-pass" classification. If higher quality data (e.g., longer time windows for measurement, higher SNR from stacking data and being acquired in a static mode) is required for more reliable classification, the inversion results from dynamic data are used to provide more efficient location coordinates for fielding a follow-up cued survey. The process of using properties of the dipole inversion - in particular, polarizabilities characteristics and data fit - to eliminate sources that are unlikely to be related to a target of interest is called "Informed Source Selection (ISS)". We developed and studied the effectiveness of various ISS techniques, and report on a number of metrics we use for screening sources. A workflow was developed that involves using Monte Carlo simulations and synthetic seeding to identify reliable screening parameters, and establish the range of these parameters for particular targets of interest. This approach is objective, and eliminates ad hoc decisions by the processor. Our informed source selection workflow was applied to MetalMapper data acquired at the Former Lowry Bombing and Gunnery Range, CO. The approach greatly reduced the number of required cued measurements and intrusive digs.

Multi-source inversions for data collected at cluttered sites

In Section 2, we report on a number of methods that were tested and developed to address the difficulties of multi-target scenarios.

1) A new inversion approach called the Temporal Orthogonal Projection Inversion (TOPI) for inverting time-domain electromagnetic data to recover location and magnetic dipole polarizabilities was developed. In this technique, the spatial temporal response matrix (STRM) is defined. The rows of the STRM correspond to measurements at difference time channels from a single transmitter receiver pair (i.e., a time-domain decay curve measured by a particular receiver). The time-domain curves are projected onto a small subspace by keeping only those vectors associated with larger singular values. A nonlinear inversion is carried out in a transformed domain, to determine source locations. Briefly, the TOPI uses the concept of a subspace to select channels. There is no involvement of either the empirical selection of channels or a formidable task of estimating unknown noise - a substantial portion of the

noise in the data is automatically winnowed from the analysis. In addition, the subspace projection has the potential for separating signal from additive Gaussian noise and thus higher quality and more robust solutions are obtained in the inverse problem. Most importantly, the TOPI is insensitive to determining the dimension of the signal subspace (SS) and is able to recover accurate source locations using a small number of temporal projections. This further reduces the size of the inverse problem and speeds up the convergence. The TOPI method is available in the UXOLab software and was tested using TEMTADS 5x5 data.

2) To improve source location estimates at cluttered sites we developed the space-time MUSIC (MUltiple Signal Classification) imaging approach. The approach is established upon a receiver array-based spatial and temporal response matrix. The multi-static response matrix-based (MSRM) MUSIC approach that requires a sufficient number of receivers and transmitters. In contrast, the new imaging scheme relaxes the condition on a large number of transmitters and is thus generalized to a wide range of sensing systems. We also investigated noise subspace estimates and its effect on algorithm performance.

The MUSIC development led to a greater understanding of the Eigen-structure of the multi-static response matrix. Introduction of the 3-way array decomposition provided the theoretical basis for the generalization of MUSIC to sensors with only a few transmitters. The method has been verified on the primary advanced sensor systems in use for UXO classification. We found that an accurate estimate of the noise subspace is not required for practical implementation of the method. An inexact, underestimate of the noise subspace is simple to obtain and makes the MUSIC viable for practical application. Image sharpness was shown to be useful for indicating number of targets present when processing using Man-Portable Vector (MPV) data and Time-domain Electromagnetic Multi-sensor Towed Array Detection System (TEMTADS) data. Our initial implementations of MUSIC were on a uniform grid of testing points. we have extended the method to work in a grid free environment.

3) We developed a “Mixed-Norm” (MN) inversion approach that formulates the inversion problem as a multi-objective function minimization subject to fitting the sensor data to within a noise-dependent amount. The standard inversion approach in AGC is to carry out a 1 source, 2 source and 3 source inversion on the data, and then use library matching to determine if any of the recovered polarizability models correspond to a target of interest. This results in cases in which there are fewer targets than sources, with the additional source(s) fitting data noise (i.e., non-target signals in the data). These spurious sources can sometimes be difficult to objectively eliminate from consideration. Using the Mixed-Norm approach encourages “less complex” models, such that redundant dipole sources that are not constrained by the data are suppressed. The MN inversion approaches were demonstrated to work well using TEMTADS and MPV sensor system data. The MN inversion reduced the occurrence of spurious sources in cases where an overdetermined inverse problem was solved. However, implementation requires defining an optimal final or “target” misfit value. Additional work is required to define the optimal misfit value before the method can be introduced into standard workflows.

4) In order to address the difficulty of local minima in the multi-source inversion problem, a Genetic Algorithm (GA) approach was used to obtain improved starting models. This work was completed in partnership with Dr. Peter Lelievre at Memorial University of Newfoundland and Labrador. The

algorithm developed by Dr. Lelievre was incorporated into our UXOLab processing software, and tested by Black Tusk Geophysics scientists using synthetic data.

5) Once a cued measurement is acquired, the standard approach is to refine the acquisition location by inverting the data for a single dipole source. The next sounding is collected by placing the cued instrument at the location of the single dipole source. By centering the sensor, we attempt to maximize the SNR and improve the angles at which the primary field illuminates the target in question. We studied the ability to better constrain dipole parameters for multi-target scenarios by simultaneously inverting multiple electromagnetic induction soundings in the vicinity of the targets. The additional data would, in principle, be better able to constrain the higher degrees of freedom of the multi-source inversion. The simultaneous inversion was tested using synthetic data.

Both the GA implementation and multi-sounding simultaneous inversion greatly improved multi-source inversion performance for 2, 3, and 4 sources. For the 5-source inversion, the GA approach did not improve performance. However, the additional data of the multi-sounding inversion resulted in a nearly three-fold improvement in the percentage of realizations that were successfully inverted (from 22.6% to 64.6%). These methods are more robust than the standard approach. Further study is required to determine the effect of sensor position error on the simultaneous inversion.

We developed a Sequential Experiment Design (SED) method to better determine the location of reacquired data during cued surveys. As we mentioned earlier, the standard approach for refining acquisition locations in the field, is to invert for a single source. This approach is not ideal at sites with high densities of metallic contamination, and multiple targets being sensed by the instrument. A series of tests were used to establish robustness of the SED to model parameter estimates (in particular, sensitivity to source location estimates). Convergence issues were addressed with the development of deterministic initialization strategies for multi-source inversion, and a distance or range constraint to control how far a sensor can move given a priori information on sensor offset sensitivity. SED was tested in the lab and at a field site we established at the University of British Columbia. We found that SED positioning can improve polarizability estimates, often with fewer soundings than the number of targets. Simultaneously inverting multiple soundings resulted in higher signal-to-noise data, and polarizabilities with better matches to the classification library.

To deal with positioning errors associated with multi-sounding inversions, we developed a method of inverting data that we call the Independent Model Location Inversion (IMLI). The IMLI solves for single set of polarizabilities for a target, but, to account for the relative error between multiple soundings, we allow for the location of the target to be slightly different for each sounding. This method was also tested using dynamic data acquired with the MPV on an IVS strip, where adjacent lines could have a relative error in position due to, for example, a bias in a measured heading. The method showed some promise, in particular for marine surveys where relative along track positioning can be accurate, though the relative positioning between adjacent transects can be inaccurate. Further development and testing are required prior to implementation.

Processing data at sites with magnetic soils

Section 3 includes methods for processing data at sites with high levels of magnetic soil response. In our previous work (SERDP MR-1573), we investigated techniques of modelling the background response and target parameters simultaneously. These techniques required accurate measurements of the geometry of the sensor relative to the ground surface. In general, EMI systems do not record this type of information. In addition, several of the techniques involved computationally intensive methods for calculating soil responses or for inverting the data for a smooth distribution of magnetic susceptibility. In this project, we focused on more practical approaches for mitigating the effects of magnetic soil. In particular, we wanted to develop methods that do not require accurate measurements of ground clearance or extensive computing power to model the soil response.

The EMI response of soils exhibiting Viscous Remnant Magnetization (VRM) have a characteristic 1/t decay. Target detection using decay comparisons were initially used on mono-static data (i.e., single transmitter and single receiver geometries like the Geonics EM61 or Geonics EM63), and were thus limited to comparing individual decays measured at a number of points over a potential target with VRM response. With the development of multi-static data, there are multiple combinations of receivers and transmitters that can be used to compare a soil model to a compact metallic object response. With this data we no longer only determine the fit to the characteristic VRM decay. The multi-static data allows us determine if the relative amplitudes of the multiple Tx/Rx combinations are consistent with magnetic soil responses. In this project, we tested using a soil model that exploits relative Tx/Rx amplitudes as well as the characteristic VRM decays to improve processing performance. The soil model can be used to identify soundings that are likely to be due to soil, and can be used as part of the inversion process.

When collecting cued EMI data, the standard practice is to acquire “background data” in the near vicinity of anomalies being investigated. These background data are then subtracted from anomaly data. This approach can be ineffective at sites where the geology includes highly magnetic soils or sites with variable amplitude background signals, as inaccurate background removal can bias the recovered models. We provided examples how scaling the background measurement should be considered at sites with magnetic soil noise to improve polarizability fits. Also, we demonstrated how multi-source inversions can help the accuracy of polarizabilities by having sources represent background soil signal that was not sufficiently removed from the data through background correction. Alternative methods of suppressing the soil effects that do not require subtracting a background measurement were investigated by using combinations or components of the data that are less sensitive to the magnetic geology. The approach defines an operator P such that the geology response is in the null-space of the operator. The P matrix transforms the observed and modeled data such that it minimizes an objective function that measures the fit to linear combinations of the data. The P matrix projects the vector secondary field onto directions orthogonal to the soil response. In the absence of a compact metallic target, these orthogonal components should have zero response.

This technique was tested using MPV3D IVS data collected as part of an ESTCP demonstration at Waikoloa, HI. We showed that for a small piece of pipe (i.e., small ISOs), the P matrix approach provided more accurate recovery of the target polarizabilities then the standard background measurement and subtraction procedure. Larger targets were less affected by the inaccuracy of the background

measurement, and no improvement was realized with the P-matrix technique. In addition to cued data, the P matrix was used to transform dynamic, full coverage MPV data from Waikoloa, HI. The transformed data was able to produce detection maps with lower magnetic soil noise. Synthetic seeding into an MPV data set collected on the magnetic soil of Waikoloa, Hawaii was used to compare the conventional approach of amplitude picking from de-median filtered data, to picking from data projected into directions orthogonal to the soil response. Conventional picking resulted in numerous missed targets due to the magnetic soil background response. In contrast, the projection matrix approach found all targets, while reducing the number of required digs by over 50%. This technique was also tested using data from Geometrics MetalMapper 2x2 surveys acquired in Hawaii. In addition to the projection matrix-based methods, we showed that using a soil misfit incorporating both the relative Tx/Rx amplitudes and time decay signal is also effective when target picking with the Geometrics MetalMapper 2x2.

During recent projects, we have used soil misfit maps for identifying metal-free locations as candidates for background measurements in cued surveys. Also, we have implemented soil match comparisons in UXOLab determining cued soundings that are not likely acquired over a metallic target. Although we have implemented the ability to calculated the projected data in both UXOLab and BTField, we believe that significant improvement in its use would be achieved if AGC sensors included instrumentation to determine ground clearance and orientation of the system with the ground.

Quality Control and review of inversion results

Our standard processing approach is to use conservative target picking parameters. For one-pass surveys, inverting multiple pick locations – and therefore multiple, data chips sampling different sections of the data – over a potential target improves the probability that a representative source for target will be obtained. For two-pass surveys, we also use relatively conversative ISS parameters to screen anomalies, and rely on the higher quality data of a cued sensor to make decisions. Data over potential targets are inverted using 1 source, 2 source and 3 source dipole models. This approach produces spurious models resulting from the overly complex model. In previous work, we have tested methods of determine the number of targets present based on balancing data fit with model complexity (i.e., number of sources). However, these methods that use information theoretic criteria (e.g., Akaiki information criterion (AIC), and Minimum Description Length (MDL)) were found to not be robust due the large dynamic range of the EMI data (i.e., data ranges over numerous orders of magnitude) and the nature of noise (e.g., non-gaussian signals) observed in EMI data. Therefore, the standard approach is to utilize N-dipole inversions, and then select polarizability models that correspond to a target of interest. However, spurious models can often sometimes have relatively good fits to library polarizabilities. For example, multi-source target inversions can often produce deep sources with large amplitude polarizabilities that may appear similar to TOI. The efficiency of classification depends on the ability to eliminate spurious models resulting from sources that are not being constrained by the data.

We have studied different approaches to reducing the number of spurious sources (e.g., the Mixed-Norm approach) or for identifying spurious models related to soil anomalies (e.g., modelling the background with large deep source). In Sections 4 and 5, we look data based and model-based metrics to help eliminate spurious models, and also methods of using metrics to identify potential TOI when that

target's polarizability is not in the site ordnance library. We refer to these different metrics as "Figures of Merit". Many of the metrics developed in this project are now part implemented in our UXOLab processing flow. The "simple, no ground truth classifier" (SNGTC) score combine a number of metrics, and is used both for non-library based identification of potential targets, as well as Informed Source Selection (ISS).

Once polarizability estimates are obtained and as many spurious sources as possible are eliminated, a library-based classification technique is used to classify UXO. When there are novel ordnance types present, and thus the site's ordnance polarizability library is incomplete, there is the potential for false negatives. We developed a pair of classification approaches that does not require a priori information of target types, and compared these techniques' performance in finding novel targets when using a complete library. The pair of non-library based classification approaches that were developed, use a combination of various data, polarizability and fit metrics to produce a score for each dipole source. Our non-library based classification approach was found to be very effective when applied to data acquired at Pole Mountain, Wyoming and Former Spencer Artillery Range, Tennessee. The methods were found to be as or even more efficient at identifying all UXO when compared to using a complete library, and will be an excellent QC check for library-based techniques.

Technology Transfer: UXOLab, BTField and Black Tusk API to UX-Analyze

A Black Tusk Application Program Interface (API) has been developed that enables software packages to access inversion routines and metrics initially developed within the UXOLab MATLAB environment. A reference manual for the API is included at the end of this report as an Appendix.

In addition to technology transfer via the API, the following papers have been published through this work:

Temporal Orthogonal Projection Inversion for EMI Sensing of UXO, IEEE Transactions on Geoscience and Remote Sensing (Volume: 53, Issue: 2, Feb. 2015)

Space-time MUSIC imaging of EMI sensing data and a subspace partition study, Journal of Electromagnetic Waves and Applications. (Volume 31, 2017 - Issue 15)

Sensor Placement via Optimal Experiment Design in EMI Sensing of Metallic Objects, Mathematical Problems in Engineering, (Volume 2016, Article ID 5856083)

Contents

Executive Summary i
Table of Figures xiii
List of Tables xxiii
List of Acronyms xxv
1. Methods for processing dynamically collected advanced EMI Data 1
Pre-inversion Data Processing 1
Estimation of IMU bias and instrument lag corrections for dynamic EMI sensors. 1
Improvements to along-line filtering 3
Temporal Orthogonal Projection Inversion for EMI Sensing of UXO 14
1. Introduction 14
2. Signal Model 15
3. Method 18
4. Experiments 21
5. Conclusion 33
Using an equivalent source methodology for target picking (1): Data reconstruction and denoising 35
Limitations of Image based picking algorithms 39
Simulations for determining the limitations of target picking from images 41
Using simulations to estimate risk of missing a TOI when using image based EM61 target picking 45
Testing Limitations of Informed Source Selection approach in cluttered setting 51
Using an equivalent source methodology for target picking (2): Source clustering 57
Comparison of profile picking, dipole clustering and dipole filter target picking 63
Methodology 63
Target picking 66
Results 71
Summary 72
Using Monte Carlo simulations for determining Source Screening Parameters 81
Lowry MetalMapper data: Establishing screening parameters 81
Redstone Arsenal, AL: Screening using total polarizability 86
2. Multi-Source Inversions for data collected at cluttered sites 89
Investigation into multi-source algorithm modifications and enhancements 89

Nonlinear inversion for multiple objects using mixed norm 89
Accelerating the multi-object inversion: An augmented matrix approach 92
Deterministic Initialization for multi-source inversion by a fast Gram-Schmidt orthogonalization ... 95
Space-Time MUSIC Imaging of EMI Sensing Data and a Subspace Partition Study 98
1. Introduction 98
2. MUSIC Imaging Method 99
3. Rank estimate and subspace partition 103
4. Experiments 106
5. Discussion 116
6. Conclusion 116
Multi-source inversion using Multi-shot data and Genetic Algorithm starting models 118
Approach 118
Measure of success and model selection process 118
Results 1: Standard N-dipole method 122
Results 2: Multi-shot inversion 125
Results 3: Using a Genetic Algorithm to find starting source locations 126
Sensor Placement via Optimal Experiment Design in EMI Sensing of Metallic Objects 127
1. Introduction 127
2. Method 128
3. Results 132
4. Conclusions 143
Inversion approach: independent model locations and common polarizations for data subsets 144
3. Advanced Processing techniques for data acquired at sites with magnetic soils 159
Simplified Modeling of the background response: Processing of MetalMapper Data at the Former Waikoloa Maneuver Area 160
Determining if a target is a soil anomaly 160
Inversion of MetalMapper data at Waikoloa 164
Target picking methods that compare to a soil model: 169
Processing dynamic MPV data from Waikoloa: 169
Inverting Projected Data: Processing cued MPV data from Waikoloa 201
Processing TEMTADS data at Redstone Arsenal, AL 208
4. Using Figure of Merit for improving data QC and assessing inversion reliability 222

5. Identification of unique targets of interest 227
6. Black Tusk API to UX-Analyze 231
References 232
Appendix: Inversion and Discrimination C++ API Reference Manual 238

Table of Figures

Figure 1. Results from cell 1, medium ISO, vertical orientation. Left: left axis is degrees showing pitch and roll values, right axis is the lag correction time. Right: left axis gives the polarizability values, right axis gives the orientation. 2
Figure 2. Results from cell 2, 4.2" projectile, vertical orientation. Left: left axis is degrees showing pitch and roll values, right axis is the lag correction time. Right: left axis gives the polarizability values, right axis gives the orientation. 2
Figure 3. Results from cell 3, large ISO w/ bentonite vertical orientation. Top plot: left axis is degrees showing pitch and roll values, right axis is the lag correction time. Bottom plot: left axis gives the polarizability values, right axis gives the orientation. 2
Figure 4. Results from cell 4, large ISO vertical orientation. Left: left axis is degrees showing pitch and roll values, right axis is the lag correction time. Right: left axis gives the polarizability values, right axis gives the orientation. 3
Figure 5. Example of de-median filtering along profile. The median value for the entire profile is near 0. 4
Figure 6. Detection channel before and after filtering for the Z-component of the centre cube (MN=9). . 4
Figure 7. Example of a short line finishing with a large anomaly. 5
Figure 8. Longer line with elevated signal and erroneous correction. 5
Figure 9. Long line where large anomaly near an end causes failure in background correction. 6
Figure 10. Filtering of a noisy line with weak amplitude anomalies. Vertical component, coaxial data are plotted. 7
Figure 11. Example of filtering a short line 8
Figure 12. A second example of filtering along a very short (i.e., less than 1m length) line. 8
Figure 13. Examples of filtering data that has larger scale target anomalies. 9
Figure 14. Detection map for MPV vertical-component data, standard de-median filter. There appear to be many instances of negative data due to overshooting of the filter correction near large anomalies. . 10
Figure 15. Detection map for corrected de-median filter. 11
Figure 16. Filtering of TEMTADS 2x2 data. Each panel shows profile data for different combinations of transmitter and receiver locations and components (RxC is the vector component, 1=X, 2=Y and 3=Z). Raw data show a DC offset. The standard filtering approach (thin red line) overshoots the correction near anomalies. The new filter (thick purple line) corrects the data such that background values are closer to zero around anomalies. (Dashed lines show estimated background for each filter). 12
Figure 17. TEMTADS detection map with standard filter (ESTCP data from Redstone Army Depot). 13
Figure 18. TEMTADS detection map using new filter. 13
Figure 19. (a) TEMTADS: a single-component multi-static system consisting of a horizontally arranged coplanar array of 5 × 5 transmitters and receivers. Each transmitter is 35 cm × 35 cm and each receiver 25 cm × 25 cm. (b) Two sets of polarizations used for the numerical experiments. The solid and dashed curves represent polarizations of a 105 mm projectile and a scrap, respectively. 22
Figure 20. Single-object case. Singular values: (a) noise free; (b) 3% noise; (c) 5% noise; and (d) 10% noise. The first seven and the last two TEVs: (e) noise free; (f) 10% additive noise. 24
Figure 21. Single-object case. For all 625 Tx/Rx pairs. (a) Noise-free decay signals. (b) Noise (10%). (c) Corrupted signals = (a)+(b). (d) Estimated signal. (e) Estimated noise. 24

Figure 22. Single-object case. 10% Noise. (a) Original data at 25 receivers with Tx-13 excitation. (b) Projected data at 25 receivers with Tx-13 excitation. (c), (d) Original and projected data of Tx-13/Rx-4 pair. (e), (f) Original and projected data of Tx-13/Rx-13 pair. 26
Figure 23. Two-object case. Singular values: (a) noise free; (b) 3% noise; (c) 5% noise; and (d) 10% noise. The first seven and the last two TEVs: (e) noise free and (f) 10% noise. 28
Figure 24. Test-pit data. (a) Singular values. (b) The first seven and the last two TEVs 29
Figure 25. Test-pit data. (a) Original data at 25 receivers with Tx-13 excitation. (b) Projected data at 25 receivers with Tx-13 excitation. (c), (d) Original and projected data of Tx-13/Rx-1 pair. (e), (f) Original and projected data of Tx-13/Rx-13 pair. 31
Figure 26. Recovered polarizabilities from test-pit data. TOPI: (a) 1 TEV, (b) 7 TEVs. Inversion of original data with time channels of: (c) 115, (d) 51, (e) 16, and (f) 13. On the polarization plots, the red curves represent the known polarizabilities of 105-mm projectile and the blue and black the recovered ones. 33
Figure 27. Example of dynamically acquired MetalMapper data from Camp Ellis. Data from time channel t=0.136ms is gridded 35
Figure 28. Comparing “Split Cube 7” and “Split Cube 5” gridded data. 36
Figure 29. Data modelled with equivalent sources 37
Figure 30. Constructing a data map that is easier to interpret and use for target picking. Time = 0.136ms. 38
Figure 31. Effect of line spacing on EM61 data 39
Figure 32. In this example, there are 3 vertical targets: a small ISO at (x,y)=(-0.40, -0.25)m and depth of 0.15m, a medium ISO at (x,y)=(0.00,0.25)m and depth of 0.30m, and a small ISO at (x,y)=(0.60,-0.50)m and depth of 0.05m. 40
Figure 33. In this example, there are 3 targets: a vertical small ISO at (x,y)=(-0.40, -0.25)m and depth of 0.15m, a vertical small scrap at (x,y)=(0.00,0.25)m and depth of 0.05m, and a horizontal 2.75” rocket at (x,y)=(0.60,-0.50)m and depth of 0.20m. 41
Figure 34. Effect of target density on target picking offset. White squares show where there are targets, grey triangles indicate target picks, and red squares indicate targets whose closes pick is greater than 0.6 m away. Data were simulated assuming a 1 m line spacing. 42
Figure 35. Example of missed targets in Realization 22. For this modeling, we assumed 1m line spacing and a density of 162 targets/acre. On the right, we include a pair of examples of inaccurate or missed picks. 43
Figure 36. Effect of line spacing on target picking accuracy 44
Figure 37. Comparison of different survey types for a range of target densities. In (a), we consider all target types (i.e., 20mm, small ISO and medium ISO). In (b), we only consider small and medium ISOs. For low target density, there is uncertainty in the percentage estimates due to fewer samples. 44
Figure 38. Modelling results for lower density area, 22 targets/acre, 2.5% TOI. 0.5m line spacing. Only one 2.75" rocket would not have target pick within 60 cm. However, since the target is isolated, there is a good possibility that the in-field inversion and reacquisition would be able to identify the target. 46
Figure 39. Higher density region (135 targets/acre, 5% TOI), 0.5 m line spacing. Simulations result in 17 of the 2.75” rockets would have picks>0.6m away. Anomalies with a red outline indicate multi-source scenarios where the infield inversion might not result in an additional cued measurement over the anomaly. There is a 2 in 30000 chance to miss TOI. 48

Figure 40. Summary of pick offset results for EM61 target picking simulations 49
Figure 41. Data collected in the vicinity of a missed QC seed (black triangle). The QC seed is a small ISO that is oriented vertically and buried at a depth of 35 cm. 51
Figure 42. Example of synthetic dataset. Vertical small ISO at a depth of 35 cm. The location of the missed seed is indicated by 'A'. 'B' and 'C' are also locations of vertical small ISO at 35 cm. The 'B' and 'C' are isolated seeds (i.e., no known nearby metallic targets). 53
Figure 43. Data and recovered polarizabilities. At locations A and C, we synthetically emplace a vertical small ISO at 30 cm, and at location B there is a synthetically emplaced vertical small ISO at 35 cm. 54
Figure 44. Data and recovered polarizabilities. Horizontal ISO at a depth of 30 cm for locations A and C. At location B, it is difficult to accurately recover depth, although the target isolated (i.e., no large anomalies in the near vicinity) 55
Figure 45. Ability to resolve a horizontal small ISO at Savanna. Data centered above the target is inverted with 1, 2, and 3 source models. Reliable estimates of the polarizabilities are not expected for depths of 25 cm and greater. 56
Figure 46. Location of recovered sources related to the missing seed. The blue dashed lines indicate the data inverted around grid location 267. The three sources are within 15 cm of each other, so they are designated as a target pick. The location of the pick is defined as the median of the three sources. 57
Figure 47. Three data tiles produced a source near the location of the missing seed. The 3 tiles – centered on 266,267, and 283 recovered a vertical target near the seed. The black dashed lines indicate the lateral limits for the sources. 58
Figure 48. Source clustering approach applied to missed seed data from Savanna 60
Figure 49. Source clustering approach applied to synthetic seeded data. Recall that when inverting the 30cm data directly over the seed, we were unable to put a source in the right spot. However, by combining inversions from adjacent targets, we have a cluster of sources. 61
Figure 50. Using data amplitude as a criteria for choosing sources. Triangles represent peaks in the reconstructed coaxial, z-component image. Red triangles are located where peaks are greater than 5 times the noise. 'x' symbols represent locations of sources, with black 'x's indicating sources located where the signal is greater than 5 times the noise. 62
Figure 51. Example of synthetic data used for testing. Black triangles mark location of synthetically emplaced seeds. 63
Figure 52. Options for "standard" profile picking method. 64
Figure 53. Example of a spurious inversion result. For this example, we consider a TEMTADS 2x2 sounding acquired at Castner Range. Intrusive results revealed that it was a 37 mm Fuse. The data were inverted with 1, 2, and 3 source inversions; resulting in 6 models to consider. Model 4 is highlighted in yellow above. The source is not constrained by the data, with the depth and location estimate sitting on the inversion constraints. The recovered polarizabilities (bottom left) have a very "noisy" looking result. These features are characteristic of a spurious source, and likely due to the problem being underdetermined, i.e., more model sources than actual targets. 67
Figure 54. Seed A, horizontal. Comparison of target picking methods performance for depths varying from 0.1 to 0.3m. The true location of seed A is marked with a cross at (0, 0). The distance, in meters, between the target picker solution and the true location of the seed is listed in brackets next to each one of the methods. 73

Figure 55. Seed A, vertical. Comparison of target picking methods performance for depths varying from 0.1 to 0.3m. The true location of seed A is marked with a cross at (0, 0). The distance, in meters, between the target picker solution and the true location of the seed is listed in brackets next to each one of the methods. 74
Figure 56. Seed B, horizontal. Comparison of target picking methods performance for depths varying from 0.1 to 0.3m. The true location of seed B is marked with a cross at (0, 0). The distance, in meters, between the target picker solution and the true location of the seed is listed in brackets next to each one of the methods. 75
Figure 57. Seed B, vertical. Comparison of target picking methods performance for depths varying from 0.1 to 0.3m. The true location of seed B is marked with a cross at (0, 0). The distance, in meters, between the target picker solution and the true location of the seed is listed in brackets next to each one of the methods. 76
Figure 58. Seed C, horizontal. The depth in each case is 35 cm. The true location of seed C is marked with a cross at (0, 0). The distance, in meters, between the target picker solution and the true location of the seed is listed in brackets next to each one of the methods. 77
Figure 59. Seed C, vertical. The depth in each case is 35 cm. The true location of seed C is marked with a cross at (0, 0). The distance, in meters, between the target picker solution and the true location of the seed is listed in brackets next to each one of the methods. 78
Figure 60. Comparison of methods based on count of missed seeds out of 100 planted horizontal seeds. A distance exceeding 0.25m from seed to closest target pick defined a missed seed. The total count of missed seeds is listed in brackets next to the method name. 79
Figure 61. Comparison of methods based on count of missed seeds out of 100 planted vertical seeds. A distance exceeding 0.25m from seed to closest target pick defined a missed seed. The total count of missed seeds is listed in brackets next to the method name 80
Figure 62. Size/Decay feature space for dynamic MetalMapper data collected on Column 13 at FLBGR. The grey stars represent targets from the ESTCP ordnance library. 81
Figure 63. Seeds emplaced in the FLBGR noise strip 82
Figure 64. Synthetic seeding of Column 13 data. Targets were emplaced in a uniform grid within the Column 13 dataset. No anomaly avoidance was used. Locations of synthetic 37 mm M59 anomalies are indicated by white triangles. 83
Figure 65. Size/Decay feature space of the synthetically seeded Column 13 data. 84
Figure 66. Decision line for the 20mm targets. 84
Figure 67. Anomalies that are screened and retained when applying screening line. 85
Figure 68. Example of artificially seeding a MK18 smoke grenade in a grid. For Grid L09, the seeded targets are buried at a depth of 0.36 m and are randomly oriented. The anomalies are subsequently inverted to determine the range of expected polarizabilities. 86
Figure 69. Recovered total polarizabilities of artificially seeded anomalies. The recovered total polarizabilities are plotted in various colours, with the minimum total polarizability indicated by a black dashed line. The solid black lines show the 6 samples of total polarizabilities of the MK18 smoke grenade from the ESTCP Library. 87
Figure 70. Screening Results for Grid L09 when assuming different clearance depths for the MK18 Grenade. 88

Figure 71. Recovered polarizabilities from the three-object inversion of synthetic noisy data. (a)-(c) Standard nonlinear least square solution; (d)-(f) Mixed norm solution; (g)-(i) Mixed norm-TOPI. 91
Figure 72. Recovered polarizabilities from the two-object inversion of field anomaly 1210 at SWPG site. Plots (a)-(b) show recovered polarizabilities when inverting using lsqlin. Plots (c)-(d) show the estimated polarizabilities when using a pseudo-inverse with α=1. Plots(e)-(f) show estimated polarizabilities when using a pseudo-inverse with α=200‖A‖_1 94
Figure 73. Gram Schmidt example 97
Figure 74. (a) MetalMapper: a multi-static system consisting of three orthogonal transmitters and seven triaxial receiver cubes. Each transmitter is 1 m ×1 m and each receiver 10 cm × 10 cm. (b) Two sets of polarizations used for the numerical experiments. The blue and black curves represent the polarizations of 37-mm and 75-mm projectiles, respectively. 106
Figure 75. Data eigenvalues. Synthetic single-object case: (a) $\theta = 90^0$; (b) $\theta = 45^0$; (c) $\theta = 0^0$. (d) Synthetic two-object case where $\theta_1 = \theta_2 = 90^0$. θ is the polar angle describing the orientation of a rod object relative to the vertical axis. 107
Figure 76. Synthetic single-object case. MUSIC 3D spatial imaging with two noise-subspace projection matrices: (a)-(b) P_N[4:21]; (c)-(d) P_N[7:21]. (b) and (d) represent the 2nd detection in each case. 108
Figure 77. Synthetic two-object case. MUSIC 3D spatial imaging: (a) PN[4:21]; (b) PN[7:21]; (c) PN[10:21]. Row 1 and 2 represent the 1st and 2nd detection for each case. 109
Figure 78. Data Eigenvalues. (a) Field data at Camp Beale. (b) Test-stand data at Lowry 110
Figure 79. Field data at Camp Beale. MUSIC 3D spatial imaging: (a) P_N[4:21]; (b) P_N[7:21]; (c) P_N[10:21]. Row 1 and 2 represent the 1st and 2nd detection. 111
Figure 80. Field data at Camp Beale. Recovered polarizabilities using MUSIC peak locations in Figure 6. (a)-(b) PN[4:21]. (c)-(d) PN[7:21]. (e)-(f) PN[10:21]. On the polarization plots, the solid red curves represent the known polarizabilities of ISO and the blue and black ones are the recovered polarizabilities. 112
Figure 81. Test-stand data at Lowry. MUSIC 3D spatial imaging: (a) PN[4:21]; (b) PN[8:21]; (c) PN[14:21]. Row 1 and 2 represent the 1st and 2nd detection. 113
Figure 82. Test-stand data at Lowrey. Recovered polarizabilities using the MUSIC peak locations in Figure 81 (a)-(b) PN[4:21]. (c)-(d) PN[8:21]. (e)-(f) PN[14:21]. On the polarization plots, the solid and dash red curves represent the known polarizabilities of 60mm and 37mm projectiles and the blue and black ones are the recovered polarizabilities. 115
Figure 83. Four-target scenario, cell 162, target 647 is a large ISO. The three other targets are medium ISOs. From left top to right bottom – models 1,2,3,4. Model #2 matches a large ISO and is the selected best model for target 647. L123 polarizability misfits for the four models are: 3.964, 0.002, 2.114, 1.737. Note that the 5 latest time channels are excluded from the misfit computations. 119
Figure 84. Four-target scenario inverted with 500 starting points, cell 19, target 73 is a medium ISO. The three other targets are: two medium ISO and one small ISO. From left top to right bottom – models 1,2,3,4. Model #3 matched a medium ISO and is the selected best model for target 73. L123 polarizability misfits for the four models respectively are: 0.6732, 2.653, 0.100, 0.612. Note that the 5 latest time channels are excluded from the misfit computations. 120
Figure 85. Five-target scenario inverted with 500 starting points, cell 499, target 2494 is a medium ISO. The four other targets are: one small ISO, one large ISO and two medium ISOs. From left top to right

bottom – models 1, 2, 3, 4, 5. Model #3 matched a medium ISO and is the selected best model for target 2494. L123 polarizability misfits for the five models respectively are: 1.152, 2.209, 0.338, 2.992, 1.713. Note that the 5 latest time channels are excluded from the misfit computations. 121
Figure 86. Comparison of the rate of success of inversion with 500 random starting points and 1000 random starting points. 124
Figure 87. (left) TEMTADS2x2: a multi-static system consisting of 4 coplanar transmitters and 4 triaxial receiver cubes. Each transmitter is 40 cm× 40 cm and each receiver 8 cm × 8 cm. (right) Two sets of polarizations used for the numerical experiments. The blue and black solid curves represent polarizations decays of 37mm and 75mm projectiles. 133
Figure 88. Experiment 1: two objects near the sensor edge. (a) Two red circles represent the true locations of the objects. The black square delineates the footprint for the initial sensor location and the other color squares indicate the predicted positions. (b) The recovered polarizabilities from the initial sounding (s1) data. (c) The recovered polarizabilities from the sounding data [s1 s2]. (d) The recovered polarizabilities from the sounding data [s1 s2 s3]. In the polarization subplots, the solid curves represent the recovered polarizabilities and the dashed ones the true ones. 134
Figure 89. Experiment 2: Two objects close to sensor edges. Caption is the same as that in Figure 88. 135
Figure 90. Map of Information gain as a function of sensor locations: (a) Experiment 1; (b) Experiment 2. The two circles denote the locations of targets. 136
Figure 91. Experiment 3: single-object close to sensor edges. Caption is the same as that in Figure 88. 137
Figure 92. (a) MPV: a multi-static system consisting of a z-directed circular transmitter with the diameter of 50 cm and x- and y-directed rectangular transmitters with size of 54 cm × 54 cm. 5 triaxial receiver cubes (each 8 cm × 8 cm) are distributed on the circular transmitter plane. (b) A snapshot of the indoor experiment setup. (c) Photos of small, medium, and large ISOs used in the experiments. 138
Figure 93. Target locations and initial sensor footprint in the SED experiment setup with the MPV. In the initial sounding (S1), a black circle denotes the sensor footprint and gray squares the true locations of the objects. 139
Figure 94. SED experiment with the MPV, two-object example. Initial sounding (S1): (a) the sensor footprint (black circle) and inverted object inverted object locations (small circles); (b)-(c) recovered polarizabilities in blue and red and the reference ones in gray dashed. Soundings S1 + S2: (d) the sensor footprint and inverted object locations; (e)-(f) recovered polarizabilities. Soundings S1 + S2 + S3: (g) the sensor footprint and inverted object locations; (h)-(i) recovered polarizabilities..... 141
Figure 95. SED experiment with the MPV, three-object example. Initial sounding (S1): (a) the sensor footprint (black circle) and inverted two-object locations (small circles); (b)-(c) recovered polarizabilities with a two-object model; (d)–(f) recovered polarizabilities with a three-object model. Soundings S1 + S2: (g) the sensor footprint and inverted two-object locations; (h)-(i) recovered polarizabilities with a two-object model; (j)–(l) recovered polarizabilities with a three-object model. Recovered polarizabilities are in blue, red, and black and the reference ones in gray dashed. 142
Figure 96. Left: Showing recovered depths for a range of standard deviation of noise added to shot locations. The true depth of 30cm is predicted well when there is no noise added to the shot locations while the recovered depth is pushed deeper for increased noise levels. Right: Showing the size of the recovered polarizabilities for a range of standard deviation of noise

added to shot locations. When no noise is added, i.e., 0 cm, the true size is estimated very well. As noise levels increase the size becomes overestimated. 144
Figure 97. Location of the sensor for each shot. The red circles indicate locations used for forward modeling, while the blue asterisks indicate noisy locations used for inversions. This example has a noise level of σ = 3cm. 145
Figure 98. Location of the receivers for each shot. The circles indicate locations used for forward modeling, while the asterisks indicate noisy locations used for inversions. Separate shots are indicated by a different color. This example has a noise level of σ = 3cm 146
Figure 99. Left: Target XY location results for both the IMLI and standard inversion procedures. For this 4-shot example the 4 independent locations are shown along with their mean value. Right: Target depth results for both the IMLI and standard inversion procedures. 147
Figure 100. Results of polarization estimations from the shot independent location and standard inversion procedures. 147
Figure 101. Left: Target location results for both the shot independent location and standard inversion procedures. For this 4-shot example, the 4 independent locations are shown along with their mean value. Right: Target depth results for both the shot independent location and standard inversion procedures. 148
Figure 102. Recovered polarizabilities for the two-target example. 148
Figure 103. Test stand setup for IMLI example. Left: MPV placed over the targets. An MPV measurement is acquired with the targets at each of the nine locations indicated in the image. Right: The targets are attached to a plastic crate to ensure consistent relative positioning. The relative positions are listed in Table 18. 149
Figure 104. Single shot inversion result 150
Figure 105. Inverting a pair of shots. 151
Figure 106. Experiment 1. Recovered polarizabilities (a) Standard inversion. (b) IMLI 152
Figure 107. Experiment 2. Recovered polarizabilities (a) Standard inversion. (b) IMLI 152
Figure 108. Experiment 3. Recovered polarizabilities (a) Standard inversion. (b) IMLI 153
Figure 109. Dynamic data collected with the MPV over an IVS strip consisting of a 3-in Stokes mortar, 75mm projectiles, medium ISO and Small ISO. An orientation of “along track” indicates the item is parallel to the travel path, and “across track” is perpendicular to the travel path. 154
Figure 110. IVS item: 3-in Stokes. Left column shows the result of the standard inversion. Right column shows the result of the IMLI. 155
Figure 111. IVS item: 75mm. Left column shows the result of the standard inversion. Right column shows the result of the IMLI 156
Figure 112. IVS Item 3: Medium ISO. Left column shows the result of the standard inversion. Right column shows the result of the IMLI. This target had the greatest improvement in polarizability estimate accuracy of all the targets. 157
Figure 113. IVS Item 4: Small ISO. The behaviour of the secondary polarizabilities suggests that a small fast decaying target also present. 158

Figure 114. Example of background measurements corrected with air. Blue lines are for positive responses, and red lines represent negative responses. Receiver Rx0 was not working properly during these measurements. 162
Figure 115. TO17 Target 785. Soil anomaly. 163
Figure 116. TO17 Target 785. Soil data can be fit well with a large, deep, plate-like target centered on the MetalMapper instrument. 165
Figure 117. TO17 Target 859. Soil data can be fit well with a large deep, plate-like target centered on the MetalMapper instrument. There is a second local minimum in the solution where the soil is fit well with two sources: one source at 40 cm and a second source at approximately 95 cm. 166
Figure 118. Recovered polarizabilities when inverting IVS measurements. The IVS data were inverted using in-air measurements for background correction, and the data were fit using (a) single source inversions, (b) two source inversions in which the location of both sources were unconstrained, and (c) two source inversions in which the location of one of the sources was constrained to be deep and centered on the MetalMapper instrument. 167
Figure 119. Size/Decay parameter plot for IVS data. 168
Figure 120. MPV data collection at Waikoloa. 169
Figure 121. Example of surveying an outcrop at Waikoloa. In the upper left, photo of acquiring data over an outcrop. Upper right: location of a survey line directly over an outcrop, though not the outcrop in the photo. Below: plots of the data and the elevation. 170
Figure 122. Profile of coaxial, vertical component data acquired on the Waikoloa IVS. Time channel 1 is plotted. The small ISO buried at a depth of 30 cm does not produce a significant anomaly. The emplaced targets are shown in (b). No photo of the sphere is available. 171
Figure 123. Examining the correlation between the response and ground clearance height. Variations in the instrument height lead to data anomalies of approximately the same size as a small ISO at a depth of 30 cm. 172
Figure 124. Comparing different components of the MPV IVS data. For a horizontal transmitter loop with receivers inside the loop, the soil noise is greatest in the vertical component and also the radial component of receivers not in the center of the transmitter loop. Non-soil components include horizontal components at the center of the loop, and azimuth components in the outer loops. 173
Figure 125. Soil response for the MPV. Data acquired over a target-free transect at Waikoloa. 174
Figure 126. Direction of secondary field and orthogonal directions used to define the $P^{nonsoil}$ matrix. 175
Figure 127. A comprison of using different projection matrices. The data multiplied by $P^{nonsoil}$ produces the most distinct anomaly for the 30 cm deep small ISO. 177
Figure 128. Comparing decays from pairs of outer receivers. 178
Figure 129. Calculating a symmetry measure for the MPV IVS data. The symmetry measure does a poor job in resolving the deeper small ISO. 179
Figure 130. Calculating a soil misift for each transmitter firing. The soil misfit for each transmitter firing is mapped to the center receiver for plotting. 180
Figure 131. Comparison of different target detection measures. The section of the 10 cm deep small ISO (left dot) and 30 cm deep small ISO (right dot) are shown. 181
Figure 132. Raw vertical component, coaxial receiver, t=1.1ms. 182
Figure 133. TOI in my mag soils study area. 182

Figure 134. Filtered vertical, coaxial data collected in time channel 10 (t=1.14 ms) over TO20A. A 150 point de-median filter was applied along profile data. Top: time channel 4, t = 0.38 ms, bottom: time channel 10, t=1.14ms 183
Figure 135. Horizontal component. TO20A. top: time channel 4, t=0.38 ms. Bottom: Time channel 10, t=1.14ms 185
Figure 136 Non-soil amplitude calculated using $P^{nonsoil}$ 186
Figure 137. Gradient amplitude calculated using P^{diff} 186
Figure 138. Combined non-soil and gradient matrix 187
Figure 139. Soil Misfit 187
Figure 140. Target TOI 542. Similar to the IVS data, the gradient measure was unable to detect the target. 189
Figure 141. Target TOI 477 190
Figure 142. Target TOI 492 191
Figure 143. Target TOI 535 192
Figure 144. A group of metallic debris. 193
Figure 145. Comparison of different detection metrics. There is an improvement in the ability to detect the targets, as well as the location accuracy. 195
Figure 146. Filtered coaxial vertical component. Black squares indicate locations of small ISOs seeded at a depth of 10 inches. 197
Figure 147. Small iso, synthetic seeds, 10 inch depth. Soil metrics. Soil misfit. All picked 198
Figure 148. Picking result for a small ISO at 6" 199
Figure 149. Small ISO: 6" depth. Random orientation. In both cases, all synthetically seeded targets found. However, TOI 542 is not found when setting the threshold this high. 200
Figure 150. Recovered polarizabilities for the medium ISO and the shallow small ISO from the Waikoloa IVS. 201
Figure 151. Applying a background correction. Multiplying the background data by 0.6 prior to subtracting from the IVS data, produces the best result. 202
Figure 152. An example of reducing background signal by taking differences between receivers. 203
Figure 153. Fitting result for Z-transmitter. Blue symbols represent observed data, and green symbols are predicted data. Plots with a red outline are components that contain soil response. Plots without a red outline represent MPV receiver components that are the azimuth components of outer cubes, or horizontal components of the center, cube. 204
Figure 154. Non-soil component data. For each receiver cube/transmitter combination, there are a pair of directions that are orthogonal to the direction of the secondary field. 205
Figure 155. Fitting gradient data components 206
Figure 156. Comparison of recovered polarizabilities when inverting with background correction and P-matrix. 206
Figure 157. Apply method to all IVS data over the small ISO and the medium ISO 207
Figure 158. Example of geologic response at Redstone: Grid R17 208
Figure 159. Comparison of in-air and background when Tx4 is fired 209
Figure 160. Comparison of background acquired over Bentonite, and background measurement acquired over the designated background location. 210

Figure 161. Comparison of recovered polarizabilities from IVS data measurements, using different background measurements. 211
Figure 162. Orthogonal directions to the secondary field. Red arrows are the direction of the geology secondary field. Blue arrows are directions orthogonal to the geology response 212
Figure 163. Comparison of in air corrected data and the data projected along the non-soil directions. 212
Figure 164. A comparison of Vertical, Coaxial components (top) to projected non-soil data amplitude (bottom). 214
Figure 165. Raw and projected data for Line 39. More distinct anomalies can be found in the projected data for seeds at x=19 m and x=23.5m. 216
Figure 166. A comparison between raw, vertical coaxial data and projected data. 217
Figure 167. Comparison of projected data ampliutde and the average of the vertical, coaxial data. 218
Figure 168. Comparison of the projected data from the seeded data set, and the projected data calculated from the target responses only. 219
Figure 169. Raw and projected data for Line 47. A more distinct anomaly can be found in the projected data for a seed at x=17.5 m, which is located in a region of high magnetic susceptibility. 220
Figure 170. Raw and projected data for Line 66. 221
Figure 171. Plotting metrics in dig list order. Once a dig list is created, we plot the metrics as a function of dig number. If there are relatively anomalous values of a metric, the analyst is able to quickly identify the problem model and data. This GUI is directly linked to the interactive QC tool for efficient checking of any problematic targets. 222
Figure 172. The BDU metric applied to TEMTADS 2x2 data. On the left, is the metric selection GUI. On the right is the BDU metric applied to the TEMTADS 2x2 Castner Data. We highlight Target 1147, which appears to have an anomalously high BDU value. The polarizability for model 4 is noisy (see inset), but matches the amplitude of a 105 mm HEAT. 223
Figure 173. Dipole inversion results for target 1147. 225
Figure 174. The Figure of Failure (FoF) metric 226
Figure 175. Example of metrics. To combine the metrics into a single score, we count the number of metrics that fall within the TOI range. 227
Figure 176. MetalMapper cued data from Pole Mountain 228
Figure 177. Digs 973 to 1008 when using the full ESTCP library. There are many items with good fits to small ordnance (i.e., 20 mm, 25 mm, and 30 mm projectiles). 229
Figure 178. MetalMapper cued data from Spencer Range. 230

List of Tables

Table 1. TOPI with single vj and various subspaces in the real data example. In this table, V1j = [v1,...,vj], j=2,3,5,7,10. V2j=[v2,...,vj,j=3,4,5,7 32
Table 2. Missed targets in the low-density region. There were 16000 total anomalies per scenario. A missed target is defined as one without a target pick (i.e., peak in gridded image) within 60 cm of the target location. 50
Table 3. Missed targets in the high-density region. There were 30000 total anomalies per scenario. A missed target is defined as one without a target pick (i.e., peak in gridded image) within 60 cm of the target location. 50
Table 4. Missed targets for entire site. The site is defined as having 30000 total anomalies, with 20977 anomalies in the lower density region and 9023 anomalies in the higher density region. 50
Table 5: Parameter values for target picking and inversion 66
Table 6. Metrics used for initial screening of data amplitude-based picks. 69
Table 7. Informed Source Selection Parameters 70
Table 8 Additional parameters used for finding additional models in each cell. 71
Table 9. MUSIC with various subspaces in the real two-object example. A projection matrix for the noise subspace is defined as $\mathrm{PNi: j = k = ik = jukuk'}$ 114
Table 10. Inversion with 500 starting points. Summary of results for 2, 3, 4, and 5 targets per cluster scenarios. 123
Table 11. Inversion with 1000 starting points – summary of results for 2, 3, 4, and 5 targets per cluster scenarios. 123
Table 12. Percentage of each of the ordnance items out of all missed targets, for 2, 3, 4, and 5 target scenarios, as a result of inversion with 500 random starting points. The percent chance of missing a larger TOI is a few orders of magnitude lower than the percent chance of missing a smaller TOI. 124
Table 13. Count of missed targets by ordnance type, for 2, 3, 4 and 5 target scenarios, as a result of inversion with 500 random starting points. Regardless the number of targets per cluster, the number of missed small ISO is significantly larger than the number of missed medium or large ISO. 124
Table 14. Percentage of missed targets out of all seeded targets of that kind, for each of the ordnance items, for 2, 3, 4, and 5 target cases, as a result of inversion with 500 random starting points. The results are consistent with previous statistics, demonstrating that smaller ordnance items that have a smaller signal response are easier to miss than larger ordnance items. 125
Table 15. Inversion of two cued measurements simultaneously applied to cases where at least one target was missed for the 2, 3, 4 and 5 targets per cluster scenarios. Multi-shot inversion tests whether addition of data improves inversion results in situations where the standard inversion method is not able to resolve all targets within a cluster 125
Table 16. Inversion with Genetic Algorithm – summary of results; percent of found targets and the rate of success for each of the 2, 3, 4, and 5 target scenarios. Detection of all targets within a cell defines a success. 126
Table 17. Location and orientation of shot locations used for synthetic modelling 145
Table 18. Location of targets in IMLI example. Depths listed are measured to center of the target. 149
Table 19. Recovered depths for each item. 154

Table 20: Polarizability misfit for each target 154
Table 21. Ground truth information for targets in Figure 144 194

List of Acronyms

2-D	Two Dimensional
BDU	“Big, Deep, and Ugly”
DC	Direct Current
DOA	Directions of Arrival
EMI	Electromagnetic Induction
ESTCP	Environmental Security Technology Certification Program
GA	Genetic Algorithm
GPS	Global Positioning System
IMLI	Independent Model Location Inversion
IMU	Inertial Measurement Unit
ISO	Industry Standard Object
ISS	Informed Source Selection
IVS	Instrument Verification Strip
MMRP	Military Munitions Response Program
MOI	Multi-Object Inversion
MN	Mixed Norm
MPT	Magnetic Polarizability Tensor
MPV	Man Portable Vector Sensor
MRM	Multi-Static Response Matrix
MUSIC	Multiple Signal Classification
NS	Noise Subspace
ROI	Region of Interest
Rx	Receiver
RxSTRM	receiver array-based spatial temporal response matrix
SED	Sequential Experimental Design
SNGTC	Simple, no ground truth, classifier
SNR	Signal-to-Noise Ratio
SOI	Single-Object Inversion
STRM	Spatial–Temporal Response Matrix
SS	Signal Subspace
SVD	Singular Value Decomposition
TEMTADS	Time-domain Electromagnetic Multi-Sensor Towed Array Detection System
TEV	Temporal Eigenvector
TOI	Target of Interest
TOPI	Temporal Orthogonal Projection Inversion
Tx	Transmitter

1. Methods for processing dynamically collected advanced EMI Data

Pre-inversion Data Processing

Estimation of IMU bias and instrument lag corrections for dynamic EMI sensors.

Recorded inertial measurement unit (IMU) values can contain significant errors due to the misalignment of the IMU when attached to the electromagnetic induction (EMI) sensor. The EMI sensor and Global Positioning System (GPS)/IMU data streams can be misaligned in time by a constant value which can lead to a misalignment of the data spatially over the target. Therefore, the objective is to determine survey correction values for both the IMU measurements and EMI sensor acquisition times such that these errors are minimized.

To meet the objective, methodology was developed to recover these survey correction values. We use measurements acquired as part of the morning and evening instrument verification strip (IVS) data. The approach solves a non-linear least squares problem where a depth constrained dipole model is estimated along with the survey correction values. For various problem configurations the recovered model will look like the following,

$$\overrightarrow{m} = \left[t_{lag}, pitch_{bias}, roll_{bias}, x_1, y_1, L1_1, L2_1, L3_1, x_2, y_2, L1_2, L2_2, L3_2, \dots\right] \quad (1)$$

where t_{lag} is the time lag between the EMI data and GPS data streams, $pitch_{bias}$, is the offset in pitch, $roll_{bias}$ is the offset in the roll, x_i and y_i is the x and y location of the i^{th} seeded target in the IVS, and $L1_i$, $L2_i$, and $L3_i$ are the polarizabilities of the i^{th} seeded target in the IVS.

This approach allows for any number of IVS seeds and survey lines over the targets. Provided the assumptions of the problem are reasonably met, the first 3 correction values can be used to correct all of the data taken during a survey day.

To bound this problem, we make a number of assumptions:

- Rx's are at the same height for each pass over the target.
- Depth is known from Cued inversions and does not change between passes.
- The lag correction is a constant value between passes.
- The IMU bias is constant between passes.

TEMTADS 2x2 from the former Redstone Arsenal, AL were used to test the approach. Initial testing used dynamic IVS data. Each target in the IVS was treated separately. Figure 1 to Figure 4 plot results for each of the 4 IVS targets, i.e., a medium industry standard object (ISO), 4.2" projectile, and large ISOs. The results for each cell consistently estimate a lag correction value across all time channels. The roll correction is somewhat stable, while the pitch correction varies significantly from target to target and time to time.

Future work could include simultaneous inversion of all targets and times for a single set of correction values. It is recommended that new data are collected to ensure that assumptions are closely met.

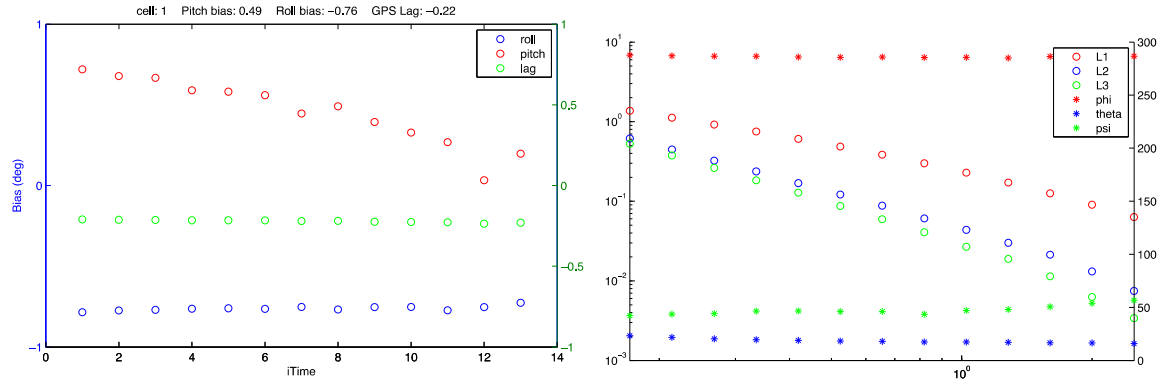

F ıtation. Left: left axis is degrees showing pitch and roll
v axis gives the polarizability values, right axis gives the
c

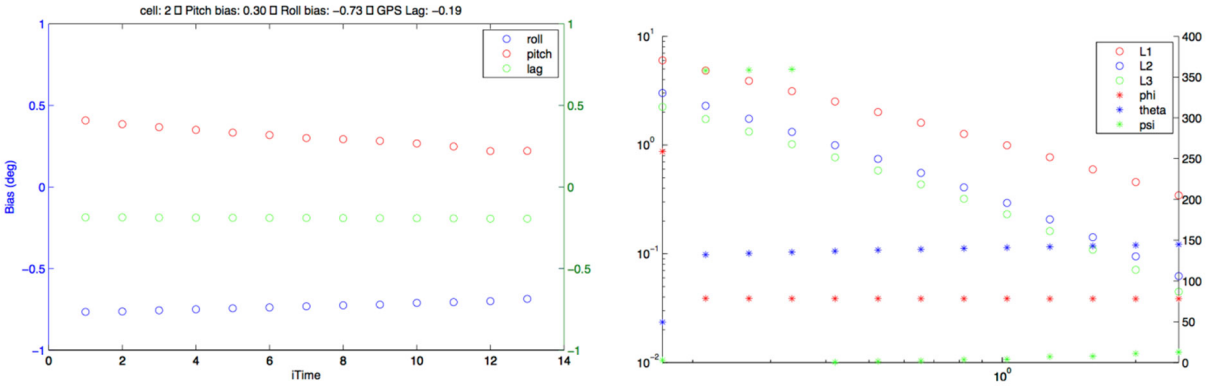

Figure 2. Results from cell 2, 4.2" projectile, vertical orientation. Left: left axis is degrees showing pitch and roll values, right axis is the lag correction time. Right: left axis gives the polarizability values, right axis gives the orientation.

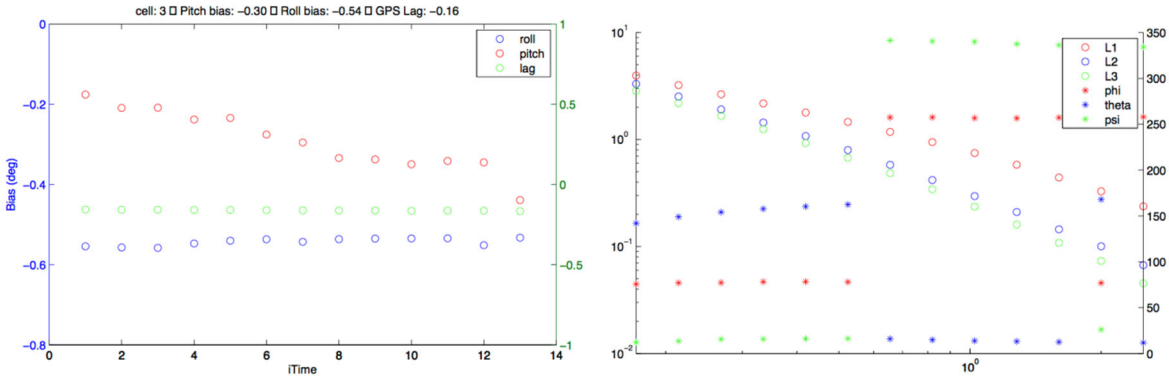

Figure 3. Results from cell 3, large ISO w/ bentonite vertical orientation. Top plot: left axis is degrees showing pitch and roll values, right axis is the lag correction time. Bottom plot: left axis gives the polarizability values, right axis gives the orientation.

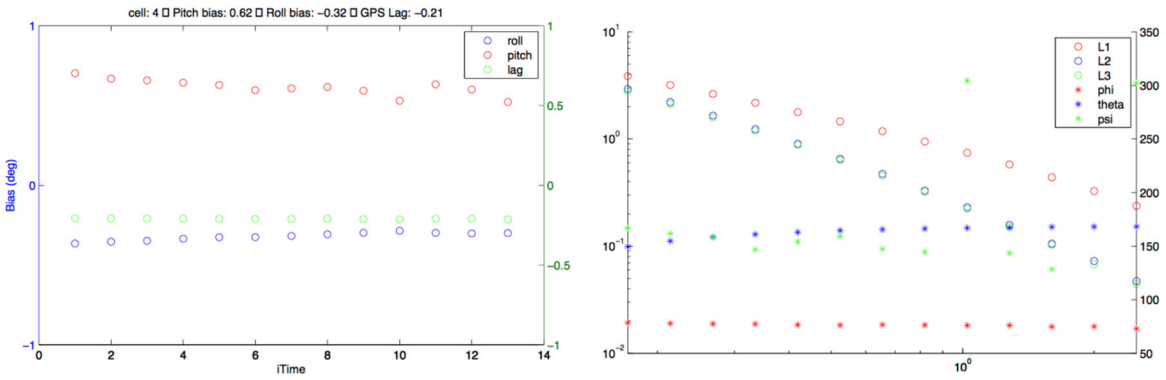

Figure 4. Results from cell 4, large ISO vertical orientation. Left: left axis is degrees showing pitch and roll values, right axis is the lag correction time. Right: left axis gives the polarizability values, right axis gives the orientation.

Improvements to along-line filtering

The motivation for investigating filtering approaches is to improve current methods for removing background effects from EMI profile data. Bringing all profile data to a common background level near zero value is critical for processing data, in particular for picking anomalies above that background, and for inverting dynamic data. Recent studies have provided cases where a target could be missed due to inadequate filtering. We have also observed that our default filtering method tend to overshoot corrections to the data near anomalies, due to biases introduced by averaging signal over a region that encompasses a transition between background, above soil, and significant signal, above a metallic object.

There are multiple sources of elevated background responses. First, a modern EMI sensor platform generally comprises of an array with multiple receivers that each have their own noise characteristics. For instance, some receivers may exhibit a DC (direct current) offset, where a constant value due to electronics configuration is added to the environmental responses. A second source of background effect can be the presence of magnetically active soil. This can generate a response that may spatially vary over the survey area. Other potential sources may be temporary external signals due to sensors emitting in a frequency window that interferes with our EMI sensor.

The current algorithm for removing background effects is based on a de-median filter along profiles. For each receiver and time channel, the median of a segment of profile data centred at a point is calculated as an estimate of the local background, and subtracted from the datum at that point. The segment of data can be defined as a number of points, or a distance. We generally prefer the distance, because background variations are mostly due to spatially varying geologic features, and because the distance is less sensitive to variation in the survey speed. The typical distance is 5-10 m.

The algorithm is formulated as an iterative process. First the moving median is calculated with a set window distance for each point of the profile and subtracted from the original data. This first correction removes trends in the data. It may be incorrect around anomalies, where there is a large variation in the data amplitude that can affect the background estimate. If so, the corrected data may have artificially high or low amplitude, similar to signal from valid anomalies that should not be used to estimate the background. To identify anomalies the corrected data are sorted by amplitude, and the extremes (below

or above a user-defined amplitude or percentile) are excluded for a second estimation of the background based on the original data. This new background estimate is interpolated at the points where extremes had been excluded, and the final background is smoothed out over a user-defined window length before being removed from the original data.

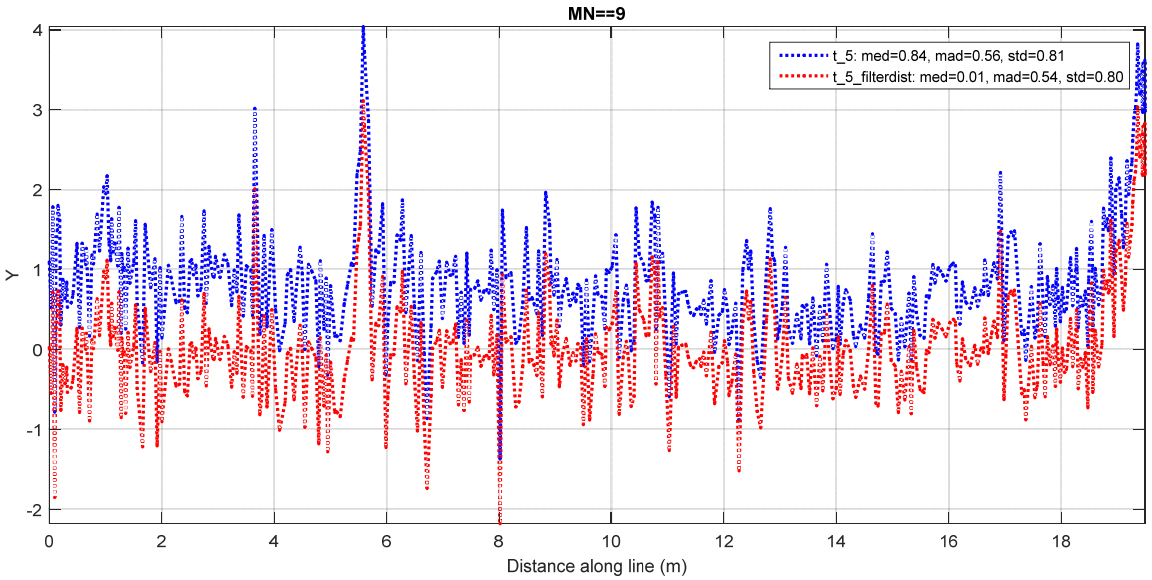

Figure 5. Example of de-median filtering along profile. The median value for the entire profile is near 0.

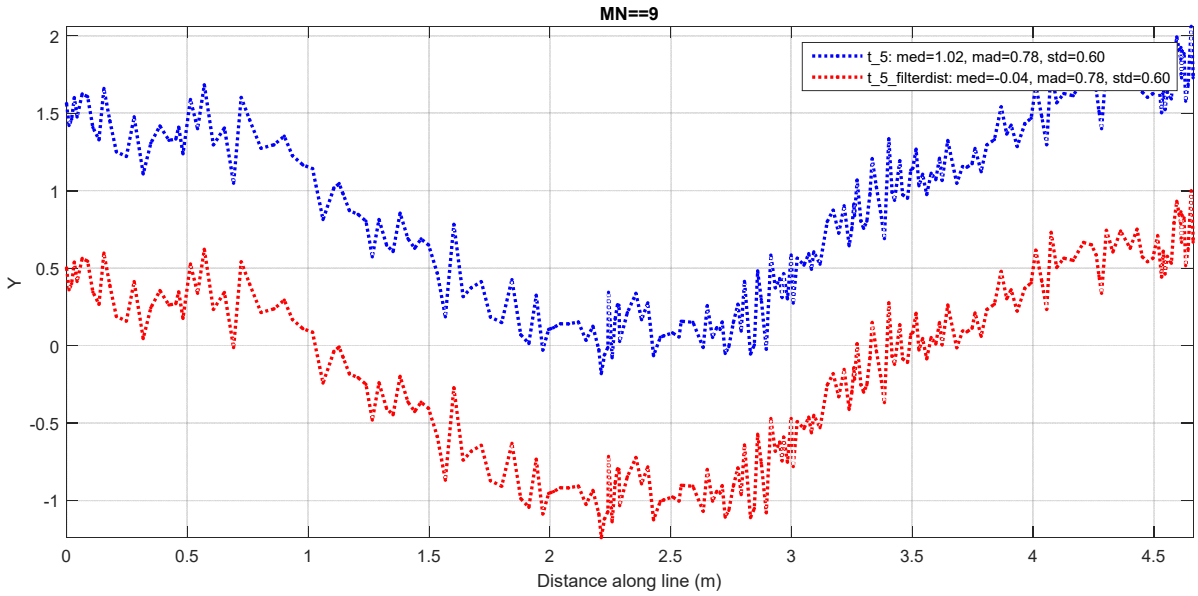

Figure 6. Detection channel before and after filtering for the Z-component of the centre cube (MN=9).

The current method leads to a missed detection due to inadequate filtering of a short line that was collected above a target. The raw and corrected data for the detection channel, the fifth time channel of the vertical component data, is shown for the centre cube in Figure 6. The background value is near 0, but the median estimate of the background has a biased value near 1 because the line is short and a

large fraction of the data is reflecting signal from a buried target (this line is a complicated case: it is a gap fill, where the operators collected 2.5 m along a line, then returned for 2 m with a slight lateral offset). This issue with the treatment of short lines can affect any short line where the median value is biased by the presence of a large anomaly, as illustrated in Figure 7.

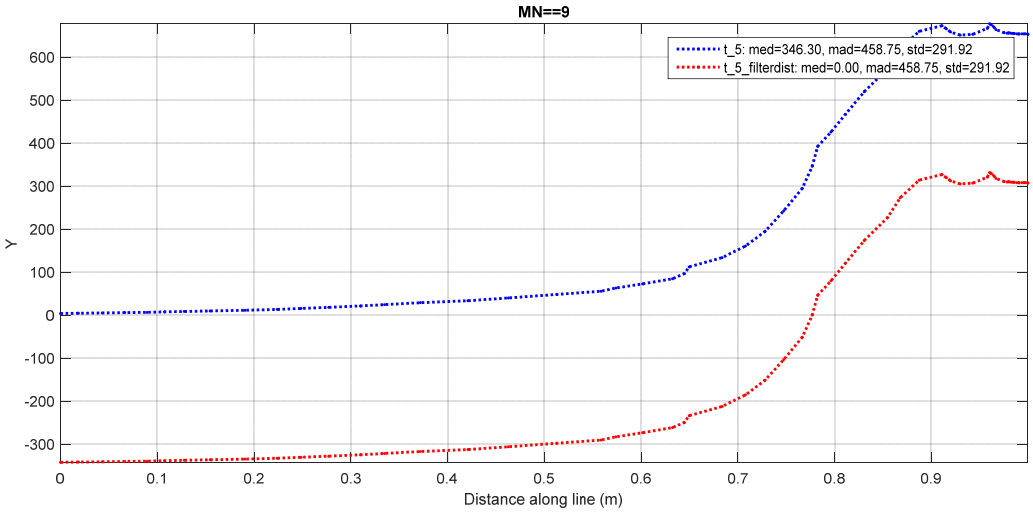

Figure 7. Example of a short line finishing with a large anomaly.

The issue of over- or under-estimating the background value through a median can affect any line with a high proportion of elevated signal. In the example of Figure 8, the line is 14 m long, when the filter window length is 5 m. The corrected data had a median value approaching 0, but it seems to be incorrect: negative values for Z-component data on either side of the anomaly located at x=11 m suggest overshooting of the correction. We suspect that correction of the entire line is incorrect because, in general, the amplitude of the Z-component data is positive for an MPV. The data presented in Figure 9 shows the example of a line where the correction seems right for most of the line, except for the left side, where a large anomaly causes large overshooting of the correction.

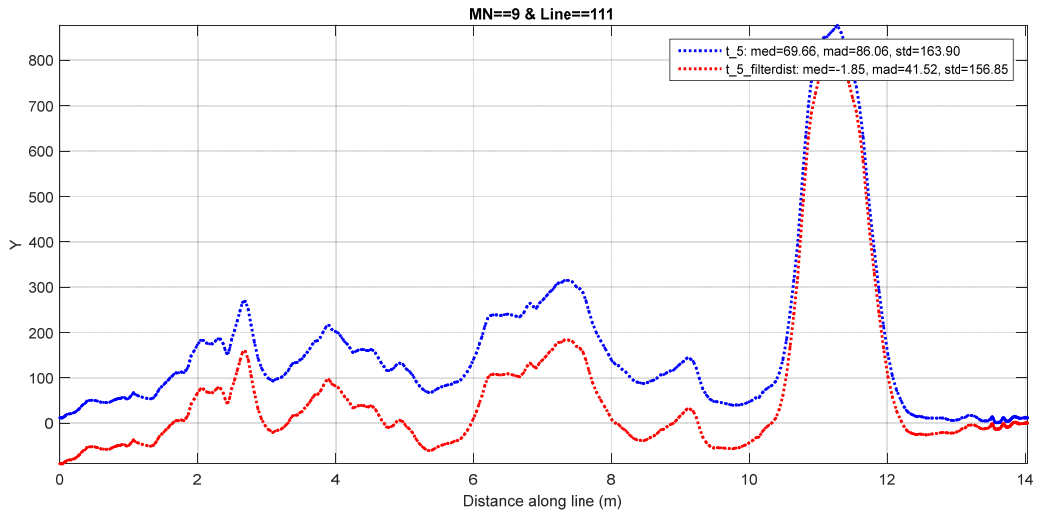

Figure 8. Longer line with elevated signal and erroneous correction.

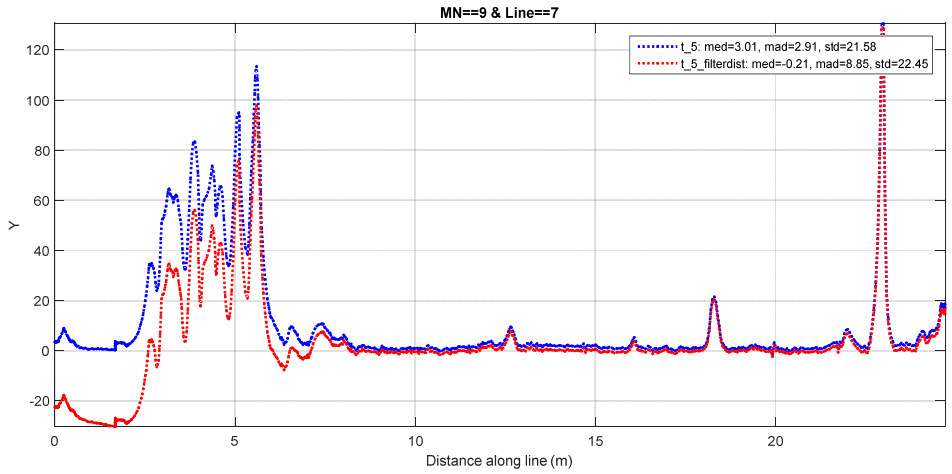

Figure 9. Long line where large anomaly near an end causes failure in background correction.

Alternative filtering method

The main source of error in the background estimate is the inclusion of valid signal from metallic objects. Since the filter may be applied to data that has a trend, eliminating signal from valid anomalies may not, in general, be as straightforward as eliminating the higher or lower values – i.e., anomalous values – within a segment of data. Our approach is to verify that the background correction is not adding energy to the data. In this way, we hope to reduce "overshooting".

The first stage of the filter runs a moving median calculation to estimate the background (B0), then subtracts that running median from the data. We then run a second moving median with a shorter window length, e.g., approximately 3 times the typical distance between consecutive points. The amplitude of the "normal" background (B0) and the shorter window background estimate (BL) are compared. At each point, we choose the background that has the one with lowest energy (or absolute amplitude).

In the second stage the background estimate is refined after identifying points where the background correction is biased.

- If the line is shorter than a user specified distance, or twice the median-window length, we assume that the 20% fraction of the points with amplitude closest to 0 best represents the background. Once outliers from the subset of data are removed, this data is used to estimate the background.

- For lines greater than the minimum length, we identify the subset of extreme points where the corrected data is in the lowest and highest percentile. There may be points where the original data was near the background, but the correction artificially increased the data amplitude. We identify some of these points by sorting the points by the absolute value and use the lowest 10% for the subsequent background estimation. Points with large variations in the signal are unlikely associated with background; these are excluded by excluding the extremes.

Once points defining the background are identified, the background is estimated, again, with a moving window median filter. The background is estimated at the excluded points by interpolation. Where the new estimated background has higher absolute amplitude than the local background (BL), we retain the local background. Finally, the background estimate is smoothed.

Examples with MPV data

Correction of profile data

Figure 10 presents an example of applying the modified filtering scheme on an, approximately, 19.5m length of data. The unfiltered profile data is presented in blue, the original filter is in red, and the modified filtering scheme result is plotted in green. For this case, the original and modified filter do not have a significant different, though the median value along the line for the new filter is slightly larger (median of 0.13 instead of 0.01).

Figure 11 considers the case of a short line that contains signal in the majority of data. In this example, approximately 70% of soundings have signal, with only a small section in the middle of the line that represents the background response. Applying the modified filtering methodology avoids the overestimate of the background response, thereby avoiding the overshooting seen in the standard median filtering approach (red line).

Figure 12 has an additional example of filtering along a very short line. In this example, there is a large anomaly at the end of the line that causes the standard de-median filter to overestimate the background signal. In this example, the modified approach is able to avoid the overshooting resulting from the standard approach.

Figure 13 contains examples of filtering data that contains multiple closely spaced targets. The targets produce regions of high amplitude that are problematic for standard de-median filtering, since the median becomes a poor estimate of the background signal for the chosen window length. These examples show that the modified filtering approach avoids the “overshooting” artifacts that affect the standard approach.

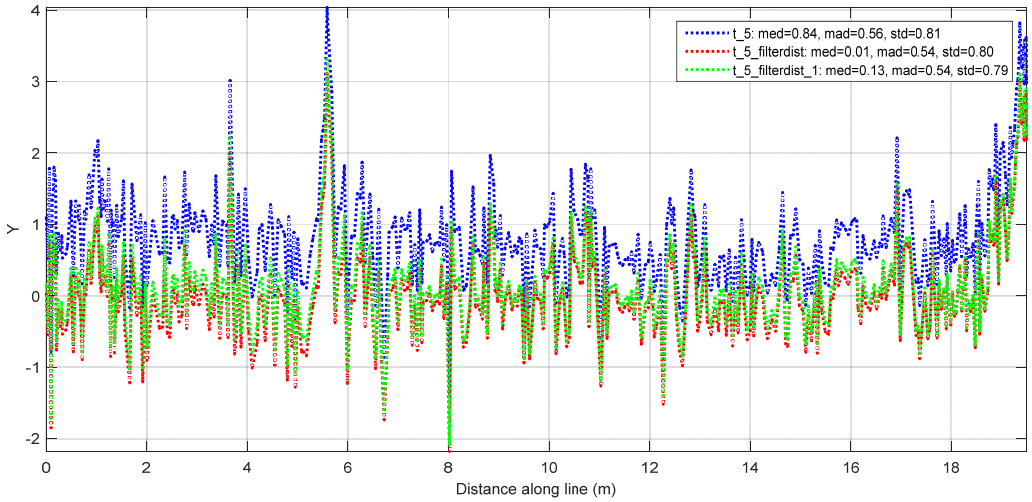

Figure 10. Filtering of a noisy line with weak amplitude anomalies. Vertical component, coaxial data are plotted.

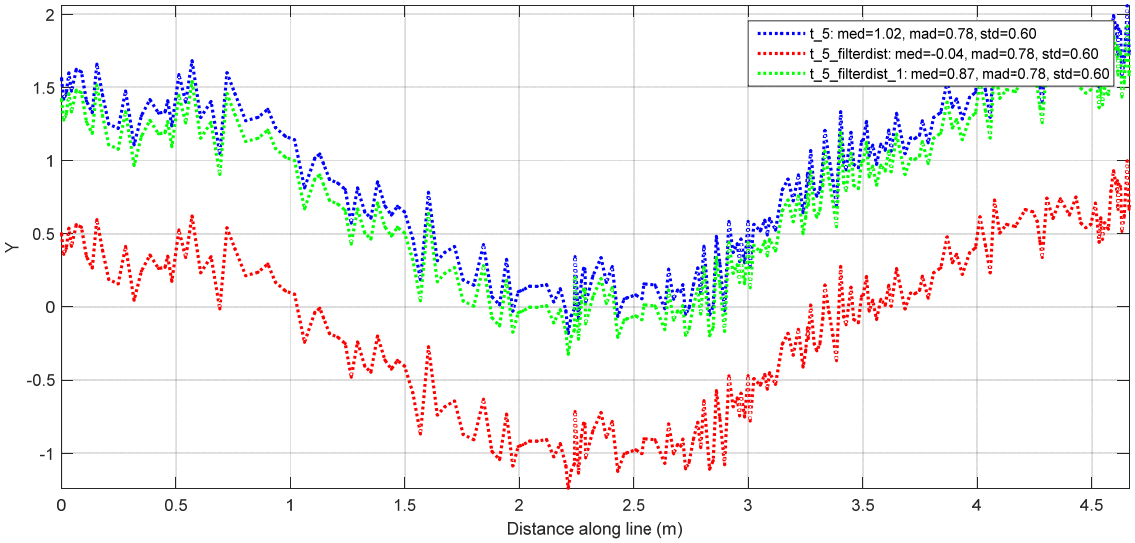

Figure 11. Example of filtering a short line

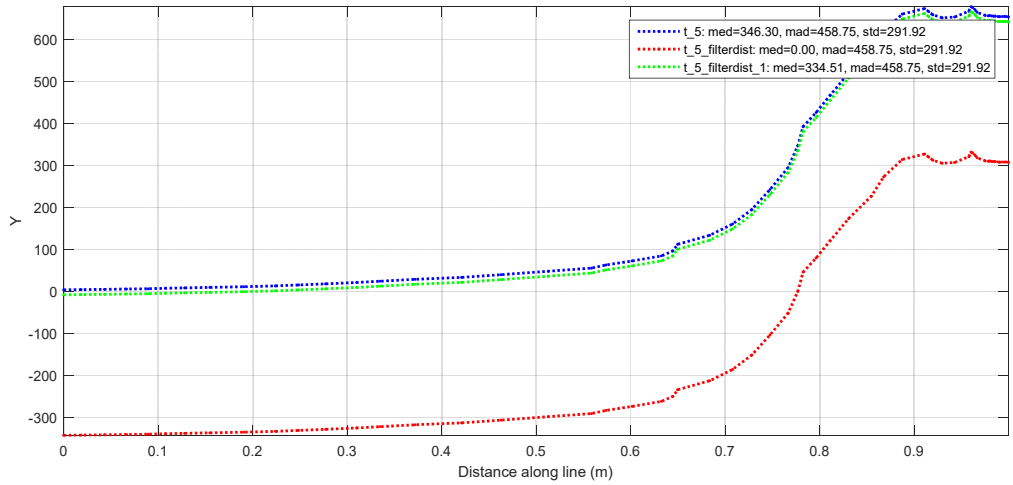

Figure 12. A second example of filtering along a very short (i.e., less than 1m length) line.

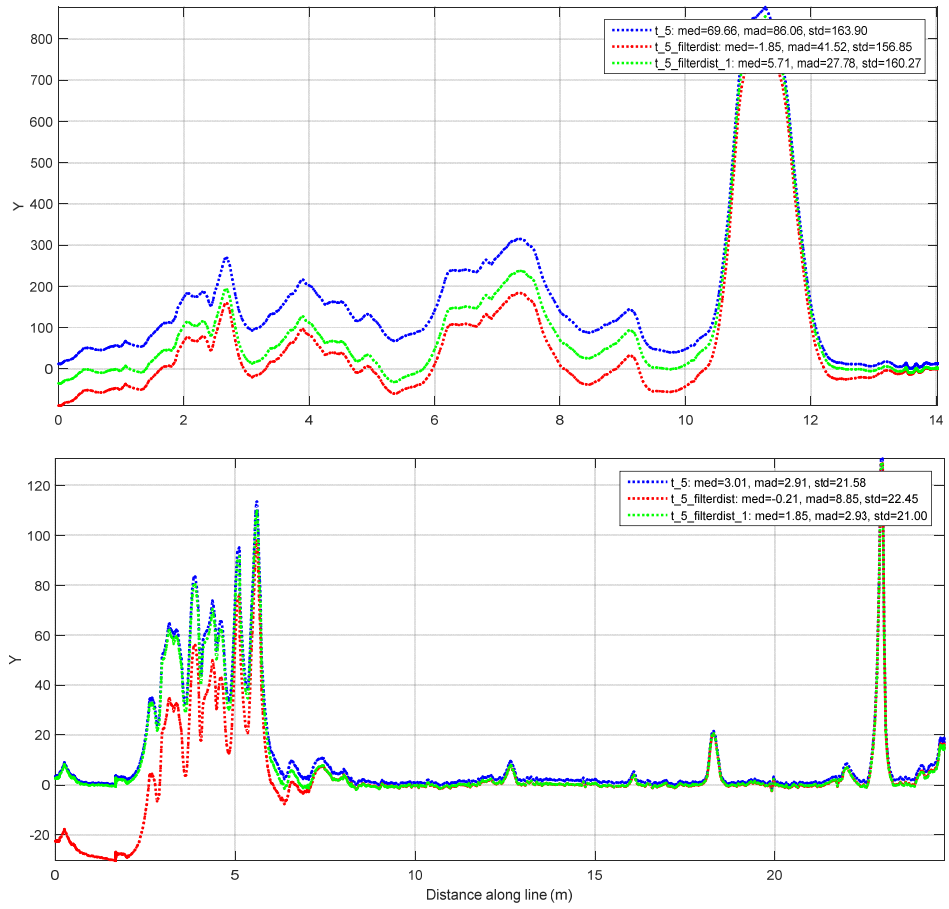

Figure 13. Examples of filtering data that has larger scale target anomalies.

Detection map

Dynamic MPV data were acquired at a number of homes in the town of Puako, Hawaii as part of an Environmental Security Technology Certification Program (ESTCP) demonstration. The data featured many short lines and magnetic soil responses. The data were filtered using the standard de-median filter approach and the modified filtering method. Figure 14 plots the gridded image of the standard de-median data at time channel 5, for the vertical component data for all 5 receivers. In the vicinity of anomalies, there are many instances of filtering artifacts (i.e., negative lobes adjacent to anomalies) due to overestimating the background values. We see that there are many sections of green pixels in regions without anomaly, indicating negative data values.

Figure 15 contains a grid with the modified filtering approach. The gridded image shows a significant improvement: the background is generally closer to zero (yellow) and fewer filtering artifacts are apparent.

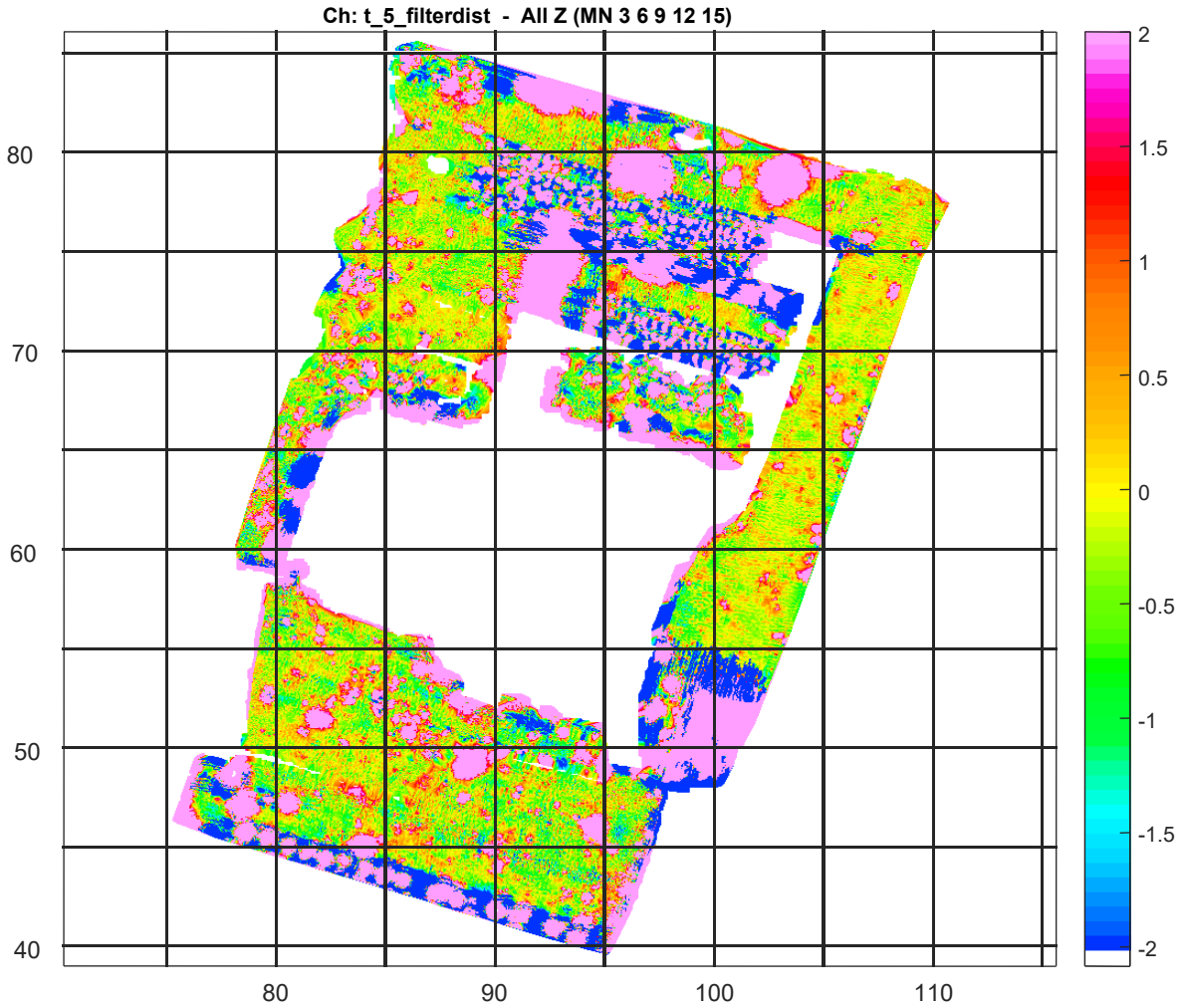

Figure 14. Detection map for MPV vertical-component data, standard de-median filter. There appear to be many instances of negative data due to overshooting of the filter correction near large anomalies.

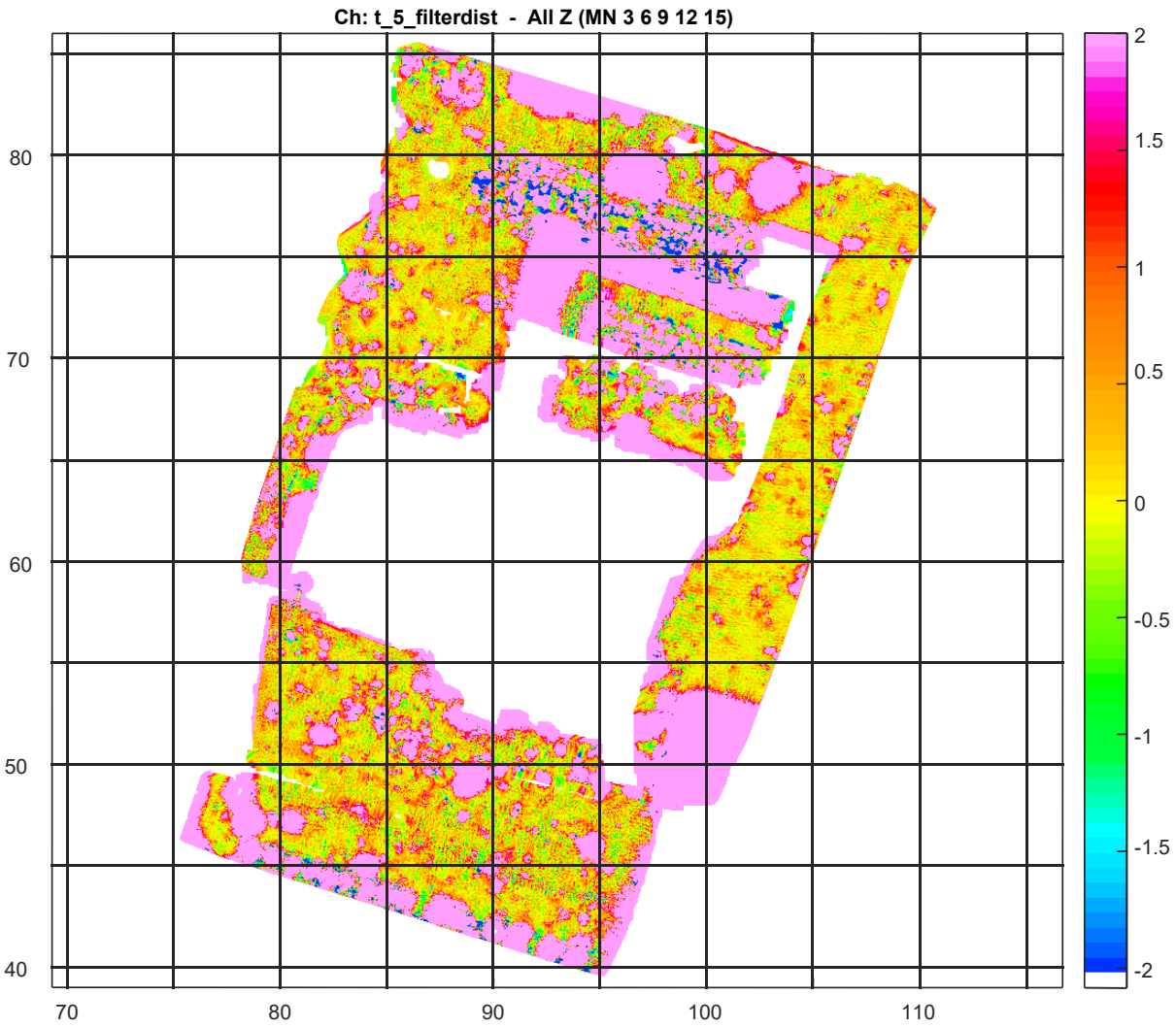

Figure 15. Detection map for corrected de-median filter.

Examples with TEMTADS2x2 data

The modified filtering approach was also tested on TEMTADS 2x2 data acquired at the former Redstone Arsenal, AL. The data featured significant DC offsets (Figure 16). An initial step was performed to remove a single offset in each data profile.

The data presented in Figure 16 shows the raw profile, the standard filter correction and the new approach for different combinations of transmitters, receivers and receiver components. The raw data has a DC offset that can be positive or negative, with an amplitude that is generally larger than the standard deviation of the data for that profile. Both filtering methods succeed at shifting the profile data near zero. However, the standard approach over-corrects near anomalies: this is particularly visible on the second panel from the top, where the shape of the signal is distorted and creates a positive anomaly before a large negative anomaly.

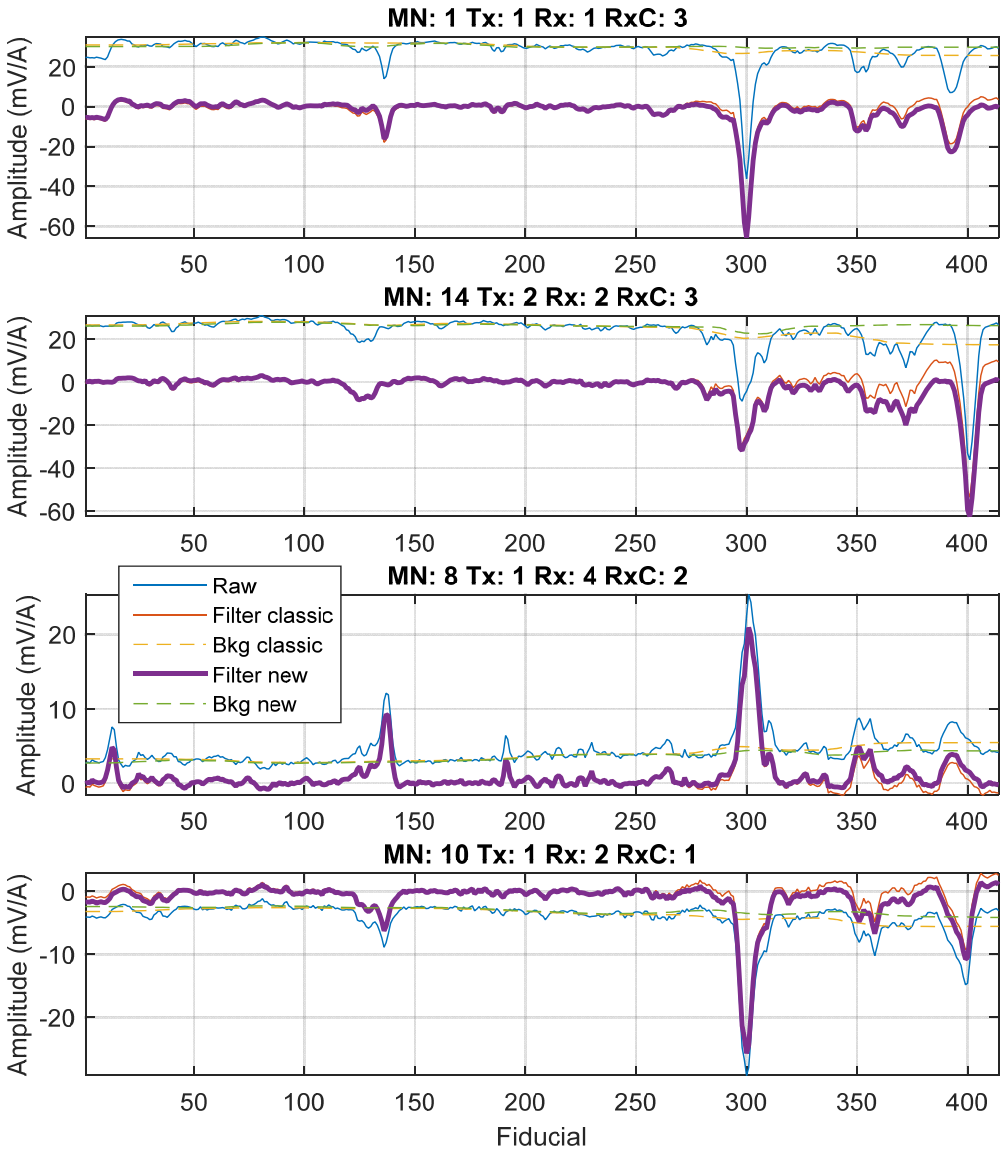

Figure 16. Filtering of TEMTADS 2x2 data. Each panel shows profile data for different combinations of transmitter and receiver locations and components (RxC is the vector component, 1=X, 2=Y and 3=Z). Raw data show a DC offset. The standard filtering approach (thin red line) overshoots the correction near anomalies. The new filter (thick purple line) corrects the data such that background values are closer to zero around anomalies. (Dashed lines show estimated background for each filter).

The data in Figure 17 shows a detection map for TEMTADS 2x2 data based on the standard filter applied to the mono-static vertical-component data. The gridded image seems to delineate anomalies reasonably well. There are only few instances of negative data (the sign of the data is flipped here so that anomalies have a positive value). The data obtained with the new filter is gridded in Figure 18. Although the image appears shows some qualitative improvements (e.g., some regions have the background response reduced and filtering artefacts removed), further testing and development is required to establish the robustness of the modified approach, and to identify improvements.

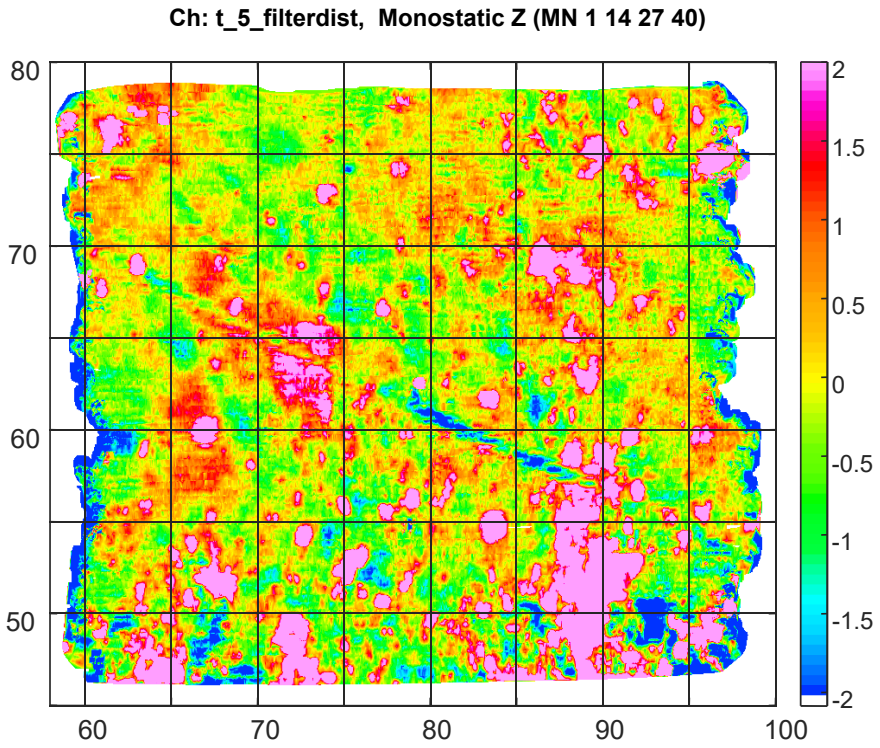

Figure 17. TEMTADS detection map with standard filter (ESTCP data from Redstone Army Depot).

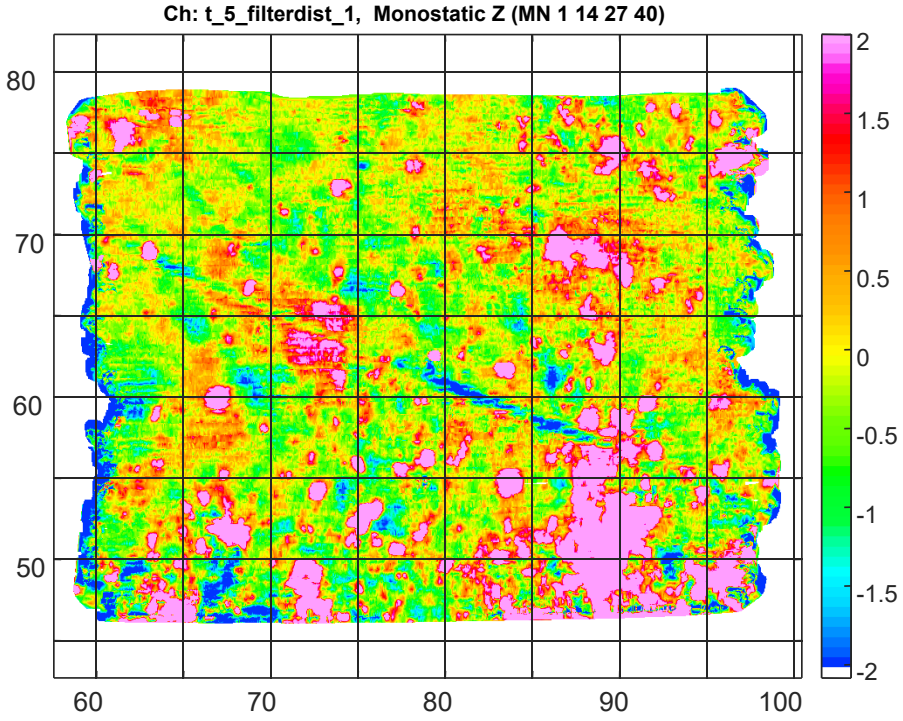

Figure 18. TEMTADS detection map using new filter.

Temporal Orthogonal Projection Inversion for EMI Sensing of UXO

We present a new approach for inverting time domain electromagnetic data to recover the location and magnetic dipole polarizations of a limited number of buried objects. We form the multichannel electromagnetic induction (EMI) sensor data as a spatial–temporal response matrix (STRM). The rows of the STRM correspond to measurements sampled at different time channels from one sensor and the columns correspond to measurements sampled at the same time channel from different sensors. The singular value decomposition of the STRM produces the left and right singular vectors that are related to the sensor and the temporal spaces, respectively. If the effective rank of the STRM is r, then the first r singular vectors span signal subspaces (SS), and the remaining singular vectors span the noise subspaces. The original data are projected onto the SS, and the temporal orthogonal projection inversion (TOPI) uses these data in a nonlinear inverse problem to solve for source locations of the objects. The polarizations of the targets are then obtained by solving a linear optimization problem in the original data domain. We present theoretical and numerical analyses to investigate the singular value system of the STRM and the sensitivity of the TOPI to the size of an SS. Only a few subspace vectors are required to generate locations of the objects. The results are insensitive to the exact choice of rank, and this differs from usual methods that involve selecting the number of time channels to be used in the inversion and carefully estimating associated uncertainties. The proposed approach is evaluated using the synthetic and real multi-static EMI data.

1. Introduction

Electromagnetic induction (EMI) sensing is a major survey in environmental remediation of unexploded ordnance (UXO) contamination [1] [2] [3] [4] [5] [6] [7] [8] [9] [10] [11] [12] [13] [14] [15] [16] [17] [18] [19] [20] [21] [22] [23] [24] [25] [26] [27] [28] [29]. Its effective use relies upon the ability to extract accurate target signatures (e.g., dipolar polarizabilities) from measured data. Those polarizabilities are subsequently used to discriminate UXO from nonhazardous clutter [20] [21] [22].

EMI signal processing is generally cast as a nonlinear overdetermined inverse problem, where the location of an object and its principal polarizations are sought [6] [7] [8] [12] [13] [23] [24] [25] [26] [27] [28] [29]. Data are acquired as a series of transient responses from an array of sensors. The noise level in the time channels vary, and later times are often particularly contaminated. A quality inversion thus begins with choosing which time channels should be included in the inversion and providing an assessment of expected noise. However, this issue has received little direct attention (see, for example, [6] [7] [8] [9] [10] [11] [12] [13] for a single object case or [23] [24] [25] [26] [27] [28] [29] multiple objects). The general approach uses the hypothesis that responses at early time channels likely have a higher signal-to-noise ratio (SNR) and a simple selection of early time channels might be empirically set up for one type of sensor or particular data. If there are a priori estimates of the unknown sensor noise, one may also choose responses above a predefined SNR threshold in order to avoid possible adverse effects of late time noisy measurement on the estimated source parameters. Overall, however, the quality of the inversion result from inclusion of noisy data is most likely degraded unless accurate error estimates are available and proper weighting is chosen [8] [12] [13] [28].

In this paper, we present a method that is less dependent upon a priori noise estimates. We first define the spatial–temporal response matrix (STRM). This is the data matrix whose rows correspond to measurements at different time channels from one sensor (i.e., a single transmitter–receiver pair). Namely, each row is the time-domain decay curve for a particular sensor. The columns of the STRM are measurements at all sensors at a single time. The singular value decomposition (SVD) of this matrix provides a well-defined set of vectors with which to expand the rows of the STRM. We project the time-domain decay curves onto a small subspace by keeping only those vectors associated with larger singular values. A nonlinear inversion is then carried out in the transformed domain to find the source locations. The procedure, which we refer to as temporal orthogonal projection inversion (TOPI), has some advantages over the usual inversion method. Briefly, the TOPI uses the concept of subspace to select channels. There is no involvement of either the empirical selection of channels or a formidable task of estimating unknown noise. In addition, the subspace projection has the potential for separating signal from additive Gaussian noise and thus higher quality and more robust solutions are obtained in the inverse problem. Most importantly, the TOPI is insensitive to determining the dimension of the signal subspace (SS) and is able to recover accurate source locations using a small number of temporal projections. This further reduces the size of the inverse problem and speeds up the convergence. Once good estimates are obtained for the locations of the targets, their polarizabilities are subsequently obtained by solving a linear optimization problem in the original data domain.

The remaining parts of this paper are organized as follows. In Section II, we present the mathematical foundation for working with data from dipole models and outline our existing nonlinear inversion algorithm. In Section III, we present the SVD analysis of the STRM that relates spatial and temporal singular bases to the physical field quantities and derive our projection inversion method. In Section IV, we evaluate and discuss the technique using synthetic and real data recorded by the new-generation sensor array systems of the Time-domain Electro-Magnetic multi-sensor Towed Array Detection System (TEMTADS) [30]. Section V gives the conclusion.

2. Signal Model

A. Polarizability Tensor and Formulation

For a UXO survey, where the target dimension is often small relative to the target-sensor distance, the primary fields around the target can be approximately uniform, and the induced eddy currents in the target are localized and dominantly produce dipole responses [31] [32]. As a leading order approximation, the transient scattering of a metallic object can be well represented by an equivalent induced dipole. This dipolar dynamic property is characterized by a 3 × 3 symmetric magnetic polarizability tensor (MPT) $P(t)$

$$P(t) = \begin{bmatrix} p_{11}(t) & p_{12}(t) & p_{13}(t) \\ p_{12}(t) & p_{22}(t) & p_{23}(t) \\ p_{13}(t) & p_{23}(t) & p_{33}(t) \end{bmatrix} \tag{2}$$

where each element $p_{ij}(t)$ represents a dipole component in the ith Cartesian direction due to a primary field in jth Cartesian direction and where t is time (for example, see [1] [2] [3] [4] [5] [6] [7] [8] [9] [10] [11] [12]). This polarizability tensor $P(t)$ has an eigenvalue decomposition as

$$P(t) = \sum_{j=1}^{3} L_j(t)\mathbf{e}_j\mathbf{e}_j^T \tag{3}$$

where $\mathbf{e}_j$(j = 1, 2, 3) is the orthonormal eigenvector representing the jth principal direction of dipolar polarization with respect to (w.r.t.) a reference system, superscript T denotes the transpose, and $L_j(t)$ is the principal polarization strength that is a function of the geometry and material of a target. In other words, $P(t)$ contains the information about the geometry and physical properties of a target, as well as its orientation. For axially symmetric objects, it is generally assumed that the principal directions are time independent. For an irregular shape object, the principal directions may vary with time [20]. However, in our inversion development, the assumption of time-independent principal directions is not critical since we work directly on the polarizability tensor $P(t)$ at each time channel rather than with its decomposition form of (3). This will be evident in the following description.

A typical survey uses multiple transmitter–receiver pairs. We assume M such pairs and denote the secondary response due to the ith Tx/Rx pair as di. This can be written in an inner product form with respect to $P(t)$, [1] [2] [3] [4] [5] [6] [7] [8] [9] [10] [11] [12] as

$$d_i(\mathbf{r}_{Rx_i}, t) = \mathbf{a}_i^T(\mathbf{r}, \mathbf{r}_{Rx_i}, \mathbf{r}_{Tx_i})\mathbf{q}(t) \tag{4}$$

where $\mathbf{a}_i(\mathbf{r}, \mathbf{r}_{Rx_i}, \mathbf{r}_{Tx_i})$ is 6 × 1 column vector representing spatial sensitivities of the ith sensor to the object located at r, and q(t) a 6 × 1 column vector, whose components are the elements of the polarizability tensor P(t) of an object. They are given by [27] [28]

$$\mathbf{a}_i(\mathbf{r}, \mathbf{r}_{Rx_i}, \mathbf{r}_{Tx_i}) = \begin{bmatrix} B_R^x B_T^x \\ B_R^x B_T^y + B_R^y B_T^x \\ B_R^x B_T^z + B_R^z B_T^x \\ B_R^y B_T^y \\ B_R^y B_T^z + B_R^z B_T^y \\ B_R^z B_T^z \end{bmatrix}, \mathbf{q}(t) = \begin{bmatrix} p_{11}(t) \\ p_{12}(t) \\ p_{13}(t) \\ p_{22}(t) \\ p_{23}(t) \\ p_{33}(t) \end{bmatrix} \tag{5}$$

where $[B_R^x B_R^y B_R^z]T$ and $[B_T^x B_T^y B_T^z]T$ are the Cartesian components of field vectors $B^R(\boldsymbol{r}, \boldsymbol{r}_{Rx_i})$ and $B^T(\boldsymbol{r}, \boldsymbol{r}_{Tx_i})$ that are generated at the object's location by the receiver and transmitter coils.

Assume that η objects are present in response to a given excitation. By neglecting EMI interaction between the objects [23] [24] [25] [26] [27] [28] [29], we model a measurement as a linear superposition of the signal from each object. That is, $d_i(\boldsymbol{r}_{Rx_i}, t) = \sum_{k=1}^{\eta} a_i^T(\boldsymbol{r}_k, \boldsymbol{r}_{Rx_i}, \boldsymbol{r}_{Tx_i})\boldsymbol{q}_k(t)$, where $a_i(\boldsymbol{r}_k, \boldsymbol{r}_{Rx_i}, \boldsymbol{r}_{Tx_i})$ defined in (4) are the spatial sensitivities of the ith sensor to the kth object located at $\boldsymbol{r}_k$ with polarizations $\boldsymbol{q}_k(t)$. The observed EMI responses for M sensors, in the presence of noise, can be conveniently expressed in a vector–matrix notation

$$\mathbf{d}(t) = \sum_{k=1}^{\eta} A(\mathbf{r}_k)\mathbf{q}_k(t) + \mathbf{n}(t) \tag{6}$$

where $d(t) = [d_1(t), \ldots, d_M(t)]^T$ is an $M \times 1$ measured data vector at time t, $\boldsymbol{n}(t)$ is the additive noise vector, and $A(\boldsymbol{r}_k)$ is an $M \times 6$ matrix denoting the sensitivities of the M sensors to the kth object located at $\boldsymbol{r}_k$. Its transpose is given by

$$A^T(\mathbf{r}_k) = \left[\; \mathbf{a}_1(\mathbf{r}_k) \; \ldots \; \mathbf{a}_M(\mathbf{r}_k) \; \right] \tag{7}$$

The position vectors of the sensor coils are suppressed in (6).

It is understood that the sensor information is subscript indexed in the recordings and in the sensitivity vectors. Equation (6) is a generic dipole-based formulation for estimating and recovering the locations and polarizabilities of EMI anomalies. We note that for a single time channel of data and for a single object that we need at least M>9 in order to have an overdetermined system. If there are η objects then M>9η.

B. Two-Step Inversion

Here, we briefly review the sequential inversion algorithm of TEM data [27] [28] since we use this generic procedure throughout this paper to solve for locations and polarizations. In the sequential inversion of η objects, the model parameters are grouped into two parts: a nonlinear part consisting of source locations $\boldsymbol{r} = vec[\boldsymbol{r}_1, \ldots, \boldsymbol{r}_\eta]$ and a linear part consisting of source polarizations $q(t) = vec[\boldsymbol{q}_1(t), \ldots, \boldsymbol{q}_\eta(t)]$ at time instant t. Here, vec [·] represents a vectorization operation, i.e., stacking all vectors into a single column. The use of notations r and q should be evident in the context of multiple objects. Denoting $A(r) = [A(r_1), \ldots, A(r_\eta)]$ and using (5), we can write our full problem of determining r and q as a minimization of the functional given by

$$\min_{\mathbf{r},\mathbf{q}(t_j)} \sum_{j=1}^{N_t} \left\| W_j \left(\mathbf{d}_{\text{obs}}(t_j) - A(\mathbf{r})\mathbf{q}(t_j) \right) \right\|^2 \tag{8}$$

where N_t is the number of time channels used during this nonlinear update, and W_j is a diagonal data weighting matrix for the data at the selected time t_j. This is diagonal matrix with values equal to $1/_i$, where i is the estimated Gaussian uncertainty for each datum.

The parameter sets [see (5)] are separable because matrix $A(r_k)$ is independent of source polarizations $\boldsymbol{q}_k(t)$. Thus, the data are a nonlinear functional of location coordinates of the object and a linear functional of the polarizations. Since the estimate of polarizations depends on the unknown locations, determining the two parameter sets simultaneously can make the problem more ill posed that requires a careful weighting for different scale sensitivity submatrices. In addition, it induces a difficult initial guess of polarizations. Rather, we solve (8) using a Gauss–Newton approach [33] [34], in which a step for finding updated target locations involves a linear inversion for polarizabilities as a subproblem.

At the nth iteration, we are provided with a location estimate $\mathbf{r}^{(n)}$ and polarizations $\mathbf{q}^{(n)}$. The linearized data equations, with a perturbation, δ**r** are

$$\mathbf{d}(\mathbf{r}^{(n)} + \delta\mathbf{r}, \mathbf{q}^{(n)}; t_j) = \mathbf{d}(\mathbf{r}^{(n)}, \mathbf{q}^{(n)}; t_j) + J(\mathbf{r}^{(n)}, \mathbf{q}^{(n)}; t_j)\delta\mathbf{r} \tag{9}$$

where

$$J(\mathbf{r}^{(n)}, \mathbf{q}^{(n)}; t_j) = \frac{\partial A(\mathbf{r})}{\partial \mathbf{r}}\Big|_{\mathbf{r}^{(n)}} \mathbf{q}^{(n)}(t_j)$$

is the Jacobian and $A(r)$ is the composite matrix defined in (8).

At each iteration, we minimize

$$\min_{\delta \mathbf{r}} \sum_{j=1}^{N_t} \left\| W_j(\delta \mathbf{d}^{(n)}(t_j) - J^{(n)}(t_j)\delta \mathbf{r} \right\| \\ \text{subject to } \|\delta \mathbf{r}\| < \Delta \tag{10}$$

where $\delta \boldsymbol{d}^{(n)}(t_j) = \boldsymbol{d}_{obs}(t_j) - d(\boldsymbol{r}^n, \boldsymbol{q}^n;\ t_j)$ and $J^{(n)}(t_j)$ is the current Jacobian. Δ is a positive scalar used to provide a local ball, within which δ**r** is allowed to change with respect to the current $\mathbf{r}^{(n)}$ [33] [34]. This is generally a highly overdetermined system. The updated location is

$$\mathbf{r}^{(n+1)} = \mathbf{r}^{(n)} + \delta \mathbf{r} \tag{11}$$

The polarizations $\mathbf{q}^{(n+1)}(t_j)$ needed for the next update are found by minimizing

$$\mathbf{q}^{(n+1)}(t_j) = \arg\min_{\mathbf{q}(t_j)} \|\mathbf{d}_{\text{obs}}(t_j) - A(\mathbf{r}^{(n+1)})\mathbf{q}(t_j)\|^2 \\ \text{s.t.} \\ p_{k,ii}(t) \geq 0 \\ |p_{k,il}(t)| \leq \frac{1}{2}\left[p_{k,ii}(t) + p_{k,ll}(t)\right], i, l = 1, 2, 3, \tag{12}$$

where the constraints imposed on the polarizability elements p_{ij} arise from the symmetric positive definite matrix in (2) [35] [36].

The iterations in equations (10)-(12) are continued until convergence criteria are satisfied. This yields a set of final locations $\tilde{\boldsymbol{r}}_k$; polarizations $\tilde{\boldsymbol{q}}_k(k = 1, \dots, \eta)$ are obtained by (12) for all time channels. Note that the solution for $\boldsymbol{q}_k(t)$ is solved at each time channel. The principal directions and polarizations might be simply obtained by the eigen-decomposition of each individual MPT. There are no numerical restrictions or physical assumptions that these directions are identical or close to each other. As suggested in [28], an average principal direction can be sought across a range of times via a joint diagonalization of the polarizability tensors.

It is observed in (10) that the computed source locations depend upon the responses at N_t selected time channels. The issue of which time channels to select is the focus of the next section.

3. Method

A. STRM and its SVD

EMI data are generally acquired with an array of sensors. Each sensor records data at times $t_1, \dots, t_j$. Assuming M Tx/Rx pairs, we arrange data as

$$D = \begin{bmatrix} d_1(t_1) & \cdots & d_1(t_J) \\ \vdots & \vdots & \vdots \\ d_M(t_1) & \cdots & d_M(t_J) \end{bmatrix} \tag{13}$$

We call this the STRM. Its rows correspond to responses sampled at different time channels from one transmitter/receiver pair and its columns to measurements sampled at the same time channel from

different transmitter/receiver combinations. The STRM can be formed for a static or a dynamic survey with monostatic or multi-static array configurations. The SVD [35] [36] of D in (13) is written as

$$D = U\Sigma V^T = \sum_{i=1}^{p} \sigma_{ii}\mathbf{u}_i\mathbf{v}_i^T \tag{14}$$

where $p = \min(M, J)$, $U = [\mathbf{u}_1, \cdots, \mathbf{u}_M]$ is an $M \times M$ left orthonormal matrix, $V = [v_1, \ldots, v_j]$

is a $J \times J$ right orthonormal matrix, and Σ is an $M \times J$ singular value matrix with elements σ_{ii} along the diagonal and zeros everywhere else. If the singular values are ordered so that

$$\sigma_{11} \geq \sigma_{22} \geq \cdots \sigma_{pp} \geq 0 \tag{15}$$

and if the matrix has a rank r < p, then the last singular values are equal to zero and the SVD of D becomes

$$D = \sum_{i=1}^{r} \sigma_{ii}\mathbf{u}_i\mathbf{v}_i^T \tag{16}$$

Equations 14 or 16 hold w.r.t. any ordering of singular values and singular vectors and sign of each of the column pairs u_i and v_i. With the decreasing ordering of singular values, as in (14), the SVD is unique up to a sign change of both left and right singular vectors.

To understand the SVD of D, we relate the triplet $\{\sigma_{ii}, \mathrm{u}_i, \mathrm{v}_i\}$ in (16) to field quantities A and $\mathbf{q}$. It is sufficient to consider data from a single object as given by (4). Replacing each entry in (13) with (4), we rewrite (13) as

$$D = A(\mathbf{r})Q^T \tag{17}$$

where $\mathrm{A(r)}$ is an $M \times 6$ array response matrix defined in (6). Q^T is a $6 \times J$ source matrix

$$Q^T = \begin{bmatrix} \mathbf{q}(t_1) & \cdots & \mathbf{q}(t_J) \end{bmatrix} \tag{18}$$

whose column corresponds to one temporal component of the dynamic polarizability tensor.

To generate an SVD form of (17), we introduce the two symmetric matrices [37]

$$W_A = (A^T A)^{\frac{1}{2}}, \quad W_Q = (Q^T Q)^{\frac{1}{2}}. \tag{19}$$

Using W_A and W_Q, we transform D in (17) into

$$D = AW_A^{-1}W_A W_Q (QW_Q^{-1})^T. \tag{20}$$

Setting

$$U_A = AW_A^{-1}, \quad V_Q = QW_Q^{-1}, \quad X = W_A W_Q, \tag{21}$$

taking the SVD of X as $U_X = U_X \Pi V_X^T$, we write (20) as

$$D = (U_A U_X)\Pi(V_Q V_X)^T \tag{22}$$

where $U_A^T U_A = I$ and $V_Q^T V_Q = I$. Equation (21) is an explicit form of SVD decomposition of D. The left singular vectors are the columns of $U_A U_X$, and the right singular vectors are the columns of $V_Q V_X$. The singular values of D are the diagonal entries of Π, i.e., the eigenvalues of the square matrix X.

With the previous discussion on the uniqueness of a SVD and comparing (22) to (16), we have

$$U_A U_{X,i} = \mathbf{u}_i, \quad V_Q V_{X,i} = \mathbf{v}_i, \quad i = 1, \cdots, r, \tag{23}$$

where $U_{X,i}$ and $V_{X,i}$ represent the ith column of U_X and V_X. Equation (23) shows that for $\sigma_{ii} > 0$ the singular vectors u_i are linear combinations of the orthonormalized array Green's function matrix U_A and form an orthonormal basis spanning the sensor-target location space, whereas the singular vectors v_i are linear combinations of the orthonormalized polarizability source matrix V_Q and form an orthonormal basis spanning the temporal space. Both left and right singular vectors contain information of the target locations and polarizabilities. The former in principle can be used in MUSIC-like imaging to estimate target location [37]. However, in this development, our scope is concentrated on the use of the latter as a basis to project original temporal responses for inversion. Finally, there is no direct connection of Π with the principal polarizabilities of L_j. The eigenvalues of an STRM cannot be simply interpreted as apparent principal polarizabilities as in the multi-static response matrix that has measurements taken at one location and requires a sufficient number of transmitters and receivers [37] [38].

B. Rank of D

From SVD analysis, the data matrix D given in (13) has rank $r \leq p = min(M,J)$. However, we also have $D = AQ^T$ [see (16)]. From the matrix analysis theory [37], we have $rank(D) = rank(AQ^T) \leq min[rank(A), rank(Q^T)]$. Provided $M \geq 6$ and $J \geq 6$ then both $rank(A) \leq 6$ and $rank(Q^T) \leq 6$, this restricts the maximum rank of D for a single object to 6. Theoretically, if there are η objects contributing to the data then the maximum rank is 6η. This is for a general case, where principal directions might be rotational with time.

For the case that the principal coordinates of the polarizability matrix are time independent, Q^T is controlled by three parameters L_j . Using (3), we can express Q^T as $Q^T = EL$ where E is a 6 × 3 matrix whose elements are related to the principal direction vectors $\boldsymbol{e}_j$ and L is a 3 × J matrix whose elements are the three principal polarizabilities in J time channels. By applying the rank inequality property, we have $rank(Q^T) = rank(EL) \leq min[rank(E), rank(L)] \leq 3$ provided $J \geq 3$. Thus, the maximum rank of Q is 3 if the data are from a single object. That rank can be reduced to 2 for a cylindrically symmetrical object that has two distinct principal polarizabilities, or to rank one for a sphere. In general, if there are η objects contributing to the data, then the maximum rank is 3η.

C. Temporal Orthogonal Projection and Inversion

Assuming that the matrix has a rank r, as described in (16), we group these SVD-constructed orthonormal vectors into the left and right SS, i.e., $U_s = [\mathbf{u}_1, \ldots, \mathbf{u}_r]$ and $V_s = [\mathbf{v}_1, \ldots, \mathbf{v}_r]$. The remaining singular vectors, $U_n = [\mathbf{u}_{r+1}, \ldots, \mathbf{u}_M]$ and $V_n = [\mathbf{v}_{r+1}, \ldots, \mathbf{v}_M]$, are correspondingly grouped as the left and right orthonormal noise subspaces (NS).

Next, we project the data onto V_s. Right-multiplying (17) with submatrix V_s, we have

$$D_s = A(\mathbf{r})Q_s^T \tag{24}$$

where

$$D_s = DV_s \tag{25}$$

is a projected data matrix of $M \times \mathrm{r}$ and

$$Q_s^T = Q^T V_s \tag{26}$$

is a projected source matrix of $6 \times \mathrm{r}$ for a single-object case. Equation (24) is a temporal orthogonal projection equation, where the original J time channels are converted into r SS temporal channels but the sensitivity matrix A remains unchanged. For numerical implementation of an inversion in the transformed domain, (24) might be rewritten as a matrix-vector form for each projected temporal channel i

$$\mathbf{d}_s(i) = \sum_{k=1}^{\eta} A(\mathbf{r}_k)\mathbf{q}_{s,k}(i) + \mathbf{n}_s(i), i = 1, \cdots, r \tag{27}$$

where $d_s(i) = [d_s, 1(i), \ldots, d_s, M(i)]T$ is an $M \times 1$ projected data vector at projected channel $i, \boldsymbol{n}_s(i)$, is the projected noise vector. Considering the decomposition of (16) and the orthonormality of vectors $\boldsymbol{v}_i$, we can see that projected data $\boldsymbol{d}_s(i) = \sigma_{ii}\boldsymbol{u}_i$. Namely, σ_{ii} controls the importance of the ith normalized channel $\boldsymbol{u}_i$.

Like the original domain (6), the transformed (27) retains the feature that $\boldsymbol{d}_s$ is linear w.r.t. source parameter $\boldsymbol{q}_s$ and nonlinear w.r.t. the locations of objects. Therefore, the same solution strategy outlined in Section II-B can be applied to (27) by replacing $\boldsymbol{d}$ and $\boldsymbol{q}$ with $\boldsymbol{d}_s$ and $\boldsymbol{q}_s$ in (10). The statistics of the projected noise are difficult to evaluate, but we make the much-used assumption for now that the noise is Gaussian and uncorrelated and that each datum has the same standard deviation. Thus, the data weighting matrix in (10) becomes a scaled identity matrix. We now proceed with the TOPI where the r SS projected temporal channels are used to localize sources via the nonlinear update. Once source locations are determined, the target polarizabilities are solved as a linear optimization problem in the original data domain via (12). The orientation of each object, if desired, can be extracted from the polarizability tensors, according to the method outlined in Section II-B [28].

4. Experiments

An important question for the TOPI concerns the size of the subspace used and the nature of the associated basis vectors. To illustrate the relationship between the rank and the polarizations of an object, and divisions between SS and NS, we perform experiments using synthetic and real TEMTADS data. TEMTADS [30] is a single-component multi-static system. It consists of a horizontally arranged coplanar array of 5 × 5 transmitters and receivers [see Figure 19(a)]. The sizes of its transmitters and receivers are 35 cm × 35 cm and 25 cm × 25 cm, respectively. Data are acquired at 115 logarithmically spaced channels between 0.042 and 24.35 ms. For each transmitter excitation, TEMTADS records the response at all receivers. Thus, it has spatial–temporal data of 625 × 115 for a static (cued) survey.

Figure 19(b) shows the two sets of polarizations that will be used for the numerical experiments. The solid and dashed curves represent polarizations of a 105-mm projectile and a scrap item, respectively. In the following numerical experiments with TEMTADS, we specify the number, location, and orientation of the objects and their polarizations. We assume that the principal directions are time independent. Given these simulation parameters, we are able to calculate sensitivity matrix $A(r_k)$ and form polarization parameter vector $\boldsymbol{q_k}(t)$. It is then straightforward to generate synthetic signals, ranging from 0.042 to 24.35 ms, in the absence or presence of noise using (6).

For all inversion experiments either in the original domain or with the TOPI, we use the multi-start strategy to initialize an Inversion (for details see [28]). Briefly, the initialization process consists of the following:

1) Creating a few hundred (e.g., 300) random trial locations for η objects within the region of interest.

2) Evaluating these trial locations within a single linear inversion to generate polarizabilities and rank the trials according to their achieved misfits.

3) Selecting a few (e.g., 5) distinct trial locations that have low misfits as starting locations for a nonlinear update. Among multiple nonlinear solutions, the one with the smallest misfit is chosen as the set of final locations.

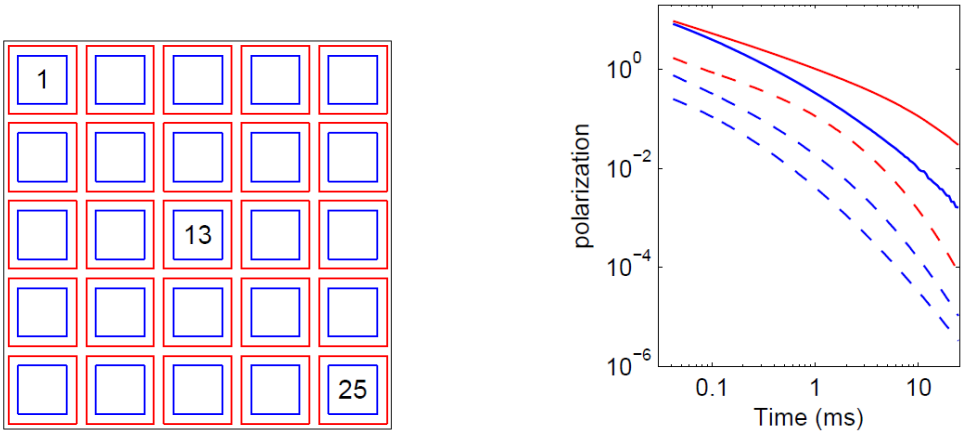

(a) TEMTADS Array (b) Polarizabilities for experiments

Figure 19. (a) TEMTADS: a single-component multi-static system consisting of a horizontally arranged coplanar array of 5 × 5 transmitters and receivers. Each transmitter is 35 cm × 35 cm and each receiver 25 cm × 25 cm. (b) Two sets of polarizations used for the numerical experiments. The solid and dashed curves represent polarizations of a 105 mm projectile and a scrap, respectively.

A. Synthetic Single Object Example

For an experiment with a single object, we consider a 105-mm projectile-like object buried at (0.00, 0.00, −0.60) m and vertically oriented. Figure 20(a) is a plot of the singular values versus their indexes for the noise-free case. Two sets of singular values, calculated from matrices D (denoted as circles) and X (denoted as crosses) in (21), are shown. The projectile has circular symmetry and hence, from our earlier analysis, the rank should be equal to 2. It is observed that there are only two large singular values and that those of D and X are equal, as they were shown to be in Section III. This numerically illustrates that

the signal singular values of STRM D are governed by those of X. The other small nonzero singular values evident in Figure 20(a) are a consequence of numerical noise.

To see how additive noise affects the singular values, we add 3%, 5%, and 10% Gaussian noise to the synthetic data. As shown Figure 20(b)–(d), this noise lifts the small nonzero singular values to a level that might be comparable to singular values of signal. In this example, however, the signal singular values are still distinguishable with 10% noise given the ground truth and suggest that the rank of D is 2. However, in reality, the number of targets and their geometries are unknown, there could be an ambiguity to determine the true rank of D. For instance, Figure 20(d) can also suggest that the rank of D is at least two and a third nonzero singular value might represent signal singular value that looks likely hidden in the noise.

Additional insight about the rank of the matrix can be gleaned from the shape of the singular vectors in V. We refer to these as temporal eigenvectors (TEVs). Figure 20(e) shows the first seven and the last two TEVs in V for noise-free case. The first two vectors are smooth, and they span the 2-D SS. The remaining singular vectors, which span the NS, have a random behavior. The TEVs for 10% additive noise are shown in Figure 20(f). The first two TEVs have almost the same structure as in the noise-free case but the remaining vectors are substantially different and are characterized by high frequency fluctuations. The number of smooth TEVs corresponds to the rank of two. In this noisy case, the singular vectors that are smooth and show progressively more zero crossings are more diagnostic in determining the rank of the D than solely inspecting singular value distribution.

With the SVD decomposition, and knowledge of the rank of the matrix, we can generate our SS and NS. To illustrate the effectiveness of this, we carry out an analysis using 10% noise. Figure 21(a)–(c) show the true noise-free decay signals, the random noise, and the corrupted signals produced at all 625 $\mathrm{Tx/Rx}$ pairs. Using the triplets of $\{\sigma_{ii}, \boldsymbol{u}_i, \boldsymbol{v}_i\}$ derived from the corrupted signals, we want to reconstruct the noise-free data using $\widetilde{D} = \sum_{i=1}^{2} \sigma_{ii}, \boldsymbol{u}_i, \boldsymbol{v}_i^T$ where the rank is 2. The remaining eigenvalues and eigenvectors can be used to estimate noise as $\widetilde{N} = \sum_{i=3}^{115} \sigma_{ii}, \boldsymbol{u}_i, \boldsymbol{v}_i^T$. As a measure of accuracy, we compute a relative error defined as $\delta = \left\| D_{true} - \widetilde{D} \right\| F \,/ \| D_{true} \| F$ where $\cdot F$ denotes the Frobenius norm [38]. Figure 21(d) shows the estimated data $\widetilde{D}$. By comparing with the noise-free signals in Figure 21(a), we observe that the additive noise has been substantially reduced. The approximation error of δ = 2.5% is much less than the noise level of 10%. Figure 21(e) shows the estimated noise. These results show that the subspace concept can be a useful tool for separating signal from unwanted noise.

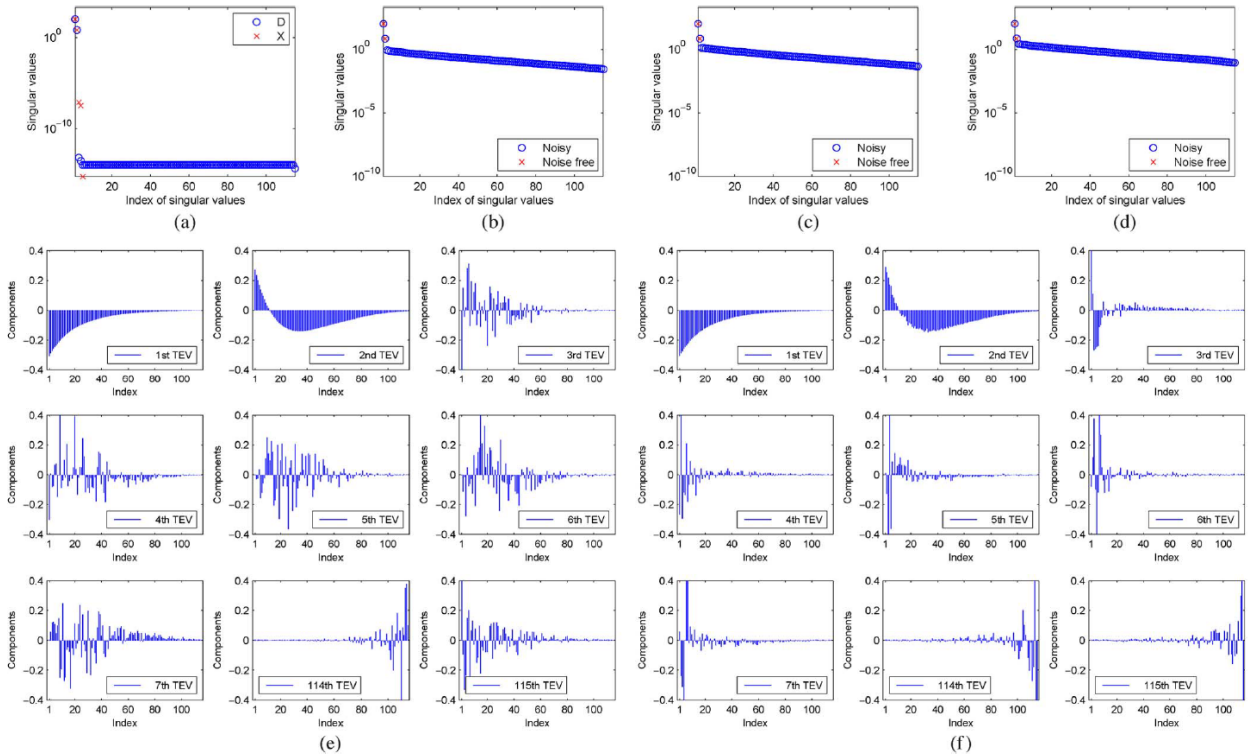

Figure 20. Single-object case. Singular values: (a) noise free; (b) 3% noise; (c) 5% noise; and (d) 10% noise. The first seven and the last two TEVs: (e) noise free; (f) 10% additive noise.

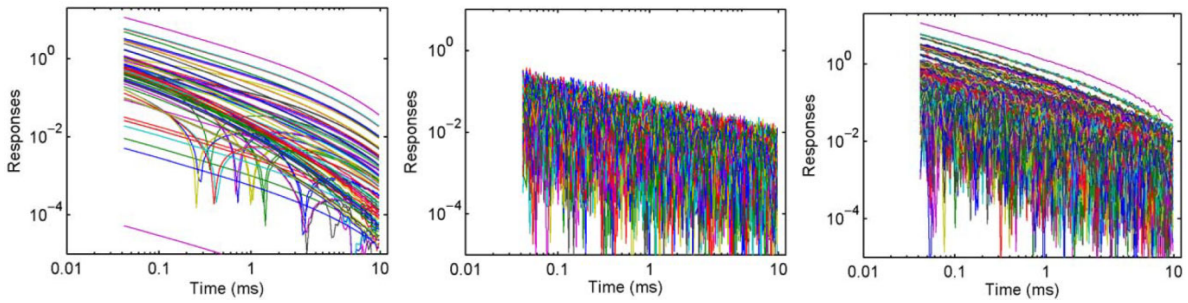

(a) Noise Free (b) 10% noise (c) Corrupted signal ((a)+(b))

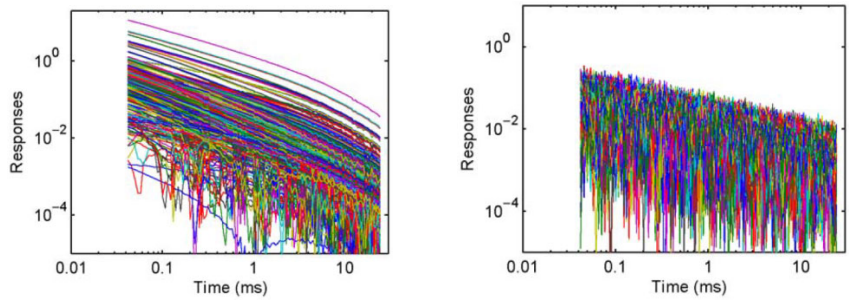

(d) Estimated Signal (e) Estimated Noise

Figure 21. Single-object case. For all 625 Tx/Rx pairs. (a) Noise-free decay signals. (b) Noise (10%). (c) Corrupted signals = (a)+(b). (d) Estimated signal. (e) Estimated noise.

The last item to explore within the decomposition concerns the projected data. As an example, Figure 22 shows the data for Transmitter 13. The projection of these data onto the space spanned by vectors V_s and V_n is also shown in that figure. The projected data consist of a few large values that correspond to the larger singular values and small random values thereafter. This character is easily understood. The first singular vector v1 is a smoothly decaying single polarity curve. Its character is similar to the data observed at many Tx/Rx pairs. Hence, the inner product of that basis with the rows of D generates a large value. Inner products with other vectors that have additional zero crossings will yield smaller data values. Eventually, inner products with highly variable vectors, and especially when those vectors have increasing amplitudes at larger times, produce projected data that contain little information and whose uncertainty greatly exceeds their values.

Let us turn to the TOPI based on (26) for the 10% noise case. We have determined that the rank of D for this single object is 2. As such, we now run the TOPI using the two projection vectors $\mathbf{v}_1$ and $\mathbf{v}_2$. The inversion returns an almost exact location $\mathbf{r}$ = (0.00, −0.01, −0.60) m. In fact, we can obtain the same result when we run the TOPI with only v_1 or only v_2. Each of these signal vectors contains enough information to allow recovery of the location. This arises because we have 625 data for each time channel, and hence, the problem is still overdetermined even with a single time channel of data. It is important that the vectors chosen for TOPI are signal vectors or at least the subspace used contains signal vectors. To illustrate this point, we run the TOPI with the vector v_3, which is a singular vector corresponding to the NS. The TOPI gives $\mathbf{r}$ = (0.61, 1.00, −1.20) m, which is a meaningless result. Finally, we carry out the inversion using the first three and then the first five vectors. Both of these inversions, which include signal vectors plus noise vectors, produce the same results $\mathbf{r}$ = (0.00, −0.00,−0.60) m. Removing v_1, we conduct the TOPI using the two subspaces of [$\mathbf{v}_2$, $\mathbf{v}_3$] and [$\mathbf{v}_2$, . . . , $\mathbf{v}_5$], respectively. Both the tests still deliver the location at $\mathbf{r}$ = (0.00, −0.01, −0.60) m. The experiments demonstrate that the TOPI is stable whenever signal vectors are used to project data. Of course, this still requires that M is large enough so that the problem is overdetermined.

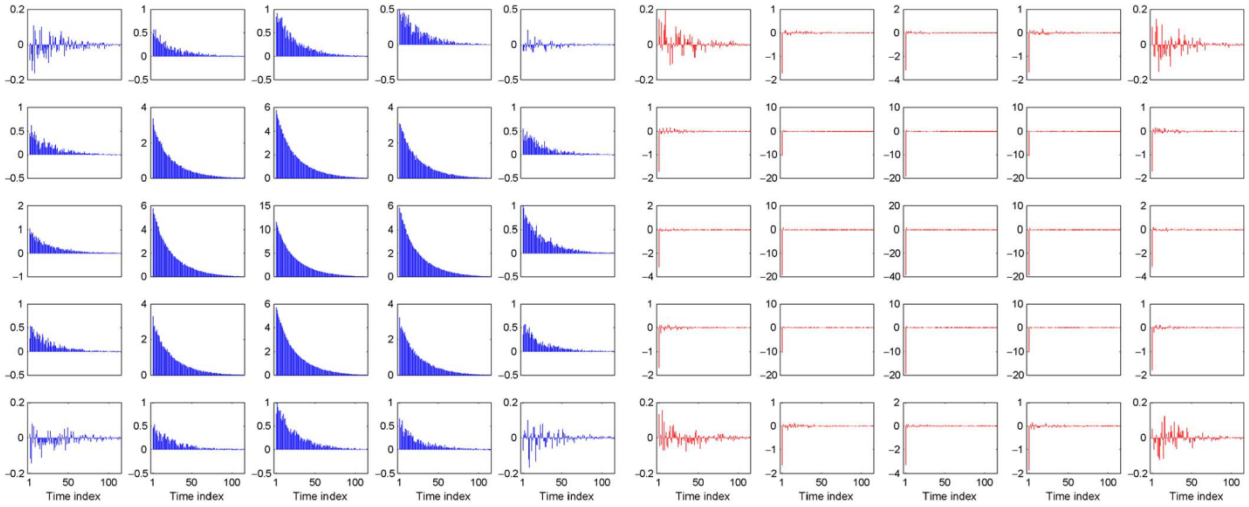

(a) Original Data (b) Projected data

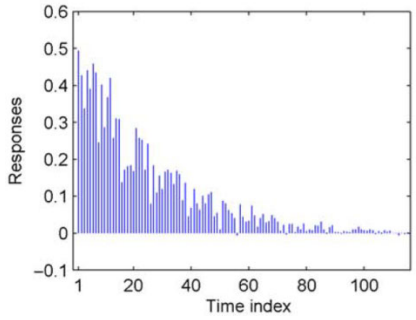

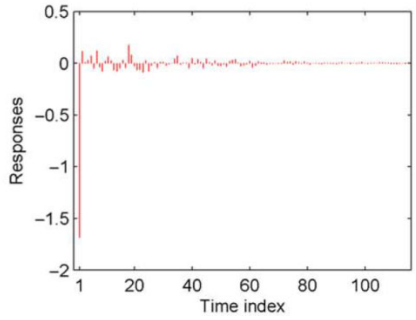

(c) Original data for Tx13, Rx4 (d) Projected data for Tx13, Rx4

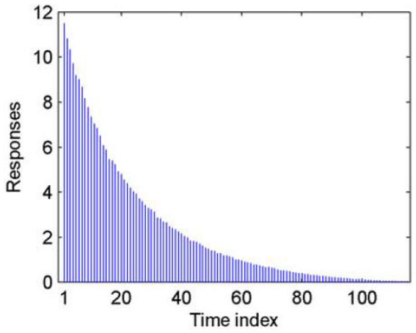

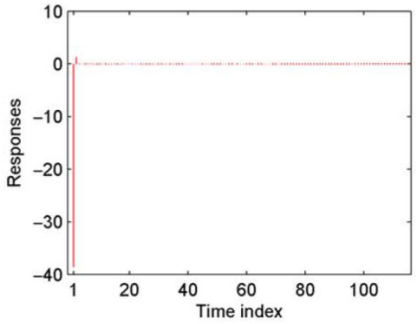

(e) Original data for Tx13, Rx13 (f) Projected data for Tx13, Rx13

Figure 22. Single-object case. 10% Noise. (a) Original data at 25 receivers with Tx-13 excitation. (b) Projected data at 25 receivers with Tx-13 excitation. (c), (d) Original and projected data of Tx-13/Rx-4 pair. (e), (f) Original and projected data of Tx-13/Rx-13 pair.

B. Synthetic Two-Object example

For a two-object example, we place a shallow object at $\mathbf{r}_2$ = (0.03, −0.01, −0.09) m and a deep object, a 105-mm projectile, at $\mathbf{r}_1$ = (0, 0, −0.60) m. The shallow object is horizontally oriented and the deep object is vertical. This simulates a practical scenario, where a piece of scrap is often buried at a shallow depth and a large UXO can penetrate into deep ground. Both polarizabilities are given in Figure 19(b). Different levels of Gaussian noise have been added to the data prior to input into the SVD. For the noise-free case, Figure 23(a) shows that both D and X have the five identical larger singular values. That is the number of distinct polarizabilities effected from a symmetric ordnance and a scrap. The remaining singular values of X and D, which ideally should be zero, are numerically small. The first five singular vectors are smooth and progressively display more zero crossings, whereas the other singular vectors behave randomly [see Figure 23(e)]. Based upon these eigen characteristics, one can define that the maximal dimension of the SS is 5 in this case. The rank of D in this case is 5. The situation changes when noise is added. Corrupting the data with 3%–10% noise produces singular values shown in Figure 23(b)–(d). The result is similar to that with a single object, where the addition of noise lifts the singular values. The three smaller signal singular values, observed in the noise-free case, are now buried in the noise. The ideal SS is also distorted by the noise. The singular vectors in Figure 23(f) associated with the three small signal singular values become oscillatory and behave like noise eigenvectors. Therefore, in these noisy examples, the effective rank, or the reduced SS of the data D, is 2 if we determine rank in terms of the significant singular values and associated smooth eigenvectors. This experiment illustrates that, in practice, one should be cautious about inferring the number of objects using a singular value spectrum.

To test the aforementioned analysis about the singular values/vectors for the 10% noise case, we first project the original signals using individual eigenvectors $\mathbf{v}_1$, $\mathbf{v}_2$, and $\mathbf{v}_3$ and the implement the TOPI, respectively. With $\mathbf{v}_1$ projection, the TOPI returns $\mathbf{r}_1$ = (0.00, −0.00, −0.61) m and $\mathbf{r}_2$ = (0.03, −0.01, −0.09) m. With the projected channel at $\mathbf{v}_2$, the TOPI returns $\mathbf{r}_1$ = (0.02, 0.02, −0.61) m and $\mathbf{r}_2$ = (0.04, −0.02, −0.08) m. The inverted locations of the objects in both cases are almost the same and close to the true values. However, using v_3 alone in the TOPI yields $\mathbf{r}_1$ = (0.43, −0.81, −0.72) m and $\mathbf{r}_2$ = (0.43, −0.81, −0.72) m. These are far from the true locations. Referring back to Figure 23(f), we see that $\mathbf{v}_3$ is a severely contaminated signal vector in contrast to the noise-free $\mathbf{v}_3$ in Figure 23(e). Thus, the inversion with $\mathbf{v}_3$ might be expected to be worse. The TOPI experiment demonstrates that the effective rank is 2, and this is consistent with the singular spectrum analysis. Nevertheless, this effective rank value cannot be used to infer that there is only a single object.

Next, we evaluate the TOPI using the channels projected onto the three subspaces of $[\mathbf{v}_1, \ldots, \mathbf{v}_j]$ (j = 2, 5, 10), respectively. These three subspaces contain the common signal eigenvectors $\mathbf{v}_1$ and $\mathbf{v}_2$. Not surprisingly, all inversions give almost exact results at $\mathbf{r}_1$ = (0.00, −0.00, −0.61) m and $\mathbf{r}_2$ = (0.03, −0.01, −0.09) m. These tests show that, like the single-object case, the TOPI is robust to a rank determination or a SS dimension if signal eigenvectors are included in the projection process. This numerical property of the TOPI is further illustrated in the following experiment.

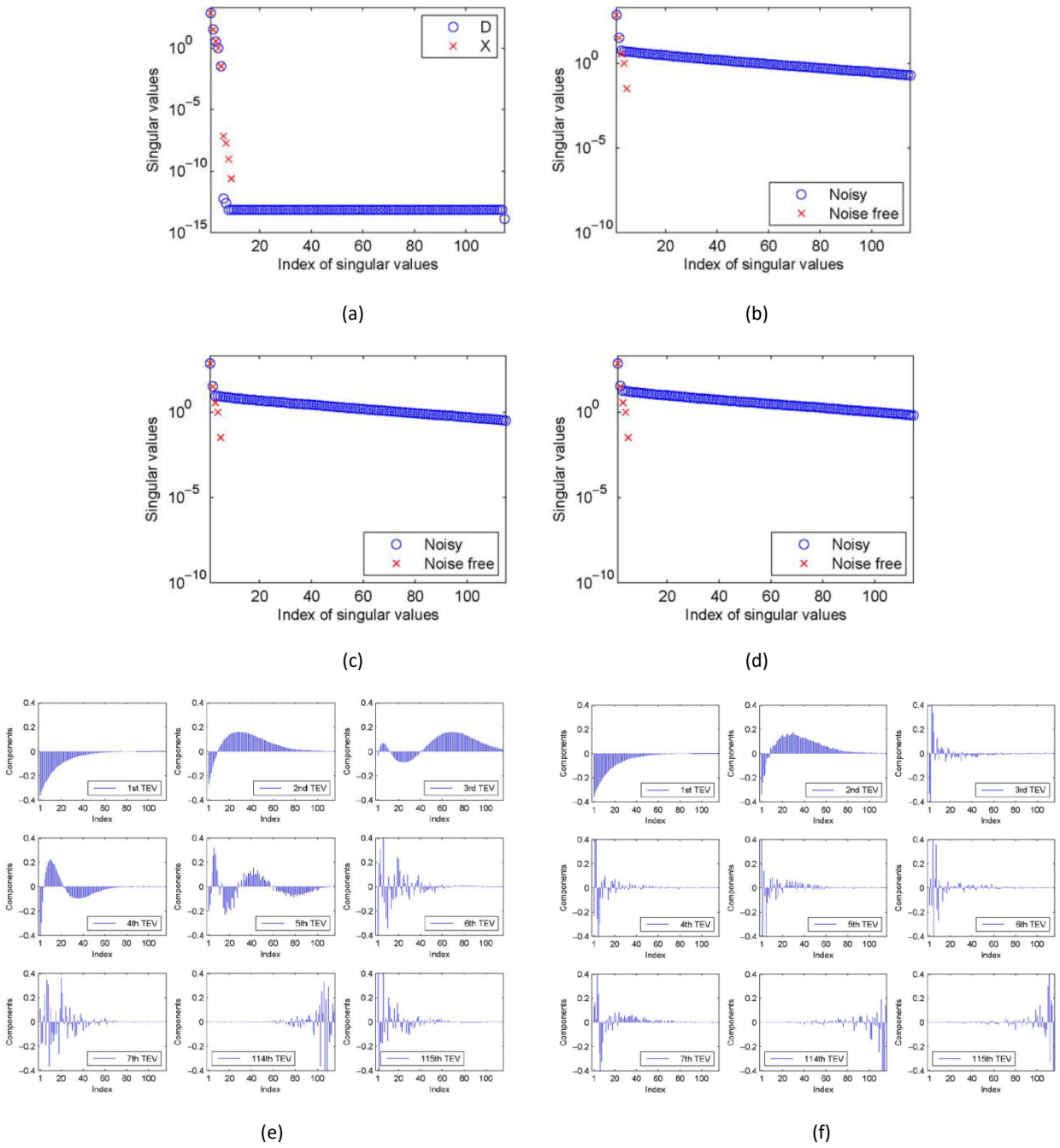

Figure 23. Two-object case. Singular values: (a) noise free; (b) 3% noise; (c) 5% noise; and (d) 10% noise. The first seven and the last two TEVs: (e) noise free and (f) 10% noise.

By including more eigenvectors, we extend the aforementioned tested subspace into $[\mathbf{v}_1, \ldots, \mathbf{v}_{39}]$. Projecting the original noisy data onto this subspace, running the TOPI with the 39 projected channels, we again obtain almost exact locations at $\mathbf{r}_1$ = (0.00, −0.00, −0.61) m and $\mathbf{r}_2$ = (0.03, −0.01, −0.09) m. The time taken to invert with 39 projected time channels was 0.13 min. We now compare these results with the inversion in the original data domain. The challenge with working in the original domain is deciding how many and which time channels to use. Certainly, late time channels can be problematic, but it is

difficult to decide where to make the cut. Here, we estimated that the first N_t = 39 time channels with time ranging from t_1 = 0.042 ms to t_{39} = 0.469 ms could be used. With this subset, the inversion yields $\mathbf{r}_1$ = (0.00, −0.01, −0.35) m and $\mathbf{r}_2$ = (0.14, −0.01, −0.02) m, which is a rather poor result; it also took 1.20 min. It is possible that different choices of time channels can still produce a good result. For instance, using the first N_t = 10 time channels produced the good locations at $\mathbf{r}_1$ = (0.00, −0.00, −0.61) m and $\mathbf{r}_2$ = (0.03, −0.01, −0.09) m). In the TOPI, we use all 115 time channels to construct TEVs. To be comparable to the TOPI, we tested the original data domain inversion using N_t = 115 time channels. The inversion gives $\mathbf{r}_1$ = (−0.01, −0.00, −0.45) m and $\mathbf{r}_2$ = (0.03, −0.01, −0.04) m). The inverted horizontal locations of the two objects are good. However, their inverted depths are shallower, shifted by −0.15 and −0.05 m as compared with true ones. It took 1.73 min. Unlike the TOPI, the simple use of all time channels in an inversion does not provide an optimal solution. The advantage of the TOPI is that much of the previous guessing about which time channels to use is removed, and the inversion with a few signal channels provides a more robust methodology. We next proceed with a real data example.

C. Real Data Example

For a real data example, we use the test-pit data collected over a 105-mm-HEAT (high explosive anti-tank) round. The length (head to tail) of the ordnance is 650 mm, and its body diameter is 105 mm. The object was oriented nose down and centered below the sensor array. The previous study [30] showed that this large, vertically oriented object is better represented by a two-object model.

Figure 24(a) shows the $\log \sigma_{ii}$ versus their indexes. There is a long tail of steadily decreasing singular values, which are indicative of noise. However, in this case, the noise may not be purely Gaussian and part may arise from the approximate modeling. There is no clear gap between the large singular values and the long tail of smaller values. The question of interest pertains to the rank of the system and the number of projected channels that should be used in the TOPI.

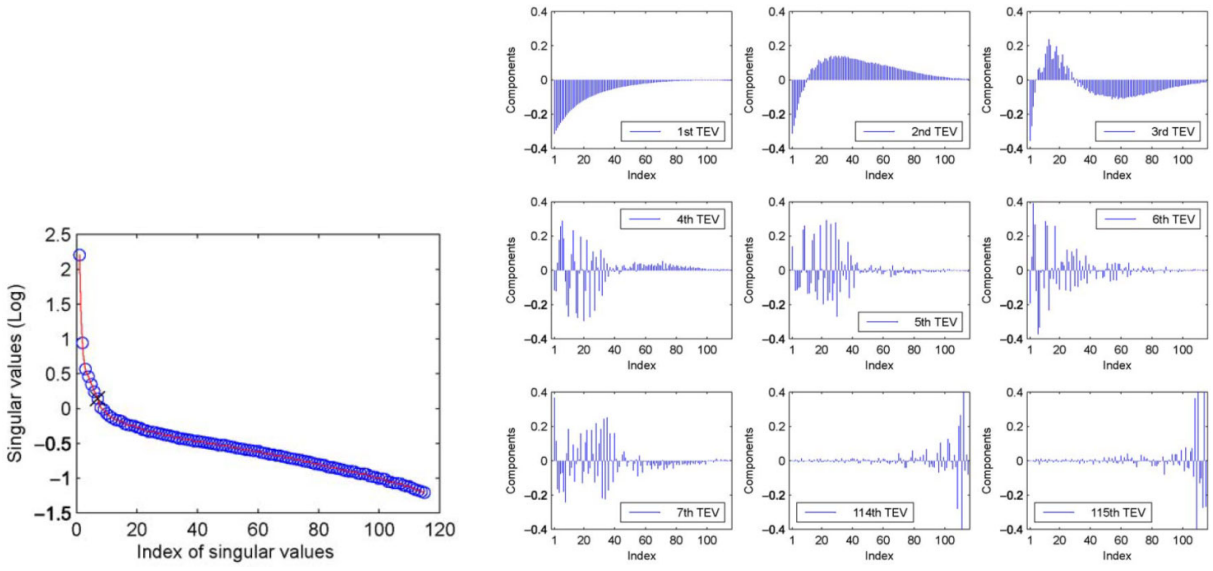

(a) Singular Values (b) The first seven and last two TEVs

Figure 24. Test-pit data. (a) Singular values. (b) The first seven and the last two TEVs

Suppose we have two objects and assume that principal directions are independent of time. Then, the maximum r is six. In addition, it is likely that the deep main part of the object is axisymmetric, whereas the nearer surface tail end is more 3-D and scrap like. If true, then the maximum rank would be five. Irrespective an estimate of the rank r can be made by the "kink" or location of highest curvature, in the singular value index space of Figure 24(a). This yields $\mathbf{r}$ = 7, and it is found as marked with a cross in Figure 24(a). This number is slightly larger than $\mathbf{r}$ = 5, or 6 assumed using the physics of the problem.

On the other hand, a useable rank can be determined by examining the TEVs. Figure 24(b) presents the first seven and the last two TEVs. The first three TEVs look like signal vectors seen in the synthetics. They are smooth and characterized by 0, 1, and 2 zero crossings. The remaining TEVs are more erratic and are characteristic of noise (Figure 24). From the insight provided by the TEVs we may infer the dimension of the reduced SS is $\mathbf{r}$ = 3.

Figure 25(a) shows the original data when Tx-13 was fired [the center transmitter, see Figure 19(a)]. The data measured at the center receivers have large amplitudes and decay smoothly; data at edge receivers have low amplitude and are noisy. From Figure 25(a), it is not straightforward to determine which combination of receivers and time channels should be used as input to the inversion.

The projected data are shown in Figure 25(b). As expected from our synthetic analysis, the maximum amplitude data are associated with the first few singular vectors, and in particular, the first one. A more detailed look is provided by Figure 25(c), which is the recorded data at Rx-1 due to an excitation of Tx-13. The data fluctuate, and responses at some time channels are larger or comparable to the responses at their preceding channels. In contrast, the projected data in Figure 25(d) show that the first temporal channel is roughly 3.1 times as large as the maximum amplitude of the original signals and is at least around 13 times as strong as the projected signals at subsequent temporal channels. A similar phenomenon is observed in Figure 25(e) and (f), where we show the recorded and projected data at Rx-13 from Tx-13. In this case, the projected signal at the first temporal channel is also about 3.1 times as large as the maximum amplitude of the original signals and is at least around 78 times strong as the projected data at subsequent temporal channels. This suggests that an inversion may be carried out using the projected data for the first temporal channel. This is further evident if looking back at the singular value spectrum. The amplitudes of singular values contain the information about the importance of the eigenvectors. One notices that σ_{11} is about 18 times larger than σ_{22} and it dominates the other singular values.

As aforementioned, the determination of r was analyzed from the known physics of the problem, singular value distribution, smoothness of the temporal singular vectors, and the behavior of the projected data. Numbers varied from one to seven. To further investigate the effects of different choices, we undertake the following analysis. We first perform the TOPI with individual vectors $\mathbf{v}_j$, j = 1, 2, 3, 4, 5, 6, 7. Table I lists the inverted locations. Both $\mathbf{v}_1$ and $\mathbf{v}_2$ produce identical locations for the large object but estimated depths for the smaller item differ by 12 cm. When any single vector from $\mathbf{v}_3$ onward is used the location estimates are quite inaccurate. Next, we test the TOPI using five different subspaces [$\mathbf{v}_1$, . . . , $\mathbf{v}_j$], j = 2, 3, 5, 7, 10 and attain all identical locations. For this real data example, the TOPI is robust to the selection of projected channels so long as at least one of the two main singular vectors are used.

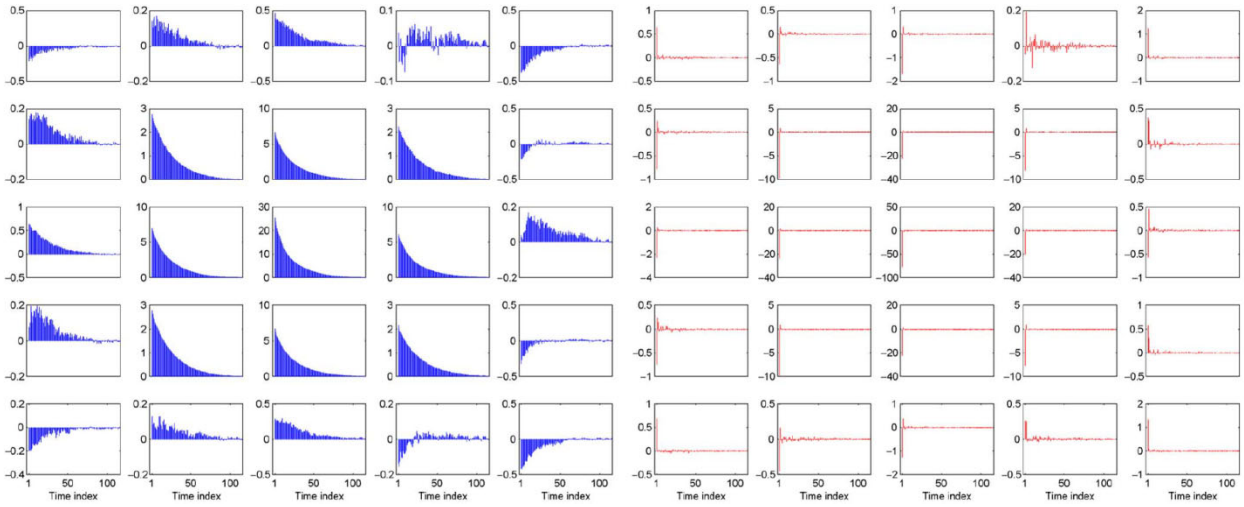

(a) Original Data

(b) Projected Data

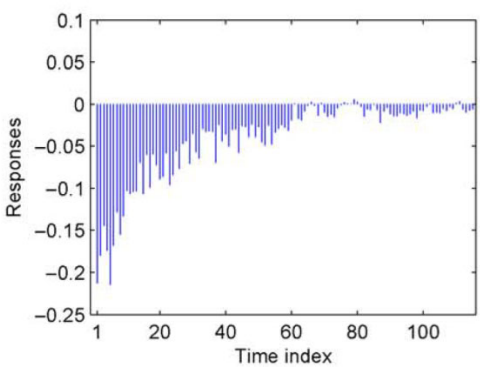

(c) Original Data, Tx13/Rx1

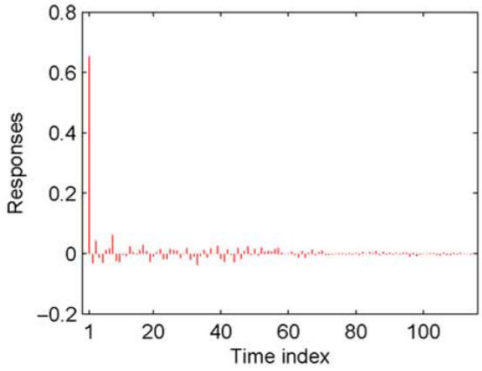

(d) Project Data, Tx13/Rx1

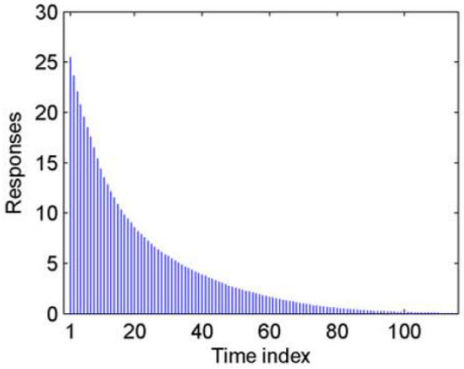

(e) Original Data, Tx13/Rx13

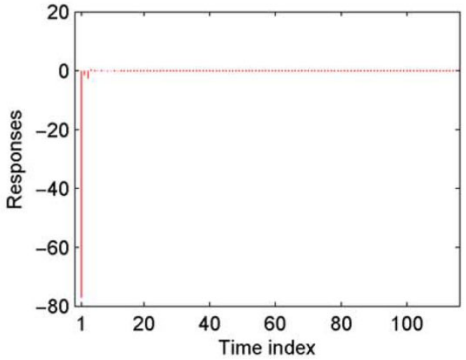

(f) Projected Data, Tx13/Rx13

Figure 25. Test-pit data. (a) Original data at 25 receivers with Tx-13 excitation. (b) Projected data at 25 receivers with Tx-13 excitation. (c), (d) Original and projected data of Tx-13/Rx-1 pair. (e), (f) Original and projected data of Tx-13/Rx-13 pair.

Further investigations can be carried out to observe the impact of the signal vector $\mathbf{v}_1$. We form the following subspaces by excluding $\mathbf{v}_1$, i.e., [$\mathbf{v}_2$, $\mathbf{v}_3$], [$\mathbf{v}_2$, . . . , $\mathbf{v}_4$], [$\mathbf{v}_2$, . . . , $\mathbf{v}_5$], and [$\mathbf{v}_2$, . . . , $\mathbf{v}_7$]. The results are summarized in Table I. All subspaces return almost the same location. The situation changes when the two major signal vectors $\mathbf{v}_1$ and $\mathbf{v}_2$ are omitted. When the TOPI is carried out with the subspaces [$\mathbf{v}_3$, $\mathbf{v}_4$], [$\mathbf{v}_3$, . . . , $\mathbf{v}_5$] and [$\mathbf{v}_3$, . . . , $\mathbf{v}_7$] erratic results are obtained for r_1 but r_2 are consistently estimated. We conclude that the signal vectors associated with the two large singular values have information about both shallow and deep objects, whereas the next few vectors have information primarily about the shallow object.

Table 1. TOPI with single vj and various subspaces in the real data example. In this table, V1j = [v1,...,vj], j=2,3,5,7,10. V2j=[v2,...,vj,j=3,4,5,7

TEVs	(x_1, y_1, z_1) (m)	(x_2, y_2, z_2) (m)
$\mathbf{v}_1$	(0.02, -0.01, -0.61)	(0.03, -0.01, -0.27)
$\mathbf{v}_2$	(0.02, -0.02, -0.61)	(0.04, -0.02, -0.15)
$\mathbf{v}_3$	(0.04, -0.33, -0.85)	(0.03, -0.33, -0.21)
$\mathbf{v}_4$	(0.26, 0.26, -0.01)	(0.26, 0.26, -0.01)
$\mathbf{v}_5$	(-0.50, -0.48, -1.20)	(-0.44, -0.50, -1.20)
$\mathbf{v}_6$	(-0.47, -0.50, -1.01)	(-0.47, -0.50, -1.01)
$\mathbf{v}_7$	(0.50, 0.26, -1.20)	(0.08, 0.56, -1.20)
V_{1j}	(0.02, -0.01, -0.60)	(0.03, -0.01, -0.26)
V_{2j}	(0.03, -0.02, -0.58)	(0.04, -0.02, -0.20)
$[\mathbf{v}_3, \mathbf{v}_4]$	(0.48, 0.36, -0.80)	(0.03, -0.03, -0.20)
$[\mathbf{v}_3, \mathbf{v}_4, \mathbf{v}_5]$	(-0.09, -0.50, -1.2)	(0.04, -0.02, -0.20)
$[\mathbf{v}_3, \cdots, \mathbf{v}_7]$	(-0.04, -0.50, -1.2)	(0.04, -0.02, -0.20)

Overall, the aforementioned tests show that the inclusion of the signal vectors [$\mathbf{v}_1$, $\mathbf{v}_2$] is sufficient to recover the locations via the TOPI. This is consistent with observations in the numerical experiments. The TOPI-recovered polarizabilities are given in Figure 26(a) and (b) for $\mathbf{r}$ = 1, 7, where the red curves represent the known polarizabilities of the 105-mm projectile, and the blue and black curves represent the recovered ones. To test the sensitivity of inversions to the selection of time channels in the original domain, we invert responses from different subsets of time channels. Generally, responses at early time channels are less prone to be noisy but the choice of the latest time to be used is difficult to assess. Here, we use responses from the first 51, 16, and 13 channels (i.e., N_t = 51, 16, 13), respectively. The first time channel is 0.042 ms and the last is, respectively 0.89, 0.124, and 0.101 ms. Similar to the two-object synthetic case, we also present the inversion with N_t = 115 time channels that are used in constructing the TOPI. Figure 26(c)–(f) present the associated inversion results of the recovered locations and polarizabilities. Using N_t = 115, 51 or 16 produces less accurate results and there is substantial difference between N_t = 16 and N_t = 13. Likely, the noise is starting to become significant in that range [see Figure 26(d) and (e)]. The result of N_t = 115 is somewhat better than those of N_t = 51 or 16 but is not optimal. In contrast, the TOPI is not sensitive to the subspace-based channel selection. In this example, the effective rank, based upon the shape of the TEVs, is estimated to be three. The TOPI returns almost identical results for inversions with rank $\mathbf{r}$ = 1, 2, 3, 5, 7, 10. This parallels the results obtained in synthetic experiments. This suggests that the new algorithm is much more robust w.r.t. the

inclusion of noise vectors and has greater potential for providing a stable correct result [e.g., Figure 26(a) and (b)].

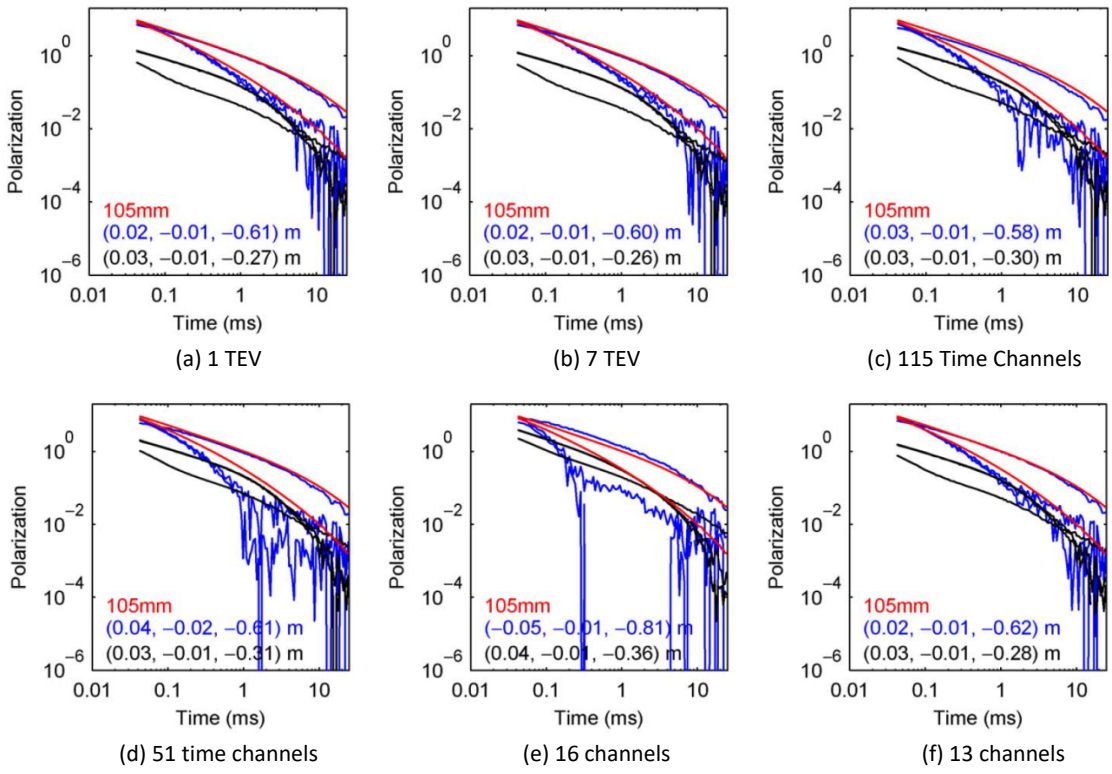

Figure 26. Recovered polarizabilities from test-pit data. TOPI: (a) 1 TEV, (b) 7 TEVs. Inversion of original data with time channels of: (c) 115, (d) 51, (e) 16, and (f) 13. On the polarization plots, the red curves represent the known polarizabilities of 105-mm projectile and the blue and black the recovered ones.

5. Conclusion

We have considered the problem of inverting multiple time channel TEM data. Tests showed that the accuracy of source localization via a traditional nonlinear inversion can be critically dependent upon the selected time channels. To address this problem, we propose a TOPI method that circumvents either the manual choice of which channels to select or the difficult task of estimating the unknown noise. The method has four steps:

1) perform the SVD of the STRM;

2) project the STRM onto the temporal SS matrix;

3) compute source locations in the projected temporal domain; and

4) obtain target polarizabilities in the original data domain.

A key step in the method is to determine the number $\mathbf{r}$ of temporal signal vectors used for projection. Information about r can be obtained from the spectrum of singular values, from the shape of the TEVs, from the values of the projected data, and from the fundamental physics of the problem. One feature that seems particularly diagnostic is the shape of the TEVs. Specifically, signal eigenvectors are smooth

and have only a few polarity changes, with generally one additional zero crossing per unit increase in rank. Noise eigenvectors are oscillatory and have a random behavior. As a result, the projected TEM responses are associated with a few early temporal indexes, and the transformed responses are suppressed at subsequent channels. Therefore, the oscillating properties of the TEVs or highly compressed projected responses make the selection of projected temporal channels easy. Moreover, tests show that the TOPI returns almost the same result with various $\mathbf{r}$ values whenever signal vectors are included. In other words, the TOPI is robust to the size of a SS. In contrast, the usual inversion in the original domain is sensitive to channel selection and can derive poor results in case of inappropriate selection.

In comparison with the standard nonlinear inversion method implemented in original time-channel domain, the TOPI can be a potentially practical tool that is not only computationally efficient but also is able to produces more accurate results since a substantial portion of the noise in the data is automatically winnowed from the analysis.

Using an equivalent source methodology for target picking (1): Data reconstruction and denoising

We have investigated a technique where full coverage DGM data is inverted for multiple sources, and these sources can be used to in data amplitude based or source clustering-based target picking algorithms. In this approach, we define a uniform grid of overlapping data tiles across the site. Each of the data tiles are then inverted for multiple dipole sources. To reduce computational time, we have often used the Temporal Orthogonal Projection Inversion described in the previous section.

The resulting set of sources can then be used to reconstruct the sensor data. Since the data is being represented by dipole sources, the high frequency along-line noise is not reproduced, resulting in a smoother, higher SNR version of the data. As an example, we consider data collected by the MetalMapper as part of the ESTCP Live Site study at Camp Ellis. Figure 27(a)-(c) show the x, y, and z component of t=0.136ms data acquired over a 15m subset of the data. The data is from a part of the site with higher target densities (Figure 27(d)).

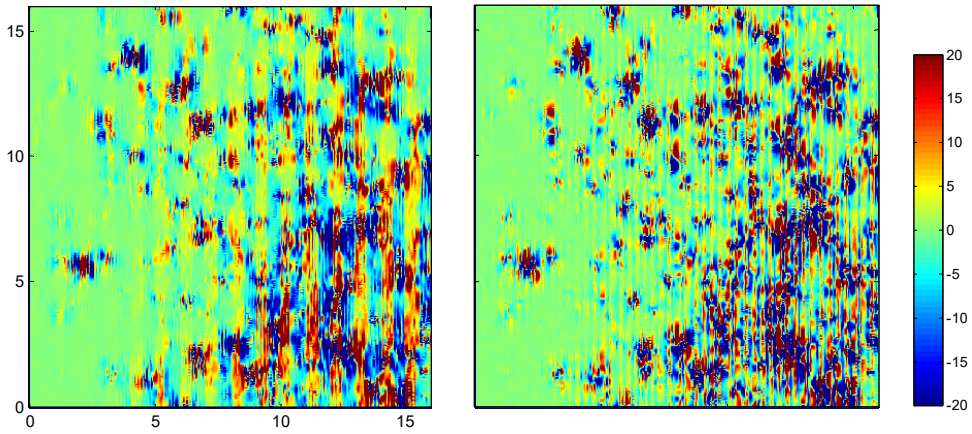

(a) x-component data (b) y-component data

(c) z-component data (d) location of data

Figure 27. Example of dynamically acquired MetalMapper data from Camp Ellis. Data from time channel t=0.136ms is gridded.

Due to the geometry of the MetalMapper (Figure 28(a)) anomalies in the gridded data image can appear complex – in particular for near surface targets – and the traditional method of applying a peak picking algorithm so image data would produce multiple spurious picks. Prior to the use of dipole source methods for target picking, a common practice was to omit the outer cubes when gridding data. This data subset was often referred to as "Split-cube 5" data. This approach does not utilize all the available data.

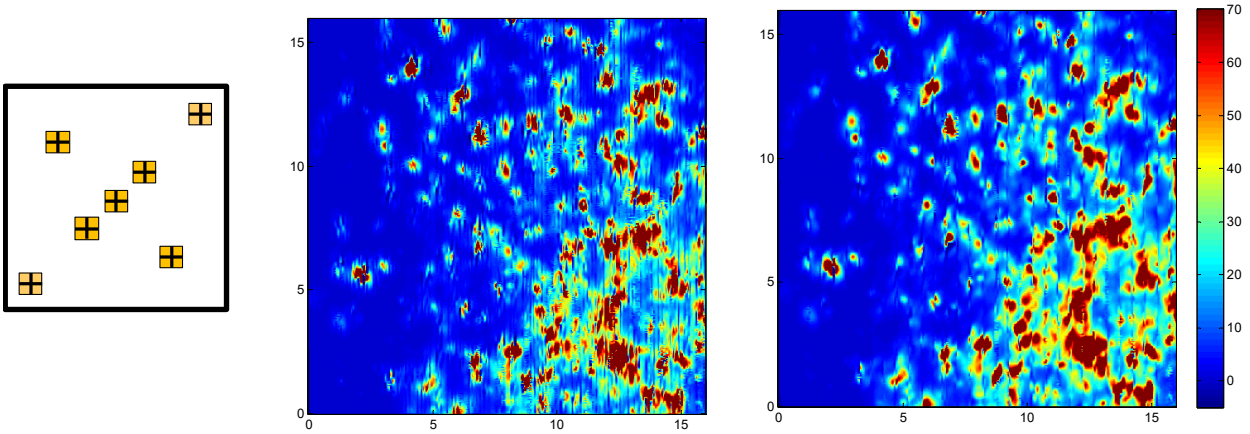

(a) Receiver locations (b) "Split-cube" 7, z-component (c) "Split-cube" 5, z-component

Figure 28. Comparing "Split Cube 7" and "Split Cube 5" gridded data.

The data in Figure 27 was used to demonstrate the equivalent source approach. Over the region of interest, we define a uniform grid of square tiles. All 21 Rx/Tx combinations within each data tile is inverted for multiple sources. Although we have used up to 5 sources to reproduce the data, we use only 3 sources for this example. In this example, we use the TOPI method outlined in the previous section. The resulting set of sources can then be used to reconstruct the data. At the locations where the data overlap, the predicted response is averaged. Figure 29 shows how the set of sources reproduce the data. By using the positioning and orientation information of the instrument, the sources are able to accurately reproduce the features in the dataset (Figure 29(d)-(f)).

Once a set of dipole sources that can accurately reconstruct the data are obtained, they can be used to in a number of different ways to assist in target picking. For example, if we want to use a peak detection algorithm applied to gridded image data or profile data, the dipole sources could be used to forward model survey data. The peak detection approach can be improved using modelled data for the following reasons:

- The resulting modelled data increases the SNR of the data, since the dipole sources are unable to model the high spatial frequency noise of the survey.
- The picking threshold is usually set to account for variations in elevation or ground clearance height. It is possible to model forward the model sources with the assumption that the instrument surveys on a level plain. This will also reduce perturbations in anomaly shape due to sudden changes in instrument standoff. A higher picking threshold could be defined.

- The threshold is often controlled by line-spacing. It is possible to model tighter line spacing. In this sense, the equivalent source technique can be thought of a way to grid one component of the data, but using all the other components were used to help interpolate.

Figure 30 shows an example of forward modeling the sources. A coaxial, z-component dataset is constructed such that an image-based target picking method be used. There would be fewer spurious picks due to reduced noise and simplified anomalies from the mono-static geometry.

Another approach to target picking is to use the sources rather than the data. We have developed a target picking method that uses a source clustering algorithm to identify likely sources. In this approach, we invert the data tiles using 1, 2, and 3 source inversions. Since the tiles overlap, there would be multiple inversions that could place a source at the location of a target, i.e., there would be a cluster of sources that would coincide with the target. In this approach, we define a target pick to be any location where some minimum number of sources are located. We demonstrate how this approach works in the Section "Using an equivalent source methodology for target picking (2): Source clustering".

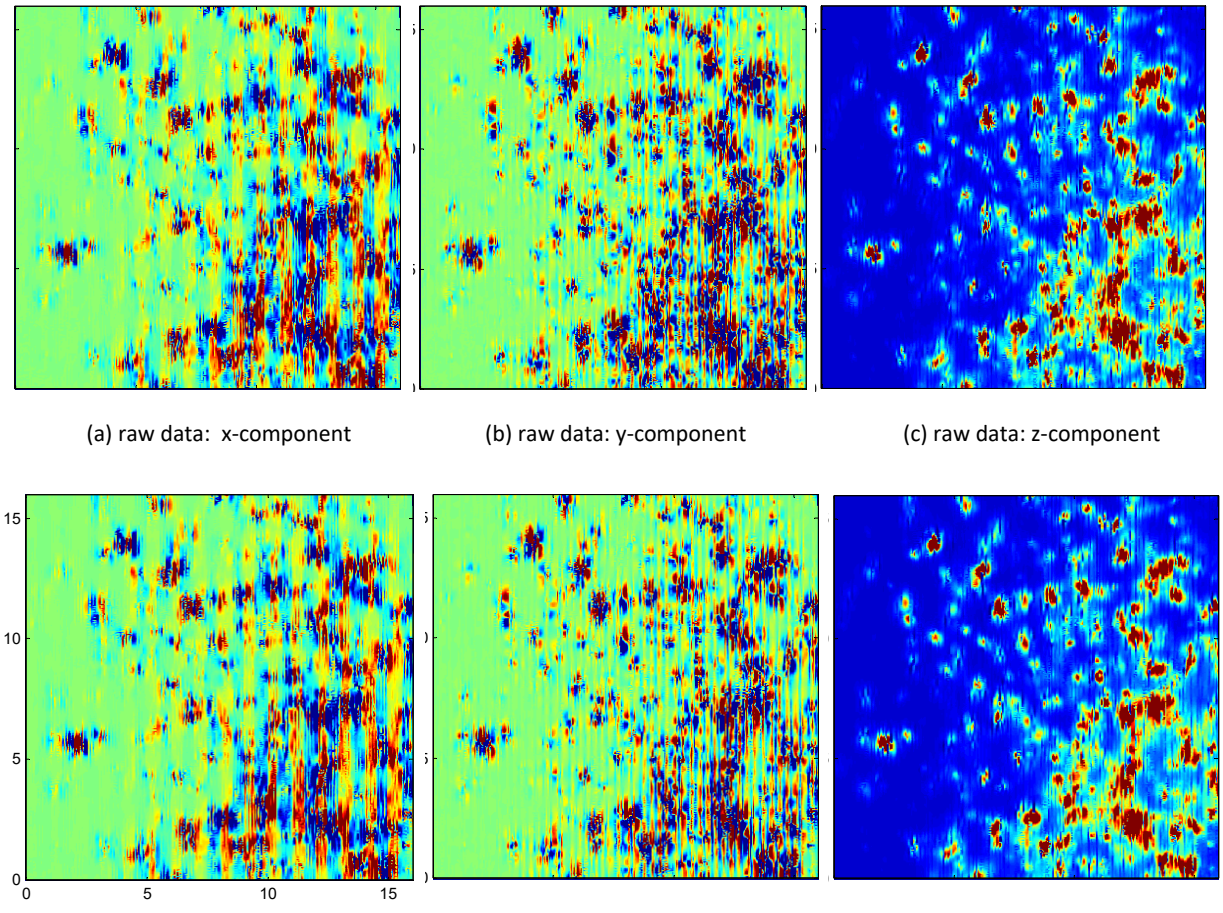

(a) raw data: x-component (b) raw data: y-component (c) raw data: z-component

(d) constructed data: x-component (e) constructed data: y-component (f) constructed data: z-component

Figure 29. Data modelled with equivalent sources

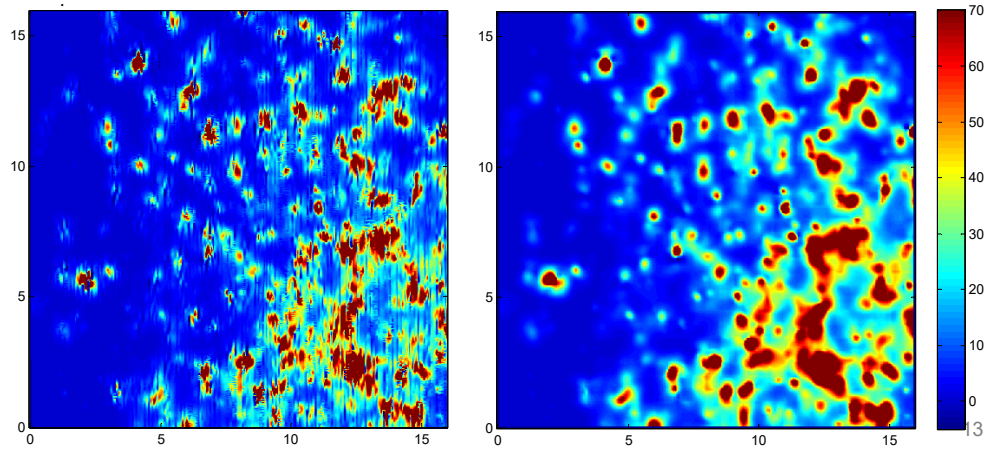

(a) Raw data, z-component, “Split-cube 7” (b) Constructed: Mono-static, z-component

Figure 30. Constructing a data map that is easier to interpret and use for target picking. Time = 0.136ms.

Limitations of Image based picking algorithms

The use of Geonics EM61 MKII data for target detection is still common practice within the UXO industry. The Geonics EM61 MkII uses a single 0.5m x 1.0 m transmitter coil and a pair of coaxial receiver coils. Due to the monostatic nature of the data and limited time decay window, inversion-based target picking approaches are generally not a good idea. The standard approach is to grid a time channel of data, and use an image-based picking algorithm.

On a recent project, there was a discussion on whether it was sufficient to use a 3-coil array with 1 m line spacing, or if it was necessary to use a 5-coil array such that the cross-track separation was only 0.5 m. Figure 31 demonstrates the importance of line-spacing on image based target picking. In this example, we synthetically create data for three small ISO's oriented vertically. Each ISO is buried at a depth of 20cm, and the location of the ISO's are indicated by white box, circle, and triangle. The data are gridded using a thin plate spline interpolation. The data are scaled, such that the maximum value is equal to one. Peaks in the image are indicated by a yellow star.

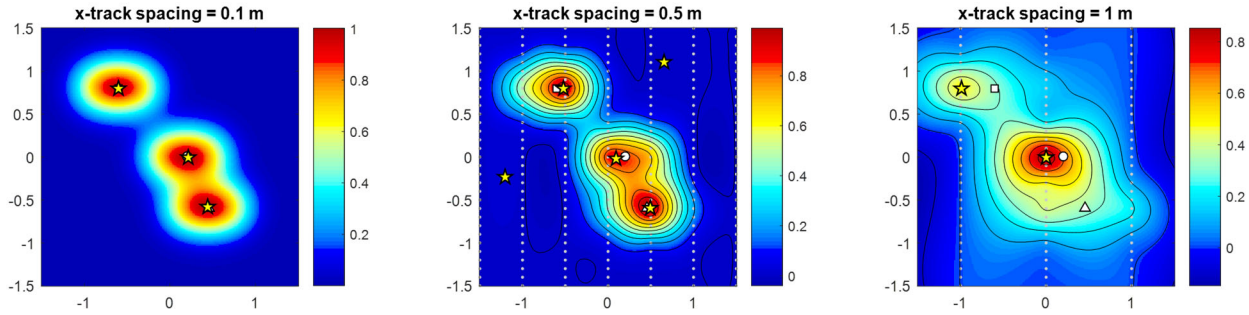

(a) line spacing = 0.1 m (b) line spacing = 0.5 m (c) line spacing = 1 m

Figure 31. Effect of line spacing on EM61 data.

For a line-spacing of 0.1 and 0.5 m, there are distinct peaks near the location of the targets. If you look at the target in the top left (square), we see that the accuracy of the pick decreases with increased line spacing. Indeed, the pick location for an isolated target has a potential error of ½ the line spacing. The target in the bottom right (triangle) is an example of the case when insufficiently sampling data results in losing a peak associated with a target. The closest pick is located 75 cm from the target. For both the upper left (square) and center (circle) targets, a follow-up cued measurement will likely find the correct target location via in-field QC and inversion. However, the bottom right target would be missed.

In addition to line-spacing, the coil size plays a role in the ability to resolve targets. Figure 32compares the vertical component coaxial data due to 3 vertical targets: a small ISO at a depth of 15cm, a medium ISO at a depth of 30cm and another small ISO at a depth of 5cm. Figure 32(a)-(c) plots the gridded response for a system with the coil geometry of a TEMTADS system, and Figure 32(d)-(f) plots the gridded response for an EM61MK2 cart. Due to the size and the square shape of the TEMTADS system, the TEMTADS anomalies are more compact and symmetrical. The three targets produce three distinct peaks in the data (note: peaks are indicated by yellow stars). Since the measured voltage in the receive

coils is an integration of change in flux over the surface of the receiver, the larger, rectangular EM61 coils produces a more “smeared” image. Indeed, when looking at the response of all the targets, the anomalies of the three target anomalies overlap and there are only two peaks in the data.

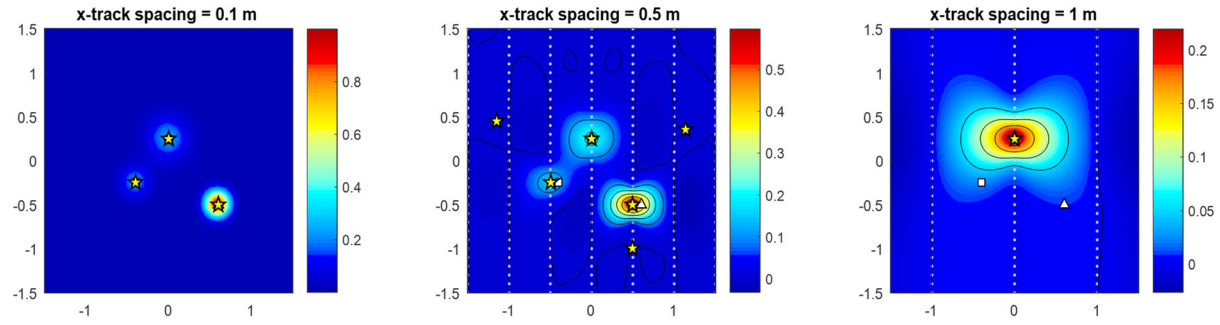

(a) TEMTADS: line spacing = 0.1m (b) TEMTADS coils: linespacing = 0.5m (c) TEMTADS coils: line spacing = 1.0m

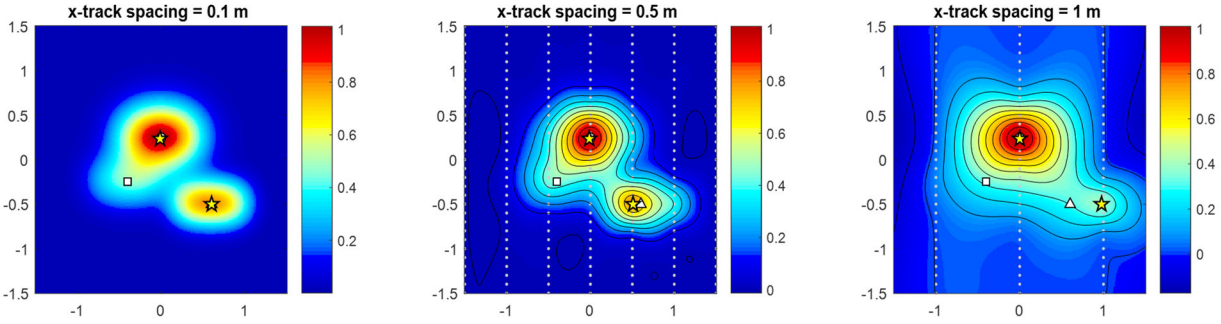

(a) EM61MK2: line spacing = 0.1m (b) EM61MK2: line spacing = 0.5m (c) EM61MK2: line spacing = 1.0m

Figure 32. In this example, there are 3 vertical targets: a small ISO at (x,y)=(-0.40, -0.25)m and depth of 0.15m, a medium ISO at (x,y)=(0.00,0.25)m and depth of 0.30m, and a small ISO at (x,y)=(0.60,-0.50)m and depth of 0.05m.

Acquiring data at 0.5 m line spacing does not produce a difference in the ability to resolve the targets. If we acquire data on 1 m line spacing it actually helps to have the larger coils, as the smaller coils of the TEMTADS would not be able to produce a peak. Of course, an actual TEMTADS sensor has coils arranged in a 2x2 configuration, such that the across track spacing is 40 cm.

Figure 33 demonstrates how horizontal targets can cause difficulties with target picking. A horizontal, rod-like target can produce a “dumbbell” shaped, two-peak anomaly. The distance between peaks is a function of the transmitter coil size. For horizontal targets, the two-peak anomaly can result in peak locations that are far from the target. In this example, the two-peak anomaly screens out the small ISO and scrap, i.e., there is no distinct data anomaly peak related to the small ISO and scrap.

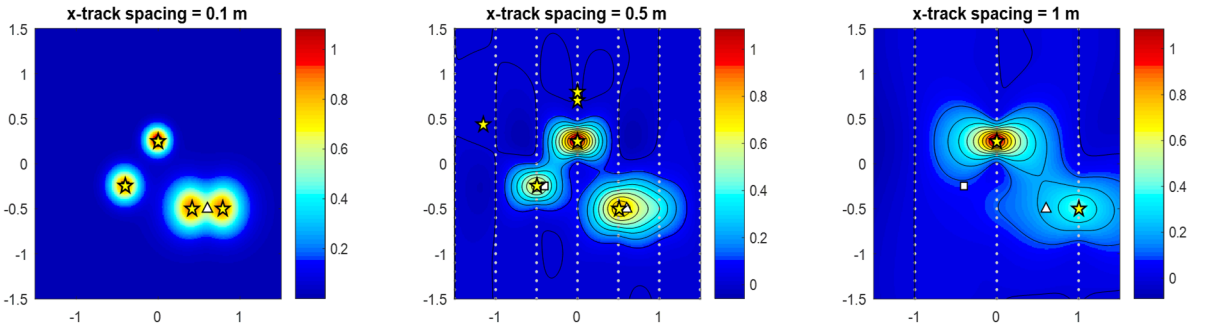

(a) TEMTADS: line spacing = 0.1m (b) TEMTADS: linespacing = 0.5m (c) TEMTADS: line spacing = 1.0m

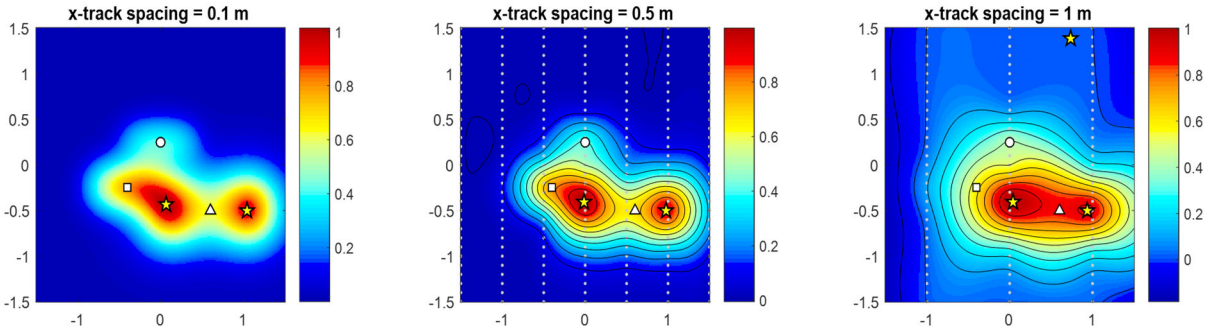

(a) EM61MK2: line spacing = 0.1m (b) EM61MK2: linespacing = 0.5m (c) EM61MK2: line spacing = 1.0m

Figure 33. In this example, there are 3 targets: a vertical small ISO at (x,y)=(-0.40, -0.25)m and depth of 0.15m, a vertical small scrap at (x,y)=(0.00,0.25)m and depth of 0.05m, and a horizontal 2.75" rocket at (x,y)=(0.60,-0.50)m and depth of 0.20m.

Simulations for determining the limitations of target picking from images

To understand the limitations of image-based target picking methods with the Geonics EM61, we simulate full coverage survey data and determine if there are anomalies corresponding to synthetically emplaced targets. In particular, we want to determine the effect of line-spacing and target density on the number of targets missed at a site.

The objective of these simulations is to determine the frequency with which there are targets that do not have target pick within 60 cm. That is, we want to find instances in which the gridded data does not produce a distinct peak within 60 cm of the target. We choose 60 cm as threshold, because exceeding this threshold would result the follow-up cued measurement possibly being unable to resolve the target accurately. For this experiment, we simulate data over a 50 m x 50 m grid, with 100 data realizations. For each 50 m x 50 m grid, we assume a uniform spatial distribution of targets across the grid. We use three targets:

- 80% 20mm, max depth of 15 cm
- 10% small ISO, max depth of 25cm
- 20% medium ISO, max depth 45 cm

A uniform depth distribution is assumed for each target. No noise is added to the data. Therefore, the results of these simulations represent the upper limit of performance that we could expect for image-based target picking.

Figure 34 contains examples of modeling results for 19 and 162 targets/acre, along with histograms indicating the offset of the closest pick to the seeded target. For these data, we assume a line spacing of 1m. In the presentation of the simulated data, the seed locations are indicated by white squares, the location of anomaly peaks (i.e., target picks) are indicated by grey triangles. Targets with a closest pick that is greater than 0.6 m is marked with a red square.

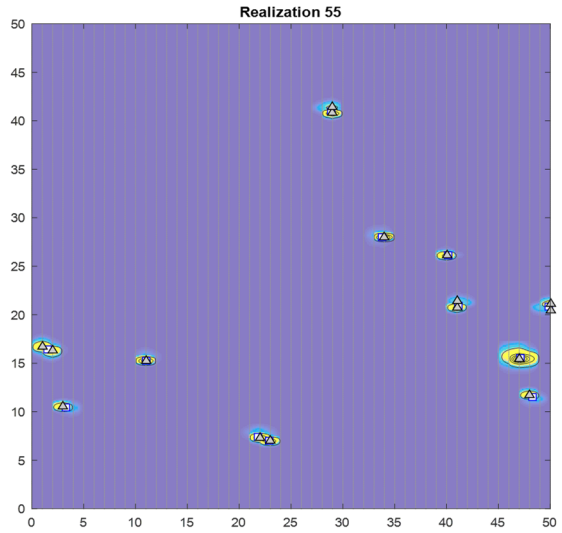

(a) Example of 50m grid with 19 targets/acre

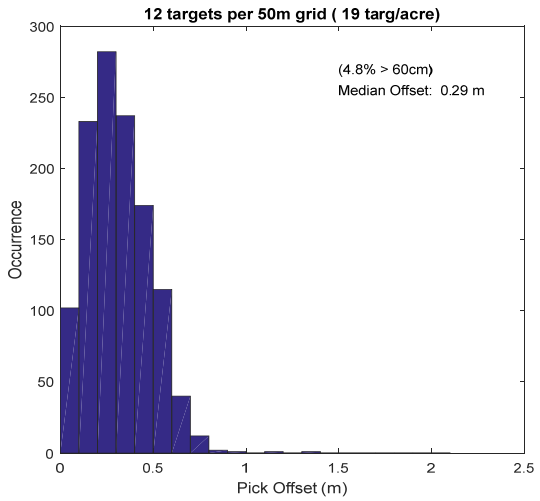

(b) Offset of distribution of peak detector

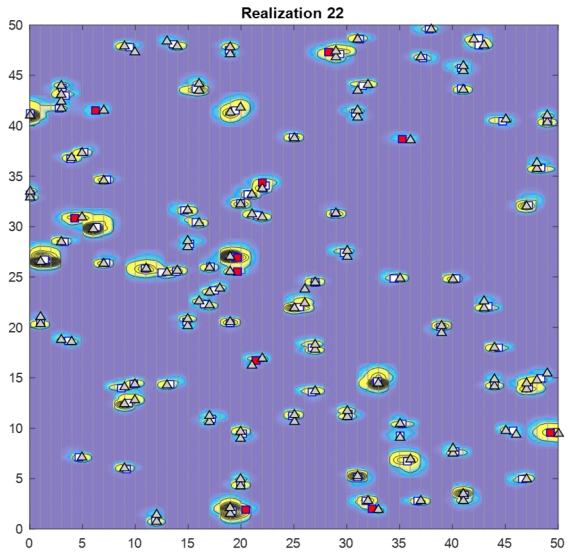

(c) Example of 50m grid with 162 targets/acre

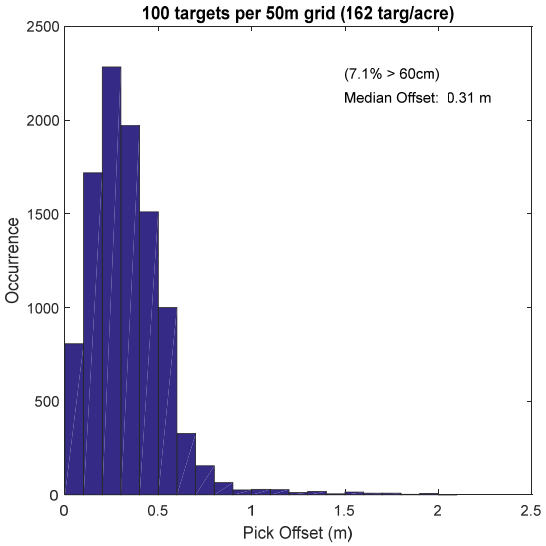

(d) Offset of distribution of peak detector

Figure 34. Effect of target density on target picking offset. White squares show where there are targets, grey triangles indicate target picks, and red squares indicate targets whose closes pick is greater than 0.6 m away. Data were simulated assuming a 1 m line spacing.

For both target densities, the median offset is approximately 30 cm. The tail of the distribution is larger for the higher density example. The percent of targets with a target pick greater than 60 cm away is slightly greater for the higher density case (i.e., 4.8% vs 7.1%). This result is consistent with the idea that missed targets can be due to multi-object scenarios. An example of a missed target is shown in Figure 35.

If the line spacing in the 162 target/acre example of Figure 34 is reduced to 0.5 m, the percentage of targets with a pick greater than 60 cm is reduced from 7.1% to 1.7 percent, and the median pick offset decreases from 31 cm to 26 cm. A comparison of pick offset histograms is found in Figure 36.

The simulations were carried out for a range of target densities. Figure 37 summarizes the results. There is an approximate linear relationship between target density and the percentage of targets that have a pick offset greater than 60 cm. There is a significant improvement in the target picking performance when reducing the line spacing from 1 m to 0.5 m.

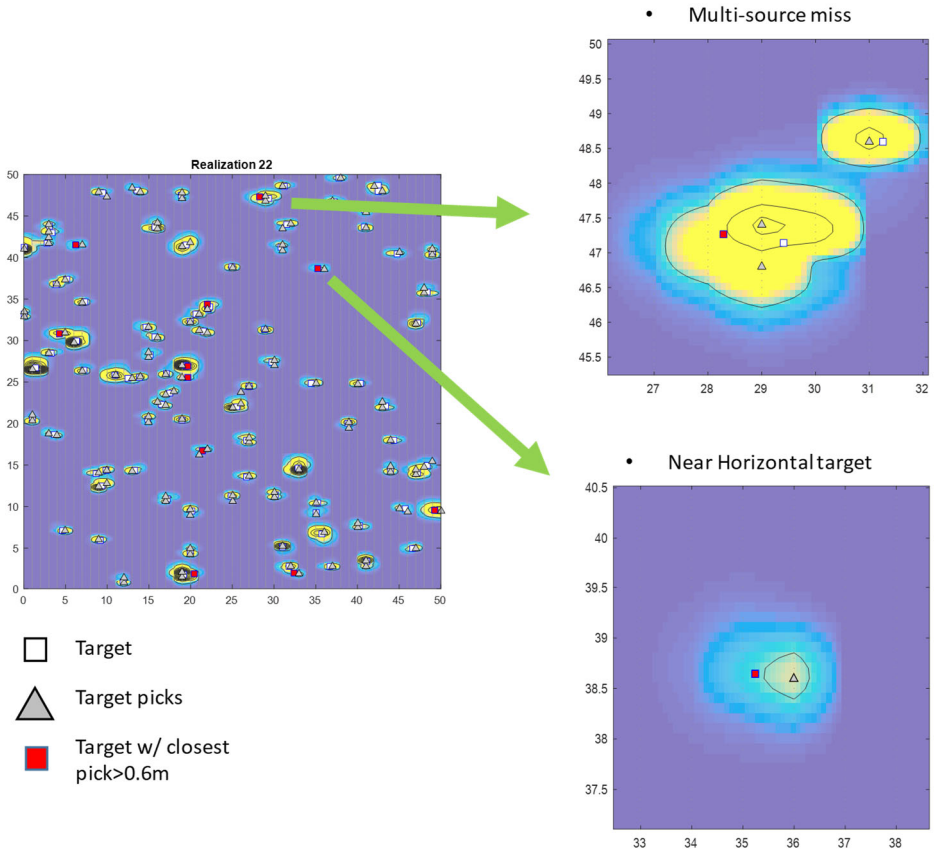

Figure 35. Example of missed targets in Realization 22. For this modeling, we assumed 1m line spacing and a density of 162 targets/acre. On the right, we include a pair of examples of inaccurate or missed picks.

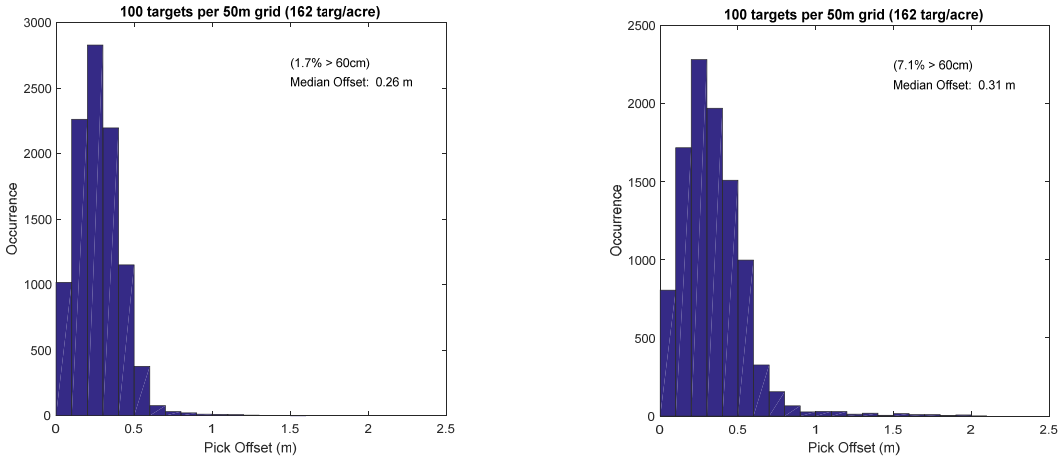

(a) Line spacing = 0.5 m (b) Line spacing = 1.0 m

Figure 36. Effect of line spacing on target picking accuracy

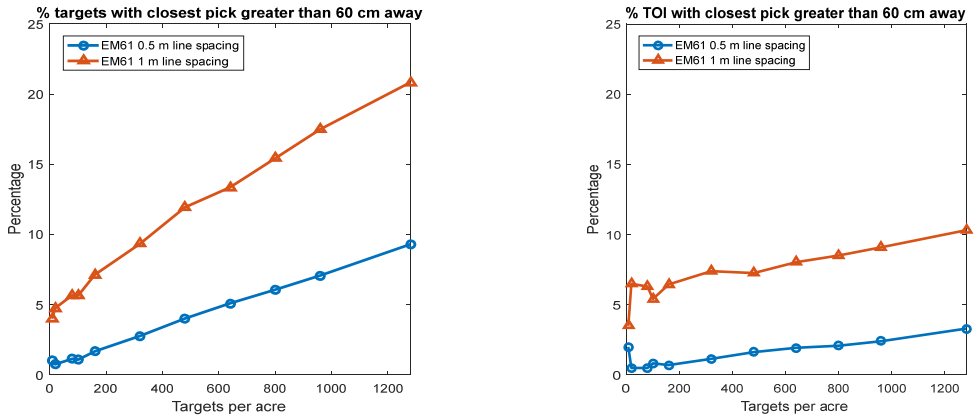

(a) All targets (b) Only small and medium ISOs

Figure 37. Comparison of different survey types for a range of target densities. In (a), we consider all target types (i.e., 20mm, small ISO and medium ISO). In (b), we only consider small and medium ISOs. For low target density, there is uncertainty in the percentage estimates due to fewer samples.

In Figure 37(b), we only consider the small and medium ISOs as TOI, omitting the 20 mm. The percentage of missed targets decrease, since the small and medium ISOs would produce a larger signal than the 20mm targets in most cases. Therefore, it would be less likely that the 20mm would shield the small and medium ISO to the extent they were missed. At lower target densities there is some uncertainty in the number of missed targets due to small number of samples.

Using simulations to estimate risk of missing a TOI when using image based EM61 target picking

During a recent project, we wanted to determine the risk of missing a TOI when using an EM61 MK2 array. In addition, we wanted to know whether there would be a significant difference when using an array with 0.5m coil spacing or 1.0m coil spacing. Intuitively, we would expect the likelihood of a missed TOI to increase as the line spacing and target density increases. In order to answer these questions, we applied the Monte Carlo type modeling approach described in the previous section.

For the project being modelled here, the EM61 data would be used to determine locations for a follow up TEMTADS 2x2 cued measurement. In the case where a target pick could be >60 cm away from the target, if there is target pick error is due to a multi-target scenario, we label the target as a miss. However, if the target is isolated and may be found through in-field inversion, we do not label the target as a miss.

For this study, we wanted to determine the likelihood of missing a 2.75" rocket to a maximum depth of 60 cm. In addition to the 2.75" rocket, we also model 20 mm projectiles to a maximum depth of 15 cm. Since we wanted to assess detectability of the 2.75" rocket amongst near surface, smaller scrap, we decided to let the 20 mm will play the role of scrap. Although we list the 20mm as scrap, the ability to detect all targets, as well as only the TOI, are reported. Both targets are uniformly distributed across the grid, and have a uniform depth distribution. Similar to the previous section, we do not add noise to the data – we focus on whether target density and line-spacing would cause targets to have missing anomaly peaks.

We assume 30,000 anomalies over a 1000-acre site. The site model consists of a lower density area and a higher density area. The lower density area is assumed to have 22 targets/acre with 2.5% of the targets being TOI. We estimated that the higher density region is approximately 67 acres, we assume a density of 135 targets/acre. We will calculate results for 2.5% and 5% of targets being TOI. Therefore, there are four scenarios that will be simulated:

1. 1 m line spacing, 5% TOI in higher density region
2. 1 m line spacing, 2.5% TOI in higher density region
3. 0.5 m line spacing, 5% TOI in higher density region
4. 0.5 m line spacing, 2.5% TOI in higher density region

We will run separate simulations for higher and lower density area, and for the different TOI densities of the higher density region. Once we obtain the probability of missing a target for these scenarios, we calculate the expected number of TOI missed for the entire site.

Figure 38(a) plots the distribution of pick offset for the lower density area (22 targets/acre, 2.5% TOI) surveyed with 0.5 m line spacing. In this scenario 0.6% (90 of 16000) of targets would have a pick greater than 60cm away. For TOI, only a single instance of a missed 2.75" rocket had a pick greater than 60cm (Figure 38 (right)). In this case, the 2.75" target was horizontal, and an infield inversion could, possibly, reposition the 2x2 over the target, since the target is isolated. We note that the infield inversion is a single source inversion.

We repeated the simulation on the lower density area with 1.0 m line spacing. The increased line spacing results in a 4 cm increase in the median pick offset (from 26 cm to 30 cm). In addition, the risk of having targets without a pick within 60cm increased from 0.6% to 4.4%. There are 36 of the 2.75" rockets that have a pick greater than 0.6 m away. In one of these cases, this is due to a multi-source anomaly, and the infield single source inversion could potentially miss this TOI. This represents a 1 in 16000 chance in missing a TOI.

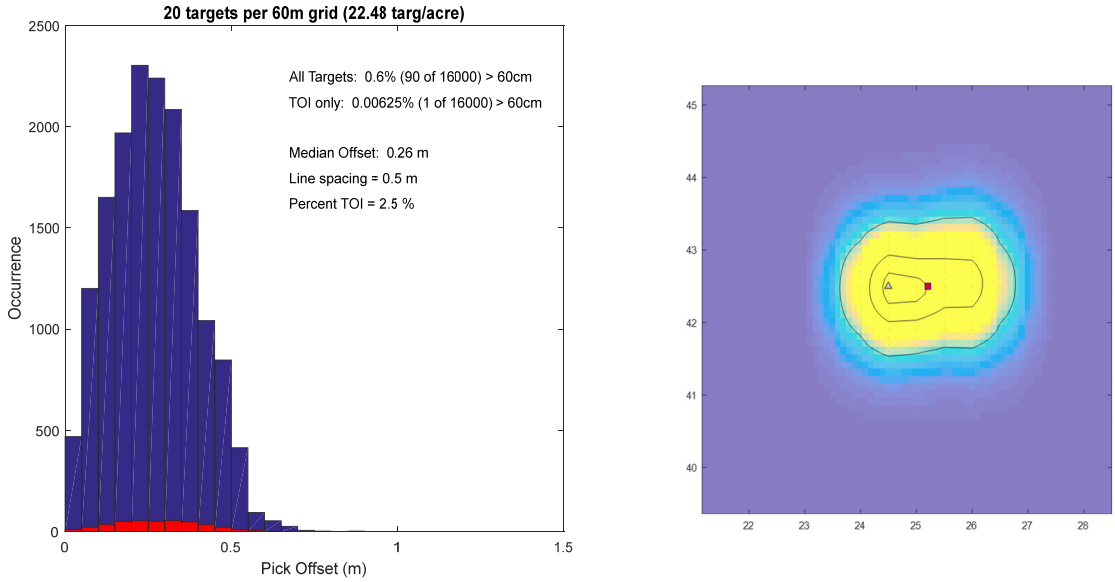

(a) Distribution of pick offsets

(b) Missed TOI

Figure 38. Modelling results for lower density area, 22 targets/acre, 2.5% TOI. 0.5m line spacing. Only one 2.75" rocket would not have target pick within 60 cm. However, since the target is isolated, there is a good possibility that the in-field inversion and reacquisition would be able to identify the target.

Figure 39 presents results from simulating target picking results in the higher density area (134.9 targets/acre, 5% TOI). Data were simulated with 0.5m line spacing. As expected, the higher density of targets results in a higher probability of missed targets. For TOI, there are 17 rockets that have a missed target pick out of the 30000 anomalies in the simulation (0.057% chance). Of the 17 missed TOI, two were multi-target scenarios, and therefore would have a lower likelihood of being detected by infield inversion. When we repeat the simulation of the high-density area (134.9 targets/acre, 5% TOI) with 1m line spacing, the number of missed TOI increases from 17/30000 (0.057%) to 110/30000 (0.37%). Of the 110 TOI, 10 of the anomalies were due to multi-source scenarios.

A summary of the simulated peak offsets is shown in Figure 40. Table 2 and Table 3 list the chance of a missed targets and the chance of a missed TOI for the low and high density regions, respectively. These simulation results are then used to calculate the number of missed targets across the entire site for the four modelling scenarios. Recall that, in the site model, there are 30000 total anomalies, with 20977 anomalies in the lower density area and 9023 anomalies in the higher density area. A summary of the number of missed targets can be found in Table 4. Using 1m line spacing will result in a large number of

targets not having a distinct peak – and therefore a target pick – within 60 cm. Using 0.5 m line spacing reduces the number of targets without a pick by an order of magnitude.

There are two ways that would reduce the number of targets without a pick. The first would be to include additional picks on anomalies that are extended and not symmetrical – i.e., include additional picks when the anomaly looks like it comes from multiple objects. The second would be through the use of an in-field QC/inversion to identify a possible location of the target. In cases where an anomaly is due to a single object, an infield QC/inversion could potentially identify the location of a target, such that the pick location could be refined by the field data acquisition crew. If the noise levels are low enough for the cued instrument to resolve sources outside the footprint of the sensor, then the number of missed TOI would be reduced. In this case, we only need to count TOI missed due to multi-targets when tabulated all missed TOI. Results for this case is shown in the far-right column of Table 4.

When interpreting the results in Table 4, we need to keep in mind that these numbers were obtained by looking at noise-free data. In addition, the difference in size between the TOI (i.e., the 2.75" rocket) and the non-TOI (a 20 mm projectile) and their depth distributions affect the frequency with which a TOI could be obscured by a non-TOI. Therefore, the numbers represent a lower limit for targets to be missed.

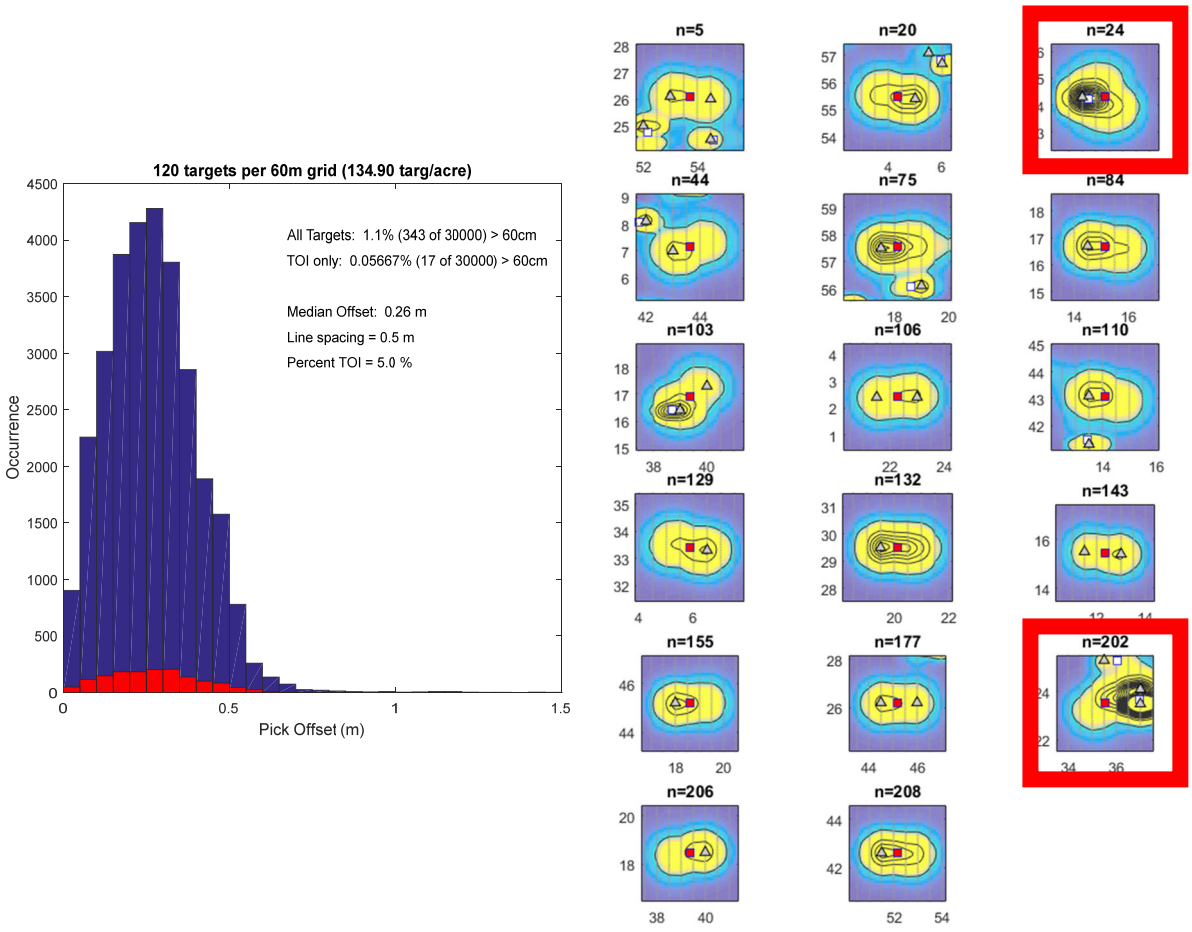

(a) Distribution of pick offsets

(b) Missed TOI

Figure 39. Higher density region (135 targets/acre, 5% TOI), 0.5 m line spacing. Simulations result in 17 of the 2.75" rockets would have picks>0.6m away. Anomalies with a red outline indicate multi-source scenarios where the infield inversion might not result in an additional cued measurement over the anomaly. There is a 2 in 30000 chance to miss TOI.

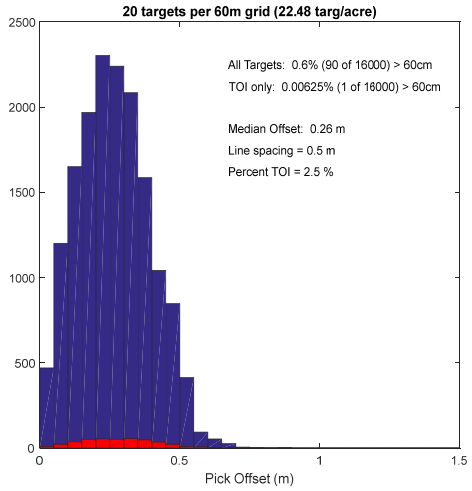

(a) Low density, 0.5 m linespacing, 2.5% TOI

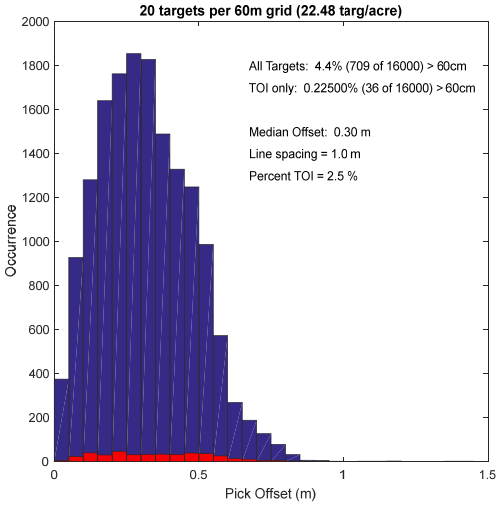

(b) Low density, 1.0 m linespacing, 2.5% TOI

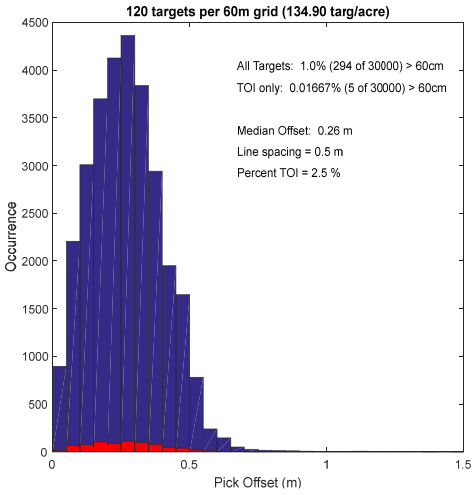

(c) High density, 0.5 m linespacing, 2.5% TOI

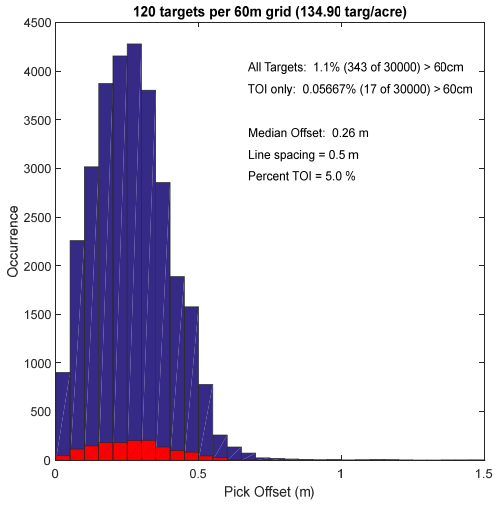

(d) High density, 0.5 m linespacing, 2.5% TOI

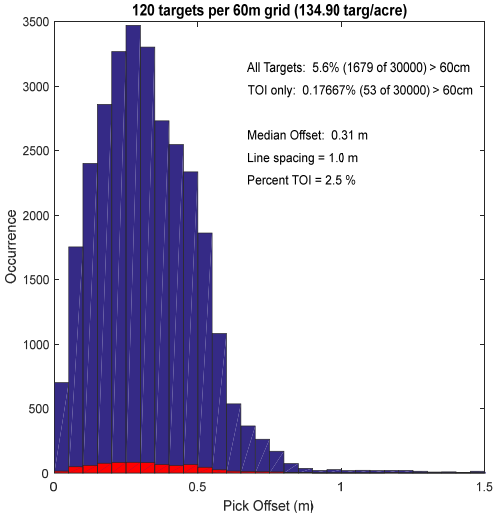

(e) High density, 1.0 m linespacing, 5% TOI

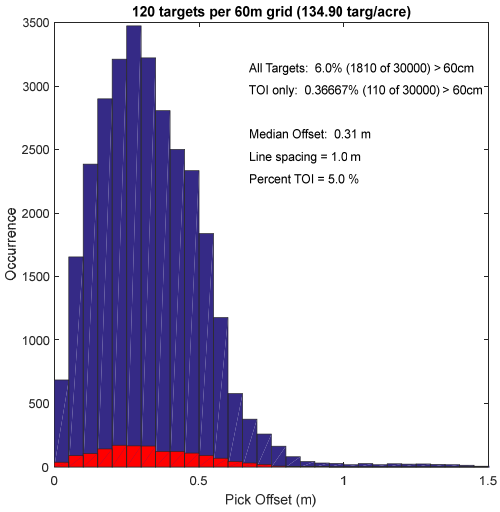

(f) High density, 1.0 m linespacing, 5% TOI

Figure 40. Summary of pick offset results for EM61 target picking simulations

Line spacing (m)	%TOI	All Targets	TOI only	TOI miss due to multi-target
0.5	2.5	0.56% (90/16000)	0.0063% (1/16000)	0.0% (0/16000)
1	2.5	4.43% (709/16000)	0.225% (36/16000)	0.0063% (1/16000)

Table 2. Missed targets in the low-density region. There were 16000 total anomalies per scenario. A missed target is defined as one without a target pick (i.e., peak in gridded image) within 60 cm of the target location.

Line spacing (m)	%TOI	All Targets	TOI only	TOI miss due to multi-target
0.5	2.5	0.98% (294/30000)	0.017% (5/30000)	0.0% (0/30000)
0.5	5	1.14% (343/30000)	0.057% (17/30000)	0.0067% (2/30000)
1	2.5	5.60% (1679/30000)	0.18% (53/30000)	0.027% (8/30000)
1	5	6.03% (1810/30000)	0.37% (110/30000)	0.033% (10/30000)

Table 3. Missed targets in the high-density region. There were 30000 total anomalies per scenario. A missed target is defined as one without a target pick (i.e., peak in gridded image) within 60 cm of the target location.

line spacing (m)	%TOI in high density region	All targets	TOI only	TOI miss due to multi-target
0.5	2.5	206.4	2.8	0.0
0.5	5	221.2	6.4	0.6
1	2.5	1434.5	63.1	3.7
1	5	1473.9	80.3	4.3

Table 4. Missed targets for entire site. The site is defined as having 30000 total anomalies, with 20977 anomalies in the lower density region and 9023 anomalies in the higher density region.

Testing Limitations of Informed Source Selection approach in cluttered setting

During analysis of dynamic MetalMapper 2x2 data, a seed was missed by the informed source selection process. The missed seed was a vertical, small ISO buried at a depth of 35 cm. In Figure 41(top), the location of the seed is indicated by a triangle. The black MM2x2 path-lines indicate that the 2x2 passed directly over the seed. Although the center of the MM2x2 produces the weakest response, the signal for the detection channel (integrated over time channels 5 to 12) was 1.1 mV/A and the noise level for that channel s 0.209 mV/A. Therefore, the amplitude is approximately 5.5 times the noise.

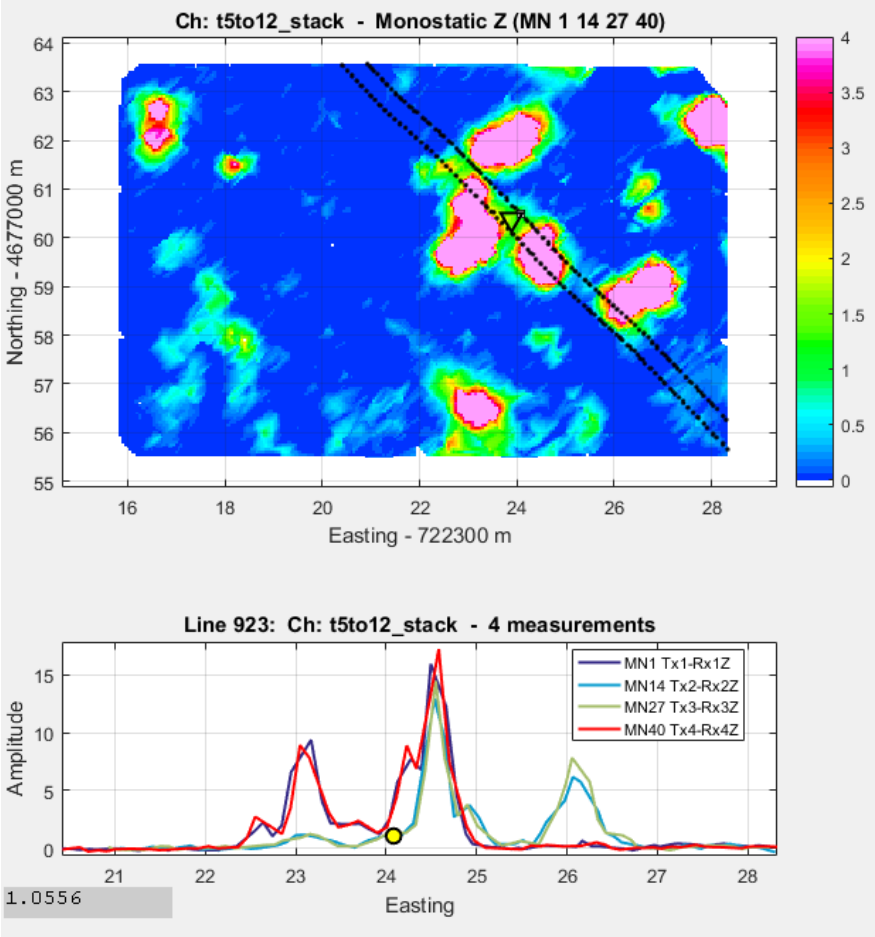

Figure 41. Data collected in the vicinity of a missed QC seed (black triangle). The QC seed is a small ISO that is oriented vertically and buried at a depth of 35 cm.

The SNR suggests that the target should be easily identified. However, the target does not appear to produce a distinct anomaly due to nearby targets. The bottom of Figure 41 shows the coaxial, z-component profile data for the detection channel. There is no distinct peak associated with the seed; the seed produces a "shoulder" on the side of the anomaly produced in the second and third transmitter (i.e., Tx2, Tx3) coaxial z-component. Not surprisingly, data amplitude picking along profile was unable to place a target pick at the location of the seed. During the processing, multi-source inversion of picks near to the seed was unable to place a source at the seed location.

Following the missed seed, we carried out a sensitivity analysis to establish our standard ISS approach to identify seeds in this multi-source scenario. For this study, we subtracted the expected response for a small ISO at the seed depth (35 cm) and orientation (vertical), from the sensor data. We then added the response of a seed at different depths. We created data sets for horizontal and vertical ISOs at depths ranging from 10 to 40 cm deep, at 1 cm intervals. For comparison, we modelled two synthetic targets in addition to the seed, for a total of 3 targets labeled A, B, and C:

A. Target at seed location, at depth d

B. Isolated target at depth = 35 cm

C. Isolated target at depth d

Locations of the seeds are indicated Figure 42(a).

We inverted the data centered on each target, using 1, 2, and 3 source inversion models. Figure 42(b) plots the estimated polarizabilities for the case of each of the small ISO targets (A, B, and C) being buried at a depth of 35 cm, and oriented vertically. In this case, there is no source found at the location of the missed seed (location A). The adjacent anomalies shield the target, and prevent the ability to recover a source. For the isolated targets, the inversion was able to recover the primary polarizability, but the data was unable to constrain the secondary polarizabilities.

When the depth of the seed is reduced to 30 cm, the amplitude of the signal from the seed is increased which produces a slight “bump” in the profile and gridded image (Figure 43). The recovered polarizabilities are shown at the bottom of Figure 43. At the location of the missed seed (A), the inversion was able to recover a source. However, due to the adjacent anomalies, the depth was overestimated. The increased depth resulted in a best fit library item being a 25 mm with cartridge (M794, NRL25-1), which has a high amplitude polarizability. When the depth of the vertical small ISO is further reduced to 25 cm, all the targets are well recovered with good matches to the library small ISO polarizability.

Figure 44 plots the data and inversion results for a horizontal ISO at 30 cm. Not surprisingly, the inversion is unable to resolve a horizontal target at the location of the missed seed (A). Figure 45 plots the recovered polarizabilities when changing the depth. The inversion was able to recover polarizabilities that match the library small ISO polarizabilities, down to a depth of 24 cm. The inversion is unable to reliably resolve a small ISO at depths of 25 cm and greater.

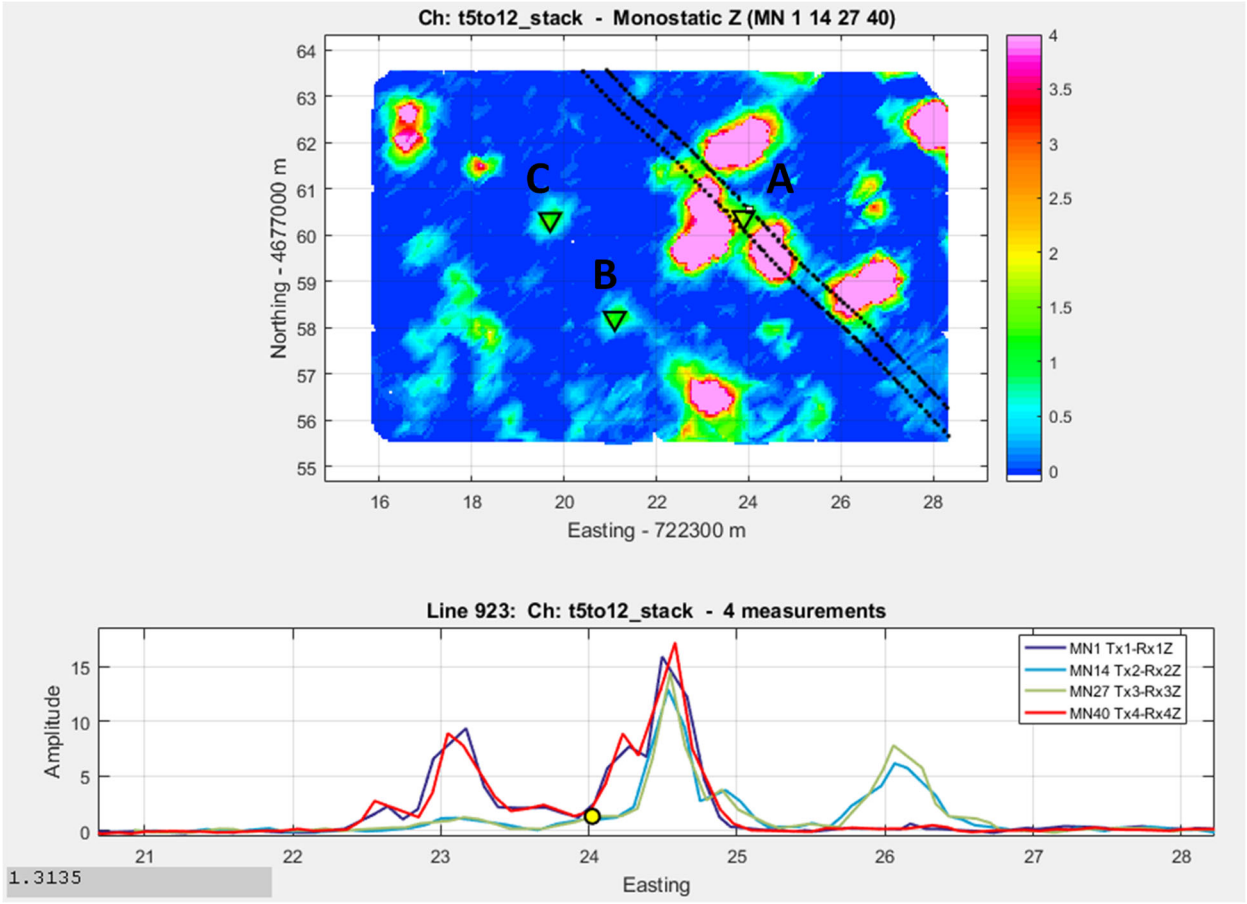

(a) Synthetic Data

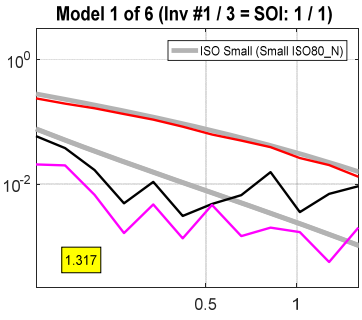

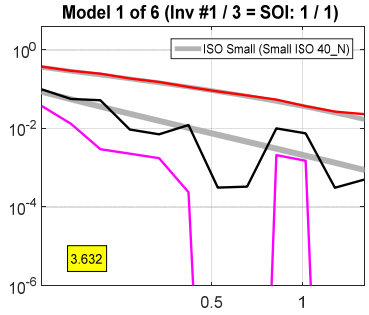

No source

Location A. Vertical, 35 cm.
No source at seed location.

Location B. Vertical, 35 cm.
recovered depth = 31 cm

Location C. Vertical, 35 cm.
Recovered depth = 37 cm.

(b) Inversion Results

Figure 42. Example of synthetic dataset. Vertical small ISO at a depth of 35 cm. The location of the missed seed is indicated by 'A'. 'B' and 'C' are also locations of vertical small ISO at 35 cm. The 'B' and 'C' are isolated seeds (i.e., no known nearby metallic targets).

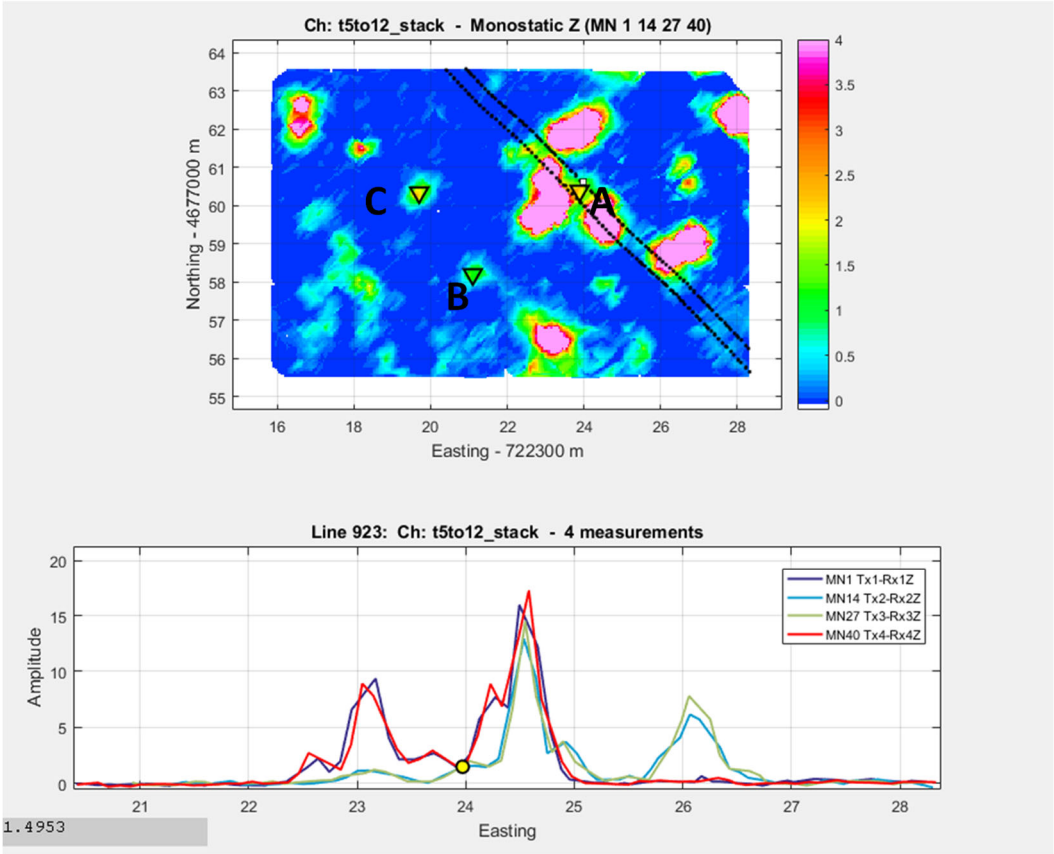

(a) Synthetic Data

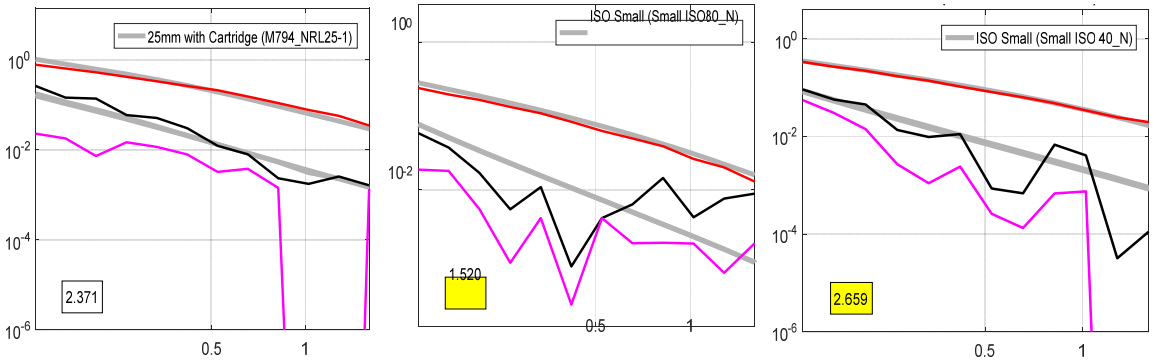

Location A. Vertical, 30 cm.
Recovered depth = 40 cm.

Location B. Vertical, 35 cm.
Recovered depth = 32 cm

Location C. Vertical, 30 cm.
Recovered depth = 30 cm.

(b) Inversion results

Figure 43. Data and recovered polarizabilities. At locations A and C, we synthetically emplace a vertical small ISO at 30 cm, and at location B there is a synthetically emplaced vertical small ISO at 35 cm.

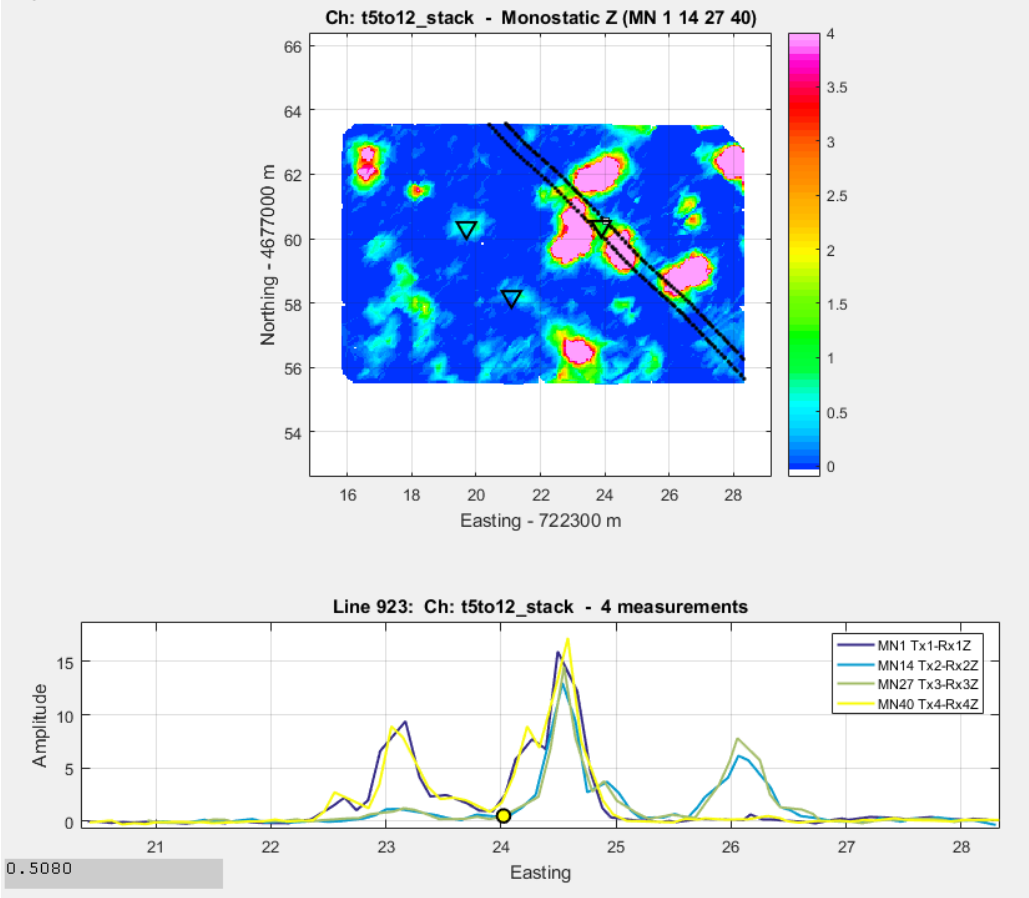

(a) Synthetic Data

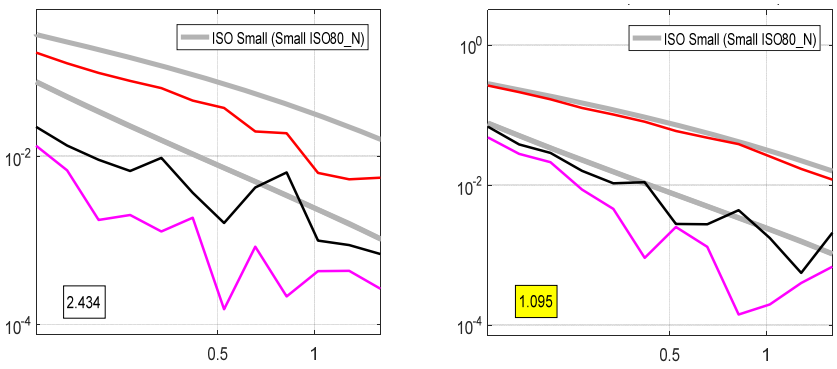

No source

Location A. Horizontal, 30 cm. No Source.

Location B. Isolated horizontal, 35 cm. recovered depth = 28 cm

Location C. Isolated horizontal, 30 cm. Recovered depth = 27 cm.

(b) Inversion results

Figure 44. Data and recovered polarizabilities. Horizontal ISO at a depth of 30 cm for locations A and C. At location B, it is difficult to accurately recover depth, although the target isolated (i.e., no large anomalies in the near vicinity)

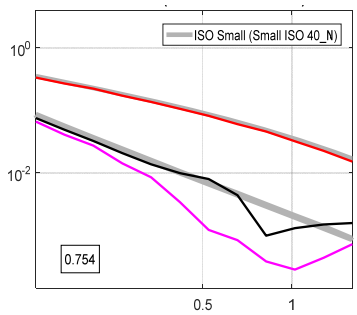

(a) depth = 20 cm

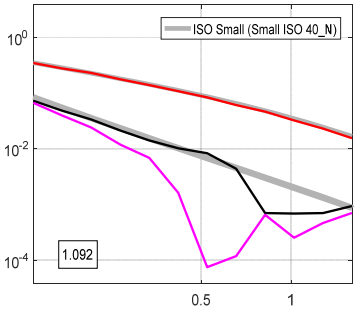

(b) depth = 21 cm

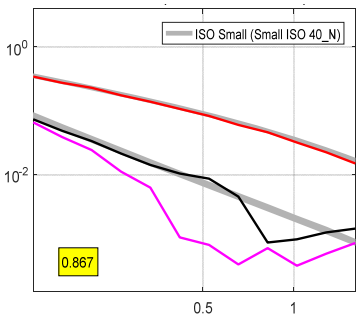

(c) depth = 22 cm

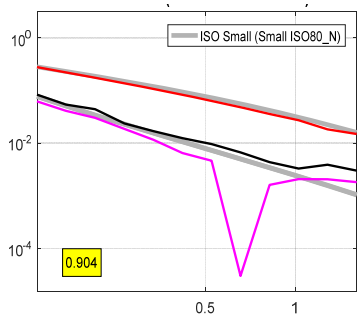

(d) depth = 23 cm

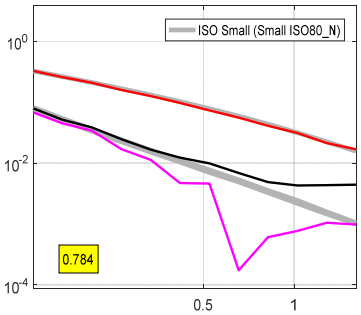

(e) depth = 24 cm

No source

(f) depth = 25 cm

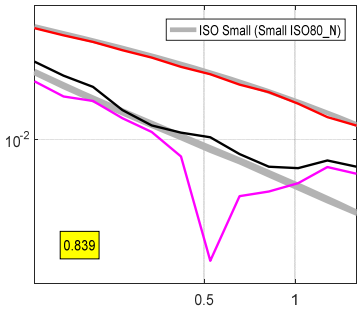

(g) depth = 26 cm

No source

(h) depth = 27 cm

No source

(i) depth = 28 cm

Figure 45. Ability to resolve a horizontal small ISO at Savanna. Data centered above the target is inverted with 1, 2, and 3 source models. Reliable estimates of the polarizabilities are not expected for depths of 25 cm and greater.

Using an equivalent source methodology for target picking (2): Source clustering

Earlier in this report, we presented the use of equivalent sources for reconstructing and denoising data to improve the performance of image or profile-based target picking methods. In this section, we use the missed seed example from the previous section to demonstrate how the target sources can be used for target picking. Recall that the missed seed was a vertical, small ISO buried at a depth of 35 cm.

We defined a grid of 1m x 1m data tiles that covers the grid containing the missed seed. The data tiles were centered on a uniform grid. Figure 46 plots the locations of the grid centers in the vicinity of the missed seed. The blue dashed line plots the border of the 1m x 1m data tile centered on grid location 267. Data tile centers are separated by 0.5m, such that the data above the seed is inverted 4 times. Each of the data tiles is inverted for 1, 2, and 3 source dipole models. We restrict sources to lie within a 2m x 2m square that is centered on the data grid.

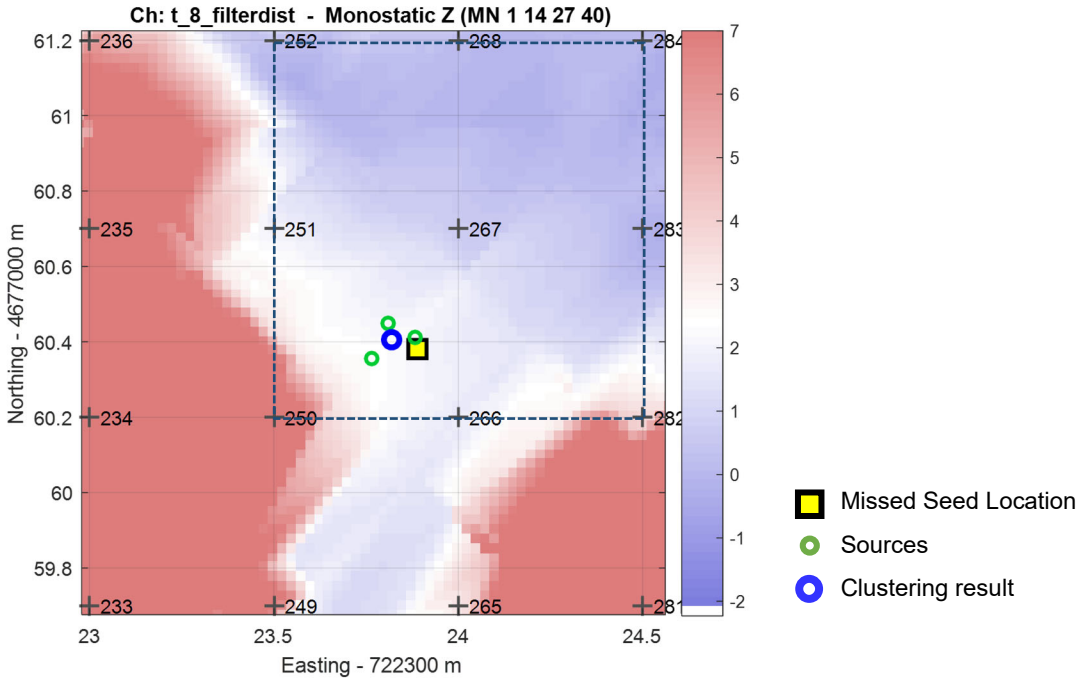

Figure 46. Location of recovered sources related to the missing seed. The blue dashed lines indicate the data inverted around grid location 267. The three sources are within 15 cm of each other, so they are designated as a target pick. The location of the pick is defined as the median of the three sources.

The inversion of data from locations 266, 267 and 283 produce sources near the location of the missed seed (black circles in Figure 47). For each of these data files, one of the sources predicts a vertical target. These three data files share two features: (1) The data of these locations are acquired near to the seed location (i.e., the seed falls within the data tile, or next to the data tile), and (2) the majority of data within the tile does not have signal from the large anomalies to the west and southeast of the seed. In the previous section, we inverted data centered directly over the target. It is possible that the inversion was unable to recover a source at the location of the missed seed, due to screening from target responses to the west of the seed.

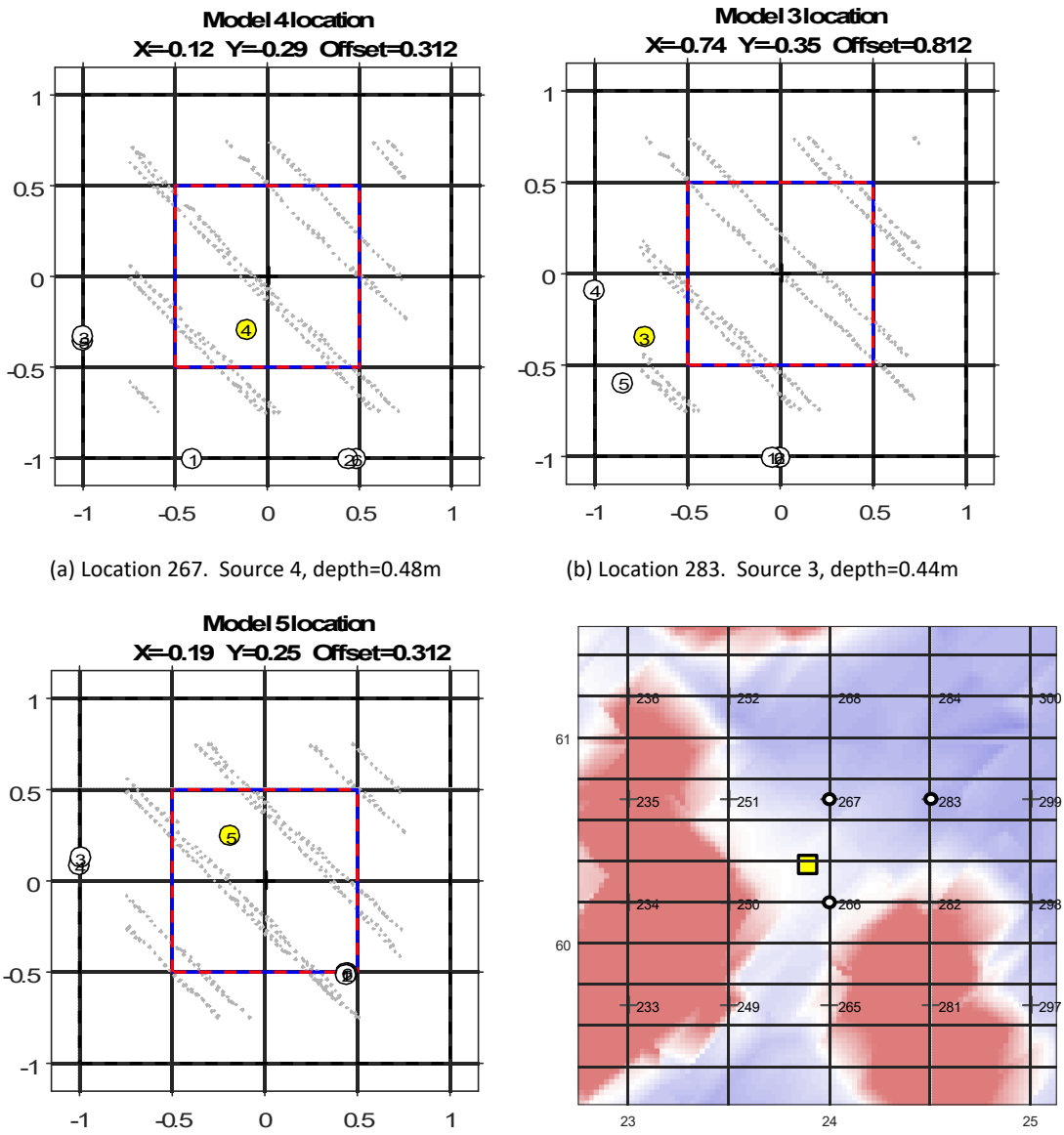

(a) Location 267. Source 4, depth=0.48m

(b) Location 283. Source 3, depth=0.44m

(c) Location 266. Source 5, depth=0.55m

(d) Location of missed seed and data tile centers

Figure 47. Three data tiles produced a source near the location of the missing seed. The 3 tiles – centered on 266,267, and 283 recovered a vertical target near the seed. The black dashed lines indicate the lateral limits for the sources.

Figure 48 plots the results of applying source clustering to a larger area surrounding the seed. The cyan dots indicate the location of all the seeds. To cluster sources into picks, we have been developing and testing a number of different clustering algorithms. The black squares indicate clustering results using the "Density-based spatial clustering of applications with noise (DBSCAN) algorithm, and the red plus signs show results of an alternate method we have developed that is more aggressive and results in more picks. For both methods, the minimum number of sources to define a cluster is 3, and the maximum distance between points to remain in the cluster is 15 cm. Although the alternate clustering

appears to miss some clusters in this example, newer versions of the method have improved, more robust performance.

Figure 49 plots the clustering results for the case of a synthetically emplaced horizontal target. In the previous section, we described an experiment where we removed the response of a vertical small ISO at 35 cm, and added the small ISO at a number of depths. The inversion of data centered above a horizontal small ISO at 30 cm did not result in a source at the seed location. However, the source clustering algorithm was able to place a target pick at the location of the small ISO (Figure 49 (a)).

The clustering algorithm was also applied to a horizontal small ISO at a depth of 35 cm. At the locations where the horizontal small ISO is isolated, the algorithm is able to add a target. At the location of the missed seed (i.e., the farthest right square), the algorithm did not add a pick at the target. It is possible that the anomaly did not have sufficient SNR to be resolved amongst the adjacent targets. Since the time that this test was initial performed, we have made a number of improvements to our N-dipole inversion code.

An additional method for choosing sources is to use data amplitude. Through modeling it is possible to determine the minimum data amplitude for a TOI to be found within its clearance depth. Figure 50 presents results of applying the approach to the dataset with the missing vertical seed. A set of sources are determined via multi-source inversion ('x' symbols) and we then use these sources to create a smooth map. The gridded image is shown in Figure 50. All sources that are located where the gridded image exceeds 5 times the noise is kept as a possible source. These sources are marked with a black 'x'. A clustering algorithm could be used to remove isolate sources for consideration.

An automated peak finder is used to determine peaks in the gridded image. The peaks are indicated by triangle symbols. Peaks that have a maximum value greater than 5 times the noise are noted with red triangles. This approach was able to find a peak at a point close to the missed seed location. We are currently doing a more extensive using the synthetic datasets presented in the next section.

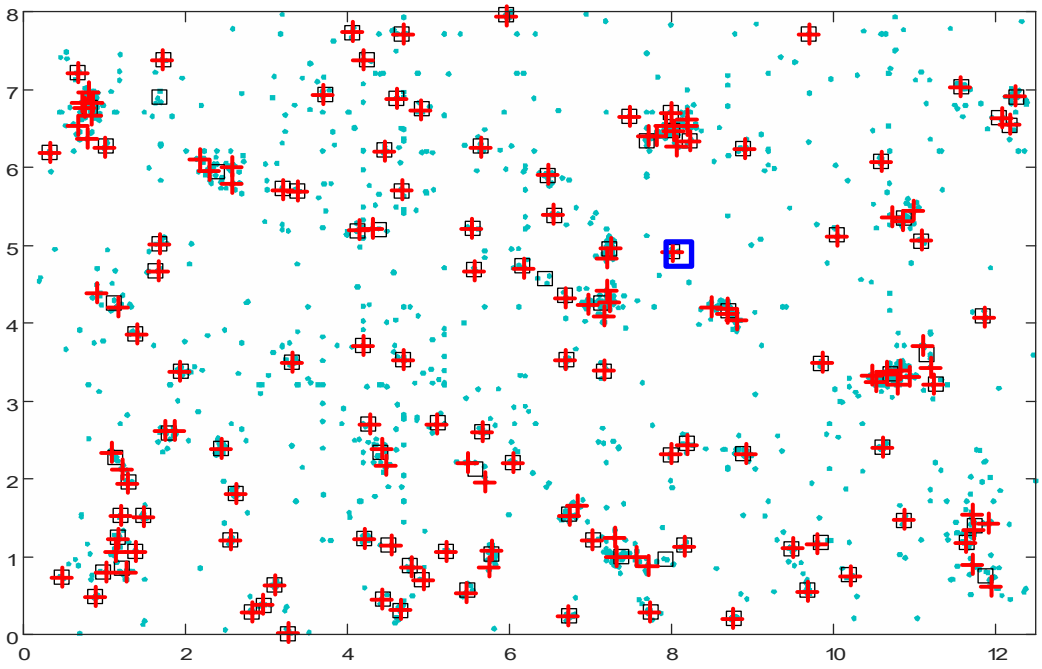

(a) Blue square: location of the missed seed. Cyan dots: sources from multi-source inversion. Black squares: source clustering using the dbscan algorithm. Red crosses: result from using a more aggressive, modified clustering algorithm.

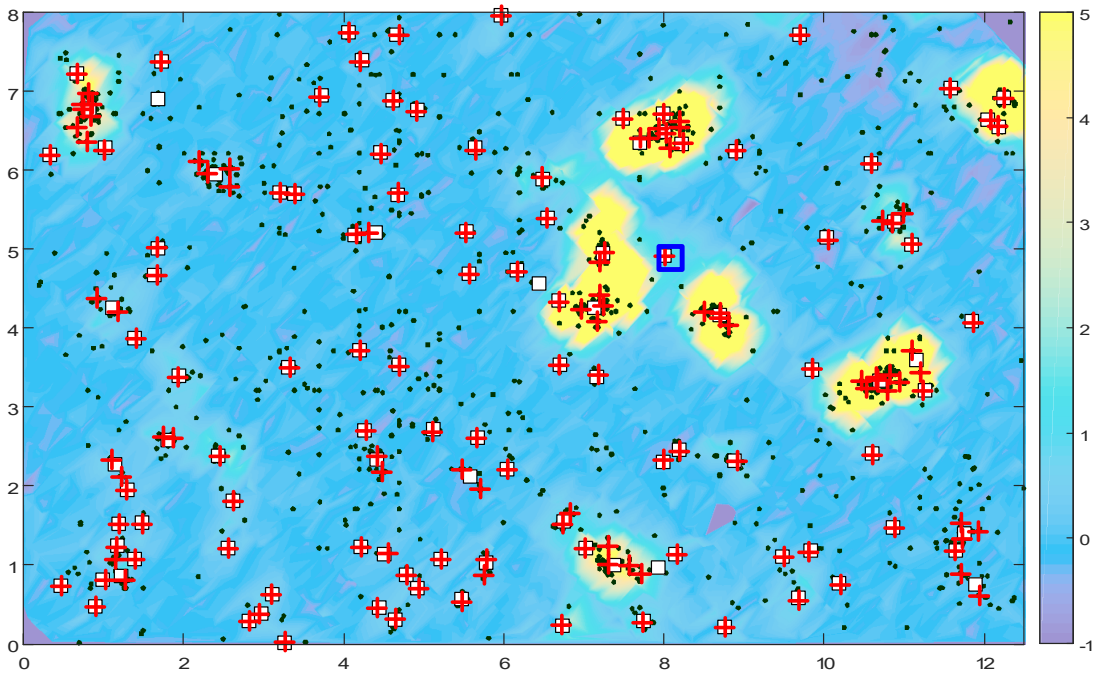

(b) Clustering results plotted over an image of the data.

Figure 48. Source clustering approach applied to missed seed data from Savanna

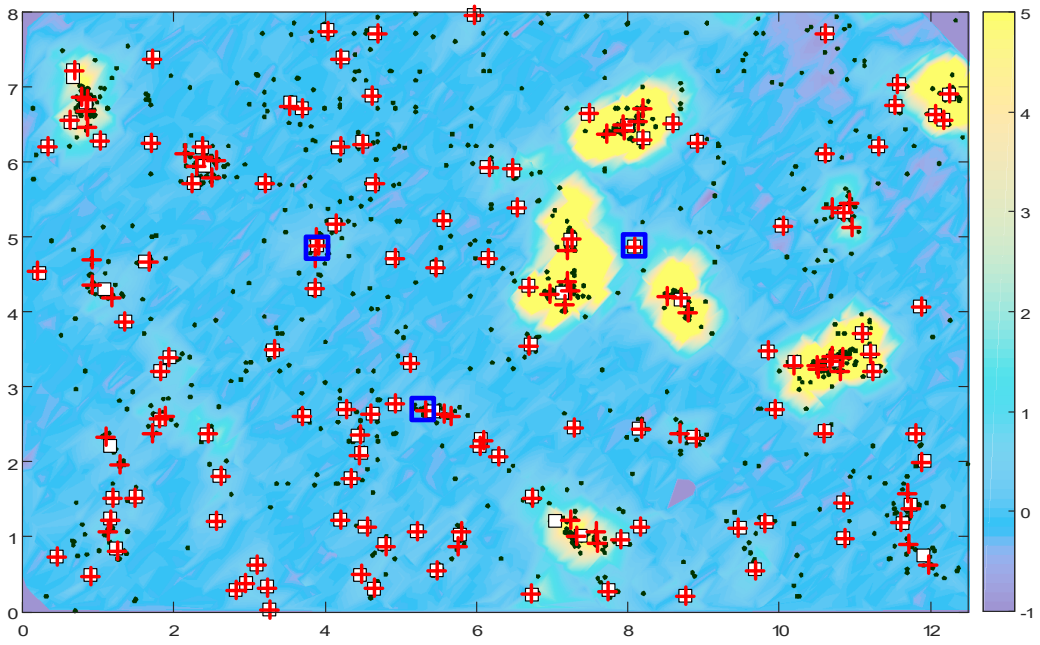

(a) top two blue squares: horizontal small ISO, depth 30cm. bottom blue square: horizontal small ISO, depth = 35 cm.

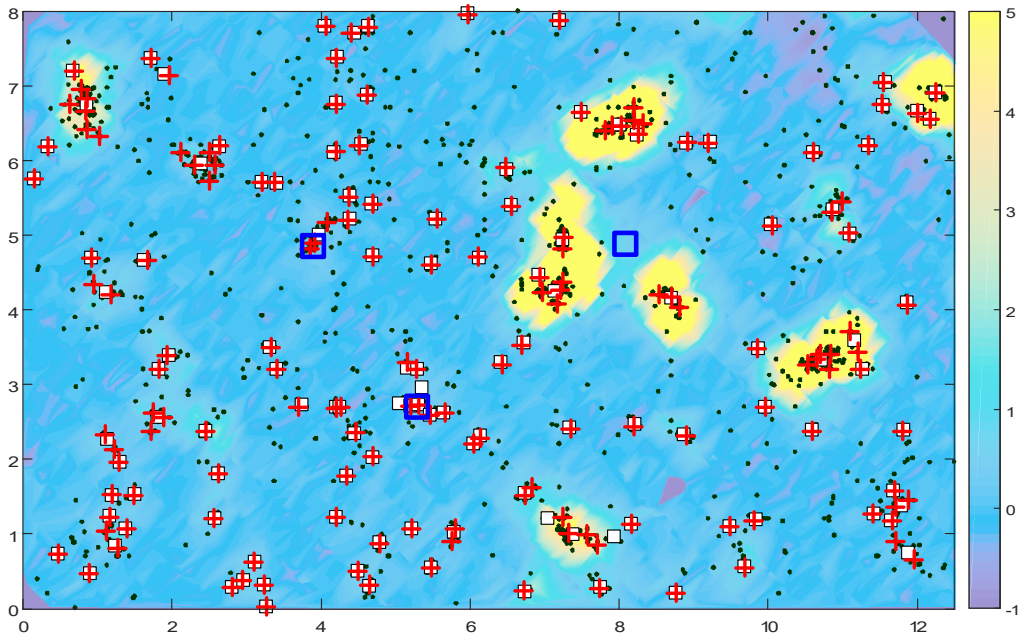

(b) All three blue squares: horizontal small ISO, depth 35cm

Figure 49. Source clustering approach applied to synthetic seeded data. Recall that when inverting the 30cm data directly over the seed, we were unable to put a source in the right spot. However, by combining inversions from adjacent targets, we have a cluster of sources.

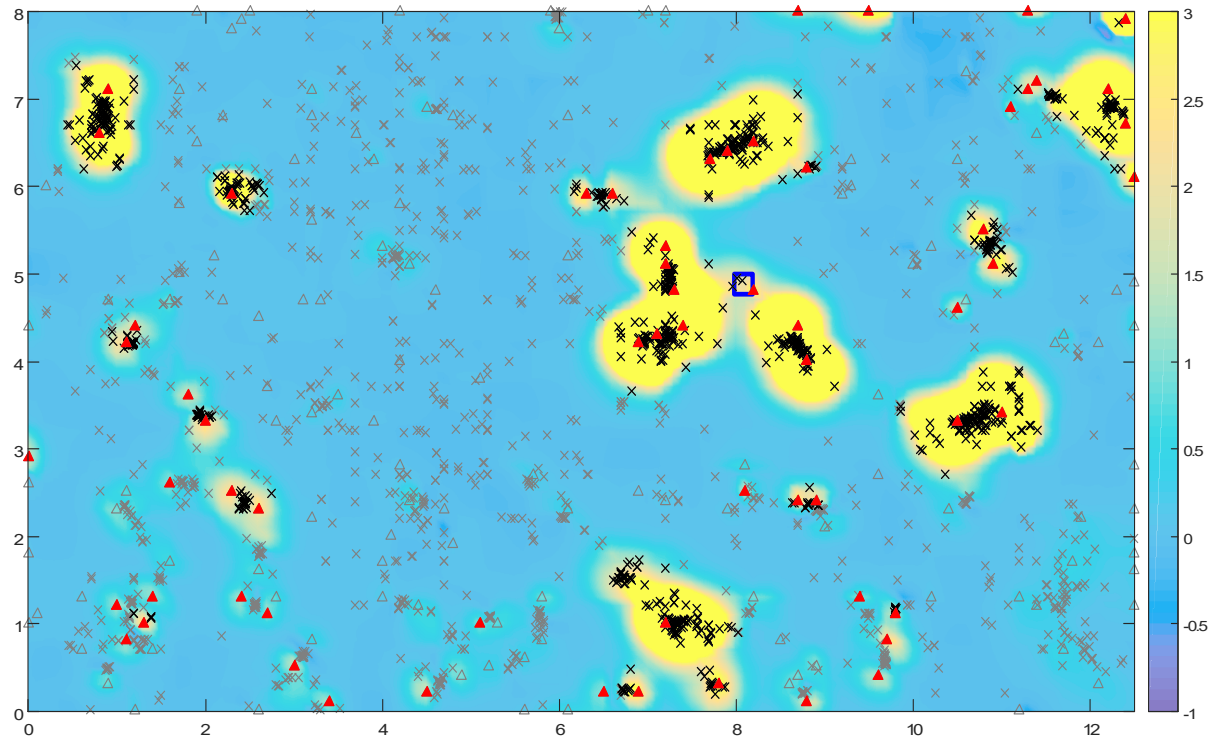

Figure 50. Using data amplitude as a criteria for choosing sources. Triangles represent peaks in the reconstructed coaxial, z-component image. Red triangles are located where peaks are greater than 5 times the noise. 'x' symbols represent locations of sources, with black 'x's indicating sources located where the signal is greater than 5 times the noise.

Comparison of profile picking, dipole clustering and dipole filter target picking

Methodology

A comprehensive comparison of the existing target picking methods was prompted by misclassification of a small ISO seed during the Savanna project. The data was collected using the TEMTADs 2x2 sensor system in the dynamic mode. For the purpose of synthetic modelling the response of the missed ISO was removed from the total signal and replaced with a synthetic target response of a small ISO seed at depths varying from 10 to 30 cm and at one of the two orientations: horizontal and vertical. Hereafter the missed ISO seed will be referred to as seed A. Two additional synthetic seeds were planted in the dynamic data; one of the reference seeds was planted at the same depth as seed A and will be referred to as target B, while the other reference seed was planted at the depth of 35 cm and will be referred to as target C.

In order to obtain a statistical assessment of the methods' performance, a raw dataset from the Savanna project was planted with 100 evenly spaced synthetic seeds that simulate small ISOs. The dataset was processed with the same parameters as the single seed datasets. Figure 51 shows a subset of the synthetically seeded dataset.

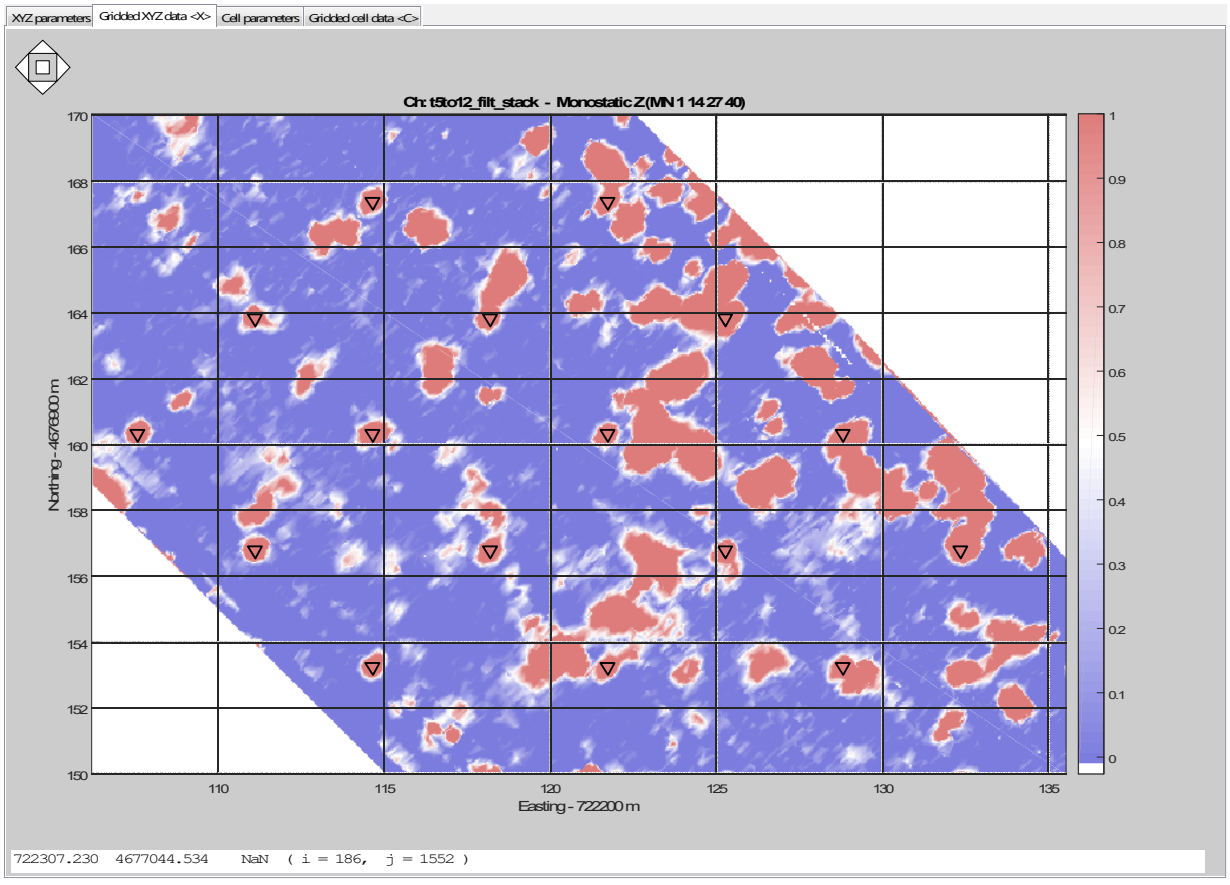

Figure 51. Example of synthetic data used for testing. Black triangles mark location of synthetically emplaced seeds.

The synthetic data was processed using methods that perform target picking along a profile. A profile consists of a line of data for a given choice of a detection channel and an Rx/Tx combination for one physical pass of the EMI sensor. For instance, the MPV sensor has 15 receivers and one transmitter; there are 15 available profiles for one physical pass. Several Rx/Tx combinations can be used for picking for each physical pass (e.g., all Z component data). An anomaly is selected wherever the profile data exceeds the detection threshold over a specified distance or a number of data points.

The standard profile picking method finds peak in segments of data where the signal exceeds a detection threshold over an analyst defined minimum number of consecutive points. The inputs for this target picking approach are shown in Figure 52.

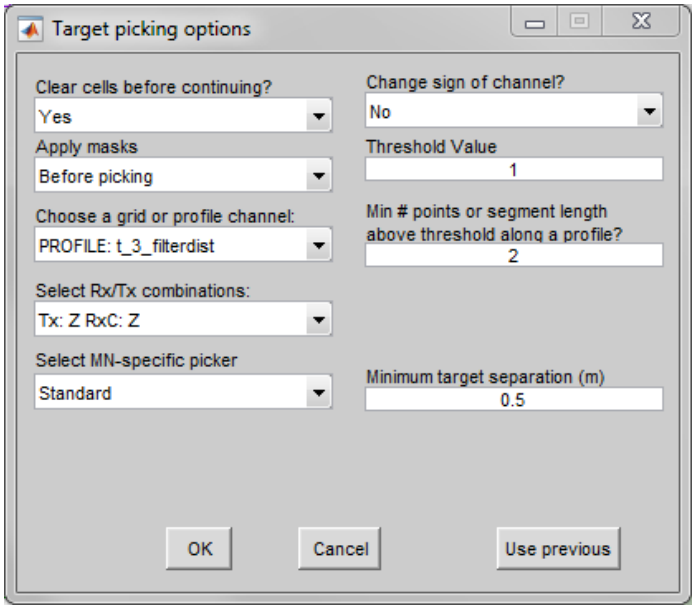

Figure 52. Options for "standard" profile picking method.

A number of modified profile picking methods have been developed. These methods have a similar framework:

- A specific threshold can be applied to each receiver/transmitter combination: different thresholds can be defined for each Rx/Tx combination to account for the specific properties of each pair (e.g., electronic gains, coupling due to geometry, Rx location relative to edge of array)
- The minimum number of profiles that see a valid anomaly can be specified: Some level of false pick rejection can be achieved by specifying that an anomaly should appear on multiple profiles. This is particularly true if the anomalies are expected to have a minimum spatial footprint.
- The picking algorithms first scans all profiles and seeks data segments that exceed the threshold. Several properties for each segment are recorded: the maximum value, pick location, the segment length, the energy (i.e., square root of the sum of squares of the data above the threshold).

- For each detected segment, the pick location can be defined as the location with maximum amplitude (i.e., the peak), the data-weighted mean location, or the average location.
- Close picks that appear on multiple profiles can be merged by defining a minimum target distance separation. Merging involves sorting all picks by their amplitude (signal or energy), then starting with the highest amplitude, finding all close picks within the minimum separation distance. These picks are then merged to a single location, which can be defined as: the location with maximum value (peak), the data-weighted mean location, or the average location. This new pick replaces the first pick, the number of close picks for this new pick is recorded, the close picks are removed from the detection list. The processes continue by moving to the next pick in the list, and finding its close neighbours, and repeating the steps.

The following methods differ in their treatment of close anomalies, where the signals from multiple buried targets may overlap and create a continuous segment of elevated EMI response where multiple peaks may be present. Each of the methods have been implemented into our in-house processing software to facilitate evaluating the different picking methods. The methods that were tested are: Standard, Peaks and sampled picks, Peaks and local maxima, Peaks above threshold, Derivatives. Further details on each of the methods are presented below.

Peaks above threshold (PAT) - This method find data segments that exceed the threshold. The method includes one special refinement to search for overlapping anomalies, for which we assume that (1) within a segment the signal would drop to a local minimum between two consecutives peaks, and (2) the peaks would be part of different segments if the detection threshold was higher than that local minimum. The picking algorithm is applied several times at multiples of the detection threshold to try and capture the peaks that are separated by a local minimum up to 25 times the detection threshold. Then all picks are sorted accorded to their energy and merged.

Peaks and sampled picks (PSP) – This method uses the basic principles of "peaks above threshold" but adds picks such that larger anomalies have additional picks added. Supplementary picks are added to the main pick if a segment of data exceeding the detection threshold value is longer than an analyst defined distance. Additional picks are added at a given spacing along the detection segment. Then all picks are sorted accorded to their energy and merged.

Peaks and local maxima (PLM) – This method also uses the basic principles of "peaks above threshold" and assumes that the presence of multiple objects could produce local minima along a detection profile. First, the method finds all data segments that exceed the threshold, then finds local minima within each segment and breaks the segments at local minima. Then picks are identified within each segment, picks are sorted accorded to their energy and merged. This method may fail to separate two overlapping targets if there is no local minimum marking the presence of the weaker anomaly and if that weaker anomaly does not individually appear on a separate profile.

Derivatives –This method also uses the basic principles of "peaks above threshold". However, this algorithm is applied to interpolated data at regular spacing to compute derivatives and locate maxima and minima to identify peaks and define their extent (or footprint). The footprint is the distance between the peak and the closest minimum or closest point before going under the detection threshold, along the interpolated profile. The footprint is used to define the merging radius for a given pick. The

maximum of the prescribed target separation, defined by the user, and the calculated pick footprint is then used for merging close picks after sorting the picks by amplitude.

In addition to the methods mentioned above, a Dipole Clustering method was tested on the multi-seed synthetic datasets.

***Dipole Clustering (DC)* -** The dipole clustering method is an inversion-based target picking approach. Each dynamic sounding (a complete cycle of transmitters firing) is inverted at a single time channel to recover a prospective single source location. We then cluster all estimated source locations to identify locations that correspond to a legitimate target. The clustering algorithm is an "agglomerative" algorithm that lumps sources together based on a specified minimum distance. A minimum number of points in each cluster must also be specified to identify clusters that will be considered as legitimate target picks.

Target picking

Target picking was performed on a stack (i.e., numerically integration) of the levelled channels 5 to 12 (0.110 ms to 0.524 ms). Mono-static (i.e., co-axial) Z-component receiver data profiles used. The threshold value used was 0.38, and the minimum target separation was defined to be 0.41 m, respectively. A minimum of two points for segment length above threshold along a profile was applied. To combine nearby picks, a weighted average of the pick locations was used. The locations were weighted by the data amplitude at the pick locations.

Once amplitude-based profile picking was completed, each pick location was inverted for 1, 2 and 3 dipole source solutions. This results in a total of 6 dipole source models. De-median filtered data from channels 6 to 17 (0.137 ms to 1.6 ms) were selected for inversion. The height of the sensor above ground was kept at 0.22 m. The number of starting models was set to 10 while the model bounds were: x∈ (-0.7 0.7), y∈ (-0.7 0.7), z∈(-1 0). The parameters for inversion are listed in Table 5.

Table 5: Parameter values for target picking and inversion

Parameter	Value
Stacked channels	5 to 12 (0.110 s to 0.524 s)
Threshold	0.38
Minimum target separation	0.41m
Cell size	2
Cell mask	1.2
Inverted channels	6 to17 (0.137 s to 1.6 s)
Sensor height above ground	0.22m
Number of starting models	10
Model bounds	X (-0.7 0.7), Y(-0.7 0.7), Z(-1 0)

Initial screening to remove spurious models

For this example, an initial screening process was used to identify dipole sources that are unlikely to be related to buried metallic targets. These are spurious models are from fitting data noise. For example, the models can be artifacts from fitting a single target with a multi-source inversion. Figure 53 contains an example of a spurious dipole source taken from a TEMTADS 2x2 data set acquired at the Former Castner Range.

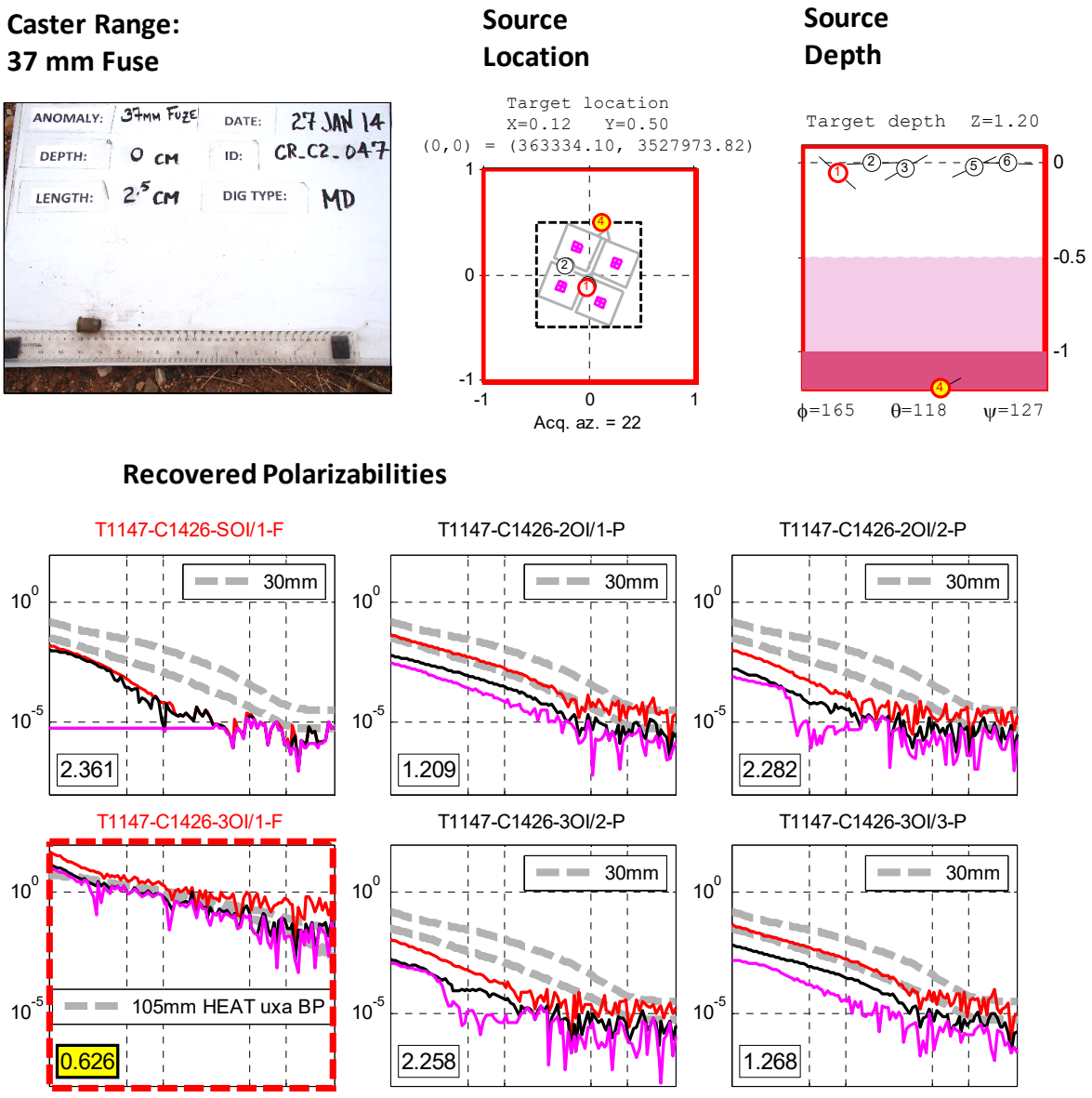

Figure 53. Example of a spurious inversion result. For this example, we consider a TEMTADS 2x2 sounding acquired at Castner Range. Intrusive results revealed that it was a 37 mm Fuse. The data were inverted with 1, 2, and 3 source inversions; resulting in 6 models to consider. Model 4 is highlighted in yellow above. The source is not constrained by the data, with the depth and location estimate sitting on the inversion constraints. The recovered polarizabilities (bottom left) have a very "noisy" looking result. These features are characteristic of a spurious source, and likely due to the problem being underdetermined, i.e., more model sources than actual targets.

In order to identify these spurious of models, we calculated 5 metrics.

- **Data fit:** Data fit metric is a measure of the similarity between observed and predicted data, with values ranging between 0 and 1. Data fit is calculated using data with an absolute amplitude greater than the cell standard deviation, thus it is important that the assigned cell standard deviation is a reasonable estimate of the noise level. Data fit is calculated as the median of the difference between observed and predicted data, scaled by amplitude so that low amplitude noisy data (typical of an empty cell) will have a data fit approximately ≥0.8. The scaled difference is converted to a value between 0 and 1 by the simple mapping $d=1/(1+m^{\propto})$, where d is the data fit, m is the scaled misfit value, and α is an exponential scale factor (usually, α=1).

  The optimal value for the threshold is site and target distribution dependent. Typically for cued data, a value >0.8 is considered a good fit. For dynamic data, the data fit values tend to be lower, thus it is necessary to get a feel for what data fit values constitute good versus poor fits.

- **Depth**: The depth of a dipole source. A depth that is equal to depth constraint suggests that the data is not constraining the dipole location well.

- **Model offset threshold.** Model offset is the distance between model location and target pick. Only models with an offset less than the specified threshold will be considered when looking for "good models". If all models for a cell have an offset greater than the threshold, the cell is flagged as category 1 (note: description of categories summarized below), and the pick location is assigned as the source location.

- **BDU ("Big, Deep, and Ugly")**: This metric helps identify models that are artifacts of multi-object inversion (MOI) – i.e., When multiple objects are not present. These models tend to have large amplitude polarizabilities, tend to be deep since their depth is not being constrained by the data, and they tend to be ugly since they often model the noise in the measurement. The metric is a product of the source depth, size, and a measure of how many time channels there are for which polarizabilities exceed the noise (e.g., polarizability reliability).

- **MOI-PB**: This metric is similar to the BDU, in that it attempts to find spurious sources based inverted model properties. In addition, to looking at the depth, size, and polarizability reliability, this metric considers the source offset from the center of the array, the "noisiness" or "smoothness" of the polarizabilities, and the amount that each source contributes to model the signal.

The threshold values used to reject models are listed in Table 6. The values were determined through analysis of previous datasets, and were chosen to be conservative. A model that fails is not considered in the ISS process. If all models for an anomaly are failed, regardless of which side of the screening line they fall, ISS will flag this cell and the target pick location will be assigned for the source location.

Table 6. Metrics used for initial screening of data amplitude-based picks.

Criteria	Value
Data-fit	>0.35
Depth	<0.99m
Model offset	<0.8m
MOI	<3
BDU	<0.3

The models that did not satisfy the conditions in Table 6 were removed from consideration (i.e., "screened out"). The remaining models were subjected to a two-step Informed Source Selection. In addition to the metrics in Table 6, consider these additional metrics.

- **Model contribution threshold.** Model contribution is the percent contribution of each model to the predicted data for a given inversion. Values range between 0 and 100. For a single object inversion, the contribution is always 100%. For a multi-object inversion, the sum of the model contributions of each model is 100%. Frequently, models with small model contribution represent insignificant models that are artefacts of the multi-object inversion process when <N objects are present in an N-object inversion. When searching for "good" models, only models with a contribution greater than the specified threshold are considered. Note that sometimes, a seemingly significant model can have a small model contribution, so this threshold, if applied, must be used cautiously.

- **SNGTC threshold**. SNGTC refers to the "simple, no ground truth classifier" score. The SNGTC score is calculated from seven model and data metrics. For each metric, the ordinal position of a model relative to all models is determined and the average of the ordinals for a given model is the SNGTC score. Models with high SNGTC tend to have polarizabilities that have properties typical of UXO. The following metrics are used in the calculation:

  1) *Polarizability size.* Higher values give higher SNGTC score.

  2) *Polarizability decay.* Higher values give higher SNGTC score.

  3) *Data noise metric:* a measure of the point-to-point jitter in the data, calculated as the average of the sum of the point-to-point difference, scaled by the absolute mean size of the data. Smaller values give higher SNGTC score.

  4) *Data fail metric:* calculated as the ratio of data misfit to data noise. High values of this metric tend to correlate with inversions that have a poor data fit with relatively high amplitude data. Smaller values give higher SNGTC score.

  5) *L2-L3 separation:* a measure of the difference between the secondary and tertiary polarizabilities. Smaller values give higher SNGTC score.

6) *Polarizability jitter:* a measure of the overall point-to-point jitter on the polarizabilities. Smaller values give higher SNGTC score.

7) *Polarizability reliability:* is the estimated time channel at which the polarizabilities become noisy. Higher values give higher SNGTC score.

- **Model Similarity Misfit Threshold.** For a given cell, model similarity is the polarizability misfit (calculated using all three polarizabilities) between each model of the cell. If more than 2 "good" models are found, the similarity of these models is considered. If a pair of these models has a similarity misfit lower than the specified misfit threshold, the one with the highest simple, no ground truth classifier (SNGTC) score is chosen. If more than one pair of models have similarity misfits lower than the specified misfit threshold, the pair with the lowest misfit is considered and the model from this pair with the lowest SNGTC score is selected. Note that, in general, in the end, if more than one "good" model is found, the tie is broken by choosing the one with the highest SNGTC score. For this step of the source selection, however, there is no threshold associated with SNGTC.
- **Acquisition to Pick Location Threshold**. In general, this threshold is not used with dynamic data. For cued data, it requires that a target pick file to be loaded in QCZilla. If a pick file is loaded, and if the distance between the acquisition location and pick location exceeds this threshold, the cell is flagged as category 7, and the pick location is assigned as the source location.

The first step was to find the best model for each cell was identified using the criteria in Table 7

Table 7. Informed Source Selection Parameters

Criteria	Value
Size threshold	-1.2
Decay threshold	0.05
Data fit threshold	-Infinity
Model offset threshold	0.4m
Model contribution threshold	1%
Model similarity misfit threshold	0.4
Acquisition-to-pick location offset threshold	0.5m

Each model was classified into one of nine categories:

Cat 1: No models near acquisition location (use acquisition location)

Cat 2: Screened: all models below size/decay thresholds

Cat 3: More than 2 "good" models w/2 similar: use model with highest SNGTC. SNGTC is the name of a metric that calculates the likelihood of a source being related to a TOI, without the use of a polarizability library.

Cat 4: More than 2 "good" models but none similar, or <= 2 "good" models: use model with highest SNGTC

Cat 5: Screened: no "good" models and models within distance threshold are all small

Cat 6: No "good" models, but >= 1 model(s) is above size/decay threshold; use model with highest SNGTC

Cat 7: Acquisition location too far from pick location (use acquisition location or ignore cell)

Cat 8: All models failed (use acquisition location)

Cat 9: Screened: passed model(s) not above size/decay threshold

The number of cells (note: the set of inversion results for an anomaly represents a cell) in each category was recorded.

In the second step additional models in each cell were found using the following criteria:

Table 8 Additional parameters used for finding additional models in each cell.

Criteria	Value
SNGTC threshold	1.6
Polarizability misfit threshold	1.5
BDU threshold	0.1

Results

Based on the findings, vertically oriented targets were, in general, easier to detect and were detected at deeper depths, as was expected. A measured distance of less than 0.25m between the modelled location and the true location of the target defined successful performance. There was a bimodal distribution of performance among the tested methods. The Standard and the Derivatives methods tend to perform similarly, while the PSP, PLM and PAT methods perform similarly to each other.

Single seed

For Seed A, the Standard and the Derivatives methods failed to perform at depths exceeding 0.1m in the horizontal orientation (Figure 54) and 0.15m in the vertical orientation (Figure 55). Whereas the other three methods: PSP, PLM, and PAT failed to perform at depths exceeding 0.2m (PLM, PAT) and 0.25m (PSP) in the horizontal orientation and 0.25m in the vertical orientation.

In the case of target B, all target picking methods performed exceptionally well (Figure 56 and Figure 57). Target B was successfully located by all methods at all tested depths in both orientations. At 0.3m depth in the horizontal orientation the target was picked at less than 7cm precision by all five methods.

In the case of target C, the orientation of the target had a notable impact on the results (Figure 59). In the vertical orientation, all methods were successful for all depths within less than 6cm. As for the horizontally oriented target, the different picking methods were unable to reliable detect the target due to lower SNR (Figure 58). We note that the noise levels for this data set were high, since they were based on one of the first MetalMapper 2x2 instruments manufactured.

Multiple seeds

The performance of the DC method was significantly lower than all other methods and plummeted with increasing depth, therefore, the DC method will be excluded from further comparisons. In the multi-seed case, statistical comparison exemplified that for vertically oriented targets there is no superior method that can be singled out; all methods performed equally (Figure 60 and Figure 61). The number of missed seeds gradually increases with increasing depth of burial. For horizontally oriented targets, the PAT, PSP and PLM methods yielded better results than the Standard and Derivative methods, particularly at shallower depths, as the depth increased the methods performance tied with their counterparts.

The distribution of distances of the picks from the seeds follows the same trend for all methods. The multi-seed case emphasized the effect of the target orientation on successful picking; the number of missed seeds is a significantly higher for horizontal seeds than for vertical seeds, i.e., ~62 vs ~14.

Summary

When the target of interest is isolated from other targets and has sufficient SNR, all the methods have the capability to locate it within high precision, regardless the orientation of the target. In non-ideal conditions, i.e., when the target of interest is near to other targets, the solution may converge to a close lying target. For the horizontal small ISO at 35 cm, this particular data did not have sufficiently high SNR for successful detection performance.

There is a gradual decrease in performance associated with increase in target depth but the influence of multi target situations on performance is certainly greater and less predictable. In order to avoid missed seeds in the future, particular multi target situations where the methods efficiency is compromised have to be characterized.

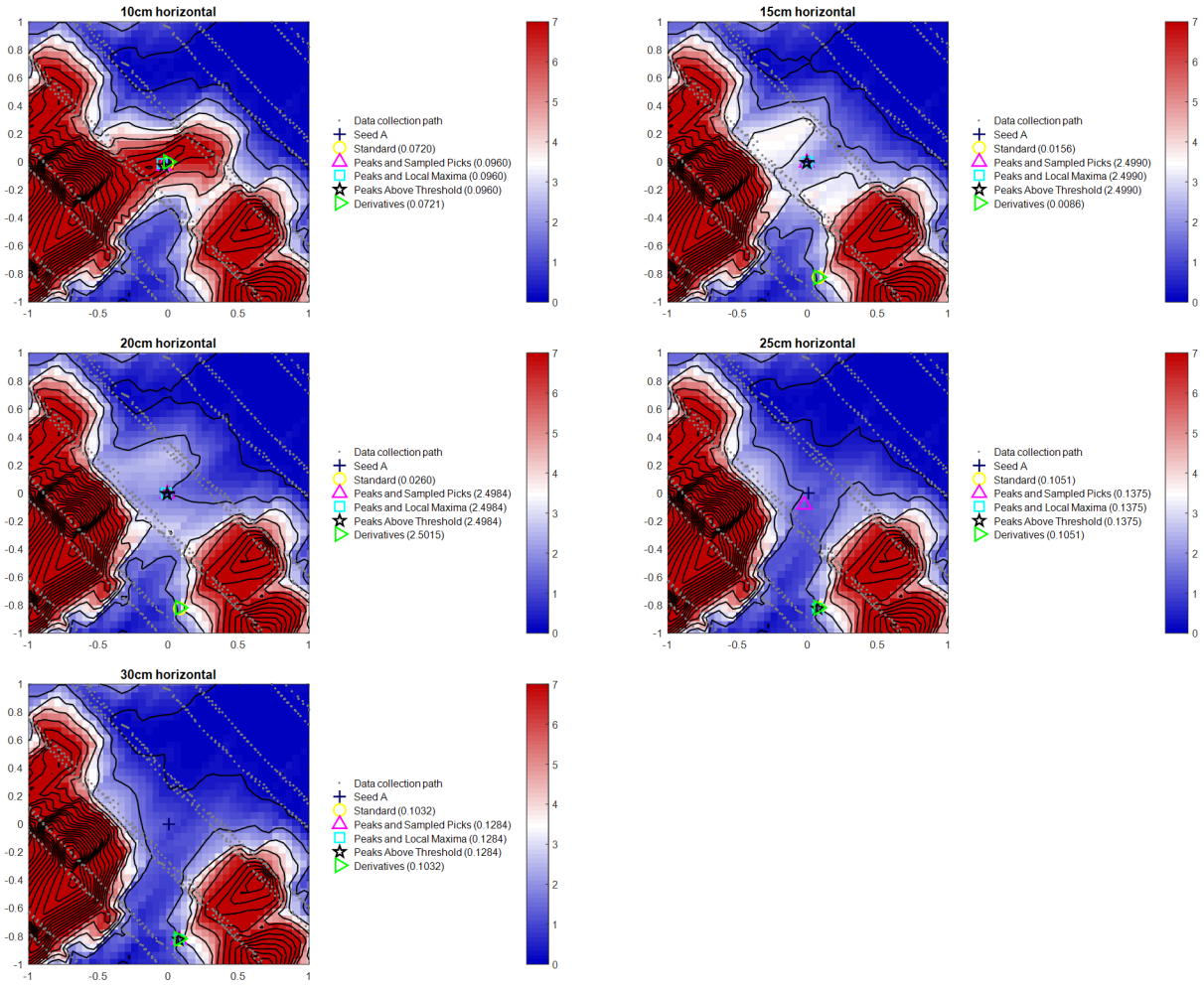

Figure 54. Seed A, horizontal. Comparison of target picking methods performance for depths varying from 0.1 to 0.3m. The true location of seed A is marked with a cross at (0, 0). The distance, in meters, between the target picker solution and the true location of the seed is listed in brackets next to each one of the methods.

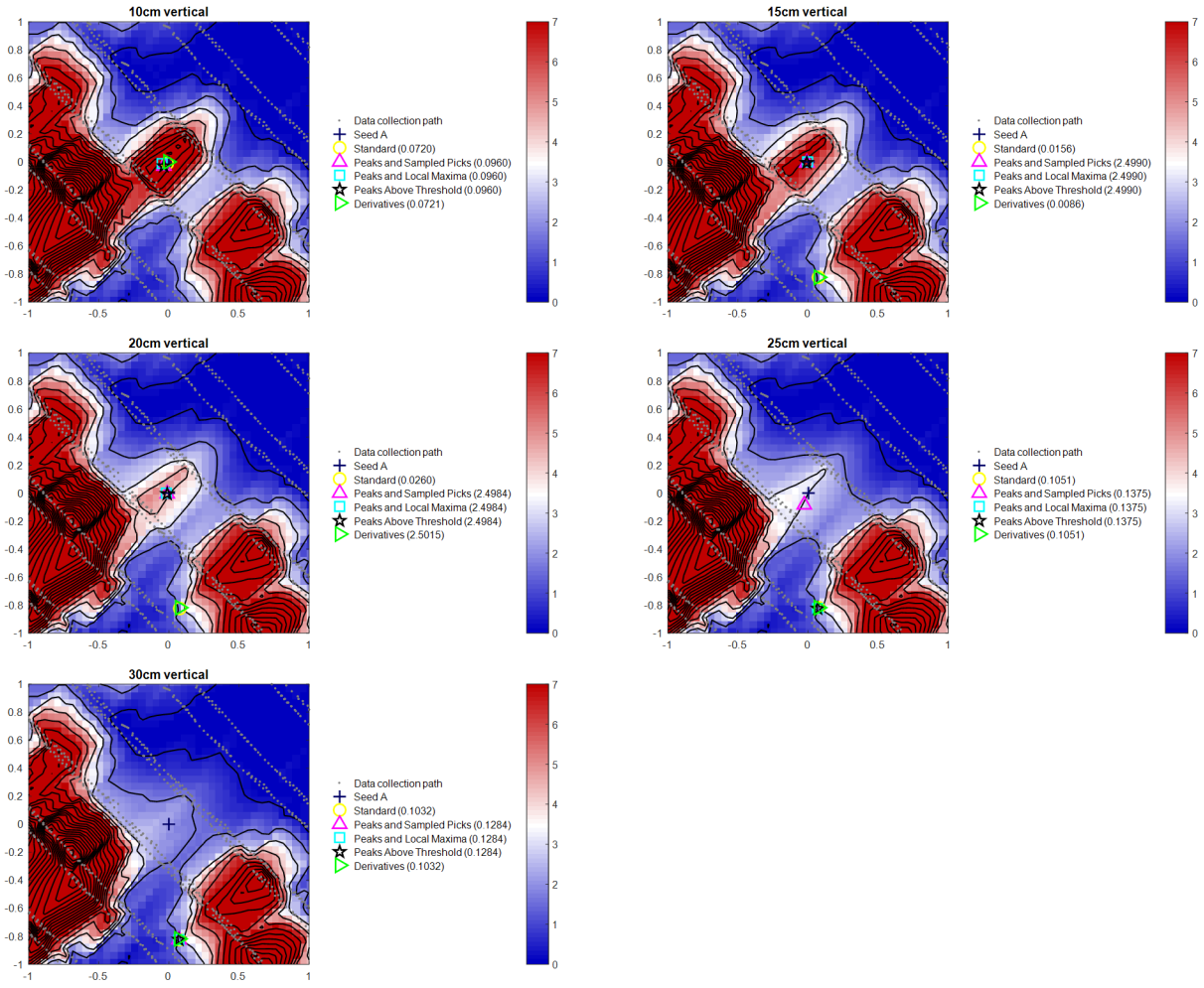

Figure 55. Seed A, vertical. Comparison of target picking methods performance for depths varying from 0.1 to 0.3m. The true location of seed A is marked with a cross at (0, 0). The distance, in meters, between the target picker solution and the true location of the seed is listed in brackets next to each one of the methods.

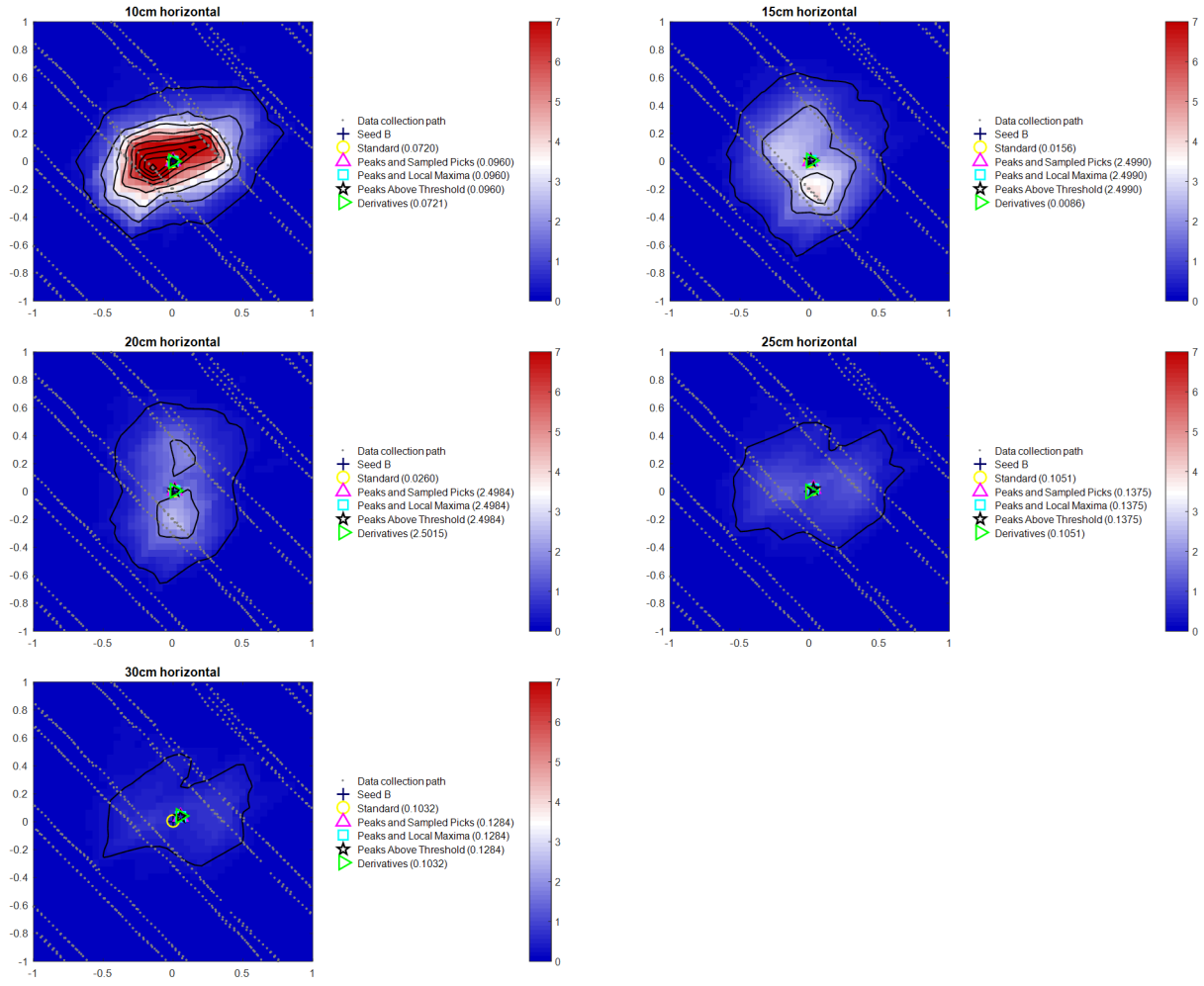

Figure 56. Seed B, horizontal. Comparison of target picking methods performance for depths varying from 0.1 to 0.3m. The true location of seed B is marked with a cross at (0, 0). The distance, in meters, between the target picker solution and the true location of the seed is listed in brackets next to each one of the methods.

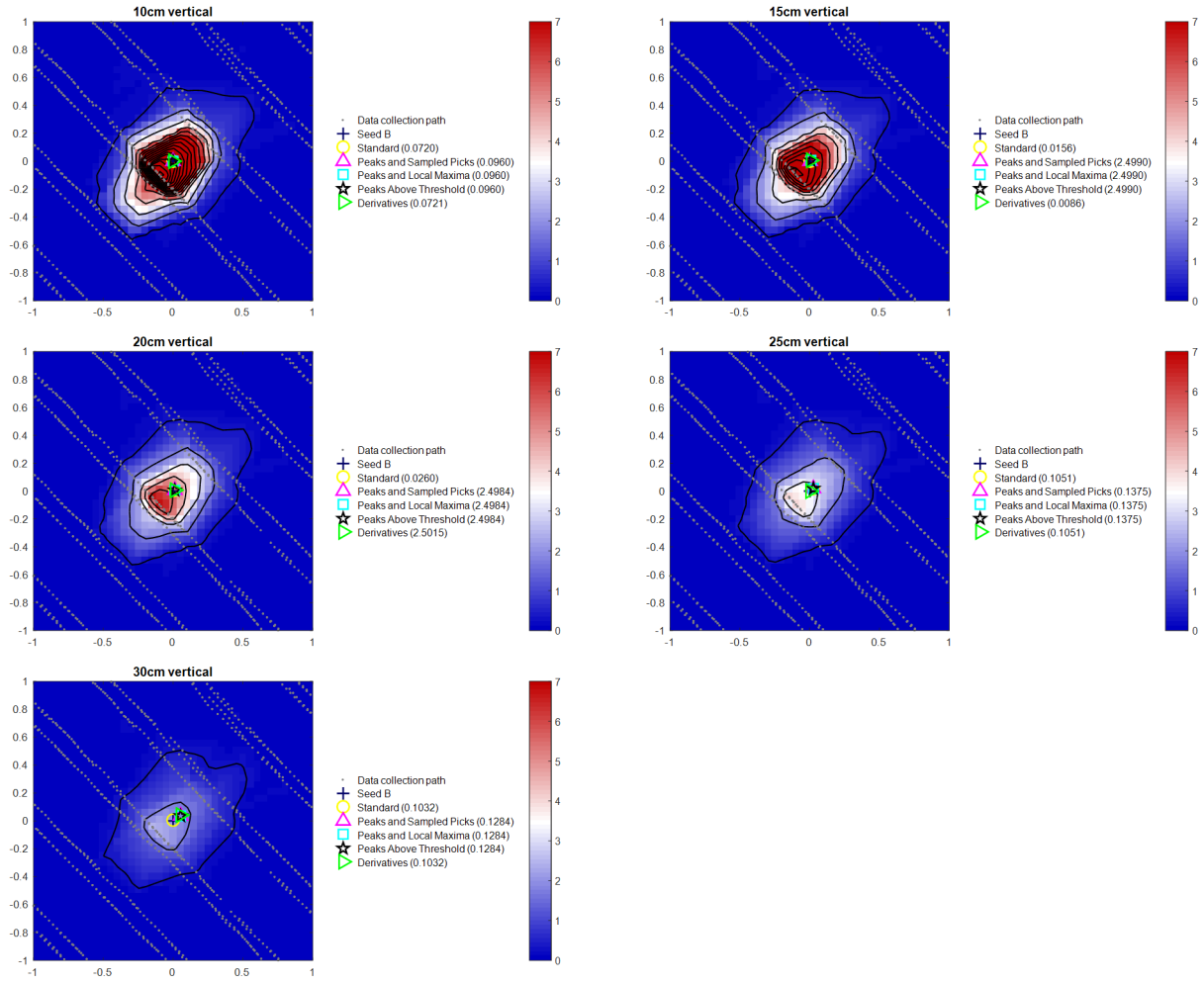

Figure 57. Seed B, vertical. Comparison of target picking methods performance for depths varying from 0.1 to 0.3m. The true location of seed B is marked with a cross at (0, 0). The distance, in meters, between the target picker solution and the true location of the seed is listed in brackets next to each one of the methods.

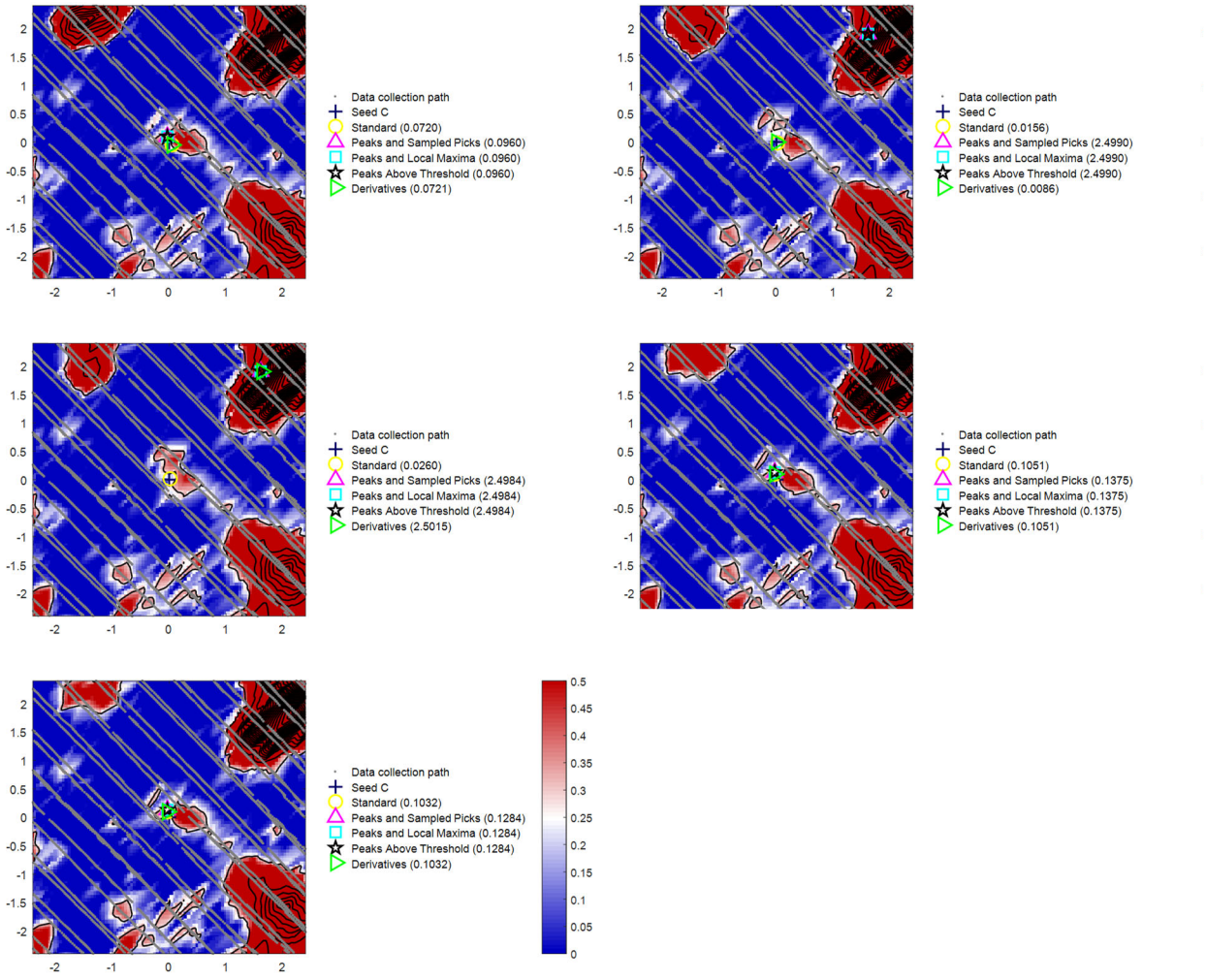

Figure 58. Seed C, horizontal. The depth in each case is 35 cm. The true location of seed C is marked with a cross at (0, 0). The distance, in meters, between the target picker solution and the true location of the seed is listed in brackets next to each one of the methods.

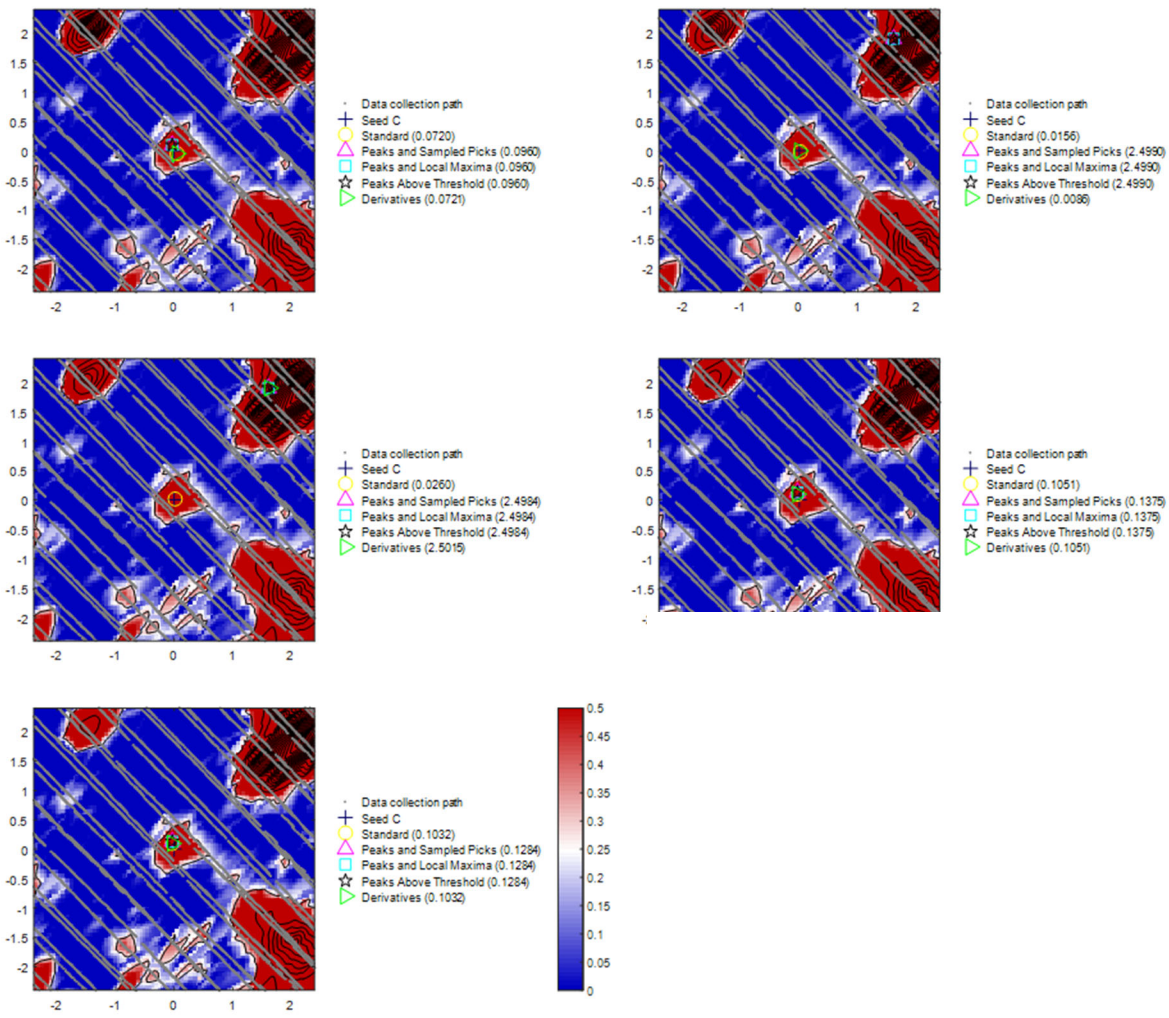

Figure 59. Seed C, vertical. The depth in each case is 35 cm. The true location of seed C is marked with a cross at (0, 0). The distance, in meters, between the target picker solution and the true location of the seed is listed in brackets next to each one of the methods.

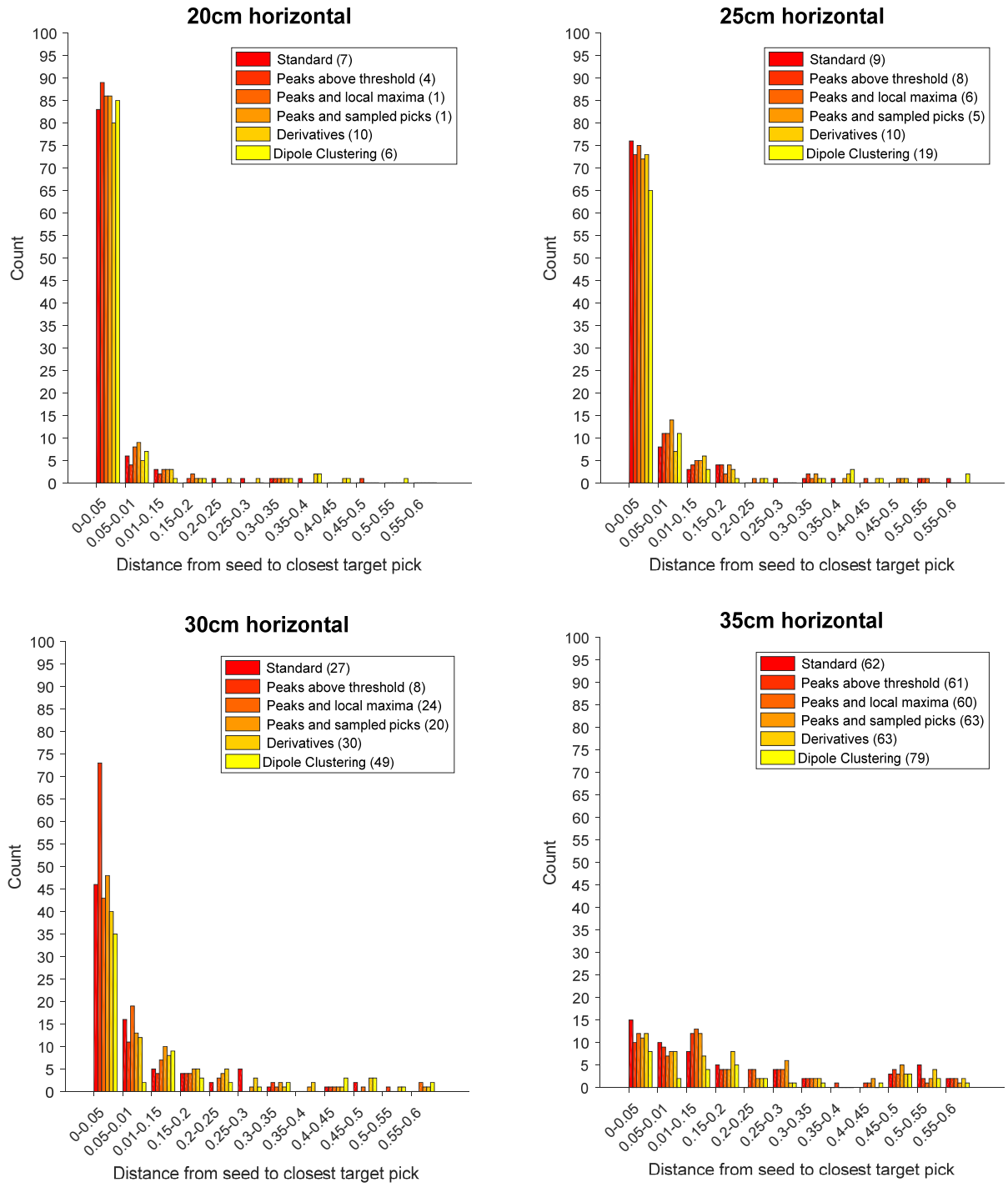

Figure 60. Comparison of methods based on count of missed seeds out of 100 planted horizontal seeds. A distance exceeding 0.25m from seed to closest target pick defined a missed seed. The total count of missed seeds is listed in brackets next to the method name.

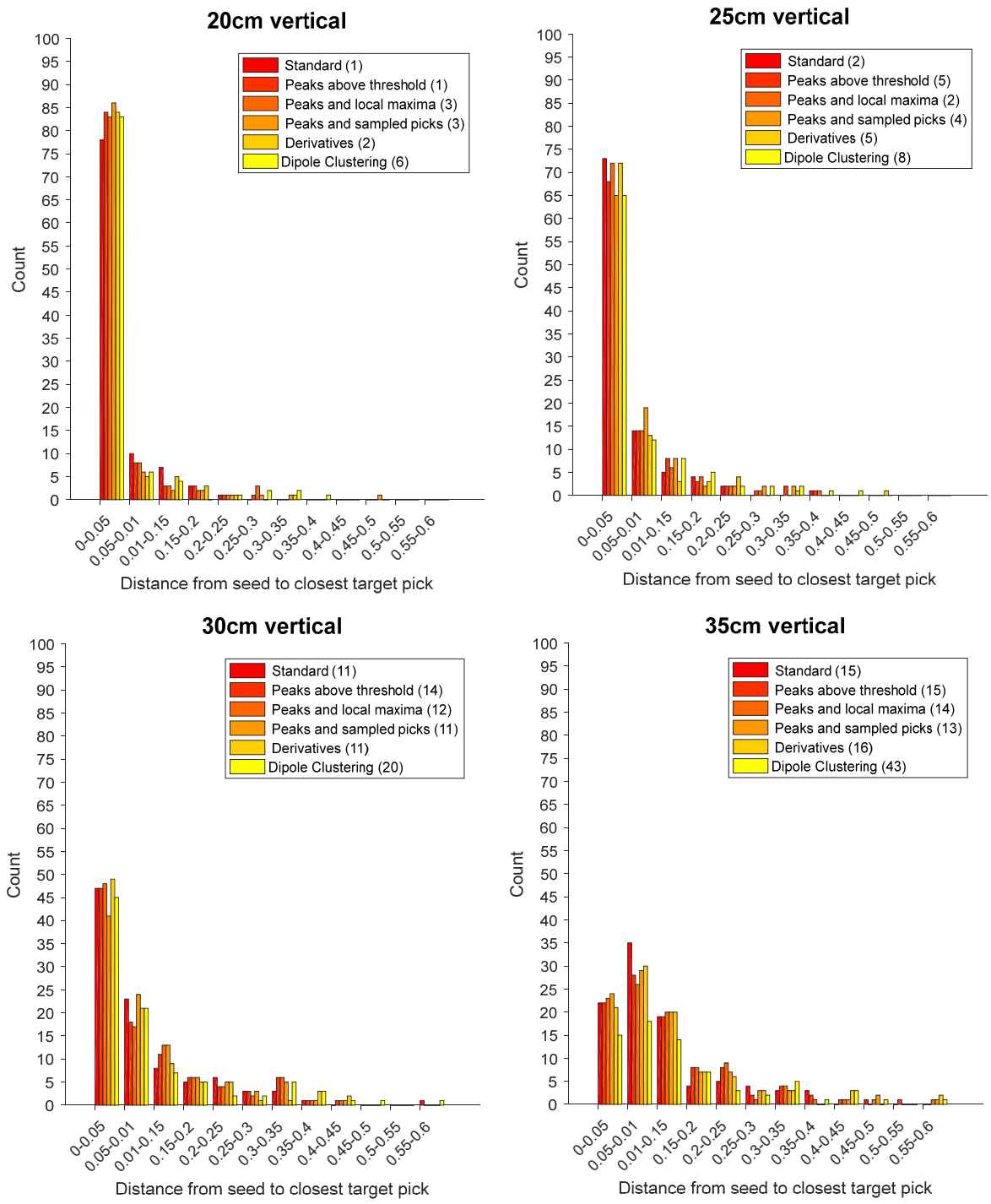

Figure 61. Comparison of methods based on count of missed seeds out of 100 planted vertical seeds. A distance exceeding 0.25m from seed to closest target pick defined a missed seed. The total count of missed seeds is listed in brackets next to the method name

Using Monte Carlo simulations for determining Source Screening Parameters

Lowry MetalMapper data: Establishing screening parameters

As part of a classification project at FLBGR, dynamic MetalMapper data was used to map the site. The "Standard" picking approach described in the section "Comparison of profile picking, dipole clustering and dipole filter target picking" was used to detect data anomalies along profiles. Data centered on each of the data anomalies were inverted dipole sources. The size and decay parameters based on the recovered polarizabilities from Column 13 data of data delivery unit 1 are shown in Figure 62.

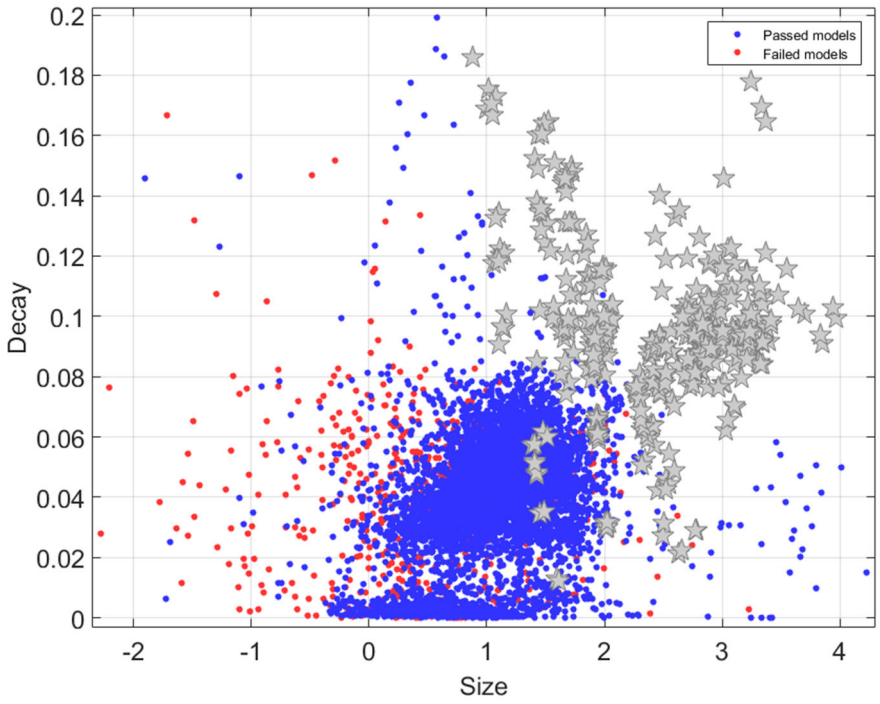

Figure 62. Size/Decay feature space for dynamic MetalMapper data collected on Column 13 at FLBGR. The grey stars represent targets from the ESTCP ordnance library.

The grey stars represent targets from the ESTCP ordnance library, the blue symbols represent models that will be used for analysis, and red symbols are models that were "failed" due to being a physically realistic model (e.g., spurious source, as determined via data and inversion metrics, see Section 4 of this report). The recovered polarizabilities suggest that the column 13 grid has many small targets (i.e., blue dots that sit to the left the grey stars) and thin walled, fast decaying targets. This suggests that the dataset would be suitable for using size and decay characteristics of the estimated dipole polarizabilities for screening.

Monte Carlo simulations were used to determine appropriate screening parameters for source selection. By synthetically seeding targets into survey data, we can obtain a measure of the expected spread in size and decay parameters. This information could then be used to partition the Size/Decay feature space into the set of anomalies to be screened, and anomalies requiring a follow-up cued measurement.

Four target types were used for the simulations: 20 mm TP M55A3B1, 20 mm AA MK7, 37 mm M80A1, and 37mm M59. These particular items were chosen, as they represent the fastest decaying and smallest sized 20mm and 37mm ESTCP library reference items, and therefore most influence the screening boundary of the size-decay feature space. To forward model responses, we used polarizabilities from the ESTCP library project.

For our first set of simulations, we seeded targets into a noise strip at the site. The targets are emplaced in a uniform grid throughout the data. The 37 mm targets were synthetically seeded at a depth of 0.254 m and the 20 mm targets were seeded at a depth of 0.13 m. The chosen 20 mm target depth corresponds to the expected clearance depth for the detection threshold. Targets were oriented randomly. Normally distributed random error with a standard deviation of 1 cm was added to the GPS positional information, and an error with a standard deviation of 1 degree was added to IMU. Each target type was synthetically seeded into the data, which created four separate data sets for analysis. A plot of the data emplaced with the smaller 37mm projectile is shown in Figure 63(a).

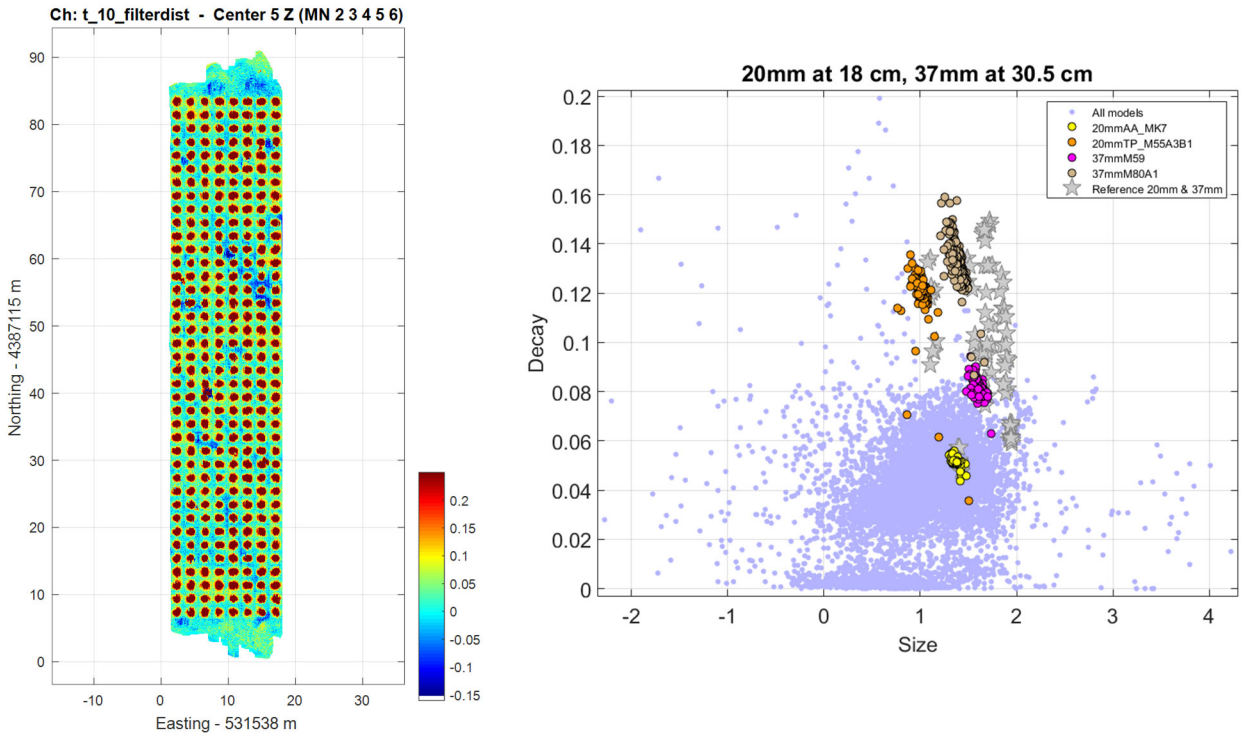

(a) synthetically seeded data

(b) spread in size and decay features

Figure 63. Seeds emplaced in the FLBGR noise strip

Figure 63(b) overlays the estimated size and decay parameters from the synthetically data onto the size/decay feature space of Column 13. Clusters of Monte Carlo realizations of the synthetically seeded noise strip are plotted as different coloured circles for both the fastest decaying and smallest sized

20mm and 37mm targets in the ESTCP library. Grey stars indicate all the 20mm and 37mm reference items from the ESTCP library.

Our initial plan was to use the results in Figure 63(b) to guide how the size/decay feature space should be partitioned for screening. However, synthetic seeding of 20mm and 37mm into the noise strip data does not address the challenge of multiple targets within the footprint of the sensor. In order to capture this more difficult scenario, synthetic seeding of those same 20mm and 37mm targets obtained through Monte Carlo simulations was performed on the Column 13 data. The synthetic seeding of Column 13 data did not involve any attempts to avoid existing target responses resulting in many cases of overlapping synthetically seeds targets with existing target signatures (Figure 64).

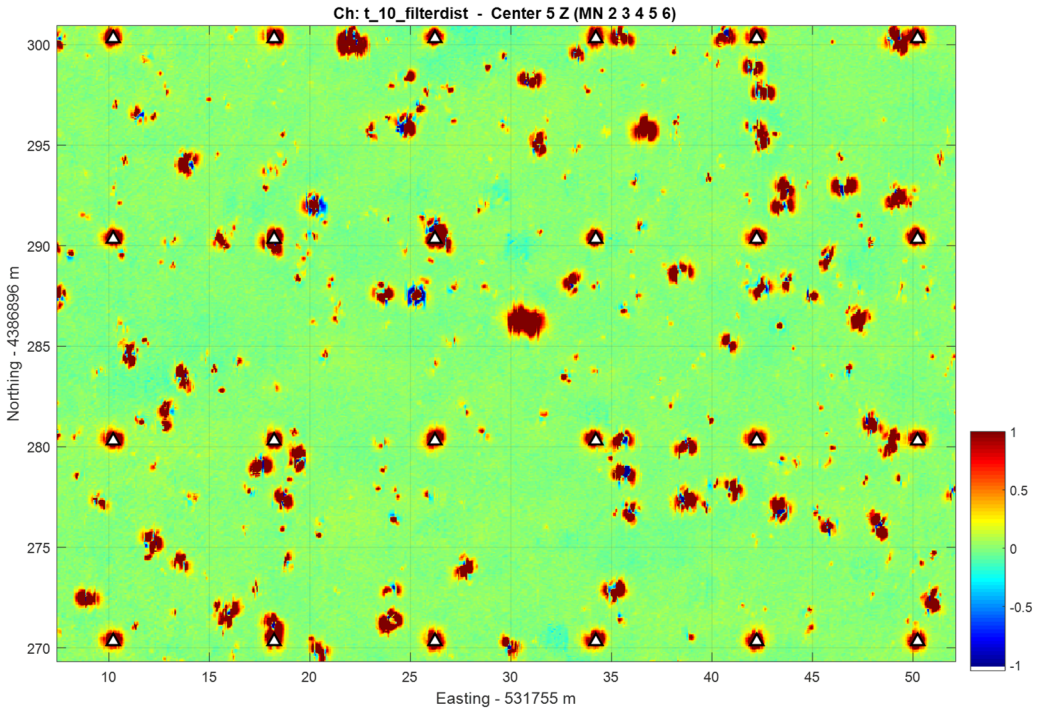

Figure 64. Synthetic seeding of Column 13 data. Targets were emplaced in a uniform grid within the Column 13 dataset. No anomaly avoidance was used. Locations of synthetic 37 mm M59 anomalies are indicated by white triangles.

The clusters resulting from the inversion of seeded Column 13 data are shown in Figure 65. The effect of having multi-source scenarios is evident: seeding the targets into Column 13 data produce a wider spread with more outliers for the fastest decaying and smallest sized ESTCP library items than was observed in the synthetically seeded noise strip data. The clusters tend to extend along a near-vertical line in size/decay space. Indeed, for lower SNR targets like the 20mm, the size parameter seems to be a more useful parameter for screening than using decay.

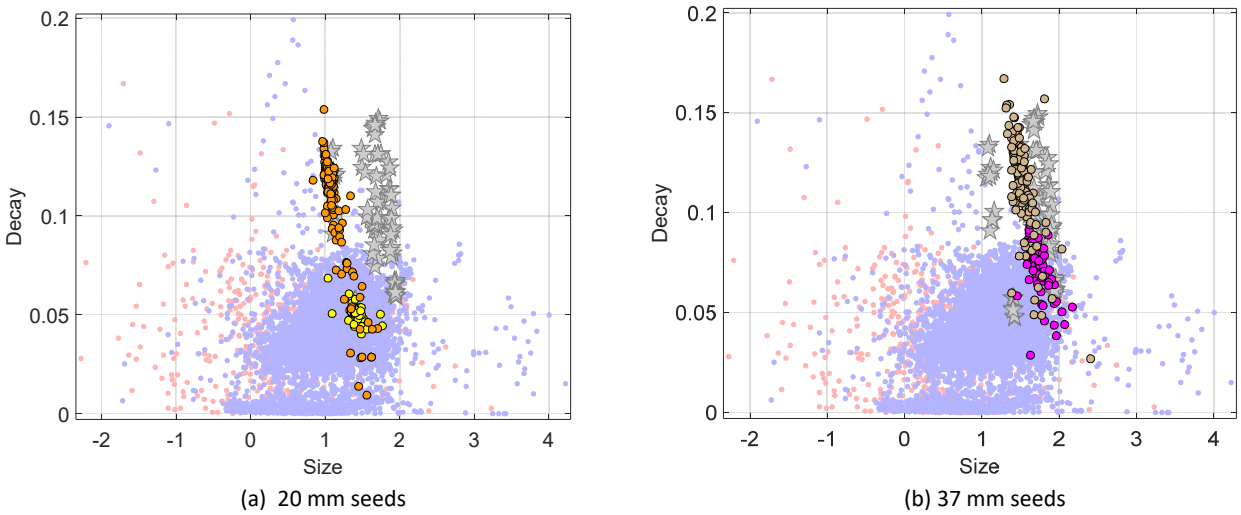

Figure 65. Size/Decay feature space of the synthetically seeded Column 13 data.

In order to define a screening line for 20 mm targets, we considered a pair of 20mm target types whose polarizabilities define the left edge of all 20 mm in the ESTCP library. A line was defined that intersected the median value of the clusters for the two types of 20mm projectiles. The median values of the clusters are indicated by white squares in Figure 66. This line is then shifted in the direction of the line's normal, until the all 20 mm outliers fall to the right of the line. We note that we operate in a normalized version of Size/Decay space, where size and decay values are divided by the median size and decay, respectively, from the Column 13 inversions. The distance *d* between the furthest outlier and the original line is calculated. In order to be conservative, the decision line is further shifted to the left such that the distance between the original line intersecting the median of the clusters and the decision line is 1.25 x *d*. The resulting decision line for the 20 mm is the thick black line in Figure 66.

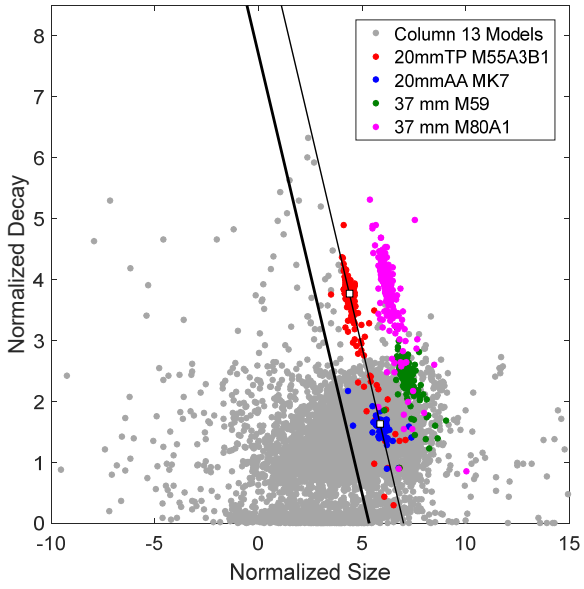

Figure 66. Decision line for the 20mm targets.

Once the screening line has been determined, only targets where all models (single and multi-source) fall to the left of the decision line will be screened. If any one of the models exceeds the screening threshold, the target will require a cued measurement. Figure 67(a) plots the targets that are not screened with a magenta box. Anomalies appearing to the left of the screening line, yet are not screened, are selected for a cued measurement because their inversion was labelled "Can't Analyze" due to data fitting issues. This conservative approach targets only small, fast decaying targets that are high confidence non-TOI for screening (see blue lines in Figure 67(b)). After the screening stage is complete, the source locations recovered from the inversions for the remaining targets are compared and sources that fall within 40cm of one another are merged to represent a single source.

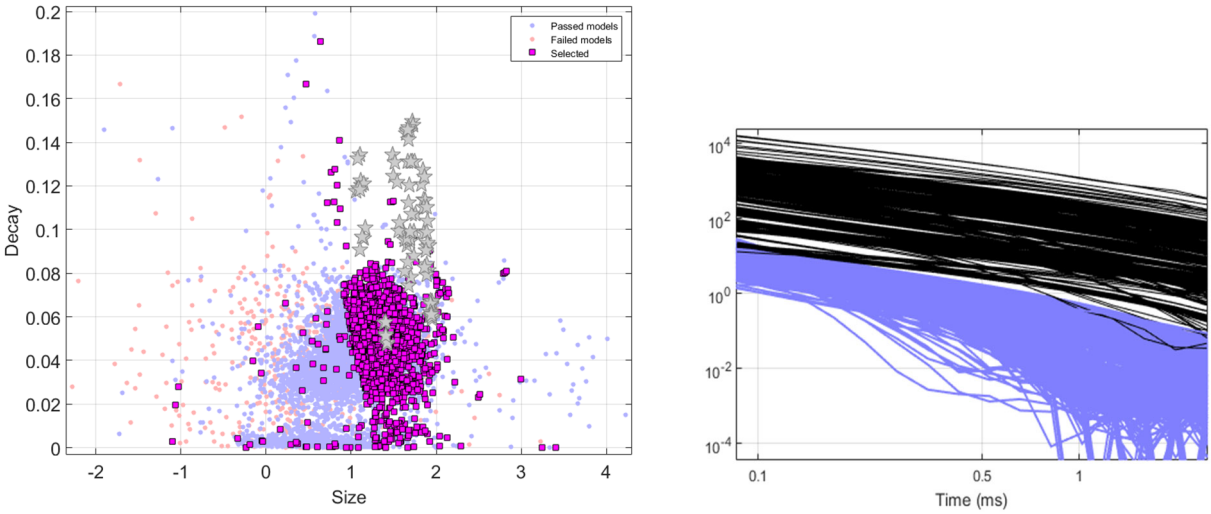

(a) Screening result

(b) Total polarizability for screened (blue) and anomalies to be cued (black)

Figure 67. Anomalies that are screened and retained when applying screening line.

Redstone Arsenal, AL: Screening using total polarizability

At the Redstone Arsenal, the TEMTADS 2x2 was used to collect full coverage dynamic data. In support of this CB&I company, we extended our Monte Carlo simulation codes to TEMTADS 2x2 data. For the Redstone project, the objective was to determine the distribution of polarizabilities for a MK18 Hand Grenade at the clearance depth for each grid. We note that the clearance depth grid dependent since the detection threshold was based on 5 times the noise, and noise characteristics changed from grid to grid.

Using MK18 Hand Grenade polarizabilities from the ESTCP library polarizability project, we synthetically seeded targets within the grid. For this project, we seeded the MK18 Hand grenade in areas where there were no picked targets and we inverted each seeded anomaly for only a single dipole source. An example of the synthetic seeding example is found in Figure 68. In Figure 68(a), we show the gridded image for the coaxial, z-component data from the 8th time channel, and in Figure 68(b) we show the gridded data after randomly oriented MK18 hand grenades were synthetically seeded at a depth of 36 cm.

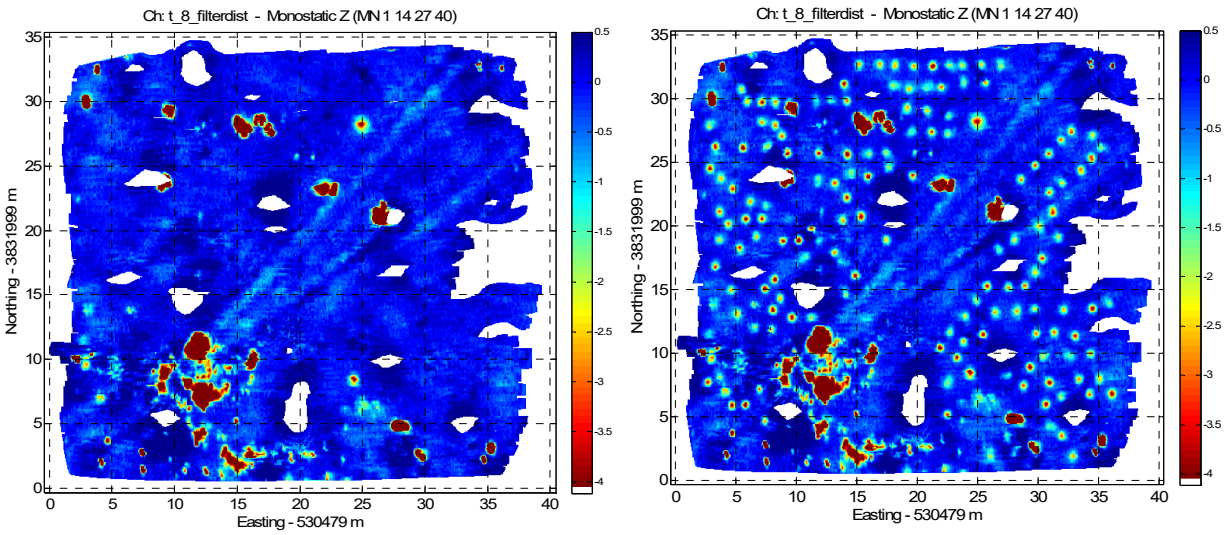

(a) Levelled Data (b) Levelled Data + Seeded MK18 Hand grenades.

Figure 68. Example of artificially seeding a MK18 smoke grenade in a grid. For Grid L09, the seeded targets are buried at a depth of 0.36 m and are randomly oriented. The anomalies are subsequently inverted to determine the range of expected polarizabilities.

In the previous section, we described how the size/decay feature space was used to screen anomalies. For this project, we decided to use the total polarizability, i.e., the trace of the dipole polarizability tensor. In this approach, we compare the recovered total polarizability to the minimum expected total polarizability for an MK18 hand grenade. The trace of the polarizability tensor is used rather than the eigenvalues, since the trace is a more robust value to estimate from noisy data.

The range of polarizabilities – and therefore the amount of screening – is a function of target depth and data noise. To demonstrate this effect, we created data sets with the MK 18 grenade buried at a depth of 25 cm and 30 cm in the L09 grid, in addition to the 36 cm deep dataset corresponding to the L09

clearance depth. Figure 69 Shows the range of recovered total polarizabilities compared to the total polarizabilities from the ESTCP library. We see that the minimum total polarizability (black dashed line) become lower in amplitude as the grenade is emplaced deeper.

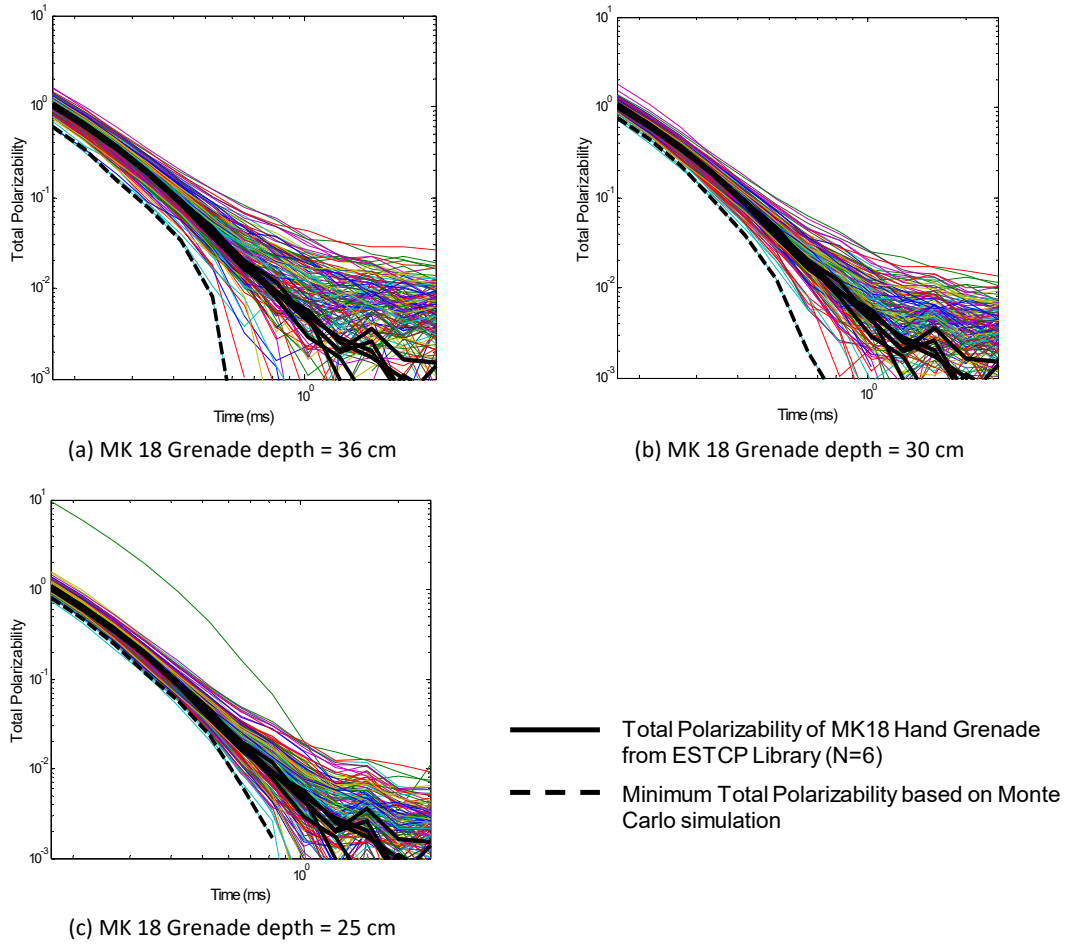

(a) MK 18 Grenade depth = 36 cm

(b) MK 18 Grenade depth = 30 cm

(c) MK 18 Grenade depth = 25 cm

Figure 69. Recovered total polarizabilities of artificially seeded anomalies. The recovered total polarizabilities are plotted in various colours, with the minimum total polarizability indicated by a black dashed line. The solid black lines show the 6 samples of total polarizabilities of the MK18 smoke grenade from the ESTCP Library.

Figure 70 shows how the number of screened targets change as a function of depth for grid L09. The 91 anomalies in grid L09 were inverted for single and multiple sources. We compare the minimum expected total polarizability to each recovered polarizability. Only the first few time channels are used for the comparison. For comparison, we include the total polarizability for a 20mm projectile and a small ISO. We see that the screened anomalies are generally smaller and faster decaying than a 20 mm. Of the 91 anomalies picked in Grid L09, only 11 anomalies have polarizabilities smaller than the Mk18 smoke grenade threshold when considering a clearance depth of 36 cm. At this site we see that, due to high noise levels and the fast-decaying smallest TOI, there is very limited screening ability with this technique. Indeed, for some of the other grids at Redstone, the Monte Carlo modeling suggested that screening would be ineffective, and that all anomalies on the grid be assigned a cued data measurement.

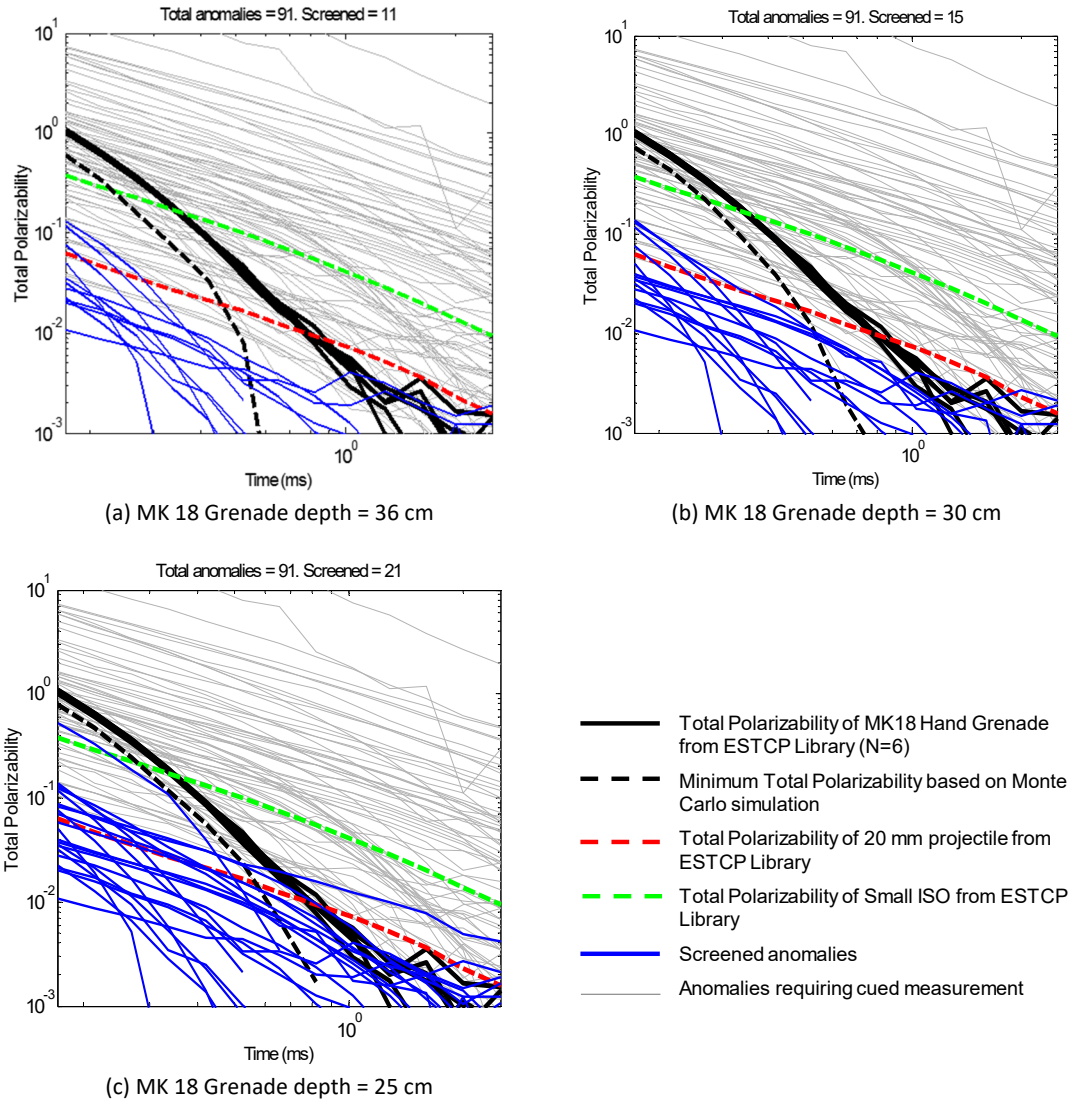

Figure 70. Screening Results for Grid L09 when assuming different clearance depths for the MK18 Grenade.

2. Multi-Source Inversions for data collected at cluttered sites

Investigation into multi-source algorithm modifications and enhancements

Nonlinear inversion for multiple objects using mixed norm

Introduction

In this study, we consider the problem of inverting multiple objects. Given measured EMI data $\mathbf{d}(t)$, we describe them as a response superposition contributed from each individual one among η sources:

$$\mathbf{d}(t) = \sum_{k=1}^{\eta} A(\mathbf{r}_k)\, \mathbf{q}_k(t), \tag{28}$$

where $A(\mathbf{r}_k)$ is the sensitivity matrix for the kth source at $\mathbf{r}_k$ and $\mathbf{q}_k(t)$ a vector representing the correspondent source polarizability. The goal of an inversion is to recover the polarizations of multiple objects, as well as their locations, i.e., $\mathbf{m}_k = (\mathbf{q}_k, \mathbf{r}_k), k = 1, \dots, \eta$. Ideally, the inversion can be deterministic if the number of objects is known exactly. However, this often is not the case in reality. Since there is no *a priori* knowledge of the number of targets within the field of sensor view, we choose a redundant representation to model EMI signals. That is, we often assume a value of η being larger than the actual number of sources. Then the model parameters $\mathbf{m}_k, k = 1, \dots, \eta$ are sought by minimizing the data misfit between the observed and predicted in the least squares sense:

$$\widehat{\mathbf{m}} = \underset{\mathbf{m}}{\operatorname{argmin}} \left\| d(t) - \sum_{k=1}^{\eta} A(\mathbf{r}_k)\mathbf{q}_k(t) \right\|_2^2 \tag{29}$$

Under a redundant model representation, we wish to avoid missing any potential targets of interest. But meanwhile we are also at a risk of over-fitting noisy data using a complex model. As a result, the accurate recovery of true targets is likely compromised.

Sparsity Perspective on representation of multiple objects

To mitigate the aforementioned issues, we re-considered the problem of the multiple source inversion from a sparsity perspective. We can view the EMI response as a linear combination of group polarization signals. Each group vector consists of polarization elements of an object to be determined. Having a larger number of objects than expected, we are to seek a redundant, yet sparse, representation of EMI signals. This is consistent with our underlying assumptions that the objects are sparse as they typically occupy a small fraction of the overall region of interest. Further by group-sparsity, we mean that only a few groups remain non-zeroes and the remainder are zeroes. By the introduction of group sparsity, we wish to relax the assumption of the number of objects by reformulating the multiple object inversion as a recovery of group-sparse signals.

Inversion using mixed norm

$l_1$norm has been widely used to measure or promote the sparsity desired in various scientific and engineering problems. For our problem here, we might follow a standard way to impose the sparsity measure on the polarizabilities when solving the nonlinear least squares optimization. However, due to the nonlinearity of the problem related to the source locations, finding a location that corresponds to near-zero polarizability is difficult by directly sparsifying polarizabilities. Instead, we consider the response as a quantity to be sparsified. As described earlier, the measurements are the sum of responses from each source, i.e., $\mathbf{d} = \mathbf{d}_1 + \mathbf{d}_2 + \cdots + \mathbf{d}_\eta$. Thus, for a redundant representation of η sources, we

expect some assumed sources that have no contributions to responses. To fulfill the goal, we introduce an objective function that consists of a sum of response contributions from each individual target: $\|\mathbf{d}_1\|_2 + \|\mathbf{d}_2\|_2 + \cdots + \|\mathbf{d}_\eta\|_2$. This is called the mixed norm measure. By minimizing such an objective function, we try to express $\mathbf{d}$ which is sparse at group level. Ideally, the non-zero components of $\mathbf{d}$ just occur at few specific groups (locations) within which the elements are non-sparse. Thus, the minimization of the mixed norm automatically boils down to seeking for a representation that uses the minimum number of objects. In other words, we optimize a problem of minimal signal contributions from all necessary targets that sufficiently explain the data.

Eventually by adding a constraint that requires the data misfit being equal or less than a threshold δ, we define the optimization problem using the mixed norm as follows:

$$\widehat{\mathbf{m}} = \underset{\mathbf{m}}{\operatorname{argmin}} \|\mathbf{d}_1\|_2 + \|\mathbf{d}_2\|_2 + \cdots + \|\mathbf{d}_\eta\|_2 \text{, subject to } \|\mathbf{d} - \mathbf{d}_{\text{pred}}\|_2^2 \leq \delta \tag{30}$$

where $\mathbf{d}_{\text{pred}}$ is the predicted response. Such a threshold δ would be set to a known or desired noise level. To make the algorithm parameter choice free, we choose to set the threshold as the sum of residuals derived from our standard non-linear inversion processing. This means that we can use the minimal contribution optimization strategy to refine the previous solution derived from the non-linear inversion. To improve computation time, we have also implemented the approach in temporally projected domain (TOPI) where a few major projected channels are required. In addition, we supply a gradient function in the minimization.

An example

Figure 71 shows a synthetic noisy example where a single-object (medium ISO) is present within the field of view. To test the algorithm, we use a redundant representation, a 3-object model, to conduct the inversions. Figure 71(a)-(c) are the recovered polarizabilities derived from our standard nonlinear least-squares approach. The response contributions are, approximately, 80%, 11%, and 9% from the inverted sources. The latter sources model sensor noise. Figure 71(d)-(f) are the recovered polarizabilities from the inversion using mixed norm. In this case, the response contributions are approximately 5.2%, 3.6%, and 91.2% from the inverted three sources. By comparison, we observe that the mixed norm solution not only minimizes the contributions to the responses from spurious sources but also estimates much smaller amplitudes of polarizabilities of these artificial sources. Similarly, Figure 71(g)-(i) are the results when the mixed norm inversion was implemented in the TOPI domain. The response contributions are approximately 2.8%, 5.6% and 91.6% from the inverted three sources.

Summary

We have proposed a new inversion approach that aims to penalize contributions from spurious sources when a redundant representation is used to model EMI signals. The problem is formulated using the notion of sparsity. In contrast to the conventional measure of sparsity, we impose a sparsity measure as a sum of l_2 norm (a mixed norm) over the group signals. By minimizing an objective function that consists of a sum of response norms subject to fit to observations, we can enforce selection of only necessary sources to explain the data. The techniques can be implanted either in the original data or TOPI domain. The tests with MPV and TEMTADS 2x2 instruments show that the new method works well but at the expenses of extra computation time when compared to our nonlinear least-squares based multiple-object inversion technique.

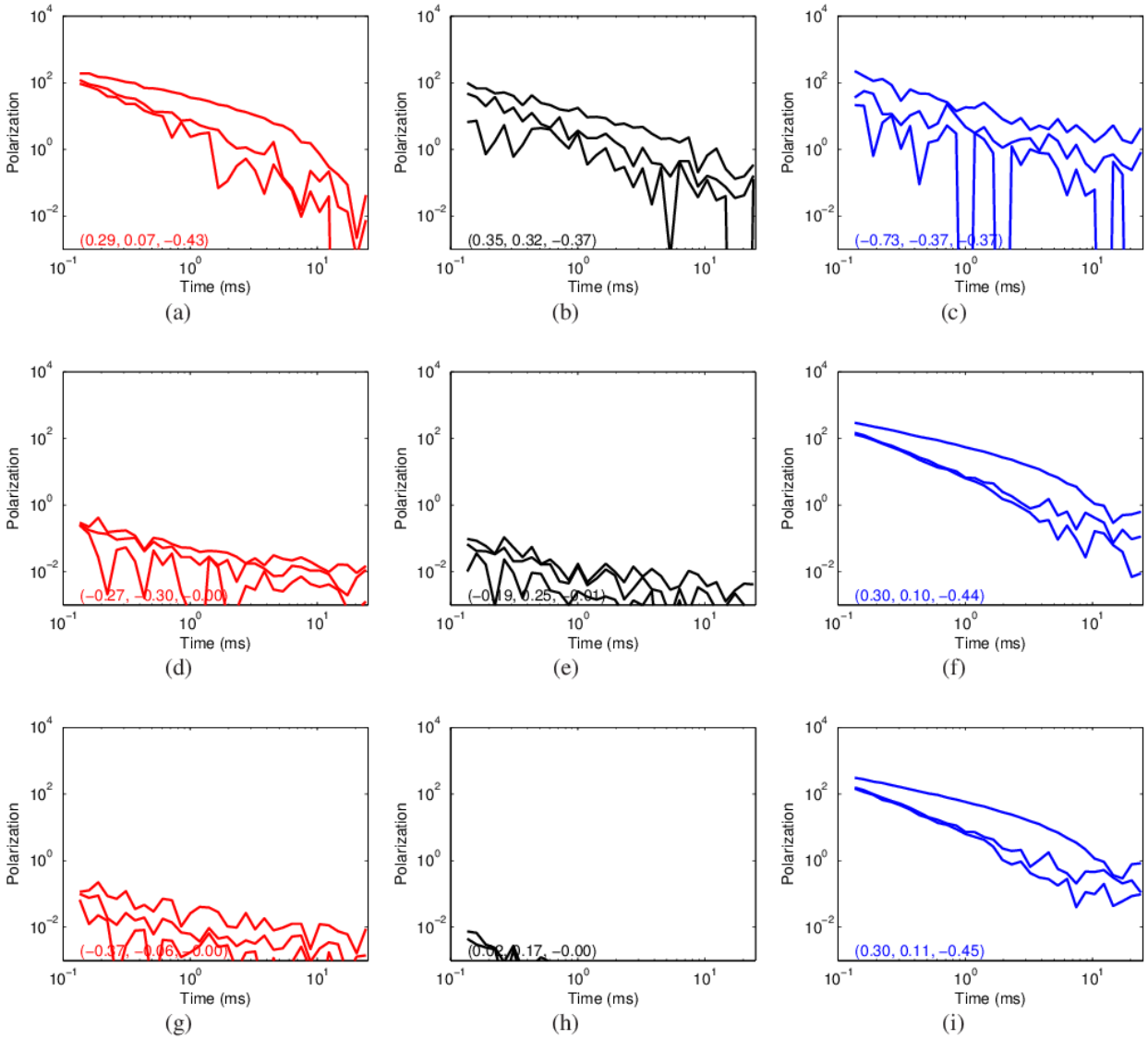

Figure 71. Recovered polarizabilities from the three-object inversion of synthetic noisy data. (a)-(c) Standard nonlinear least square solution; (d)-(f) Mixed norm solution; (g)-(i) Mixed norm-TOPI.

Accelerating the multi-object inversion: An augmented matrix approach

Introduction

In our standard nonlinear multi-object inversion technique, a constrained linear least-squares optimization is embedded for solving the time-dependent polarizabilities of targets for a given set of locations. Mathematically, the problem is expressed as

$$\min_{\mathbf{q}(t)} ||\mathbf{d}(t) - A(\mathbf{r})\mathbf{q}(t)||_2^2 \qquad \text{subject to } C\mathbf{q}(t) \leq \mathbf{b}, \tag{31}$$

where $\mathbf{q}(t)$ is a vector composed of polarizability tensor elements, $\mathbf{d}(t)$ a vector of the observed data, $A(\mathbf{r})$ is a sensitivity matrix at locations $\mathbf{r}$, C a constraint matrix derived from the positive definiteness of the polarizability tensor, $\mathbf{b}$ an associated constraint vector. This linear optimization problem is numerically solved for data at each time channel separately. We use an iterative algorithm, a MATLAB solver lsqlin to perform the task. For *N* channels, we need to solve the problem *N* times.

Augmented matrix approach

Notice that the EMI responses are nonlinear with respect to source locations $\mathbf{r}$ and linear source polarizabilties (t) . As both parameter sets are separable, the sensitivity matrix $A(\mathbf{r})$ that is the function of source locations is identical for all dynamic polarizations. Therefore, a pseudo-inverse A^+ is also the same for data at all time channels and can be constructed in a closed-form to solve the least-squares problem. With the pseudo-inverse, it seems impossible to impose positive definite constraints on the polarizabilities as does via the MATLAB numerical solver lsqlin. However, by introducing slack variables $\mathbf{s}$, we can convert those inequality constraints into equality constraints $C\mathbf{q} + \mathbf{s} = \mathbf{b}$. Further treating these constraints as "virtual measurements" and appending them into the measurement equation $\mathbf{d} = A\mathbf{q}$, then we have an augmented matrix and an associated pseudo-inverse. This approach is similar to solving the regularized inverse problem by reformulating as a least squares solution. Once the pseudo-inverse of the augmented matrix is constructed, obtaining the solution $\mathbf{q}(t)$ at each time channel becomes a matrix-vector product. Consequently, using the augmented pseudo-inverse saves the inversion significantly, roughly 6-7 times faster than the use of the iterative solution method.

Modified augmented matrix approach

In a number of tests with the pseudo-inverse based inversion, we observed a phenomenon that the inversion tends to produce collocated false sources for a multi-source model (see the example below). This might be attributed to the ill-conditioning of the augmented matrix. If this is the case, the question arises how we can regularize the inverse problem and increase the numerical stability.

Recall that we are solving the problem in a least-squares sense. A well-known property in a least-squares solution is that residual vector is orthogonal to the columns of the sensitivity matrix, i.e., $A^T\mathbf{e} = 0$, $\mathbf{e} = \mathbf{d} - A\mathbf{q}$. Thus, by enforcing this orthogonal property and introducing residual vector as extra unknowns, we obtain a new modified augmented matrix system:

$$\begin{bmatrix} A & \alpha I & 0 \\ 0 & A^T & 0 \\ C & 0 & I \end{bmatrix} \begin{bmatrix} \mathbf{q} \\ \alpha^{-1}\mathbf{e} \\ \mathbf{s} \end{bmatrix} = \begin{bmatrix} \mathbf{d} \\ \mathbf{0} \\ \mathbf{b} \end{bmatrix} \tag{32}$$

Keep in mind that among the unknowns only $\mathbf{q}$ is needed. In the new formulation, we can add a scalar α to improve the condition of a matrix.

Summary with an example

We have done a number of tests on the use of a pseudo-inverse of the modified augmented matrix. We have found that the scalar plays a role in regularizing a solution. To illustrate, we process anomaly 1210 from the TEMTADS 2x2 data set acquired at SWPG. Figure 72 shows the recovered polarizabilities from a two-object model inversion. Figure 72(a)-(b) are the results with the iterative solver lsqlin; Figure 72 (c)-(d) the pseudo-inverse of the augmented approach with $\alpha = 1$; Figure 72(e)-(f) the pseudo-inverse of the augmented approach with $\alpha = 200\|A\|_1$. In this example, the lsqlin-base inversion appears to provide a somewhat suspected TOI anomaly at (-0.06, 0.01, -0.46) m but with noisy polarizabilities that probably due to the impact of the second source at (-0.05, 0.07, -0.43) m. As shown in Figure 72 (c)-(d) with the pseudo-inverse approach ($\alpha = 1$), the inversion yields the collocated sources at (-0.04, 0.08, -0.41) m that are physically impossible. However, when we empirically applied a large value of α, the results changed. The result in Figure 72 (e)-(f) is the one that we attempted an automatic yet heuristic way to set the α in the augmented matrix. Now at we recovered an anomaly at (-0.06, 0.01, -0.46) m with much cleaner polarizabilities. For classification, we are certain to dig such an anomaly and ignore the second source that is related to data noise. With the modified augmented matrix, it looks promising that the stability issue of pseudo-inverse-based method can be effectively resolved and the inversion can be significantly accelerated without compromising the recovery accuracy.

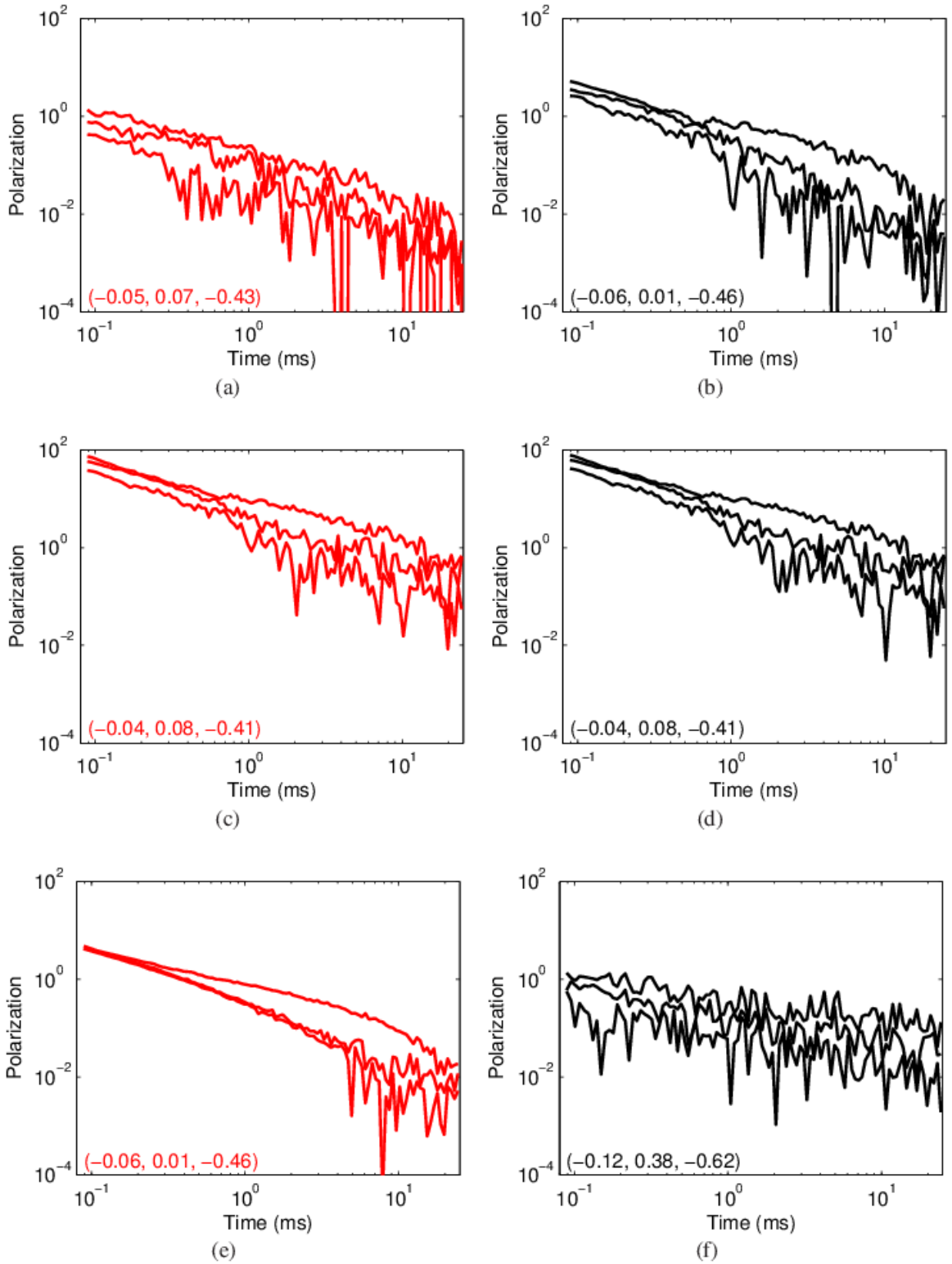

Figure 72. Recovered polarizabilities from the two-object inversion of field anomaly 1210 at SWPG site. Plots (a)-(b) show recovered polarizabilities when inverting using lsqlin. Plots (c)-(d) show the estimated polarizabilities when using a pseudo-inverse with α=1. Plots(e)-(f) show estimated polarizabilities when using a pseudo-inverse with α=200||A||_1.

Deterministic Initialization for multi-source inversion by a fast Gram-Schmidt orthogonalization

Introduction

A primary problem facing EMI data processing is to accurately determine source locations. Often, the problem is solved by minimizing a misfit between observed and predicted data in a least-square sense. Since EMI responses are nonlinearly related to the source locations, the minimization is a nonlinear optimization process and requires an initialization. Since the final solution of the minimization depends on its initial estimate, an initialization appears critical. We have developed a multi-start strategy to initialize an inversion by a random sampling over a region of interest. The initialization procedure has been demonstrated being computationally efficient. Yet, the uncertainty nature inherent with random sampling may lead to missing good initial locations or possibility of being trapped in local minima due to limited sampling. Such probable scenarios might be mitigated by increasing the number of sampling points at the expense of computational times. But to avoid stochastic components embedded in the optimization, we consider an alternative way, deterministic, to initialize a multi-object inversion.

Uniform 3D grid and sequential search initialization

To initialize in a deterministic way, first we define a region of interest (ROI) that is sufficiently large to cover the active objects. Second, we create a uniform 3D grid to sample the space and treat each grid point as a potential source location. Probably, the simplest way of initializing is to do an exhaustive search over the grid for any combinations of candidate points. However, this immediately turns out to be prohibited since it can produce an astronomical number of possible source configurations. For example, we wish to initialize *n* sources over *M* grids (*M* >> *n*). There would be $\binom{M}{n}$ source combinations to be evaluated. Consider even a coarse grid of 11 × 11 × 11 over a volume of 1 m × 1 m × 1 m and *M* = 1331, for *n* = 2 we end up with an enormous search over 885115 potential pairs of sources.

To make the problem tractable, we proposed a sequential procedure over a given 3D grid:

1) Search for the first source by solving a single-source linear least-squares problem;

$$\hat{\mathbf{r}}_1 = \underset{\mathbf{r}_1}{\operatorname{argmin}}\, \epsilon(A(\mathbf{r}_1), \mathbf{d}), \tag{33}$$

where $A(\mathbf{r}_1)$ is the sensitivity matrix at a candidate location $\mathbf{r}_1$ and $\hat{\mathbf{r}}_1$ is the solution after minimizing the least-squares data misfit ϵ with respect to observed data $\mathbf{d}$.

2) Given the searched first source at $\hat{\mathbf{r}}_1$, we find the second source at $\mathbf{r}_2$ by solving a two-source linear problem, i.e.,

$$\hat{\mathbf{r}}_2 = \underset{\mathbf{r}_2}{\operatorname{argmin}}\, \epsilon(A(\hat{\mathbf{r}}_1), A(\mathbf{r}_2), \mathbf{d})\,; \tag{34}$$

3) Similar step continues to find the *k*th source given the *k-1* searched sources, i.e.,

$$\hat{\mathbf{r}}_k = \underset{\mathbf{r}_k}{\operatorname{argmin}}\, \epsilon(A(\hat{\mathbf{r}}_1), \ldots A(\hat{\mathbf{r}}_{k-1}), A(\mathbf{r}_k), \mathbf{d})\,; \tag{35}$$

In the process, we use the SVD (singular value decomposition)-like algorithm as our basic least-squares solver for ensuring the stable and accurate result.

This strategy avoids a large amount of computation in an exhaustive search for multiple objects. Nevertheless, it is increasing to solve a large system of equations like $[A_1 \ldots A_k]$ and its computational complexity is increasing rapidly. As a result, such initialization can slow down with an increasing number of objects.

Fast Gram-Schmidt method

In the sequential initialization of multiple sources, we need to solve an increasingly appended system that is proportional to the number of sources. Is there a way that we can avoid appending when adding more sources to search? If so, then computation cost can be saved. Following the path, we present a fast Gram-Schmidt (FGS) method to speed up the deterministic initialization algorithm. The Gram-Schmidt (GS) orthogonalization is a well-known QR decomposition that decomposes a matrix as a product of an orthogonal matrix and unit upper triangular matrix. The usual GS orthogonalization, which is commonly referred to dealing with the columns of a matrix, has been widely studied and used to solve a least-squares problem. In the research of MR-1572, the GS procedure was applied to the multiple-object case where the orthogonalization was implemented over sub-matrices A_i not the columns of a matrix. This might be viewed as a block GS method. The conventional block GS method explicitly constructs orthogonal matrices and its computation is roughly equivalent to a SVD-based least squares solver.

Because of using the orthogonal matrices in the GS algorithm, we noticed that the data misfit can be computed without a need of appending sub-matrices. It is this property that allows to evaluate each candidate grid in the deterministic initialization. By introducing some intermediate correlations quantities, we can carry out a new Gram-Schmidt procedure without a need to construct the orthogonal matrices explicitly. In the new GS procedure, we recursively calculate: 1) correlations between data and the orthogonal matrices of already selected sources; 2) correlations between candidate matrices and the selected orthogonal matrices. This procedure can be implemented rapidly since its major operations only involves matrices and vectors with dimesons of 6 x 6 and 6 x 1 and also a number of quantities can be pre-computed and used repeatedly.

In a test with TEMTADS data, we use 3025 grid points to produce five initial models. In a two-object case, it took a standard LS or the block GS about 0.07 minutes to initialize the task. For the same two-object case, it took the FGS 0.04 minutes. The FGS improves about 43% of computation over the usual LS method. In a three-object case, it took the usual LS/the block GS about 0.15 minutes to finish initialization. On the other hand, it costed the FGS 0.08 minutes. As a result, the FGS saves about 46% of the usual LS computation (See Figure 73(b)).

Summary

In this study, we propose a sequential search initialization scheme over a uniform 3D grid for the nonlinear multiple source inversion. To further reduce the computational load of the initialization process, we implement a fast Gram-Schmidt procedure that mainly involves operations of small matrices and short vectors. The test showed that the speedy performance of the FGS. Therefore, the FGS-based deterministic initialization can be an alternative choice to the random multi-starting starting scheme.

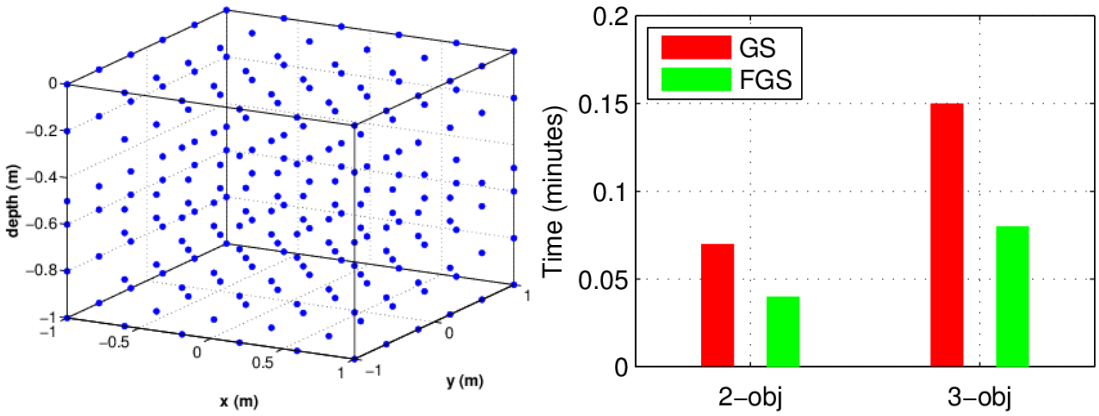

Figure 73. Gram Schmidt example

Space-Time MUSIC Imaging of EMI Sensing Data and a Subspace Partition Study

To localize sources in electromagnetic induction (EMI) sensing, we propose a spacetime MUSIC (MUltiple SIgnal Classification) imaging approach. Under the EMI physical model, the approach is established upon a receiver array-based spatial and temporal response matrix. In contrast to the multi-static response matrix-based MUSIC imaging approach that requires a sufficient number of receivers and transmitters, the new imaging scheme relaxes the condition on a large number of transmitters and thus becomes applicable to a wide range of EMI sensing systems. We also investigate the issue of forming a noise subspace - an essential determiner to the MUSIC performance. Our theoretic analysis indicates that the choice of an underestimated noise subspace is appropriate for the imaging. Thus, it implies, when doing a subspace partition required in the MUSIC, that a difficult task of exactly distinguishing signal from noise eigenvalues can be eased greatly in a practical eigenvalue distribution map. The technique is evaluated through the synthetic and real data. The results show that the space-time MUSIC can be used to detect sources with an EMI system consisting of multiple receivers but a few transmitters. As predicted from the theoretical analysis, the tests show that the MUSIC-source locations are robust to under-estimates of the dimension of the noise subspace.

1. Introduction

In EMI sensing, identifying buried metallic objects in terms of the extracted polarizations requires accurate estimates of target locations [39] [21] [22]. Several existing methods might be used to approach this problem. Usually, localization of sources can be formulated as nonlinear inverse scattering problem by minimizing a data misfit from a starting model [8] [7] [6] [12] [16] [29] [28]. Other noniterative methods of localizing EMI sources have been attempted like an adaptive focusing technique [40] adapted from radar and sonar array processing [41] and a multi-static response matrix (MRM)-based MUSIC (MUltiple SIgnal Classification) imaging algorithm [37]. On the MRM-MUSIC, Ammari and his colleagues [42] [43] proposed it to locate electromagnetic small inclusions buried in subsurface at a fixed frequency. Their important theoretical and numerical results of MRM-MUSIC reactivate the studies of this technique introduced by Schmidt [44]: including the resolution and stability analysis using MUSIC [45], the use of Hadamard's matrices in order to enhance the signal-to-noise ratio in the measurements [46], the investigation of a relationship between imaging functionals and Bessel functions of the first kind of integer order in 2D [47]. For a detailed mathematical and statistical aspects of multi-static imaging and other direct imaging approaches like Kirchhoff imaging, backpropagation, etc., readers may refer to the excellent monograph [48]. In the quasi-magnetostatic approximation where the displacement and electrical conduction currents are negligible, Song et al. later [37] presented a multi-time channel multi-static MUSIC-type algorithm for imaging UXO-like objects with a loop transmitters and receivers and evaluated it with field EMI data. The analytical expressions in [37], which relates signal singular vectors of the MRM with the steering field vectors either from transmitter or receiver side, are similar to the ones in Ammari et al.'s earlier work in frequency domain [42] [43].

In the context of EMI based detection, previously developed multi-static response matrix (MRM) based MUSIC [37] is suitable for a system like the TEMTADS 5x5 [30] that consists of multiple transmitters and receivers. The MRM-based MUSIC requires the numbers of transmitters and receivers larger than the number of targets to be detected [42] [43] [37]. However, in practice, such a condition might not be

always satisfied for implementing MRM-based MUSIC. Some smaller EMI sensing instruments with a few transmitters have been designed and widely used for cost-effective survey in challenging environments. Such a typical system is the MetalMapper [49] (having three orthogonal transmitters).

To make the MUSIC a practical application in EMI sensing, one goal of this study is to remedy the technical difficulty encountered in the MRM-based MUSIC for a system consisting of multiple receivers but a few transmitters. Inspired by the original MUSIC [44] that uses space-time array data to find the directions of arrival (DOA) in radar applications [50] [51], we reformulate the MUSIC imaging approach using the receiver array-based spatial and temporal response matrix under the EMI physical model. The newly formulated imaging approach overcomes the limitation of MRM-based imaging approach with only a few of transmitters.

There is also the key issue of estimating the noise subspace. The core idea of the MUSIC algorithm estimating sources is to use the orthogonality between signal and noise subspaces and to seek the minimum projections of the array Green's functions onto a noise subspace [44]. To define a noise subspace *a priori*, a common way is to enumerate signal eigenvalues and noise eigenvalues of a data matrix [52]. However due to measurement errors that alter signals and model approximations to a real-world problem, there is often no ideal gap in an eigenvalue map to distinguish them [37] [52]. The significant eigenvalues may be statistically determined assuming a known noise distribution [53]. In turn, one practically faces an inexact estimate of signal and noise subspaces, and is not clear how such an estimate can affect the performance of the MUSIC. To understand the issue, another task is to investigate the sensitivity and stability of the MUSIC algorithm with respect to various estimates of a noise subspace. Further we aim to establish a theoretic foundation that can be used to guide estimating noise subspace for the accurate MUSIC imaging.

The remaining parts of this paper are organized as follows. In section II, we describe the data model and present the new formulation of the MUSIC imaging technique based upon receiver-based spatial-temporal response matrix. In section III, we present a theoretic analysis shows how estimated subspace partitions can affect the projection in the imaging process. In section IV, the synthetic and real data are used to evaluate the new MUSIC imaging technique and examine effects of the estimated noise subspaces on source localization. In section V, we discuss the theoretic and numerical results about subspace partition and propose a simple rule to form an underestimated noise subspace. Section VI concludes the paper.

2. MUSIC Imaging Method

2.1 Signal model and receiver-based spatial-temporal response matrix

In active EMI sensing, a primary field emitted from a transmitter illuminates the subsurface and its abrupt changes with time induce eddy currents in the metal object. These induced currents produce a transient secondary magnetic field that is measured by a receiver. For a UXO survey where the target dimension is often small relative to the target-sensor distance, the primary fields around the target are approximately uniform and the induced eddy currents in the target are localized and predominantly produce dipole responses [31] [32]. The EMI scattering nature of a metal target can generally be well

represented by an equivalent induced dipole. Here we assume that dipole location is independent of time. If the target location is denoted by $\mathbf{r}$ then the induced dipole moment $\mathbf{m}(t)$ at time t is represented by [1] [8] [6] [12]

$$\mathbf{m}(\mathrm{t}) \;=\; P(\mathrm{t})\mathbf{B}_T\,(\mathbf{r}, \mathbf{r}_{Tx}), \tag{36}$$

where $\mathbf{B}_T$ is the exciting magnetic field vector at the target location from a transmitter at $\mathbf{r}_{Tx}$ and $P(t)$ is a 3 × 3 symmetric magnetic polarizability tensor (MPT)

$$P(t) = \begin{bmatrix} p_{11}(t) & p_{12}(t) & p_{13}(t) \\ p_{12}(t) & p_{22}(t) & p_{23}(t) \\ p_{13}(t) & p_{23}(t) & p_{33}(t) \end{bmatrix}. \tag{37}$$

where each element $p_{ij}(t)$ represents a dipole component in the ith Cartesian direction due to a primary field in jth Cartesian direction and where t is time. This polarizability tensor $P(t)$ has an eigen-decomposition as

$$P(t) = \sum_{s=1}^{3} L_j(t)\mathbf{e}_s\mathbf{e}_s', \tag{38}$$

where $\mathbf{e}_s$ (s = 1,2,3) is the orthonormal eigenvector representing the jth principal direction of dipolar polarization with respect to a reference system, and $L_s(t)$ is the principal polarization strength that is a function of the geometry and material of a target. In other words, $P(t)$ contains the information about the geometry and physical properties of a target as well as its orientation. The prime denotes a transpose.

Consider a multi-static array consisting of M receivers and J time channels, i.e., i = 1,⋯ ,M, j = 1,⋯ ,J, and N transmitters. The measured secondary response of a target to the nth exciting field might be designated as $d_{ij,n}$ [1] [8] [12] [28]

$$d_{ij,n}(\mathbf{r}_{Rx_i}, \mathbf{r}_{Tx_n}, t_j) = \mathbf{B}'_R(\mathbf{r}, \mathbf{r}_{Rx_i})\mathbf{m}_n(t_j), \tag{39}$$

where $\mathbf{m}_n(t_j) = P(t_j)\mathbf{B}_T(\boldsymbol{r}, \boldsymbol{r}_{Tx_n})$, $\mathbf{B}_T(\boldsymbol{r}, \boldsymbol{r}_{Tx_n})$ is the field vector at target location $\mathbf{r}$ generated by the n^{th} transmitter and $\mathbf{B}'_R(\mathbf{r}, \mathbf{r}_{Rx_i})$ is the field which would be produced at $\mathbf{r}$ by a current flowing in the ith receiver. t_j is the jth time instant. Equation (39) describes the basic EMI process of illuminating, scattering, and sensing and it is the model from which we begin our formulation of the MUSIC imaging methodology. Collect all measured responses together in the following way:

$$D_n(t) = \begin{bmatrix} d_{11,n} & \cdots & d_{1J,n} \\ \vdots & \vdots & \vdots \\ d_{M1,n} & \cdots & d_{MJ,n} \end{bmatrix},\ n = 1, \cdots, N. \tag{40}$$

We say that Equation (40) defines a Rx-based $M \times J$ spatial-temporal response matrix (RxSTRM) for a given transmitter. In Equation (40), its row corresponds to measurements from the same receiver at

different time channels and its column corresponds to measurements from different receivers (a receiver array) at a given temporal channel.

Replacing each entry in Equation (40) with Equation $d_{ij,n}(\mathbf{r}_{Rx_i}, \mathbf{r}_{Tx_n}, t_j) = \mathbf{B}'_R(\mathbf{r}, \mathbf{r}_{Rx_i})\mathbf{m}_n(t_j)$, (39), we rewrite Equation (40) as

$$D_n = G_{Rx}(\mathbf{r})Q'_n, \tag{41}$$

where $G_{Rx}(\boldsymbol{r})$ is an $M\times 3$ the receiver array response matrix defined as

$$G_{Rx} = \begin{bmatrix} \mathbf{B}'_R(\mathbf{r}, \mathbf{r}_{Rx_1}) \\ \vdots \\ \mathbf{B}'_R(\mathbf{r}, \mathbf{r}_{Rx_M}) \end{bmatrix}, \tag{42}$$

and Q'_n is a $3 \times J$ the moment matrix given by

$$Q'_n = \begin{bmatrix} \mathbf{m}_n(t_1) & \cdots & \mathbf{m}_n(t_J) \end{bmatrix}, \tag{43}$$

whose column corresponds to induced moment components at one temporal channel for the nth transmitter. Equations (40) and (41) has similar forms to the data matrix and the signal model used in the MUSIC-based DOA estimation [44] [50] [51].

2.2 Singular vectors and receiver array Green's function

In the following discussion, we drop off the subscript n for simple notation. Taking the singular value decomposition (SVD) [36] of D corresponding to one excitation in Equation (40) and assuming its rank $k \leq \min(M,J)$, we can express D as

$$D = \sum_{i=1}^{k} \sigma_{ii}\mathbf{u}_i\mathbf{v}'_i \quad . \tag{44}$$

where the $\mathbf{u}_i$ and $\mathbf{v}_i$ are the ith left and right singular vectors, respectively. Theoretically, the singular values σ_{ii} arranged in decreasing order are zeros for $i= k+1,\cdots, M$ if $M< J$.

To interpret the SVD of D in (44), we relate the triplet $\{\sigma_{ii},\mathbf{u}_i,\mathbf{v}_i\}$ to field quantities G_{Rx} and M. Following [35, 27], we can transform the mathematical representation D of a data matrix in Equation (41) into a semi-analytical SVD form:

$$D = (G_{Rx}W_{Rx}^{-1}U_X)\Pi(QW_Q^{-1}V_X)', \tag{45}$$

where $W_{Rx} = (G'_{Rx}G_{Rx})^{\frac{1}{2}}$, $W_Q = (Q'Q)^{\frac{1}{2}} \cdot U_X, V_X$,and Π are the SVD quantities of matrix $X = W_{Rx}W_Q = U_X\Pi V'_X$. Its left and right singular vectors are the columns of the product matrix $G_{Rx}W_{Rx}^{-1}U_X$ and the product matrix $QW_Q^{-1}V_X$, respectively. The nonzero singular values of D are the diagonal entries of Π, i.e., the eigenvalues of the square matrix X. Therefore, the singular values derived from measured

data depend upon the three factors: the intrinsic target polarization, its orientation, and field strength that are encoded in the product matrix X.

For noise-free data, the two SVDs in Equations (44) and (45) are identical and the rank k of D will be three if there is a single object. By equating the singular vectors in the two SVDs, we might express the relationship between the left and right singular vectors in Equation (44) as

$$\mathbf{u}_i = G_{Rx}\mathbf{c}_i,\ \mathbf{v}_i = Q\mathbf{f}_i,\ i = 1, \cdots, 3, \tag{46}$$

where $c_i = W_{Rx}^{-1}U_{X,i}$ and $f_i = W_Q^{-1}V_{X,i}$ represent the ith coefficient vectors. We see that for $\sigma_{ii} > 0$ the singular vector $\mathbf{u}_i$ are the linear combinations of the receiver array Green's function matrix G_{Rx} and form an orthonormal basis for receiver array space, whereas the singular vectors $\mathbf{v}_i$ are linear combinations of the orthonormalized moment source matrix Q and form an orthonormal basis spanning the temporal space. Both left and right singular vectors contain information of the target locations and moment polarizabilities. The former, i.e., left singular vectors $\mathbf{u}_i$ will be used in MUSIC-like imaging to estimate target location. Finally, there is no direct connection of Π with the principal polarizabilities of L_j. The eigenvalues of an RxSTRM cannot be simply interpreted as apparent principal polarizabilities as in the multi-static response matrix that is composed of measurements taken with a sufficient number of transmitters and receivers [37].

The SVD analysis tells that the data matrix D given in Equation (40) has rank $k \leq p = \min(M, J)$. However, we have $D = G_{Rx}Q'$ (see Equation (41). From matrix analysis theory [35], we infer that $rank(D) = rank(G_{Rx}Q') \leq \min[rank(G_{Rx}), rank(Q')]$. Provided $M \geq 3$ and $J \geq 3$ then both $rank(G_{Rx}) \leq 3$ and $rank(Q') \leq 3$, this restricts the maximum rank of D for a single object to be 3. This is the number of the principal polarizations manifested in Equation (38).

The above analysis is similarly applied to a general case of multiple objects. Suppose that there are η objects contributing to the data. The sizes of matrices G_{Rx} and Q'_n in Equation $D_n = G_{Rx}(\mathbf{r})Q'_n$, (41) become of $M \times 3\eta$ and $3\eta \times J$, respectively. Then the maximum rank for a RxSTRM is 3η assuming that $M \geq 3\eta$ and $J \geq 3\eta$.

2.3 MUSIC imaging function

We use the left singular matrix derived from a RxSTRM to form the projection matrices related to the MUSIC spatial function and to discuss the subspace partition subsequently.

Given that the matrix has a rank k in Equation (44), we can group these SVD constructed orthonormal vectors into the left signal subspace, i.e., $U_s = [\mathbf{u}_1, \cdots, \mathbf{u}_k]$. The remaining singular vectors, $U_n = [\mathbf{u}_{k+1}, \cdots, \mathbf{u}_M]$ forms the left noise subspaces.

Signal and noise projection matrices P_S and P_N are given by

$$P_S = U_s U_s' = \sum_{i=1}^{k} \mathbf{u}_i \mathbf{u}_i',\ P_N = U_n U_n' = \sum_{i=k+1}^{M} \mathbf{u}_i \mathbf{u}_i' \quad . \tag{47}$$

Both projection matrices obey a constrained relation

$$P_S + P_N = I \tag{48}$$

where I is an identity matrix with an appropriate size.

As shown in Equation (46), the array function G_{Rx} corresponding to a target location lies in the subspace spanned by the U_s. Then the projection of the array Green's functions G_{Rx} onto the noise subspaces spanned by U_n will be zero, i.e.,

$$P_N G_{Rx} = 0. \tag{49}$$

From the property of Equation $P_N G_{Rx} = 0$. (49), we introduce a MUSIC-type functional or spatial spectrum for source imaging or localization.

$$\mathcal{S}(\mathbf{r}) = \sum_{i=1}^{3} \frac{\|G_{Rx,i}(\mathbf{r})\|^2}{\|P_N G_{Rx,i}(\mathbf{r})\|^2}, \tag{50}$$

where $||\cdot||$ denotes the 2-norm of a vector. Equation (50) measures the inverse projections of components $G_{Rx,i}$ onto the noise subspace, which can sharp the spatial imaging. We would expect that $\mathrm{S}(\mathbf{r})$ peaks at or near a target location where $G_{Rx}(\boldsymbol{r})$ lies in the signal subspace.

For the MRMs with multiple channel responses, the common singular vectors of the MRMs are sought [27] by employing the joint diagonalization technique [36]. To implement the RxSTRM-based MUSIC with a few excitations, we also want to find the common left singular matrix U shared for $D_1,\cdots,D_n$. From the SVD of Equation (44), we know that the eigenvectors of the square matrix $C_n = D_n D_n'$ are the left singular vectors of D_n. Thus, forming a set of real-valued square matrices

$$\{C_1, \cdots, C_N\} = \{D_1 D_1', \cdots, D_N D_N'\}, \tag{51}$$

we can simply perform joint diagonalization and obtain the common left singular matrix U that "diagonalizes" all the given matrices as:

$$C_1 = U\tilde{\Sigma}_1 U', \cdots, C_N = U\tilde{\Sigma}_N U', \tag{52}$$

where $\tilde{\Sigma}_1, \ldots, \tilde{\Sigma}_N$ are diagonal matrices. Then these common singular vectors in are used in the MUSIC imaging to localize the objects.

3. Rank estimate and subspace partition

In this section, we provide a theoretic analysis to get an insight into the projection consequence of a subspace partition.

3.1 Exact estimate of rank

Assume that an exact estimate of the rank is k. Using the relation in Equation (46), we might rewrite the signal projection matrix as

$$P_S = \sum_{i=1}^{k} \mathbf{u}_i \mathbf{u}_i' = G_{Rx} \left(\sum_{i=1}^{k} \mathbf{c}_i \mathbf{c}_i' \right) G_{Rx}' \quad . \tag{53}$$

According to the definitions in Equations (45) and (46), we have

$$\sum_{i=1}^{k} \mathbf{c}_i \mathbf{c}_i' = W_{Rx}^{-1} \left(\sum_{i=1}^{k} U_{X,i} U_{X,i}' \right) W_{Rx}^{-1} \quad . \tag{54}$$

As we assumed that k is the exact estimate of the rank, $U_{\Omega,i}$ is complete. That is,

$$\sum_{i=1}^{k} U_{X,i} U_{X,i}' = I. \tag{55}$$

It follows that, from Equation (53), Equation (52) reduces to

$$\sum_{i=1}^{k} \mathbf{c}_i \mathbf{c}_i' = W_{Rx}^{-2} = (G_{Rx}' G_{Rx})^{-1} \quad . \tag{56}$$

Thus, given an exact estimate of rank k, we will have

$$P_S = G_{Rx}(G_{Rx}' G_{Rx})^{-1} G_{Rx}' = P_{G_{Rx}}, \; P_S G_{Rx} = G_{Rx}, \; P_N G_{Rx} = (I - P_S) G_{Rx} = 0. \tag{57}$$

Therefore, P_S obtained from the data is ideally equal to the analytical one $P_{G_{Rx}}$ that is the signal projection matrix when source locations are known.

3.2 Overestimate of rank

Assume that we overestimate the size of signal subspace, $k' = k + l$. In this case, we have

$$P_S = \sum_{i=1}^{k} \mathbf{u}_i \mathbf{u}_i' + \sum_{i=k+1}^{k+l} \mathbf{u}_i \mathbf{u}_i' \quad . \tag{58}$$

Using Equations (51) and (54), we can rewrite Equation (56)

$$P_S = P_{G_{Rx}} + \sum_{i=k+1}^{k+l} \mathbf{u}_i \mathbf{u}_i' \quad . \tag{59}$$

We see that the estimated P_S contains an additional term, which is formed from the noise eigenvectors. We will see that this inexact estimate does not hurt the MUSIC operation.

Projecting the signal Green's function onto the estimated signal subspace define in Equation (56), we obtain

$$P_S G_{Rx} = G_{Rx} + \left(\sum_{i=k+1}^{k+l} \mathbf{u}_i \mathbf{u}_i' \right) G_{Rx} \quad . \tag{60}$$

To deal with the second term in (58), we can express G_{Rx}using Equation (46):

$$G_{Rx} = U_s C^{-1} . \tag{61}$$

where $U_s = [\mathbf{u}_1 \cdots \mathbf{u}_k]$ and $C = [\mathbf{c}_1 \cdots \mathbf{c}_k]$. That is, G_{Rx}can be expressed as the linear combination of signal singular vectors. As a result, substituting Equation (59) into the second term of Equation (58) leads to

$$\left(\sum_{i=k+1}^{k+l} \mathbf{u}_i \mathbf{u}_i' \right) G_{Rx} = \left(\sum_{i=k+1}^{k+l} \mathbf{u}_i \mathbf{u}_i' \right) U_s C^{-1} = 0 \quad . \tag{62}$$

Therefore, with an overestimate of the signal subspace, or equivalently an underestimate of the noise subspace, the following orthogonality still holds for the MUSIC:

$$P_S G_{Rx} = G_{Rx}, \; P_N G_{Rx} = (I - P_S) G_{Rx} = 0 . \tag{63}$$

3.3 Underestimate of rank

Assume that we underestimate the size of signal subspace, say $k' < k$. Again, using the relations in Equations (45) and (46), we have

$$P_S = \sum_{i=1}^{k'} \mathbf{u}_i \mathbf{u}_i' = G_{Rx} \left(\sum_{i=1}^{k'} \mathbf{c}_i \mathbf{c}_i' \right) G_{Rx}' \tag{64}$$

and

$$\sum_{i=1}^{k'} \mathbf{c}_i \mathbf{c}_i' = W_{Rx}^{-1} \left(\sum_{i=1}^{k'} U_{X,i} U_{X,i}' \right) W_{Rx}^{-1} \quad . \tag{65}$$

As estimated rank $k' < k, U_{X,i}$ is no longer complete. That is,

$$\sum_{i=1}^{k'} U_{X,i} U_{X,i}' \neq I. \tag{66}$$

Thus

$$\left(\sum_{i=1}^{k'} \mathbf{c}_i \mathbf{c}_i' \right) \neq (G_{Rx}' G_{Rx})^{-1} \tag{67}$$

and it is unable to guarantees the orthogonality, i.e.,

$$P_S G_{Rx} \neq G_{Rx}, \; P_N G_{Rx} \neq 0. \tag{68}$$

For an underestimated signal subspace, or equivalently, an overestimated noise subspace, we can't have the property of the zero-projection required in the MUSIC. In principle, all above analysis would apply to the use of an MRM-based MUSIC approach.

4. Experiments

In this part, we present the results using the synthetic and the real MetalMapper data to evaluate the performance of localizing sources using a RxSTRM-based MUSIC imaging approach. It includes the inspection of how MUSIC imaging can be sensitive to a subspace partition and examination of our theoretical analysis presented in section III.

The MetalMapper [49] is a 3-component multi-static system. It consists of three orthogonal transmitters (roughly 1 m × 1m) and seven three-component receiver cubes of 0.1 m. Its configuration is given in Figure 74(a). The MetalMapper has 42 logarithmical time gates ranging from 0.106 ms to 7.91 ms. At one static sounding, the MetalMapper can record spatial-temporal data of 63 × 42. The size of a RxSTRM is 21 × 42. This is a system that has a few transmitters and multiple receivers and is practical to test the RxSTRM-based MUSIC applicability.

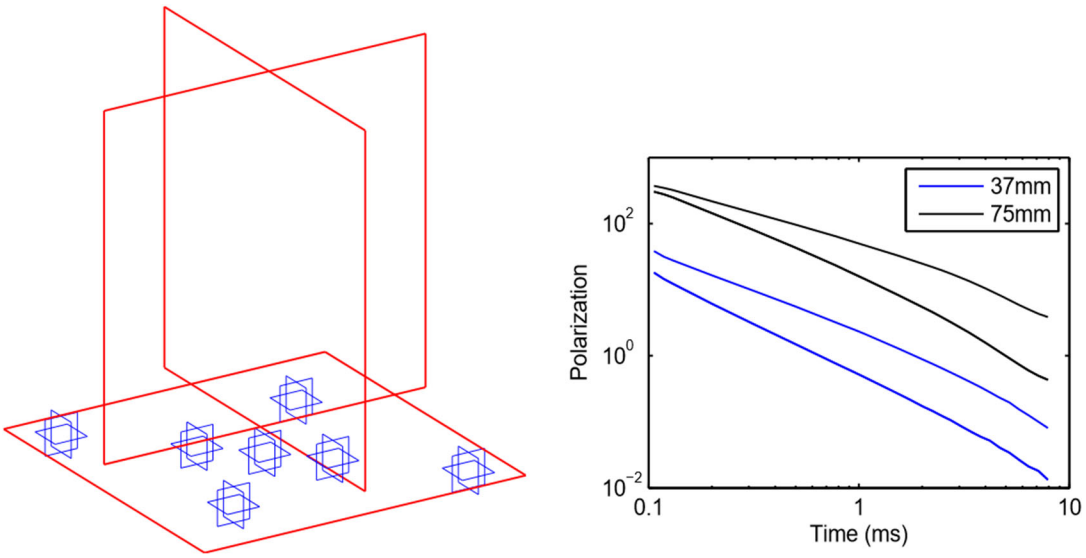

(a) MetalMapper coil geometry (b) Polarizabilities of a 37 mm and 75 mm projectile

Figure 74. (a) MetalMapper: a multi-static system consisting of three orthogonal transmitters and seven triaxial receiver cubes. Each transmitter is 1 m ×1 m and each receiver 10 cm × 10 cm. (b) Two sets of polarizations used for the numerical experiments. The blue and black curves represent the polarizations of 37-mm and 75-mm projectiles, respectively.

To generate synthetic response matrix $D(t)$ of Equation (40), we will specify the simulation parameters like the number, location, and orientation of the objects and their polarizations. Figure 74(b) shows the two sets of polarizations that will be used for the numerical experiments. The blue and black curves respectively represent the polarizations of a 37mm projectile and a 75mm projectile. Each projectile has circular symmetry with one major polarization and two equal minor polarizations. To seek the maximum defined in Equation (50), we define a region of interest (ROI) that is large enough to cover potential sources. In this present test, a 3D ROI of 2 m × 2 m × 1 m is discretized into grids with intervals of Δx = 0.05 m, Δy = 0.05 m, and Δz = 0.025 m. It creates 41 × 41 × 41 = 68921 grids representing possible source locations to be scanned.

The MUSIC is a non-iterative method to find a source in contrast to a standard non-linear inversion algorithm [42] [43] [37]. The MUSIC can be implemented very fast for that (1) the array Green functions over a 3D grid can be pre-calculated and stored for subsequent application; (2) the computation of the MUSIC spatial spectrum of Equation (50) can be parallelized.

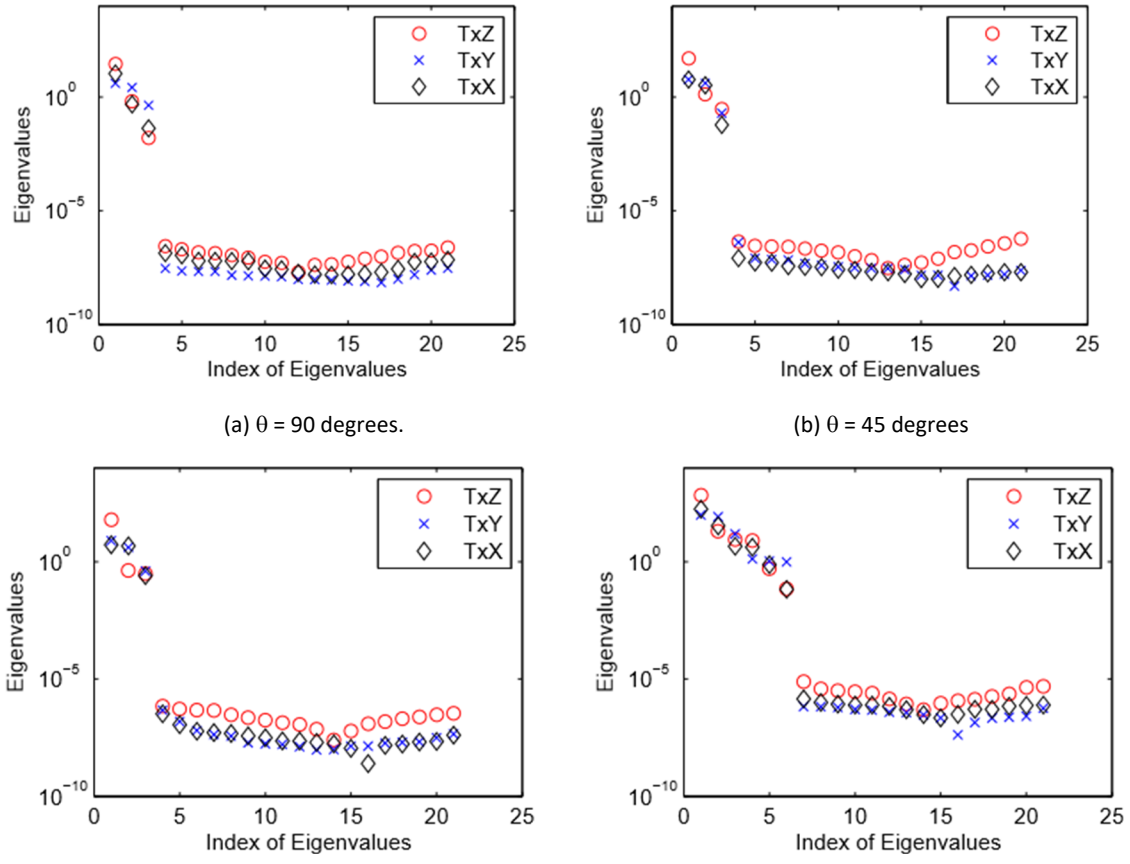

(a) θ = 90 degrees.

(b) θ = 45 degrees

(c) θ = 0 degrees.

(d) Synthetic two-object cases, $\theta_1 = \theta_2 = 0$ degrees

Figure 75. Data eigenvalues. Synthetic single-object case: (a) θ = 90⁰; (b) θ = 45⁰; (c) θ = 0⁰. (d) Synthetic two-object case where $\theta_1 = \theta_2 = 90^0$. θ is the polar angle describing the orientation of a rod object relative to the vertical axis.

4.1 Synthetic single-object example

For an experiment with a single object, we consider a 37mm projectile-like object buried at (0.10, 0.15, −0.35) m. Figure 75(a)-(c) show the data eigenvalues of DD' after performing joint diagonalization when the object has three different orientations: $\vartheta = 90^0, 45^0, 0^0$. ϑ is the polar angle describing the orientation of a rod object relative to the vertical axis. For the ideal cases, one can observe the three significant eigenvalues for each of the three excitation transmitters. There are clear gaps between them and other small values that are treated as numerical zeros

We apply the MUSIC to the horizontal case for localizing the source. In the first test, we have exact estimate of rank k = 3. That is, the corresponding noise subspace projector is given by

$$P_{N[4:21]} = \sum_{i=4}^{21} \mathbf{u}_i \mathbf{u}_i' \quad . \tag{69}$$

Using $P_{N[4:21]}$ in Equation (50), we obtain the MUSIC spatial spectrum over the defined 3D ROI grids. The peak in the image of Figure 76(a) exactly indicates the source at $\boldsymbol{r}_{mu}$ = (0.10,0.15,−0.35) m. We can do a sequential MUSIC detection by zeroing the contribution of the first detected source $\mathbf{r}_1$ from the signal subspace with the projectors, where $P^{\perp}_{G_{Rx,1}}$ to G_{Rx} where

$$P^{\perp}_{G_{Rx},1} = I - G_{Rx}(\mathbf{r}_1)[G'_{Rx}(\mathbf{r}_1)G_{Rx}(\mathbf{r}_1)]^{-1}G'_{Rx}(\mathbf{r}_1). \tag{70}$$

The image of the second MUSIC scanning in Figure 76(b) becomes uniformly diffusive all over the ROI. It shows that there are no more sources.

To test the numerical sensitivity of the MUSIC on a subspace partition, we set up k= 6. In the other words, we will image the ROI using $P_{N[7:21]}$ that underestimates the size of true noise subspace of $P_{N[4:21]}$. The results in Figure 76(c)-(d) show that the first detection of the MUSIC exactly localize the source and the second detection renders a non-focused image that signs no more sources.

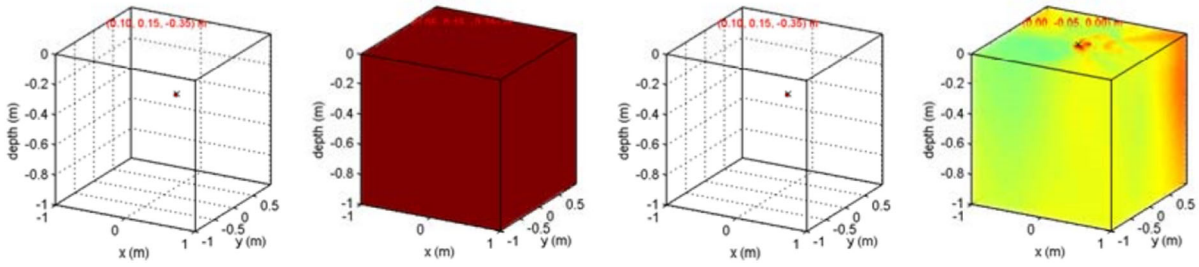

(a) (b) (c) (d)

Figure 76. Synthetic single-object case. MUSIC 3D spatial imaging with two noise-subspace projection matrices: (a)-(b) $P_{N[4:21]}$*; (c)-(d)* $P_{N[7:21]}$*. (b) and (d) represent the 2nd detection in each case.*

4.2 Synthetic two-object example

For a two-object example, we place the 37mm projectile-like object at $\boldsymbol{r}_1$ = (0.20,0.25,−0.15) m and a 75mm projectile-like at $\boldsymbol{r}_2$ = (0.10,0.15,−0.35) m. Both objects are oriented horizontally. The data

eigenvalues produced by the joint diagonalization in Figure 75(d) show six significant values for each transmitter excitation, which is well separated from remaining 15 values. The exact estimate of rank is 6.

We apply the MUSIC to the ideal two-object case using the three subspace partitions: $P_{M[4:21]}$, $P_{M[7:21]}$, $P_{M[10:21]}$. These correspond to an overestimate, an exact estimate, and an underestimate of the noise subspace. For $P_{M[4:21]}$, the MUSIC imaging incorrectly detects two sources spatially closed at $\boldsymbol{r}_{mu,1}$ = (0.15, 0.20, −0.35) m and $\boldsymbol{r}_{mu,2}$ = (0.15,0.20,0.00) m in

Figure 77(a). A very smeared image in the second detection (the bottom row in Figure 77(a)) can lead to a false inference that there is likely one object. Decreasing the size of the noise subspace P_N[4:21] to P_N[7:21], we see that the MUSIC imaging is clearly focused in Figure 77(b) and exactly localize the two sources at $\boldsymbol{r}_{mu,1}$ = (0.20,0.25,−0.15) m and $\boldsymbol{r}_{mu,2}$ = (0.10,0.15,−0.35) m. Further with the underestimated noise subspace $P_{M[10:21]}$, the MUSIC returns the same exact results as the one with $P_{M[7:21]}$.

The numerical tests are consistent with the theoretic suggestion that an underestimated noise subspace established in section III can make the MUSIC implementation robust and accurate in the source localization. This implies that in reality we don't need to concern too much about how many significant eigenvalues should be counted when doing a subspace partition. With real data examples, we further elaborate this next.

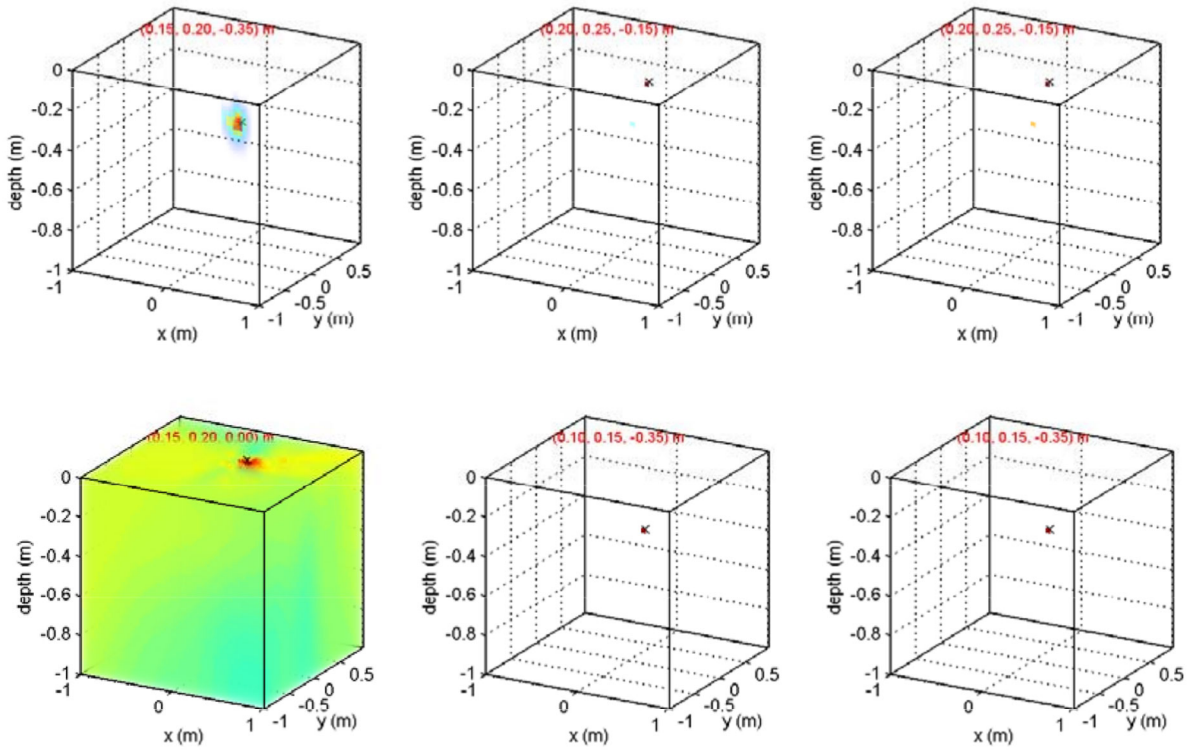

(a) (b) (c)

Figure 77. Synthetic two-object case. MUSIC 3D spatial imaging: (a) PN[4:21]; (b) PN[7:21]; (c) PN[10:21]. Row 1 and 2 represent the 1st and 2nd detection for each case.

4.3 Real data: A single-object case

A set of field data collected at Camp Beale (an ESTCP demonstration site) is used in the evaluation. The data anomaly was arisen from an ISO (Industry Standard Object, a steel pipe with a length of about 10 cm).

The eigenvalues are shown in Figure 78(a) for the three excitations. Unlike in the ideal synthetic cases, there is not a clear gap in the eigenvalue distributions probably due to measurement noise or model approximation or both. We could have 3 significant values if using a high threshold, or 5 or 7 using a lower threshold or the elbow of the curve distribution. It appears a quite subjective matter of how to define a threshold level. We are interested to do source localization tests and see how such an ambiguity of enumerating significant eigenvalues can affect the result.

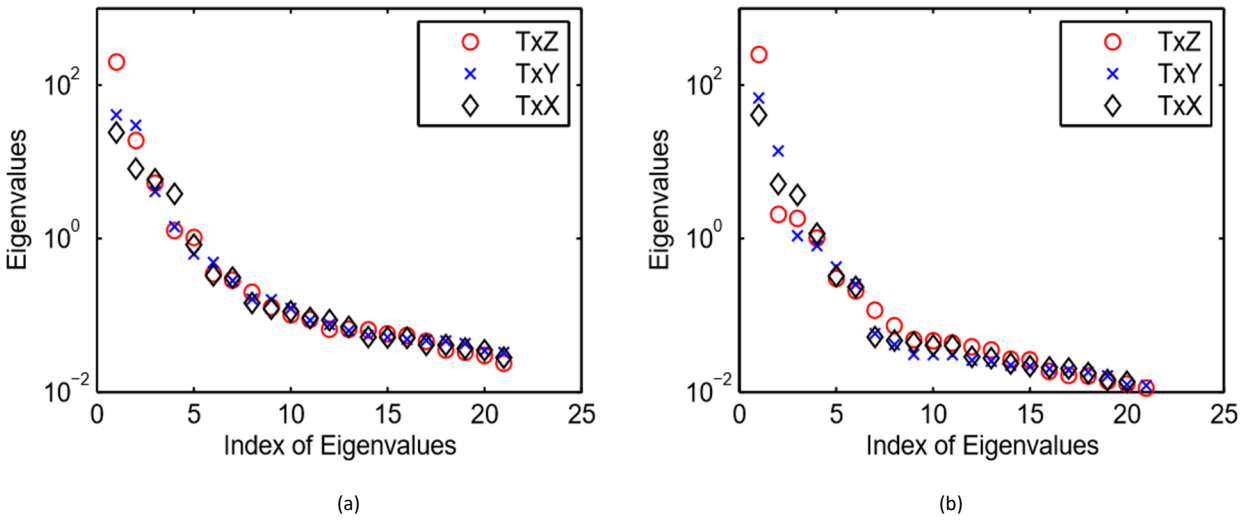

Figure 78. Data Eigenvalues. (a) Field data at Camp Beale. (b) Test-stand data at Lowry

As in the synthetic cases, we use $P_{\mathcal{N}[4:21]}$, $P_{\mathcal{N}[7:21]}$, $P_{\mathcal{N}[10:21]}$ in the MUSIC. The latter two represent the underestimated noise subspaces relative to the theoretic value of k = 3. From the top row of Figure 79, we see that first detected locations are stable with respect to the three subspace partitions: $\boldsymbol{r}_{mu,1}$ = (0.05, 0.15, −0.23) m. Using the source locations, we can solve a linear inverse problem and obtain the polarizabilities for this target anomaly [28]. Figure 80(a), (c), and (e) show the three sets of the recovered polarizabilities for three subspace partitions. All are consistent and agree well with the reference ISO (red curves). Continuing the second MUSIC detection, we observe the blurred images (the bottom row of Figure 79) that could indicate no existence of another real source and those locations are either close to edge or very deep: $\boldsymbol{r}_{mu,2}$ = (−0.05,−1.0,0.00) m, or $\boldsymbol{r}_{mu,2}$ = (0.30,1.00,−1.00) m, $\boldsymbol{r}_{mu,2}$ = (0.10,1.00,−1.00) m. Even assuming a two-object case and using the detected $\boldsymbol{r}_{mu,1}$ and $\boldsymbol{r}_{mu,2}$, we obtain the first set of the recovered polarizabilites that still matches with the ISO ones and the second set of the recovered polarizabilities that are noisy in Figure 80(b), (d), and (f) and can be ignored. This real case illustrates that attempting to exactly enumerate significant eigenvalues is not critical in the MUSIC imaging process.

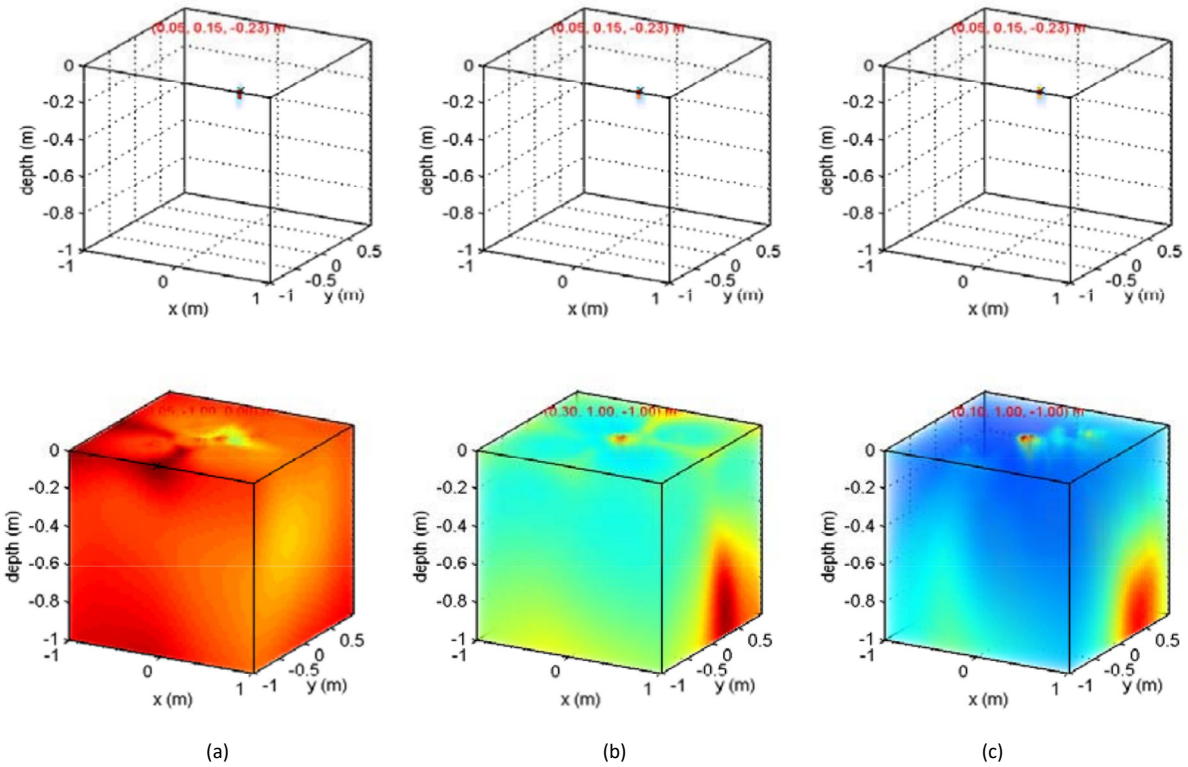

Figure 79. Field data at Camp Beale. MUSIC 3D spatial imaging: (a) $P_{N[4:21]}$; (b) $P_{N[7:21]}$; (c) $P_{N[10:21]}$. Row 1 and 2 represent the 1st and 2nd detection.

4.4 Real data: A two-object case

This is a set of the test-stand data collected over two horizontally oriented objects: a 60mm projectile was placed at $\boldsymbol{r}_1$ = (0.00,0.00,0.365) m and a 37mm projectile at $\boldsymbol{r}_2$ = (−0.20, −0.20, 0.365) m.

Figure 78(b) shows the data eigenvalues of the three excitations. As compared to the ideal synthetic two-object case in Figure 75(d), the eigenvalues Figure 78(b) does not show a clear cluster of 6 significant as expected. Again, we may say there is 3 significant ones if assuming the presence of at least one object, or 4 or 7 based upon the small gap or the elbow point on the eigenvalue distribution. Similar to the real one-object case, it is uncertain to do a rank estimate in this real two-object example. However, we have learned that, from the last location tests, such an ambiguous task of counting significant eigenvalues can be relaxed. That is, we rather choose k larger than the one that eigenvalue map can provide to form a noise subspace.

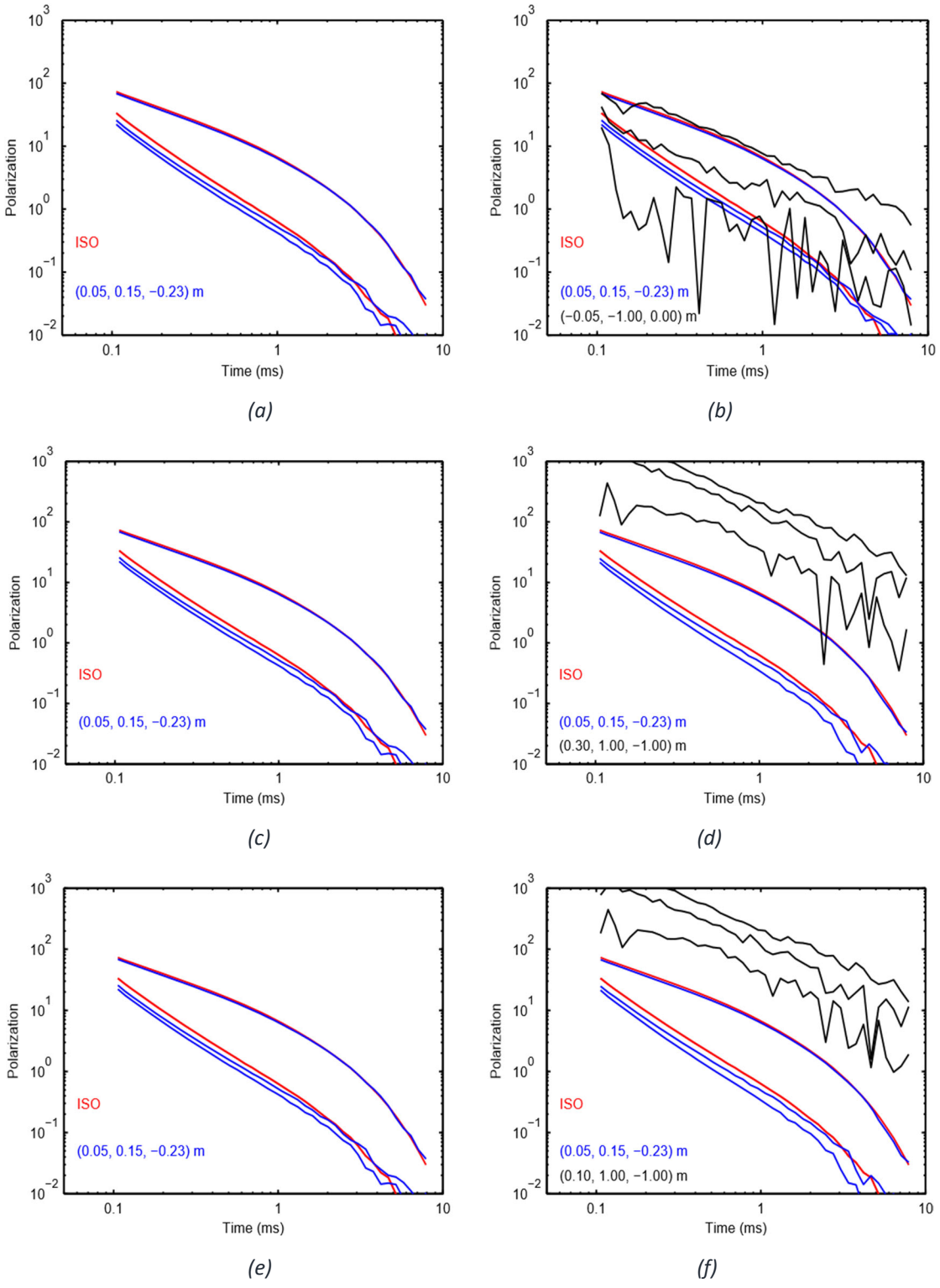

Figure 80. Field data at Camp Beale. Recovered polarizabilities using MUSIC peak locations in Figure 6. (a)-(b) PN[4:21]. (c)-(d) PN[7:21]. (e)-(f) PN[10:21]. On the polarization plots, the solid red curves represent the known polarizabilities of ISO and the blue and black ones are the recovered polarizabilities.

As a test, we start with $P_{N[4:21]}$. This is an overestimated noise subspace relative to the theoretic value of k = 6. Correspondingly, the MUSIC derives the peak locations at $\mathbf{r}_{\mathrm{mu},1}$ = (−0.05, −0.05, −0.40) m and $\mathbf{r}_{\mathrm{mu},2}$= (−0.20, −0.30, −0.30) m. The image of the second detection in the bottom row of Figure 81(a) is not focused due to the overestimated noise subspace, a similar observation in the synthetic two-object case. And, the recovered polarizabilities (blue and black curves) in Figure 82(a) and (b) using the two peak locations cannot match with the reference ones (red solid and dash curves). To further examine the effects of subspace partition on the imaging of the real data, we gradually use a smaller sized noise subspace and obtain a series of the peak locations listed in Table I. As we can see that the peak locations are the same over $\mathrm{P_{N[8:21]}} \cdots \mathrm{P_{N[14:21]}}$, close to the ground truth ones. Even with more smaller sizes of noise subspace $\mathrm{P_{N[15:21]}}$ to $\mathrm{P_{N[18:21]}}$, detected peak locations are still not far from the ground truth ones. For the cases of using $\mathrm{P_{N[8:21]}}$, $\mathrm{P_{N[14:21]}}$, Figure 81(b)-(c) and Figure 82(c) - (f) present the location images and the recovered polarizabilities that match well with the reference polarizabilities.

The MUSIC function in Equation (50) is computed over the pre-defined grids. It might not be realistic to assume that sources fall on the discretized grids. To solve the off-grid issue, we consider to refine the peak locations via an optimization and also check if there are improvements. For instance, we might optimize the MUSIC function of Equation (50) via the MATLAB function fmincon. For $P_{N[7:21]}$ case in Table 9, the peak locations at $\boldsymbol{r}_{mu,1}$= (0.00,0.00,−0.40) m, $\boldsymbol{r}_{mu,2}$= (−0.20,−0.20,−0.375) m were updated as $\tilde{\boldsymbol{r}}_{mu,1}$ = (−0.024,−0.010,−0.374) m, $\tilde{\boldsymbol{r}}_{mu,2}$ = (−0.210,−0.220,−0.366) m. For $P_{N[15:21]}$, the peak locations at $\boldsymbol{r}_{mu,1}$ = (0.00,0.00′−0.35) m $\boldsymbol{r}_{mu,2}$ = (−0.20,−0.20,−0.40) m were tuned as $\tilde{\boldsymbol{r}}_{mu,1}$= (−0.009,0.007,−0.357) m, $\tilde{\boldsymbol{r}}_{mu,2}$= (−0.198,−0.214,−0.381) m. The optimized peak locations are improved as compared to the ground truth ones.

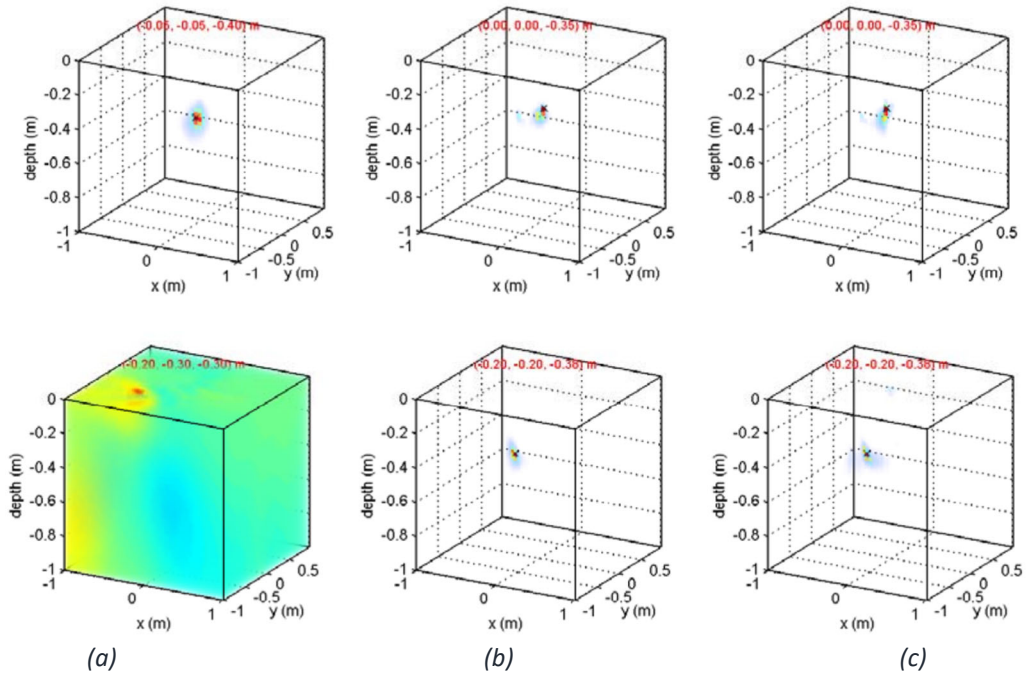

Figure 81. Test-stand data at Lowry. MUSIC 3D spatial imaging: (a) PN[4:21]; (b) PN[8:21]; (c) PN[14:21]. Row 1 and 2 represent the 1st and 2nd detection.

Table 9. MUSIC with various subspaces in the real two-object example. A projection matrix for the noise subspace is defined as $P_{N[i:j]} = \sum_{k=i}^{k=j} \boldsymbol{u}_k \boldsymbol{u}_k'$

Projection matrix	(x1, y1, z1) (m)	(x2, y2, z2) (m)
PN[4:21]	(-0.05, -0.05, -0.400)	(-0.20, -0.30, -0.30)
PN[5:21]	(-0.05, -0.05, -0.400)	(-0.20, -0.25, -0.325)
PN[6:21]	(-0.05, -0.05, -0.400)	(-0.20, -0.25, -0.375)
PN[7:21]	(0.00, 0.00, -0.400)	(-0.20, -0.20, -0.375)
PN[8:21]	(0.00, 0.00, -0.350)	(-0.20, -0.20, -0.375)
PN[9:21]	(0.00, 0.00, -0.350)	(-0.20, -0.20, -0.375)
PN[10:21]	(0.00, 0.00, -0.350)	(-0.20, -0.20, -0.375)
PN[11:21]	(0.00, 0.00, -0.350)	(-0.20, -0.20, -0.375)
PN[12:21]	(0.00, 0.00, -0.350)	(-0.20, -0.20, -0.375)
PN[13:21]	(0.00, 0.00, -0.350)	(-0.20, -0.20, -0.375)
PN[14:21]	(0.00, 0.00, -0.350)	(-0.20, -0.20, -0.375)
PN[15:21]	(0.00, 0.00, -0.350)	(-0.20, -0.20, -0.40)
PN[16:21]	(0.00, 0.00, -0.350)	(-0.20, -0.20, -0.40)
PN[17:21]	(0.00, 0.00, -0.350)	(-0.25, -0.20, -0.375)
PN[18:21]	(0.00, 0.05, -0.350)	(-0.25, -0.20, -0.375)
PN[19:21]	(0.00, 0.05, -0.350)	(-0.40, -0.30, -0.775)
PN[20:21]	(1.00, -0.40, -0.825)	(1.00, 0.55, -0.350)
PN[21:21]	(-0.95, -0.55, -0.050)	(1.00, 0.00, -0.975)

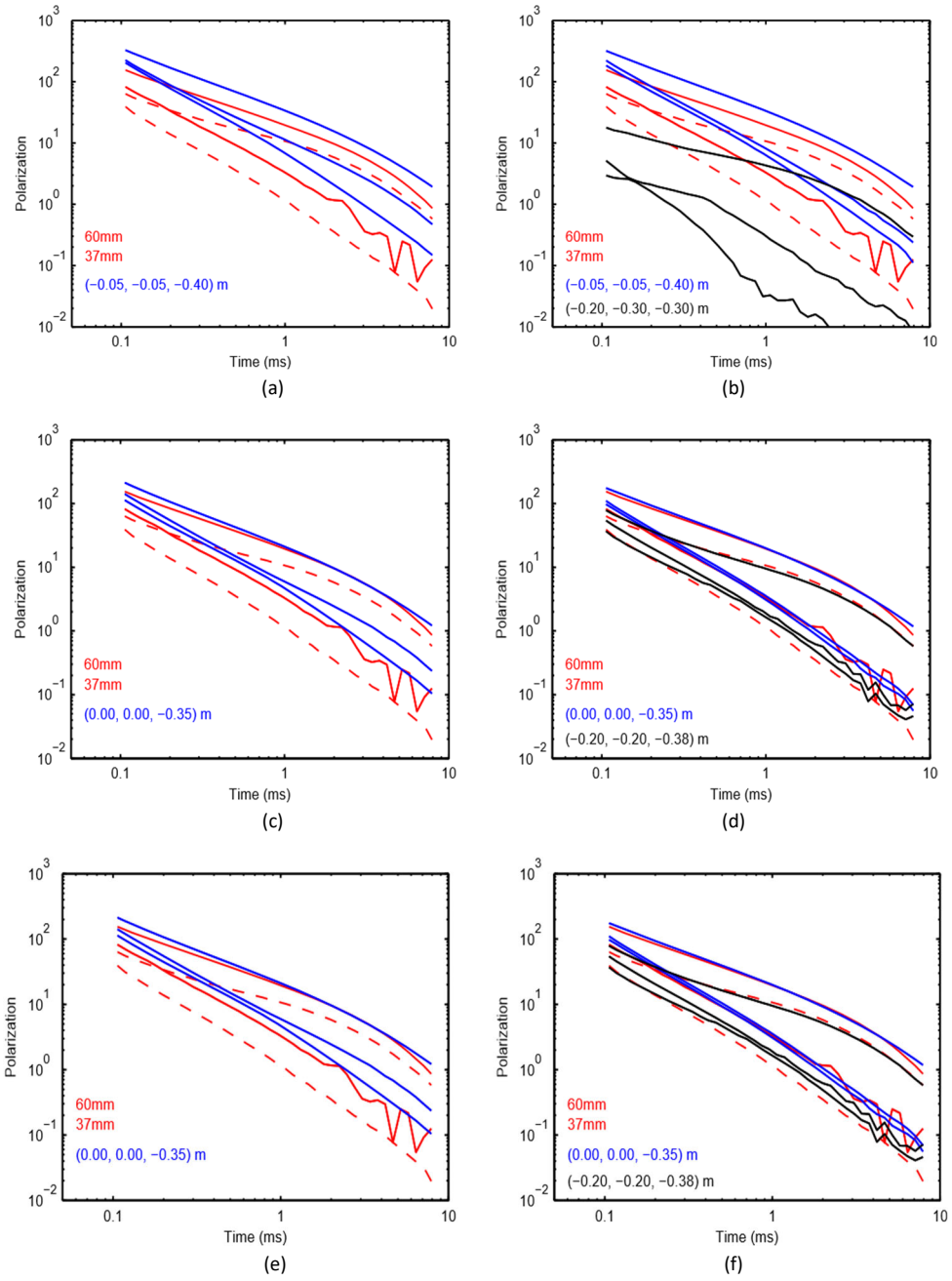

Figure 82. Test-stand data at Lowrey. Recovered polarizabilities using the MUSIC peak locations in Figure 81 (a)-(b) PN[4:21]. (c)-(d) PN[8:21]. (e)-(f) PN[14:21]. On the polarization plots, the solid and dash red curves represent the known polarizabilities of 60mm and 37mm projectiles and the blue and black ones are the recovered polarizabilities.

5. Discussion

For an EMI sensing system with a few of transmitters like MetalMapper system [49], the above tests show that the newly formulated RxSTRM-based MUSIC imaging approach is able to localize sources. On estimating a noise subspace, we found that an underestimated noise subspace is appropriate for the MUSIC imaging to accurately identify sources; an overestimated noise subspace would likely produce inaccurate results. Traditionally, estimating noise subspace is transformed to estimating the rank of a matrix via its eigenvalue distribution in the problem. However, estimating an exact rank often faces a big ambiguity of where to cut signal and noise eigenvalues as data eigenvalues distribute without a clear gap in reality. Our studies suggest that trying to exactly enumerate significant eigenvalues seems unnecessary in the context of the MUSIC imaging. Rather a simple general rule to form a noise subspace can be set up in the EMI application: given a possible number η to be detected or a rough estimate of η from a distribution of signal eigenvalues and assuming an existence of a sufficiently large dimension of noise subspace, we can form a noise subspace starting from an index of eigenvectors $3\eta + \tau$. τ is used to avoid including any signal eigenvectors in the imaging process. Based upon our numerical tests, $\tau = 4$ is suggested. A slightly larger τ might be used. However, it does not mean that we can have an arbitrarily small noise subspace. Recall the identity constraint in (48) between the signal and noise projection matrices. Mathematically, partitioning subspaces into signal and noise ones equivalently splits an identity into two projection parts. If choosing very large τ, we will have a very small dimensional noise subspace and meanwhile create a false signal projection matrix that approaches to the identity. This means that the projection of any array Green's function onto the noise subspace is approaching zero. Therefore, using a very small size noise subspace, we will lose the ability to resolve sources in the MUSIC. For example in the real two-object case, with $\tau = 13$ and $P_{\mathcal{N}[19:21]}$, we have $\boldsymbol{r}_{mu,1}$ = (0.00,0.05,−0.350) m and $\boldsymbol{r}_{mu,2}$= (−0.40,−0.30,−0.775) m; with $\tau = 14$ and $P_{\mathcal{N}[20:21]}$, we have $\boldsymbol{r}_{mu,1}$= (1.00,−0.40,−0.825) m, $\boldsymbol{r}_{mu,2}$= (1.00,0.55,−0.350) m; with $\tau = 15$ and $P_{\mathcal{N}[21:21]}$, we have $\boldsymbol{r}_{mu,1}$= (−0.95,−0.55,−0.050) m, $\boldsymbol{r}_{mu,2}$= (1.00,0.00,−0.975) m. The use of a very small sized noise subspace is unable to correctly localize sources. In principle, this analysis is applied to the MRM-based MUSIC imaging [27] with TEMTADS-like system [30].

6. Conclusion

We have proposed a space-time MUSIC imaging approach that applies to multi-static EMI data with only a few of transmitters. This is a step toward to practical application of MUSIC to an EMI sensor system like MetalMapper with 3 transmitters, which has been widely used in site surveys. The new MUSIC imaging scheme is formulated in terms of a receiver array-based spatial temporal response matrix (RxSTRM). We show that the left singular vectors in a RxSTRM contain location information of targets and can be used to detect sources in the MUSIC. The introduction of RxSTRM only assumes sufficient numbers of receivers and temporal channels, which can be satisfied in most of advanced EMI sensor systems. In contrast, the MRM-based imaging technique requires a system having sufficient numbers of both transmitters and receivers, which can be expensive and impractical. As a result, the RxSTRM-based MUSIC imaging is able to overcome the technical difficulty and the practical limitations in the MRM-MUSIC scheme.

Given that enumerating signal eigenvalues can be ambiguous in practice, we have further investigated the effects of an estimated noise subspace on the performance of the RxSTRM-based MUSIC imaging. Both theoretic analysis and numerical evaluations indicate that an underestimated noise subspace is appropriate for the MUSIC imaging to accurately identify sources; an overestimated noise subspace would likely produce inaccurate results. Based upon the synthetic and real data tests, we have proposed a simple rule to form an underestimated noise subspace that ease the difficult exercise of figuring out significant and noise eigenvalues. This study is carried out in the context of the EMI application, but it might provide an insight into a subspace partition issue for the MUSIC used in the other areas.

The development of RxSTRM MUSIC algorithm in principle applies to multi-frequency case for imaging small inclusions when a sensor array has a limited number of either transmitters or receivers.

Multi-source inversion using Multi-shot data and Genetic Algorithm starting models

Approach

To compare our standard multi-source inversion to inversions using multi-shot data and inversions that initialize starting models using a Genetic Algorithm (GA), we constructed a synthetic MPV data set that consisted of 500 0.5m by 0.5m cells. Each data set cell (i.e., target scenario) contained 2, 3, 4 or 5 targets. The targets within each cell were random combinations of TOI. The TOI used were small, medium and large ISOs. The targets were placed within detection limits; the depth of the small ISOs ranged 0.05-0.3m, the depth of the medium ISOs 0.1-0.45m and the large ISOs 0.15-0.6m. All targets were randomly oriented. Within each cell the targets were separated by a minimum distance of 0.1m from each other. The data sets were created using a Gaussian distribution of noise collected at UBC.

The number of inverted sources matched the number of targets in each cell for the dataset, i.e., cells with 5 targets were inverted using 5 source inversion etc. The datasets were inverted with 500 random starting points to determine source locations. Of these 500 results, the 10 source locations that achieved the best fit to the data were then inverted for polarizability tensor and orientation. Inversion with a larger number of random starting points (i.e., 1000 points) was also tested and the results compared to 500-point default.

Measure of success and model selection process

For this test, the N-dipole inversion was considered successful only when n targets are found within the cell. For each target, the models that are within the cut off distance from the true target location are selected for consideration. Among the close models the model with the smallest misfit is considered. The misfit is calculated between the three polarizabilities and the polarizabilities of the target's true polarizabilities based on the ground truth. If that model has a sufficiently small polarizability misfit it is selected and the target is flagged 'found'.

The acceptable separation between the true target location and the model location was under 0.1m and the acceptable misfit below 1.7. Due to SNR considerations, the final 5 time channels were omitted from the polarizability misfit computation.

Examples of inversion results are shown in Figure 83, Figure 84, and Figure 85.

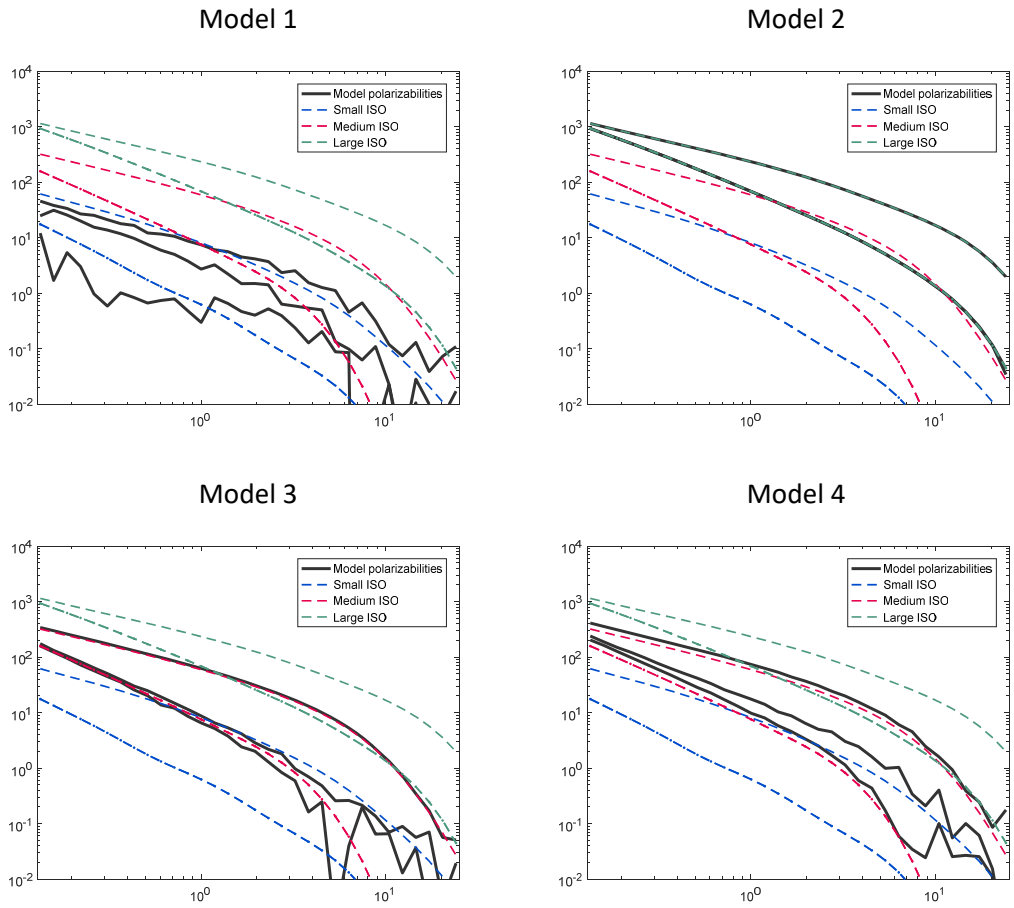

Figure 83. Four-target scenario, cell 162, target 647 is a large ISO. The three other targets are medium ISOs. From left top to right bottom – models 1,2,3,4. Model #2 matches a large ISO and is the selected best model for target 647. L123 polarizability misfits for the four models are: 3.964, 0.002, 2.114, 1.737. Note that the 5 latest time channels are excluded from the misfit computations.

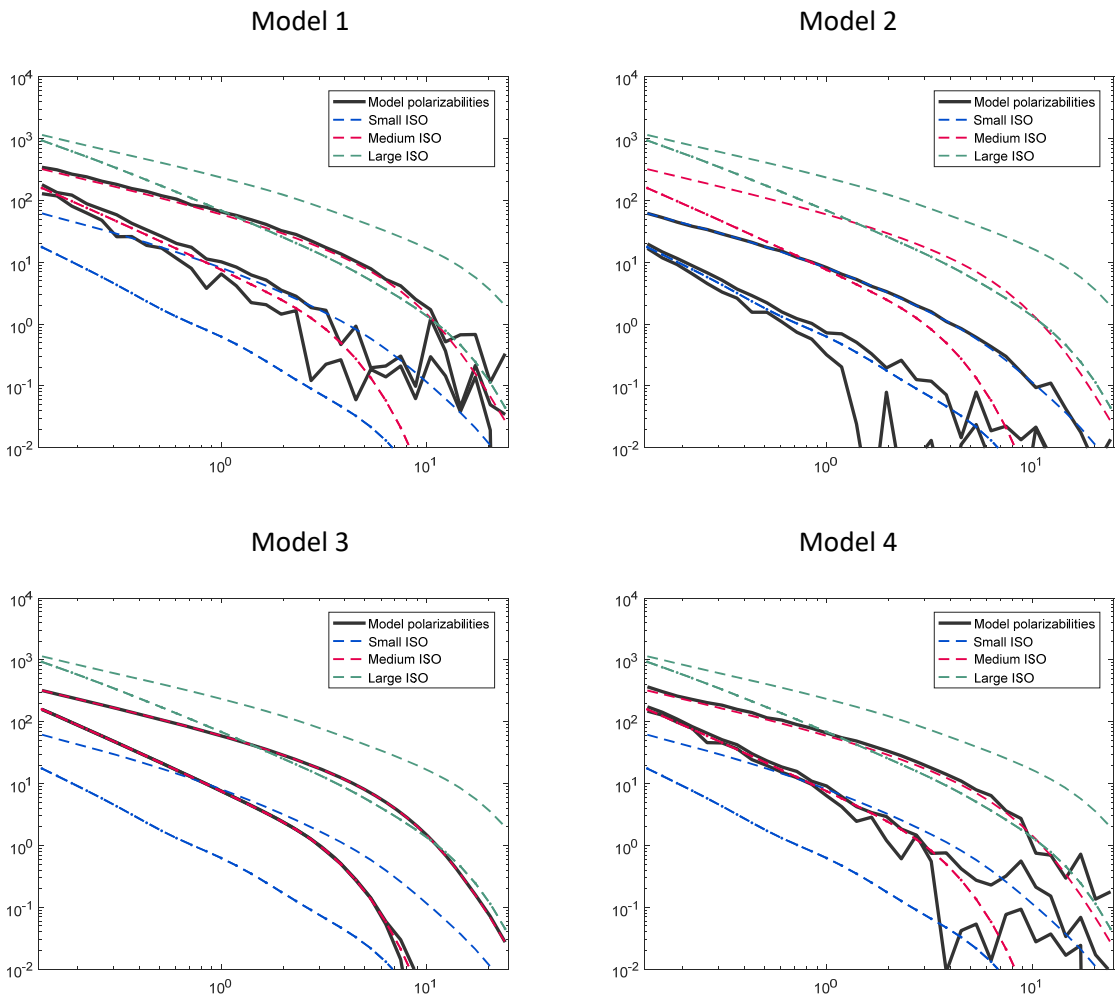

Figure 84. Four-target scenario inverted with 500 starting points, cell 19, target 73 is a medium ISO. The three other targets are: two medium ISO and one small ISO. From left top to right bottom – models 1,2,3,4. Model #3 matched a medium ISO and is the selected best model for target 73. L123 polarizability misfits for the four models respectively are: 0.6732, 2.653, 0.100, 0.612. Note that the 5 latest time channels are excluded from the misfit computations.

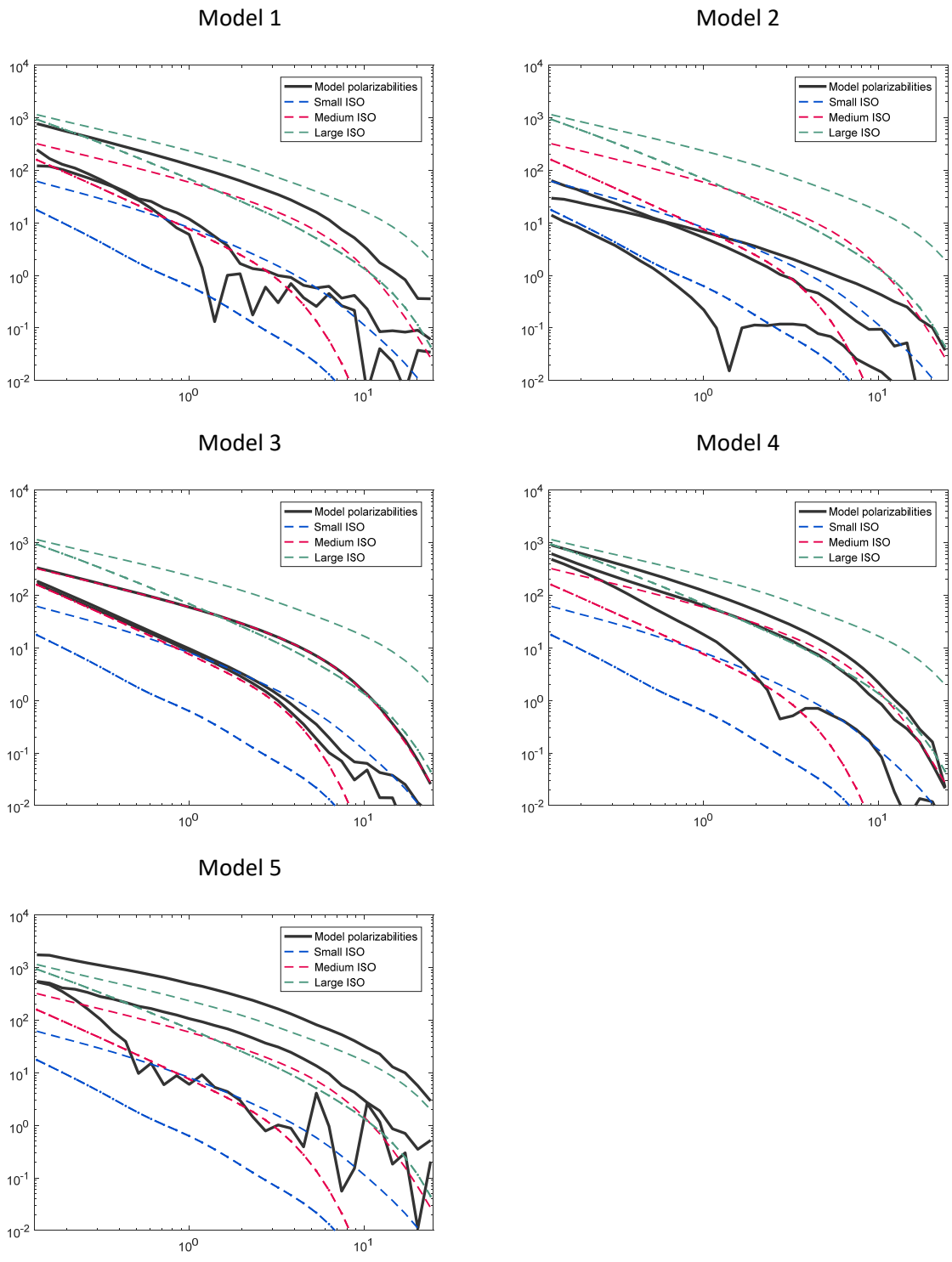

Figure 85. Five-target scenario inverted with 500 starting points, cell 499, target 2494 is a medium ISO. The four other targets are: one small ISO, one large ISO and two medium ISOs. From left top to right bottom – models 1, 2, 3, 4, 5. Model #3 matched a medium ISO and is the selected best model for target 2494. L123 polarizability misfits for the five models respectively are: 1.152, 2.209, 0.338, 2.992, 1.713. Note that the 5 latest time channels are excluded from the misfit computations.

Results 1: Standard N-dipole method

Following the above selection process the results were as follows:

- In the two-target case 98.1% of the total number of targets were found while the chance of finding all the targets in each cell cluster is 97.2%. The chance of finding one target out of two in a cluster is 1.8% and the chance of finding no targets at all in a cluster 1.0%.
- In the three-target case 97.1% of the total number of targets were found while the chance of finding all the targets in each cell cluster is 91.8%. The chance of finding one target out of three in a cluster is 0.6% and the chance of finding two targets out of three is 7.6%.
  There was a drastic decline in the rate of success as the number of targets in a cluster increased from 3 to 4.
- In the four-target case 87.3% of the total number of targets were found while the chance of finding all the targets in each cell cluster is 60.6%. The chance of finding one target out of four in a cluster is 1.6% and the chance of finding two targets out of four is 7.2%. The chance of finding at least 3 out of 4 targets in a cluster is 90.8%.
- In the five-target case 68.8% of the total number of targets were found while the chance of finding all the targets in each cell cluster is 19.6%. The chance of finding at least 4 out of 5 targets was 55.2% while the chance of finding at least 3 out of 5 targets is 79.4%.

The chance of completely missing the cluster appears to be independent of the number of targets in the cluster and fluctuates between 0 and 2%.

Regardless the number of targets in the cluster the chance of missing a small ISO is 2 to 3 times higher than the chance of missing a medium ISO. Similarly, the chance of missing a medium ISO is 2 to 3 times higher than the chance of missing a large ISO.

The case of a single target per cell was also explored. The shot was placed directly above the target. The rate of success in this case was 100%. All 500 targets were found even when the maximum offset distance between the model and the ground truth location was decreased to 0.05cm. The maximum polarizability misfit was as low as 0.45.

Increasing of the number of inversion starting points from 500 to 1000 resulted in a slight increase in the rate of success in the 2, 3 and 5 target case (Figure 86). The rate of success increased by 0.6-2% which translated to up to 15 additional cells where all targets are found. The improvement is most noticeable in the 5-target case. In the 4-target case the rate of success remained unaltered.

These results are summarized in Table 10 to Table 14.

Table 10. Inversion with 500 starting points. Summary of results for 2, 3, 4, and 5 targets per cluster scenarios.

total # of targets	total # of found targets	# of cells with 0 found targets	# of cells with 1 found targets	# of cells with 2 found targets	# of cells with 3 found targets	# of cells with 4 found targets	# of cells with 5 found targets	% of found targets	% of success
1000	981	5 (1.0%)	9 (1.8%)	486 (97.2%)	0	0	0	98.10%	97.20%
1500	1456	0 (0.0%)	3 (0.6%)	38 (7.6%)	459 (91.8%)	0	0	97.10%	91.80%
2000	1745	2 (0.4%)	8 (1.6%)	36 (7.2%)	151 (30.2%)	303 (60.6%)	0	87.30%	60.60%
2500	1720	10 (2.0%)	31 (6.2%)	62 (12.4%)	121 (24.2%)	178 (35.6%)	98 (19.6%)	68.80%	19.60%

Table 11. Inversion with 1000 starting points – summary of results for 2, 3, 4, and 5 targets per cluster scenarios.

total # of targets	total # of found targets	# of cells with 0 found targets	# of cells with 1 found targets	# of cells with 2 found targets	# of cells with 3 found targets	# of cells with 4 found targets	# of cells with 5 found targets	% of found targets	% of success
1000	982	6 (1.2%)	6 (1.2%)	488 (97.6%)	0	0	0	98.20%	97.60%
1500	1452	2 (0.4%)	4 (0.8%)	34 (6.8%)	460 (92.0%)	0	0	96.80%	92.00%
2000	1747	3 (0.6%)	3 (0.6%)	41 (8.2%)	150 (30.0%)	303 (60.6%)	0	87.35%	60.60%
2500	1800	1 (0.2%)	22 (4.4%)	54 (10.8%)	135 (27.0%)	175 (35.0%)	113 (22.6%)	72.00%	22.60%

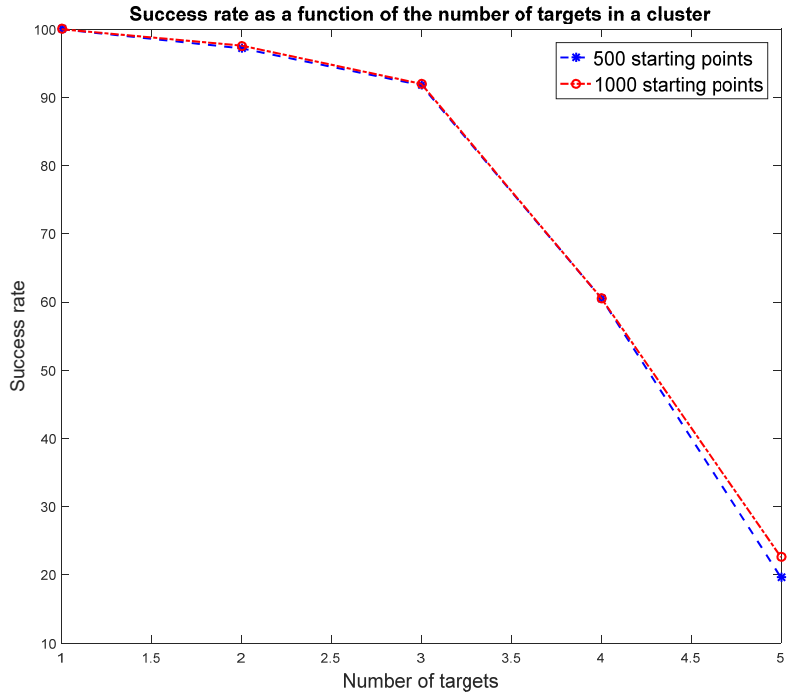

Figure 86. Comparison of the rate of success of inversion with 500 random starting points and 1000 random starting points.

Table 12. Percentage of each of the ordnance items out of all missed targets, for 2, 3, 4, and 5 target scenarios, as a result of inversion with 500 random starting points. The percent chance of missing a larger TOI is a few orders of magnitude lower than the percent chance of missing a smaller TOI.

	2 target case	3 target case	4 target case	5 target case
% of small ISO out of all missed targets	78.90%	72.70%	60.00%	51.40%
% of medium ISO out of all missed targets	21.10%	20.50%	29.80%	30.30%
% of large ISO out of all missed targets	0.00%	6.80%	10.20%	18.30%

Table 13. Count of missed targets by ordnance type, for 2, 3, 4 and 5 target scenarios, as a result of inversion with 500 random starting points. Regardless the number of targets per cluster, the number of missed small ISO is significantly larger than the number of missed medium or large ISO.

	2 target case	3 target case	4 target case	5 target case
Total number of targets missed	19	44	255	780
Number of missed small ISO	15	32	153	401
Number of missed medium ISO	4	9	76	236
Number of missed large ISO	0	3	26	143

Table 14. Percentage of missed targets out of all seeded targets of that kind, for each of the ordnance items, for 2, 3, 4, and 5 target cases, as a result of inversion with 500 random starting points. The results are consistent with previous statistics, demonstrating that smaller ordnance items that have a smaller signal response are easier to miss than larger ordnance items.

	2 target case	3 target case	4 target case	5 target case
% of missed small ISO out of total small ISO seeded	4.50%	6.30%	22.00%	45.90%
% of missed medium ISO out of total medium ISO seeded	1.20%	1.90%	11.60%	29.10%
% of missed large ISO out of total large ISO seeded	0.00%	0.60%	4.00%	17.50%

Results 2: Multi-shot inversion

Inversion of cued measurements over areas of multiple closely spaced targets may benefit from addition of a second shot location to help resolve more of the targets. To test this concept in each of the datasets the multi- shot approach was applied to the cells where none or not all targets were found. For each unsuccessful/failed cell another cell was created with the same targets. To replicate the field procedures as closely as possible the second shot was placed using the model location of the single object inversion for the cell. The two cells were merged into a single cell and inverted simultaneously.

Addition of a second shot is highly efficient for multi- source inversions. As many as 52% to 75% of the failed cases, where not all targets are found, can be corrected by simultaneously inverting an additional sounding.

Table 15. Inversion of two cued measurements simultaneously applied to cases where at least one target was missed for the 2, 3, 4 and 5 targets per cluster scenarios. Multi-shot inversion tests whether addition of data improves inversion results in situations where the standard inversion method is not able to resolve all targets within a cluster

dataset	# of failed cells	total # of targets	total # of found targets	# of cells with 0 found targets	# of cells with 1 found targets	# of cells with 2 found targets	# of cells with 3 found targets	# of cells with 4 found targets	# of cells with 5 found targets	multi-shot success rate
2 targets per cell	14	28	19 (67.9%)	3 (21.4%)	3 (21.4%)	8 (57.1%)	0 (0.0%)	0 (0.0%)	0 (0.0%)	57.10%
3 targets per cell	41	123	110 (89.4%)	1 (2.4%)	1 (2.4%)	8 (19.5%)	31 (75.6%)	0 (0.0%)	0 (0.0%)	75.60%
4 targets per cell	197	788	711 (90.2%)	2 (1.0%)	4 (2.0%)	6 (3.0%)	45 (22.8%)	140 (71.1%)	0(0.0%)	71.10%
5 targets per cell	402	2010	1673 (83.2%)	2 (0.5%)	14 (3.5%)	20 (5.0%)	55 (13.7%)	101 (25.1%)	210 (52.2%)	52.20%

Results 3: Using a Genetic Algorithm to find starting source locations

The same synthetic data sets were inverted using the Genetic Algorithm (GA) optimization method developed by Peter Lelievre for selecting starting models. The results are remarkably better than the results of inversion with 500 random starting points or 1000 random starting points. The GA is also efficient in terms of inversion time. The inversion time varies from 0.88 minutes/cell for 1-2 object inversion to 1.67 minutes/cell for 1-3 object inversion to 2.02 minutes/cell for 1-5 object inversion. These inversion times are up to 3 times shorter than inversion with 1000 starting points. However, inversion time also depends on the processor and the number of workers used in parallel pool.

Table 16. Inversion with Genetic Algorithm – summary of results; percent of found targets and the rate of success for each of the 2, 3, 4, and 5 target scenarios. Detection of all targets within a cell defines a success.

total # of targets	total # of found targets	# of cells with 0 found targets	# of cells with 1 found targets	# of cells with 2 found targets	# of cells with 3 found targets	# of cells with 4 found targets	# of cells with 5 found targets	percent of found targets	percent of success
1000	1000	0 (0.0%)	0 (0.0%)	500 (100%)	0	0	0	100.00%	100.00%
1500	1497	0 (0.0%)	0 (0.0%)	3 (0.6%)	497 (99.4%)	0	0	99.80%	99.40%
2000	1875	0 (0.0%)	4 (0.8%)	15 (3.0%)	83 (16.6%)	398 (79.6%)	0	93.75%	79.60%
2500	1749	9 (1.8%)	28 (5.6%)	60 (12.0%)	120 (24.0%)	174 (34.8%)	109 (21.8%)	70.00%	21.80%

The performance of the GA was compared to the performance of the multi-shot in problematic cases. The two approached were applied to 41 cells were not all 3 targets per cell were resolved. The GA successfully resolved all targets in 53.6% of those cells while the multi-shot resolved 75.6%. Nonetheless, modifying the parameters of the GA search resulted in 97.6 % success. The parameter that was altered was the Population Size Factor which was doubled from 10 to 20. Population Size Factor of 20 means that the number of individuals in the population is at least 20 times the number of variables. This parameter adjustment resulted in increase of the inversion time to 2.4 minutes/ cell.

Situations when multi-shot is beneficial are difficult to define and second shot data is not always available. In that regard, the GA is more practical, has better time efficiency and is easier to implement.

Sensor Placement via Optimal Experiment Design in EMI Sensing of Metallic Objects

This work, under the optimal experimental design framework, investigates the sensor placement problem that aims to guide electromagnetic induction (EMI) sensing of multiple objects. We use the linearized model covariance matrix as a measure of estimation error to present a sequential experimental design (SED) technique. The technique recursively minimizes data misfit to update model parameters and maximizes an information gain function for a future survey relative to previous surveys. The fundamental process of the SED seeks to increase weighted sensitivities to targets when placing sensors. The synthetic and field experiments demonstrate that SED can be used to guide the sensing process for an effective interrogation. It also can serve as a theoretic basis to improve empirical survey operation. We further study the sensitivity of the SED to the number of objects within the sensing range. The tests suggest that an appropriately overrepresented model about expected anomalies might be a feasible choice.

1. Introduction

EMI data are collected in either a dynamic mode or cued mode [54]. In a dynamic mode, the sensor is moved across the area of interest to map data anomalies that indicate metallic contamination. In a cued survey mode, the sensor is placed at locations of data anomalies identified in the dynamic survey. The cued survey helps to acquire high signal-to-noise ratio (SNR) data by increased stacking. In addition, instrument position errors are minimized. Therefore, a follow-up cued survey is often used to acquire data for improving polarizability estimates.

In this section, we focus on the sensor placement problem in cued survey. For sites where anomalies are well separated, the current practice of cued sounding likely positions a sensor directly over a nearby target. For some circumstances the instrument might be repositioned above the target by inspecting the offset between the sensor location and the estimated location of an assumed single target. In this way, the SNR of cued data is maximized as possible. For sites with high anomaly density, we likely encounter instances where more targets are present in the field of view of the instrument. The objects near the sensor-edge might be poorly characterized due to the signal being dominated by objects closest to the center of the sensor. Additional soundings may be desired to better characterize the anomalies. Ideally, the addition of new data would reduce model uncertainty. The extent to which model uncertainty is reduced depends on the sensing locations. Therefore, we can treat adding soundings as an optimal experimental design (OED) problem [55] [56] in which optimal sensor positions are predicted in order to collect the most informative data for accurately estimating model parameters.

The theory of optimal experimental design has been well documented in statistics and extensively applied to various scientific and engineering fields [55] [56]. The OED theory contains design and model parameters. In the context of EMI sensing of UXO, the design parameter refers to the number and locations of sensors that control the survey quality. The model parameters refer to locations and polarizabilities of targets (see a brief review of the signal model in Section 2). An optimal survey design is implemented using statistical criterion [55] [56]. A common choice is the D-criterion that minimizes the determinant of the model covariance matrix. The determinant in the D-criterion is a function of both design and model parameters. When the true model parameters are known or specified, it can be

relatively straightforward to find design parameters. For the EMI classification problem, we face a nonlinear optimization problem where optimizing design parameters depends on the model parameters that are unknown before the survey. To make the problem tractable, we consider a sequential design procedure [57] [58] that forecasts a new sensor placement using estimated model parameters given an initial/current survey. We then update model parameters using additional new data. This procedure is repeated until a stopping criterion is satisfied. A stopping criterion could be a predefined threshold of information gain or a maximum number of sensing.

The remaining parts of this paper are organized as follows. In Section 2, the linearized model and the associated optimality design criteria are discussed. Then the sensor placement problem is formulated as a sequential experimental design (SED) process. In Section 3, the results from the synthetic and experimental data are presented to evaluate the SED technique. Section 4 summarizes the section.

2. Method

Our objective is to estimate model parameters m that describe targets within view of the sensor and design parameters ψ, in particular the location of the sensor. We follow the same signal model and notation as defined in the section "Temporal Orthogonal Projection Inversion for EMI Sensing of UXO" (page 14).

The model parameters m are the target polarizations and locations. For η objects within the sensor field of view, they might be collectively expressed as

$$\mathbf{m} = \begin{bmatrix} \mathbf{r} \\ \mathbf{q} \end{bmatrix} \tag{71}$$

where $\mathbf{r}$ contains the location vectors for the η objects and $\mathbf{q}$ contains their respective polarizabilities. For a single time channel, the dimension of r is $3\eta \times 1$ and the dimension of $\mathbf{q}$ is $6\eta \times 1$. The dimension of $\mathbf{m}$ is $N \times 1$, where $N = 3\eta+6\eta$. The design parameters ψ related to sensor location are contained in the modeling matrix A. We can represent the data as

$$\mathbf{d} = \mathcal{F}(\mathbf{m}, \psi) + \mathbf{n}(\psi) \tag{72}$$

where $\mathcal{F}(\mathbf{m}, \psi)$ denotes the nonlinear forward function that maps the m and ψ on the data. $\mathbf{n}(\psi)$ is the data noise associated with a particular survey design ψ. For simplicity, we have suppressed the variable t in (71) and (72).

In standard data processing, the set of experiment design parameters are fixed, and a nonlinear inverse problem is solved for finding model parameters $\mathbf{m}$ [59]. On the other hand, the optimal experiment design problem aims to find the design parameters that are expected to achieve the minimum model uncertainty [55] [56]. Experiment designs are compared using statistical criteria based on the information matrix. Calculation of the information matrix requires estimating the model covariance matrix. For the nonlinear optimal experiment design problem, we will linearize the forward model function (72) about a reference model. A design criterion based on the linear problem will then be utilized.

2.1 Linearized Model Uncertainty and Optimal Design Criteria

To obtain the analytical expression of a model covariance matrix in the nonlinear inverse problem, we linearize the data functional about a prior estimated model $\mathbf{m}_0$ [59]

$$\mathbf{d} \approx \mathcal{F}(\mathbf{m}_0, \psi) + J\Delta\mathbf{m} \tag{73}$$

where $\Delta\mathbf{m} = \mathbf{m} - \mathbf{m}_0$ and J is the $M \times N$ Jacobian matrix comprising the partial derivatives of the data functional evaluated at $\mathbf{m}_0$ for the design ψ,

$$J = \left.\frac{\partial \mathcal{F}}{\partial \mathbf{m}}\right|_{\mathbf{m}_0} \tag{74}$$

A solution to the linearized equation of (73) can be achieved by minimizing an objective function [17]

$$\phi = \left\| W_d^{-1/2} (\Delta\mathbf{d} - J\Delta\mathbf{m}) \right\|^2 + \left\| C_0^{-1/2} \Delta\mathbf{m} \right\|^2 \tag{75}$$

where $\Delta\mathbf{d} = \mathbf{d} - F(\mathbf{m}_0, \psi)$ are the data residuals between the measured data and the data predicted at the model $\mathbf{m}_0$. W_d is generally treated as a data covariance matrix and C_0 is a prior model covariance matrix. The first term in (75) is the data misfit, measuring the discrepancies between the observed and theoretical quantities. The second term is a damping or regularization term that plays a role in controlling the size of a solution model relative to model $\mathbf{m}_0$. The formal linearized least square solution for (75) is given by [59]

$$\mathbf{m} \approx \mathbf{m}_0 + \left(J^T W_d^{-1} J + C_0^{-1}\right)^{-1} J^T W_d^{-1} \left(\mathbf{d} - \mathcal{F}(\mathbf{m}_0, \psi)\right) \tag{76}$$

The corresponding posterior covariance matrix C_m can be approximated as [59]

$$C_m \approx \left(J^T W_d^{-1} J + C_0^{-1}\right)^{-1} \tag{77}$$

As indicated in [57] [59], a model $\mathbf{m}_0$ used for the linearization is often obtained as a local optimum point through an iterative optimization algorithm. The posterior C_m of (77) estimated at convergence is viewed as a linearized measure of uncertainty in the estimated model parameters. This estimate forms the basis for various experimental design approaches [55] [56].

In the standard experimental design approaches, the model covariance matrix is converted into some scalar functions such as its determinant or trace, that is, $\Phi_D = |C_m|$ or $\Phi_A = \mathrm{tr}C_m$. Then an optimal design ψ might be sought in terms of the D- and A-criteria [55] [56], given by $\min_\psi \Phi_D$ and $\min_\psi \Phi_A$, respectively. Under assumption that the estimates are multivariate Gaussian, C_m in the model space might be pictured as an ellipsoidal confidence region about the parameter estimates. Geometrically, Φ_D or Φ_A measures the size of this ellipsoid either in terms of its volume or its average semi-axes lengths. The smaller the ellipsoidal region, the smaller the uncertainty in parameter estimates. Posing Φ_D or Φ_A as a function of experimental parameters ψ makes it possible to seek an optimal experiment over the experiment space and render the minimal post experimental uncertainty in model estimates.

The optimization of experimental designs ψ in our case is conditional on the assumed model $\mathbf{m}_0$. In principle, the optimal design can be achieved only when the prior estimate $\mathbf{m}_0$ is close to the true parameters. In reality, such an assumption might not always hold. Thus, for a nonlinear model, it is necessary to have a procedure in which the design can be sequentially updated upon the improved estimate of the model parameters after each experiment. In the following we present a D-criterion-based sequential experimental design.

2.2 Sequential Experimental Design Optimization

In this section, we follow the approaches of augmenting experimental data [55] [56] [58]. to obtain a sequential experimental design criterion and procedure in terms of the posterior covariance matrix.

Starting a current survey stage denoted as s, we wish to find or predict the next sounding, denoted as future stage s+1. The sensitivity matrix at stage s+1 can be expressed as

$$B_{s+1} = \begin{bmatrix} B_s \\ J_{s+1} \end{bmatrix} \tag{78}$$

where

$$B_s^T = [J_1^T, \ldots, J_s^T] \tag{79}$$

is a composite of the sensitivitymatrices for s experiments at stage s and J_{s+1} represents a sensitivity matrix that is to be determined via optimizing the criterion below. B_{s+1} is formed by appending a future J_{s+1} to the existing B_s [55] [57] [58]. This is equivalent to adding data from a new sounding. Denote the model covariance matrix at stage s as C_s. With (77), its inverse can be expressed as

$$C_s^{-1} = \left(B_s^T W_s^{-1} B_s + C_0^{-1}\right) \tag{80}$$

Where W_s is the data covariance matrix at the s^{th} stage, given by

$$W_s = \begin{pmatrix} \Sigma_1 & 0 & 0 \\ 0 & \ddots & 0 \\ 0 & 0 & \Sigma_s \end{pmatrix} \tag{81}$$

where Σ_s is a block data covariance matrix of size $M \times M$ at the s^{th} sounding. For stage s+1, the posterior covariance matrix is given by

$$C_{s+1}^{-1} = \left(B_{s+1}^T W_{s+1}^{-1} B_{s+1} + C_0^{-1}\right) \tag{82}$$

Inserting (12) and using (13), the inverse posterior covariance matrix of (82) at step s + 1 may be rewritten as

$$C_{s+1}^{-1} = \left(B_s^T W_s^{-1} B_s + C_0^{-1} + J_{s+1}^T \Sigma_{s+1}^{-1} J_{s+1}\right)$$
$$= \left(C_s^{-1} + J_{s+1}^T \Sigma_{s+1}^{-1} J_{s+1}\right). \tag{83}$$

Using the matrix determinant lemma [60], we can have

$$\left|C_{s+1}^{-1}\right| = \left|C_s^{-1} + J_{s+1}^T \Sigma_{s+1}^{-1} J_{s+1}\right|$$
$$= \left|C_s^{-1}\right| \left|I_M + \tilde{J}_{s+1} C_s \tilde{J}_{s+1}^T\right| \tag{84}$$

where I_M is an identity matrix with the size of $M \times M$ and

$$\tilde{J}_{s+1} = \Sigma_{s+1}^{-1/2} J_{s+1}. \tag{85}$$

Therefore, we can introduce a new function as

$$\mathcal{J}_D = \ln \frac{\left|C_{s+1}^{-1}\right|}{\left|C_s^{-1}\right|} = \ln \frac{\left|C_s\right|}{\left|C_{s+1}\right|} = \ln \left|I_M + \tilde{J}_{s+1} C_s \tilde{J}_{s+1}^T\right|. \tag{86}$$

Equation (86) is a scalar measure of the model covariance reduction that can be obtained by adding a new sounding to the previous s soundings. Conversely, $\mathcal{J}_D$ may be called an expected information gain. The core part in the objective function $\mathcal{J}_D$ is $\tilde{J}_{s+1} C_s \tilde{J}_{s+1}^T$ that is a model covariance matrix C_s-weighted product of the scaled sensitivity matrix $\tilde{J}_{s+1}$ at the candidate sensing location. If the elements of model covariance matrix are larger at previous s stages, $\mathcal{J}_D$ will tend to be large by seeking a new experiment that can increase sensitivities in $\tilde{J}_{s+1}$ and thus reduce the model uncertainty expressed in (82). On the other hand, if the elements of model covariance matrix are already smaller at the previous s stages at which large sensitivities were built upon, the value of $\mathcal{J}_D$ would be small when adding a new experiment that likely resembles one of the previous ones.

The above presentation is general and can be reduced to some specific case. The form of (86) is similar to those in [57] [58], but its inclusion of the covariance matrices makes it convenient to incorporate available a priori knowledge about the model and accommodate various types of measurement noise into an optimal experimental design process. Specifying the prior covariance matrices requires statistical noise models that are representative of the experiment. However, such statistical noise models are not always known or easily defined in reality. To simplify, one common practice is to ignore C_0 and assume a uniform uncorrelated data noise [57] [58]. In our current implementation, we also simply choose C_0^{-1} = 0 which represent no prior information about model in the beginning. However, in the sequel, this choice is automatically updated as shown in (83) where C_s from the previous survey locations can be viewed as prior model information for a next intended survey location and is embedded in (86). For a data covariance matrix, we consider an uncorrelated nonuniform error distribution in this study. That is, a standard error is assigned as a summation of the baseline error δ_j and a percentage ϑ of an observed datum [16]. Then the diagonal entry of W_{ii} is written

$$W_{ii} = (\delta_i + \vartheta |d|_{\text{obs},i})^2 \tag{87}$$

for i^{th} datum.

Having obtained the D-optimality function (86), we can implement a sequential experimental design (SED) for sensor placement in the following manner.

Step 1. Given the survey parameters as ψ_s at the s^{th} stage, finding the best model parameters m is stated as the minimization of a nonlinear least squares function with some constraints (for algorithm details see [28] [33] [34])

$$\begin{aligned} \widehat{\mathbf{m}}_s &= \arg\min_{\mathbf{m}} \left\{ \left\| W_s^{-1/2} \left(\mathbf{d} - \mathcal{F}\left(\mathbf{m}, \psi_s\right) \right) \right\|^2 : \mathbf{m} \right. \\ &\left. = (\mathbf{r}, \mathbf{q}), \ \ \|\Delta \mathbf{r}\| \le \Delta_r, \ \ \mathbf{q} \in S_+ \right\}, \end{aligned} \tag{88}$$

where Δr is a positive scalar used to provide a local trust region within which Δr is allowed to change and q ∈ S_+ represents that q is constrained to be the elements of the set S_+ of symmetric positive semidefinite matrices.

Step 2. Given the current model $\widehat{\mathbf{m}}_s$ and starting from the most recent sensor position in ψ_s, we predict next sensing location represented as ψ_{s+1} by maximizing

$$\begin{aligned} \psi_{s+1} &= \arg\max_{\psi} \mathcal{J}_D \left(\widehat{\mathbf{m}}_s, \psi_s, \psi \right) \\ &= \arg\max_{\psi} \ln \left| I_M + \tilde{J}\left(\psi\right) C_s \tilde{J}^T \left(\psi\right) \right|. \end{aligned} \tag{89}$$

The optimization can be carried out via the MATLAB [61] function fmincon.

Repeat this survey augmenting process until a stopping criterion is attained. This stopping criterion may be a predefined threshold of information gain or a maximum number of sensing stages.

3. Results

In this section, we evaluate the SED with two portable EMI sensor systems: one is the TEMTADS2x2 (Transient Electromagnetic Multi-Sensor Towed Array Detection System) [62]; the other is the MPV (Man Portable Vector sensor) [63] [64]. Each sensor is described in the related subsections.

3.1. Synthetic Experiments with TEMTADS2x2. First, we present results with synthetic TEMTADS2x2 time-domain data with a noise level of 7% to illustrate the capability of the optimal experimental design for the sensor placement.

TEMTADS2x2 is a sensor system that consists of 4 coplanar small transmitters and 4 sets of tri-axial receiver cubes [23] (Figure 87(a)). The sizes of each transmitter and receiver are 40 cm × 40 cm and 8 cm × 8 cm. Two objects, 37mm and 75mm projectiles, are used in the numerical experiments. Their polarizabilities are shown in Figure 87(b).

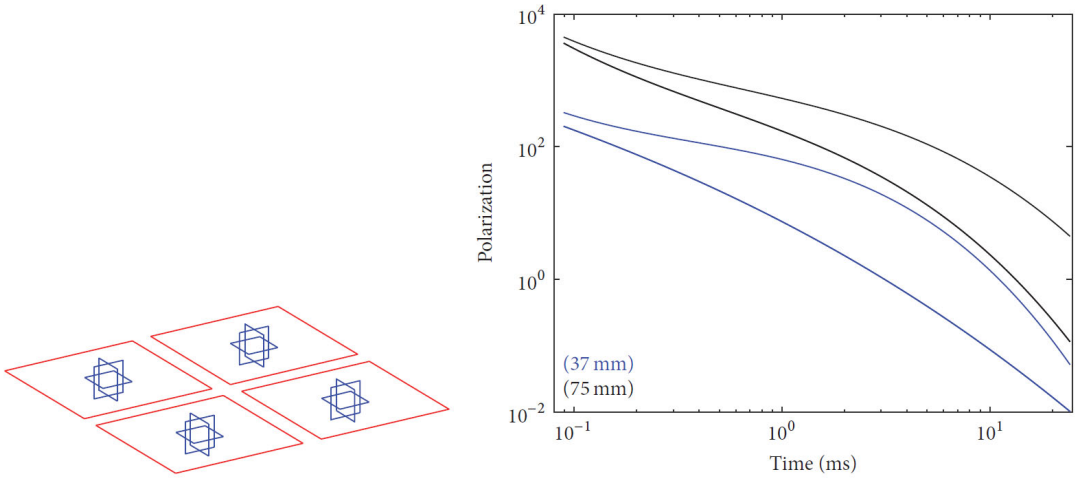

Figure 87. (left) TEMTADS2x2: a multi-static system consisting of 4 coplanar transmitters and 4 triaxial receiver cubes. Each transmitter is 40 cm× 40 cm and each receiver 8 cm × 8 cm. (right) Two sets of polarizations used for the numerical experiments. The blue and black solid curves represent polarizations decays of 37mm and 75mm projectiles.

In the first experiment, we consider a scenario where the two objects are initially sensed near the edge of the instrument. The locations of the two objects are r1 = (0.20, 0.30, −0.15) m, r2 = (0.10, 0.15, −0.35) m. Figure 88(a) shows the relative position in the first place between the sensor footprint (the black dashed square) and the object locations (the two red circles).We inverted the initial sounding data and obtained the estimated locations of the two objects:˜r1 = (0.17, 0.36, −0.15) m,˜r2 = (0.11, 0.10, −0.24) m. Figure 88(b) shows that the recovered polarizabilities (the solid curves) are fluctuated and far from the true ones (dashed curves).

Given current model information extracted from the initial sounding data, we ran the SED to predict the next sounding location. The expected information gain is 98.10 if moving sensor from previous sounding 1 to predicted sounding 2. At the suggested place (green cross) in Figure 88(a)the sensor (the green square) would center on top of the two objects. Following the SED forecast, we took the second sounding and inverted the combined data from the two soundings. As a result (Figure 88 (c)), we obtained significant improvements over the estimated locations of the two objects and the recovered polarizabilities. As an experiment, we continued to run the SED for a next sounding given the previous measurements. Relative to first two soundings, the SED predicted that the expected information gain would be 14.42 at another new sounding, shown as a blue square in Figure 88(a). Again, taking the measurements in this newly intended sensor location from the SED and inverting all three sounding data simultaneously, we further achieved some improvements in the recovery of polarizabilities of 37mm projectile. Subsequently, we would have a small information gain of 7.43 for a 4^{th} future sounding relative to the previous three soundings. Given decreasing information gain gradually from the SED, we stopped taking any more measurements.

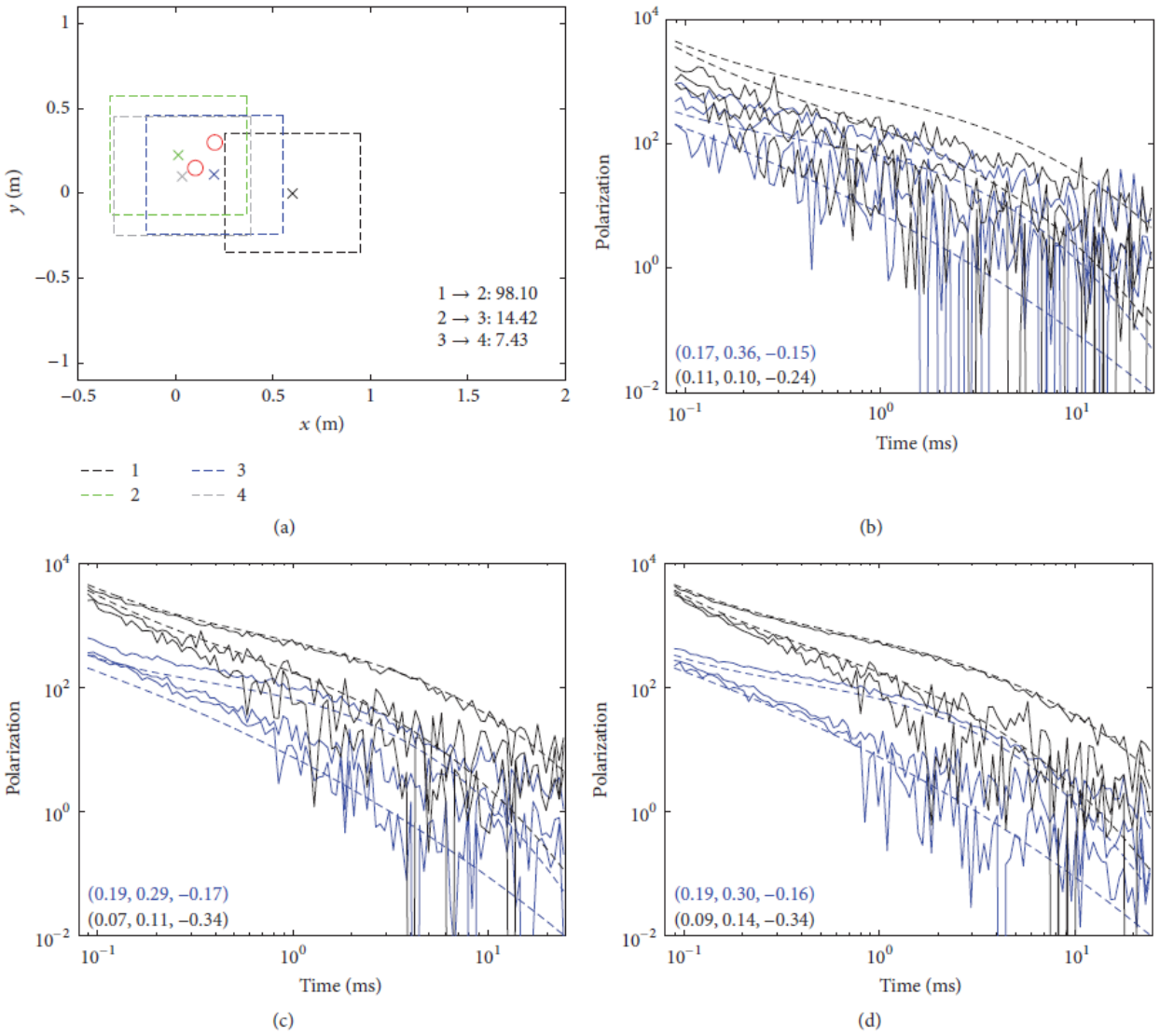

Figure 88. Experiment 1: two objects near the sensor edge. (a) Two red circles represent the true locations of the objects. The black square delineates the footprint for the initial sensor location and the other color squares indicate the predicted positions. (b) The recovered polarizabilities from the initial sounding (s1) data. (c) The recovered polarizabilities from the sounding data [s1 s2]. (d) The recovered polarizabilities from the sounding data [s1 s2 s3]. In the polarization subplots, the solid curves represent the recovered polarizabilities and the dashed ones the true ones.

In the second experiment, we mimic another real case where both objects are close to the sensor edges but one is inside the sensor footprint and the other one is outside of it. The locations of the objects are at $\mathbf{r}_1$ = (0.45, −0.21, −0.15) m and $\mathbf{r}_2$ = (0.10, 0.15, −0.35) m. Figure 90(a) shows the relative position initially between the sensor footprint (the black dashed square) and the object locations (the two red circles). Inverting the first sounding data derives the locations of the two objects: $\widetilde{\mathbf{r}}_1$ = (0.44, −0.21, −0.14) m, $\widetilde{\mathbf{r}}_2$ = (0.17, 0.12, −0.36) m. For the 37 mm projectile, its recovered polarizabilities (in the blue solid curves) are acceptable although the secondary polarizabilities show some fluctuation in late times (Figure 90(b)). But for 75mm projectile that is outside of sensor footprint, the recovered polarizabilities

are noisy. However, the situation improves after applying the SED method. For example, the suggested new sounding (the green square) in Figure 90(a)would cover both objects within sensor footprint. The corresponding expected information gain is 31.23 assuming measurements would be taken in this place. By taking the measurements as suggested by the SED and then inverting composite data from both soundings, we not only obtain the cleaner polarizabilities of the 37mm projectile but also well recover the polarizabilities of the 75mm projectile (Figure 90(c)). After that, we might want to know what the SED can continuously forecast. Relative to the current measurements, the expected information gain would be 10.30 for the next sounding. Taking the measurements at the suggested 3rd sounding location, we further pin down the fluctuation of the recovered polarizabilities in the late times. Similar to the first experiment, we ran the SED to examine a possible fourth sounding and observe that only the small information gain of 6.2 can be achieved. We decided not to acquire additional data with the suggested sounding.

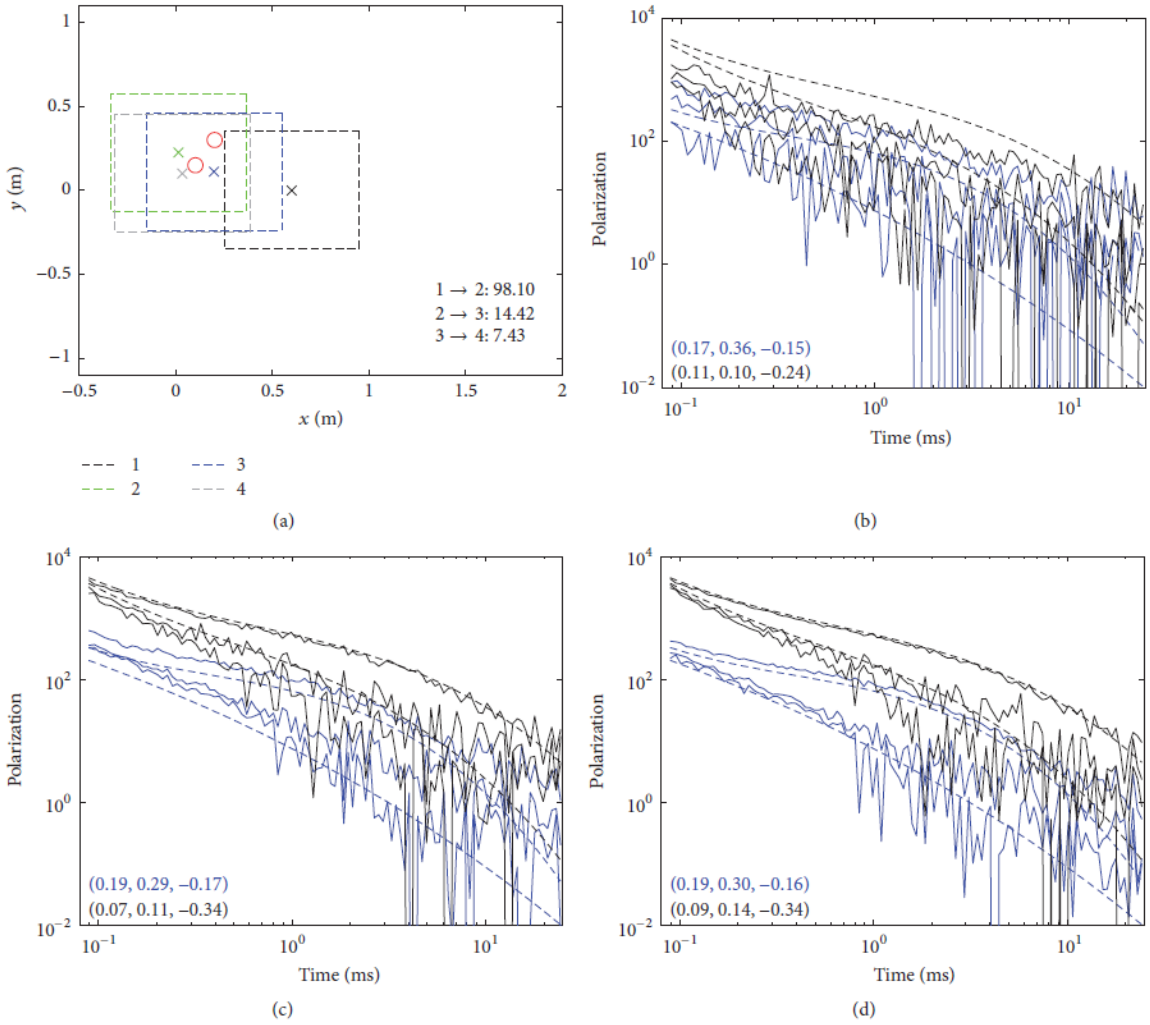

Figure 89. Experiment 2: Two objects close to sensor edges. Caption is the same as that in Figure 88.

From the above experiments, we see that the SED predicts to place a sensor toward the locations of objects. Recall that EMI sensing is quasi-static and signals fall off rapidly about $1/r^6$, where r is the distance from a sensor to an object. By reducing that distance in an optimal way, the SED attempts to increase sensing sensitivities and the SNR as well. This is consistent with the physical nature of the problem. As shown in Figure 91, the information gain in (86) as a function of sensing location can achieve maximum values around the objects' locations. This concave property justifies the use of the D optimality-based optimal experimental design to forecast an optimal sensor placement.

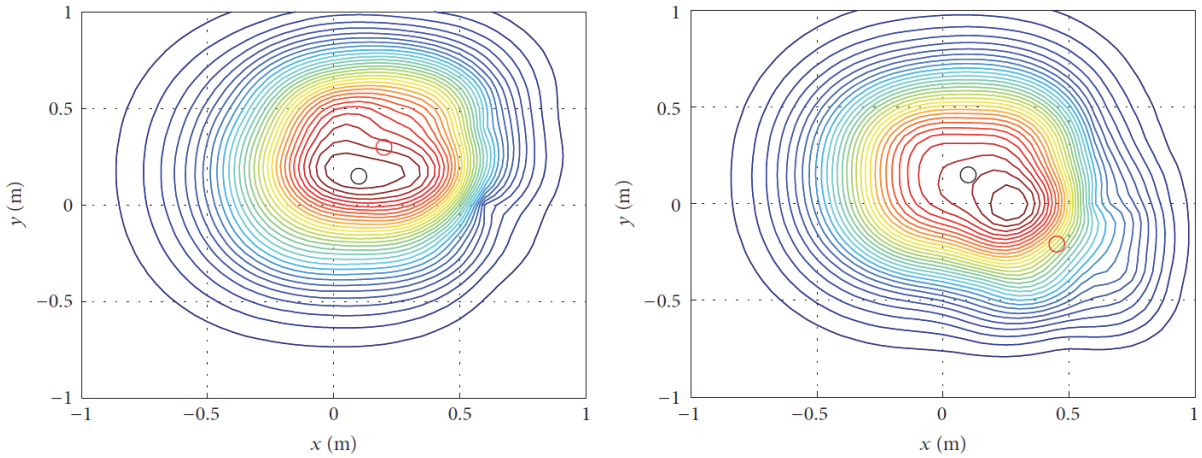

(a) Experiment 1 (b) Experiment 2

Figure 90. Map of Information gain as a function of sensor locations: (a) Experiment 1; (b) Experiment 2. The two circles denote the locations of targets.

The previous studies on inversions of multiple objects (e.g., [27] [29] [28]) have shown that a single-object model may lead to the adverse consequence of missing targets of interest and is often not sufficient to guarantee an accurate recovery of target polarizabilities. Similarly, in the SED test when assuming a single-object model for the above two-object examples, we obtained incorrect results: missing recovery of one anomaly or both (not shown here). Next, we are interested to establish whether the SED is effective for an overrepresented model, that is, assuming the number of objects larger than the actual one.

In the third experiment, we inspect the SED result given an overestimated number of objects. Consider a single object (37mm projectile) at $\mathbf{r}$ = (0.10, 0.15, −0.35) m. The object is outside of the sensor footprint. Figure 91(a) shows the initial sensing position relative to the object. In the following, we simply suppose a two-object model. Given the initial sounding data that were collected over a single object anomaly, we inverted them as if there were two objects. Figure 91(b) shows the recovered polarizabilities in the first location. The black jittery curves correspond to a false source at $\widetilde{\mathbf{r}}_1$ = (−0.33, 0.10, −0.36) m. For the actual object (blue solid curves), its primary polarizability decay curve is somehow recovered but its amplitude is smaller than the true one (dashed curves). The secondary polarizabilities are noisy. The estimated location of the true object is given by $\widetilde{\mathbf{r}}_2$ = (0.13, 0.17, −0.30) m. Given the current inaccurate information extracted from the initial sounding data, the SED predicts a new sensing place (the position

of the green square in Figure 91(a)) with the expected information gain of 128.12. Conducting the measurements as the SED forecasted and performing the inversion with the two-sounding data, we immediately get the recovered polarizabilities that match well with the true ones (Figure 91 (c)). Meanwhile, the false source is inverted now as being outside of the current sounding range and the associated polarizabilities are with very small amplitudes. The third SED predicted sounding (the blue square in Figure 91(a)) suggests a place covering the spurious source inverted in the current model parameters. The expected information gain is achieved as 12.77 with respect to the two previous real soundings. Assume that we continued to take the measurements according to the SED prediction. The results of inverting all three sounding data are quite similar to those of inverting the two sets of data (Figure 91(c) and (d)). After the three soundings, the fourth theoretic sensing location is directly over 37mm projectile. However, with the relatively small information gain of 6.73, it is unnecessary to acquire more data.

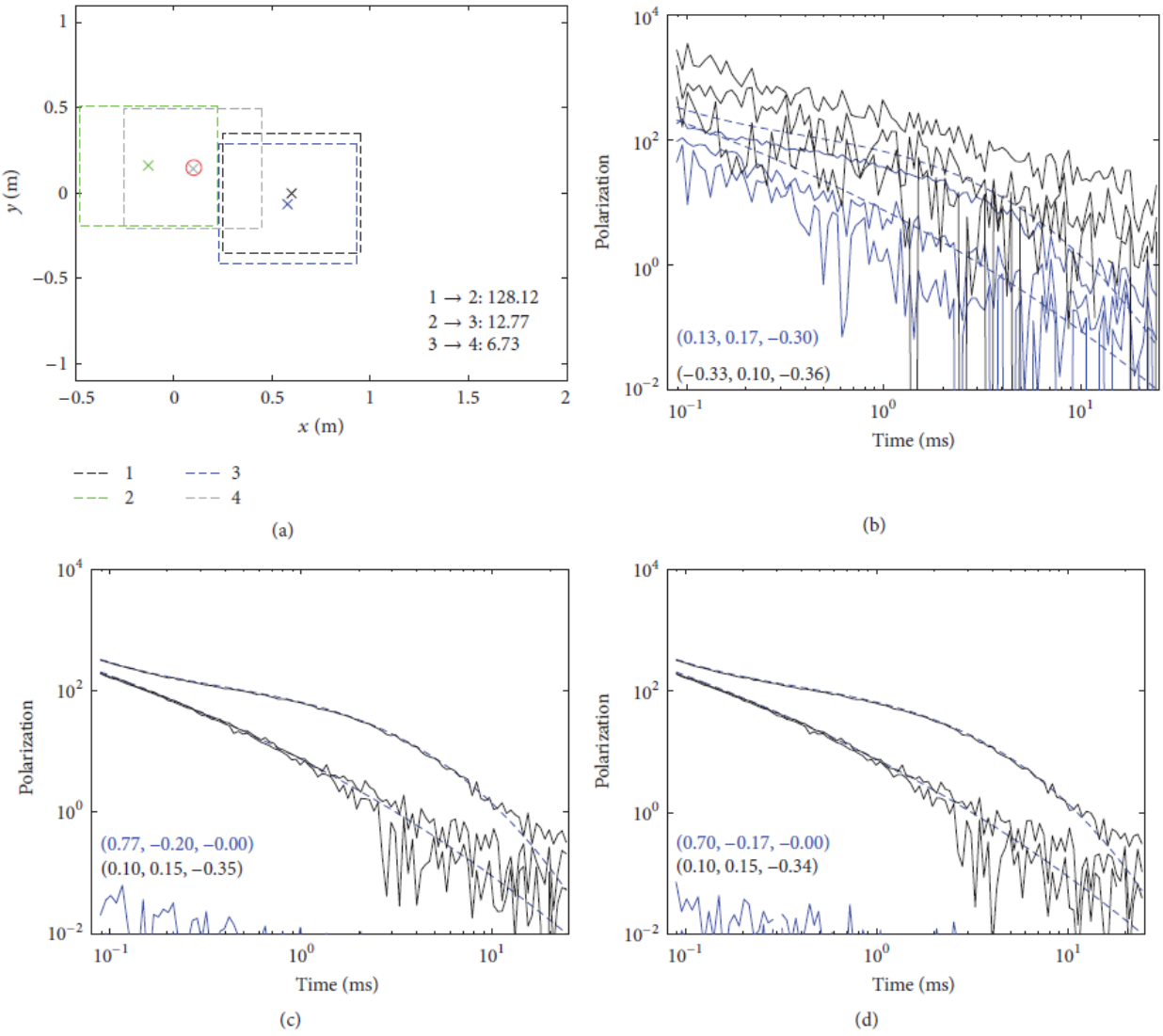

Figure 91. Experiment 3: single-object close to sensor edges. Caption is the same as that in Figure 88.

This experiment shows that an over-representation model in the SED might be a simple, feasible way to deal with the unknown number of objects.

3.2. Experiments with the MPV

To further evaluate the SED, we conducted experiments with the MPV [63] [64]. Figure 92(a) schematically shows the MPV. The MPV is a multi-static sensor system that consists of three orthogonal transmitters: a z-directed circular one with the diameter of 50 cm and x- and y- directed rectangular ones with the sizes of 54 cm× 54 cm and 54 cm× 50 cm, respectively. Five sets of triaxial receiver cubes (each 10 cm × 10 cm) are distributed on the circular transmitter plane. Referring to Figure 92(b), the sensor in the setup would be moved manually on the wood plate to a specified mark and targets were positioned below the plate for a desired configuration. Experimental objects include small, medium, and large ISOs (Industrial Standard Object) (Figure 92(c)). Note that the experiments were taken in the Black Tusk Geophysics office in the day time where noise was strong probably due to various nearby inside and outside electronic interferences. These environment factors might introduce correlated noise. That noise was compensated by taking a background measurement in the absence of the test items before each experiment and by subsequently subtracting background contribution from the data. Considering that the method would be deployed on a real-time system, we assumed an uncorrelated nonuniform noise model. As shown below the SED performance, the assumption appears reasonable.

(a) MPV system (b) Photo of setup (c) ISO targets

Figure 92. (a) MPV: a multi-static system consisting of a z-directed circular transmitter with the diameter of 50 cm and x- and y-directed rectangular transmitters with size of 54 cm × 54 cm. 5 triaxial receiver cubes (each 8 cm × 8 cm) are distributed on the circular transmitter plane. (b) A snapshot of the indoor experiment setup. (c) Photos of small, medium, and large ISOs used in the experiments.

As mentioned previously, we attempted to simulate multiple- target cases that might be encountered in real scenarios: for example, there might be one or two targets that are near or outside the footprint of the instrument. The goal of the experiments is to evaluate how the SED would guide to characterize targets near the instrument edges by taking an additional data sounding. We presented two SED experiments with two object and three-object cases, respectively.

In the two-object case shown in Figure 93(a), there are small and large ISOs (denoted by gray squares) that were positioned at the opposite sides of the sensor footprint (black circle). Inverting the initial

sounding data (S1) provided a rough estimation of target locations, denoted by the small circles in Figure 94(a). The recovered polarizabilities are presented in Figure 94(b) and (c), with the dashed gray curves showing the reference polarizabilities of the ISOs. Overall, the primary polarizabilities of both targets were fairly recovered with some level of jitter at late times. However, the recovered secondary and tertiary polarizabilities for both small and large ISOs appear noisy (Figure 94(b) and (c)). Given the model parameters derived from the initial sounding (S1), the SED predicted the second sounding at (0.28, 0.32) m with a large expected information gain of 83.75. It suggested to position the instrument over the inverted small target. Shown as a green circle in Figure 94(d), we moved the sensor to the second sounding location as the SED guided and acquired the additional data. The inversion with the additional sounding seems to mainly affect recovery of the small object. Its location has some adjustments relative to that derived from the initial sounding inversion. Its polarizabilities become smooth in Figure 94(e). Under the updated model parameters, the SED suggested a third sounding at (−0.14, −0.28) m with information gain of 23.39. We followed the SED to move the sensor in the new position (the big blue circle in Figure 94(g)) that covers the deep and large target. By inverting all three sets of data, we obtained improvements on the recovered polarizabilities of the small and large targets, which became smoother and cleaner. One possible advantage of the SED is that it is able to provide some knowledge about the future state but without a need of real action. For instance, after we took three shots of measurements, the running of the SED points out a fourth sounding at (−0.22, −0.16) m, which is a small offset relative to the third sounding location. And the expected information gain is 8.12 for the new sounding, which is small as compared to previously taking second and third soundings. Thus, in this example, we can stop collecting data for either reaching a predefined number of sounding or having a small expected information gain.

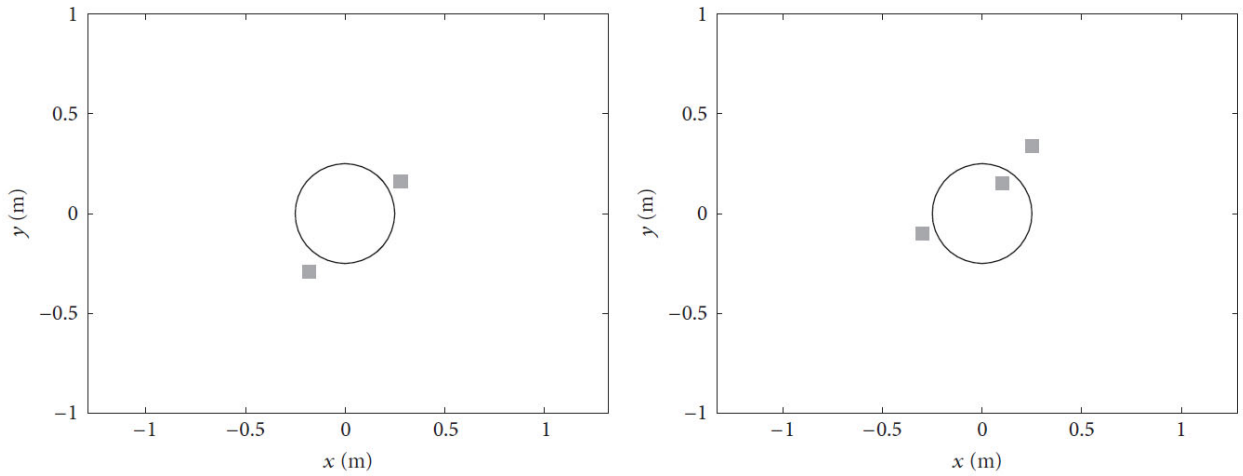

(a) Two-object example

(b) Three-object example

Figure 93. Target locations and initial sensor footprint in the SED experiment setup with the MPV. In the initial sounding (S1), a black circle denotes the sensor footprint and gray squares the true locations of the objects.

In the three-object case shown in Figure 93(b), a medium ISO was inside of the sensor footprint and a small and a large ISO were both outside of the sensor footprint. Data acquired at the initial stage (S1) were initially inverted by assuming a two-object model. The polarizabilities of the medium and large ISOs were well inverted and their recoveries appear not affected by the presence of outside small ISO. The signal contribution of the small ISO to the data S1 is negligible relative to the two other objects. This was verified by inverting the data S1 for a three-object model. Results in Figure 95(d)–(f) show inversion of the initial sounding data does not render a small ISO-like object, rather an additional, false medium ISO-like object (Figure 95 (d)). In other words, the use of the single sounding data is not sufficient to accurately resolve the three targets in this configuration. In practice, we conducted the SED using the results of the two-object inversion. The SED suggested moving the sensor to a position of (0.11, 0.19) m to cover the upper-right target in the current inversion result. The expected information gain was 28.46 for the next possible sounding. We took the second measurement and inverted the two sets of data simultaneously with a two-object model. In Figure 95(g), the big green circle denotes the new sensor location and the two small circles the inverted locations of the two objects. In the updated inversion, the polarizabilities of the medium ISO were recovered with some overshoot relative to the reference ones. However, unlike the inversion in S1 stage, we did not see the polarizabilities matching the large ISO. Instead, we obtained one different, new set of recovered polarizabilities that agree with those of the small ISO. This suggested that an additional target was present, distinct from the two targets found at S1. This motivated the use of a three-target inversion. Using a 3-object model and inverting the two sets of sounding data, we were able to resolve all three targets (their locations and polarizabilities) in a noisy setting (Figure 95(j)–(l)). We stopped collecting data after reaching the sounding number of 2, although the SED suggested the third sounding at (0.26, 0.35)m, a position that would cover the small ISO.

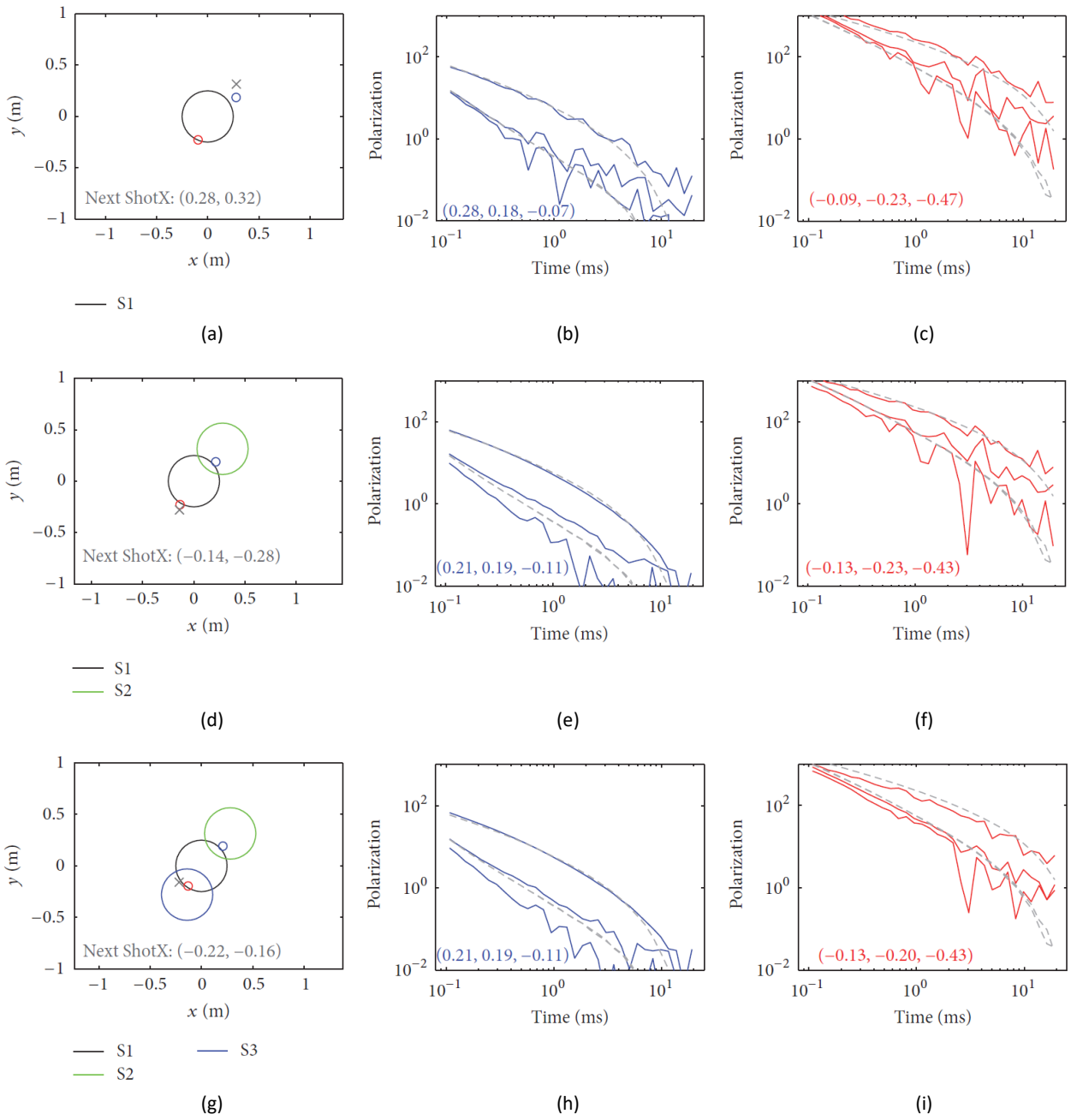

Figure 94. SED experiment with the MPV, two-object example. Initial sounding (S1): (a) the sensor footprint (black circle) and inverted object inverted object locations (small circles); (b)-(c) recovered polarizabilities in blue and red and the reference ones in gray dashed. Soundings S1 + S2: (d) the sensor footprint and inverted object locations; (e)-(f) recovered polarizabilities. Soundings S1 + S2 + S3: (g) the sensor footprint and inverted object locations; (h)-(i) recovered polarizabilities.

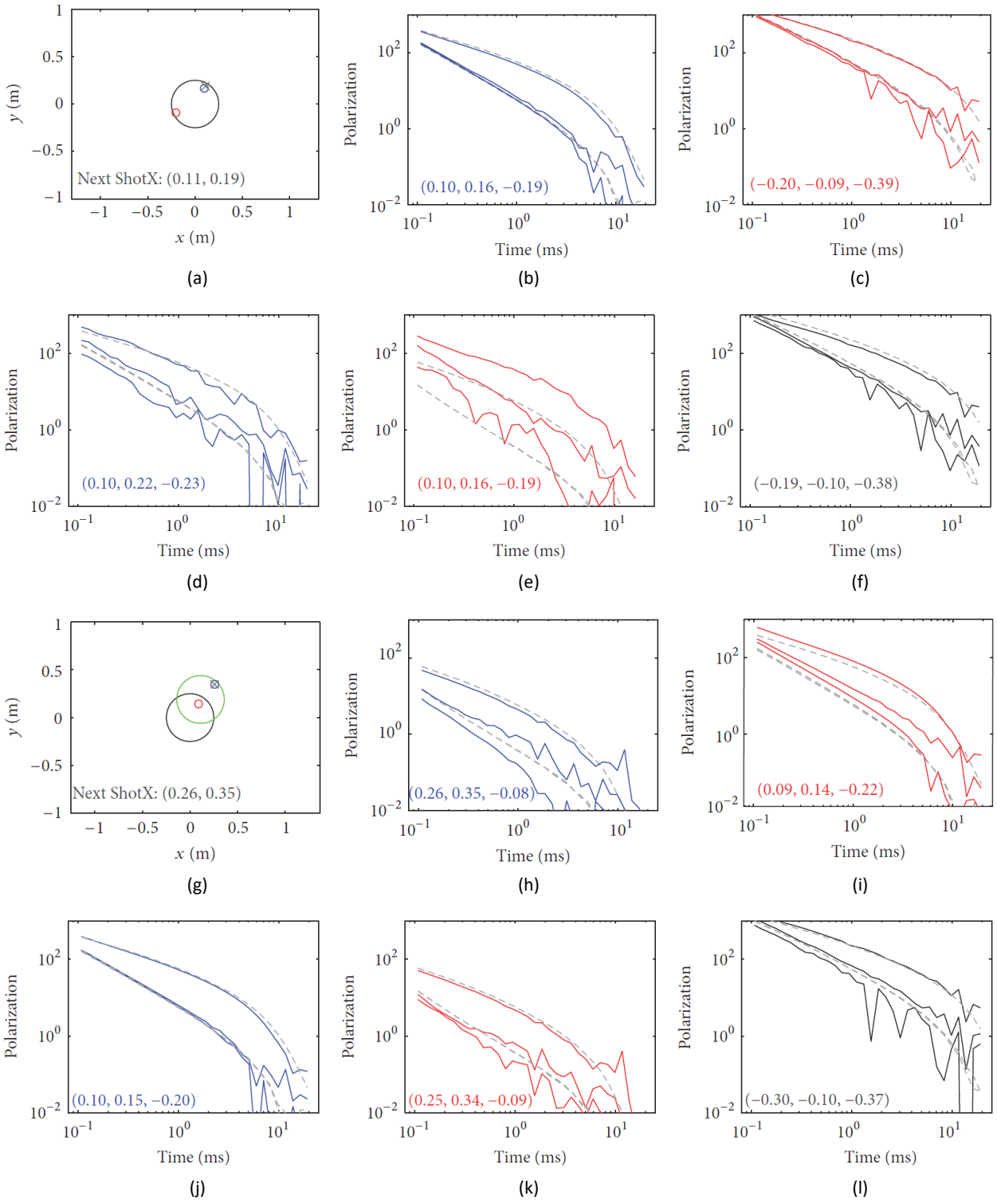

Figure 95. SED experiment with the MPV, three-object example. Initial sounding (S1): (a) the sensor footprint (black circle) and inverted two-object locations (small circles); (b)-(c) recovered polarizabilities with a two-object model; (d)–(f) recovered polarizabilities with a three-object model. Soundings S1 + S2: (g) the sensor footprint and inverted two-object locations; (h)-(i) recovered polarizabilities with a two-object model; (j)–(l) recovered polarizabilities with a three-object model. Recovered polarizabilities are in blue, red, and black and the reference ones in gray dashed.

4. Conclusions

In this work, we have investigated the application of the experiment design approach to guiding a sensor placement that aims to achieve optimal measurements in practice. The experimental design theory includes the two sets of parameters of interest: the model parameters (locations of targets and their polarizabilities) and design parameter (sensing location). Since determining the optimal design parameter depends on the model parameters that are unknown before an experiment, we adopted the sequential experimental design (SED) technique. By the linearized model covariance matrix that quantifies model uncertainty, an information gain function (a variant of the D-criterion) can be defined as a measure of model uncertainty reduction between previous and future surveys. The SED approach recursively solves the target parameters by minimizing the data misfit and forecast the next desired sensor location by maximizing the information gain function. The sequential experimental design algorithm is presented in a generic form which allows to incorporate available prior information about model and data into the process through the covariance matrices. In this preliminary study, we consider the simple case assuming $C_0^{-1} = 0$ and a non-uniform diagonal data covariance matrix.

The synthetic and real tests show that the SED can be a promising tool that can help guide a sensor placement. We further studied the impact of the unknown number of targets on the SED performance. In the TEMTADS2x2 experiments with a single near sensor-edge object, we observed that the SED is able to suggest a new sounding location that covers the true anomaly under an overestimated 2-object model. After adding one-step guided sensing, the polarizabilities of the actual anomaly were much better recovered than those with the initial sounding. Meanwhile the polarizabilities of the false anomaly become small, remain noisy, and are negligible. However, for the case of two objects that are close to sensor edges, an underestimated single-object model could mislead the SED to focus on only one of the targets. As a result, the addition of soundings through the SED brought no improvement to polarizability recovery. In the real MPV experiment with a 3-object case, assuming only two objects for the initial inversion worked for the SED to predict an informative sensing location. The reason was that both the initial sounding and the SED-suggested sounding mainly sensed two objects while the third object remained fairly far from the field view for each survey location. However, inverting the two sets of data simultaneously required a three-object model to account for the signal contribution of each of the three buried items. As a general rule, an appropriate overrepresentation model in the SED appears to be workable to deal with an unknown number of objects.

In the future, it could be interesting to investigate a noise statistical model that properly specifies correlated noise in EMI measurements. Then for measurement errors known to be correlated, a nondiagonal data covariance matrix can be used to take these correlations into account in the optimal experimental design for the sensor placement problem.

Inversion approach: independent model locations and common polarizations for data subsets

The estimation of model parameters from geophysical sensors can be poor when location and orientation of the sensor is measured inaccurately. Here we consider cued MPV data, for which relative location and orientation of the transmitter and receivers are accurately known for a single shot due to those Tx and Rx being rigidly fixed to the sensor frame. When considering multiple shots, the relative location/orientations can be off by ~3-5cm. For the MPV, we define a shot as measurements consisting of 1 firing of each of the 3 transmitters, where all data share a single location measurement from the GPS. This location will be referred to as a shot location. In previous sections, we investigated the possibility of inverting multiple shots simultaneously as a way to improve recovered polarizabilities. In principle, additional sensor data should better constrain dipole model parameters. However, error in the relative position of multiple shots will lead to inaccurate inversion results.

To demonstrate the error in inversion results from inaccurate positioning, we use synthetically generated data from 4 MPV shots (Figure 96). Random positional noise is introduced to shot locations. As relative uncertainty between shot locations increases, both the estimated depth and polarizabilities increase. At very low noise levels of 3-5 cm the polarizabilities are grossly overestimated making it very difficult to match to a library item.

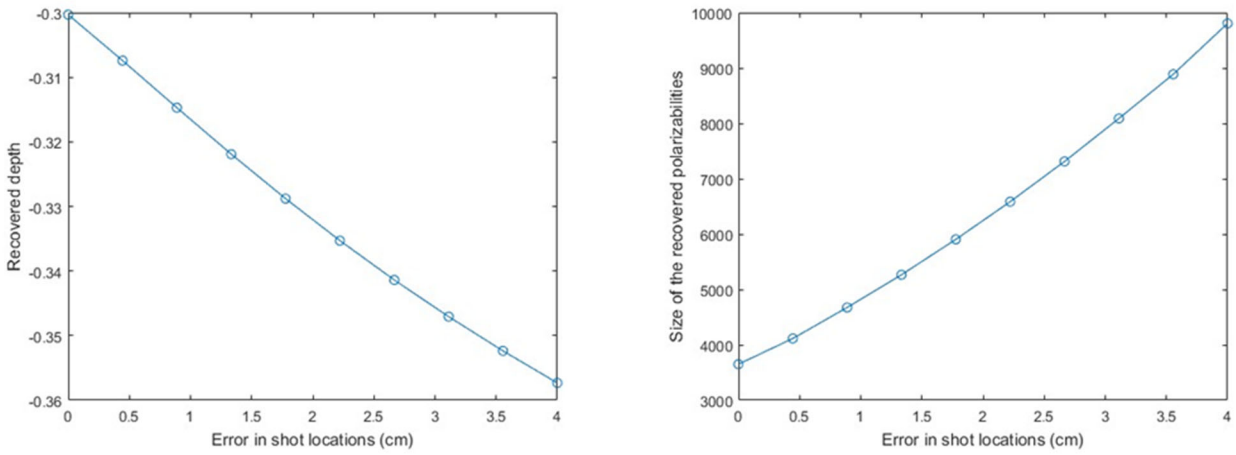

Figure 96. Left: Showing recovered depths for a range of standard deviation of noise added to shot locations. The true depth of 30cm is predicted well when there is no noise added to the shot locations while the recovered depth is pushed deeper for increased noise levels. Right: Showing the size of the recovered polarizabilities for a range of standard deviation of noise added to shot locations. When no noise is added, i.e., 0 cm, the true size is estimated very well. As noise levels increase the size becomes overestimated.

We tested a new approach to recovering polarizabilities under this type of noisy conditions. This approach allows each shot location to have an independent model location while solving for common

polarizabilities for a target. This new approach will be referred to as Independent Model Location Inversion, or IMLI.

We first tested the concept using a i.e., single target, with a single source inversion. Shot locations shown in Table 17 and Figure 97 were assigned around a target. Random gaussian noise was then assigned to each shot location with a σ = 3cm. These locations are labeled inversion locations. Figure 98 shows the resulting Rx locations for both sets of shot locations. In addition to noise placed on the shot locations, gaussian random noise was assigned to the data as 0.01*max(abs(data))/t.

Table 17. Location and orientation of shot locations used for synthetic modelling

Easting	Northing	Elevation	Heading	Pitch	Roll
-0.05	-0.1	0.05	pi/5	0	0
0.3	0	0.05	0	0	0
-0.4	0	0.05	pi/4	0	0
0	0.2	0.05	0	0	0

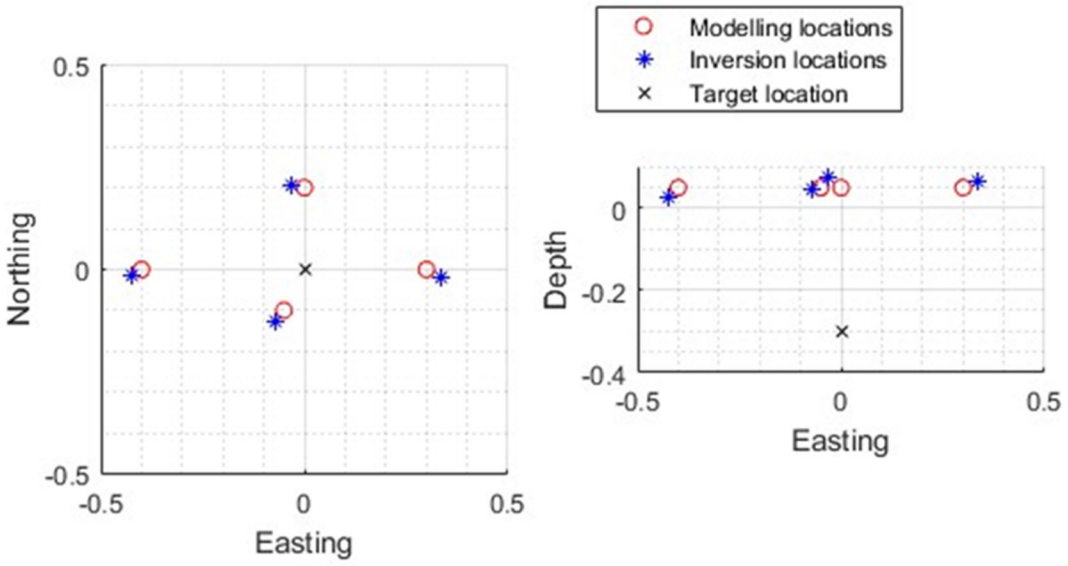

Figure 97. Location of the sensor for each shot. The red circles indicate locations used for forward modeling, while the blue asterisks indicate noisy locations used for inversions. This example has a noise level of σ = 3cm.

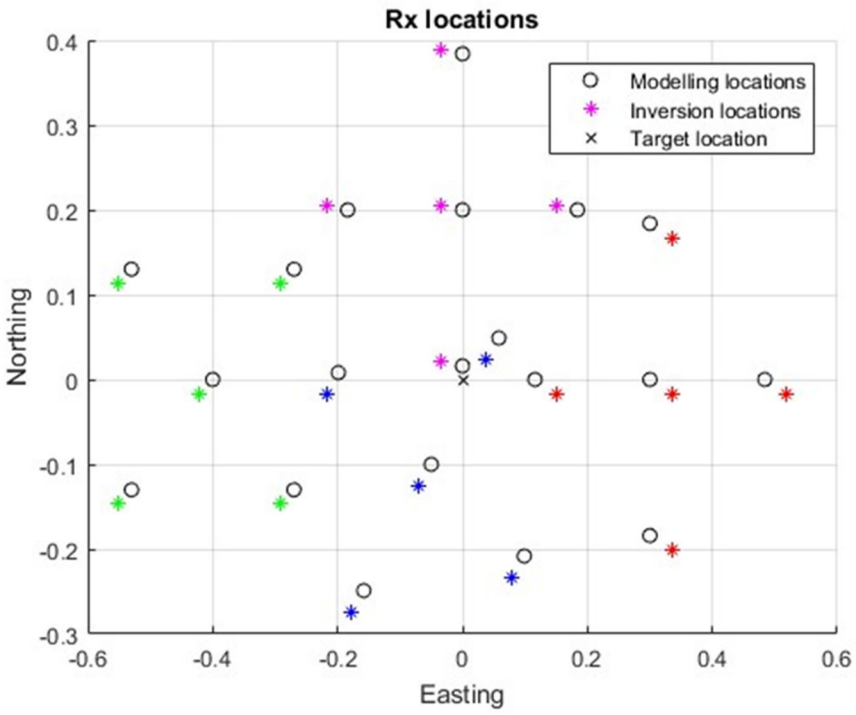

Figure 98. Location of the receivers for each shot. The circles indicate locations used for forward modeling, while the asterisks indicate noisy locations used for inversions. Separate shots are indicated by a different color. This example has a noise level of σ = 3cm

Recovered source location and depth is shown in Figure 99. The true location is indicated by a purple circle that is labeled 'model'. The estimated location (diamond) based on the mean of IMLI source locations, is more accurate than using the location estimated by the standard inversion. The standard inversion method predicts a source that is deeper than the actual model location. This results in an estimate in the dipole polarizabilities that is larger is magnitude than the actual polarizabilities (Figure 100). This overestimate of size and depth is consistent with the modelling results we showed earlier in Figure 96.

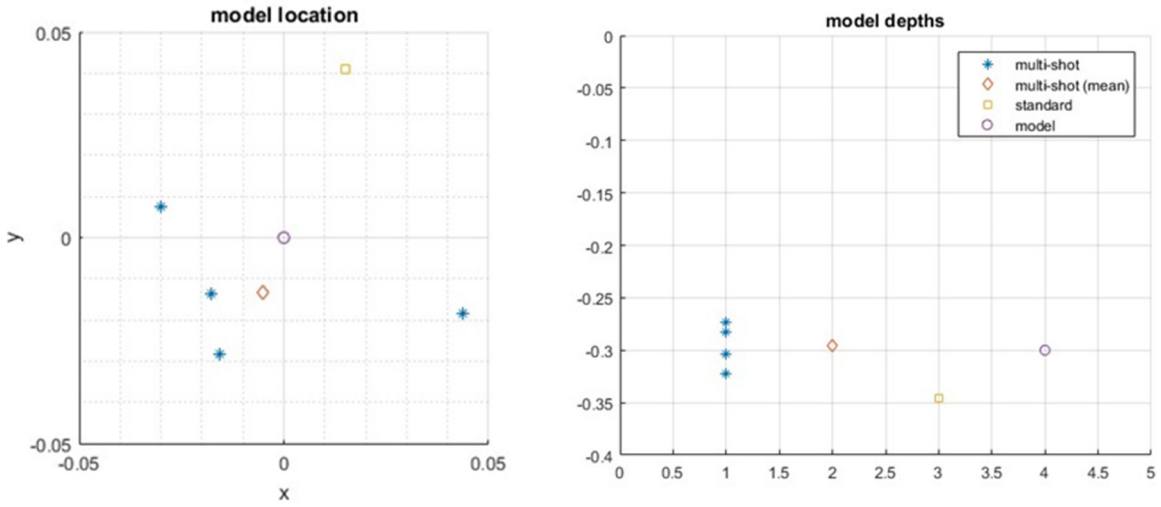

Figure 99. Left: Target XY location results for both the IMLI and standard inversion procedures. For this 4-shot example the 4 independent locations are shown along with their mean value. Right: Target depth results for both the IMLI and standard inversion procedures.

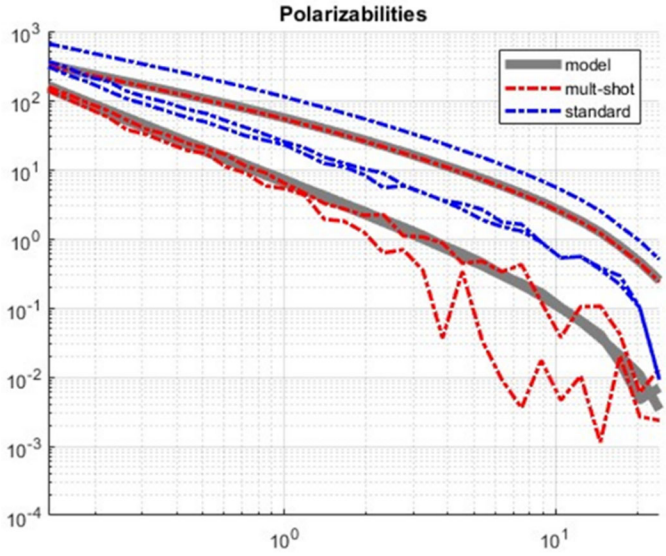

Figure 100. Results of polarization estimations from the shot independent location and standard inversion procedures.

We repeat this experiment using two targets. Figure 101 shows the result for two targets separated by 10cm in the x-direction, and at depths of 25 and 35 cm. As with the single target example, 4 shots of the MPV are used in this test. Similar to the single target example, the standard inversion over predicts the depth and over estimates the target size (i.e., the polarizability amplitudes).

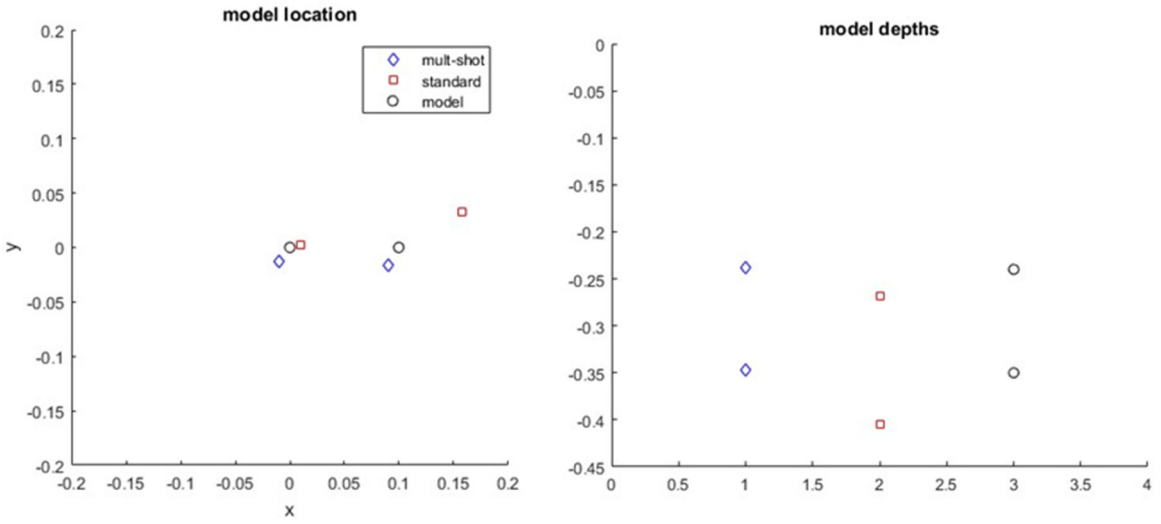

Figure 101. Left: Target location results for both the shot independent location and standard inversion procedures. For this 4-shot example, the 4 independent locations are shown along with their mean value. Right: Target depth results for both the shot independent location and standard inversion procedures.

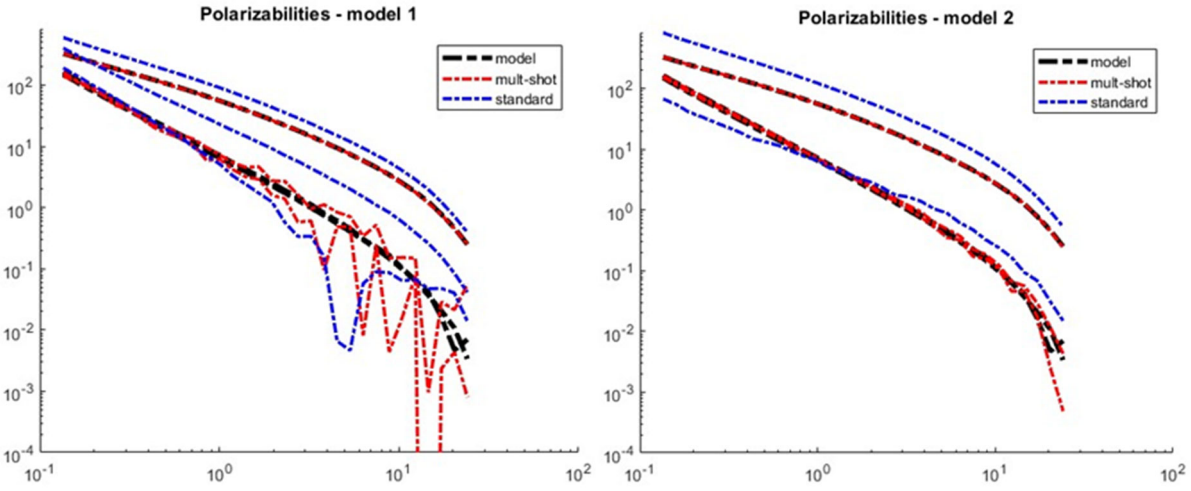

Figure 102. Recovered polarizabilities for the two-target example.

Data collected on a test stand with the MPV was used to test the IMLI. Figure 103 shows the test stand setup. To simulate collecting multiple shots over an anomaly, the targets are moved beneath the MPV. Data are collected with the MPV at nine positions relative to the targets. The relative position between the targets remains constant by attaching them to a plastic crate.

For this test, we collect data over four targets: A 20 mm simulant bolt, 2 small ISOs, and a medium ISO. The top edges of the 20mm simulant bolt and two small ISOs are at the same depth, with the medium ISO is deeper. The depth to center of target and relative positions are listed in Table 18.

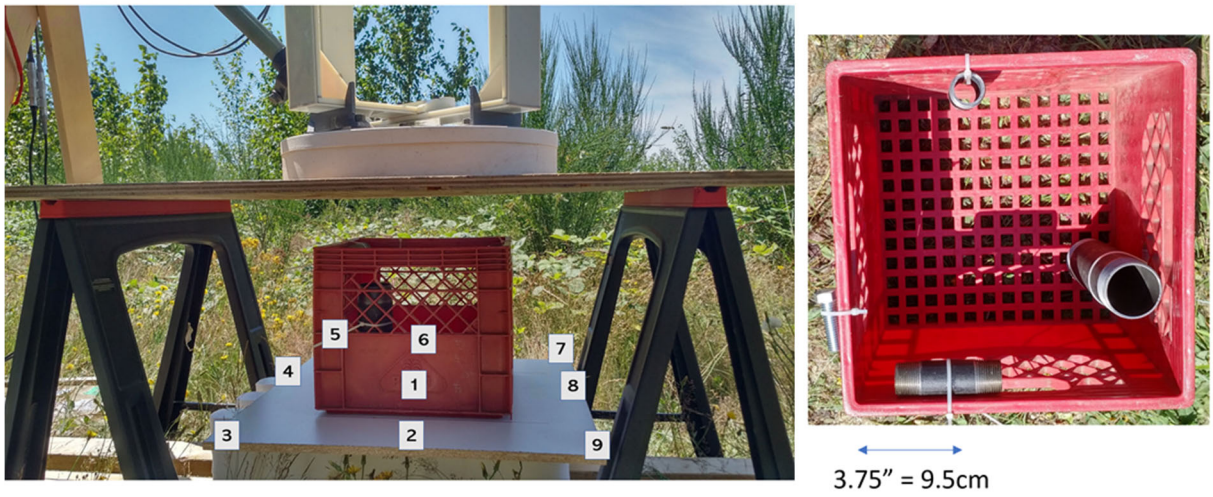

Figure 103. Test stand setup for IMLI example. Left: MPV placed over the targets. An MPV measurement is acquired with the targets at each of the nine locations indicated in the image. Right: The targets are attached to a plastic crate to ensure consistent relative positioning. The relative positions are listed in Table 18.

Table 18. Location of targets in IMLI example. Depths listed are measured to center of the target.

Target	**Orientation**	**Depth to Center of Target**	**X (cm)**	**Y (cm)**
Bolt (20mm)	Horizontal	11.5 cm	-19.1	-5.8
Small ISO	Vertical	16 cm	-5.1	13.2
Medium ISO	Vertical	27.5 cm	11.4	-7.4
Small ISO	Horizontal	11.6 cm	-7.5	-13.0

We first inverted each of the nine shots individually, using a 4-dipole source model. The single shot inversions had difficult resolving the source locations and polarizabilities of the each of the four items. The most successful result occurs when the MPV is centered on the targets (i.e., position 1 in Figure 103, left).

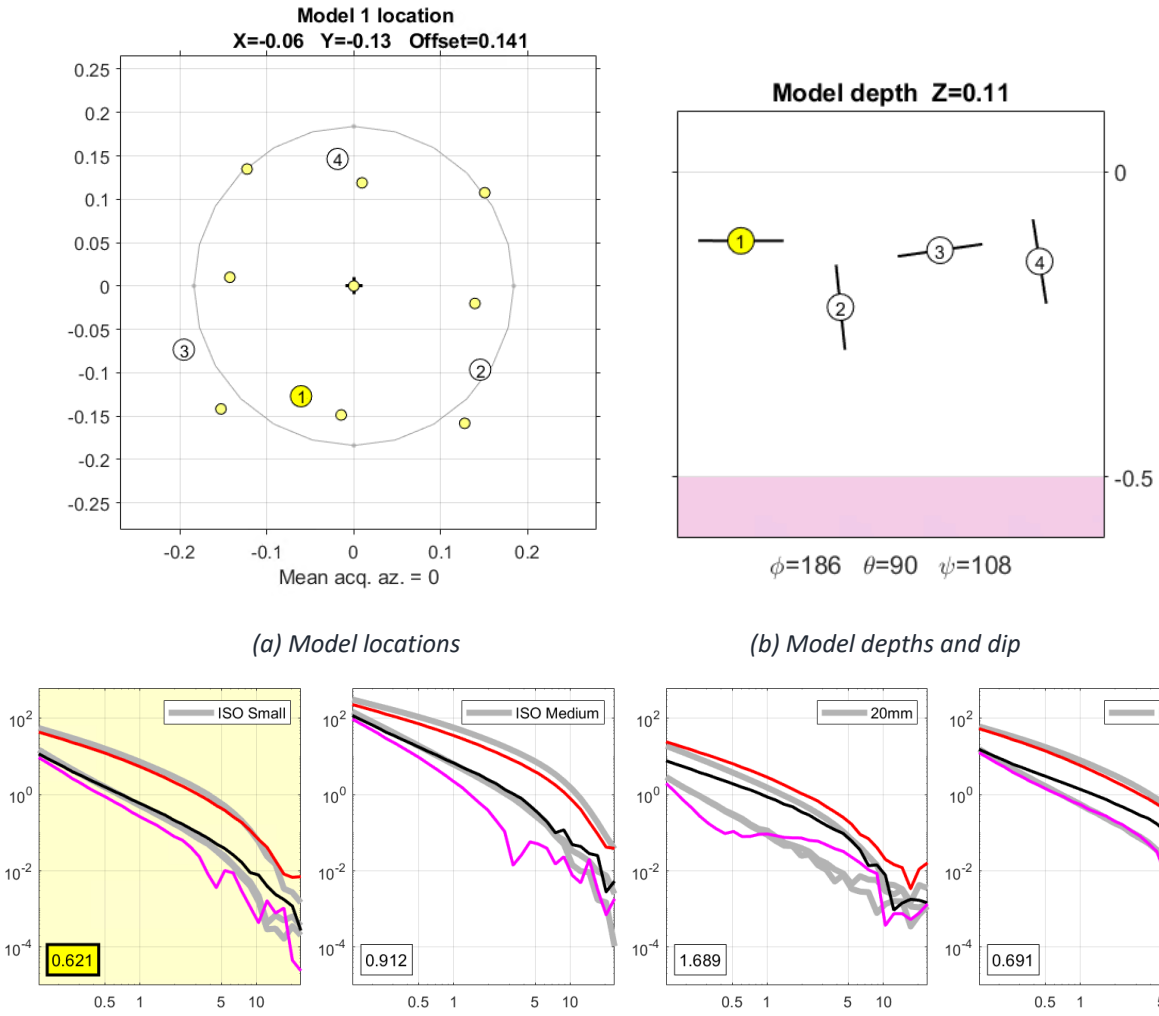

(a) Model locations *(b) Model depths and dip*

(c) polarizabilities for each of the 4 dipole sources

Figure 104. Single shot inversion result

Figure 104 contains the result from inverting the center shot over the targets. Figure 104(a) indicates the location of the estimated source locations relative to the center of the MPV sensor head. The MPV sensor head has a 50 cm diameter, and the 4 outer receiver cubes are 18.4 cm from the center of the sensor head. The grey circle has a radius of 18.4 cm. The source locations are indicated by a circle with a number indicating the source. The small yellow circles indicate the location of shots 1 to 9. Figure 104(b) indicates the depths of the recovered sources and the dip. Figure 104(c) show the estimated polarizabilities for the 4 sources. The source locations, depths and orientations are accurate, though the secondary polarizabilities for the 20mm simulant bolt are not well constrained. This may be due to, in part, the location of the 20mm being furthest away from the center of MPV and being the smallest target.

We repeat the inversion using 2 shot locations (Figure 105(a)). Using a pair of shots results in some improvement of the secondary polarizability estimates, resulting in a decrease in the polarizability misfit for 3 of the 4 targets.

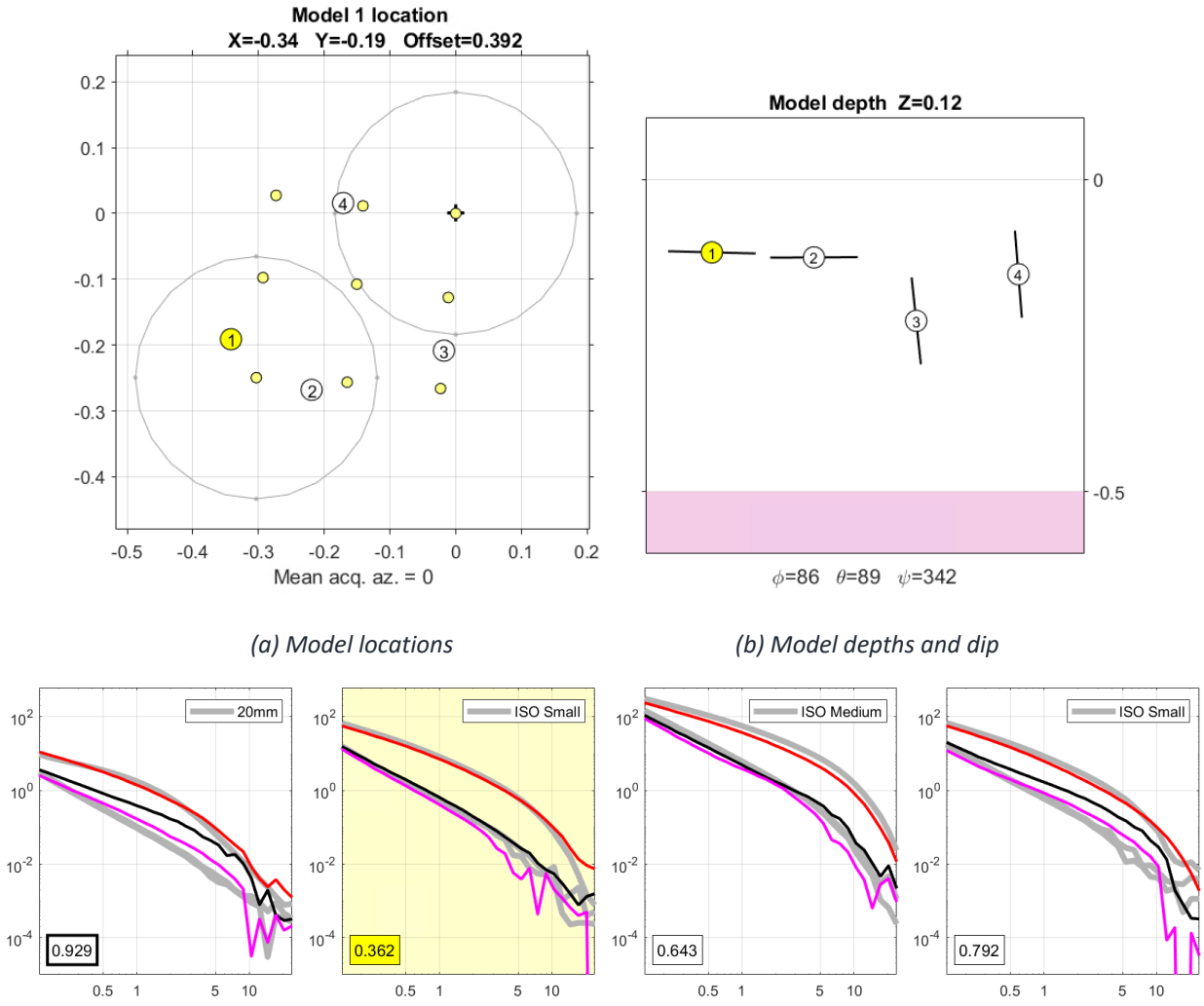

(a) Model locations *(b) Model depths and dip*

(c) polarizabilities for each of the 4 dipole sources

Figure 105. Inverting a pair of shots.

We then apply the IMLI to this data. We randomly chose 3 pairs of soundings to invert. We first invert in the standard way, and then we use the IMLI. The resulting polarizabilities are show in Figure 106 to Figure 108. The results do not show significant improvement when using the IMLI. There are however, some minor improvements in each case, and the result in Experiment 2 (Figure 107) has the best overall results. For N shots, the current implementation of the IMLI allows for a N source locations per target, but require that both the polarizability and orientation of each source is the same for each target. For future work, the IMLI should be implemented to allow for both location and orientation of each source to vary for each sounding.

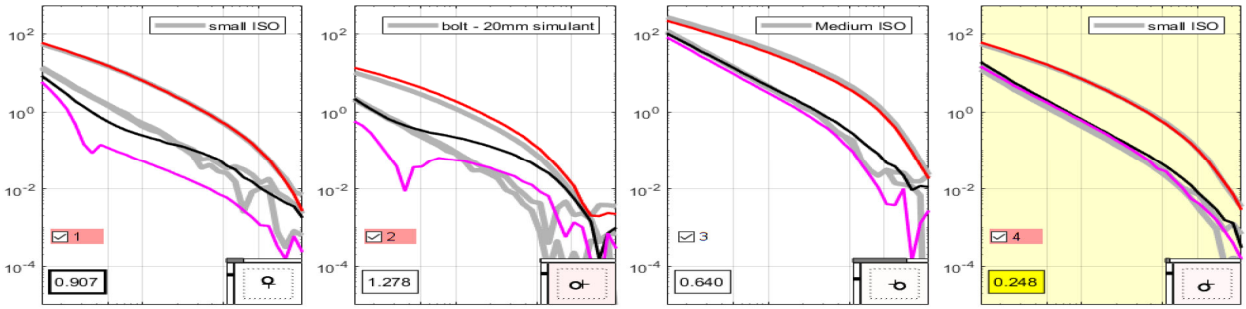

(a) *Standard inversion*

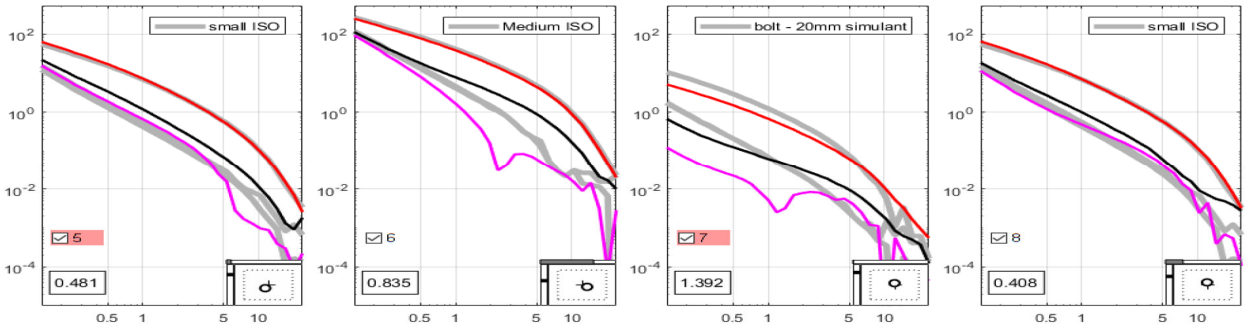

(b) Independent location inversion

Figure 106. Experiment 1. Recovered polarizabilities (a) Standard inversion. (b) IMLI

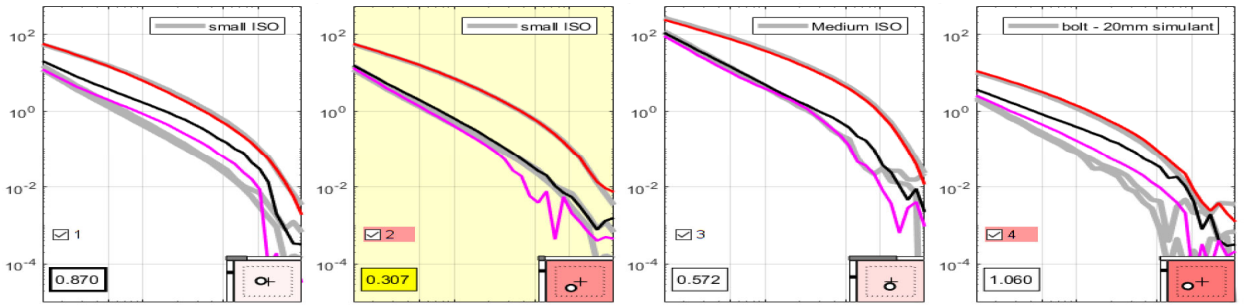

(a) standard inversion.

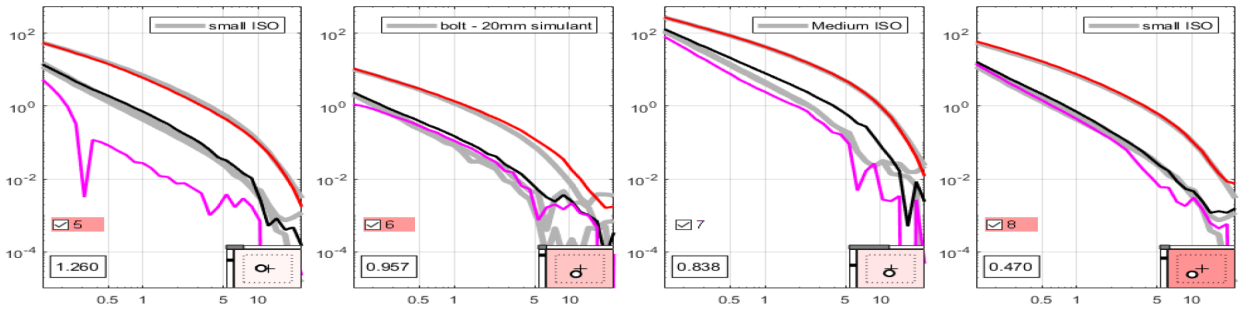

(b) independent location inversion

Figure 107. Experiment 2. Recovered polarizabilities (a) Standard inversion. (b) IMLI

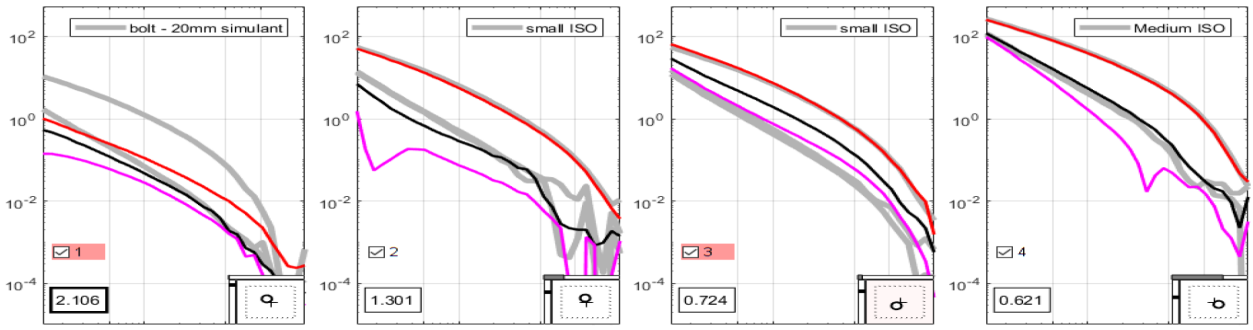

(a) standard inversion.

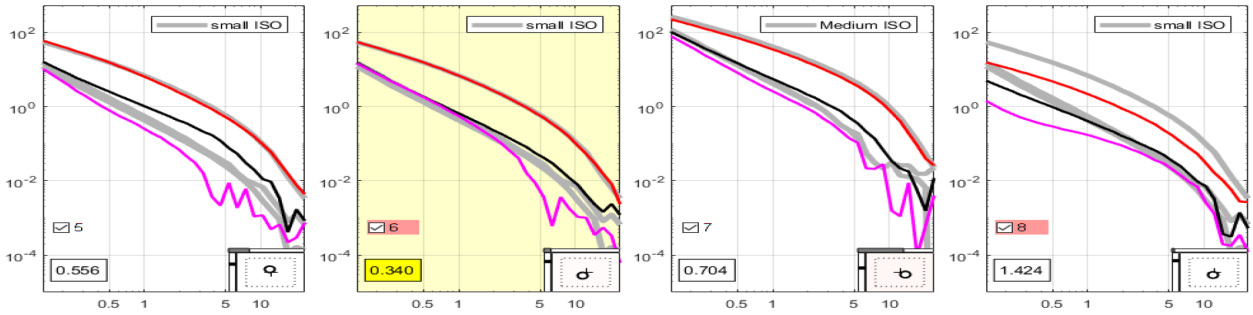

(b) independent location inversion

Figure 108. Experiment 3. Recovered polarizabilities (a) Standard inversion. (b) IMLI

We tested the IMLI on dynamic data. A common challenge when processing MPV dynamic data is to resolve the time lag between the EMI, GPS and IMU data streams. Corrections to account for the time lag are typically applied line-by-line and have a relative amount of uncertainty associated with them. If we consider relative errors in sensor location for data belonging to the same line versus data belonging to neighboring lines, we expect there to be a large difference in those errors. It follows that we should expect an improvement in recovered polarizabilities if we allow each line to have an independent model location in our inversion problem.

In order to test the IMLI on dynamic data, we used IVS data at Spring Valley. An example of one of the IVS datasets and the items in the IVS lane are shown in Figure 109. Results are presented from 4 IVS datasets. Each dataset consists 4 lines, with 2 lines passing in opposite directions centered on the targets and 2 more lines offset ~0.2 meters.

Using the approach outlined above we inverted each dataset with both the standard inversion and the IMLI. Table 19 shows the recovered depths from each inversion. We note that the recovered depth from the IMLI is a result of the mean depth of the 4 model locations from each of the 4 lines. Figure 110 to Figure 113 present the recovered polarizabilities along with their best match to the reported ground truth item. Table 20 shows the polarization misfit to the ground truth item. There is a general improvement of the polarizability misfit, with the Medium ISO having the greatest improvement in polarizability accuracy. The improvement in the Medium ISO performance may be due to the close proximity to the sensor, such that the impact of positional inaccuracy in larger.

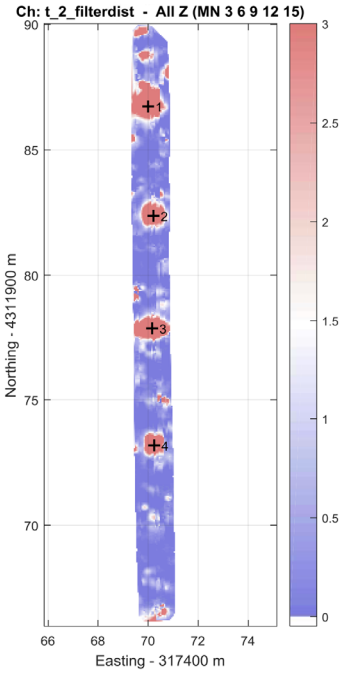

Target	Type	Orientation	Depth (m)
1	3-in Stokes	Horizontal, along track	0.26
2	75 mm	Horizontal, along track	0.32
3	Medium ISO	Horizontal, across track	0.10
4	Small ISO	Horizontal, along track	0.20

Figure 109. Dynamic data collected with the MPV over an IVS strip consisting of a 3-in Stokes mortar, 75mm projectiles, medium ISO and Small ISO. An orientation of "along track" indicates the item is parallel to the travel path, and "across track" is perpendicular to the travel path.

Table 19. Recovered depths for each item.

Source depths (m)	3-in Stokes Depth=0.26 Along track		75mm Depth = 0.32m Along track		Medium ISO Depth = 10cm		Small ISO Depth = 20 cm	
Dataset	**Standard**	**IMLI**	**Standard**	**IMLI**	**Standard**	**IMLI**	**Standard**	**IMLI**
(1) SV_WE_IVS_dyn_180618_AM	0.27	0.29	0.37	0.36	0.14	0.12	0.14	0.13
(2) SV_WE_IVS_dyn_ 80618_PM	0.28	0.28	0.35	0.33	0.14	0.12	0.13	0.12
(3) SV_WE_IVS_dyn_180619_AM	0.26	0.31	0.32	0.42	0.13	0.10	0.12	0.14
(4) SV_WE_IVS_dyn_180725_AM	0.34	0.34	0.38	0.35	0.14	0.14	0.14	0.14

Table 20: Polarizability misfit for each target

Polarizability misfit	3-in Stokes Depth=0.26 Along track		75mm Depth = 0.32m		Medium ISO Depth = 10cm		Small ISO Depth = 20 cm	
Dataset	**Standard**	**IMLI**	**Standard**	**IMLI**	**Standard**	**IMLI**	**Standard**	**IMLI**
(1) SV_WE_IVS_dyn_180618_AM	1.023	0.186	1.515	0.188	0.702	0.286	0.761	0.565
(2) SV_WE_IVS_dyn_ 80618_PM	0.514	0.162	0.233	0.219	0.605	0.255	0.753	0.711
(3) SV_WE_IVS_dyn_180619_AM	0.125	0.137	0.295	0.287	0.585	0.184	0.602	0.759
(4) SV_WE_IVS_dyn_180725_AM	0.927	1.124	0.289	0.182	0.174	0.214	0.431	0.558

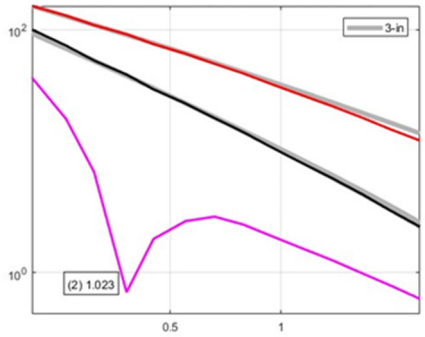

(1) SV_WE_IVS_dyn_180618_AM: Standard

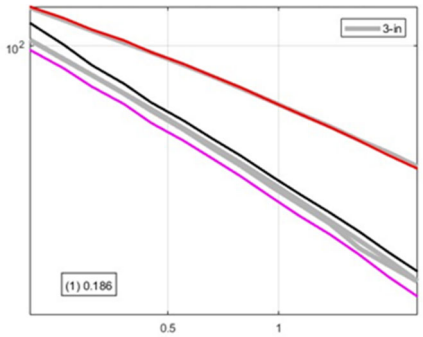

(1) SV_WE_IVS_dyn_180618_AM: IMLI

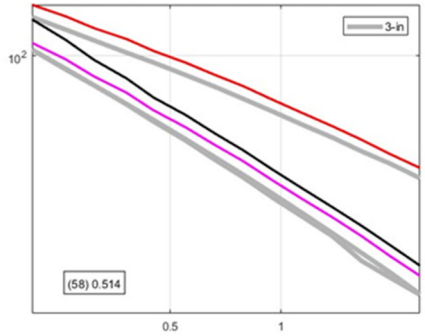

(2) SV_WE_IVS_dyn_80618_PM: Standard

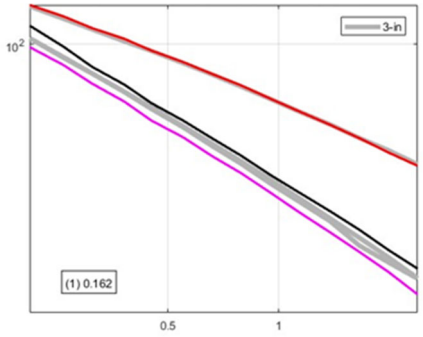

(2) SV_WE_IVS_dyn_80618_PM: IMLI

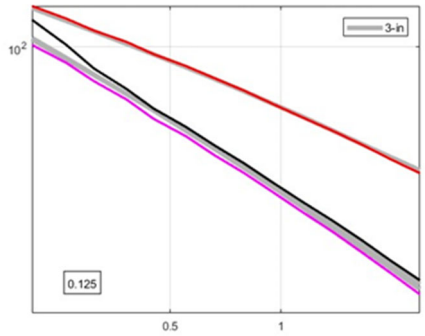

(3) SV_WE_IVS_dyn_180619_AM: Standard

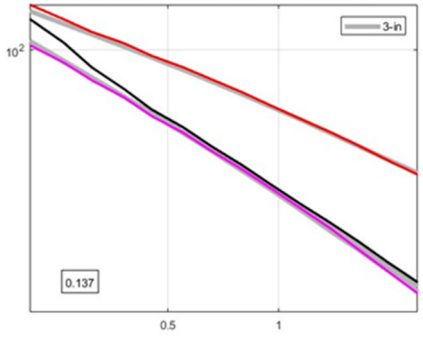

(3) SV_WE_IVS_dyn_180619_AM: IMLI

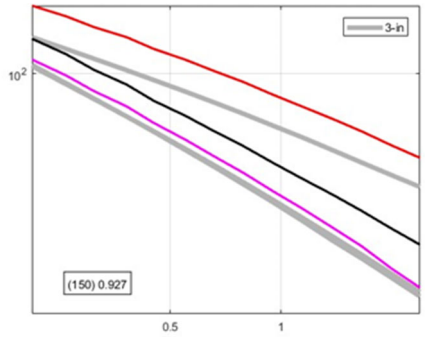

(4) SV_WE_IVS_dyn_180725_AM: Standard

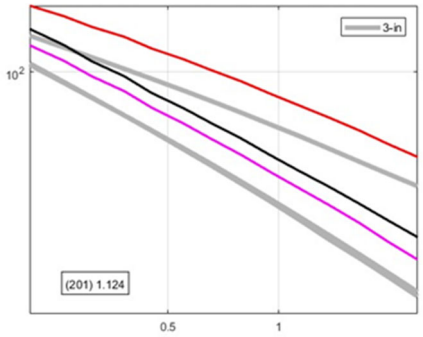

(4) SV_WE_IVS_dyn_180725_AM: IMLI

Figure 110. IVS item: 3-in Stokes. Left column shows the result of the standard inversion. Right column shows the result of the IMLI.

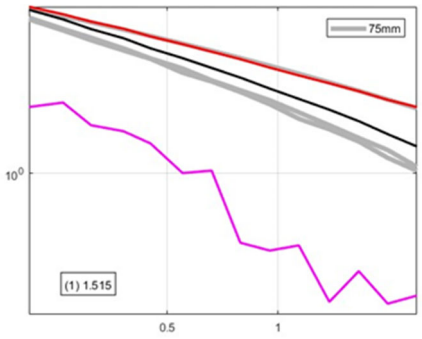

(1) SV_WE_IVS_dyn_180618_AM: Standard

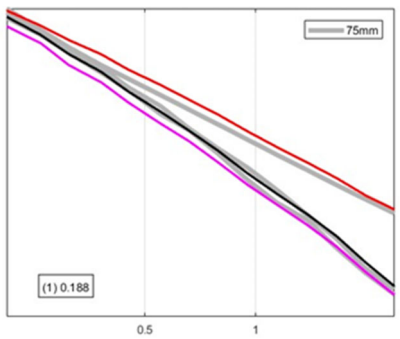

(1) SV_WE_IVS_dyn_180618_AM: IMLI

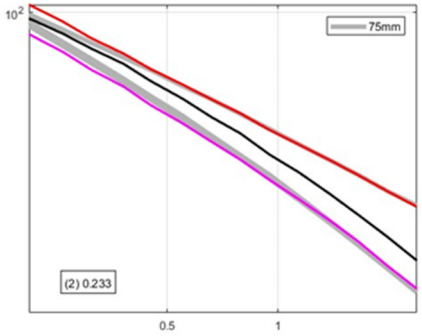

(2) SV_WE_IVS_dyn_80618_PM: Standard

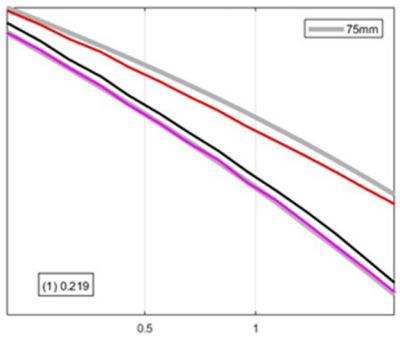

(2) SV_WE_IVS_dyn_80618_PM: IMLI

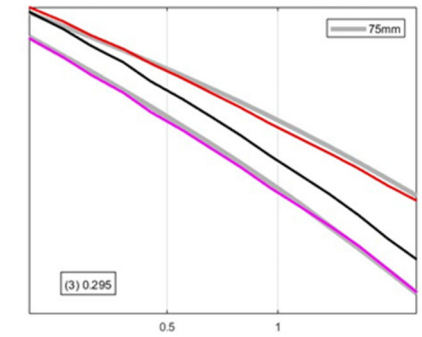

(3) SV_WE_IVS_dyn_180619_AM: Standard

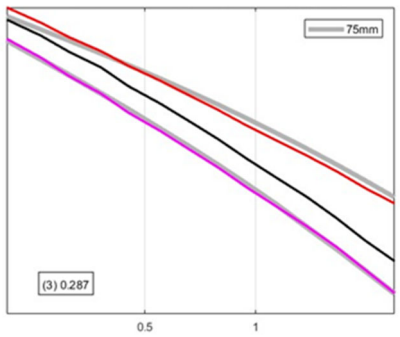

(3) SV_WE_IVS_dyn_180619_AM: IMLI

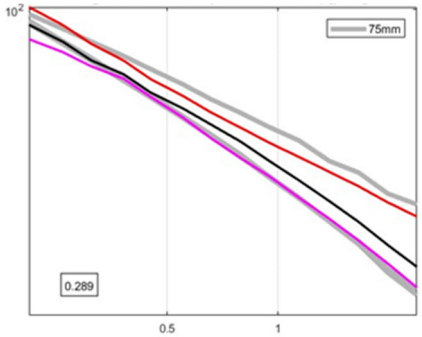

(4) SV_WE_IVS_dyn_180725_AM: Standard

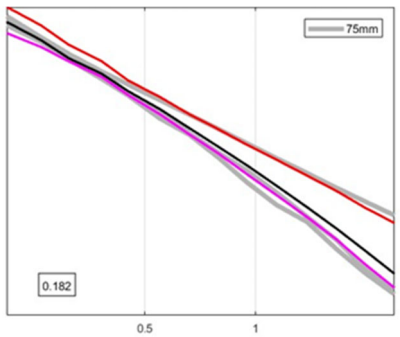

(4) SV_WE_IVS_dyn_180725_AM: IMLI

Figure 111. IVS item: 75mm. Left column shows the result of the standard inversion. Right column shows the result of the IMLI

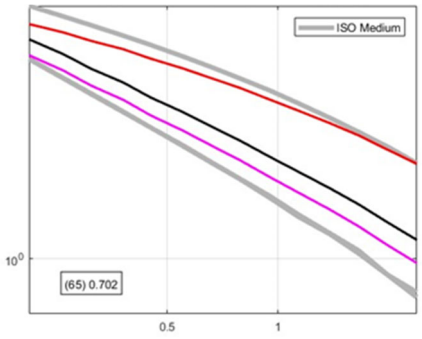

(1) SV_WE_IVS_dyn_180618_AM: Standard

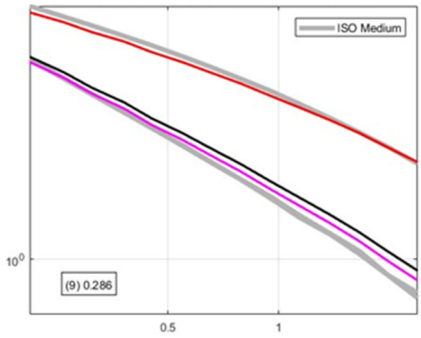

(1) SV_WE_IVS_dyn_180618_AM: IMLI

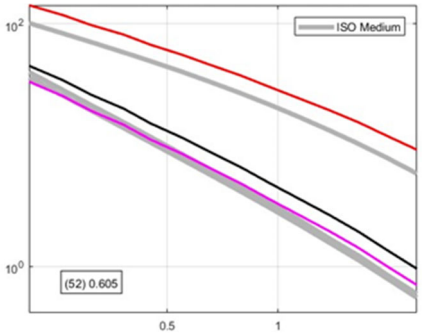

(2) SV_WE_IVS_dyn_80618_PM: Standard

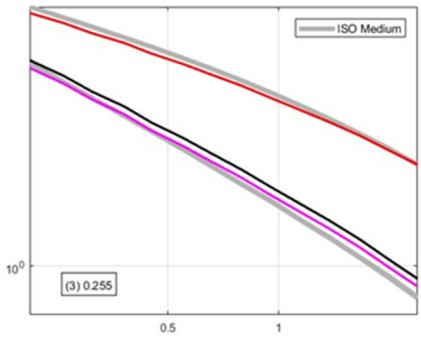

(2) SV_WE_IVS_dyn_80618_PM: IMLI

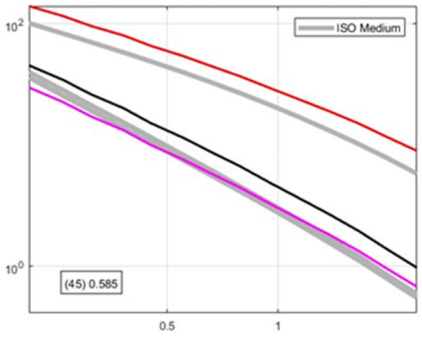

(3) SV_WE_IVS_dyn_180619_AM: Standard

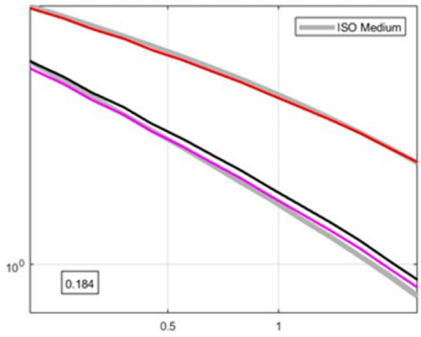

(3) SV_WE_IVS_dyn_180619_AM: IMLI

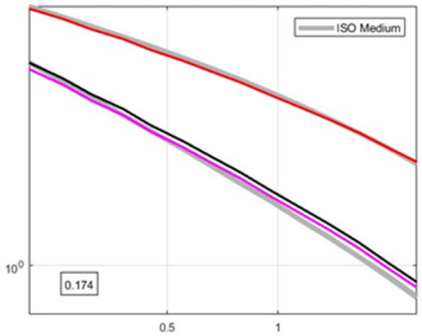

(4) SV_WE_IVS_dyn_180725_AM: Standard

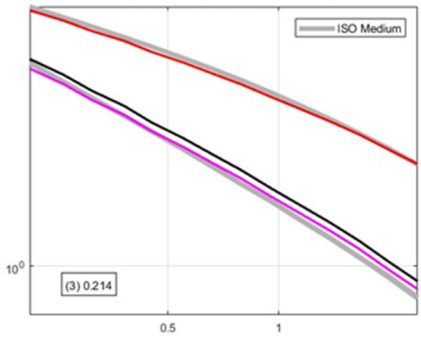

(4) SV_WE_IVS_dyn_180725_AM: IMLI

Figure 112. IVS Item 3: Medium ISO. Left column shows the result of the standard inversion. Right column shows the result of the IMLI. This target had the greatest improvement in polarizability estimate accuracy of all the targets.

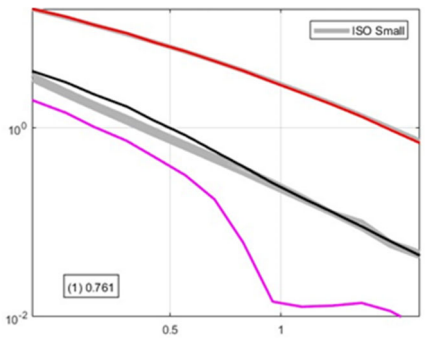

(1) SV_WE_IVS_dyn_180618_AM: Standard

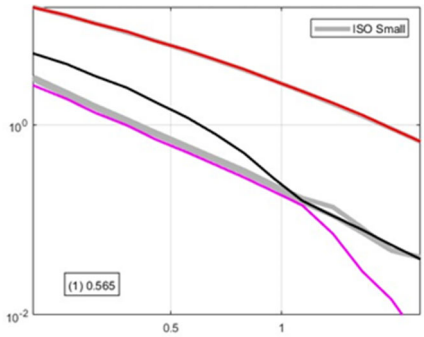

(1) SV_WE_IVS_dyn_180618_AM: IMLI

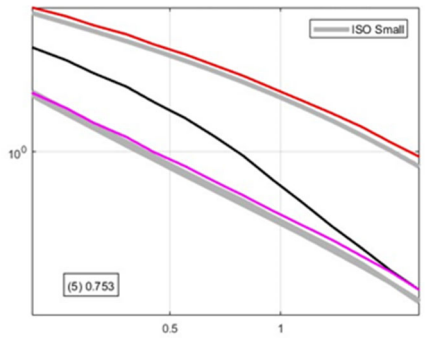

(2) SV_WE_IVS_dyn_80618_PM: Standard

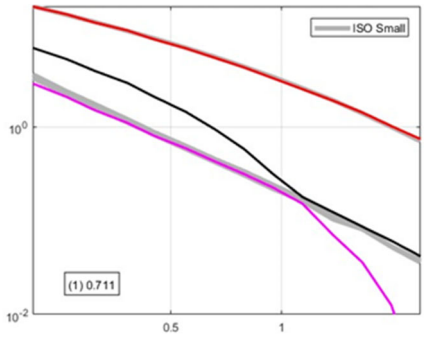

(2) SV_WE_IVS_dyn_80618_PM: IMLI

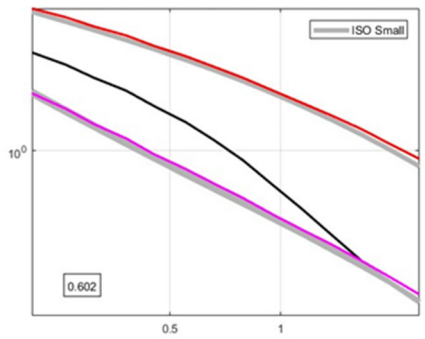

(3) SV_WE_IVS_dyn_180619_AM: Standard

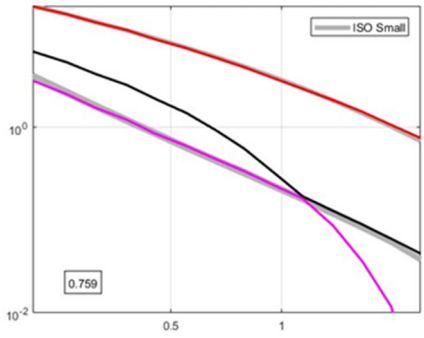

(3) SV_WE_IVS_dyn_180619_AM: IMLI

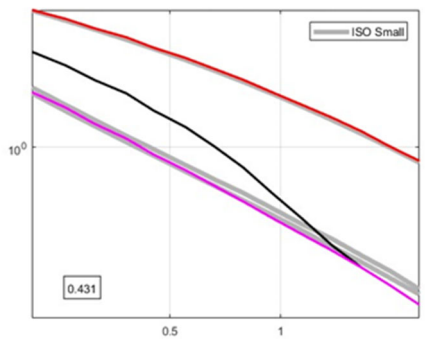

(4) SV_WE_IVS_dyn_180725_AM: Standard

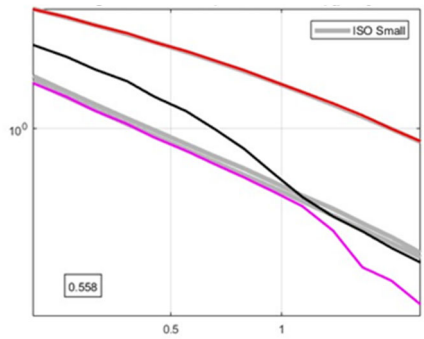

(4) SV_WE_IVS_dyn_180725_AM: IMLI

Figure 113. IVS Item 4: Small ISO. The behaviour of the secondary polarizabilities suggests that a small fast decaying target also present.

3. Advanced Processing techniques for data acquired at sites with magnetic soils

The task of UXO discrimination is more difficult when sensor data are collected at sites where an electromagnetically active host contributes a large background signal. In general, UXO dipole modeling assumes that the object of interest is in free-space. Any influence of the background medium is assumed to have been removed by pre-processing or filtering the data. However, the spatial variations of the background signal can be the same size as UXO anomalies. These signal variations can result from small scale topography (due to bumps or dips in the surface), changes in the orientation and height of the sensor relative to the ground, and spatial variations in the electromagnetic properties of the soil (i.e., conductivity and magnetic susceptibility). A high pass filter to remove the geologic signal is often unable to remove smaller scale spatial variations. In addition, this filtering step often introduces artifacts that can bias estimates of the target parameters.

In SERDP MR-1573 we developed methods for processing EMI data collected at sites with a substantial magnetic geology background response due to the presence of viscous remnant magnetic soils. The first approach considered in SERDP MR-1537 modeled the background response and target parameters simultaneously. Variations in the signal due to sensor position variations over the soil could be modeled, thereby reducing the bias on dipole polarizability estimates. In SERDP MR-1537 we developed soil modeling methods for a several advanced sensors (e.g., MPV, TEMTADS, BUD).

In this project, we study several techniques for mitigating the effects of magnetic soil.

- To determine if a data anomaly is due to soil or a compact metallic object, we compare soundings do a soil model. This is equivalent to solving for a best fit soil model. We studied this approach using mono-static data (e.g., Geonics EM63) in SERDP MR-1573. We revisit this approach due to the availability of multi-static data. With this data we no longer only determine the fit to the characteristic VRM decay – the multi-static data allows us compare if the relative amplitudes of the multiple Tx/Rx combinations are consistent with magnetic soil responses.
- We model the response of the background soil with the additional dipole sources. We first considered this approach in SERDP MR-1573, and in this project we constrain the dipole sources representing the background response. The introduction of constraints stabilizes the inverse problem and improves estimates of target parameters.
- We reduce the effect of magnetic soil on estimated target parameters by transforming data to reduce the amount of magnetic soil coupling, i.e., solve for data components that are less sensitive to the magnetic soil response. In this approach, the magnetic soil response is not modelled and the background soil properties are not estimated. This results in a simpler inverse problem.

Simplified Modeling of the background response: Processing of MetalMapper Data at the Former Waikoloa Maneuver Area

Advanced EMI data were collected on the Former Waikoloa Maneuver Area at three sites: Task Order (TO) 17, TO20 Area A and TO20 Area B. The significant background soil response at Waikoloa presented additional challenges for target picking and classification. The magnetic geology produces a large amplitude background instrument response that varies spatially across the site. The spatially varying geology and ground clearance variations due to cart movement can produce data anomalies that exceed the target picking threshold. In addition to difficulties with target picking, the background soil response can bias estimated target parameters when inverting data. Therefore, special care is required when removing or accounting for the magnetic soil background response.

There were two main objectives: (1) avoid unnecessary digs due to spurious anomaly picks due to magnetic geology and (2) determine if it is possible to accurately estimate dipole source parameters for targets buried in the highly magnetic geology of Waikoloa. The standard survey approach is to collect background measurements at locations close to an anomaly, and then to subtract the background measurement from the anomaly data. This "background corrected" data can then be inverted using the simplified model of a target in free-space. Unfortunately, there were an insufficient number of background soundings to reliably background correct the data. In addition, the spatial variability of the background geology, strength of the magnetic field, and the effect of inconsistent ground clearance height between anomaly data collection and background measurements can produce inaccurate estimates of the background response. We adopted an approach where the background response was estimated as part of a constrained inversion process. More specifically, a deep dipole source was used to model the effect of magnetic soil.

Determining if a target is a soil anomaly

Electromagnetic induction instruments are sensitive to ferri-magnetic minerals such as magnetite. When these minerals are exposed to a magnetic field, there is a non-instantaneous change in magnetization. Pulse induction instruments such as the MetalMapper, TEMTADS and MPV measure the secondary field in the off time produced by the magnetic grains as the aligned magnetization relaxes to a more random state. The secondary field amplitude is a function of the concentration of ferri-magnetic minerals in the soil, the distribution of time constants characterizing the relaxation times, and the geometry between the transmitters, receivers, and ground.

In order to identify cases where the MetalMapper measured data over a magnetic geology anomaly instead of a metallic target, we compare the MetalMapper data with a soil model. Background measurements were used to determine the MetalMapper's characteristic magnetic soil response. Figure 114 plots the background response for five of the background measurements. Receiver Rx0 was not working properly during these measurements. The measurements were corrected using in-air measurements. When the MetalMapper is parallel to flat ground, we would expect that the coaxial component of the secondary response measured by the center receiver (Rx3) would be at a maximum. Conversely, the transverse components would be null-coupled. For example, the X and Y-component

receivers should measure only noise when the Z-component transmitter is firing. When the instrument is not parallel to the ground surface, there will be some signal in these transmit/receive pairs.

The first step to building a soil model was to use the decays measured by the MetalMapper to determine how the MetalMapper transmitter waveform modified the characteristic 1/t decay of the magnetic soil. The decay characteristic is independent of the ground clearance height and orientation of the sensor relative to the soil surface. The consistent decay character for the different Tx/Rx combinations can be seen in Figure 114. The decay character is well modeled by the function:

$$f(t) = \frac{1}{t} - \frac{1}{t + \Delta t}$$

This function is the characteristic 1/t VRM response convolved with a finite pulse transmitter waveform.

If we assume that the ground clearance height and sensor orientation is approximately constant over the course of the survey, then the relative strength of the magnetic soil response between each Tx/Rx combination can be assumed to be constant during the survey. The background measurements suggested that the variations in the relative amplitude of soil responses between each Tx/Rx combination were not significant. Therefore, it is reasonable to construct a soil model consisting of the decay character f(t) which multiplies an amplitude for each Tx/Rx combination. This result simplifies the soil fitting analysis. Instead of requiring potentially inaccurate estimates of ground clearance height and sensor orientation to model the background response, we can simply estimate a single scaling parameter that multiplies our soil model. If the ground clearance and sensor orientation is constant during the survey, the value of the single scaling parameter provides a measure of the soil magnetic susceptibility.

For each MetalMapper measurement, the soil model is fit to the measured data. The misfit between the best fit soil model and data reflects the likelihood that the measurement was acquired in the presence of a metallic target. Figure 115 has an example of soil model fitting using data over Target 785 on the Western edge of the TO17 area. The absolute value of the observed data is plotted as blue circles, with a solid blue circle indicating positive data and unfilled (i.e., white) circles with a blue outline indicating negative data. A black dashed line indicates the best fit soil model. There is a very good match between the observed data and the soil model. For the null-coupled Tx/Rx combinations, the soil model predicts some signal. This is consistent with analysis of the background data files and suggests that the MetalMapper was consistently slightly tilted when acquiring the cued data. When reviewing inversion results, the analyst is provided a soil misfit to assist in determining if the data anomaly is due to soil.

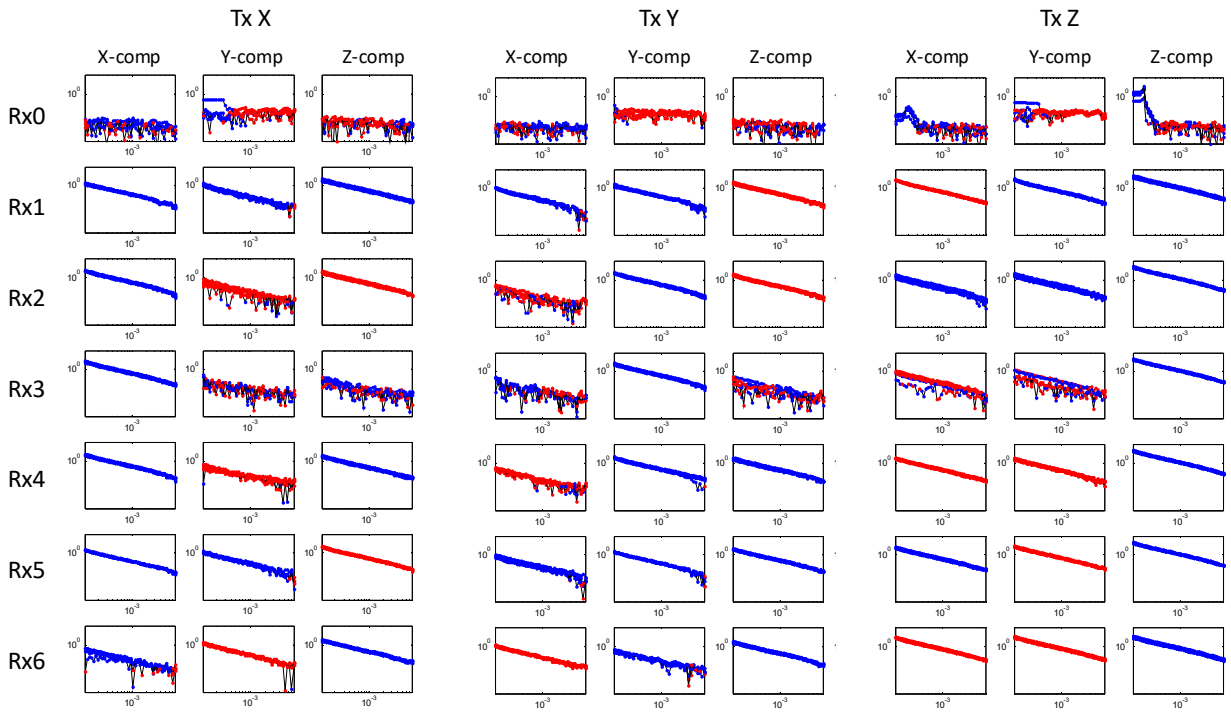

Figure 114. Example of background measurements corrected with air. Blue lines are for positive responses, and red lines represent negative responses. Receiver Rx0 was not working properly during these measurements.

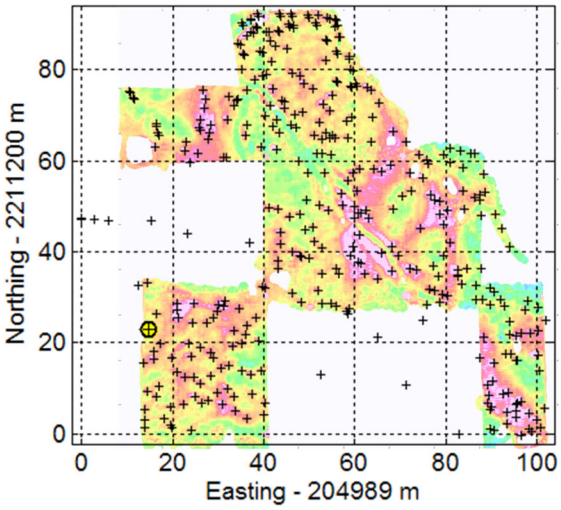

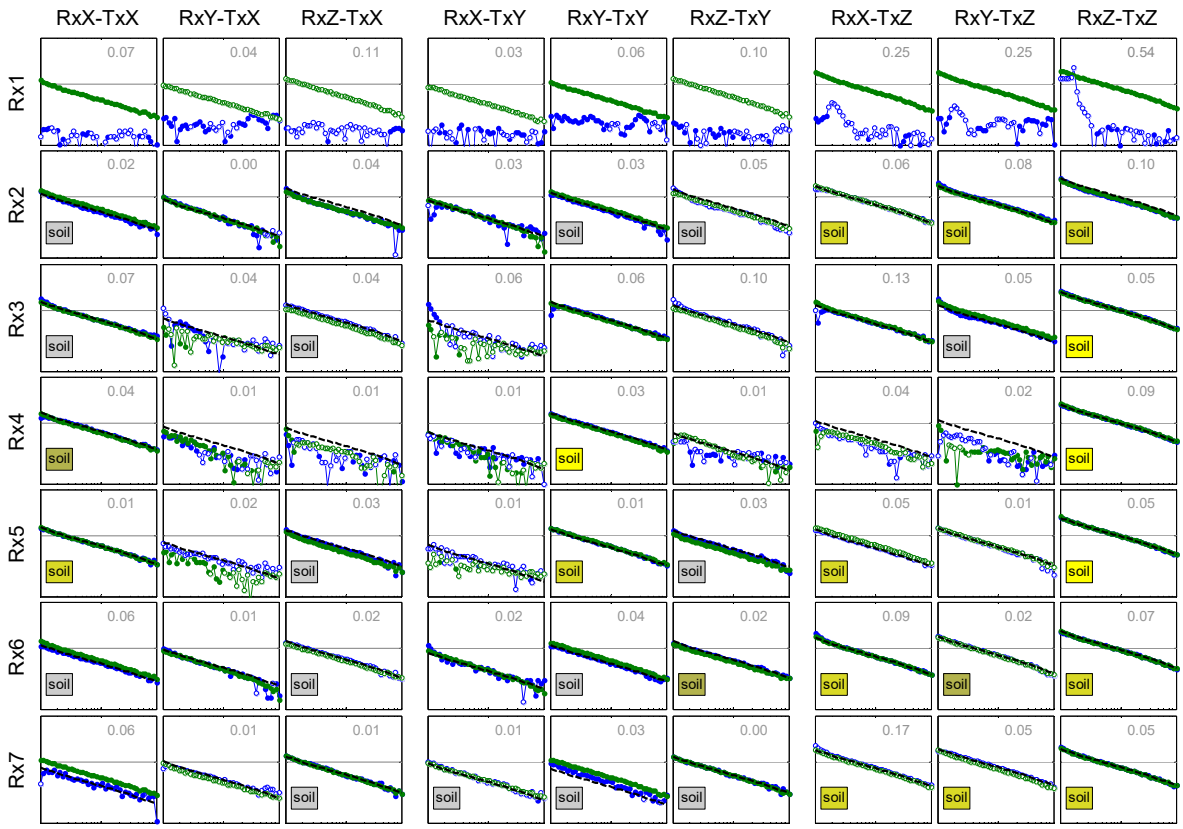

- **Blue**: Observed data
- **Green**: Data fit using a deep source
- **Black** dashed line: best fit soil model

Figure 115. TO17 Target 785. Soil anomaly.

Inversion of MetalMapper data at Waikoloa

The standard procedure when collecting cued EMI data is to take background measurements. These background measurements are then subtracted from data acquired over targets. These "background corrected" data can be modeled as a dipole in free-space. This approach requires a background measurement acquired close enough to each anomaly such that there is an accurate estimate of the background signal for each anomaly. At sites with large magnetic soil response, this approach can have limited success. This is because small changes in ground clearance and changes in orientation of the MetalMapper can result in a significant change in amplitude of the soil response. A change in ground clearance of only a few centimeters can result in a change of background response of several tens of percent. Overestimating or underestimating the background response will reduce the accuracy with which the dipole polarizabilities are estimated.

An alternative to subtracting a background measurement prior to the inverting the data is to solve for the soil response as part of the data inversion. Several modeling-based approaches were considered in SERDP 1573. It was noted in SERDP 1573 that, for cued MetalMapper data, the magnetic soil response could be modeled well with a deep dipole source. For the Waikoloa cued MetalMapper data, we developed a multi-dipole source inversion, where the location of a deep source is fixed beneath the center of the array. This single deep source will model the background response due to soil, and the remaining sources will model any buried metallic targets.

Figure 115 contains a typical result when fitting cued MetalMapper data taken over a soil anomaly with a dipole source. Three lines are shown on each plot: observed data are plotted in blue, the best fit soil model is plotted in black, and the predicted data when using a single source inversion is plotted in green. The observed data is fit well with both the best fit soil model and the single deep source. The recovered dipole polarizabilities and relative depths when inverting for 1, 2, and 3 sources are shown in Figure 116. The single source inversion shows that the soil can be fit with a plate-like target oriented with the normal of the plate parallel to the horizontal direction. Solving for two dipole sources results in a deep plate-like target, and a shallow small amplitude target that fits noise. Three sources add a second small amplitude target at the surface. To represent the soil response, we choose to use the simpler model of a single deep source. Analysis of background measurements corrected with an in-air sounding were used to determine that a source depth of 95 cm would model the soil response well. Figure 117 shows that there is a second local minimum in the fitting problem where the soil is fit well with two sources: one source at 40 cm and a second source at approximately 95 cm.

IVS data were used to test the deep-source soil modeling methodology. The IVS contains 3 targets. Targets 1 and 3 are the same 37 mm. Targets 1 and 2 are horizontal and buried such that the geometric center of the target is at a depth of 10 cm. Target 3 is vertical, with the geometric center of the target being at 12 cm. The IVS data were inverted using in-air measurements for background correction, and the data were fit using (a) single source inversions, (b) two source inversions in which the location of both sources were unconstrained, and (c) two source inversions in which the location of one of the sources was constrained to be deep and centered on the MetalMapper instrument. Figure 116compares the recovered polarizabilities from the three types of inversions. When inverting for a single source, the amplitudes of the polarizabilities are overestimated since the source is trying to fit

both the 37 mm projectile and the soil response simultaneously. Inverting for a pair of sources improves the amplitude of the polarizability estimates. Inverting for a pair of sources, with one source fixed deep to represent the background soil response produces similar results to the unconstrained two source response for IVS target 1 and IVS target 2, with only marginal improvements in the spread of recovered polarizabilities. There is a more pronounced improvement when fitting IVS Target 3, with a larger spread in recovered polarizabilities when inverting for two unconstrained sources. Fitting IVS target 3 with a deep source improves the accuracy of the recovered polarizabilities.

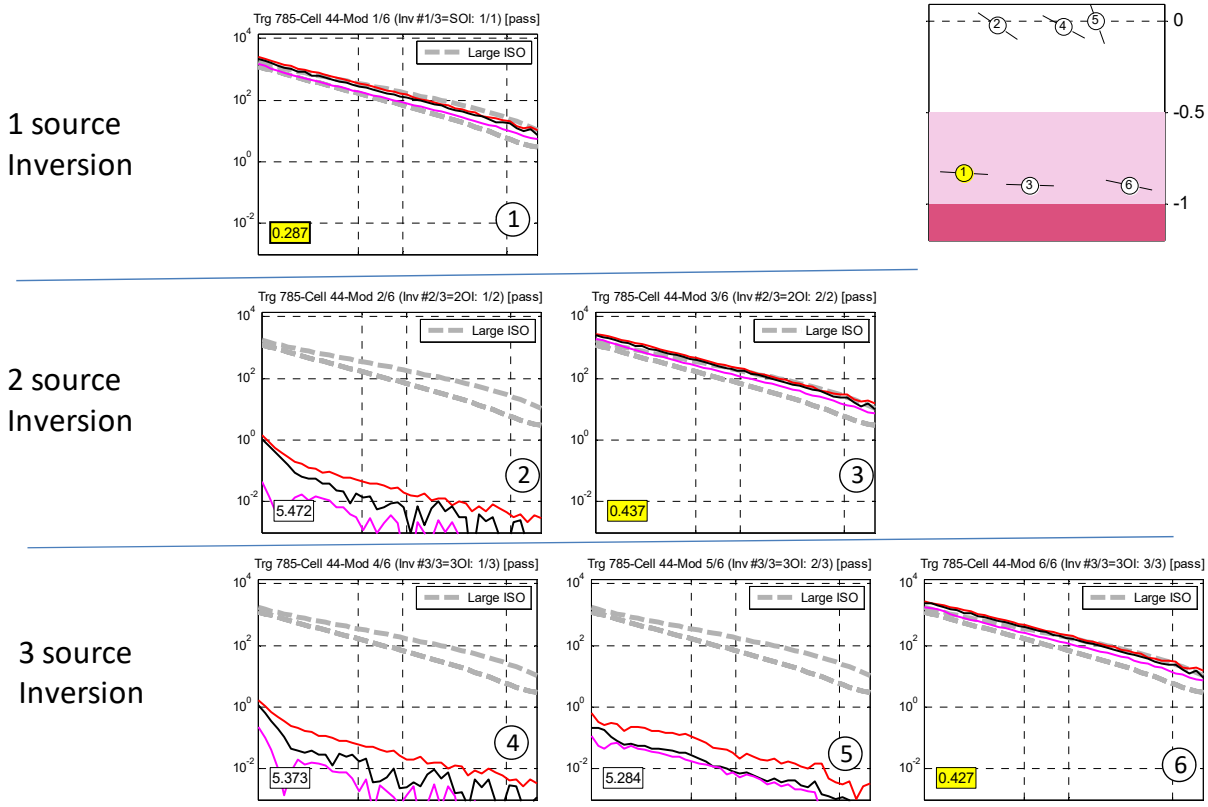

Figure 116. TO17 Target 785. Soil data can be fit well with a large, deep, plate-like target centered on the MetalMapper instrument.

Figure 119 compares the size vs. decay feature plot for the IVS inversions. Figure 119(a) shows that, when inverting the data with only a single source inversion, there is a bias in the recovered feature clusters since the polarizability size is overestimated and the estimated decay rate slower than expected due to the dipole source trying to fit both the target response and soil. When inverting the data with two unconstrained sources, the second source models the response of the ground, and the bias seen in (a) is removed (Figure 119(b)). The size and decay features associated with the source that models the soil is outlined with a black dashed line. Figure 119(c) shows that the feature clusters are better constrained for the IVS targets when the second source is constrained to be deep and centered at the center of the anomaly. In addition, using the constrained inversion results in the size and decay characteristics of the soil sources being constrained better than in (b).

We processed the Waikoloa MetalMapper cued data using both the soil modeling method described above, and also using the standard background correction method using available background measurements. One, two, and three source inversions for the two background correction methods resulted in 12 models for each anomaly. From these set of models, the coordinates of any models characteristic of a compact metallic target was recorded as a potential location for a dig team to visit.

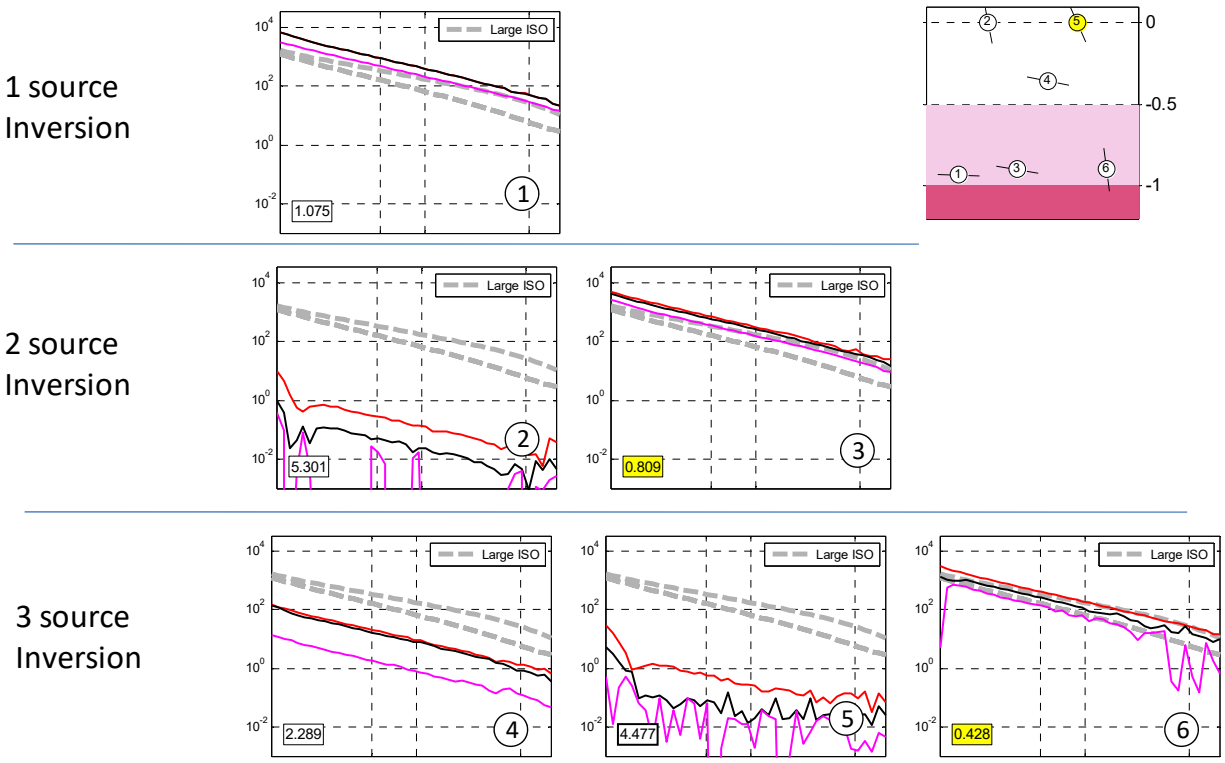

Figure 117. TO17 Target 859. Soil data can be fit well with a large deep, plate-like target centered on the MetalMapper instrument. There is a second local minimum in the solution where the soil is fit well with two sources: one source at 40 cm and a second source at approximately 95 cm.

(a) IVS Target 1. Horizontal 37 mm, geometric center of target located at a depth of 10 cm.

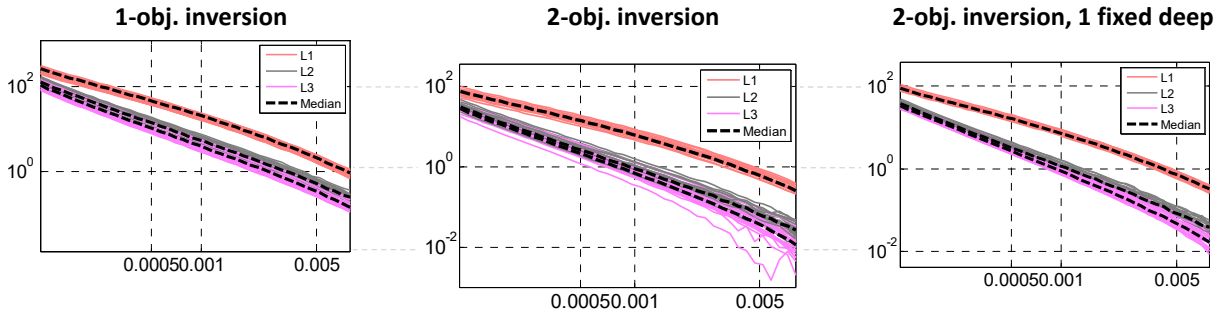

(b) IVS Target 2. Horizontal 37 mm, geometric center of target located at a depth of 10 cm.

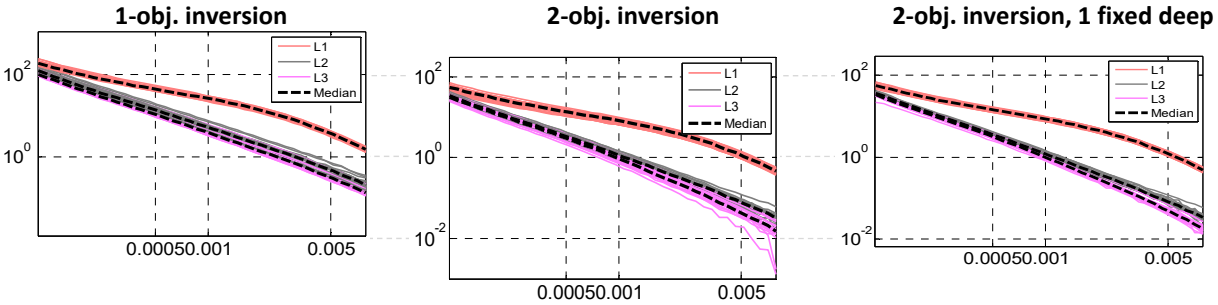

(c) IVS Target 3. Vertical 37 mm, geometric center of target located at a depth of 12 cm. Same type of 37 mm as IVS Target 1.

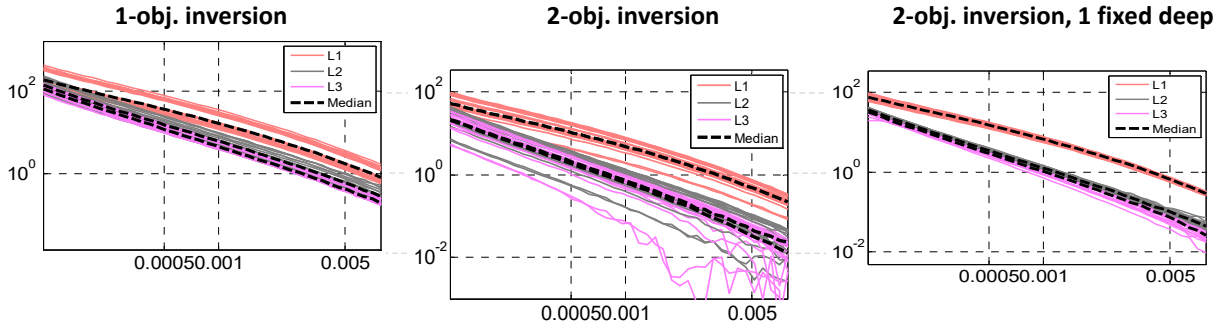

Figure 118. Recovered polarizabilities when inverting IVS measurements. The IVS data were inverted using in-air measurements for background correction, and the data were fit using (a) single source inversions, (b) two source inversions in which the location of both sources were unconstrained, and (c) two source inversions in which the location of one of the sources was constrained to be deep and centered on the MetalMapper instrument.

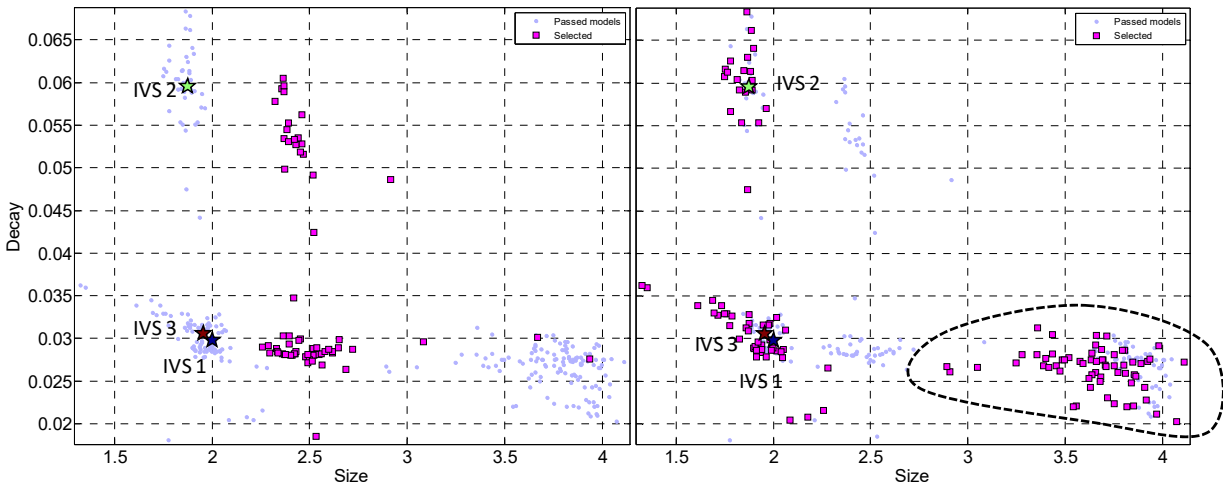

(a) Single source inversions.

(b) Two source inversion (unconstrained)

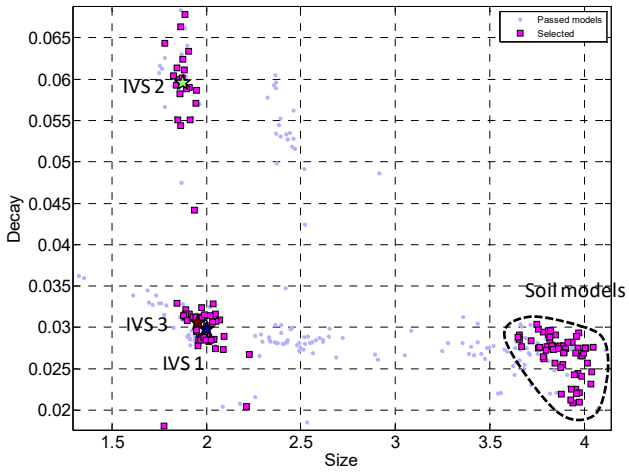

(c) Two source inversion - One source fixed deep.

Figure 119. Size/Decay parameter plot for IVS data.

Target picking methods that compare to a soil model:

In this section, we test a method for reducing the effect of magnetic soils on estimated target parameters by transforming data to reduce the amount of magnetic soil coupling. By working with this transformed data, estimated target parameters will be less affected by the presence of magnetic soil. These data transformations exploit the spatial symmetry and shape of the magnetic soil response (for example, Figure 125). Unlike the simultaneous inversion methods developed in SERDP MR-1573, these new techniques do not require modeling the background response (either by estimating the magnetic susceptibility of the background soil or solving for dipole sources to produce the soil response).

Processing dynamic MPV data from Waikoloa:

In addition to MetalMapper Classic (i.e., 3 orthogonal transmitters and 7 receivers) and Geonics EM61 data, MPV data were also collected at Former Waikoloa Maneuver Area. Both dynamic full coverage data, and cued data were collected at the site. In this section, we will focus on data collected on grid Task Order 20A (TO20A) (Figure 120(d)).

(a) Dynamic MPV data collection

(b) Cued data collection

(c) Iron Oxide rich soil

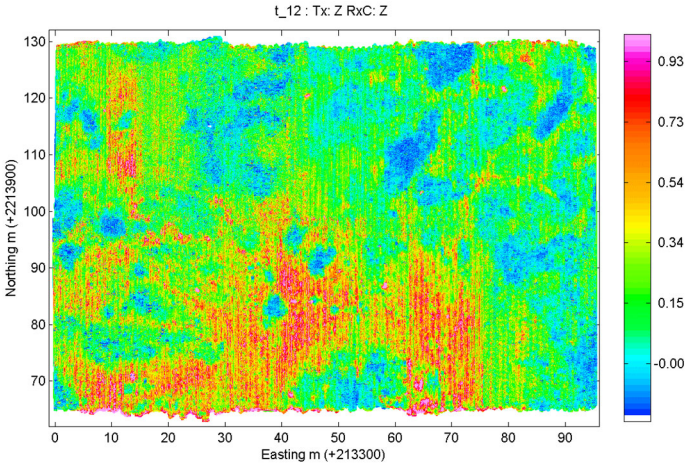

(d) Example of Mono-static z-component data. Data from TO20A.

Figure 120. MPV data collection at Waikoloa.

As we noted in the previous section, the geologic signal at Waikoloa is significant and varies in magnitude across grid TO20A. The larger length scale variations are due to changes in the level of viscous remnant magnetization in the host geology. Some of the small spatial scale variations in the signal can be attributed to variations in instrument height and orientation above the ground. The blue regions in Figure 121(d) are low amplitude areas corresponding to surveying on rocky outcrops. The topography related to outcropping rock, forces the MPV to be raised higher above the ground surface to avoid rocks. Figure 121(c) shows how the amplitude of the geologic signal decreases as the local elevation of the sensor head increases. In addition, there is also less soil on the outcrops. Magnetic soil that originates from weathering of magnetite rich host rock will generally have a higher viscous remnant susceptibility than the rock (see SERDP 1573 for additional details on complex magnetic susceptibility).

(a) Example of surveying over an outcrop

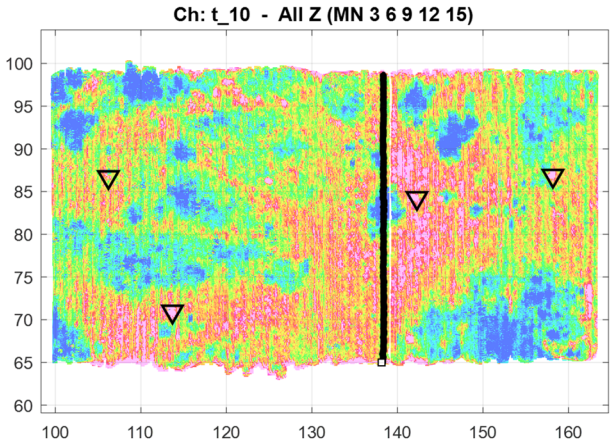

(b) location of transect for data shown below

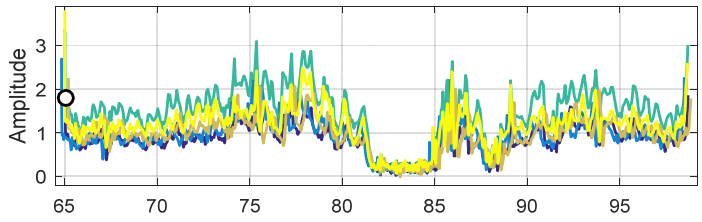

(c) Time channel 10, t=1.14ms, vertical component data

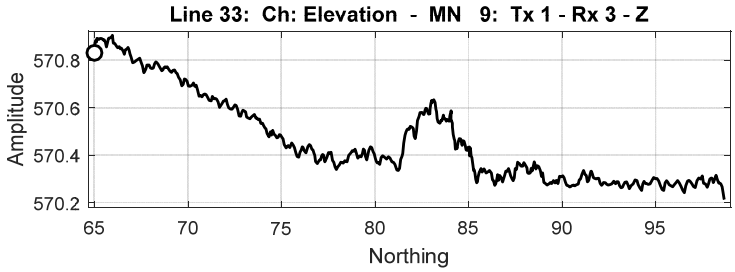

(d) Elevation in meters

Figure 121. Example of surveying an outcrop at Waikoloa. In the upper left, photo of acquiring data over an outcrop. Upper right: location of a survey line directly over an outcrop, though not the outcrop in the photo. Below: plots of the data and the elevation.

At the beginning and end of each survey day, dynamic data were acquired over an Instrument Verification Strip (IVS). The IVS contained 5 emplaced targets: a sphere, medium ISO, Large ISO, and a pair of small ISOs buried at 10 and 30 cm. Figure 122(a) plots a profile of data acquired on a line directly over the 5 targets. The vertical component of the coaxial receiver (i.e., the center receiver) data, recorded in time channel 10 (t=1.14 ms) is plotted. The sphere produces a weak anomaly (labelled A). The next 3 targets (i.e., B-D) produce a distinct data peak in the data profile. The small ISO buried at 30 cm (i.e., target location E) does not appear to produce a significant anomaly when looking at the coaxial, vertical component data. Traditional target picking methods using coaxial, vertical data amplitude would be unable to reliably detect the small ISO.

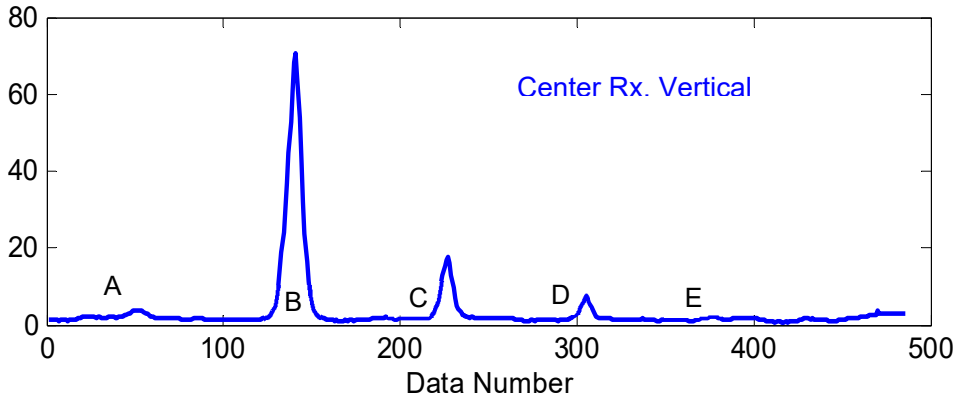

(a) profile view of dynamic data acquired on a line over the targets. Time channel 10 (t=1.14 ms) is plotted.

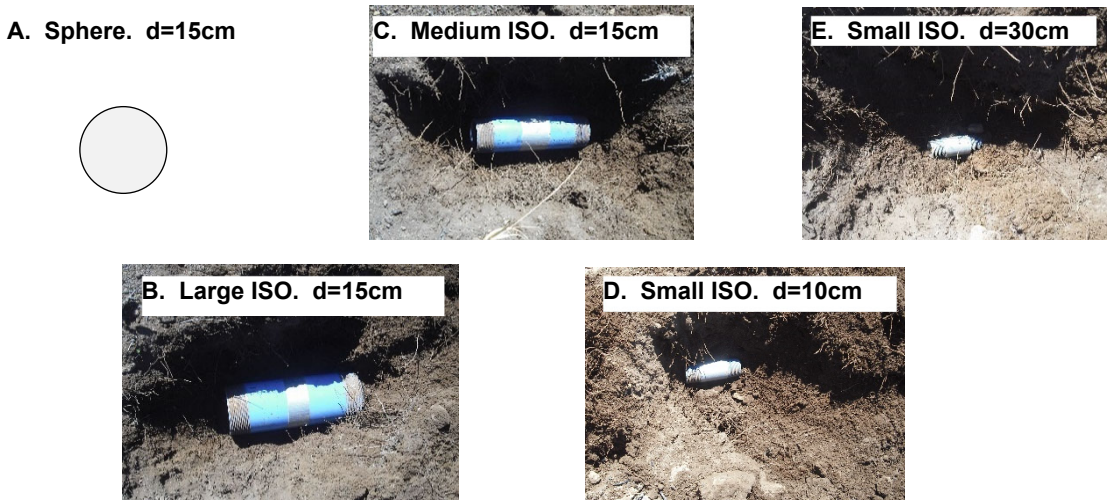

(b) Targets emplaced in the IVS

Figure 122. Profile of coaxial, vertical component data acquired on the Waikoloa IVS. Time channel 1 is plotted. The small ISO buried at a depth of 30 cm does not produce a significant anomaly. The emplaced targets are shown in (b). No photo of the sphere is available.

Figure 123 focuses in on the section of data collected over the small ISO buried at 30 cm. In the top plot, the locations of the small ISOs are indicated by red arrows. In the bottom plot, we compare the MPV coaxial, z-component data with the elevation. Since data amplitude increases as ground clearance decreases, we plot the negative of the data in the first time channel (t=0.21 ms) to better illustrate the correlation. Since the IVS strip is located on a relatively flat area, we can estimate the ground clearance height of the sensor head from the elevation (green line). At the end of line, the sensor was placed on the ground, therefore we can infer that the height of the sensor head during this line is between 5 and 15 cm above the ground. It is clear that there is a correlation between the measured signal and the ground clearance.

In addition, the data anomalies introduced by sensor height variations could, potentially, have similar amplitude to TOI. Through forward modeling of library polarizabilities, we can determine that a small ISO at a depth of 30 cm would have an expected amplitude in the first time (t=0.21 ms) channel of approximately 6 mV/amp (note: and 0.38 mV in the 10th time channel, t=1.14ms). For the magnetic susceptibility levels at the IVS strip, the anomalies due to height variations are approximately 5 mV/amp. It is for this reason that coaxial, monostatic instruments such as the Geonics EM61 have limited detection ability at sites with high levels of viscous remnant magnetization. Modern EMI instruments for UXO detection are multi-static and multi-time channel. These data facilitate the development of processing algorithms that use our understanding of the shape of the secondary field and characteristic time decay of magnetic soils.

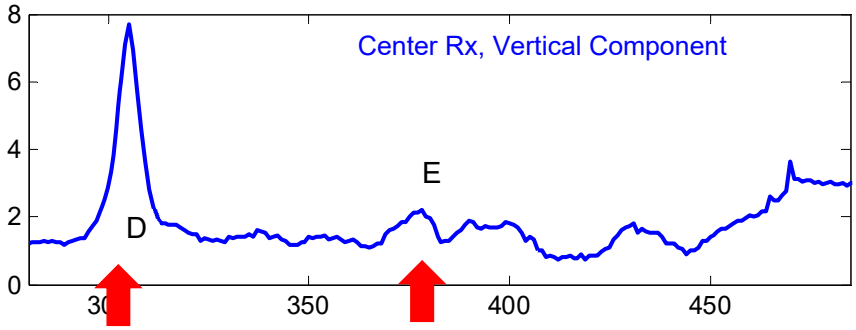

(a) Plot of coaxial, z-component data. Time channel 10 (t=1.14ms) is plotted here.

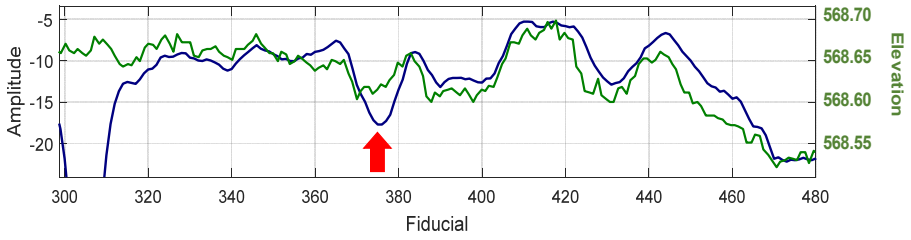

(b) Comparison of elevation and MPV. The negative of the first time channel of coaxial, z-component MPV data is plotted here.

Figure 123. Examining the correlation between the response and ground clearance height. Variations in the instrument height lead to data anomalies of approximately the same size as a small ISO at a depth of 30 cm.

Figure 124 and Figure 125 plots profiles of the different components of the geology response at t=1.14 ms. Figure 124(a) and (b) plot components that are sensitive to the response of soil. The components that are sensitive to the soil response are indicated in Figure 125(b). The top plot shows the response over the entire length of the IVS. A close up of the data acquired on the small ISOs (dashed grey line in the top plot) are shown in the bottom plot. Although the plots appear to have an anomaly at the location of the small ISO buried at a depth of 30m, a portion of the anomaly amplitude can be attributed to the sensor head being closer to the ground surface (see Figure 123(b)). We also note that the sphere also does not have a significant response.

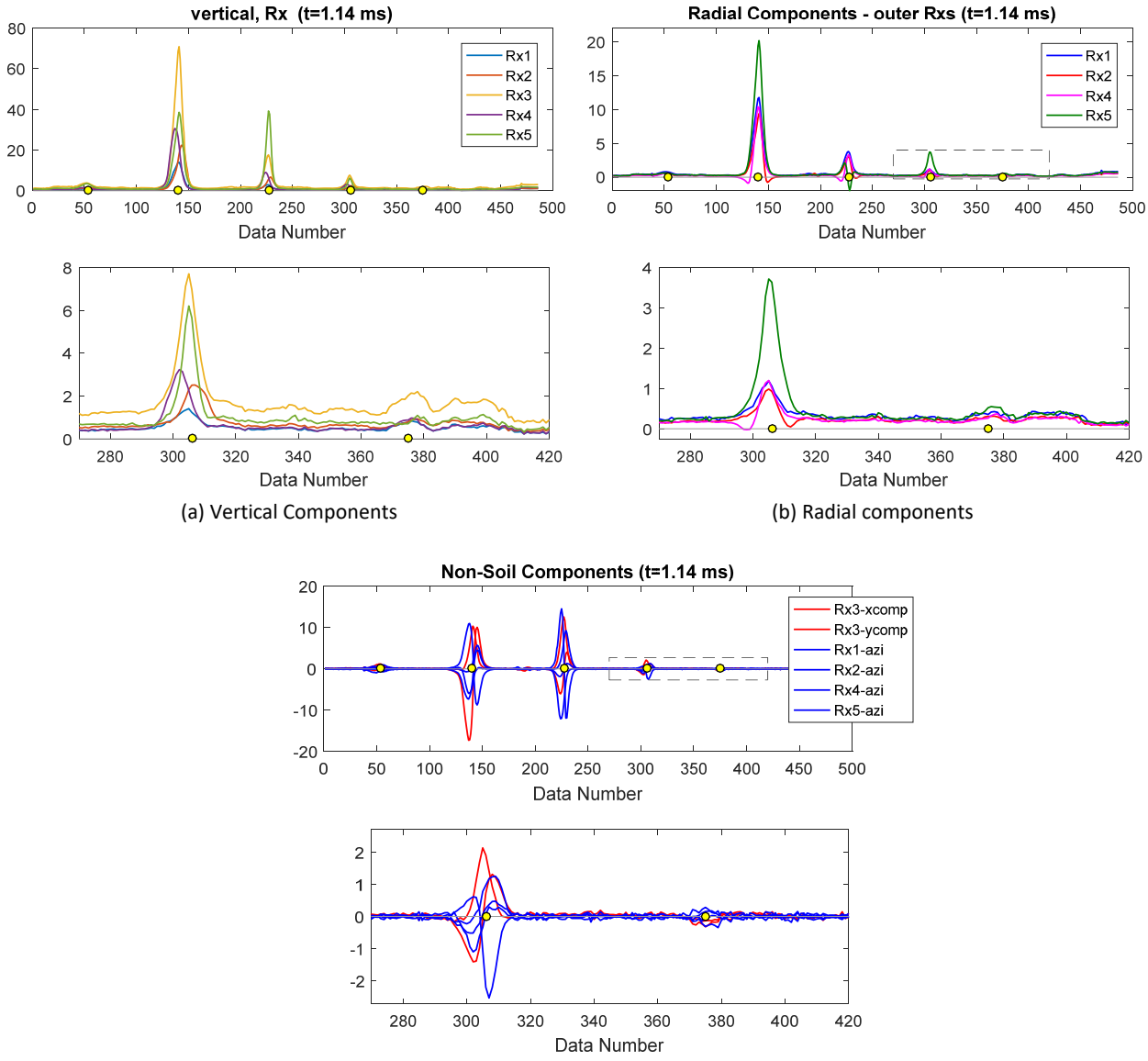

(a) Vertical Components

(b) Radial components

(c) Non-soil Tx/Rx combinations.

Figure 124. Comparing different components of the MPV IVS data. For a horizontal transmitter loop with receivers inside the loop, the soil noise is greatest in the vertical component and also the radial component of receivers not in the center of the transmitter loop. Non-soil components include horizontal components at the center of the loop, and azimuth components in the outer loops.

Figure 124(c) plots receiver components that are not coupled to the soil. These components are in directions that are orthogonal to the secondary field. The color of the plotted lines corresponds to the red and blue arrows in see Figure 125(a). Due to symmetry, the field at the center receiver (i.e., Rx3) is in the vertical direction, and the x and y components of the field are insensitive to the soil (red arrows in see Figure 125(a)). The azimuth components of the field at the outer receivers (i.e., Rx1, 2, 4 and 5, blue arrows in see Figure 123(a)) are also insensitive to the soil. When looking at a closeup of the data, we see that there is no significant soil response and that the only response corresponds to locations of the seeded items (Figure 124(c)). We see that there is a small anomaly in the non-soil components at the location of the small ISO at a depth of 30 cm. This suggests that the multi-static, multi-component data could, potentially, be utilized to improve detection.

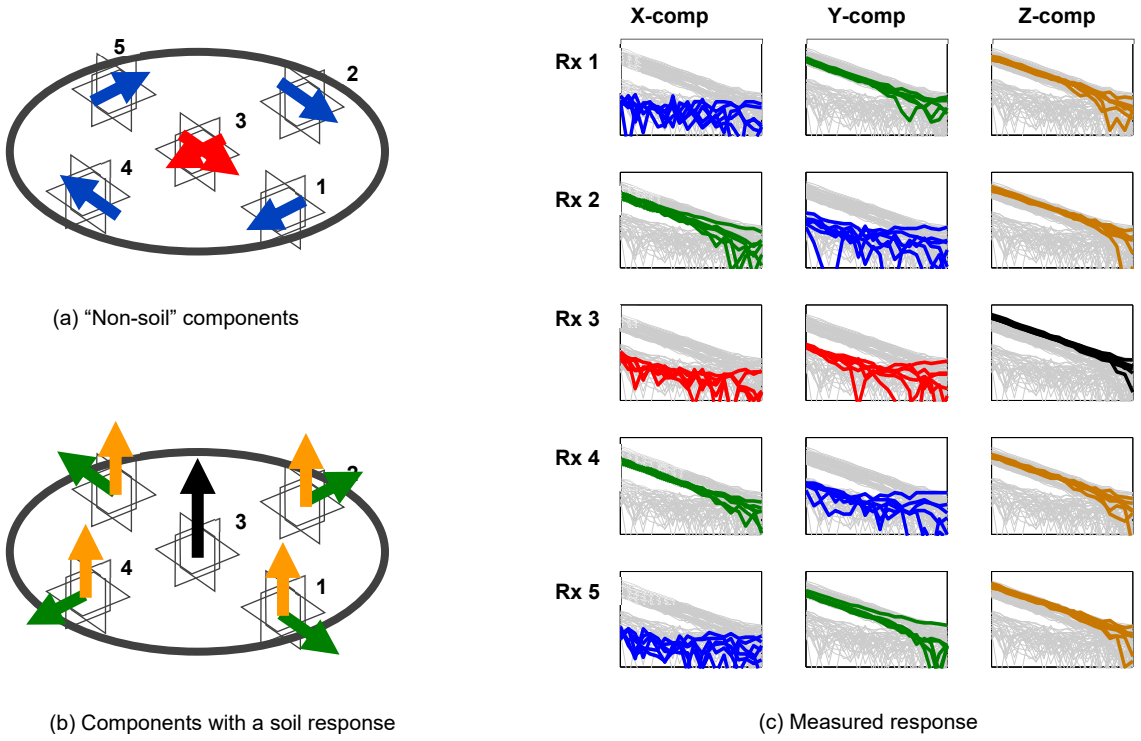

Figure 125. Soil response for the MPV. Data acquired over a target-free transect at Waikoloa.

Due to the geometry of the MPV transmitters and receivers – i.e., 4 receiver cubes in the same horizontal plane and equidistant from the center of the transmitter – there will be receiver components that measure the amplitude due to the symmetry of the magnetic soil response. Figure 125 shows the symmetry of the magnetic soil field response. This symmetry can be observed in two sets of measurements: (1) vertical components measured in the outer receivers (yellow arrows) and (2) the radial components (green arrows). If a horizontal transmitter loop (i.e., the z-component transmitter) is parallel to a flat surface, and the magnetic properties is laterally uniform in the view of the instrument, then amplitude of the vertical components should be the same, and the amplitude of the radial components should also be the same. Figure 125(c) shows the decays for the vertical components

are approximately the same, and the amplitude of the radial components are approximately the same. All the soil decays follow the characteristic. The decays follow the characteristic power-law decay.

Calculating linear combinations that exploit secondary field shape for improved detection

The conventional approach to removing soil response from data is to apply a detrend or de-median filter. Earlier, we presented an example of how the soil response can produce anomalies of the same amplitude of targets. In these instances, a spatial filtering approach might be ineffective. Our objective is to investigate the use of combinations or components of the data that are less sensitive to the magnetic geology.

In Figure 125 we noted that 6 of the 15 MPV measurements are insensitive to the magnetic soil signal when the MPV sensor head is parallel to the ground. These components are insensitive to soil noise because they are orthogonal to the magnetic field from the soil. At each receiver, we define a pair of vectors that are orthogonal to the direction of the secondary. In this work, we determine the direction of the field by using MPV data acquired in an area without metallic targets. However, if accurate ground clearance and MPV orientation data were available, the direction of the secondary field can be calculated numerically.

Figure 126 plots the direction of the soil secondary field in red, when the vertical component transmitter fires (left) and when the Y-component transmitter fires (right). The direction of the field was determined through MPV measurements in an area without targets. Once the direction of the background soil response is obtained, it is straightforward to define a pair of orthogonal vectors that is perpendicular to that direction (blue arrows).

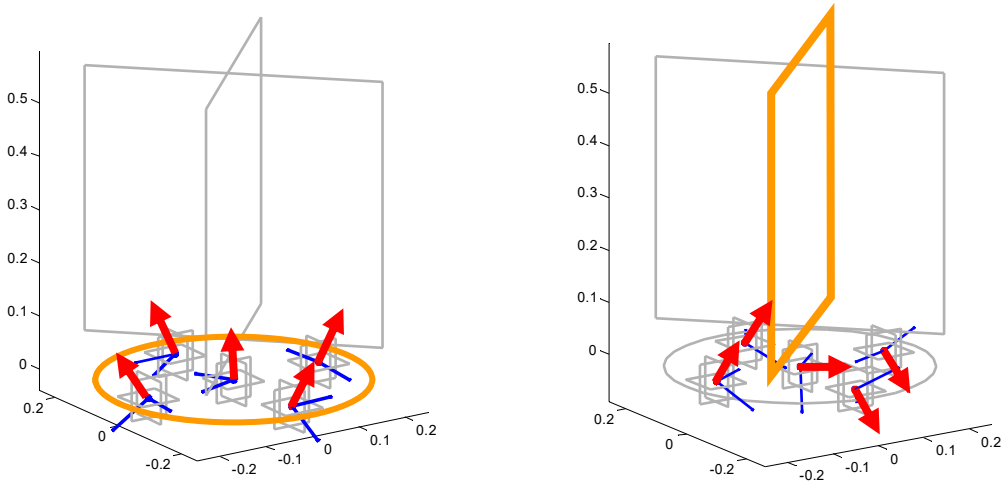

(a) z-component transmitter (b) horizontal component transmitter

Figure 126. Direction of secondary field and orthogonal directions used to define the $P^{nonsoil}$ matrix.

To calculate a new data, we define an operator P that calculates linear combinations of the data. Ideally, the operator P

$$\tilde{d} = Pd^{raw} = Pd^{target} + Pd^{geology}$$

where the ideal operator P is defined such that the geology response is in the null-space of the operator, i.e., $Pd^{geology}=0$. The amount that the soil response can be "nulled" in the projected data depends on the accuracy with which the direction of the field can be calculated. This error increases in regions of high viscous remnant magnetization.

The data matrix d^{raw} is a *15 x Ntimes* matrix (where *Ntimes* = number of time channels) that contains, along rows, the decays of the 3 receiver components of each of the 5 receiver cubes. The matrix $P^{nonsoil}$ is a *10 x 15* matrix with rows containing vectors orthogonal to the secondary field. The matrix is constructed such that it takes the transforms the data matrix to a new *10 x Ntimes* data matrix where the rows correspond to the response projected along the two non-soil directions at each receiver. To quantify the amplitude of the non-soil response, we simply take the vector sum of the projected field.

The projection matrix P can be used to form gradients between receiver components in the outer receivers. In this way, we are able to take advantage of the radial symmetry of the soil response. For these tests, we only take differences between 2 pairs of receivers: Rx1 and Rx5, and Rx2 and Rx4. Figure 128 compares the soil response in these pairs of receivers when the horizontal, z-component coil is fired. Rx1 and Rx5 are the leading and trailing receivers, respectively. Therefore, the azimuth direction is in the x-component. We see in Figure 128(a) that the y and z components are significantly larger than the x-component. The x-component is non-zero, which is likely due to the sensor head not being parallel to the ground. A similar behavior can be seen when comparing Rx2 and Rx4, i.e., the azimuth signal (this time in the y-component, since Rx2 and Rx4 is offset in the x-direction, in the sensor fixed coordinate system). The x and z component data are similar, with the difference between decays of the same component but different receiver being and order of magnitude less than the raw data.

Since we have 1 transmitter, 2 pairs of receivers, and 3 components, the matrix P^{diff} is 6 x $Ntimes$. Figure 127(b) plots the result of multiplying the data by P^{diff}, and taking the norm of the resulting gradient data. The profile of data shows that there is an anomaly at the location of the 30 cm deep small ISO. However, the anomaly is not as pronounced as when multiplying the raw data by $P^{nonsoil}$.

The P^{diff} and $P^{nonsoil}$ matrices can be combined in the following manner.

$$P^* = \begin{bmatrix} P^{diff} \\ P^{nonsoil} \end{bmatrix}$$

Figure 127(c) plots the profile when multiplying the data by P*.

In addition to calculating gradients, we calculate a symmetry measure that is the standard deviation of the vertical components of the outer receivers added to the standard deviation of the radial components of the outer receivers. Figure 129 plots the profile of this measure. This target picking measure was not able to detect the 30 cm deep, small ISO.

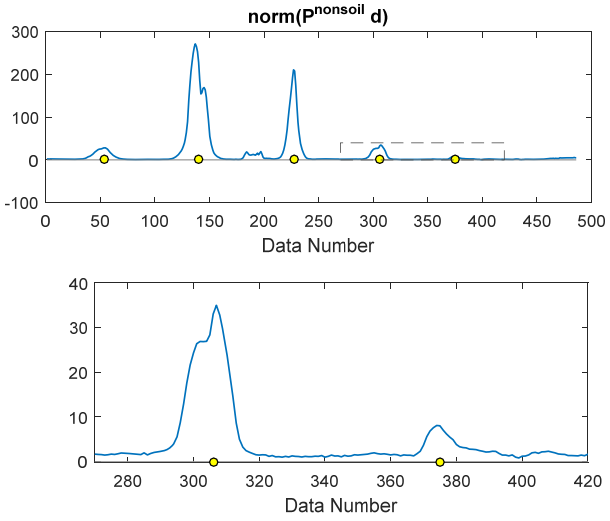

(a) Non-soil components

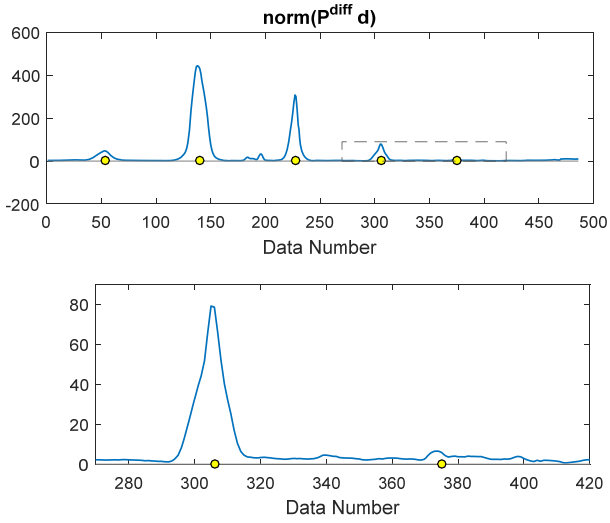

(b) A gradient, or difference matrix.

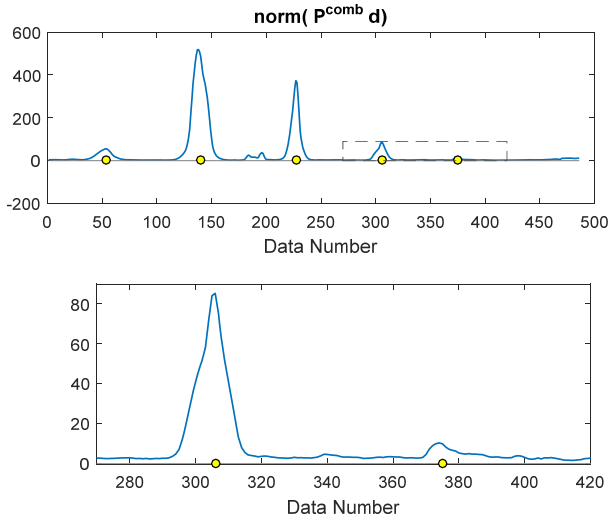

(c) Combining the Non-coil components and difference matrices.

Figure 127. A comprison of using different projection matrices. The data multiplied by $P^{nonsoil}$ produces the most distinct anomaly for the 30 cm deep small ISO.

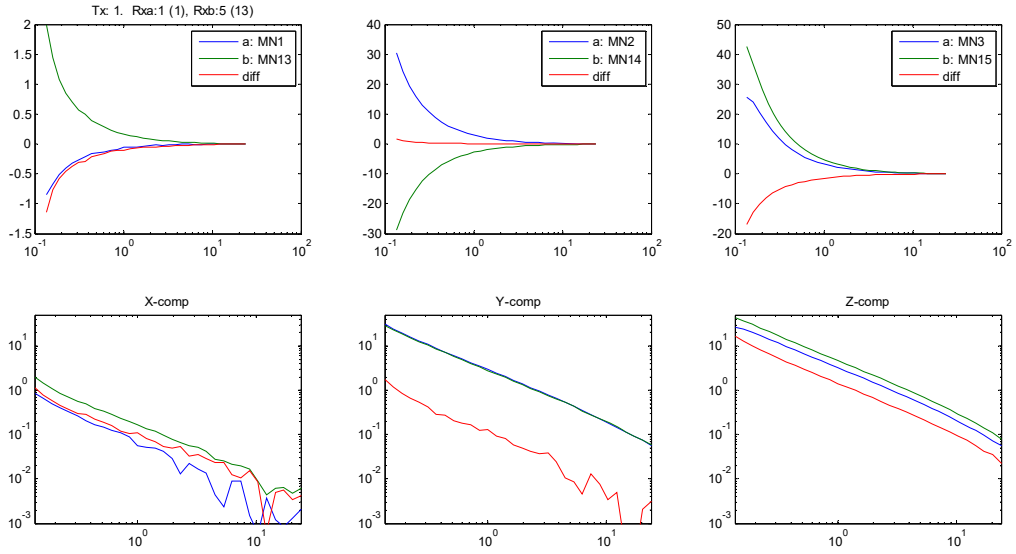

(a) Receivers 1 and 5

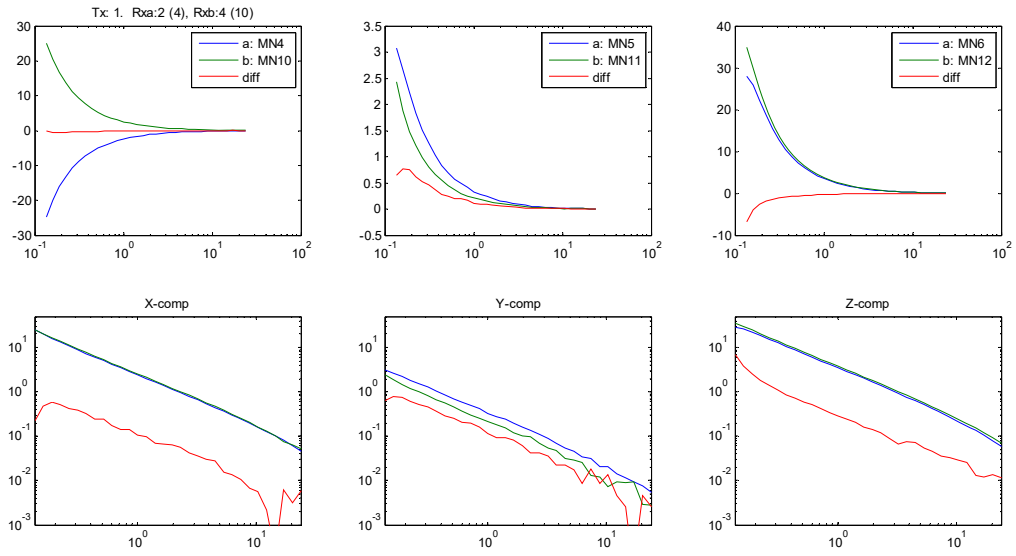

(b) Receivers 2 and 4

Figure 128. Comparing decays from pairs of outer receivers.

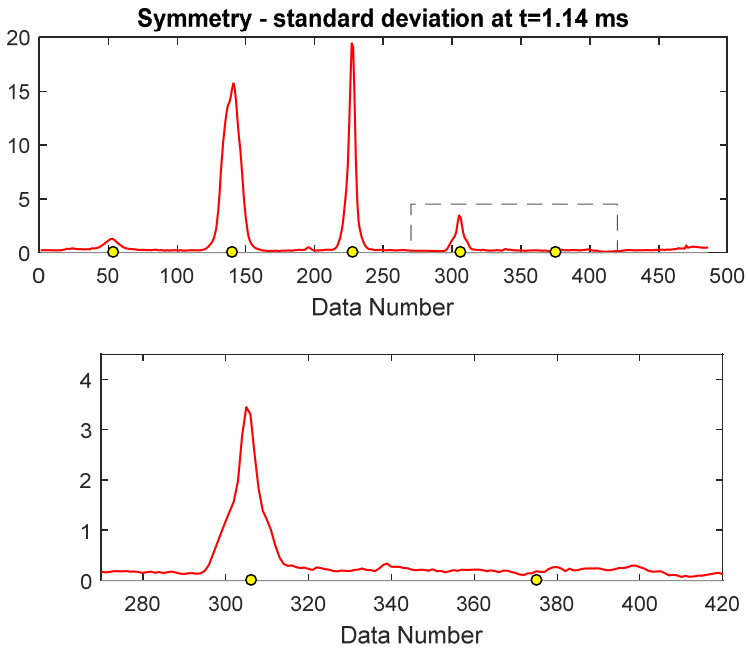

Figure 129. Calculating a symmetry measure for the MPV IVS data. The symmetry measure does a poor job in resolving the deeper small ISO.

Fitting a soil model

The soil response at each measurement location could be solved for explicitly if we know the orientation and ground clearance. Since we do not have the ability to accurately estimate ground clearance –and also for the sake of simplicity – we assume that the sensor height and orientation of the instrument is constant throughout the dynamic survey. By making this assumption, we can define the relative amplitude between the different Rx/Tx combinations will be equal throughout the dynamic survey. The absolute amplitude of the signal will only change as a function of the magnetic soil quadrature susceptibility (i.e., viscous remnant magnetization).

For the examples here, a soil model is constructed from MPV measurements. A region of data is selected that does not have metallic targets. Each of the 15 transmitter/receiver combinations are then fit with the decay function

$$f_i(t) = a_i\left(\frac{1}{t} - \frac{1}{t+\Delta t}\right)$$

where $f_i(t)$ is the decay of the i^{th} transmitter receiver combination (i.e., i=1..15). The characteristic $1/t$ power law decay is modified to account for the length of the finite pulse width.

For each transmitter firing, we fit the soil model to time channels 3 to 12. We note that this choice of time channels was arbitrarily chosen and should be optimized. For each set of 15 decays (i.e., 5 receivers with 3 components), we find the amplitude of the soil model that produces a minimum misfit to the response. To quantify the fit to a soil model, we calculate and store the L2-norm misfit between the observed and predicted data. Figure 130 plots the result of fitting a soil model. There is a distinct peak at the location of the deeper small ISO.

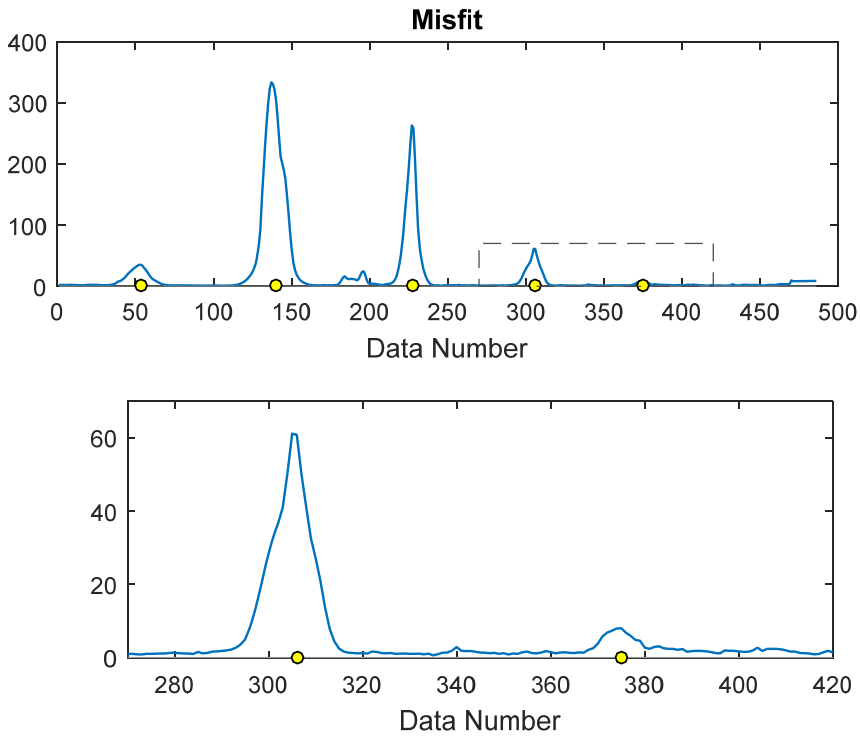

Figure 130. Calculating a soil misift for each transmitter firing. The soil misfit for each transmitter firing is mapped to the center receiver for plotting.

A comparison of the different detection measures is shown in Figure 131. The section of the data above the small ISOs are shown. The projection matrix transformed data and the soil misfit are easily able to detect the shallow small ISO (left dot). The deeper small ISO (right dot) is best detected using either the projected non-soil components or the soil misfit. The symmetry measure (i.e., standard deviation when comparing vertical or radial components of the outer MPV receivers) was unable to detect the deep ISO.

We again note that with all of these approaches we assumed that the sensor height and orientation is constant throughout the survey. This assumption simplified the implementation by allowing us to use a single soil model or P matrix across the entire length of the IVS. However, the optimal P matrix or soil model may change throughout the dataset. For example, different MPV operators may have different ground clearance heights and sensor head orientation offset due to different instrument backpack adjustments. Future implementations of this approach should have options for varying the soil model throughout the site.

Analysis of Waikoloa grid TO20A

To further test the project matrix and soil model fitting approach, we apply the techniques to the TO20A grid at Waikoloa, Hawaii. At this grid, there were multiple data sets collected as part of an ESTCP demonstration. MPV data were acquired along North-South lines with a nominal line spacing of 0.5 m. Figure 132 plots the vertical component coaxial data from the 10th time channel (t=1.14 ms). The gridded data over the site show spatially varying magnetic soil response.

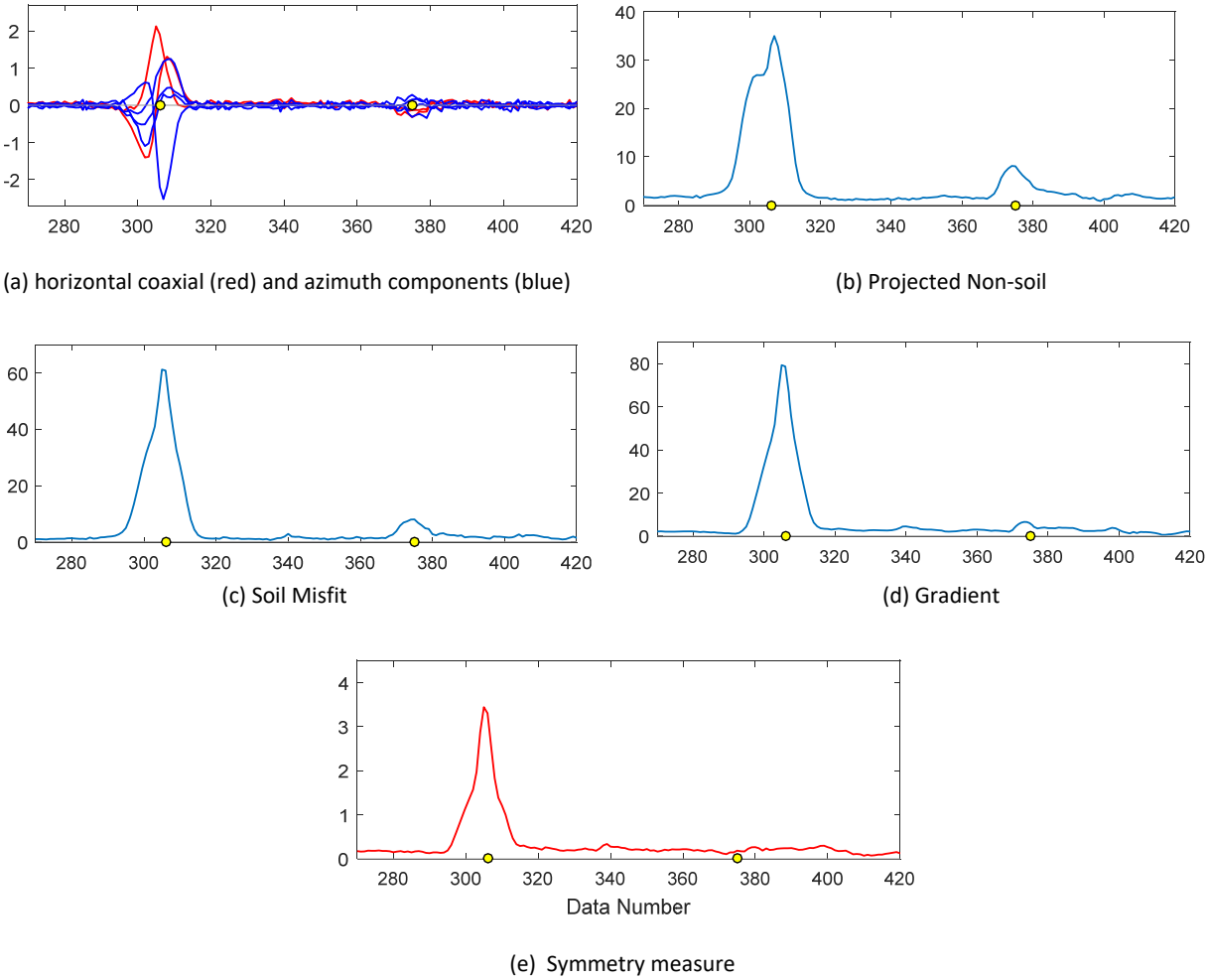

Figure 131. Comparison of different target detection measures. The section of the 10 cm deep small ISO (left dot) and 30 cm deep small ISO (right dot) are shown.

Dig and seed information from the site was provided by the ESTCP program office. The initial target picking list was generated using Geonics EM61 data. The target list was then augmented with data amplitude picks from MPV z-component data. Picks that were found to be due to soil are indicated by circles, picks that were metallic non-TOI, are plotted as triangles, and TOI are plotted as squares with the target ID also shown. The 4 TOI are:

- WK-477: 81 mm mortar, depth = 37 cm
- WK-492: Medium ISO, depth = 15 cm
- WK-535A: 37 mm AP, depth = 0 cm (surface)
- WK-542A: 37 mm TP, depth = 21 cm

Photos of the 4 TOI are shown in Figure 133.

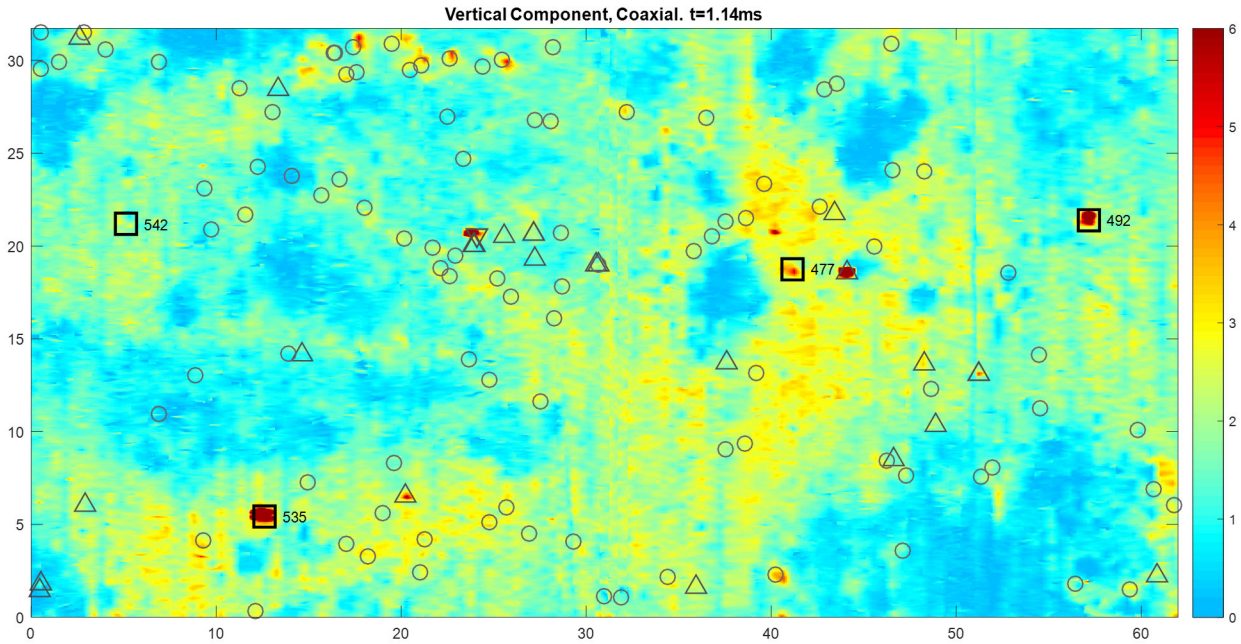

Figure 132. Raw vertical component, coaxial receiver, t=1.1ms.

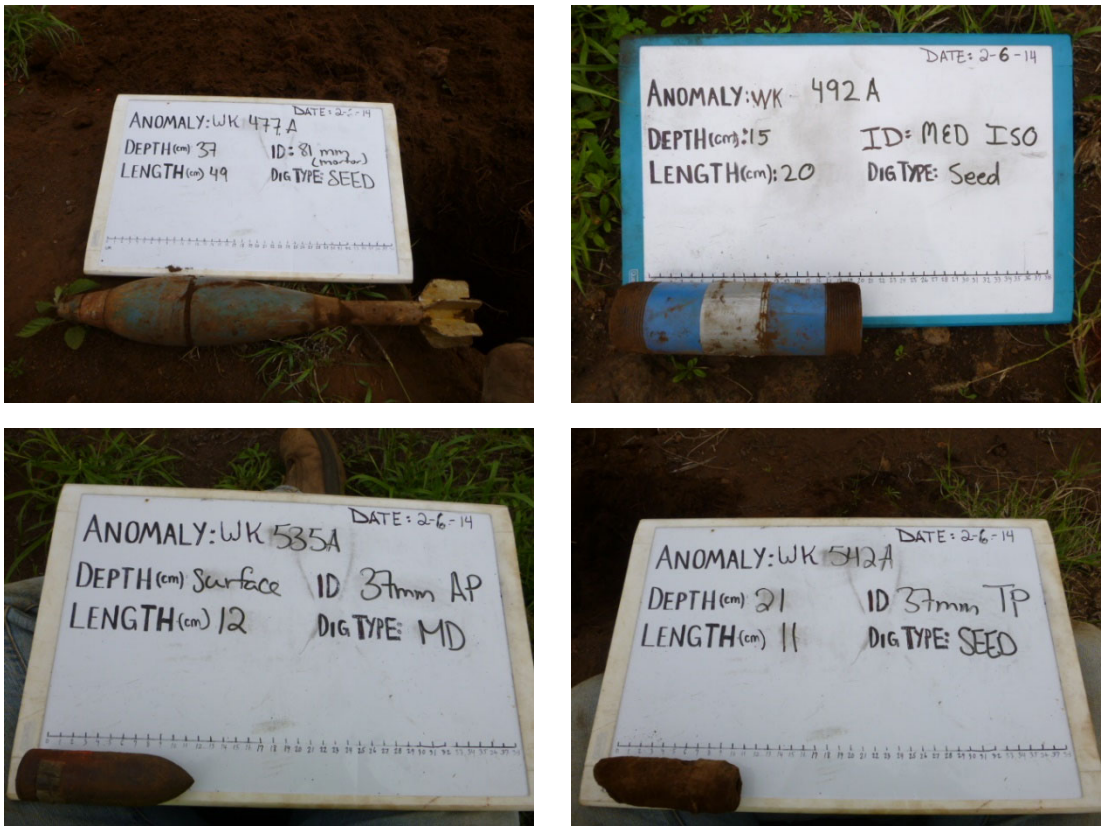

Figure 133. TOI in my mag soils study area.

Figure 134 shows de-median filtered vertical component, coaxial data. The de-median filter was applied to profile data using a 150-point filtering window. For the walking speed of the field crew, the 150-point window corresponds to an, approximately, 10 m filtering widow. Since the filter was run along North-South lines, the filtering was unable to remove some larger scale geology in the East-West direction. We see that along these linear geologic features there are often a collection of the geology related picks (i.e., circles). An effective detection metric would reduce the number of false alarms due to soil, while producing an anomaly for all TOI.

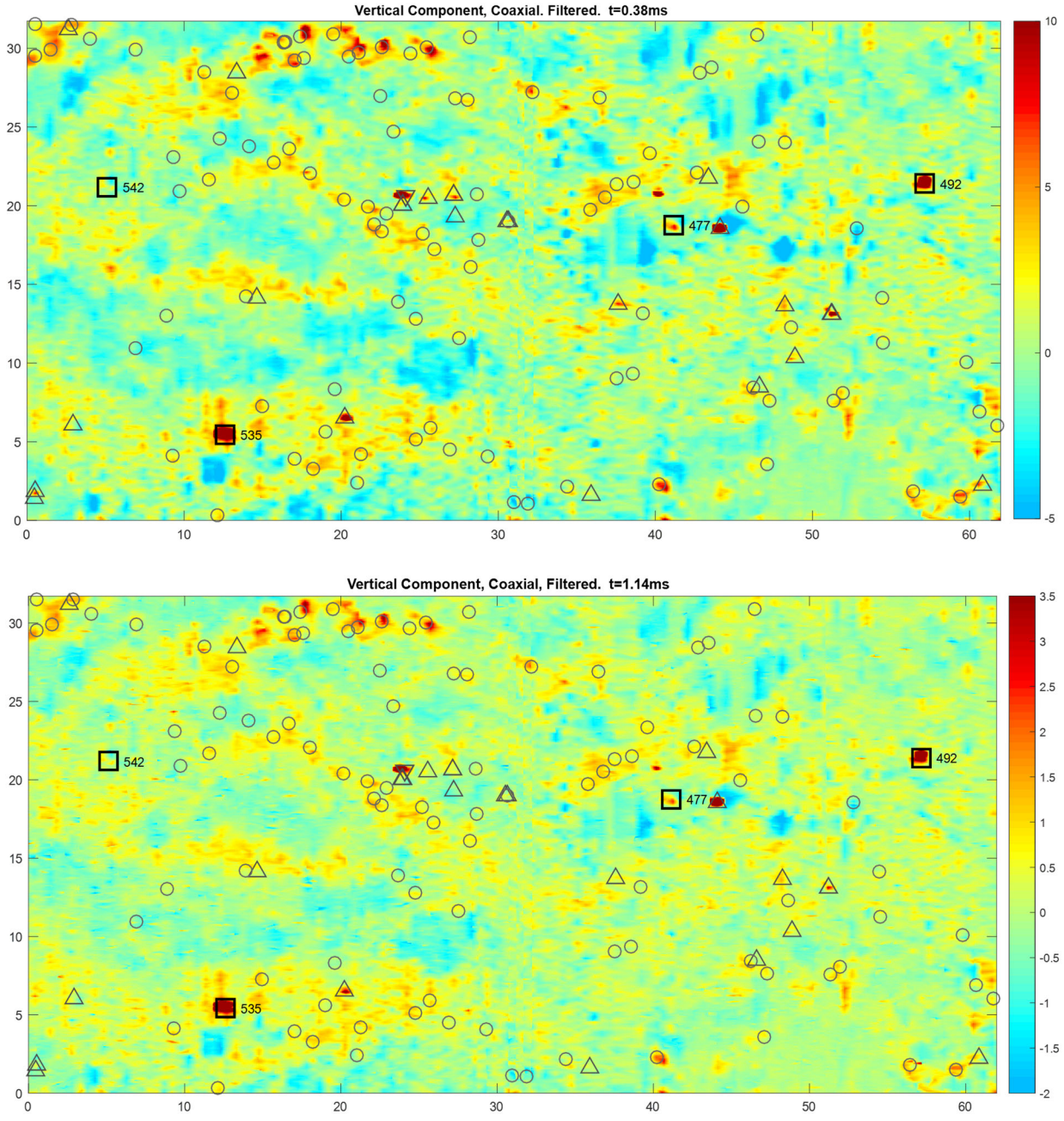

Figure 134. Filtered vertical, coaxial data collected in time channel 10 (t=1.14 ms) over TO20A. A 150 point de-median filter was applied along profile data. Top: time channel 4, t = 0.38 ms, bottom: time channel 10, t=1.14ms

When looking at the known TOI, we see that targets 477, 492 and 535 have a data anomaly. However, target 542 (37 mm, depth 21 cm) does not produce a significant response in the vertical coaxial component. The standard method of picking on vertical component amplitude has difficulty detecting one of the TOI (i.e., WK-542), and can produce multiple false alarms due to soil. We can now look at some of the different detection measures developed earlier can improve detection performance.

We first look at the horizontal component of the coaxial receiver. The horizontal component is defined $sqrt(d_x^2 + d_y^2)$ where d_x and d_y are the x and y components of the center receivers. Recall that, at the center of a horizontal transmitter loop, the secondary field due to magnetic soil will be in the vertical direction. Figure 135 grids the horizontal component of the coaxial receiver for the channels t=0.38 ms and t=1.14 ms. In the horizontal component image, the magnetic soil response has been largely suppressed. However, TOI WK-542 does not produce a significant anomaly.

Figure 136 plots gridded data from calculating the amplitude of the data projected along non-soil directions by using the $P^{nonsoil}$ matrix. The projected data suppresses the background response. However, the projected data amplitude is elevated in regions where there is higher magnetic soil signal (as indicated by a larger background response in the vertical, coaxial data). Each of the four TOI produce detectable signal. The amplitude of the non-soil response produces a greater number of distinct anomalies when compared to either the vertical or horizontal coaxial data. In particular, for several of the metallic non-TOI targets (i.e., MD or OD), there is signal in the non-soil amplitude data while the raw data does not appear to produce a distinct response.

The gradient amplitude map is shown in Figure 137. The resulting image appears to be similar to the non-soil amplitude. As was seen in the non-soil amplitude data, there is elevated background signal in regions of higher magnetic response. Similar to the non-soil amplitude case, this detection map would result in fewer magnetic soil picks resulting in empty holes than when using the raw data for detection. However, target 542 does not produce a significant anomaly. Figure 138 plots the combined non-soil and gradient measure. The resulting image appears to have more noise, but also is able to produce an anomaly at the location of target 542.

Figure 139 is a grid of fitting the soil model. All TOI – including WK-542 – are easily detected, and many of the soil anomalies do not result in a data anomaly. As with the other techniques, there is elevated signal in regions of higher magnetic soil signal. Future work should include investigating the optimal time channels and data weighting to improve the soil misfit result. In addition, we should investigate whether both the soil misfit and projected data approach should be combined. The soil misfit approach takes advantage of the decay of the signal to differentiate metal from soil, while the projected data does not.

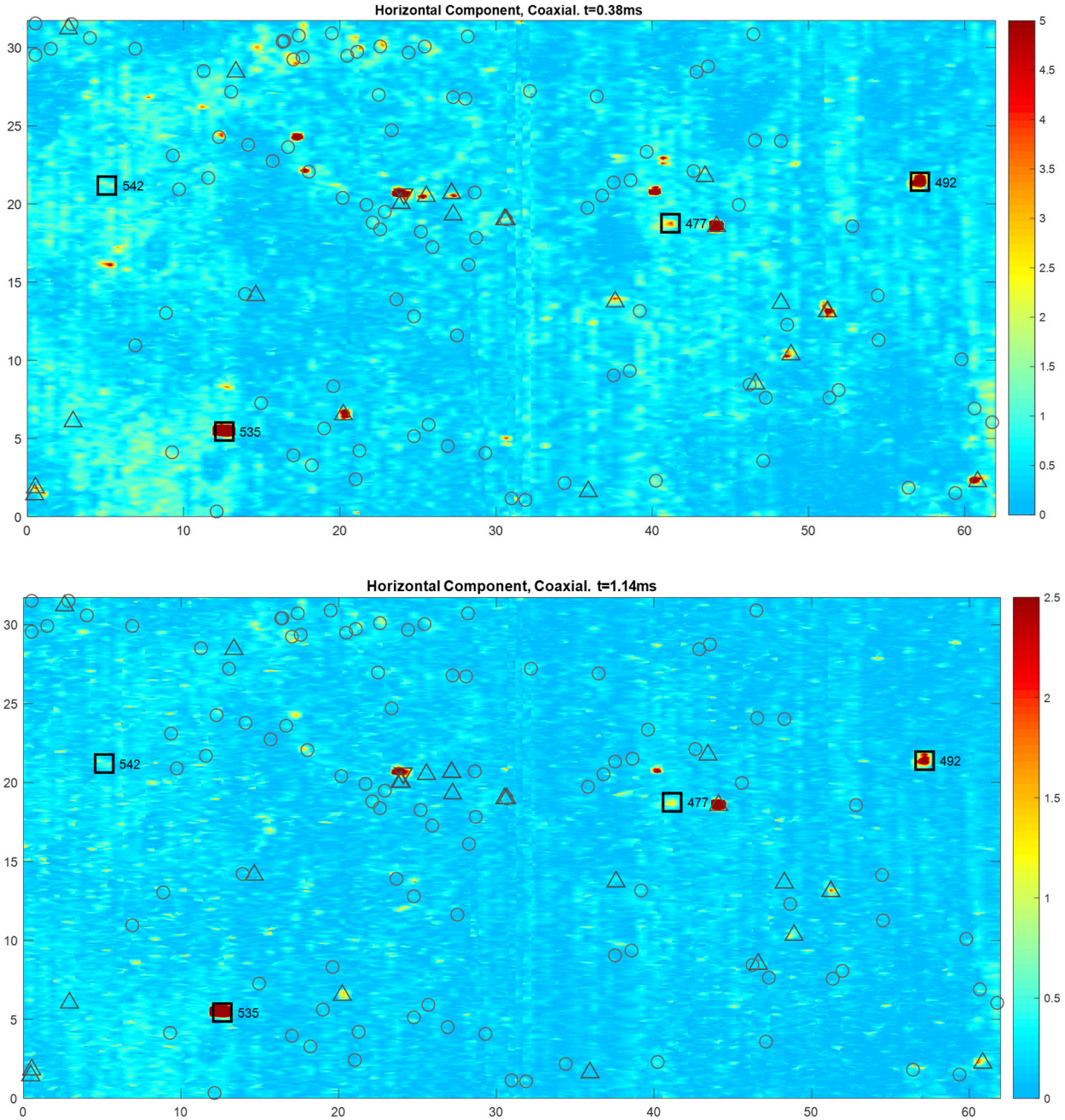

Figure 135. Horizontal component. TO20A. top: time channel 4, t=0.38 ms. Bottom: Time channel 10, t=1.14ms

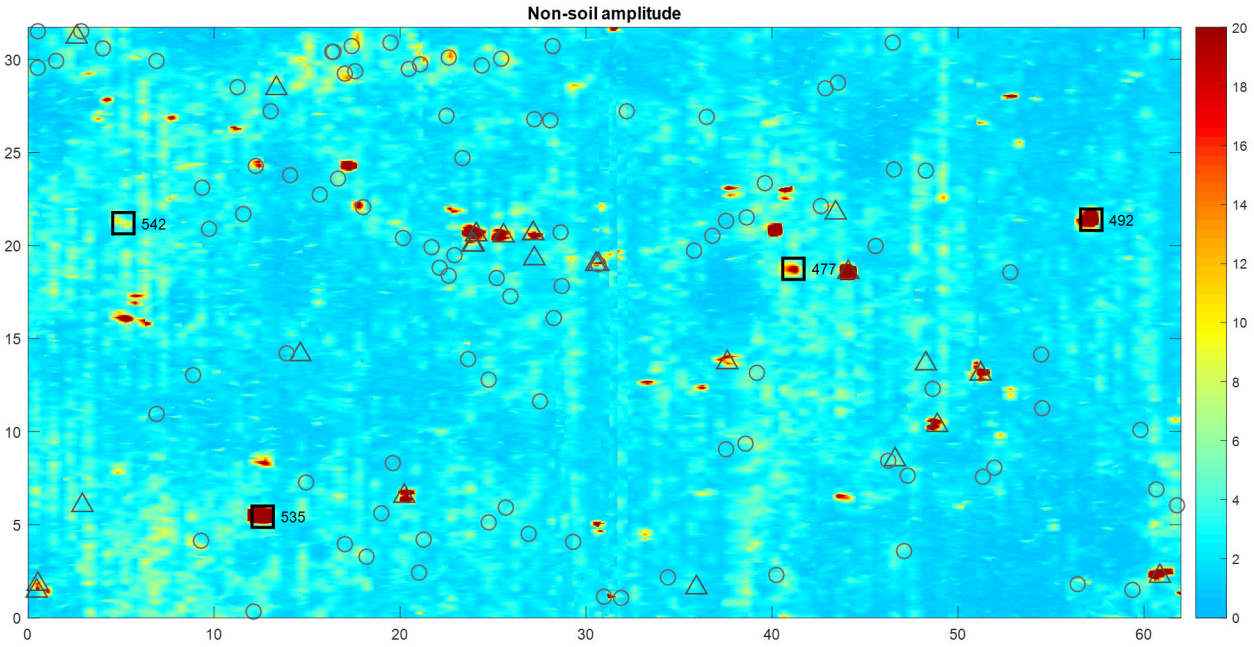

Figure 136 Non-soil amplitude calculated using $P^{nonsoil}$

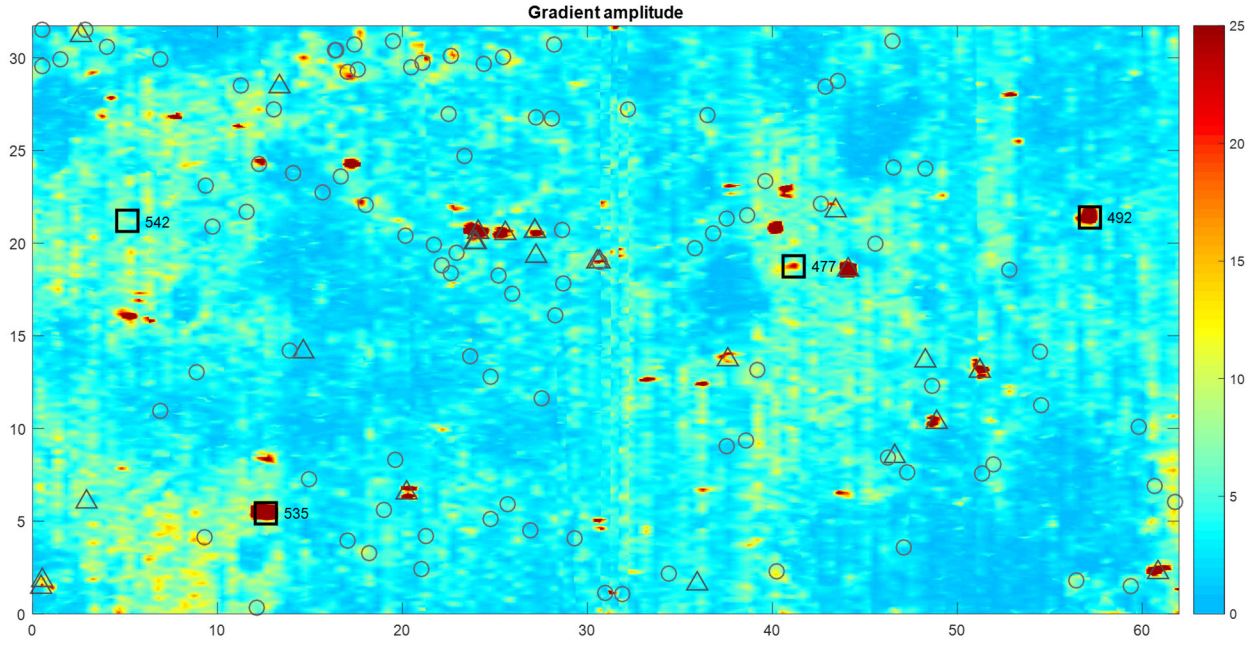

Figure 137. Gradient amplitude calculated using P^{diff}

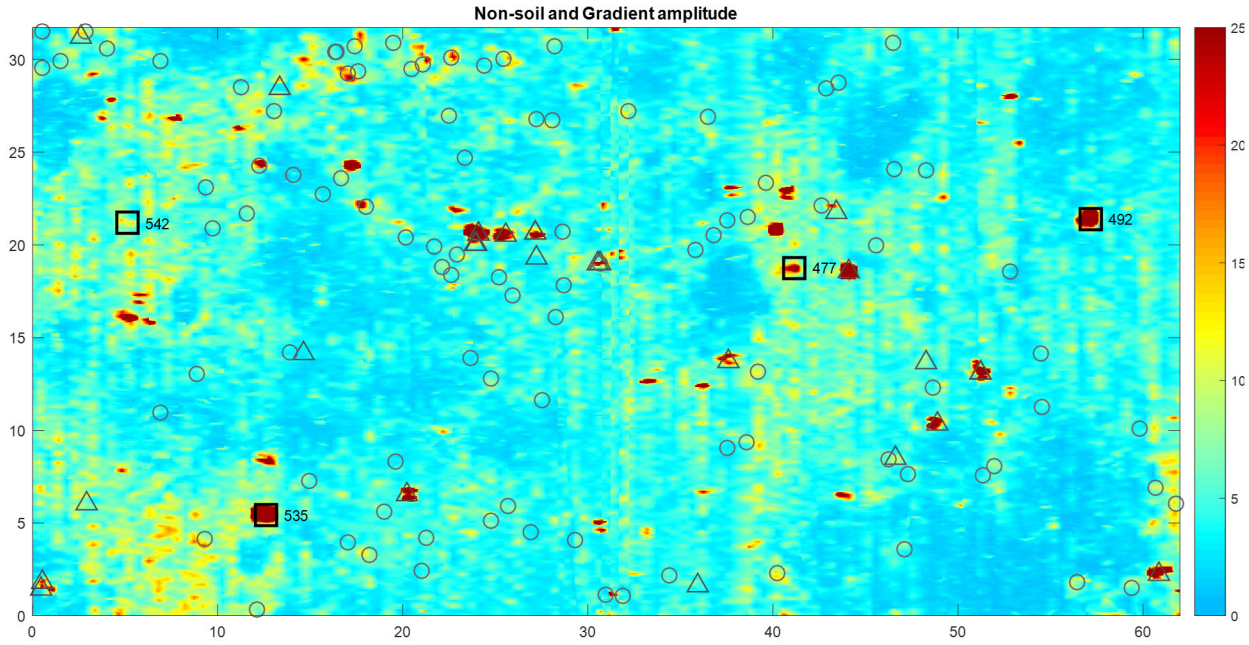

Figure 138. Combined non-soil and gradient matrix

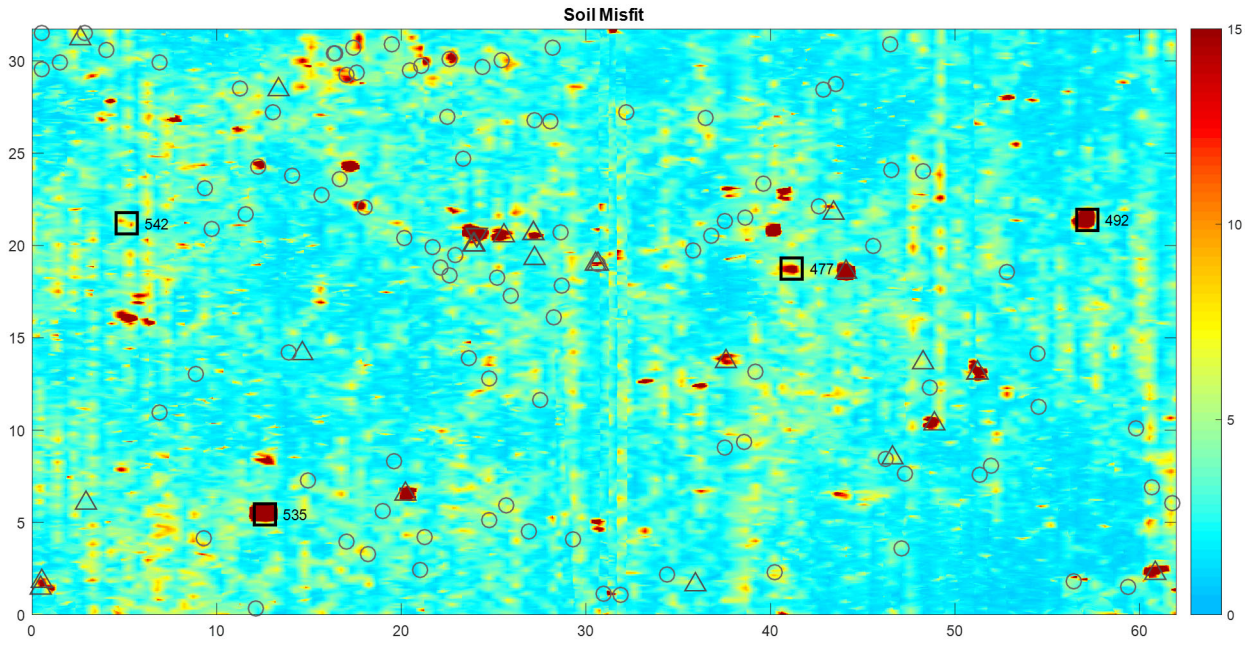

Figure 139. Soil Misfit

To get a better sense of the relative performance of the different approach, we now take a closer look at a number of the different anomalies. The most problematic target is TOI WK-542. Recall that target 542 is a 37 mm projectile buried at a depth of 21 cm. Figure 140(a) grids a 3m x 3m square of data centered on target 542. In the top row of Figure 140(a), the unfiltered vertical and horizontal co-axial data at t=1.14ms is gridded. The location of the target is indicated by a white dot. The vertical component data contains the elevated background due to the background soil, and the target does not produce a well-defined anomaly. The horizontal component does produce a pair of anomalies on either side of the target location. The horizontal component anomaly is relatively small relative to the noise across the grid, and there would be many soil based false positives picked if the horizontal component was used for detection. The problematic noise level can be seen by comparing the anomaly amplitude to the signals is Figure 135.

The bottom row of Figure 140(a), show the soil misfit, non-soil component and gradient measures. These images have the same "dumbbell" shape that was seen in the horizontal component. The misfit and non-soil measures provide a clear anomaly at the location of target 542, but the gradient is not an effective method for detection.

Figure 140(b) and (c) plot data (top plot) and soil metrics (bottom plot) along a North-South profile on the east and west side of the target. There is slight anomaly in the horizontal components. The view clearly indicates that the soil-misfit and non-soil amplitude detection maps would perform best for detecting 542.

For completeness, we plot closeups of the other three TOI (477, 492, 535) in Figure 141 to Figure 143. The other three TOI, are easily detected using any method, and therefore are not useful in comparing performance.

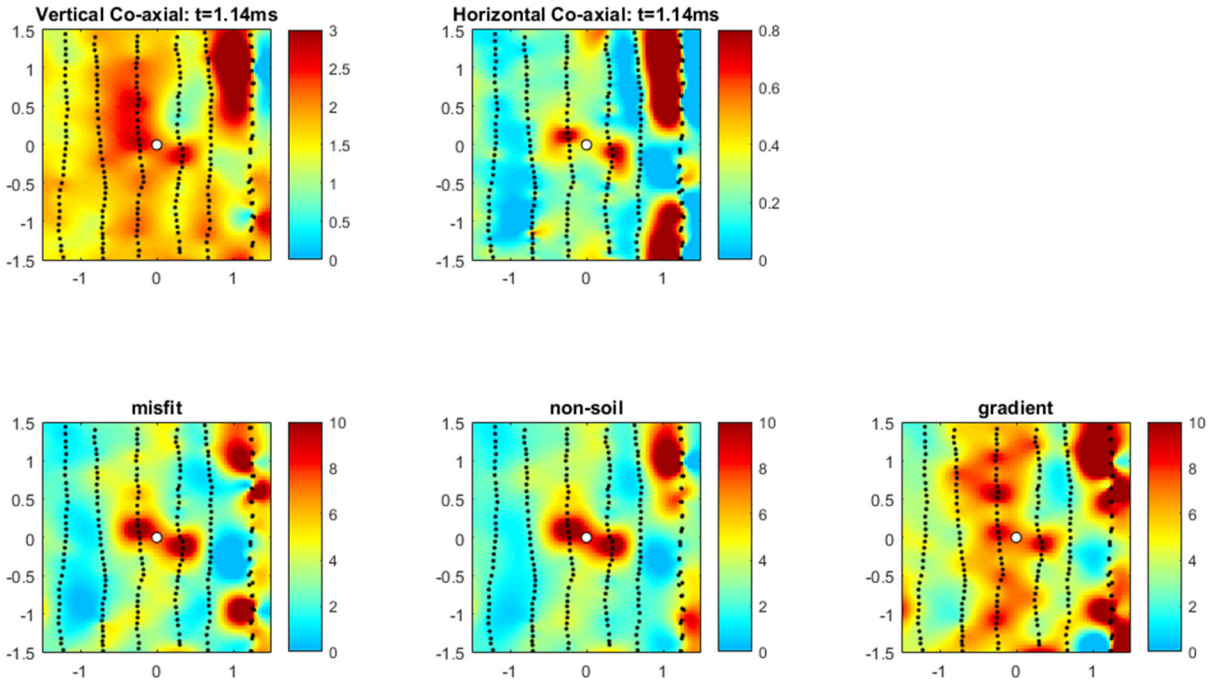

(a) Comparison of different methods.

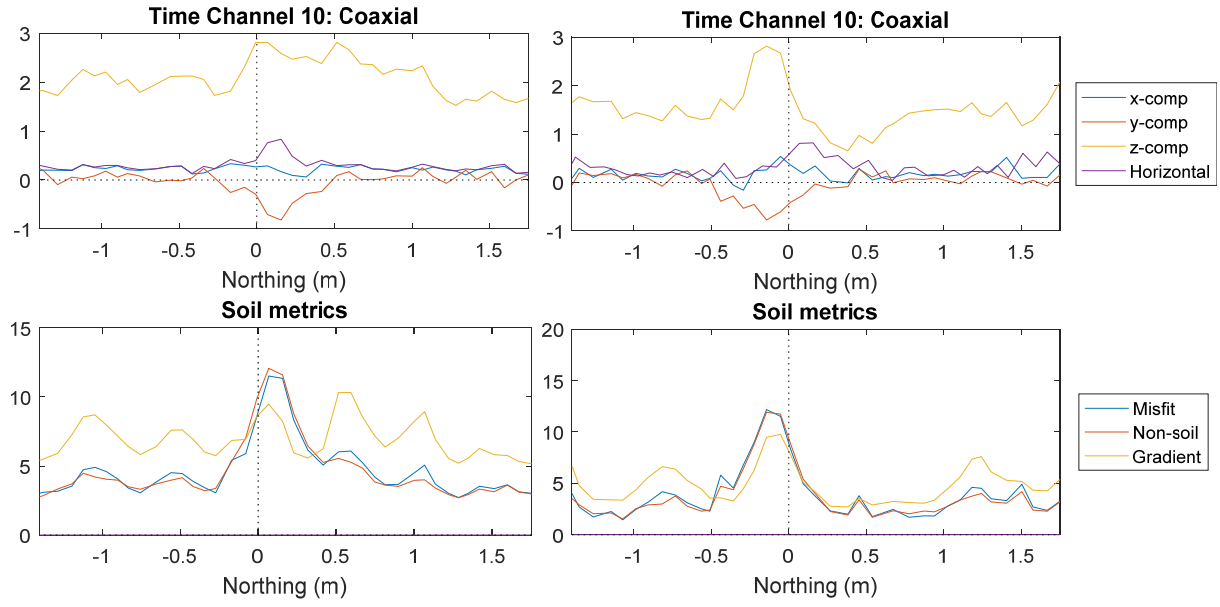

(b) line to west of target

(c) line to east of target

Figure 140. Target TOI 542. Similar to the IVS data, the gradient measure was unable to detect the target.

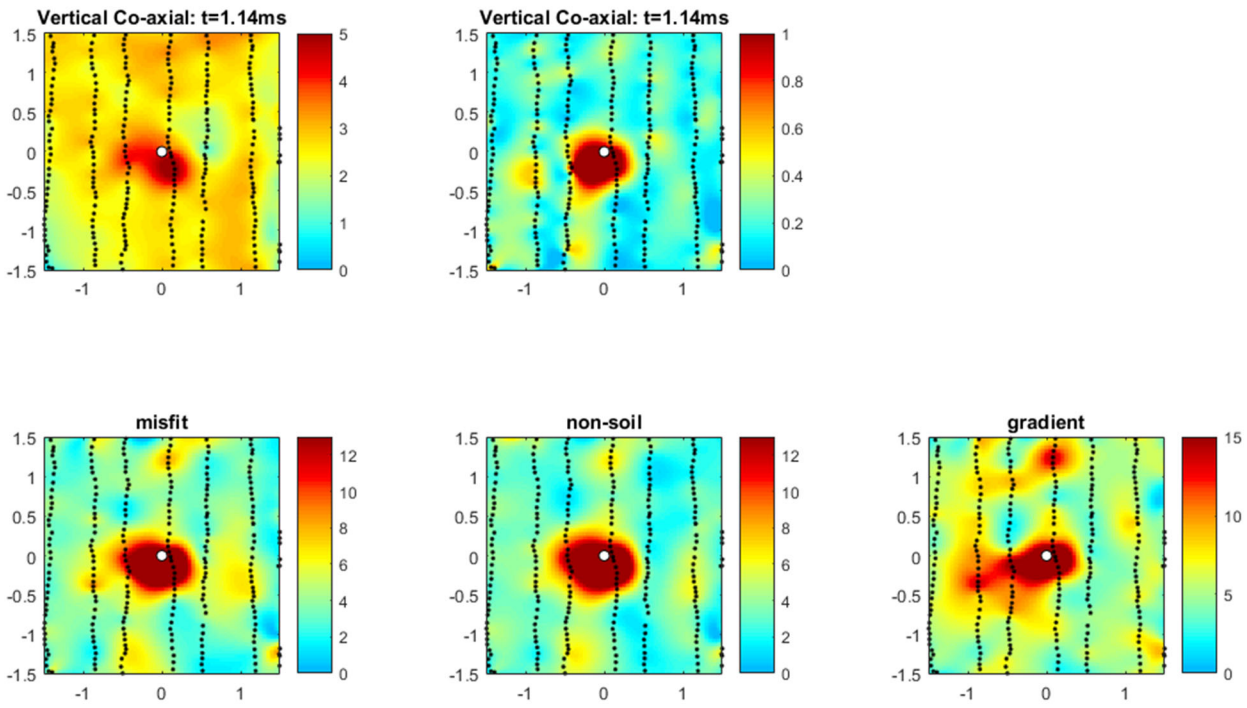

(a) GPS'ed location of target is located at white circle

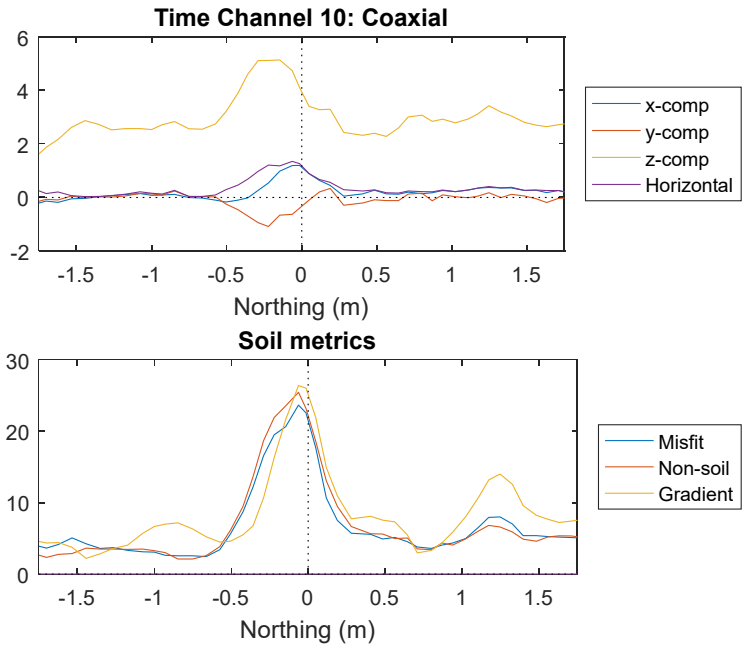

(b) profile at line closest to the target.

Figure 141. Target TOI 477

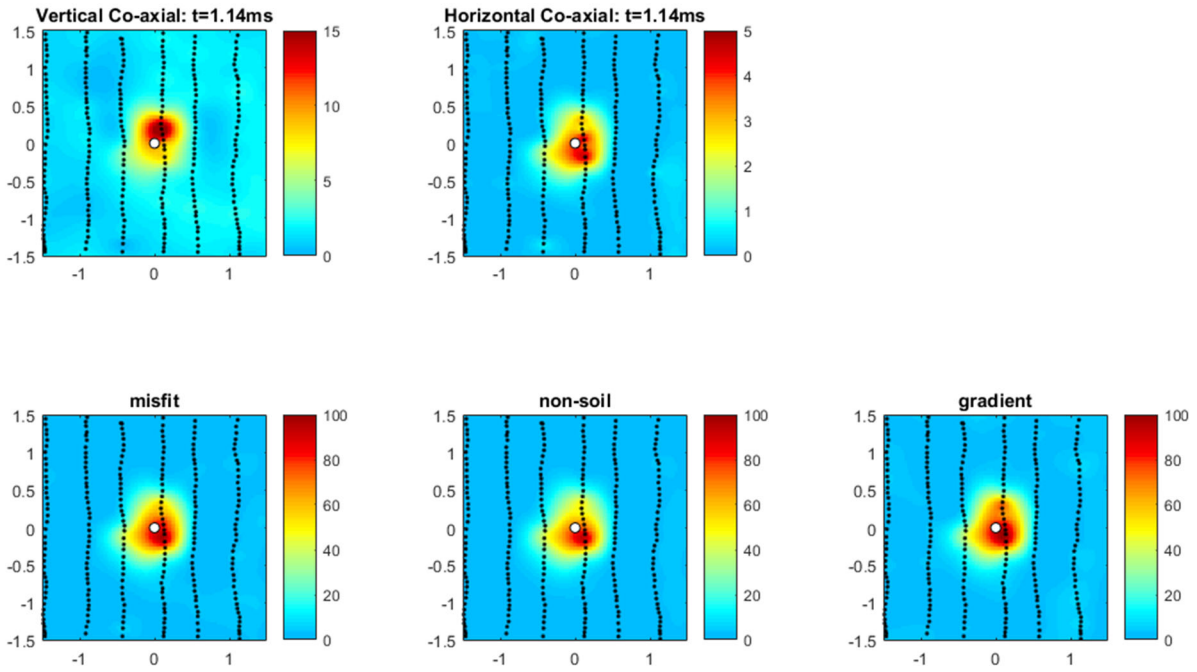

(a)

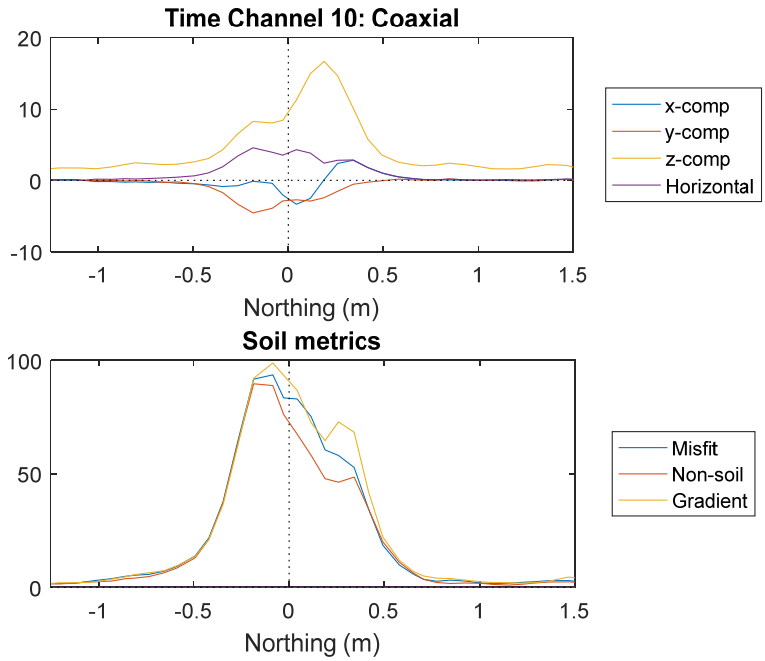

(b)

Figure 142. Target TOI 492

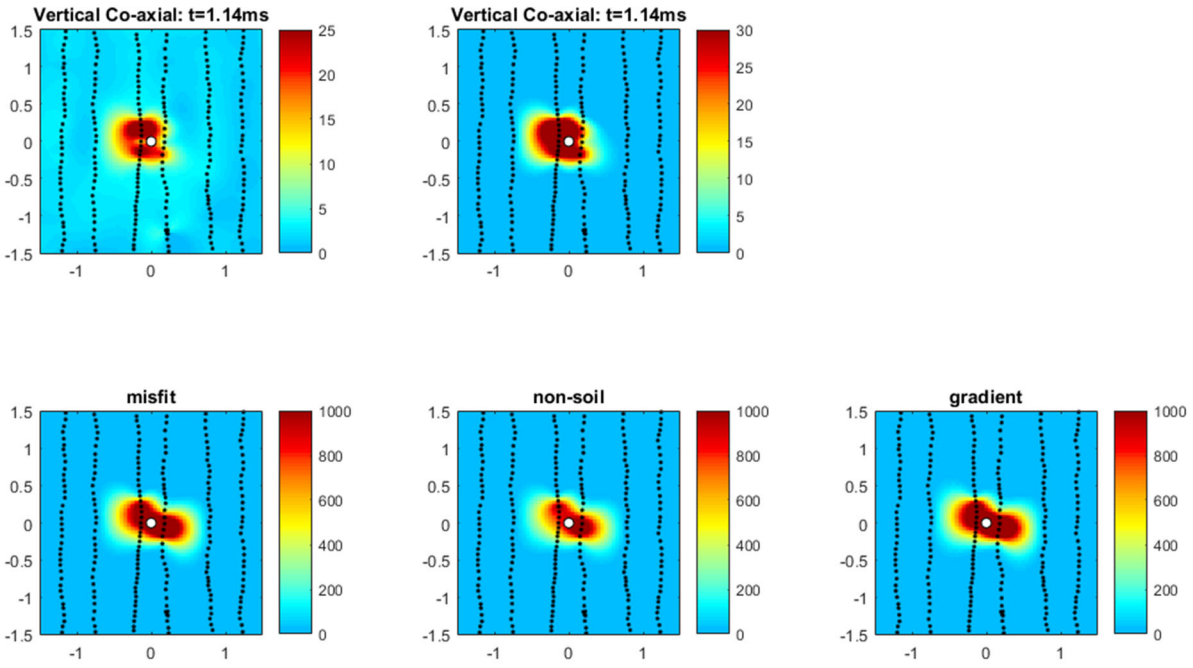

(a)

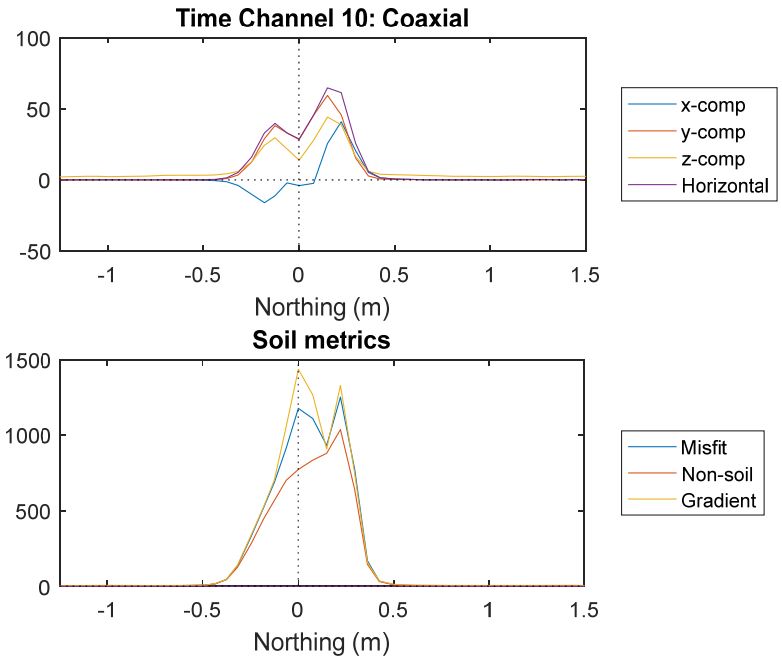

(b)

Figure 143. Target TOI 535

An additional example is the group of targets at (x,y)=(25,20)m in Figure 132. A closer look at the vertical and horizontal components of the coaxial data are shown in Figure 144, with Figure 144(a) plotting the response at time channel 4 (t=0.38ms), and Figure 144(b) plotting the response at time channel 10 (t=1.14ms).

Table 21 contains ground truth information. In the vertical and horizontal components, there are anomalies near to the locations of 487/488 (horseshoe and 7 cm frag), 489 (16cm frag) and 493 (3 and 10 cm frag). These anomalies are not well centered on the ground truth locations. The anomalies close to targets 489 and 493 are not visible at t=1.14ms. There is no anomaly present for target 482 (6cm frag).

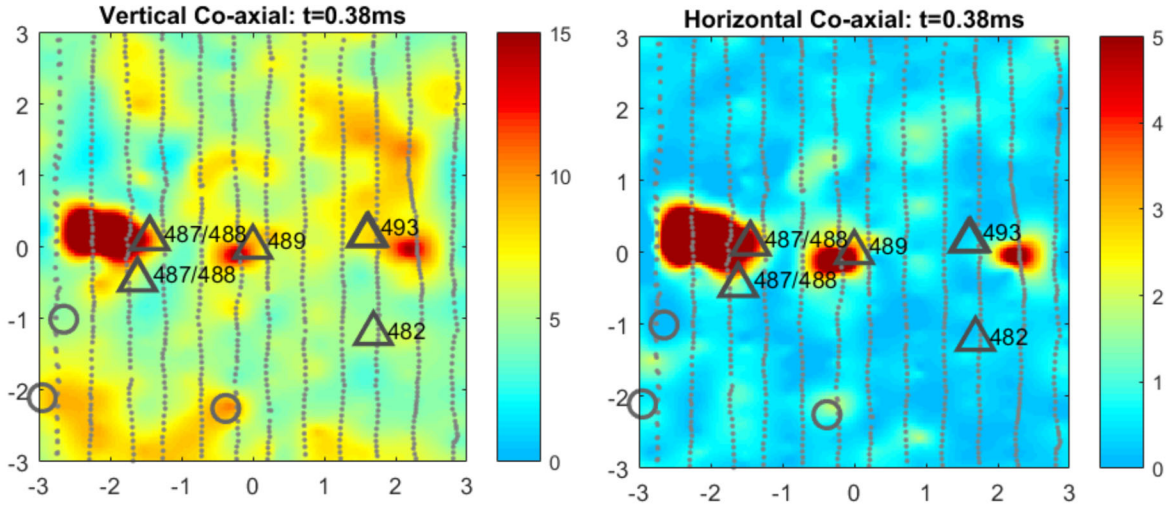

(a) time channel 4: t=0.38ms

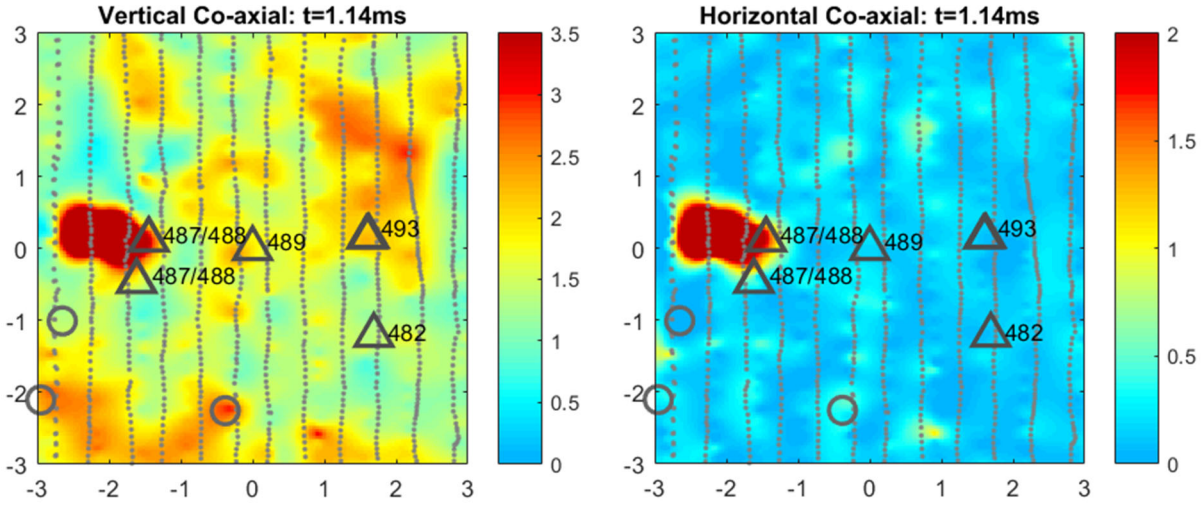

(b) time channel 10: t=1.14ms

Figure 144. A group of metallic debris.

Target ID	Recovered Item Count	Depth	Description	Item Length (cm)	Anomaly Type
WK-482A	1	0	Frag	6	MD
WK-487A	1	3	Horse Shoe - same as 488A	11.5	OD
	2	0	Frag - same as 488A	7	MD
WK-488A	1	3	Horse Shoe - same as 487A	11.5	OD
	2	0	Frag - same as 487A	7	MD
WK-489A	1	0	Frag	16	MD
WK-493A	1	0	Frag	10	MD
	2	0	Frag	3	MD

Table 21. Ground truth information for targets in Figure 144

Figure 145 compares the different target picking image (i.e., non-soil components, misfit, and gradient amplitude) to the horizontal component data (lower right). For all cases, target 482 does not have an anomaly. Since target WK-482 is a small frag, missing WK-482 may be due to low SNR. For the remaining targets, the location of the anomaly is better centered on the ground truth location. Some investigation is required to determine why the positioning of the anomaly is worse with the raw data. It is possible that signal variations due to magnetic noise sufficiently modifies the anomaly shape to shift the anomaly peak. In addition, the raw data only has a single peak for the 487/488 target pair, while the misfit/non-soil/gradient images contain a pair of targets corresponding to the two targets of 487/488.

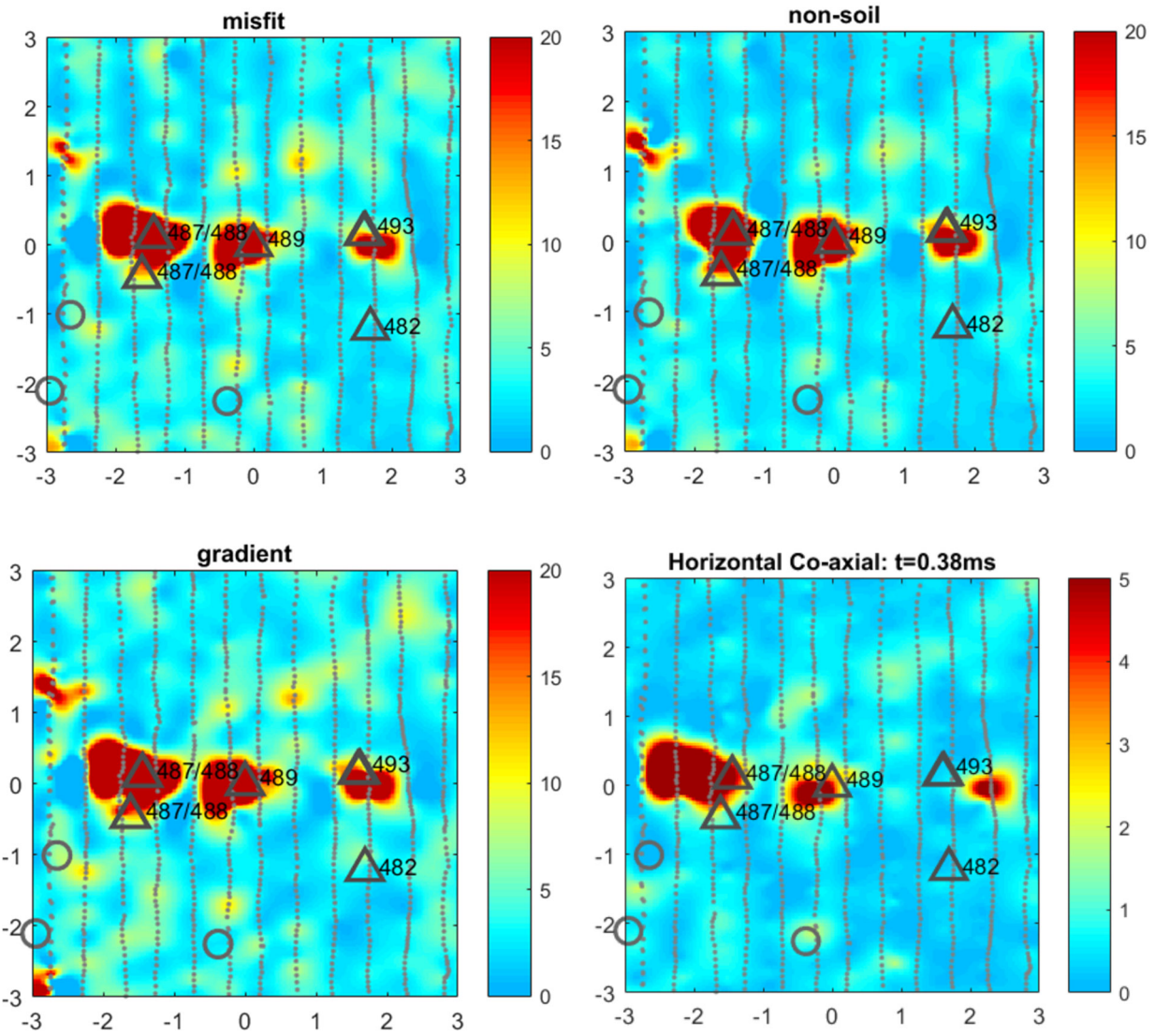

Figure 145. Comparison of different detection metrics. There is an improvement in the ability to detect the targets, as well as the location accuracy.

Simulations to study effectiveness of target picking

In the previous section, we looked at field data from Waikoloa to demonstrate how using transformed data or looking at the fit of soundings to a soil model can be used for target picking. Since there were only 4 targets of interest, the example did not have enough targets to determine if there was any improvement in target picking when using these newer measures.

To better assess performance, we again use the TO20A MPV data set, but we synthetically seed the dataset with small ISOs. The ISOs are randomly oriented and placed in a uniform grid. The rectangular seed area covers a portion of the site that has the highest level of magnetic soil noise. We create a pair of datasets, corresponding to a 10" burial depth and a 6" burial depth.

Figure 146 plots the vertical component, coaxial data with small ISOs seeded at a depth of 10 inches. The locations of seeded small ISOs are indicated by squares. There are 126 seeded small ISOs. For data collected with 50 cm line spacing, and using the time channel 10 (t=1.14ms) for detection, a small ISO at 10" has a picking threshold of 0.68 mV/A. Using this threshold with an image based target picker results in 481 target picks. Regions with higher levels of magnetic soil response tend to have a higher density of picks.

If we define a successful detection as having a pick within 50 cm of the true location, then applying the target picker results in 116 of 126 detections. We investigated if lower the threshold could result in all seeds being picked. We found that a number of the seeds do not have a distinct peak. This can be due to magnetic soil noise or filtering artifacts. We note that Target 542 (small ISO at 21 cm), that was investigated in the previous section was picked.

Figure 147 plots target picks when using the non-soil amplitude and the soil misfit for detection. Unlike picking using the filtered coaxial vertical component, it is possible to define a threshold that all seeds are found. Fort this example, we choose thresholds such that all seeds are selected by the target picker. Applying the peak picking algorithm to the gridded non-soil amplitude image with a threshold of 9.6, results in 176 target picks. Using the soil misfit data with a threshold of 9.5 results in 207 picks. Therefore, using these different approaches is able to detect all the seeds, while also being able to reduce the number of picks in half.

We repeat the target picking test on the dataset with small ISOs seeded at a depth of 6 inches (Figure 148(a)). Using the detection modeler code developed in SERDP MR-2226, we determined that the detection threshold is 1.87mV/Amp when picking from coaxial, vertical component data in the 10^{th} time channel. A total of 146 anomalies are detected when using this threshold, and 118 of 126 seeded targets are picked. The missed picks may be due to filtering artifacts as well as soil response variability due to sensor ground clearance changes.

In order to detect all seeds, the threshold would have to be lowered to 1.00mV/A (Figure 148(b)). However, this results in 304 target picks, with many of the corresponding to regions of high magnetic susceptibility.

Figure 149 shows the gridded non-soil amplitude and soil misifit images for the small ISO seeded at 6 inch depth. The detection thresholds were chosen in order to detect all seeds. There are 141 picks

when applying the peak detection algorithm to the non-soil data, and 145 picks when using the soil misfit.

In both the 6” and 10” depth cases, using the soil misfit or non-soil amplitude was a more robust and efficient way to detect the small ISOs. For both datasets, the traditional method of picking with vertical, coaxial data missed seeded targets, while requiring more target picks than the soil misifit or non-soil amplitude. The non-soil amplitude picking and soil misfit picking had similar performance, with the soil misfit approach having slightly more picks.

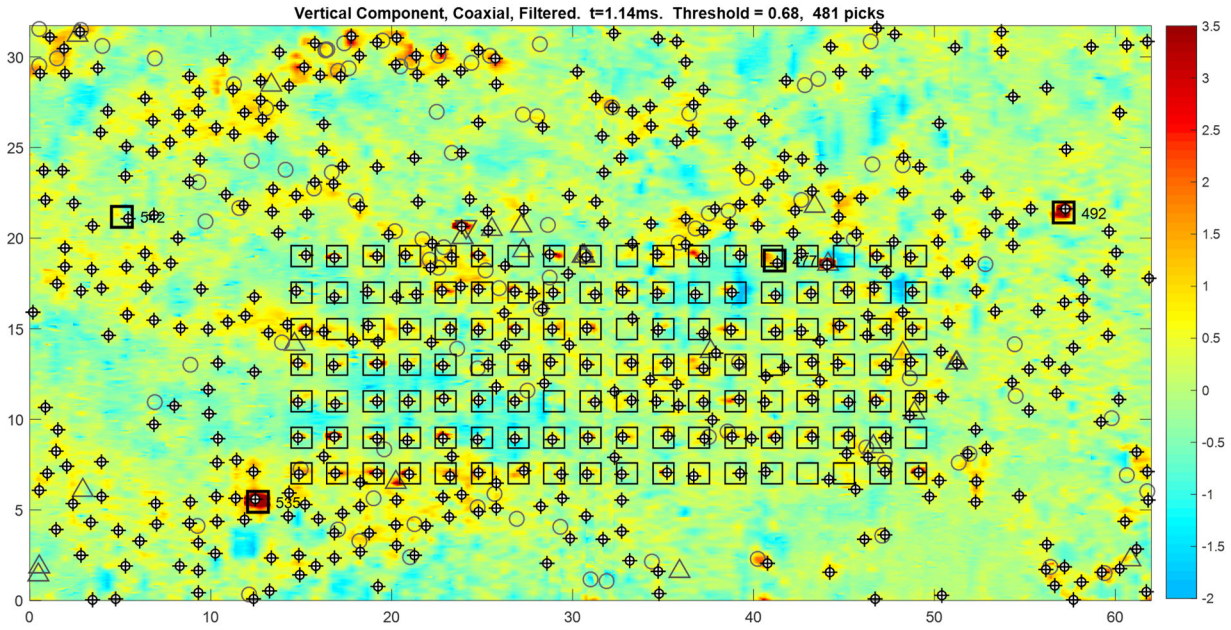

Figure 146. Filtered coaxial vertical component. Black squares indicate locations of small ISOs seeded at a depth of 10 inches.

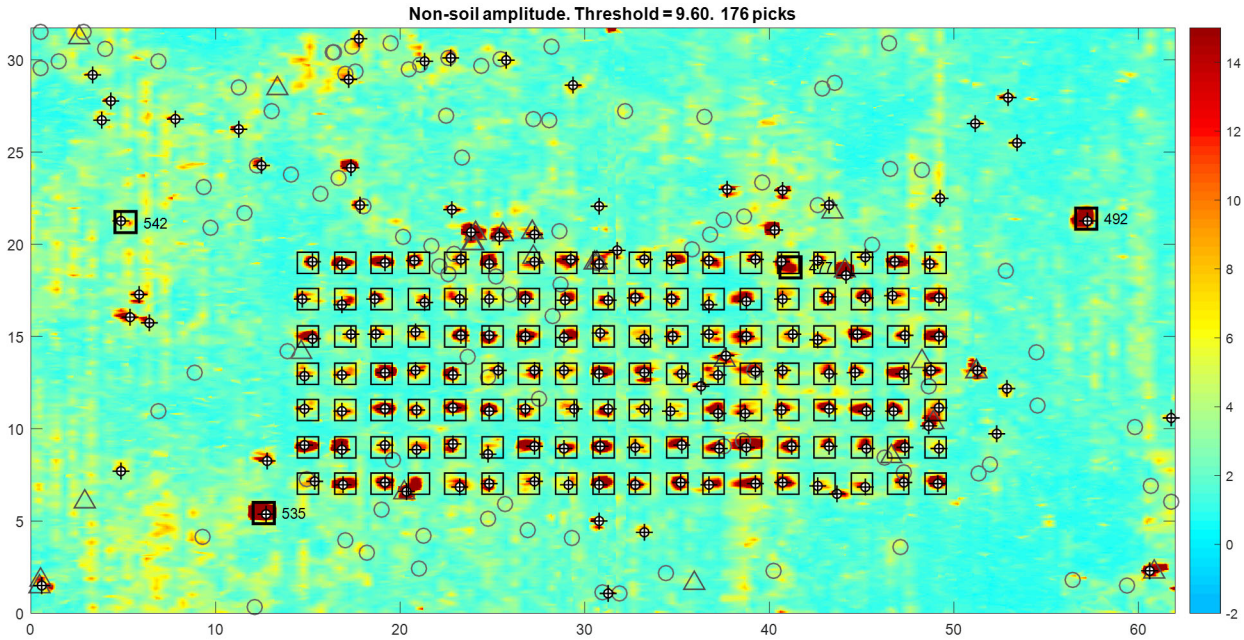

(a) projected, non-soil component.

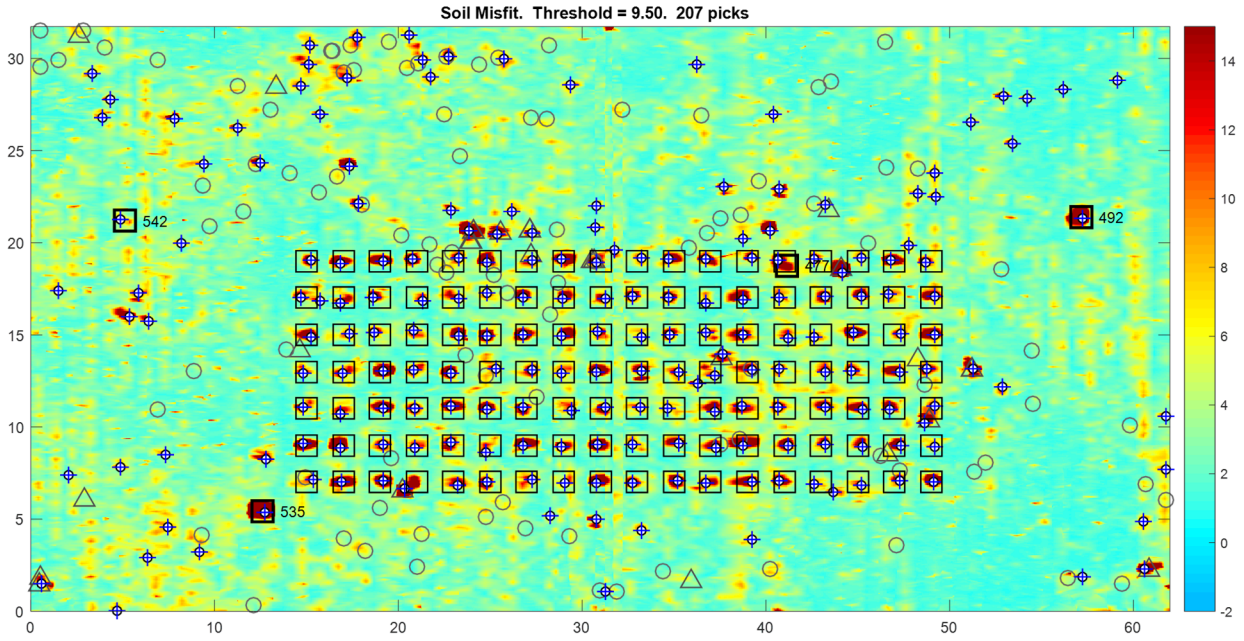

(b) soil misfit

Figure 147. Small iso, synthetic seeds, 10 inch depth. Soil metrics. Soil misfit. All picked

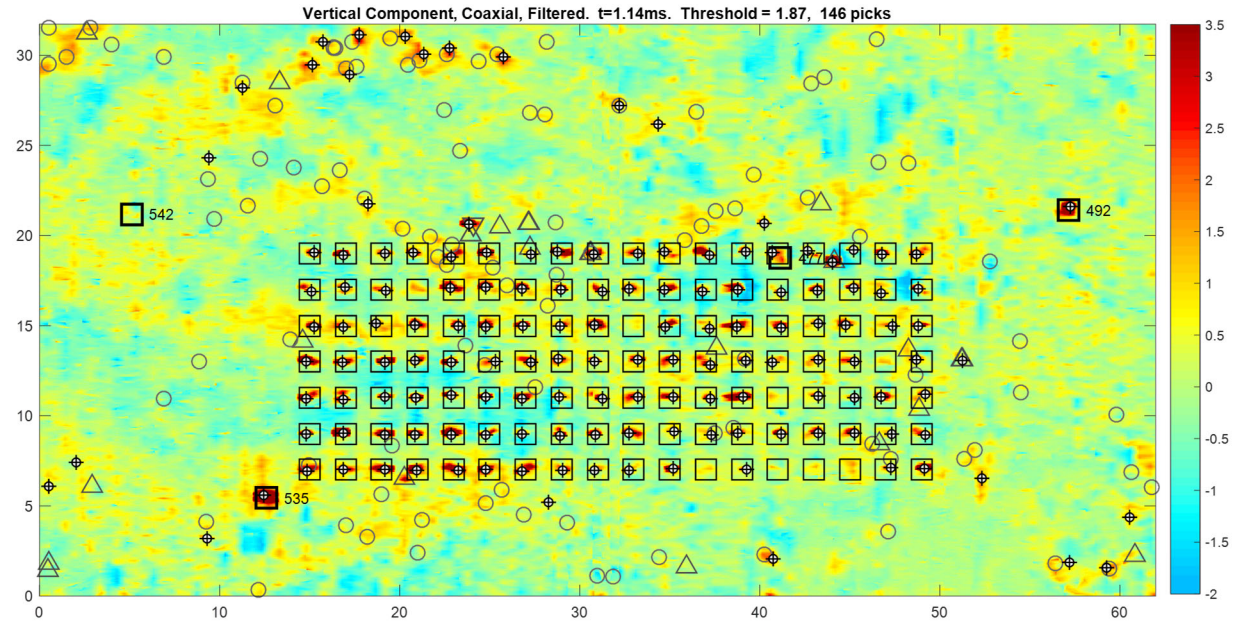

(a) Threshold = 1.87, chosen with detector. 146 picks.

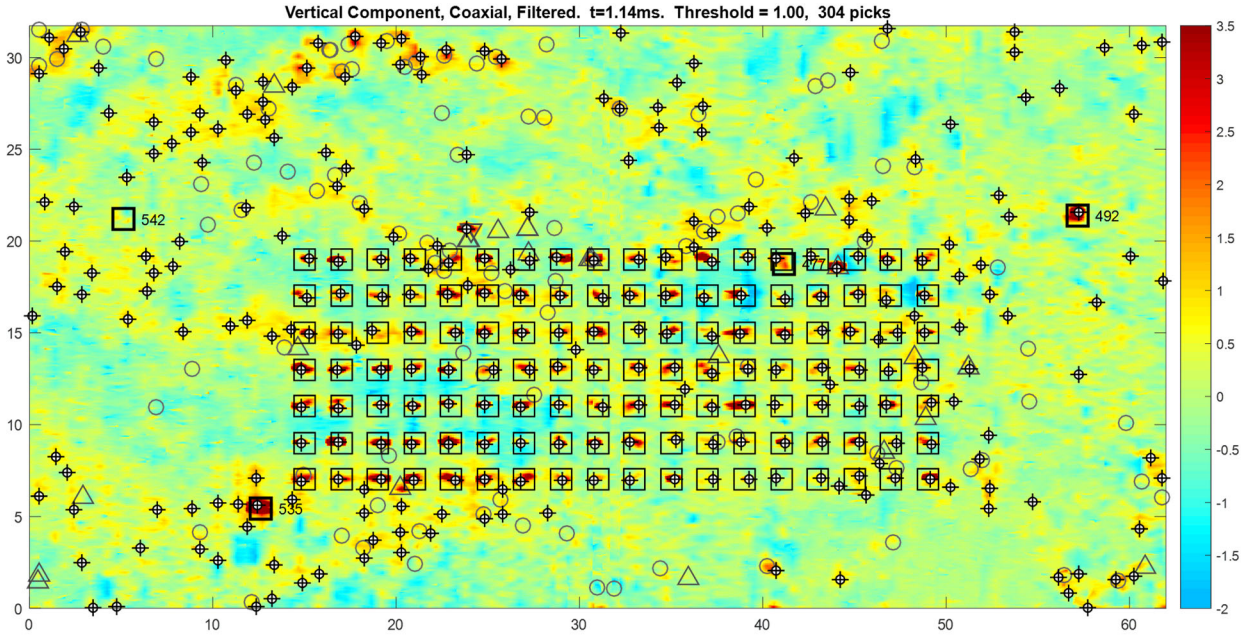

(b) Threshold = 1.00, chosen to get all seeds. 304 picks.

Figure 148. Picking result for a small ISO at 6”

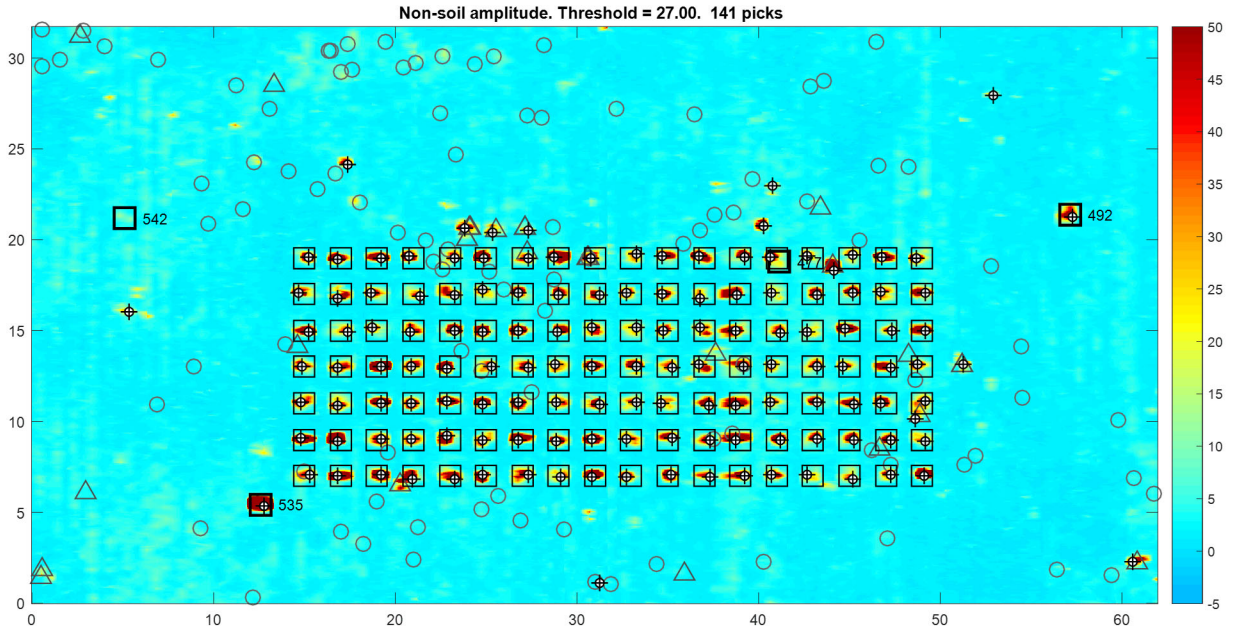

(a) non- soil amplitude

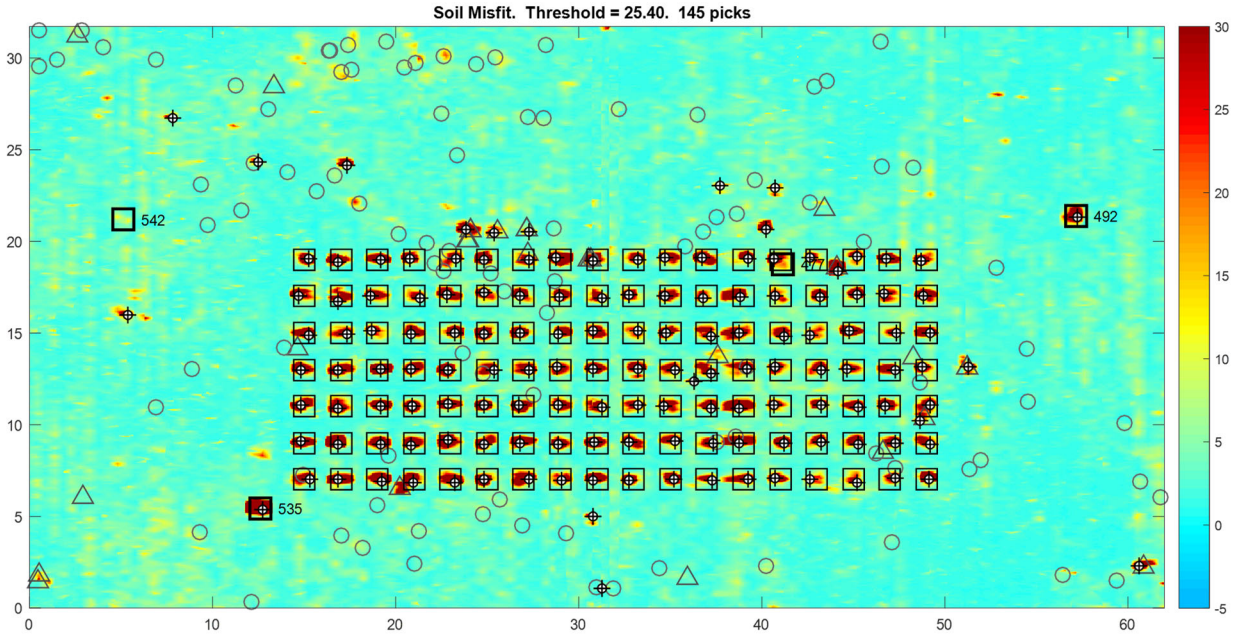

(b) soil misfit.

Figure 149. Small ISO: 6" depth. Random orientation. In both cases, all synthetically seeded targets found. However, TOI 542 is not found when setting the threshold this high.

Inverting Projected Data: Processing cued MPV data from Waikoloa

In the previous section, we used the amplitude of projected data to improve target picking performance. In this section, we study the ability to invert the projected data. To demonstrate this method, we consider cued IVS data collected with the MPV3D at the Former Waikoloa Maneuver Area (Figure 122). When the MPV3D operates in a cued mode, there are 3 transmitters that fire sequentially. The secondary response is then measured by 5 receiver cubes that measure 3 orthogonal directions of the secondary field.

At the beginning and end of each survey day, cued IVS measurements were acquired. Figure 150 plots the recovered polarizabilities from all the IVS measurements for the medium ISO and the shallower small ISO (depth = 10 cm). The grey dashed lines are library polarizabilities. The polarizabilities from the medium ISO match the library polarizability for a medium ISO. The polarizabilities for a small ISO buried, horizontally, at 10 cm were consistent, but underestimated the expected amplitude for a small ISO.

The reason for underestimating the polarizability amplitude is due to a poor background subtraction. The location for the IVS background measurements was approximately 10 m south of the locations of the small ISO, and the background measurement is, potentially, not representative of the soil response at the location of the small ISO.

(a) Medium ISO, depth = 15 cm

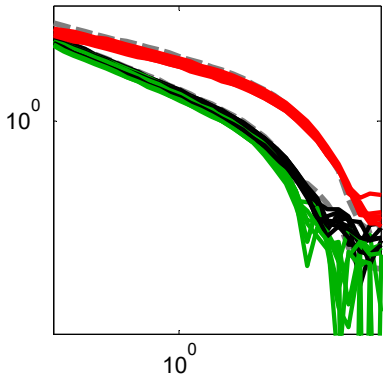

(b) Recovered polarizabilities

(c) Small ISO, depth = 10 cm

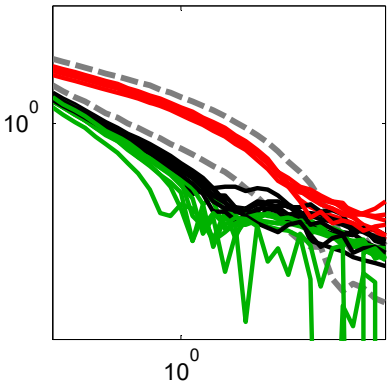

(d) Recovered polarizabilities

Figure 150. Recovered polarizabilities for the medium ISO and the shallow small ISO from the Waikoloa IVS.

To demonstrate the sensitivity of the small ISO estimated polarizabilities to the background subtraction, we compare the recovered polarizabilities when subtracting out different amounts of soil response. The background correction is represented by this equation

$$d^{corr} = d^{raw} - kd^{bg}$$

where the background measurement d^{bg} is the sum of the instrument response (i.e., the response of the instrument in air) and the magnetic soil response at the location that the background measurement is acquired. Recall that in low electric conductivity environments, the magnitude of the soil response is proportional to the magnetic susceptibility. If k=0, then there is no background correction, and we see the polarizabilities follow the characteristic viscous remnant magnetization power law decay. The standard correction – i.e., where we assume that the magnetic soil properties of the background location is equivalent to where the sounding was acquired – is represented by setting k=1. The standard correction results in an overestimated background response where the amplitude of the recovered polarizabilities is lower than the in-air measurement. The optimal background subtraction would've been to remove only 60% of the background measurement. At sites where there is a significant background soil response, it is useful to use multiple background with different scaling to account for spatial variability of the magnetic properties. If an in-air measurement is available, the corrected data d^{corr} could be

$$d^{corr} = d^{raw} - kd^{bg} - d^{in-air}$$

where $d^{in\text{-}air}$ is an in-air measurement to obtain the instrument response.

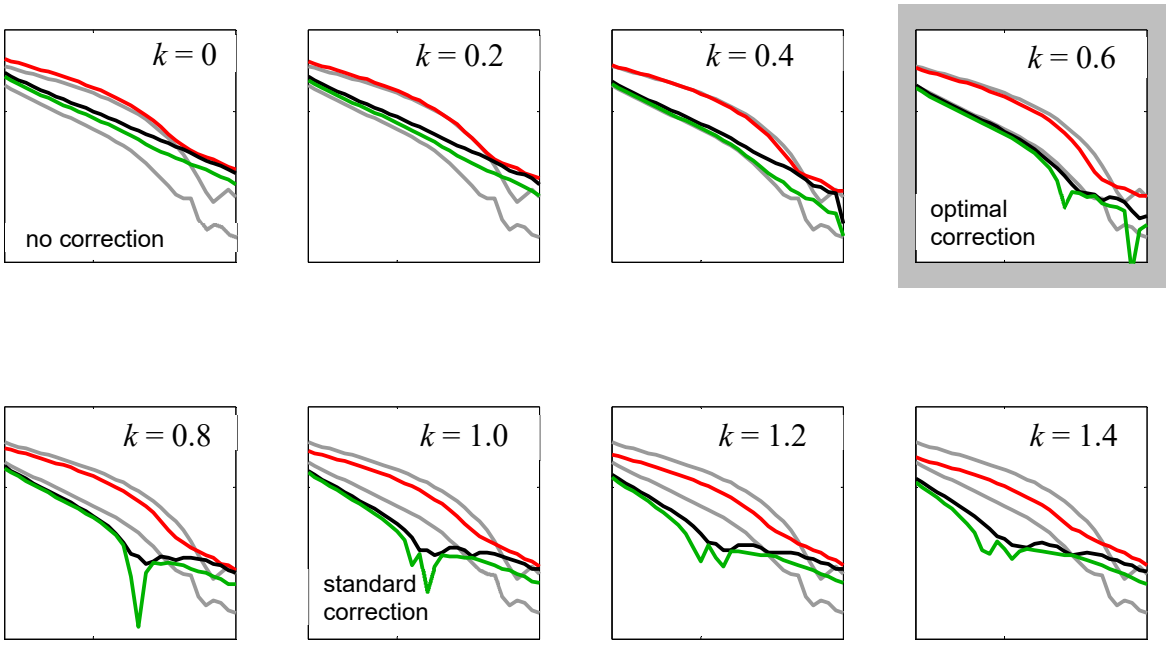

Figure 151. Applying a background correction. Multiplying the background data by 0.6 prior to subtracting from the IVS data, produces the best result.

In the previous, we demonstrated a method for suppressing the soil response that doesn't require subtracting a background measurement. Instead, we will use combinations or components of the data that are less sensitive to the magnetic geology. We define an operator P such that we don't fit the sensor data directly, but rather linear combinations of the data:

$$\tilde{d} = Pd^{raw} = Pd^{target} + Pd^{geology}$$

where the ideal operator P is defined such that the geology response is in the null-space of the operator, i.e., $Pd^{geology}=0$. The operator P is introduced into the data misfit of the inverse problem:

$$\Phi(r) = \left\| Pd^{raw}(t_j) - \sum_{k=1}^{\eta} PA(r_k)q_k(t_k) \right\|^2$$

We will solve the inverse problem using the 3 projection matrices P that were defined for the target picking approaches in the previous section. The size of the matrix will be different, since the cued survey uses 3 transmitters instead of one. The $P^{nonsoil}$ matrix is constructed by using cued background measurements to determine the expected direction of the magnetic geology secondary field. Once the direction of the field is determined, we define a pair of orthogonal vectors perpendicular to the field direction. The total number of Rx/Tx combinations are 3 Transmitters x 5 Receivers x 2 orthogonal directions, resulting in 30 decay soundings.

A difference matrix is constructed in the same manner as was described for the target picking case. For cued measurements, we have additional symmetry pairs due to the two horizontal component transmitters that are fired in static mode surveying. Figure 152 compares the decays for one of the receiver pairs. For these examples, we only consider pairs Rx1/Rx5 and Rx2/Rx4. The total number of Rx/Tx combinations are 3 Transmitters x 2 Receiver pairs x 3 receiver components, for 18 decay soundings. In future work, we can consider forming additional receiver pairs, e.g., adjacent receivers Rx1/Rx2, etc.

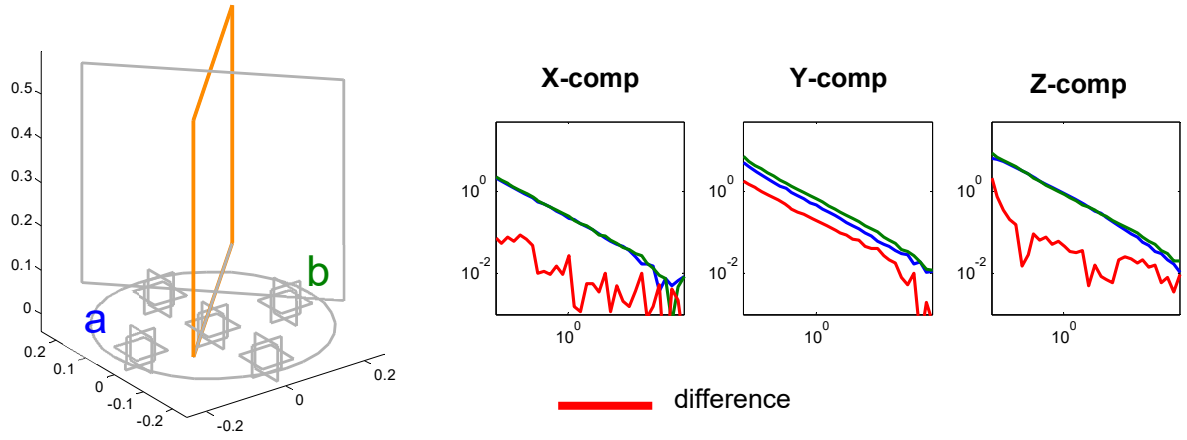

Figure 152. An example of reducing background signal by taking differences between receivers.

The transformed data has fewer decays than the 45 decays that we would have with 3Tx x 5Rx x 3 components. With fewer decays available, it will be necessary to determine if the transformed data are able to constrain model parameters. Of course, the multi-sounding inversion approach may provide a way to alleviate this problem. In addition, we note that the effectiveness with which the gradient matrix can null the soil signal will depends on the smoothness of the ground and how parallel the sensor head is to the ground.

We invert the IVS data in Figure 151 by using the P-matrix transformation. We demonstrate the technique by combining the $P^{nonsoil}$ and P^{diff} matrices:

$$P^* = \begin{bmatrix} P^{diff} \\ P^{nonsoil} \end{bmatrix}$$

In Figure 153, we compare the measured data (blue dots) with the predicted data (green dots) for data when the Z-transmitter is firing. We note that the objective is not to fit the measured data, but a transformed version of the measured data (i.e., P^*d).

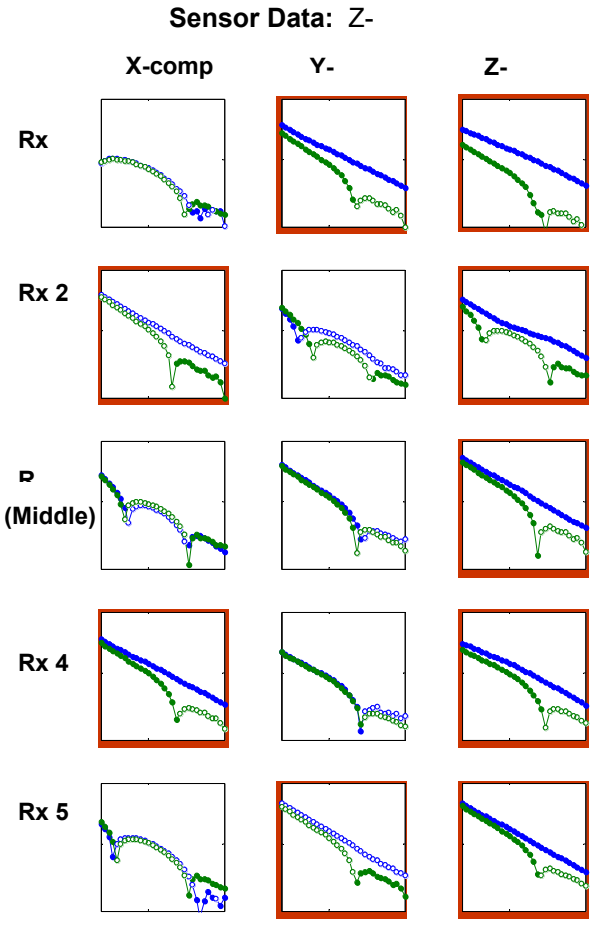

Figure 153. Fitting result for Z-transmitter. Blue symbols represent observed data, and green symbols are predicted data. Plots with a red outline are components that contain soil response. Plots without a red outline represent MPV receiver components that are the azimuth components of outer cubes, or horizontal components of the center, cube.

The transmitter/receiver pairings that are coupled to the magnetic soil response are outlined in red. For these soundings, we see that the observed data follows the characteristic viscous remnant magnetization decay since we are not subtracting out the background response. The predicted data (green) for these soundings do not match the observed data, since we are not fitting the magnetic soil response. The soundings plotted without a red border represent components that are not coupled to the soil response (i.e., the horizontal components at the center of the transmitter, and the azimuth components on the outer receiver). We see that for these soundings, the predicted data does fit the responses. The actual data fit is shown in Figure 154 and Figure 155. The non-soil components are plotted in Figure 154, and the gradient components are plotted in Figure 155. The predicted data matches the projected sensor data well.

Figure 156 compares the recovered polarizabilities when inverting the data with different P matrices and when using the standard background subtraction method with optimal scaling. The different methods produce, approximately, the same level of fit to the library polarizability for a small ISO.

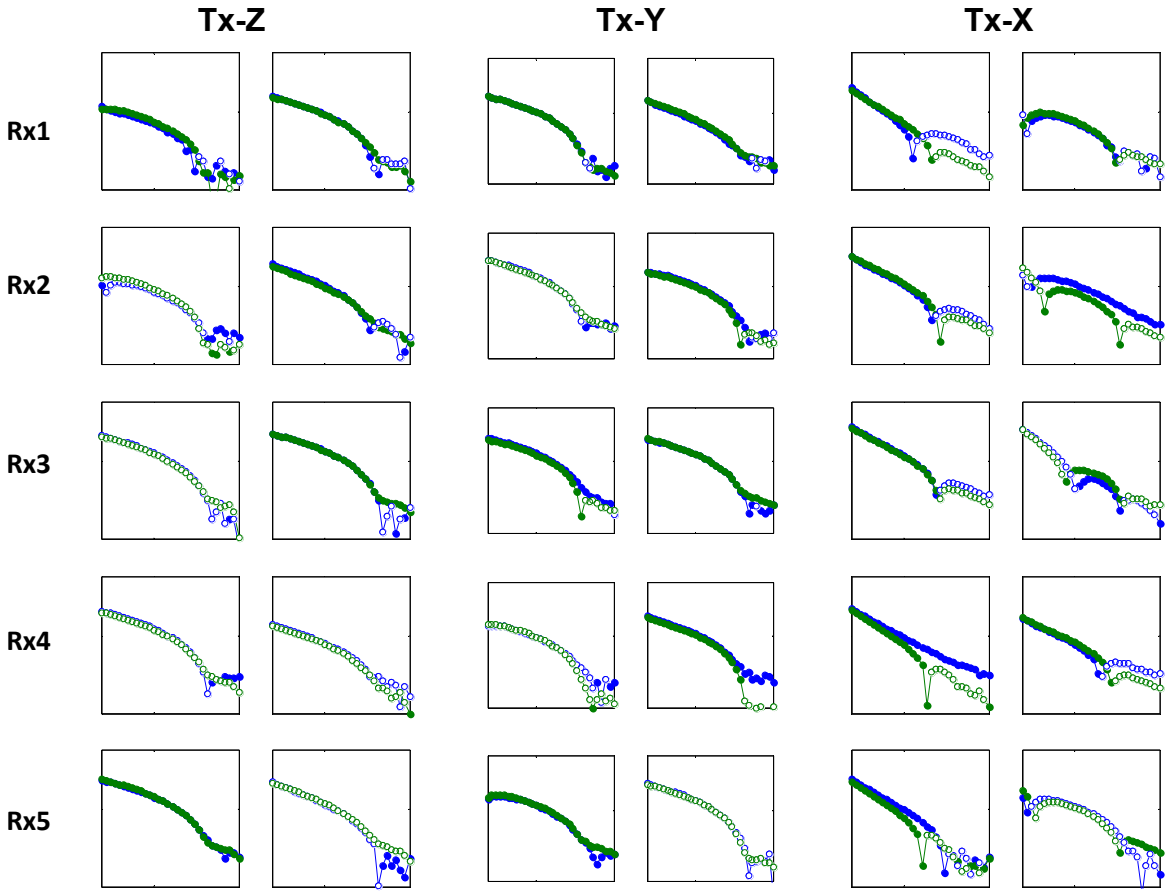

Figure 154. Non-soil component data. For each receiver cube/transmitter combination, there are a pair of directions that are orthogonal to the direction of the secondary field.

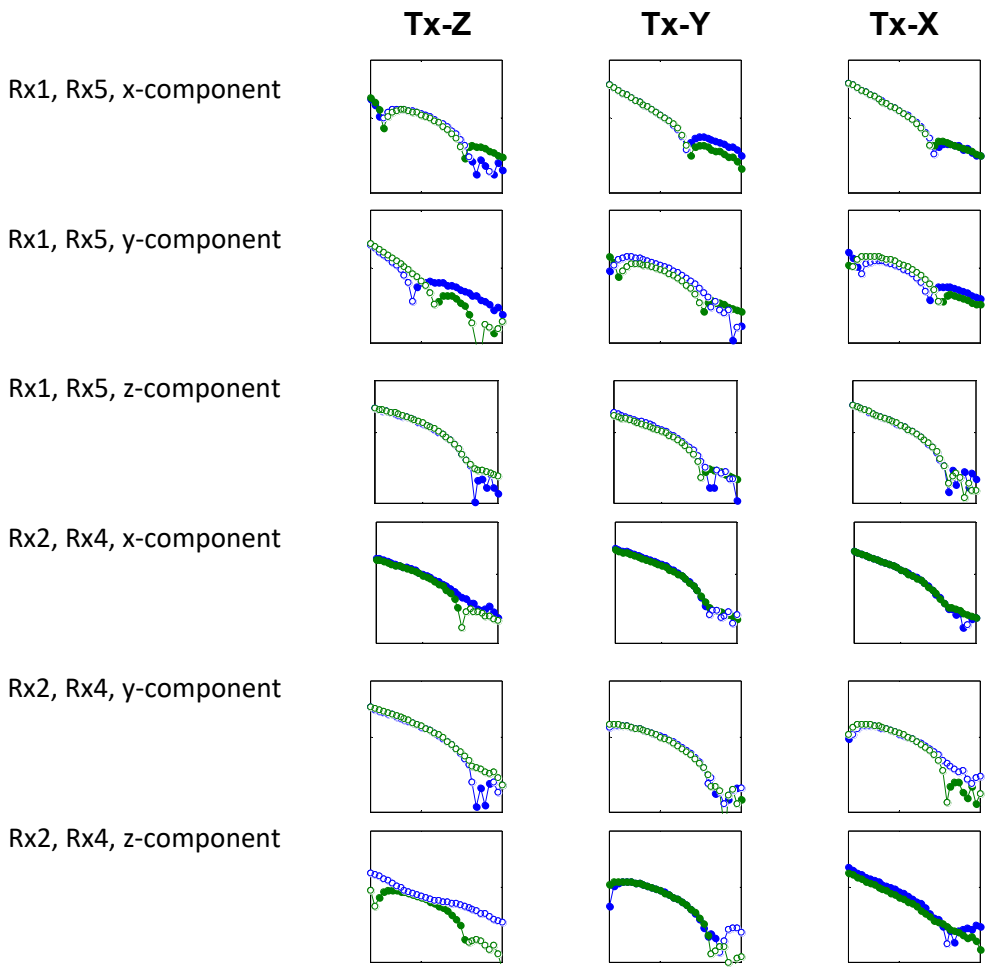

Figure 155. Fitting gradient data components

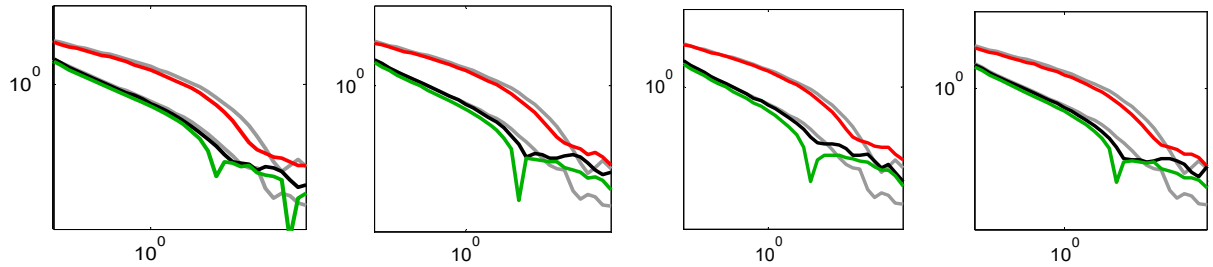

(a) $d = d\text{-}k\,d^{bg}$ with k=0.6

(b) Gradient data and non-soil components: P^*

(c) Gradient data only P^{diff}

(d) Non-soil component: $P^{nonsoil}$

Figure 156. Comparison of recovered polarizabilities when inverting with background correction and P-matrix.

We proceed to invert all the cued IVS data for the shallow small ISO and the Medium ISO. Figure 157 plots the set of recovered polarizabilities using the background subtraction without scaling the background measurement, and the set of recovered polarizabilities when inverting the non-background corrected data that has been transformed with the P matrix. When inverting the small ISO data, it is clear that the inverting the transformed data produces more accurate estimates of the small ISO polarizabilities. Inverting the medium ISO data with the default background correction produces accurate recovery of polarizabilities. The background correction is appropriate for this target location. When inverting the transformed data, there may be a slight improvement in the amplitude of the primary polarizability, but there is a greater spread in the secondary polarizabilities.

Further study is required to determine the ability to understand how the polarizability recovery performance is affected by transforming the data. Future work includes studying limitation of the approach by inverting various scenarios that are modeled synthetically by adding forward modelled target responses to background measurements acquired in the field.

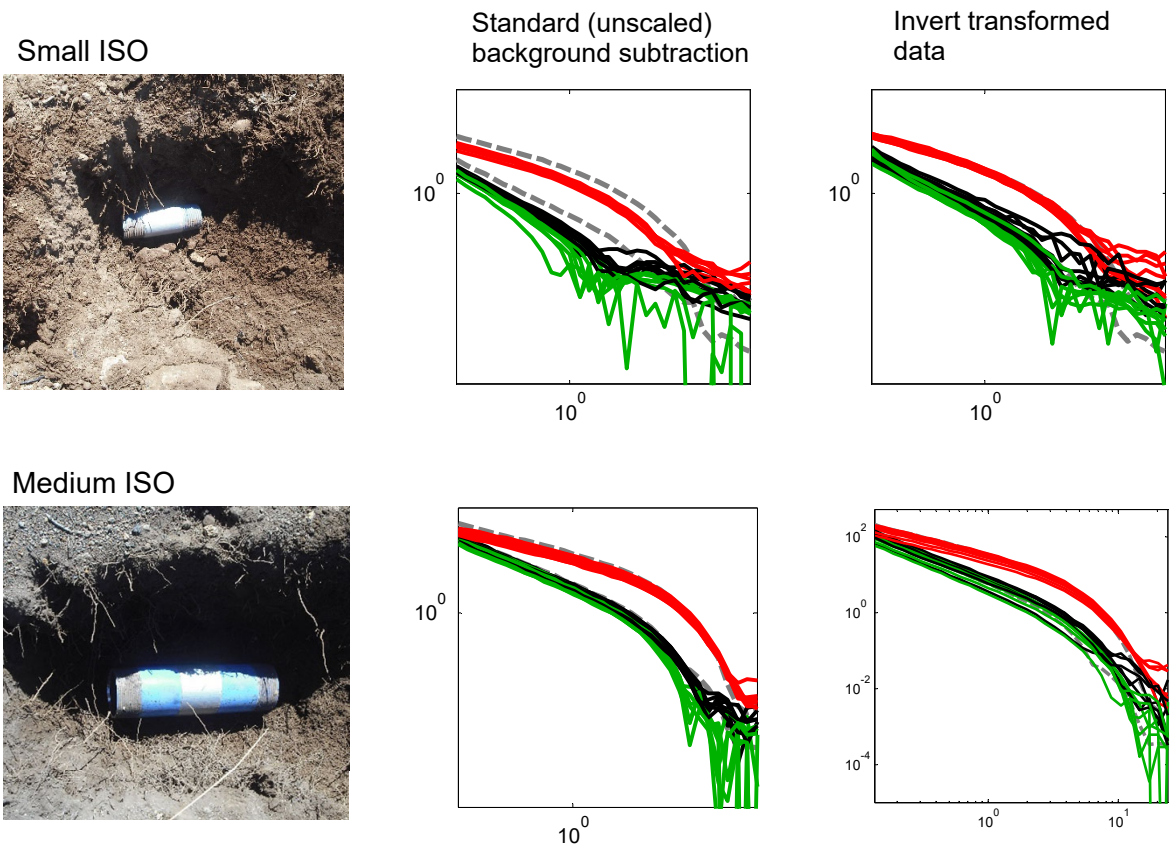

Figure 157. Apply method to all IVS data over the small ISO and the medium ISO

Processing TEMTADS data at Redstone Arsenal, AL

As part of an ESTCP demonstration at Redstone Arsenal, we processed cued and dynamic data acquired with the TEMTADS 2x2 sensor. The Redstone Arsenal site featured high levels of both geologic and viscous remnant magnetization background noise. Figure 158 plots the data from Grid R17 at Redstone. The coaxial, z-component measured at the center of each of the 4 receivers are gridded. Surprisingly, the amplitude of some of the background responses are comparable to what was encountered in Waikoloa, Hawaii. Dynamic TEMTADS data were used for detection, and anomalies were then interrogated with a cued measurement.

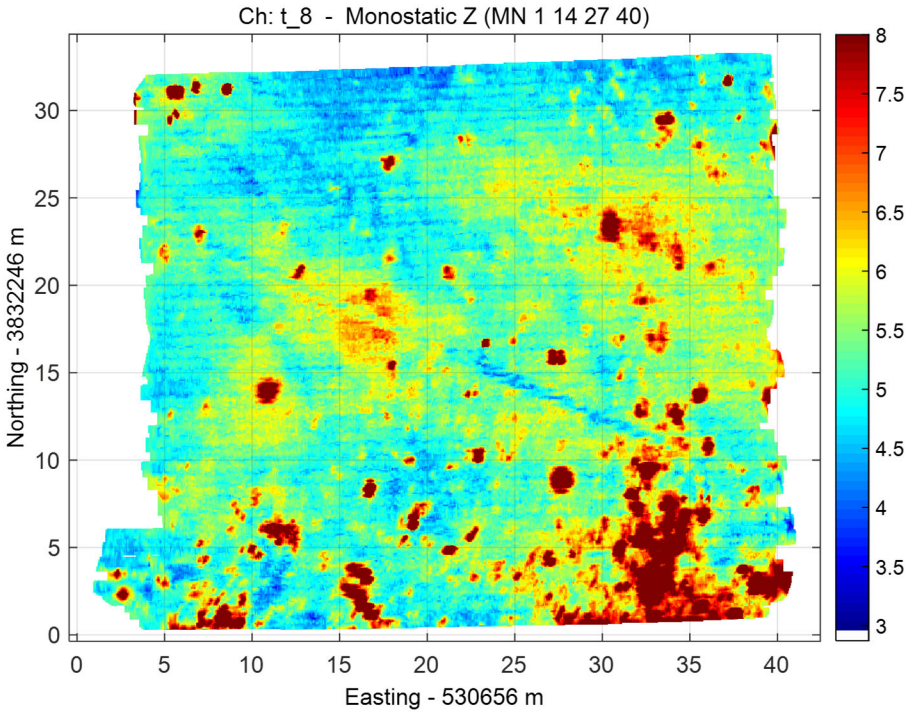

Figure 158. Example of geologic response at Redstone: Grid R17

Processing Cued data

Figure 159 compares TEMTADS 2x2 soundings with the cart on the ground and in the air. The data was acquired at a location designated for background measurements (i.e., the location was confirmed to be clear of metal objects). The sounding with the instrument in the air is plotted in blue. The largest self-response is recorded by the coaxial, z-component receiver (i.e., Rx-4, Z-comp). The red lines are the background measurement with the TEMTADS on the ground. For these plots, the in-air measurement subtracted from the signal. For a single TEMTADS 2x2 transmitter firing, there are 12 decays measured by the 4 receivers that measure 3 orthogonal components of the field. Four of the 12 decays are less sensitive to magnetic soil noise. We see that for the horizontal components at the center of the transmitter, there is a null coupling to the background response. Additional null coupled components are Rx1, X-comp and Rx3, Y-comp since they are azimuthal components of the secondary field. The remaining receivers exhibit the characteristic viscous remnant magnetization decay.

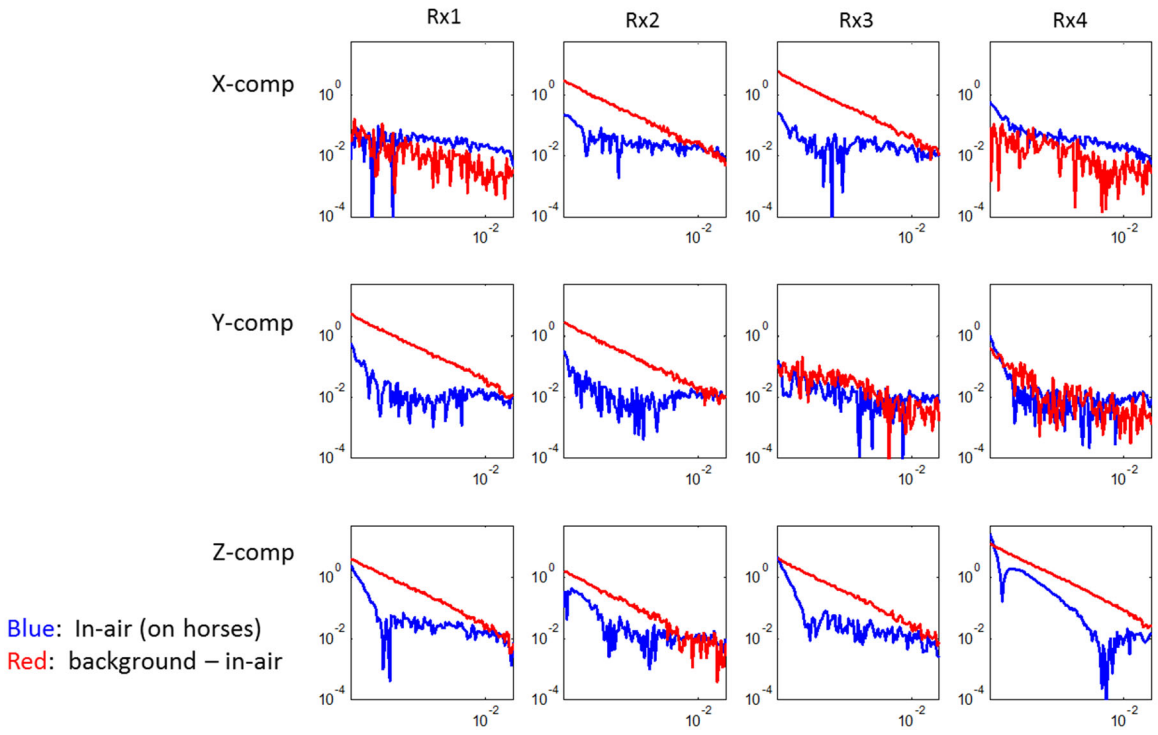

Figure 159. Comparison of in-air and background when Tx4 is fired

We compared inversions of cued IVS data when using the standard background location, and a sounding acquired at a location with Bentonite as the background sounding. The relative locations of the IVS seeds and the background locations are shown in Figure 160(a). Data over Bentonite were acquired to help determine if the Bentonite on site would affect classification on the site. Figure 160(b) compares the regular background data (blue) and the background collected over a pit with Bentonite. The Bentonite is slightly lower in magnitude than the standard background. At first glance, the subtle difference in amplitude does not suggest that there would be much difference in the result regardless of which background was chosen.

However, Figure 161 shows that this presumably small difference in background measurement does, indeed, affect the result. We choose one set of the IVS data collection for demonstration purposes. Subtraction of the background response from the designated background location result in an underestimate of the recovered polarizabilities, and misfit measures of 0.551 and 0.407 for the medium ISO and large ISO, respectively. When the Bentonite background is used, we find that the medium ISO polarizabilities have an improved misfit of 0.289. By using a lower amplitude background, the polarizabilities no longer underestimate the library result. The recovered Large ISO polarizabilities showed no improvement in estimated polarizabilities. In Figure 161(c) and (f) we plot the recovered polarizabilities for the medium and large iso, respectively when subtracted a scaled version of the background response from the designated background location. The misfit for the medium ISO is reduced to 0.268, and the misfit for the large ISO is reduced to 0.151. Although this improvement is subtle, a decision was made to process all the data at the Redstone site with multiple backgrounds. That is, for each anomaly, we would invert the data with different scaling factor of the background.

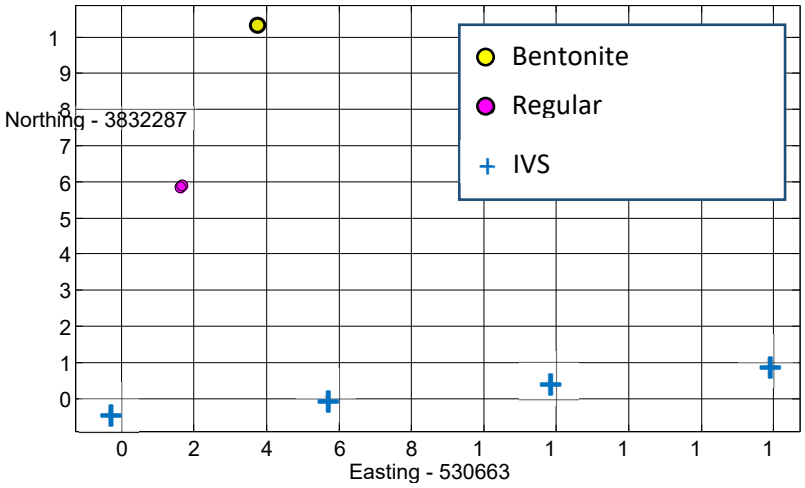

(a) Relative locations of IVS seed

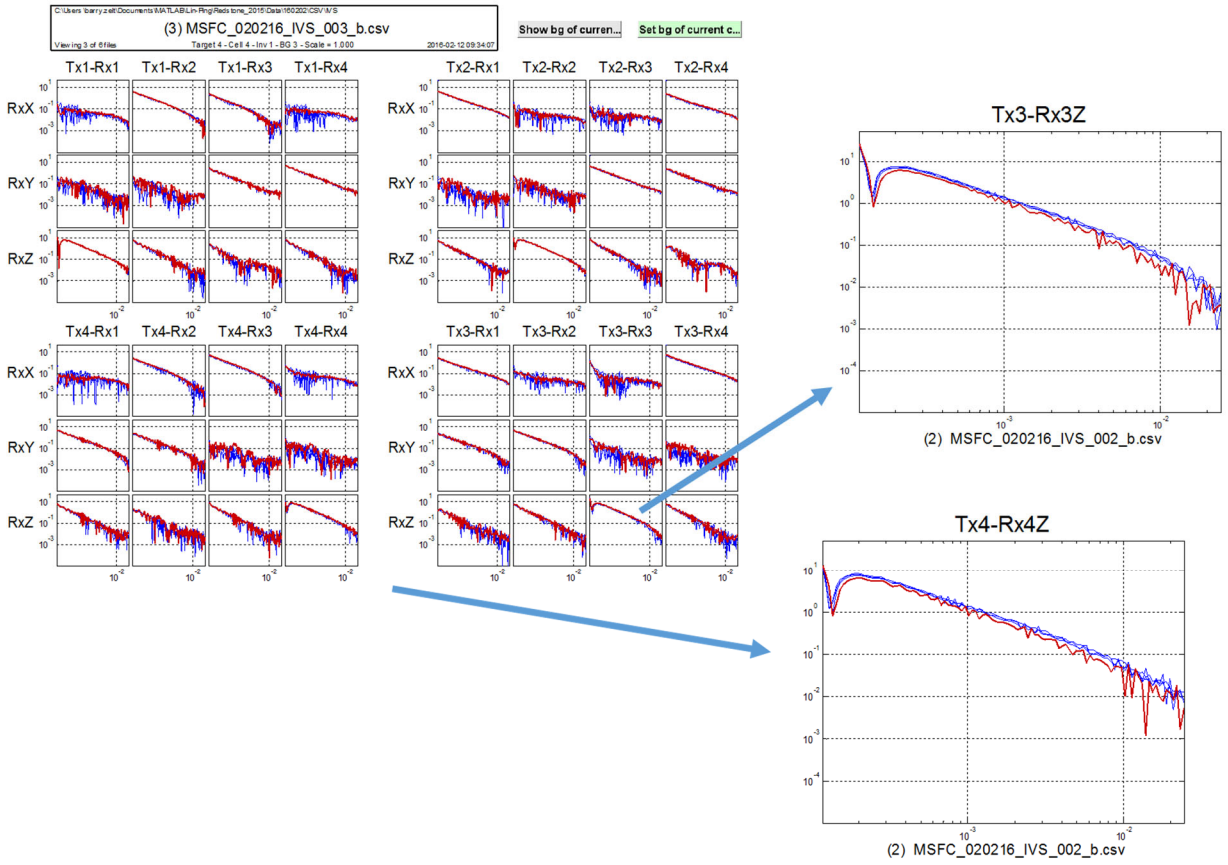

(b) Comparison of background responses

Figure 160. Comparison of background acquired over Bentonite, and background measurement acquired over the designated background location.

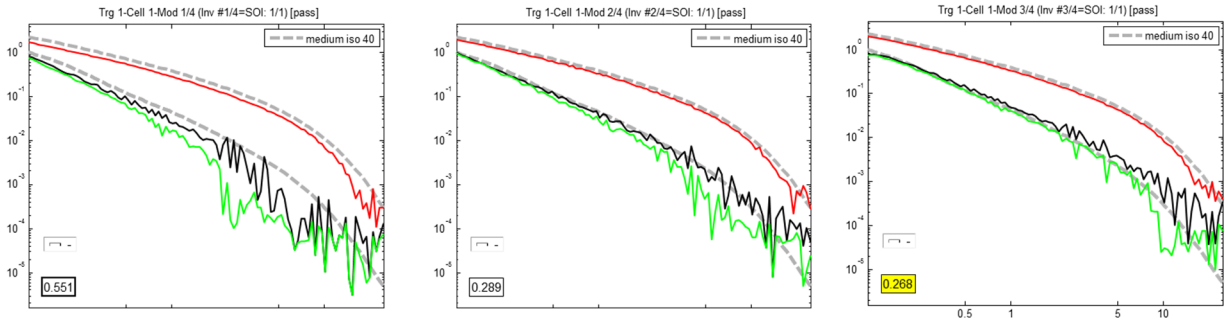

(a) Medium ISO (IVS 1), Regular background. Misfit = 0.551

(b) Medium ISO (IVS 1), bentonite background. Misfit = 0.289

(c) Medium ISO (IVS 1), 70 % of regular background. Misfit = 0.268

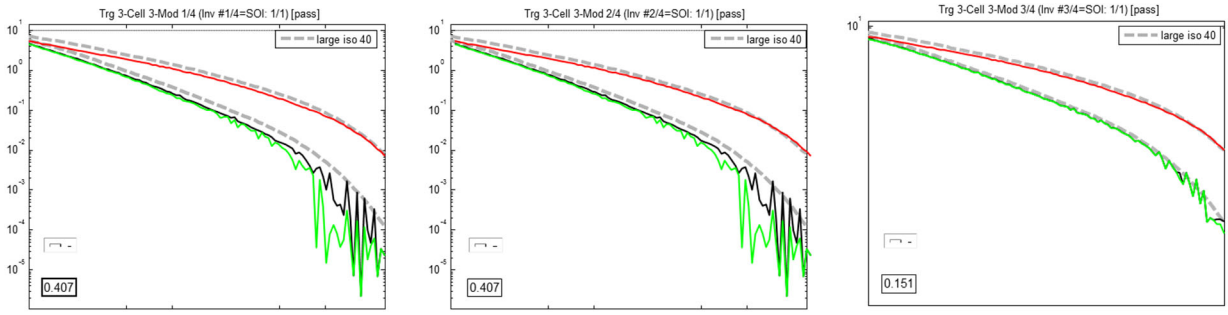

(d) Large ISO (IVS 3), Regular background. Misfit = 0.407

(e) Large ISO (IVS 3), bentonite background. Misfit = 0.407

(f) Large ISO (IVS 3), 70 % of regular background. Misfit = 0.151

Figure 161. Comparison of recovered polarizabilities from IVS data measurements, using different background measurements.

Dynamic data: TEMTADS, from most recent IPR

In the section "Calculating linear combinations that exploit secondary field shape for improved detection" (Page 175), we studied the use of non-soil components for improved detection. We apply the same approach here to TEMTADS 2x2 dynamic data.

Figure 162 plots the secondary field for each of the four TEMTADS transmitters. The transmitters are shown in yellow, with the secondary field due to magnetic soil plotted in red. We calculate a pair of orthogonal vectors that are perpendicular to the direction of the secondary field. Therefore, components of the secondary field along these directions will be due to non-geologic sources.

To project the data onto these orthogonal directions, a matrix $P^{nonsoil}$ is constructed. This matrix has dimension 32 x *Ntimes*, therefore reducing the number of soundings from 48 to 32. Figure 163 plots the decays collected along a short line of data acquired on a portion of the site without metallic targets. On the top row of the plots, is the measured decays with the instrument response subtracted. On the bottom row of plots, are the decays estimated by multiplying by the non-soil project matrix $P^{nonsoil}$. For comparison, the instrument response corrected raw data are plotted in the background in light grey. We can see that the projected data does not have the large characteristic soil decays in the raw data.

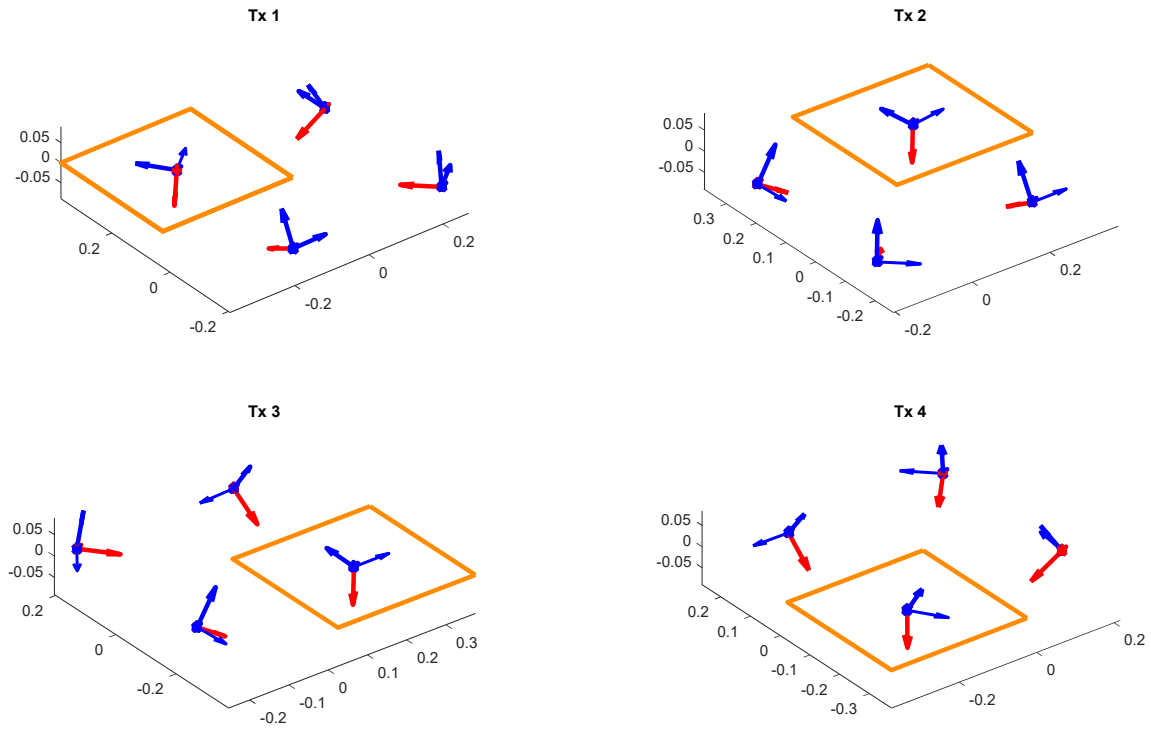

Figure 162. Orthogonal directions to the secondary field. Red arrows are the direction of the geology secondary field. Blue arrows are directions orthogonal to the geology response

$\mathbf{d}$ = Raw data – Estimated instrument response

Log (d)

d

Time (ms)

$\mathbf{d}^{p} = \mathbf{P}^{non\text{-}soil}\,\mathbf{d}$ = Projected data

Log(d)

d

Time (ms)

Figure 163. Comparison of in air corrected data and the data projected along the non-soil directions.

Detection performance with the projected data is investigated using data from Grid R17 that has been synthetically seeded with small ISOs. A uniform grid of target locations is defined. Seeds are separated by 2.5 m in both the East and West directions. At these seed locations, we add the response of a small ISO buried at a depth of 30 cm and in a random orientation. The detection threshold for a small ISO buried at a depth of 30 cm, is 0.7 mV/A if we are picking from the t=0.214ms time channel. This threshold corresponds to the TEMTADS 2x2 passing directly over a horizontal small ISO that is oriented in the along-track direction. The maximum possible signal is 4.65 mV/A, which occurs when one of the transmitter coils passes directly above a vertical target. In Figure 164(a), the gridded image of the vertical, coaxial data collected at t=0.214 ms is presented. The locations of the seeds are indicated by squares. Since the background signal varies from, approximately, 4 to 6 mV/A, we expect that it could be challenging to detect the horizontal ISO. In most cases, there is an anomaly within the black squares that mark each seed.

The non-soil components are calculated by multiplying the data by the matrix $P^{nonsoil}$. A $P^{nonsoil}$ matrix is calculated for each survey line of data. For each transect, we determine the shape of the soil model response by calculating the median value of the response for all soundings along the line. For each transmitter firing cycle (i.e., Tx1-4), the norm of the projected data is calculated. Figure 127(b) plots the gridded images of the amplitude of the projected data mapped to the center of the cart. The larger scale features due to magnetic soil that are seen in the vertical coaxial components, are not seen in the projected non-soil data amplitude. Individual anomalies appear wider than in Figure 164(a). This is because Figure 164(b) grids data that has a contribution from all Tx/Rx combinations, whereas Figure 164(a) grids only the data from the receiver at the center of the transmitter that is firing.

We compare responses along a 3 data transects in Figures 128 to 130. Figure 128 compares data acquired at a northing of approximately 15 m, in the local coordinate system. The top image of Figure 128 shows the cart path on the gridded data. The second plot from the top contains the data from all transmitter/receiver combinations acquired at t=0.214ms. The Easting location of the seeds are indicated by black triangles. The coaxial, vertical component is clearly most affected by magnetic geology. There is a vertical component data anomaly associated with each seed. The data components that are not affected by magnetic soil – i.e., azimuth directions in non-coaxial receivers, and horizontal components at the center of the transmitter – are plotted in the third plot. Although these responses do not have a non-zero offset related to the presence of magnetic soil, the seed responses are not significantly greater than the noise.

The fourth plot provides a more detailed look at the vertical, coaxial data. The TEMTADS cart is moving from west to east, and along a line that is not exactly parallel with a row of seeds. At the start of the line, the left side of the cart (receivers 1 and 4) is aligned with the row of seeds. At the end of the line, the right side of the cart (receivers 2 and 3) is aligned with the row of seeds. The relative position of the cart to the row of seeds explains why the anomalies on the left side of the profile are blue/purple (Rx1,Rx4) and anomalies on the right side of the profile are red/yellow (Rx2,Rx3). The seed at approximately x=19 m and x=36.5 m does not have a significant response. The low amplitude signal for the seed towards the end of the line (i.e., x=36.5 m) is due to the cart not passing over the seed (see top image in Figure 165). Figure 166(a) plots the small ISO responses that were added to the Grid R17 data.

The target signal for the seed at x=19 m is 1.68 mV/A in Rx4. For the data variations due to magnetic soil response, it would be difficult to detect this target using the standard approach of picking off of images from de-median filtered data.

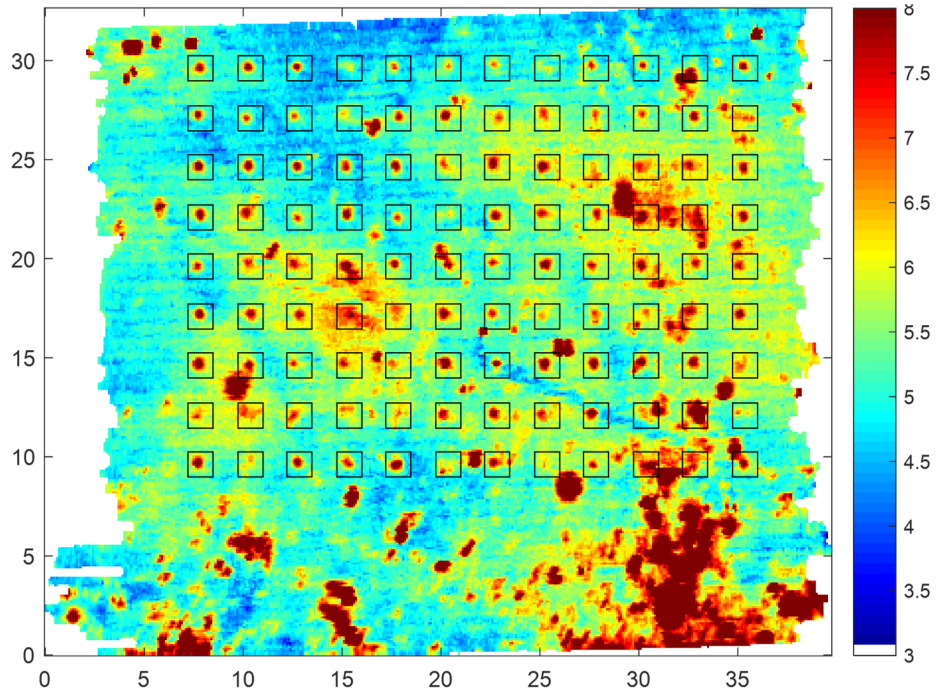

(a) Vertical component, co-axial data for t=0.214ms

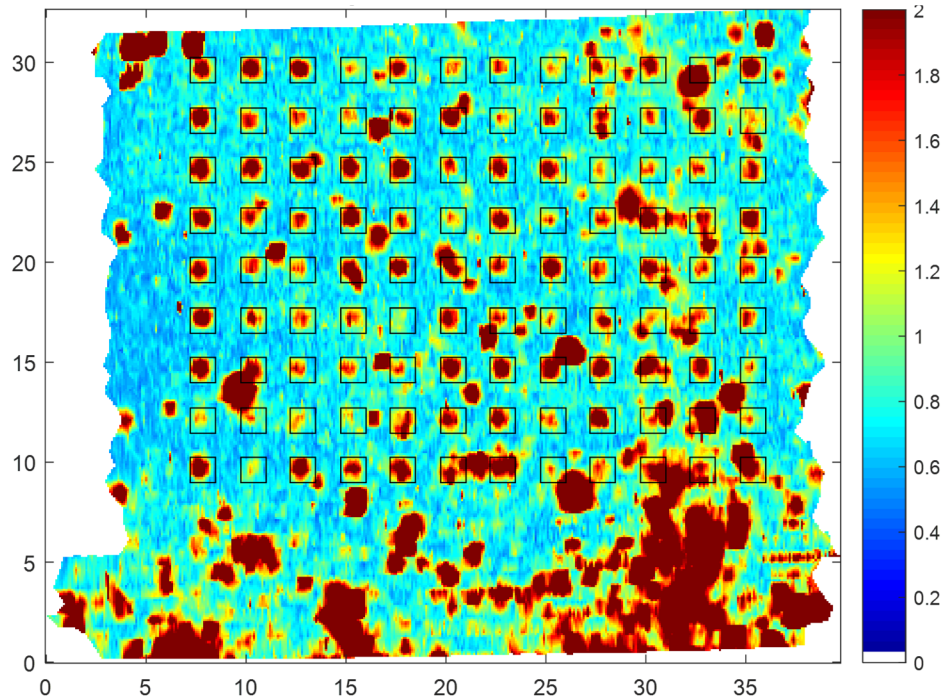

(b) Projected data. The norm of the non-soil components is mapped to the center of the cart and gridded.

Figure 164. A comparison of Vertical, Coaxial components (top) to projected non-soil data amplitude (bottom).

The bottom plot of Figure 165 contains the amplitude of the projected data. Ignoring the seed at x=36.5m, the projected data amplitude produces a distinct peak at each of the seed locations. In particular, the seed located at x=19.5 that would be difficult to detect directly from the sensor data, would be easier to pick using the projected data amplitude. The seed at x=24m is located in a region there is a low in the background response. Detection of this target might be difficult when using amplitude detection. A contributing factor for the relatively low data amplitude is that the cart passes directly above this target. In this sensor/target geometry, the TEMTADS measures a low amplitude response, since the target lies directly beneath the edge of the transmitter coils. However, the projected data uses responses from data measured from all the transmitters, and combines them. As a result, there is a significant response when the TEMTADS is directly above the target. Figure 165 shows that the all four receivers produce an anomaly in the profile data. By combining these responses in the projected data, a relatively large response is produced.

Figure 167 illustrates that the $P^{non\text{-}soil}$ projected data is similar to a combination of the responses from all the transmitter firings. The average response of the four coaxial, vertical component synthetic target response data is plotted in orange, and the amplitude of the projected data is plotted in blue. The anomalies in the two profiles have similar relative amplitudes.

In Figure 165, we see that the projected data amplitude does not have the spatially varying background responses seen in the vertical, coaxial data. However, there appears to be a constant background response that is slightly less than 1mV/Amp. This dc signal in the projected response is related to inaccuracies in the direction of the soil model. Figure 168 compares the projected data of the target response only (blue) and the combined target and background response (red). Unlike the raw data case, the combined target and background projected data amplitude response, is not simply the linear combination of the 1mV/Amp background signal and the targets. Further investigation is required to understand this signal.

Figure 169 and Figure 170 compare the projected data to the raw data for a couple of other lines (i.e., Line 47 and 66). The results for Lines 47 and 66 are similar; the projected data amplitude provides an improved measure of detection than the vertical coaxial data.

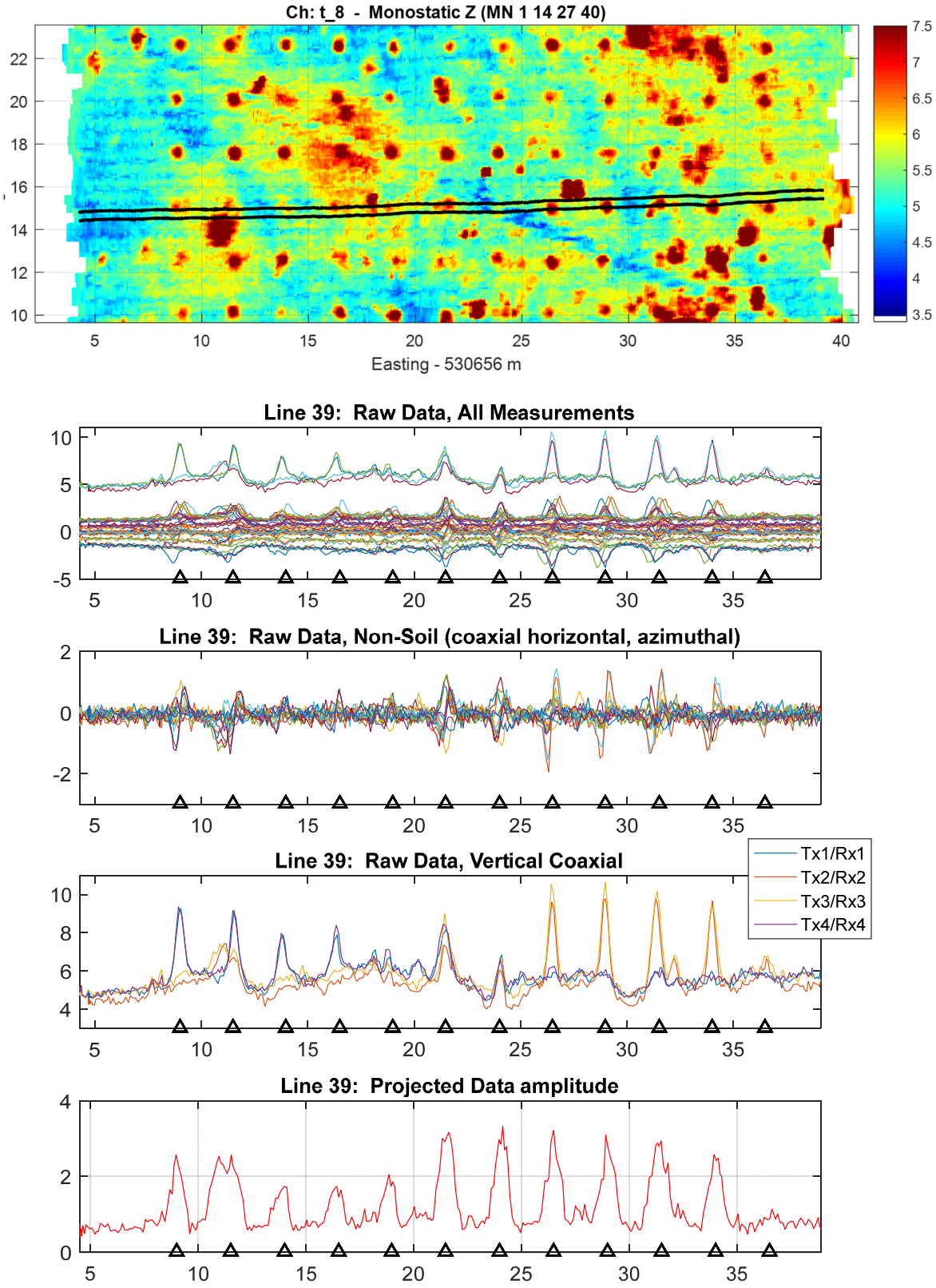

Figure 165. Raw and projected data for Line 39. More distinct anomalies can be found in the projected data for seeds at x=19 m and x=23.5m.

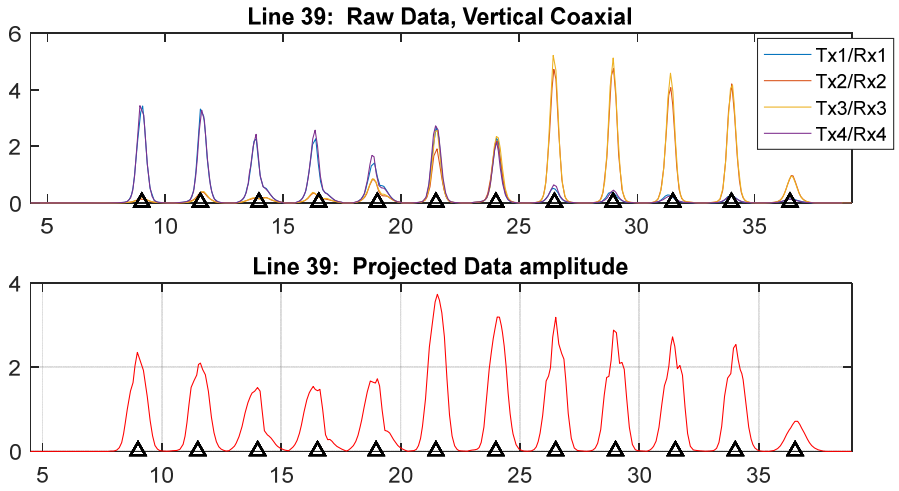

(a) Line 39. Y is approximately 15m.

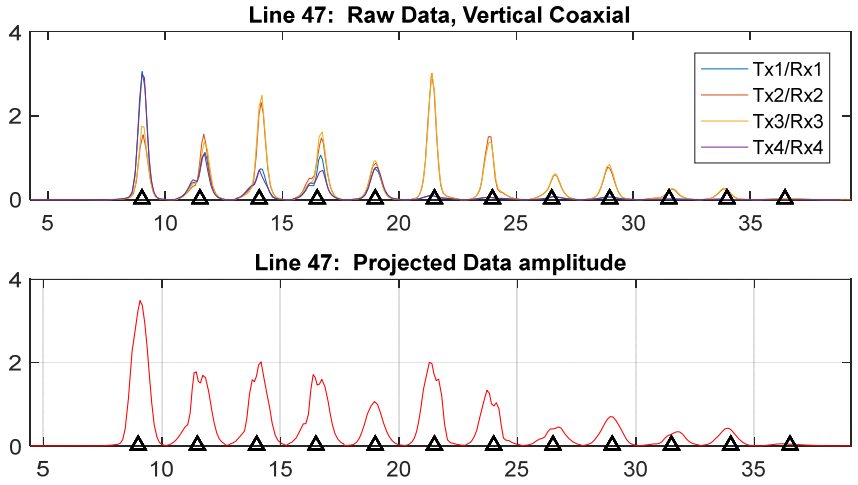

(b) Line 47. Y is approximately 17m.

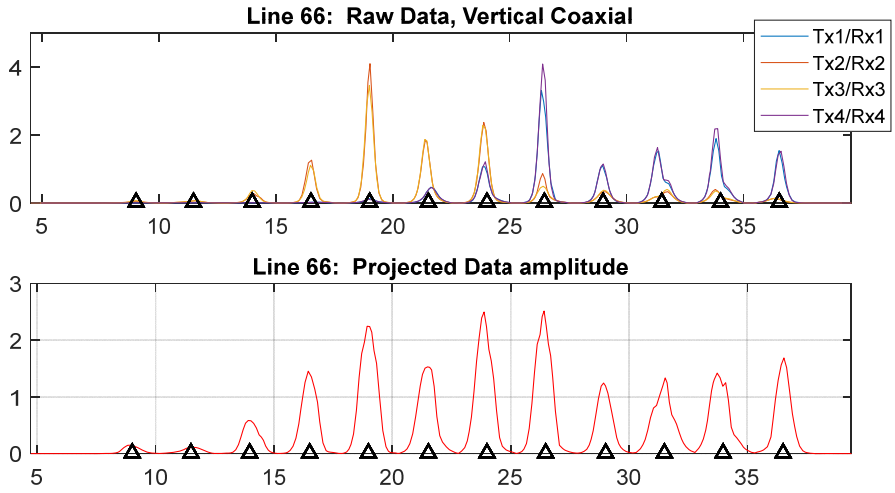

(c) Line 39. Y is approximately 25m.

Figure 166. A comparison between raw, vertical coaxial data and projected data.

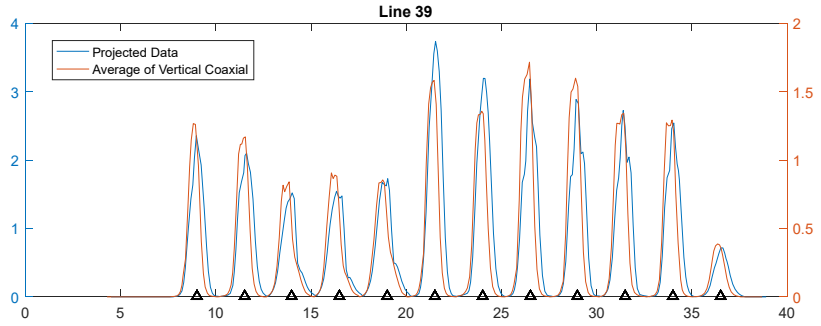

(a) Line 39. y is approximately 15m.

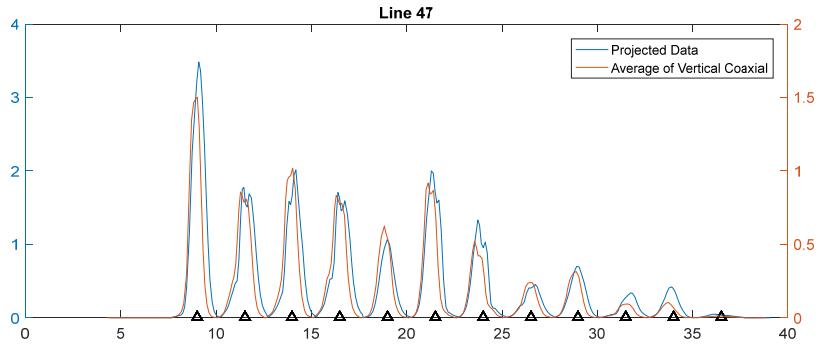

(b) Line 47. y is approximately 17m.

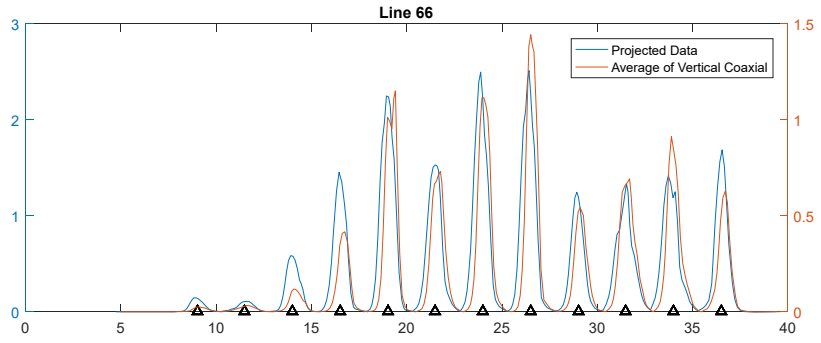

(c) Line 39. y is approximately 25m.

Figure 167. Comparison of projected data ampliutde and the average of the vertical, coaxial data.

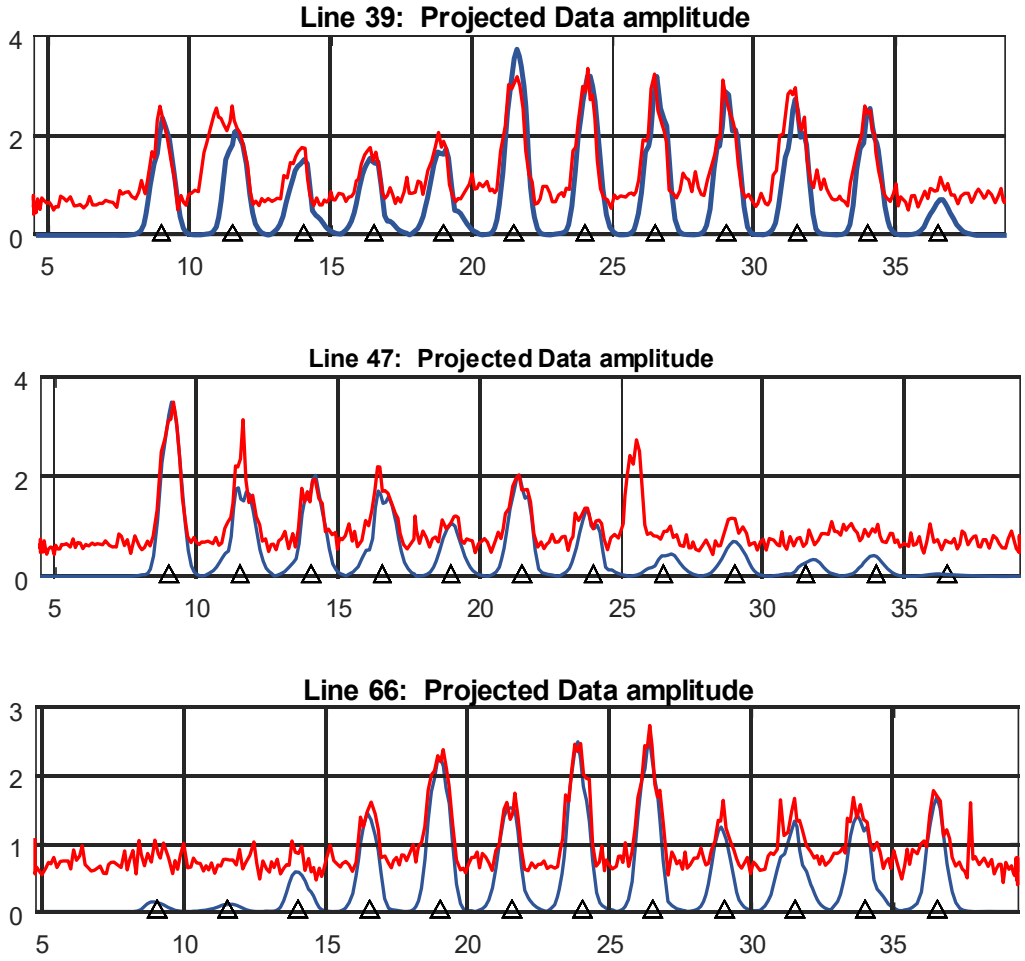

Figure 168. Comparison of the projected data from the seeded data set, and the projected data calculated from the target responses only.

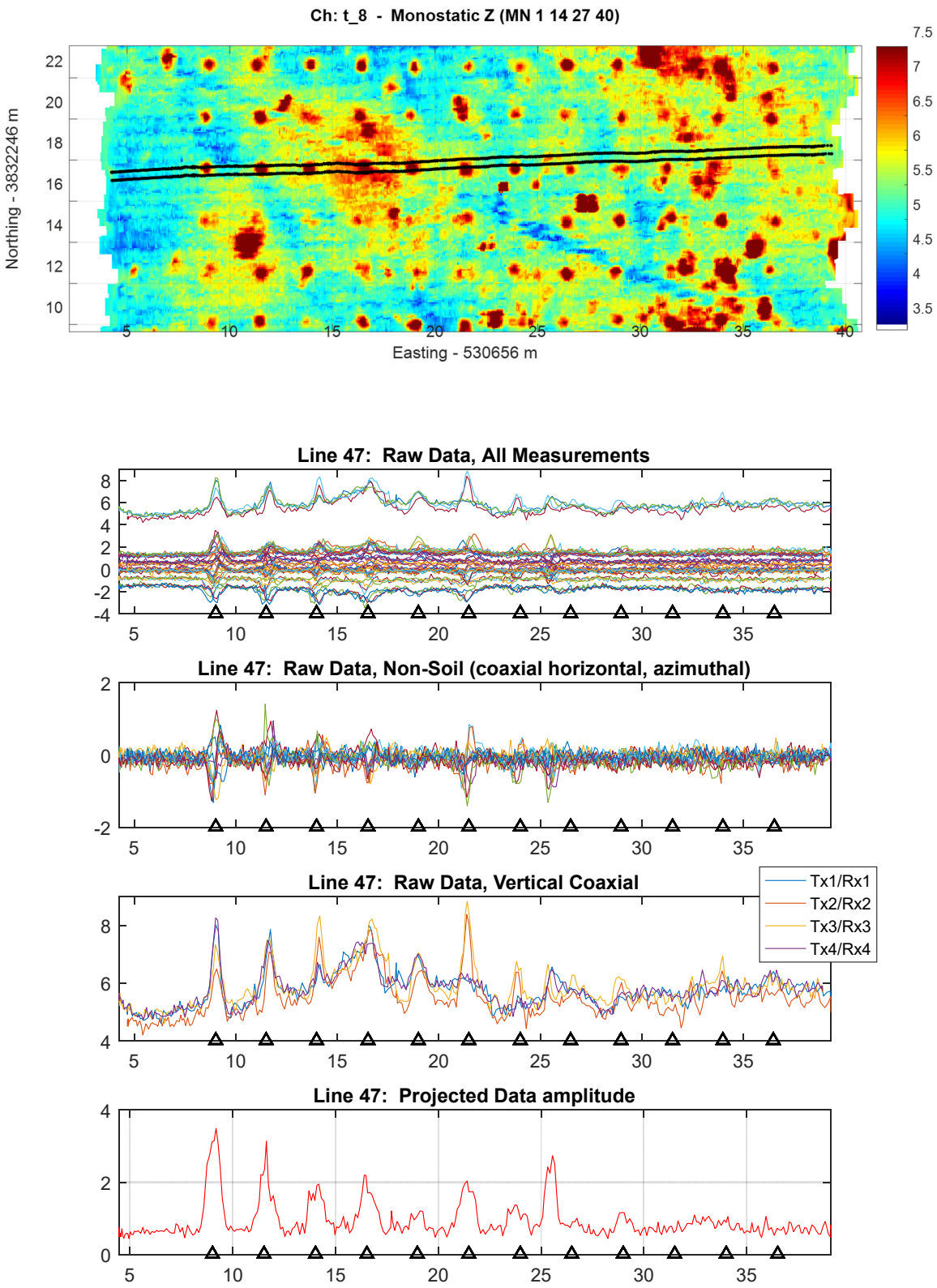

Figure 169. Raw and projected data for Line 47. A more distinct anomaly can be found in the projected data for a seed at x=17.5 m, which is located in a region of high magnetic susceptibility.

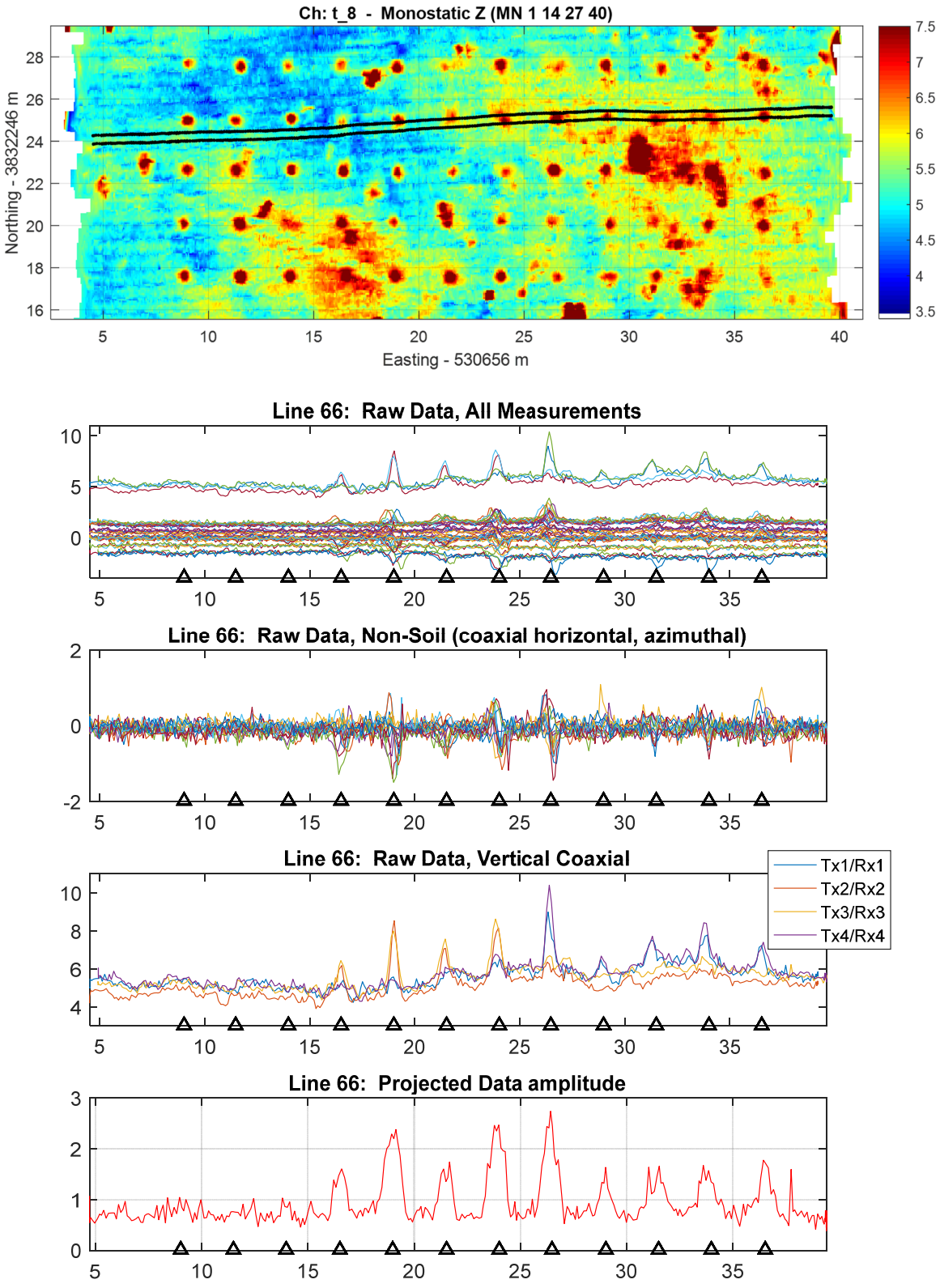

Figure 170. Raw and projected data for Line 66.

4. Using Figure of Merit for improving data QC and assessing inversion reliability

Figure of Merit metrics are an important part of our workflows for processing both dynamic and static data. These metrics help us to efficiently QC inversion results, and to identify spurious models that should not be included in the classification process. We have presented a number of results during Interim Progress Reviews. We present some examples here, but will provide a complete report of our progress in our next report.

We use TEMTADS 2x2 cued data acquired as part of the ESTCP demonstration at Castner Range, Fort Bliss. Figure 171 shows our GUI for reviewing metrics in dig list order. In this view, the analyst chooses a number of different metrics for inspection and comparison. The analyst is able to quickly identify targets and models with an anomalous metric, and review data and inversion results since this GUI is linked to the interactive QC tool.

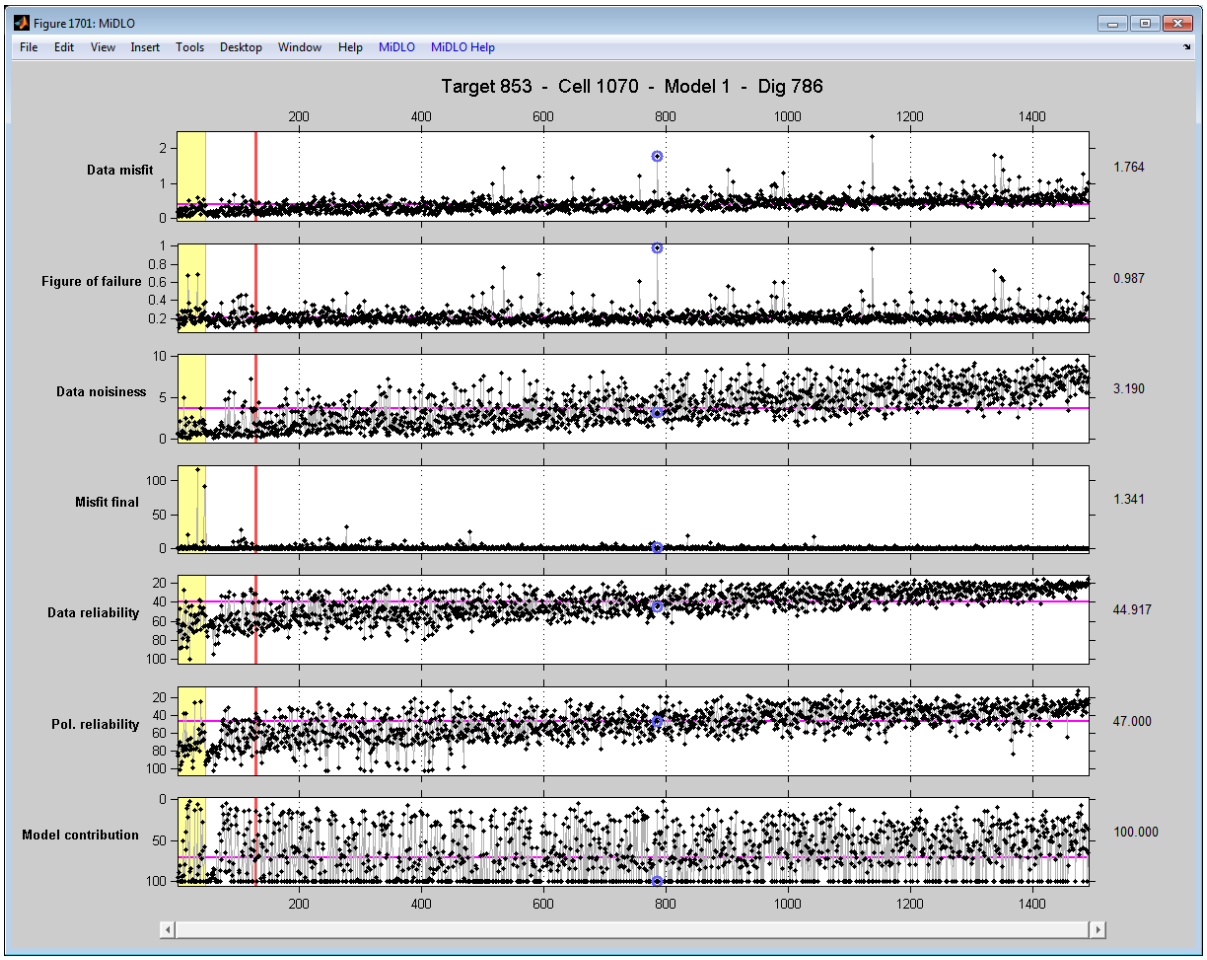

Figure 171. Plotting metrics in dig list order. Once a dig list is created, we plot the metrics as a function of dig number. If there are relatively anomalous values of a metric, the analyst is able to quickly identify the problem model and data. This GUI is directly linked to the interactive QC tool for efficient checking of any problematic targets.

Figure 172 takes a closer look at the BDU metric applied to the same Castner Range TEMTADS 2x2 dataset used in Figure 171. This interface plots various metrics as a function of model number or data cell – or plot the metrics against each other. The BDU metric helps identify models that are artifacts of multi-source inversions. When there are more sources than actual targets present, there are sources that are unconstrained. In these cases, it is possible to have a deep source with large amplitude polarizabilities. These spurious sources do not have the typically smooth polarizabilities of metallic targets with sufficient SNR, but, rather, they tend to look "ugly" since they often model the noise in the measurement.

In Figure 172, Model 4 of Target 1147 is highlighted by a square, and has a BDU score of approximately 0.025. The majority of models have a BDU of less than 0.005. Digging results found that Target 1147 was a 37 mm fuse (Figure 173(a)). The data for Target 1147 was inverted for 1, 2, and 3 source inversions. The source for the single source inversion is labelled '1', the sources for the two-source inversion are models '2' and '3', and the sources for the three-source inversion is '4', '5', and '6'. Therefore model 4, is a source from the 3-source inversion. The locations of the recovered sources are plotted in Figure 173(b). The yellow circle indicates the location for dipole source 4. The source is on the Y=0.5 m inversion bounds, since the data is not constraining its location. Figure 173(c) shows that the depth of dipole source is not constrained by the data. We note that, in our current processing SOPs, the source location inversion bounds are set greater than 0.5 m.

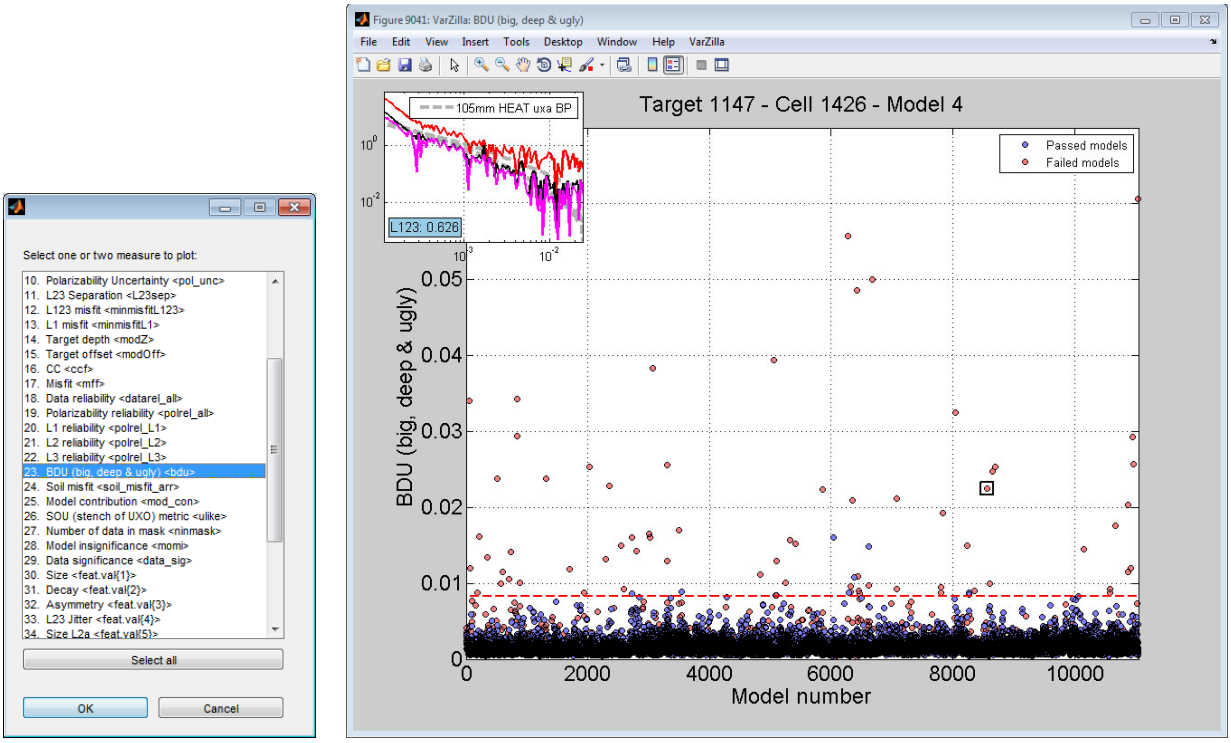

Figure 172. The BDU metric applied to TEMTADS 2x2 data. On the left, is the metric selection GUI. On the right is the BDU metric applied to the TEMTADS 2x2 Castner Data. We highlight Target 1147, which appears to have an anomalously high BDU value. The polarizability for model 4 is noisy (see inset), but matches the amplitude of a 105 mm HEAT.

Figure 173(d) compares the recovered polarizabilities for the 1, 2, and 3 source inversions. The three-source inversion has 2 sources (i.e., models 5 and 6) that match the sources from the 2-source inversion (i.e., models 2 and 3). Model 4 is problematic since it has the lowest polarizability misfit (0.626) since it has the same amplitude of the '105 mm HEAT uxa BP' polarizability, and the other polarizabilities are smaller than a 30 mm polarizability (note: the minimum size target at the site was a 37 mm projectile). Since the polarizability misfit defines the dig order, this target would be ranked higher than it should be due to the inclusion of this spurious set of polarizabilities.

In practice, an analyst would define a cutoff value, above which the models should be further investigated. The analyst can do a visual QC of this limited subset of model, ensuring that the analyst puts greatest focus on the problematic targets. In Figure 172, a cutoff of just below 0.01 is defined and any models with a BDU greater than this cutoff is flagged for potential deletion. Prior to deleting this subset of models greater than the cutoff, the analyst would review the data and inversion for each member of the subset. The analyst would review the inversion result for Target 1147, and conclude that model 4 should be excluded from classification.

Figure 174 contains an example for the "Figure of Failure" (FoF) metric. This metric combines the data misfit and data noisiness. If the data has sufficient SNR and the data misfit is poor, then the FoF will have a high value. A high FoF suggest that the inversion is not fitting the data well. Inversions with high values of FoF are candidates for classification as "Can't Analyze". In Figure 174, we consider Target CR-806. Model 1 (i.e., the single source inversion model) has a FoF higher than the cutoff. The analyst, would review this model and conclude that that the receiver Rx1 is not working properly. The inversion results for this target would be considered invalid, and the target would be assigned a "Can't Analyze" designation.

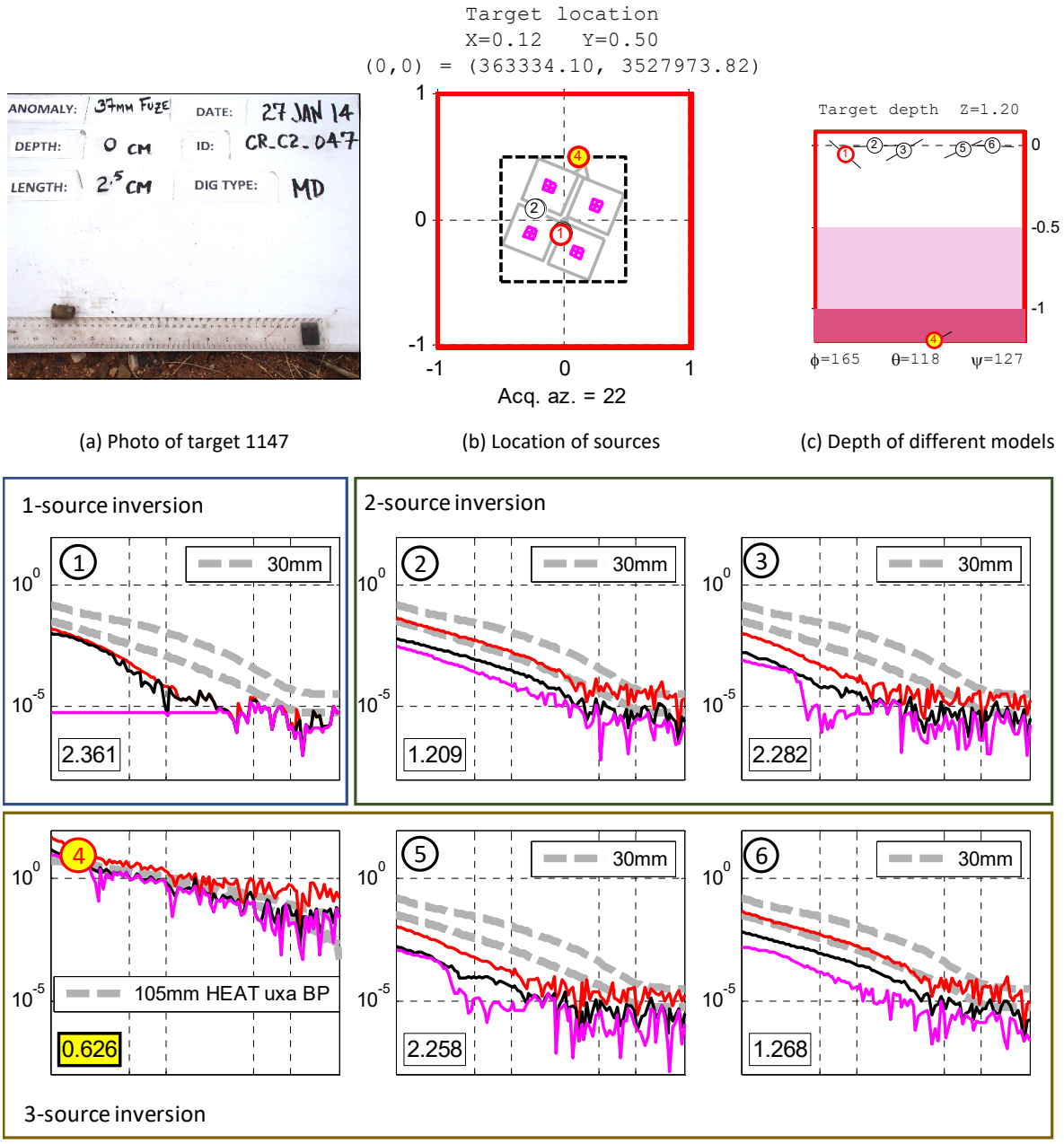

(a) Photo of target 1147 (b) Location of sources (c) Depth of different models

(d) Recovered polarizabilities from the 1, 2, and 3 source dipole inversions. The polarizability misfit is in the lower left of each plot.

Figure 173. Dipole inversion results for target 1147.

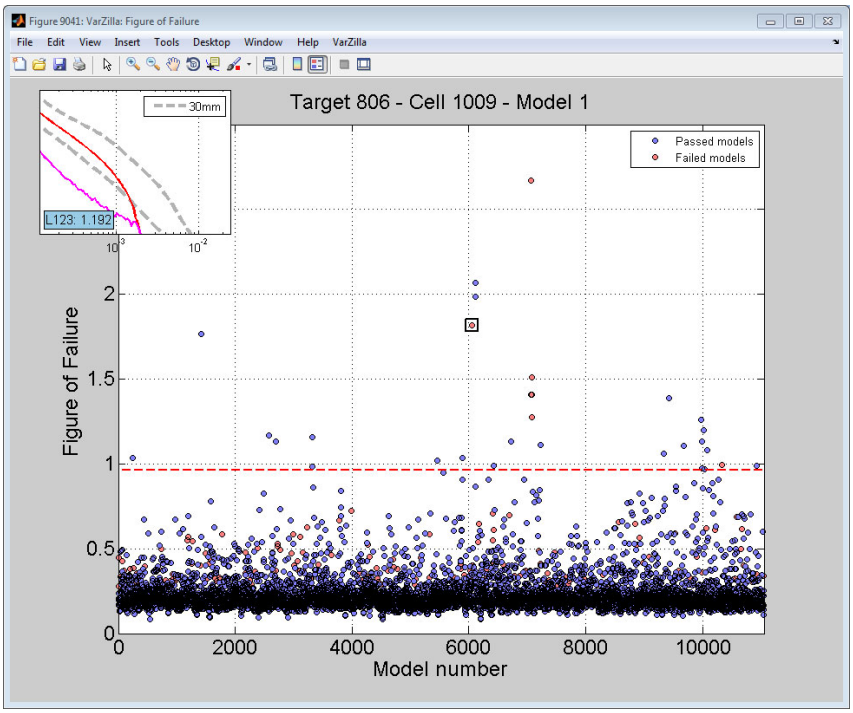

(a) Figure of failure metric applied to Castner Range TEMTADS 2x2 cued data

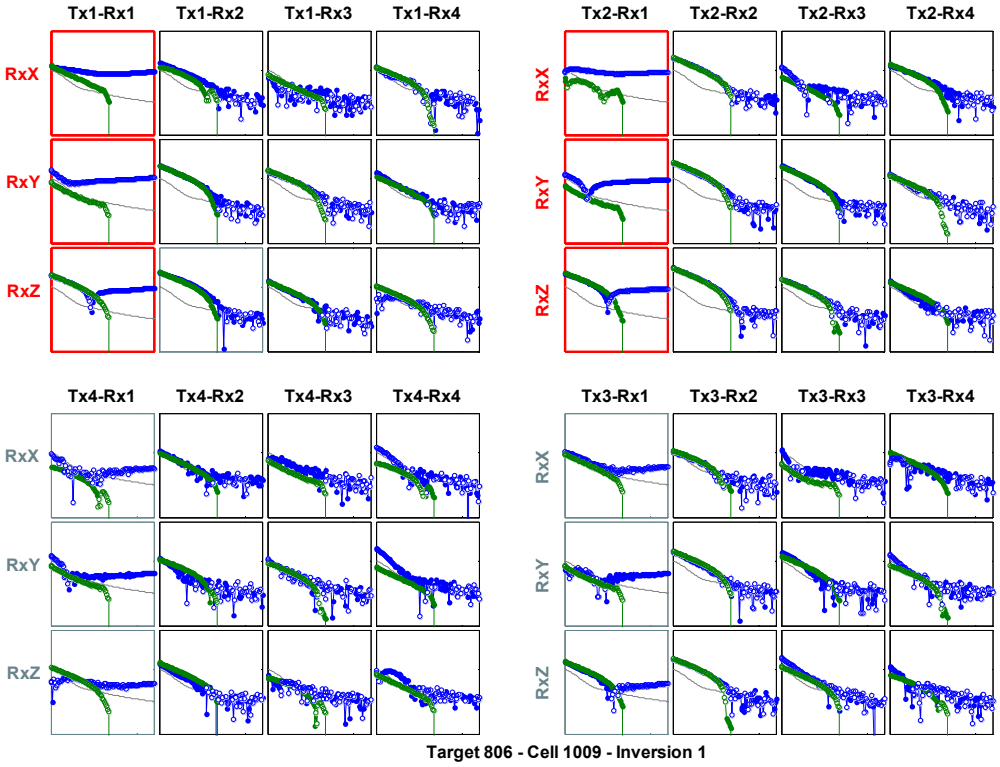

(b) Data fit for inversion of Target CR-806, which is highlighted by a square in (a)

Figure 174. The Figure of Failure (FoF) metric

5. Identification of unique targets of interest

For this task, there were two subtasks: “Subtask 5.1: Classification without a priori information on target types” and “Subtask 5.2: Identifying “Ones-sies/Two-sies” by Library matching to an extensive ordnance Library”. The work performed under this task had similar objectives with work in SERDP MR-2226. Therefore, some of the work performed for MR-2318, has been reported in MR-2226. An article containing work from this task is "Risk Assessment for Unexploded Ordnance Remediation" in the journal "Stochastic Environmental Research and Risk Assessment." March 2015, Volume 29, Issue 3, pages 1051-1061.

Since the publication of the article, we have continued testing and comparing non-library methods and using an extensive library for classification. There are a number of non-library matching based developed within this project. These rule-based methods use a number of data and inversion-based metrics. An example of these metrics is found in Figure 175. The CCR score for a given model, determines which metrics fall within a specified range for TOI, and awards a point. These points are summed to obtain the final score. This score may be a useful for identifying targets that are not in the library, for identifying items that could be considered for analyst calibration digs (e.g., training digs), or as a QC step.

Metric (m_i)	Description	Formula	TOI range (A_i)
Size	Amplitude of pol.	$\text{size}(t_i) = [L_1^2(t_i) + L_2^2(t_i) + L_3^2(t_i)]^{1/2}$	$1.5 < \log_{10}(\text{size}(t_1)) < 5$
Decay	Decay rate of pol.	$\text{decay}(t_m, t_n) = \text{size}(t_m)/\text{size}(t_n)$	$0.02 < \text{decay}(t_{29}, t_1)$
Model contribution (mc)	Contribution of TOI model i to predicted data for inversion with M objects	$\text{mc} = 100 \times [(d_i^{pred})^2 / \sum_{k=1}^{M} (d_k^{pred})^2]$	$75 < \text{mc} < 100$
Alpha	Difference between log-transformed axial and mean transverse pols.	$\alpha_L(t_i) = 1/3 \lvert \log_{10}\left(\frac{L_1(t_i)}{(L_2(t_i)L_3(t_i))^{1/2}}\right) \rvert$	$0.4 < \sum_{t_i=t_1}^{t_{29}} \frac{\alpha_L(t_i)}{t_{29}-t_1+1}$
Beta	Difference between log-transformed transverse pols.	$\beta_L(t_i) = 1/2 \lvert \log_{10}(L2(t_i)) - \log_{10}(L3(t_i)) \rvert$	$0.1 < \sum_{t_i=t_1}^{t_{29}} \frac{\beta_L(t_i)}{t_{29}-t_1+1} < 0.2$
Skewness	Skewness of pol. tensor	$\text{skewness}(t_m, t_n) = \sum_{t_i=t_m}^{t_n} \frac{2\alpha_L(t_i)(\alpha_L(t_i)^2 - \beta_L(t_i)^2)}{t_m - t_n + 1}$	$0 < \text{skewness}(t_1, t_{29}) < 0.11$
Variance	Variance of pol. tensor	$\text{variance}(t_m, t_n) = \sum_{t_i=t_m}^{t_n} \frac{2/3(3\alpha_L(t_i)^2 + \beta_L(t_i)^2)}{t_m - t_n + 1}$	$0.5 < \text{variance}(t_1, t_{29})$
Asymmetry	Relative difference between transverse pols.	$\text{asymmetry}(t_m, t_n) = \frac{\sum_{t_i=t_m}^{t_n} [L_2(t_i) - L_3(t_i)]}{\sum_{t_i=t_m}^{t_n} L_2(t_i)}$	$0.2 < \text{asymmetry}(t_4, t_{20}) < 0.4$
Shape	Difference between transverse pols. as a function of axial pol.	$\text{shape}(t_m, t_n) = \frac{\sum_{t_i=t_m}^{t_n} [L_2(t_i) - L_3(t_i)]}{\sum_{t_i=t_m}^{t_n} L_1(t_i)}$	$0.15 < \text{shape}(t_1, t_{42}) < 0.2$
Aspect ratio (ar)	Ratio of axial to mean transverse pols.	$\text{ar}(t_m, t_n) = \frac{\prod_{t_i=t_m}^{t_n} L_1(t_i)}{[\prod_{t_i=t_m}^{t_n} L_2(t_i) L_3(t_i)]^{1/2}}$	$50 < \text{ar}(t_1, t_{42}) < 60$
Pol jitter	Total variation of pols. between adjacent channels	$\text{jitter} = \sum_{t_i=t_1}^{t_{N-1}} \sum_{k=1}^{3} \log_{10}\left(\frac{L_k(t_{i+1})}{L_k(t_i)}\right)$	$12 < \text{jitter} < 15$
L_2, L_3 separation	Average separation between transformed transverse pols.	$\text{separation}(\gamma) = \text{mean}(\lvert L_2(t_i)^\gamma - L_3(t_i)^\gamma \rvert) \times \text{mean}(\lvert L_2(t_i)^\gamma \rvert)$	$0.05 < \text{separation}(0.09) < 0.1$
L_2, L_3 amplitude	Mean amplitude of log transformed transverse pols.	$\text{amplitude} = \sum_{t_i=t_1}^{t_N} \frac{\log_{10}[L_2(t_i) \cdot L_3(t_i)]}{2}$	$-50 < \text{amplitude} < 120$
Depth	Estimated target depth		$0.01 < z < 0.9$

Figure 175. Example of metrics. To combine the metrics into a single score, we count the number of metrics that fall within the TOI range.

To demonstrate the CCR, we apply the metrics to cued MetalMapper data acquired at Pole Mountain (Figure 176). Figure 176(a) plots the ROC curve when using a library match classifier using all of the three polarizabilities, for a refined library, i.e., the library was optimized to 11 target polarizabilities through the use of analyst classifier digs to remove targets from the library that were ruled to be

unlikely. In this case, all TOI are detected with 39 false alarms. Figure 176(b) plots the decision metric as a function of dig number. The decision metric is defined as the reciprocal of the polarizability misfit. The classification using the complete ESTCP library is shown in Figure 176(c). There are 1641 polarizabilities in the classification library. Due to the large number of polarizabilities in the library that match non-TOI, the classifier requires 425 non-TOI digs to recover all TOI.

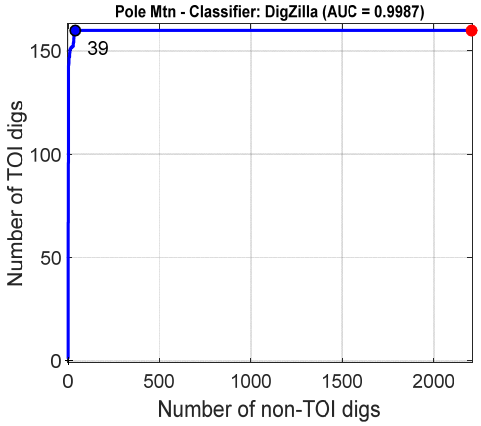

(a) ROC for classification using a refined library (11 polarizabilities)

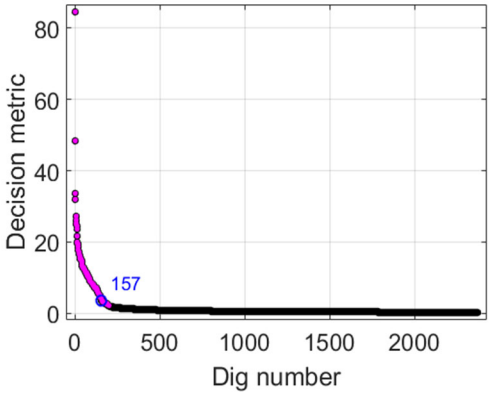

(b) Decision metric when using a refined library

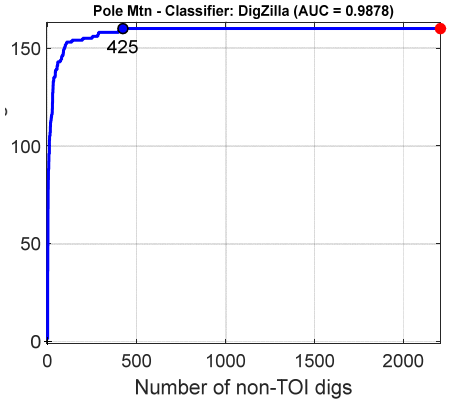

(c) ROC for classification using the ESTCP Library (1641 pols.)

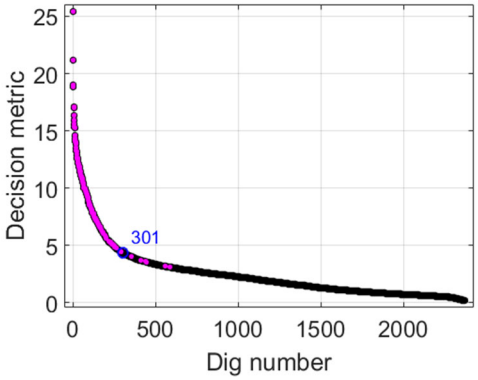

(d) Decision metric when using a refined library

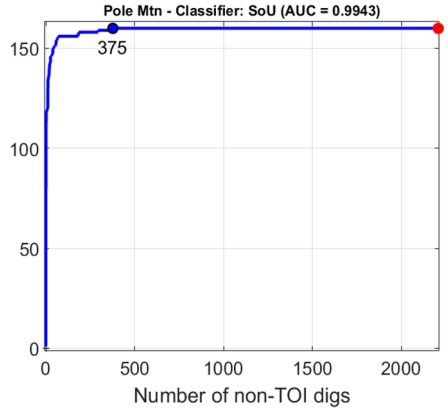

(e) ROC when using SNGTC ranking, i.e., no library

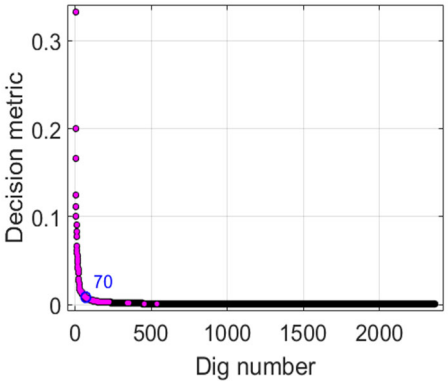

(f) Decision metric when using SNGTC ranking, i.e., no library

Figure 176. MetalMapper cued data from Pole Mountain

We note that without training data to bound the smallest TOI, there would have to be many additional digs beyond the 425 non-TOI digs. Figure 177 plots digs 973 to 1008 compared to their best fit polarizability. Within the Pole Mountain data set, there are many items with good fits to small ordnance (i.e., 20 mm, 25 mm, and 30 mm projectiles). Figure 176(d) shows that the L-curve of the decision metric has a smooth elbow, which suggests there is increased overlap between items in the polarizability library and non-TOI. The ROC from the CCR, non-library classifier is shown in Figure 176(e). The non-library based classifier finds all TOI with 375 non-TOI digs, performing better than using the complete ESTCP library.

Figure 178 compares classification results using MetalMapper cued data from Spencer Range. In this example, using the ESTCP library produced poorer results than the non-library based classifier. This is, in part, due to the seeded ISOs used. The Spencer Range small ISOs were slightly "fatter" than the standard small ISOs. As a result, more digs were required to recover all ISOs.

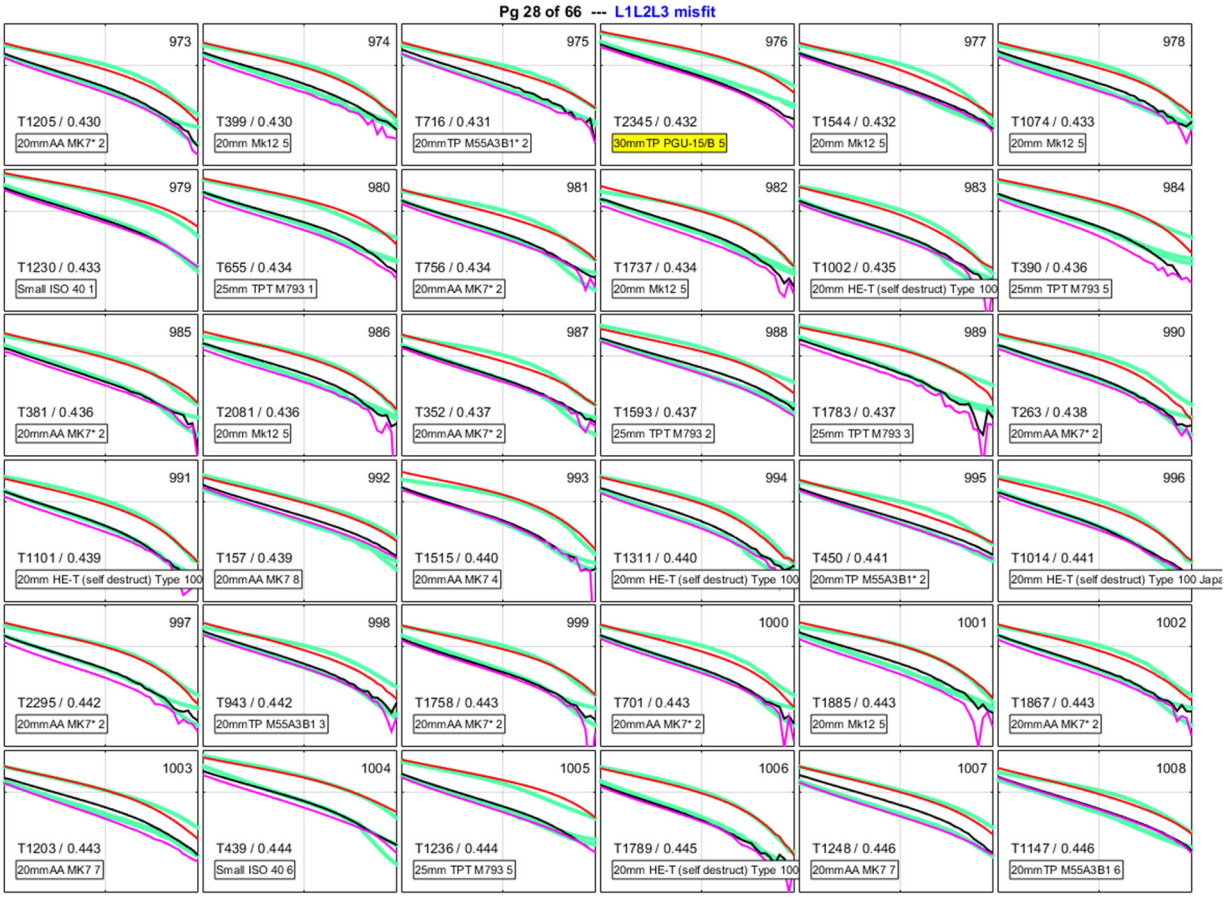

Figure 177. Digs 973 to 1008 when using the full ESTCP library. There are many items with good fits to small ordnance (i.e., 20 mm, 25 mm, and 30 mm projectiles).

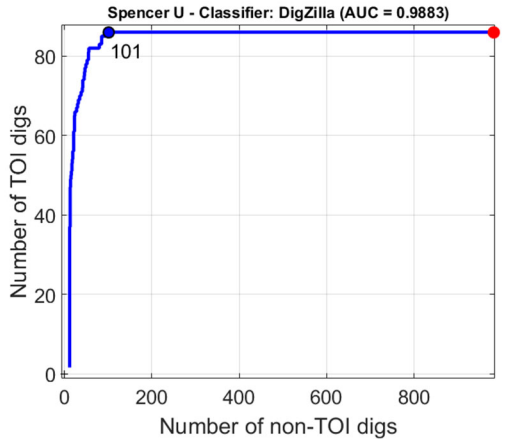

(a) ROC for classification using a refined library (11 polarizabilities)

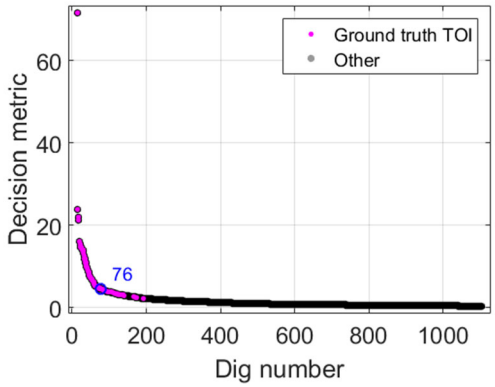

(b) Decision metric when using a refined library

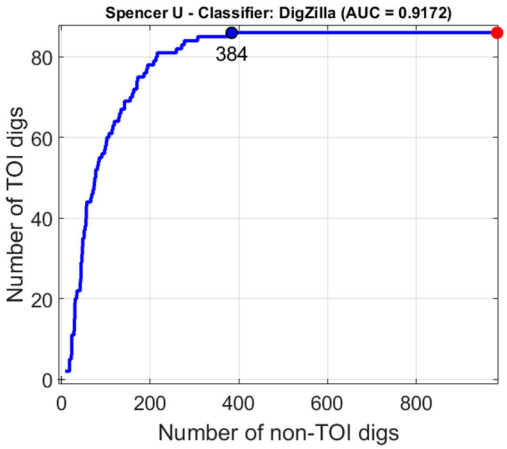

(c) ROC for classification using the ESTCP Library (1641 pols.)

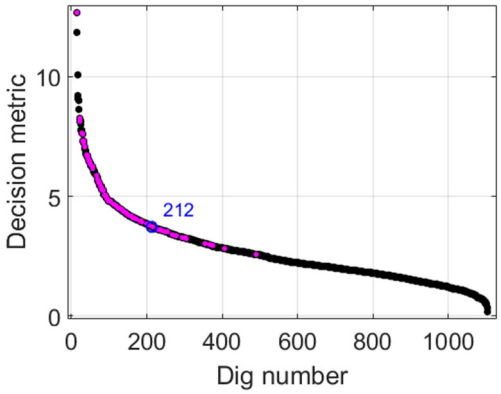

(d) Decision metric when using a refined library

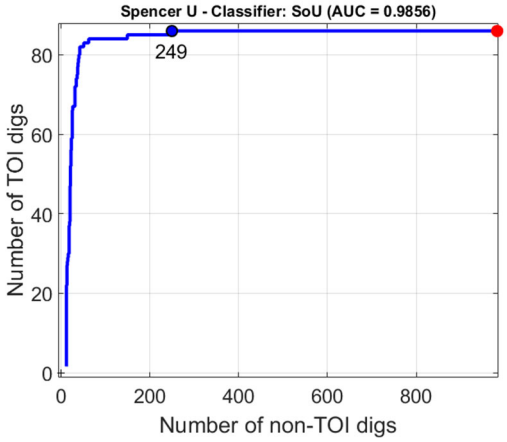

(e) ROC when using SNGTC ranking, i.e., no library

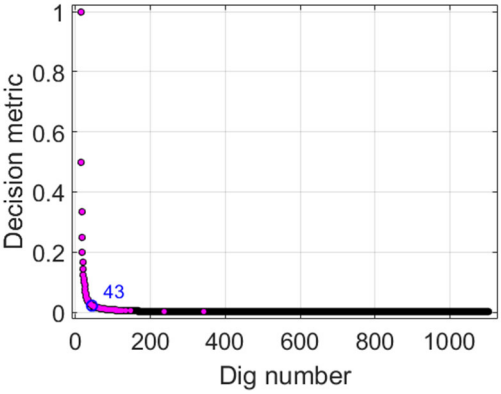

(f) Decision metric when using SNGTC ranking, i.e., no library

Figure 178. MetalMapper cued data from Spencer Range.

6. Black Tusk API to UX-Analyze

The Black Tusk Inversion and Discrimination Application Programming Interface provides inversion capability for AGC instrument systems including the MetalMapper 2x2, MPV, TEMTADS 2x2, and UltraTEM. The API can be called from either a C++ Windows application or a .NET Windows application. It supports several advanced EM systems including MetalMapper, MetalMapper 2x2, MPV, TEMTADS 2x2, and UltraTEM. Inversion metrics are also calculated and returned to the calling application to provide additional discrimination functionality.

References

[1] Y. Das, J. McFee, J. Toews and G. Stuart, "Analysis of an electromagnetic induction detector for real-time localization of buried objects," *IEEE Transactions on Geoscience and Remote Sensing,* vol. 28, no. 3, pp. 278-288, May 1990.

[2] A. Sebak, L. Shafai and Y. Das, "Near-zone fields scattered by threedimensinal highly conducting permeable objects in the field of an arbitrary loop," *IEEE Transactions on Geoscience and Remote Sensing,* vol. 29, no. 1, pp. 9-15, 1191.

[3] N. Geng, K. Baum and L. Carin, "On the low frequency natural responses of conducting and permeable target," *IEEE Transactions on Geoscience and Remote Sensing,* vol. 37, no. 1, pp. 347-359, 1999.

[4] B. Barrow and H. Nelson, "Model-based characterization of electromagnetic induction signatures obtained with the MTADS electromagnetic array," *IEEE Transactions on Geoscience and Remote Sensing,* vol. 39, no. 6, pp. 1279-1285, 2001.

[5] J. Miller, T. Bell, J. Soukup and D. Keiswetter, "Simple phenomenological models for wideband frequency-domain electromagnetic induction," *IEEE Transactions on Geoscience and Remote Sensing,* vol. 39, no. 6, pp. 1294-1298, 2001.

[6] T. Bell, B. Barrow and J. Miller, "Subsurface discrimination using electromagnetic induction sensors," *IEEE Transactions on Geoscience and Remote Sensing,* vol. 39, no. 6, pp. 1286-1293, 2001.

[7] L. S. Riggs, J. E. Mooney and D. E. Lawrence, "Identification of metallic mine-like objects using low frequency magnetic fields," *IEEE Transactions on Geoscience and Remote Sensing,* vol. 39, no. 1, pp. 56-66, 2001.

[8] L. R. Pasion and D. W. Oldenburg, "A discrimination algorithm for UXO using time domain electromagnetics," *Journal of Engineering and Environmental Geophysics,* vol. 28, no. 2, pp. 91-102, 2001.

[9] L. Carin, H. Yu, Y. Dalichaouch, E. Perry, P. Czipott and C. E. Baum, "On the wideband EMI response of a rotationally symmetric permeable and conducting target," *IEEE Transactions on Geoscience and Remote Sensing,* vol. 39, no. 6, pp. 1206-1213, 2001.

[10] H. Huang and I. J. Won, "Characterization of UXO-like targets using broadband electromagnetic induction sensors," *IEEE Transactions on Geoscience and Remote Sensing,* vol. 41, no. 3, pp. 652-663, 2003.

[11] Y. Zhang, L. Collins, H. Yu, C. Baum and L. Carin, "Sensing of unexploded ordnance with magnetometer and induction: Theory and signal processing," *IEEE Transactions on Geoscience and Remote Sensing,* vol. 41, no. 5, pp. 1005-1015, 2003.

[12] J. T. Smith and H. F. Morrison, "Estimating equivalent dipole polarizabilities for the inductive response of isolated conductive bodies," *IEEE Transactions on Geoscience and Remote Sensing,* vol. 42, no. 6, pp. 1208-1214, 2004.

[13] D. D. Snyder, D. C. George, S. C. MacInnes and J. T. Smith, "An assessment of three dipole-based programs for estimating UXO target parameters with induction EM," in *SEG Technical Program Expanded Abstracts*, Las Vegas, 2008.

[14] S. L. Tantum and L. M. Collins, "A comparison of algorithms for subsurface target detection and identification using time-domain electromagnetic induction data," *IEEE Transactions on Geoscience and Remote Sensing,* vol. 39, no. 6, pp. 1299-1306, 2001.

[15] A. B. Tarokh, E. L. Miller, I. J. Won and H. Huang, "Statistical classification of buried objects from spatially sampled time or frequency domain electromagnetic induction data," *Radio Science,* vol. 39, no. 4, 2004.

[16] L. R. Pasion, *Inversion of Time Domain Electromagnetic Data for the Detection of Unexploded Ordnance, Ph.D. Dissertation,* Vancouver, BC: University of British Columbia, 2007.

[17] A. Aliamiri, J. Stalnaker and E. L. Miller, "Statistical classification of buried unexploded ordnance using nonparametric prior models," *IEEE Transactions on Geoscience and Remote Sensing,* vol. 45, no. 9, pp. 2794-2806, 2007.

[18] D. Williams, C. P. Wang, X. J. Liao and L. Carin, "Classification of unexploded ordnance using incomplete multisensor multiresolution data," *IEEE Transactions on Geoscience and Remote Sensing,* vol. 45, no. 7, pp. 2364-2373, 2007.

[19] Q. H. Liu, X. J. Liao and L. Cain, "Detection of unexploded ordnance via efficient semisupervised and active learning," *IEEE Transactions on Geoscience and Remote Sensing,* vol. 46, no. 9, pp. 2558-2567, 2008.

[20] E. Gasperikova, , J. T. Smith, H. F. Morrison, A. Becker and K. Kappler, "UXO detection and identification based on intrinsic target polarizabilities," *Geophysics,* vol. 74, no. 1, pp. 1-9, 2009.

[21] S. D. Billings, L. R. Pasion, L. Beran, N. Lhomme, L. P. Song, D. W. Oldenburg, K. Kingdon, D. Sinex and J. Jacobson, "Unexploded ordnance discrimination using magnetic and electromagnetic sensors: Case study from a former military site," *Geophysics,* vol. 75, no. 3, pp. 103-114, 2010.

[22] L. Beran, B. Zelt, L. Pasion, S. Billings, K. Kingdon, N. Lhomme, L. P. Song and D. W. Oldenburg, "Practical strategies for classification of unexploded ordnance," *Geophysics,* vol. 78, no. 1, pp. 41-46, 2013.

[23] T. Bell, "Adaptive and iterative processing techniques for overlapping signatures," AETC inc., Arlington, VA, 2006.

[24] F. Shubitidze, K. O'Neill, B. E. Barrowes, I. Shamatava, J. P. Fernandez, K. Sun and K. D. Paulsen, "Application of the normalized surface magnetic charge model to UXO discrimination in cases with overlapping signals," *Journal of Applied Geophysics,* vol. 61, no. 3-4, pp. 292-303, 2007.

[25] F. Shubitidze , "Applying a volume dipole distribution model to nextgeneration sensor data for multi-object data inversion and discrimination," in *SPIE Proceedings*, 2010.

[26] J. T. Miller, "Source separation using sparse-solution linear solvers," in *Proceedings of SPIE*, 2010.

[27] L. P. Song, D. W. Oldenburg, L. R. Pasion and S. D. Billings, "Transient electromagnetic inversion of multiple targets," in *SPIE proceedings*, 2009.

[28] L. P. Song, L. R. Pasion, S. D. Billings and D. W. Oldenburg, "Nonlinear inversion for multiple objects in transient electromagnetic induction sensing of unexploded ordnance: Technique and applications," *IEEE Transactions on Geoscience and Remote Sensing ,* vol. 49, no. 10, pp. 4007-4020, 2011.

[29] T. M. Grzegorczyk, B. E. Barrowes, F. Shubitidze, J. P. Fernandez and K. O'Neill, "Simultaneous identification of multiple unexploded ordnance using electromagnetic induction sensors," *IEEE Transactions on Geoscience and Remote Sensing,* vol. 49, no. 7, pp. 2507-2517, 2011.

[30] H. H. Nelson, "EMI Array for Cued UXO Discrimination," Environmental Security Technology Certification Program, Alexandria, VA, 2008.

[31] F. S. Grant and G. F. West, Interpretation Theory in Applied Geophysics, New York, NY: McGraw-Hill, 1965.

[32] J. D. Jackson, Classical Electrodynamics, New York, NY: Wiley, 1975.

[33] J. J. More, "The Levenberg–Marquardt Algorithm: Implementation and Theory," in *Numerical Analysis, Lecture Notes in Mathematics 630*, Dundee, 1977.

[34] T. F. Coleman and Y. Li, "An interior, trust region approach for nonlinear minimization subject to bounds," *SIAM Journal on Optimization,* vol. 6, no. 2, pp. 418-445, 1996.

[35] R. A. Horn and C. R. Johnson, Matrix Analysis, Cambridge, U.K.: Cambridge University Press, 1985.

[36] G. H. Golub and C. F. Van Loan, Matrix Computations, Baltimore, MD: The Johns Hopkins University Press, 1989.

[37] L. P. Song, L. R. Pasion and D. W. Oldenburg, "Estimating source locations of unexploded ordnance using the multiple signal classification algorithm," *Geophysics,* vol. 77, no. 4, pp. 127-135, 2012.

[38] F. Shubitidze, J. P. Fernandez, I. Shamatava, B. E. Barrowes and K. O'Neill, "Joint diagonalization applied to the detection and discrimination of unexploded ordnance," *Geophysics,* vol. 77, no. 4, pp. 149-160, 2012.

[39] E. Gasperikova , J. T. Smith, H. F. Morrison, A. Becker and K. Kappler, "UXO detection and identification based on intrinsic target polarizabilities," *Geophysics,* vol. 74, pp. 1-9, 2009.

[40] L. P. Song, D. W. Oldenburg, L. R. Pasion and S. D. Billings, "Adaptive Focusing for Source Localization in EMI Sensing of Metallic Objects: A Preliminary Assessment," *Journal of Environmental and Engineering Geophyics,* vol. 13, pp. 131-145, 2008.

[41] B. D. Van Veen and K. M. Buckley, "Beamforming: A Versatile Approach to Spatial Filtering," *IEEE Signal Processing Magazine,* vol. 5, pp. 4-24, 1988.

[42] H. Ammari, E. Iakovleva and D. Lesselier, "A MUSIC algorithm for locating small inclusions buried in a half-space from the scattering amplitude at a fixed frequency," *Multiscale Modeling & Simulation,* vol. 3, no. 3, pp. 597-628, 2005.

[43] H. Ammari, E. Iakovleva, D. Lesselier and G. Perrusson, "MUSIC-type electromagnetic imaging of a collection of small three-dimensional inclusions," *SIAM Journal of Scientific Computering,* vol. 29, 2007.

[44] R. O. Schmidt, "Multiple emitter location and signal parameter estimation," *IEEE Transactions on Antennas and Propagation,* vol. 34, no. 3, pp. 276-280, 1986.

[45] H. Ammari, J. Garnier and V. Jugnon, "Detection, reconstruction, and characterization algorithms from noisy data in multistatic wave imaging," *Discrete and Continuous Dynamical Systems - Series S,* vol. 8, no. 3, pp. 389 - 417, 2015.

[46] H. Ammari, J. Chen, Z. Chen, J. Garnier and D. Volkov, "Target Detection and Characterization from Electromagnetic Induction Data," *J. Math. Pures Appl.,* vol. 9, no. 1, pp. 54-75, 2014.

[47] Y. K. Ma and W. K. Park, "Analysis of MUSIC-type imaging functionals for small twodimensional electromagnetic inhomogeneities," *Journal of Electromagnetic Waves and Applications,* vol. 29, no. 11, pp. 1430-1439, 2015.

[48] H. Ammari, J. Garnier, W. Jing, H. Kang, M. Lim, K. Solna and H. Wang, Mathematical and statistical methods for multistatic imaging Lecture Notes in Mathematics, Springer, 2013.

[49] D. D. Snyder, M. Prouty, S. Jose, D. C. George, T. King, Z. Blackhawk, M. Poulton and A. Szidarovszky, "Discrimination at camp san luis obispo with the metalmapper," in *Symposium on the Application of Geophysics to Engineering and Environmental Problems (SAGEEP)*, Keystone, CO, 2010.

[50] J. Foutz, A. Spanias and M. K. Banavar, "Narrowband Direction of Arrival Estimation for Antenna Arrays," *Synthesis Lectures on Antennas,* 2008.

[51] M. F. Manzano, J. F. Valenzuela-Valdes, I. T. Castro and L. Landesa, "Looking in complex angles for improving the accuracy of antenna array DoA estimation," *Journal of Electromagnetic Waves and Applications,* vol. 27, no. 3, pp. 345-354, 2013.

[52] M. Wax and T. Kailath, "Detection of signals by information theoretic criteria," *IEEE Transactions on Acoustics, Speech, and Signal Processing ,* vol. 33, no. 2, pp. 387-392, 1985.

[53] H. Ammari, J. Garnier, H. Kang, W. K. Park and K. Solna, "Imaging schemes for perfectly conducting cracks," *SIAM J. Appl. Math,* vol. 71, 2011.

[54] A. Andrews and H. Nelson, "Implementing advanced classification on munitions response sites: a guide to informed decision making for project managers, regulators, and contractors," Environmental Security Technology Certification Program (ESTCP), Alexandria, VA, 2011.

[55] V. V. Fedorov, Theory of Optimal Experiments, New York, NY: Academic Press, 1972.

[56] A. C. Atkinson, A. N. Doney and R. Tobias, Optimum Experimental Designs, with SAS, Oxford, UK: Oxford Science Publications, 2007.

[57] D. J. MacKay, "Information-based objective functions for active data selection," *Neural Computation,* vol. 4, no. 4, pp. 590-604, 1992.

[58] X. Liao and L. Carin, "Application of the theory of optimal experiments to adaptive electromagnetic-induction sensing of buried targets," *IEEE Transactions on Pattern Analysis and Machine Intelligence,* vol. 26, no. 8, pp. 961-972, 2004.

[59] A. Tarantola, Inverse Problem Theory and Methods for Model Parameter Estimation, Philadelphia, PA: SIAM, Society for Industrial and Applied Mathematics (SIAM).

[60] C. D. Meyer, Matrix Analysis and Applied Linear Algebra, Society for Industrial and Applied Mathematics, 2000.

[61] The Math Works Inc., Optimization Toolbox Users Guide, Natick, MA, 2013.

[62] Environmental Security Technology Certification Program (ESTCP), "ESTCP Live Site Demonstrations: Former Camp Beale," ESTCP, Alexandria, VA, 2011.

[63] J. P. Fernandez, B. E. Barrowes, T. M. Grzegorczyk, N. Lhomme, K. O'Neill and F. Shubitidze, "A man-portable vector sensor for identification of unexploded ordnance," *IEEE Sensors Journal,* vol. 11, no. 10, pp. 2542-2555, 2011.

[64] K. A. Kingdon, N. Lhomme and D. C. George, "A man portable EMI system for detection and classification of unexploded ordnance in challenging environments," *FastTimes,* vol. 19, no. 3, pp. 31-41, 2014.

[65] M. Wei, W. R. Scott and J. H. McClellan, "Robust Estimation of the Discrete Spectrum of Relaxations for Electromagnetic Induction Responses," *IEEE Transactions on Geoscience and Remote Sensing ,* vol. 48, pp. 1169-1179, 2010.

[66] J. F. Cardoso and A. Souloumiac, "Jacobi angles for simultaneous diagonalization," *SIAM Journal on Matrix Analysis and Applications,* vol. 17, no. 1, pp. 161-164, 1996.

Inversion and Discrimination C++ API

REFERENCE MANUAL

Version: v12.8

Black Tusk Geophysics Inc. 2018

Overview

The Inversion and Discrimination API provides 64-bit Windows applications with high performance single and multi-object inversion capability for both static and dynamic EM data. The API can be called from either a C++ Windows application or a .NET Windows application. It supports several advanced EM systems including MetalMapper, MetalMapper 2x2, MPV, TEMTADS 2x2, and UltraTEM. Inversion metrics are also calculated and returned to the calling application to provide additional discrimination functionality.

Developer Installation

Unzip the InvDiscimAPI.zip file to your application's project folder. A .NET x64 application will only need to reference the UXOCoreCompNet.dll found in the InvDiscimAPI\lib folder. If you have a Windows C++ x64 application, you will first need to update your application's linker command line to add the InvDiscimAPI\lib folder as an additional library folder. In Visual Studio, this can be done by editing the "Additional Library Directories" of your Linker properties. You will also need to add the InvDiscimAPI\include folder to your "Additional Include Directories" in your C/C++ properties. Once this is done, your C++ app should be able to find the UXOCoreComp.dll and BTGAPI.h files.

int InvertTEM (ref SensorConfig SenConfig, ref EMInversionConfig InvConfig,
int NumObsLoc, int[] EMObsLen, bool ObsLocUseAllTx,
double[][][][][] EMObs, int[] TxSensor, int[] RxSensor,
int[] VLine, int NumVLines,
bool[][][][][] EMSenMask,
double[] Easting, double[] Northing, double[] Elevation,
double[] Roll, double[] Pitch, double[] Yaw,
double[][][] ModelParams,
double[][][] PolarizLong, double[][][] PolarizTrav1, double[][][] PolarizTrav2,
double[][][][][] Pred, double[][][][][] Resid, double[] Corr,
bool CalcInvMetrics, int MetricsTGRange, double[] ModelSNR,
double[][] LastRelTGAve, double[][] BigDeep, double[][]Size, double[][]Decay,
double[][] PolQuality, double[][]SNGT)

Inverts the cell data for the presence of one, two, or three objects, and returns polarizabilities, predicted, and residual results. Additional inversion metrics are optionally calculated.

SensorConfig SenConfig	a structure holding the sensor configuration
InversionConfig InvConfig	a structure holding the inversion configuration
int NumObsLoc	total number of physical observation locations
int[] EMObsLen	number of physical observation locations for each Tx
bool ObsLocUseAllTx	flag indicating whether each physical observation location is associated with all Tx (applies to multi-Tx systems only)
double[][][][][] EMObs	4D array referencing the data to be inverted [NumTx][NumComp][NumTG][EMObsLen]
int[] TxSensor	array of length NumObsLoc holding the associated Tx sensor index of each observation location
int[] RxSensor	array of length NumObsLoc holding the associated Rx sensor index of each observation location
int[] Vline	array of length NumObsLoc holding the vehicle line index of each observation location
int NumVLines	total number of vehicle lines in the survey
bool[][][][][] EMSenMask	4D array referencing a mask for the inversion [NumTx][NumComp][NumTG][EMObsLen]
double[] Easting	Easting positions of each observation location
double[] Northing	Northing positions of each observation location
double[] Elevation	Elevation positions of each observation location
double[] Roll	Roll at each observation location (radians)

double[] Pitch	Pitch at each observation location (radians)
double[] Yaw	Yaw at each observation location (radians)
double[][][] ModelParams	3D array holding the 6 fitted results (i.e. x,y,z, phi, theta, and gamma) of each object. [NumInv][NumObj][6]
double[][][] PolarizLong	3D array holding the principal axis polarizability of each object. [NumInv][NumObj][NumTG]
double[][][] PolarizTrav1	3D array holding the first transverse axis polarizability of each object. [NumInv][NumObj][NumTG]
double[][][] PolarizTrav2	3D array holding the second transverse axis polarizability of each object. [NumInv][NumObj][NumTG]
double[][][][][] Pred	5D array holding the predicted data [NumInv][NumTx][NumComp][NumTG][EMObsLen]
double[][][][][] Resid	5D array holding the residual data [NumInv][NumTx][NumComp][NumTG][EMObsLen]
double[] Corr	correlation score for each inversion performed
bool CalcInvMetrics	flag indicating whether inversion metrics should also be calculated
int MetricsTGRange	time gate range for the inversion metrics calculations
double[] ModelSNR	signal-to-noise ratio of the model for each inversion
double[][] LastRelTGAve	average last reliable time gate index of each object [NumInv][NumObj]
double[][] BigDeep	score for objects that are likely big and deep [NumInv][NumObj]
double[][] Size	measure of size for each object [NumInv][NumObj]
double [][]Decay	measure of decay for each object. Higher values indicate a fast decay of the object. [NumInv][NumObj]
double [][]PolQuality	polarizability quality of each object. Higher values indicate less noise and jitter. [NumInv][NumObj]
double [][]SNGT	Simple-No-Ground-Truth measure of each object (a.k.a. Library-Free classification). Higher values indicate a greater likelihood of UXO [NumInv][NumObj]

Sample Code for calling from a .NET application

```
//****for our sample code, we want show how application data would get loaded into
//  the data format required by the API.  Let's assume the calling application holds its data
//in the following variables:

//1D array for holding Tx [sensor] centers
UXOCompClass.Point3D[] m_MyAppTxCenter;

//2D arrays for holding Tx [sensor][component] geometry
int[][] m_MyAppTxLoopShape;
double[][] m_MyAppTxLoopSizeW;
double[][] m_MyAppTxLoopSizeH;

double[][] m_MyAppTxLoopPitch;
double[][] m_MyAppTxLoopRoll;
double[][] m_MyAppTxLoopYaw;

double[][] m_MyAppTxLoopOffsetX;
double[][] m_MyAppTxLoopOffsetY;
double[][] m_MyAppTxLoopOffsetZ;


//1D array for holding Rx [sensor] centers
UXOCompClass.Point3D[] m_MyAppRxCenter;

//2D arrays for holding Rx [sensor][component] geometry
int[][] m_MyAppRxLoopShape;
double[][] m_MyAppRxLoopSizeW;
double[][] m_MyAppRxLoopSizeH;

double[][] m_MyAppRxLoopPitch;
double[][] m_MyAppRxLoopRoll;
double[][] m_MyAppRxLoopYaw;

double[][] m_MyAppRxLoopOffsetX;
double[][] m_MyAppRxLoopOffsetY;
double[][] m_MyAppRxLoopOffsetZ;


//the picked target location
PointF m_MyAppPickedTarget;

//positional data
double[] m_MyAppEasting;
double[] m_MyAppNorthing;
double[] m_MyAppElev;
```

```
//attitude data
double[] m_MyAppRoll;
double[] m_MyAppPitch;
double[] m_MyAppYaw;

//arrays hold Tx, Rx and vehicle line indexes
int[] m_MyAppTxSensorIndexOfReading;
int[] m_MyAppRxSensorIndexOfReading;
int[] m_MyAppVehicleLineIndexOfReading;

//array holding all the observations
double[,,][] m_MyAppCellObs;

int m_MyAppNumVehicleLines;
double[] m_MyAppRxTimes;



//sample function that loads data and calls the API:

private void button1_Click(object sender, EventArgs e)
{
   //create an instance of the class that allows your .NET code to call the API
   UXOCompEMInversionClass EMInversion = new UXOCompEMInversionClass();

   //create an inversion configuration for the API
   UXOCompEMInversionClass.EMInversionConfig InvConfig = EMInversion.CreateInversionConfig();

   //set the lower bounds for the inversion
   InvConfig.LowerBnds[0] = -0.05;  // x
   InvConfig.LowerBnds[1] = -0.05;  // y
   InvConfig.LowerBnds[2] = -1.00;  // z
   InvConfig.LowerBnds[3] =  0.0;  // phi
   InvConfig.LowerBnds[4] =  0.0;  // theta
   InvConfig.LowerBnds[5] =  0.0;  // gamma

   //set the upper bounds for the inversion
   InvConfig.UpperBnds[0] = 0.05;  // x
   InvConfig.UpperBnds[1] = 0.05;  // y
   InvConfig.UpperBnds[2] = 0.00;  // z
   InvConfig.UpperBnds[3] = 6.28;  // phi
   InvConfig.UpperBnds[4] = 3.14;  // theta
   InvConfig.UpperBnds[5] = 6.28;  // gamma

   InvConfig.BaseErr = 0.005;
   InvConfig.PercentErr = 0.005;
   InvConfig.MinS2N = 1.5;  //good for most cases
   InvConfig.NumStartModels = 3;


   //set the target pick location
```

```
   InvConfig.Target = new UXOCompClass.Point3D();
   InvConfig.Target.X = m_MyAppPickedTarget.X;
   InvConfig.Target.Y = m_MyAppPickedTarget.Y;
   InvConfig.Target.Z = UXOCompClass.CALC_PICKED_ELEV;  //ask the API to calculate a weighted
dist elev


   //we don't know the orientation, so just set it to zero
   InvConfig.Orien = new UXOCompClass.Orien3D();
   InvConfig.Orien.phi = 0;
   InvConfig.Orien.theta = 0;
   InvConfig.Orien.gamma = 0;

   InvConfig.NumInversions = 1; // perform one inversion

   //The API can perform 1,2, or 3 object inversions
   InvConfig.NumObjects[0] = 1; // this inversion will invert for one object

   //now create a sensor configuration for the API
   UXOCompEMInversionClass.SensorConfig SenConfig = EMInversion.CreateSensorConfig(true);
   SenConfig.NumTx = 1;
   SenConfig.NumTxComponents = 3;

   //copy the Tx geometry from your application into the API Sensor Configuration
   for (int s=0; s < SenConfig.NumTx; s++)
   {
      //set the Tx center
      SenConfig.Tx[s].Center.X = m_MyAppTxCenter[s].X;
      SenConfig.Tx[s].Center.Y = m_MyAppTxCenter[s].Y;
      SenConfig.Tx[s].Center.Z = m_MyAppTxCenter[s].Z;

      //set the tx component loops (in x,y,z order (i.e. c=0,1,2))
      for (int c = 0; c < SenConfig.NumTxComponents; c++)
      {
         //default initialize to a rectangular loop
         int NumLoopCrns = UXOCompEMInversionClass.NUM_RECT_LOOP_CORNERS;
         SenConfig.Tx[s].Comp[c].Area = m_MyAppTxLoopSizeW[s][c] *
m_MyAppTxLoopSizeH[s][c];

         if (m_MyAppTxLoopShape[s][c] == UXOCompEMInversionClass.LOOP_SHAPE_CIRC)
         {
            //circular loop so calculate corners and area
            NumLoopCrns = UXOCompEMInversionClass.NUM_PTS_CIRCULAR_LOOP;
            double Rad = m_MyAppTxLoopSizeW[s][c] / 2.0;
            SenConfig.Tx[s].Comp[c].Area = Math.PI * Rad * Rad;
         }

         //now calculate the loop corner positions relative to the center of the loop

         // Note: MyAppTxLoopPitch, MyAppTxLoopRoll, and MyAppTxLoopYaw
         // are the angular deviations from the regular orthogonal position of the Tx loop
```

```
        //  (will typically be = 0.0, except for MPV static)

        double[][] CornerComp = EMInversion.CalcLoopCorners(m_MyAppTxLoopShape[s][c],
                                    c,
                                    m_MyAppTxLoopSizeW[s][c] / 2.0,
                                    m_MyAppTxLoopSizeH[s][c] / 2.0,
                                    m_MyAppTxLoopPitch[s][c],
                                    m_MyAppTxLoopRoll[s][c],
                                    m_MyAppTxLoopYaw[s][c]);

        //now calculate the corner positions relative to the center of the GPS
        SenConfig.Tx[s].Comp[c].NumLoopCorners = NumLoopCrns;
        for (int cn = 0; cn < NumLoopCrns; cn++)
        {
           SenConfig.Tx[s].Comp[c].LoopCornersX[cn] = SenConfig.Tx[s].Center.X +
                                    m_MyAppTxLoopOffsetX[s][c] + CornerComp[cn][0];
           SenConfig.Tx[s].Comp[c].LoopCornersY[cn] = SenConfig.Tx[s].Center.Y +
                                    m_MyAppTxLoopOffsetY[s][c] + CornerComp[cn][1];
           SenConfig.Tx[s].Comp[c].LoopCornersZ[cn] = SenConfig.Tx[s].Center.Z +
                                    m_MyAppTxLoopOffsetZ[s][c] + CornerComp[cn][2];
        }

     }  //next Tx loop component
     SenConfig.Tx[s].Gain = 1.0;
  } //Next Tx sensor location



  //copy the Rx geometry from your application into the API Sensor Configuration
  for (int s=0; s < SenConfig.NumRx; s++)
  {
     //set the Rx center
     SenConfig.Rx[s].Center.X = m_MyAppRxCenter[s].X;
     SenConfig.Rx[s].Center.Y = m_MyAppRxCenter[s].Y;
     SenConfig.Rx[s].Center.Z = m_MyAppRxCenter[s].Z;

     //set the Rx component loops (in x,y,z order (i.e. c=0,1,2))
     for (int c = 0; c < SenConfig.NumRxComponents; c++)
     {
        //default initialize to a rectangular loop
        int NumLoopCrns = UXOCompEMInversionClass.NUM_RECT_LOOP_CORNERS;
        SenConfig.Rx[s].Comp[c].Area = m_MyAppRxLoopSizeW[s][c] *
m_MyAppRxLoopSizeH[s][c];

        if (m_MyAppRxLoopShape[s][c] == UXOCompEMInversionClass.LOOP_SHAPE_CIRC)
        {
           //circular loop so calculate corners and area
           NumLoopCrns = UXOCompEMInversionClass.NUM_PTS_CIRCULAR_LOOP;
           double Rad = m_MyAppRxLoopSizeW[s][c] / 2.0;
           SenConfig.Rx[s].Comp[c].Area = Math.PI * Rad * Rad;
        }
```

```
      //now calculate the loop corner positions relative to the center of the loop

      // Note: MyAppRxLoopPitch, MyAppRxLoopRoll, and MyAppRxLoopYaw
      // are the angular deviations from the regular orthogonal position of the Rx loop
      //  (will typically be = 0.0, except for MPV static)

      double[][] CornerComp = EMInversion.CalcLoopCorners(m_MyAppRxLoopShape[s][c],
                                    c,
                                    m_MyAppRxLoopSizeW[s][c] / 2.0,
                                    m_MyAppRxLoopSizeH[s][c] / 2.0,
                                    m_MyAppRxLoopPitch[s][c],
                                    m_MyAppRxLoopRoll[s][c],
                                    m_MyAppRxLoopYaw[s][c]);

      //now calculate the corner positions relative to the center of the GPS
      SenConfig.Rx[s].Comp[c].NumLoopCorners = NumLoopCrns;
      for (int cn = 0; cn < NumLoopCrns; cn++)
      {
         SenConfig.Rx[s].Comp[c].LoopCornersX[cn] = SenConfig.Rx[s].Center.X +
                                       m_MyAppRxLoopOffsetX[s][c] + CornerComp[cn][0];
         SenConfig.Rx[s].Comp[c].LoopCornersY[cn] = SenConfig.Rx[s].Center.Y +
                                       m_MyAppRxLoopOffsetY[s][c] + CornerComp[cn][1];
         SenConfig.Rx[s].Comp[c].LoopCornersZ[cn] = SenConfig.Rx[s].Center.Z +
                                       m_MyAppRxLoopOffsetZ[s][c] + CornerComp[cn][2];
      }
   }  //next Rx loop component
} //Next Rx sensor location


//the API will invert all time gates that are passed to it, so load from the first time gate
// selected by the user
int AllTG = 54;
int FirstTG = 8;
SenConfig.NumTimeGates = AllTG - FirstTG;

for (int tg = 0; tg < SenConfig.NumTimeGates; tg++)
   SenConfig.RxTimes[tg] = m_MyAppRxTimes[tg];

//set your cell data to a 4D jagged array EMObs [NumTx][NumComp][NumTG][EMObsLen]
int NumTx = SenConfig.NumTx;
int NumComp = SenConfig.NumTxComponents * SenConfig.NumRxComponents;
int NumTG = SenConfig.NumTimeGates;

int[] EMObsLen = new int[NumTx];

double[][][][] EMObs = new double[NumTx][][][];
for (int tx = 0; tx < NumTx; tx++)
{
   //the number of observations for this tx is:
   EMObsLen[tx] = m_MyAppCellObs[tx, 0, 0].Length ;
```

```
   EMObs[tx] = new double[NumComp][][];
   for (int c = 0; c < NumComp; c++)
   {
      EMObs[tx][c] = new double[NumTG][];
      for (int tg = 0, tgFirst = FirstTG; tg < NumTG; tg++, tgFirst++)
      {
         //set the data channel references
         EMObs[tx][c][tg] = m_MyAppCellObs[tx, c, tgFirst];
      }
   }
}

int NumInv = InvConfig.NumInversions;


//create two 5D jagged arrays to hold the Predicted and Residual results
//  Pred[NumInv][NumTx][NumComp][NumTG][EMObsLen]
//  Resid[NumInv][NumTx][NumComp][NumTG][EMObsLen]

double[][][][][] Pred = new double[NumInv][][][][];
double[][][][][] Resid = new double[NumInv][][][][];
for (int i = 0; i < NumInv; i++)
{
   Pred[i] = new double[NumTx][][][];
   Resid[i] = new double[NumTx][][][];

   for (int tx = 0; tx < NumTx; tx++)
   {
      Pred[i][tx] = new double[NumComp][][];
      Resid[i][tx] = new double[NumComp][][];
      for (int c = 0; c < NumComp; c++)
      {
         Pred[i][tx][c] = new double[NumTG][];
         Resid[i][tx][c] = new double[NumTG][];
         for (int tg = 0; tg < NumTG; tg++)
         {
            //allocate for pred and resid results of this inversion
            Pred[i][tx][c][tg] = new double[EMObsLen[tx]];
            Resid[i][tx][c][tg] = new double[EMObsLen[tx]];
         }
      }
   }
}

//allocate for inversion metrics
double[] Corr = new double[NumInv];
double[] ModelSNR = new double[NumInv];
double[][] LastRelTGAve = new double[NumInv][];
double[][] BigDeep = new double[NumInv][];
double[][] Size = new double[NumInv][];
```

```
    double[][] Decay = new double[NumInv][];
    double[][] PolQuality = new double[NumInv][];
    double[][] SNGT = new double[NumInv][];


    //allocate for polarizability results
    double[][][] PolarizLongAxis = new double[NumInv][][];
    double[][][] PolarizTrav1Axis = new double[NumInv][][];
    double[][][] PolarizTrav2Axis = new double[NumInv][][];
    double[][][] Model = new double[NumInv][][];

    for (int i = 0; i < NumInv; i++)
    {
       int NumObj = InvConfig.NumObjects[i];
       PolarizLongAxis[i] = new double[NumObj][];
       PolarizTrav1Axis[i] = new double[NumObj][];
       PolarizTrav2Axis[i] = new double[NumObj][];
       Model[i] = new double[NumObj][];

       LastRelTGAve[i] = new double[NumObj];
       BigDeep[i] = new double[NumObj];
       Size[i] = new double[NumObj];
       Decay[i] = new double[NumObj];
       PolQuality[i] = new double[NumObj];
       SNGT[i] = new double[NumObj];

       for (int n = 0; n < NumObj; n++)   //there are 3 polarizabilities for each object
       {
          PolarizLongAxis[i][n] = new double[NumTG];
          PolarizTrav1Axis[i][n] = new double[NumTG];
          PolarizTrav2Axis[i][n] = new double[NumTG];
          Model[i][n] = new
double[UXOCompEMInversionClass.MAX_MODEL_PARAMS_POS_ORIEN];
       }
    }

    int NumVLines = m_MyAppNumVehicleLines;  //the total number of vehicle lines in the survey
    int NumObsLoc = m_MyAppEasting.Length;   //number of physical observation locations

    //Metrics can be optionally calculated. Set to false if you just want the polarizabilities
    // and the correlation measure.
    bool CalcInvMetrics = true;

    //Set the time gate range that will be used by the metrics calculations
    int MetricsTGRange = 30;


    //NOTE:  set m_ObsLocUseAllTx = true if we have a multiple Tx system
    //         that has applied the same timestamp to all Tx firings.  The result of this is that
    //        each physical observation location is associated with ALL Tx.
    //        This is often the case with multi tx systems running in static mode
```

```
  //For systems running dynamic mode, we typically set m_ObsLocUseAllTx = false
  //For single transmitter systems, we always set m_ObsLocUseAllTx = false
  bool ObsLocUseAllTx = false;


  //create a 4D jagged array sensor mask that will allow you to exclude specific combinations of
  //lines, Rx sensors, Tx sensors, and components
  //EMSenMask[NumVLines][RxSenIdx][NumTx][NumComp]

  bool[][][][] EMSenMask = new bool[NumVLines][][][];

  int NumRx = SenConfig.NumRx;

  for (int VL = 0; VL < NumVLines; VL++)
  {
     EMSenMask[VL] = new bool[NumRx][][];
     for (int rx = 0; rx < NumRx; rx++)
     {
        EMSenMask[VL][rx] = new bool[NumTx][];
        for (int tx = 0; tx < NumTx; tx++)
        {
           EMSenMask[VL][rx][tx] = new bool[NumComp];
           for (int c = 0; c < NumComp; c++)
           {
              //set the bool sensor mask for the API
              //setting all true here for this example
              EMSenMask[VL][rx][tx][c] = true;
           }
        }
     }
  }


  //call the EM inversion
  int Res = EMInversion.InvertTEM(ref SenConfig, ref InvConfig, NumObsLoc, EMObsLen,
                    ObsLocUseAllTx, EMObs,
m_MyAppTxSensorIndexOfReading, m_MyAppRxSensorIndexOfReading,
m_MyAppVehicleLineIndexOfReading,
                    m_MyAppNumVehicleLines,
                    EMSenMask,
                    m_MyAppEasting, m_MyAppNorthing, m_MyAppElev,
                    m_MyAppRoll, m_MyAppPitch, m_MyAppYaw,
                    Model, PolarizLongAxis, PolarizTrav1Axis, PolarizTrav2Axis,
                    Pred, Resid, Corr, CalcInvMetrics, MetricsTGRange, ModelSNR,
                    LastRelTGAve, BigDeep, Size, Decay, PolQuality, SNGT);



}
```

int InvertEM_C(EMSensorConfig *pSenConfig, EMInversionConfig *pInvConfig,
int NumObsLoc, int *pEMObsLen, bool ObsLocUseAllTx,
double ****pEMObs, int *pTxSensor, int *pRxSensor,
int *pVLine, int NumVLines, bool ****pEMSenMask,
double *pEasting, double *pNorthing, double *pElevation,
double *pRoll, double *pPitch, double *pYaw,
double ***pEMModelParams,
double ***pEMPolarizLong, double ***pEMPolarizTrav1, double ***pEMPolarizTrav2,
double *****pEMPred, double *****pEMResid, double *pCorr,
bool CalcInvMetrics, int MetricsTGRange, double *pModelSNR,
double **pLastRelTGAve, double **pBigDeep, double **pSize, double **pDecay,
double **pPolQuality, double **pSNGT)

Inverts the cell data for the presence of one, two, or three objects, and returns polarizabilities, predicted, and residual results. Additional inversion metrics are optionally calculated.

*EMSensorConfig *pSenConfig*	a structure holding the sensor configuration
*EMInversionConfig *pInvConfig*	a structure holding the inversion configuration
int NumObsLoc	total number of physical observation locations
*int *pEMObsLen*	number of physical observation locations for each Tx
bool ObsLocUseAllTx	flag indicating whether each physical observation location is associated with all Tx (applies to multi-Tx systems only)
*double ****EMObs*	4D array referencing the data to be inverted [NumTx][NumComp][NumTG][EMObsLen]
*int *TxSensor*	array of length NumObsLoc holding the associated Tx sensor index of each observation location
*int *RxSensor*	array of length NumObsLoc holding the associated Rx sensor index of each observation location
*int *Vline*	array of length NumObsLoc holding the vehicle line index of each observation location
int NumVLines	total number of vehicle lines in the survey
*bool ****EMSenMask*	4D array referencing a mask for the inversion [NumTx][NumComp][NumTG][EMObsLen]
*double *Easting*	Easting positions of each observation location
*double *Northing*	Northing positions of each observation location
*double *Elevation*	Elevation positions of each observation location

*double *Roll*	Roll at each observation location (radians)
*double *Pitch*	Pitch at each observation location (radians)
*double *Yaw*	Yaw at each observation location (radians)
*double ***ModelParams*	3D array holding the 6 fitted results (i.e. x,y,z, phi, theta, and gamma) of each object. [NumInv][NumObj][6]
*double ***PolarizLong*	3D array holding the principal axis polarizability of each object. [NumInv][NumObj][NumTG]
*double ***PolarizTrav1*	3D array holding the first transverse axis polarizability of each object. [NumInv][NumObj][NumTG]
*double ***PolarizTrav2*	3D array holding the second transverse axis polarizability of each object. [NumInv][NumObj][NumTG]
*double *****Pred*	5D array holding the predicted data [NumInv][NumTx][NumComp][NumTG][EMObsLen]
*double *****Resid*	5D array holding the residual data [NumInv][NumTx][NumComp][NumTG][EMObsLen]
*double *Corr*	correlation score for each inversion performed
bool CalcInvMetrics	flag indicating whether inversion metrics should also be calculated
int MetricsTGRange	time gate range for the inversion metrics calculations
*double *ModelSNR*	signal-to-noise ratio of the model for each inversion
*double **LastRelTGAve*	average last reliable time gate index of each object [NumInv][NumObj]
*double **BigDeep*	score for objects that are likely big and deep [NumInv][NumObj]
*double **Size*	measure of size for each object [NumInv][NumObj]
*double **Decay*	measure of decay for each object. Higher values indicate a fast decay of the object. [NumInv][NumObj]
*double **PolQuality*	polarizability quality of each object. Higher values indicate less noise and jitter. [NumInv][NumObj]
*double **SNGT*	Simple-No-Ground-Truth measure of each object (a.k.a. Library-Free classification). Higher values indicate a greater likelihood of UXO [NumInv][NumObj]

Sample Code for calling from a C++ application

```
#include “BTGAPI.h”

//****for our sample code, we want show how application data would get loaded into
//  the data format required by the API.  Let's assume the calling application holds its data
//in the following variables:

//1D array for holding Tx [sensor] centers
Point3D *m_MyAppTxCenter;

//2D arrays for holding Tx [sensor][component] geometry
int **m_MyAppTxLoopShape;
double **m_MyAppTxLoopSizeW;
double **m_MyAppTxLoopSizeH;

double **m_MyAppTxLoopPitch;
double **m_MyAppTxLoopRoll;
double **m_MyAppTxLoopYaw;

double **m_MyAppTxLoopOffsetX;
double **m_MyAppTxLoopOffsetY;
double **m_MyAppTxLoopOffsetZ;


//1D array for holding Rx [sensor] centers
Point3D *m_MyAppRxCenter;

//2D arrays for holding Rx [sensor][component] geometry
int **m_MyAppRxLoopShape;
double **m_MyAppRxLoopSizeW;
double **m_MyAppRxLoopSizeH;

double **m_MyAppRxLoopPitch;
double **m_MyAppRxLoopRoll;
double **m_MyAppRxLoopYaw;

double **m_MyAppRxLoopOffsetX;
double **m_MyAppRxLoopOffsetY;
double **m_MyAppRxLoopOffsetZ;

//the picked target location
Point2D m_MyAppPickedTarget;

//positional data
double *m_MyAppEasting;
double *m_MyAppNorthing;
double *m_MyAppElev;
```

```
//attitude data
double *m_MyAppRoll;
double *m_MyAppPitch;
double *m_MyAppYaw;


//arrays holding Tx, Rx and vehicle line indexes
int *m_MyAppTxSensorIndexOfReading;
int *m_MyAppRxSensorIndexOfReading;
int *m_MyAppVehicleLineIndexOfReading;


//array holding all the EM observations we want to invert
//[NumTx][NumComp][NumTG][EMObsLen]
double ****m_MyAppCellObs;

int *m_MyAppEMObsLen;  //array holding Number of physical observation locations for each Tx
int m_MyAppNumObsLoc;  //total number of physical observation locations
int m_MyAppNumVehicleLines;
double *m_MyAppRxTimes;


//create an inversion configuration
EMInversionConfig InvConfig;

//set the lower bounds for the inversion
InvConfig.LowerBnds[0] = -0.05;  // x
InvConfig.LowerBnds[1] = -0.05;  // y
InvConfig.LowerBnds[2] = -1.00;  // z
InvConfig.LowerBnds[3] = 0.0;  // phi
InvConfig.LowerBnds[4] = 0.0;  // theta
InvConfig.LowerBnds[5] = 0.0;  // gamma

//set the upper bounds for the inversion
InvConfig.UpperBnds[0] = 0.05;  // x
InvConfig.UpperBnds[1] = 0.05;  // y
InvConfig.UpperBnds[2] = 0.00;  // z
InvConfig.UpperBnds[3] = 6.28;  // phi
InvConfig.UpperBnds[4] = 3.14;  // theta
InvConfig.UpperBnds[5] = 6.28;  // gamma

InvConfig.BaseErr = 0.005;
InvConfig.PercentErr = 0.005;
InvConfig.MinS2N = 1.5;  //good for most cases
InvConfig.NumStartModels = 3;


//set the target pick location
InvConfig.Target = Point3D();
InvConfig.Target.X = m_MyAppPickedTarget.X;
```

```
InvConfig.Target.Y = m_MyAppPickedTarget.Y;
InvConfig.Target.Z = CALC_PICKED_ELEV;  //ask the API to calculate a weighted dist elev

//we don't know the orientation, so just set it to zero
InvConfig.Orien = Orien3D();
InvConfig.Orien.phi = 0;
InvConfig.Orien.theta = 0;
InvConfig.Orien.gamma = 0;

InvConfig.NumInversions = 1; // perform one inversion

//The API can perform 1,2, or 3 object inversions
InvConfig.NumObjects[0] = 1; // this inversion will invert for one object

//now create a sensor configuration for the API
EMSensorConfig SenConfig;
SenConfig.NumTx = 1;
SenConfig.NumTxComponents = 3;


//copy the Tx geometry from your application into the API Sensor Configuration
for (int s = 0; s < SenConfig.NumTx; s++)
{
        //set the Tx center
        SenConfig.Tx[s].Center.X = m_MyAppTxCenter[s].X;
        SenConfig.Tx[s].Center.Y = m_MyAppTxCenter[s].Y;
        SenConfig.Tx[s].Center.Z = m_MyAppTxCenter[s].Z;

        //set the tx component loops (in x,y,z order (i.e. c=0,1,2))
        for (int c = 0; c < SenConfig.NumTxComponents; c++)
        {
                //default initialize to a rectangular loop
                int NumLoopCrns = NUM_RECT_LOOP_CORNERS;
                SenConfig.Tx[s].Comp[c].Area = m_MyAppTxLoopSizeW[s][c] *
  m_MyAppTxLoopSizeH[s][c];

                if (m_MyAppTxLoopShape[s][c] == LOOP_SHAPE_CIRC)
                {
                        //circular loop so calculate corners and area
                        NumLoopCrns = NUM_PTS_CIRCULAR_LOOP;
                        double Rad = m_MyAppTxLoopSizeW[s][c] / 2.0;
                        SenConfig.Tx[s].Comp[c].Area = PI * Rad * Rad;
                }

                //now calculate the loop corner positions relative to the center of the loop

                // Note: MyAppTxLoopPitch, MyAppTxLoopRoll, and MyAppTxLoopYaw
                // are the angular deviations from the regular orthogonal position of the Tx loop
                //  (will typically be = 0.0, except for MPV static)

                double **CornerComp = CalcLoopCorners_C(m_MyAppTxLoopShape[s][c], c,
```

```
m_MyAppTxLoopSizeW[s][c] / 2.0,
m_MyAppTxLoopSizeH[s][c] / 2.0,
m_MyAppTxLoopPitch[s][c],
m_MyAppTxLoopRoll[s][c],
m_MyAppTxLoopYaw[s][c]);

                //now calculate the corner positions relative to the center of the GPS
                SenConfig.Tx[s].Comp[c].NumLoopCorners = NumLoopCrns;
                SenConfig.Tx[s].Comp[c].pLoopCornersX = new double[NumLoopCrns];
                SenConfig.Tx[s].Comp[c].pLoopCornersY = new double[NumLoopCrns];
                SenConfig.Tx[s].Comp[c].pLoopCornersZ = new double[NumLoopCrns];

                for (int cn = 0; cn < NumLoopCrns; cn++)
                {
                        SenConfig.Tx[s].Comp[c].pLoopCornersX[cn] = SenConfig.Tx[s].Center.X +
                                m_MyAppTxLoopOffsetX[s][c] + CornerComp[cn][0];
                        SenConfig.Tx[s].Comp[c].pLoopCornersY[cn] = SenConfig.Tx[s].Center.Y +
                                m_MyAppTxLoopOffsetY[s][c] + CornerComp[cn][1];
                        SenConfig.Tx[s].Comp[c].pLoopCornersZ[cn] = SenConfig.Tx[s].Center.Z +
                                m_MyAppTxLoopOffsetZ[s][c] + CornerComp[cn][2];
                }
        }  //next Tx loop component
        SenConfig.Tx[s].Gain = 1.0;
} //Next Tx sensor location


//copy the Rx geometry from your application into the API Sensor Configuration
for (int s = 0; s < SenConfig.NumRx; s++)
{
        //set the Rx center
        SenConfig.Rx[s].Center.X = m_MyAppRxCenter[s].X;
        SenConfig.Rx[s].Center.Y = m_MyAppRxCenter[s].Y;
        SenConfig.Rx[s].Center.Z = m_MyAppRxCenter[s].Z;

        //set the Rx component loops (in x,y,z order (i.e. c=0,1,2))
        for (int c = 0; c < SenConfig.NumRxComponents; c++)
        {
                //default initialize to a rectangular loop
                int NumLoopCrns = NUM_RECT_LOOP_CORNERS;
                SenConfig.Rx[s].Comp[c].Area = m_MyAppRxLoopSizeW[s][c] *
                                                m_MyAppRxLoopSizeH[s][c];

                if (m_MyAppRxLoopShape[s][c] == LOOP_SHAPE_CIRC)
                {
                        //circular loop so calculate corners and area
                        NumLoopCrns = NUM_PTS_CIRCULAR_LOOP;
                        double Rad = m_MyAppRxLoopSizeW[s][c] / 2.0;
                        SenConfig.Rx[s].Comp[c].Area = PI * Rad * Rad;
                }

                //now calculate the loop corner positions relative to the center of the loop
```

```
                // Note: MyAppRxLoopPitch, MyAppRxLoopRoll, and MyAppRxLoopYaw
                // are the angular deviations from the regular orthogonal position of the Rx loop
                //  (will typically be = 0.0, except for MPV static)
                double **CornerComp = CalcLoopCorners_C(m_MyAppRxLoopShape[s][c], c,
m_MyAppRxLoopSizeW[s][c] / 2.0, m_MyAppRxLoopSizeH[s][c] / 2.0, m_MyAppRxLoopPitch[s][c],
m_MyAppRxLoopRoll[s][c],
m_MyAppRxLoopYaw[s][c]);

                //now calculate the corner positions relative to the center of the GPS
                SenConfig.Rx[s].Comp[c].NumLoopCorners = NumLoopCrns;
                SenConfig.Rx[s].Comp[c].pLoopCornersX = new double[NumLoopCrns];
                SenConfig.Rx[s].Comp[c].pLoopCornersY = new double[NumLoopCrns];
                SenConfig.Rx[s].Comp[c].pLoopCornersZ = new double[NumLoopCrns];

                for (int cn = 0; cn < NumLoopCrns; cn++)
                {
                        SenConfig.Rx[s].Comp[c].pLoopCornersX[cn] = SenConfig.Rx[s].Center.X +
                                m_MyAppRxLoopOffsetX[s][c] + CornerComp[cn][0];
                        SenConfig.Rx[s].Comp[c].pLoopCornersY[cn] = SenConfig.Rx[s].Center.Y +
                                m_MyAppRxLoopOffsetY[s][c] + CornerComp[cn][1];
                        SenConfig.Rx[s].Comp[c].pLoopCornersZ[cn] = SenConfig.Rx[s].Center.Z +
                                m_MyAppRxLoopOffsetZ[s][c] + CornerComp[cn][2];
                }
        }  //next Rx loop component
} //Next Rx sensor location



//the API will invert all time gates that are passed to it, so load from the first time gate
// selected by the user
int AllTG = 54;
int FirstTG = 8;
SenConfig.NumTimeGates = AllTG - FirstTG;

for (int tg = 0; tg < SenConfig.NumTimeGates; tg++)
        SenConfig.RxTimes[tg] = m_MyAppRxTimes[tg];


//set your cell data to a 4D  array EMObs [NumTx][NumComp][NumTG][EMObsLen]
int NumTx = SenConfig.NumTx;
int NumComp = SenConfig.NumTxComponents * SenConfig.NumRxComponents;
int NumTG = SenConfig.NumTimeGates;
int *EMObsLen = new int[NumTx];

double ****EMObs = new double ***[NumTx];
for (int tx = 0; tx < NumTx; tx++)
{
        //the number of observations for this tx is:
        EMObsLen[tx] = m_MyAppEMObsLen[tx];
```

```
		EMObs[tx] = new double **[NumComp];
		for (int c = 0; c < NumComp; c++)
		{
			EMObs[tx][c] = new double *[NumTG];
			for (int tg = 0, tgFirst = FirstTG; tg < NumTG; tg++, tgFirst++)
			{
				//set the data channel references
				EMObs[tx][c][tg] = m_MyAppCellObs[tx][c][tgFirst];
			}
		}
}

int NumInv = InvConfig.NumInversions;


//create two 5D arrays to hold the Predicted and Residual results
//  Pred[NumInv][NumTx][NumComp][NumTG][EMObsLen]
//  Resid[NumInv][NumTx][NumComp][NumTG][EMObsLen]
double *****Pred = new double ****[NumInv];
double *****Resid = new double ****[NumInv];
for (int i = 0; i < NumInv; i++)
{
		Pred[i] = new double ***[NumTx];
		Resid[i] = new double ***[NumTx];

		for (int tx = 0; tx < NumTx; tx++)
		{
			Pred[i][tx] = new double **[NumComp];
			Resid[i][tx] = new double **[NumComp];
			for (int c = 0; c < NumComp; c++)
			{
				Pred[i][tx][c] = new double *[NumTG];
				Resid[i][tx][c] = new double *[NumTG];
				for (int tg = 0; tg < NumTG; tg++)
				{
					//allocate for pred and resid results of this inversion
					Pred[i][tx][c][tg] = new double[EMObsLen[tx]];
					Resid[i][tx][c][tg] = new double[EMObsLen[tx]];
				}
			}
		}
}

//allocate for inversion metrics
double *Corr = new double[NumInv];
double *ModelSNR = new double[NumInv];
double **LastRelTGAve = new double *[NumInv];
double **BigDeep = new double *[NumInv];
double **Size = new double *[NumInv];
double **Decay = new double *[NumInv];
double **PolQuality = new double *[NumInv];
```

```
double **SNGT = new double *[NumInv];


//allocate for polarizability results
double ***PolarizLongAxis = new double **[NumInv];
double ***PolarizTrav1Axis = new double **[NumInv];
double ***PolarizTrav2Axis = new double **[NumInv];
double ***Model = new double **[NumInv];

for (int i = 0; i < NumInv; i++)
{
        int NumObj = InvConfig.NumObjects[i];
        PolarizLongAxis[i] = new double *[NumObj];
        PolarizTrav1Axis[i] = new double *[NumObj];
        PolarizTrav2Axis[i] = new double *[NumObj];
        Model[i] = new double *[NumObj];

        LastRelTGAve[i] = new double[NumObj];
        BigDeep[i] = new double[NumObj];
        Size[i] = new double[NumObj];
        Decay[i] = new double[NumObj];
        PolQuality[i] = new double[NumObj];
        SNGT[i] = new double[NumObj];

        for (int n = 0; n < NumObj; n++)   //there are 3 polarizabilities for each object
        {
                PolarizLongAxis[i][n] = new double[NumTG];
                PolarizTrav1Axis[i][n] = new double[NumTG];
                PolarizTrav2Axis[i][n] = new double[NumTG];
                Model[i][n] = new double[MAX_MODEL_PARAMS_POS_ORIEN];
        }
}


int NumVLines = m_MyAppNumVehicleLines;  //the total number of vehicle lines in the survey
int NumObsLoc = m_MyAppNumObsLoc;   ////total number of physical observation locations

//Metrics can be optionally calculated. Set to false if you just want the polarizabilities
// and the correlation measure.
bool CalcInvMetrics = true;

//Set the time gate range that will be used by the metrics calculations
int MetricsTGRange = 30;


//NOTE:  set m_ObsLocUseAllTx = true if we have a multiple Tx system
//        that has applied the same timestamp to all Tx firings.  The result of this is that
//       each physical observation location is associated with ALL Tx.
//       This is often the case with multi tx systems running in static mode

//For systems running dynamic mode, we typically set m_ObsLocUseAllTx = false
```

```
//For single transmitter systems, we always set m_ObsLocUseAllTx = false
bool ObsLocUseAllTx = false;


//create a 4D array sensor mask that will allow you to exclude specific combinations of
//lines, Rx sensors, Tx sensors, and components
//EMSenMask[NumVLines][RxSenIdx][NumTx][NumComp]

bool ****EMSenMask = new bool ***[NumVLines];

int NumRx = SenConfig.NumRx;

for (int VL = 0; VL < NumVLines; VL++)
{
	EMSenMask[VL] = new bool **[NumRx];
	for (int rx = 0; rx < NumRx; rx++)
	{
		EMSenMask[VL][rx] = new bool *[NumTx];
		for (int tx = 0; tx < NumTx; tx++)
		{
			EMSenMask[VL][rx][tx] = new bool[NumComp];
			for (int c = 0; c < NumComp; c++)
			{
				//set the bool sensor mask for the API
				//setting all true here for this example
				EMSenMask[VL][rx][tx][c] = true;
			}
		}
	}
}


//call the EM inversion
int Res = InvertEM_C(&SenConfig, &InvConfig, NumObsLoc, EMObsLen,
	ObsLocUseAllTx, EMObs,
	m_MyAppTxSensorIndexOfReading, m_MyAppRxSensorIndexOfReading,
	m_MyAppVehicleLineIndexOfReading,
	m_MyAppNumVehicleLines,
	EMSenMask,
	m_MyAppEasting, m_MyAppNorthing, m_MyAppElev,
	m_MyAppRoll, m_MyAppPitch, m_MyAppYaw,
	Model, PolarizLongAxis, PolarizTrav1Axis, PolarizTrav2Axis,
	Pred, Resid, Corr, CalcInvMetrics, MetricsTGRange, ModelSNR,
	LastRelTGAve, BigDeep, Size, Decay, PolQuality, SNGT);
```